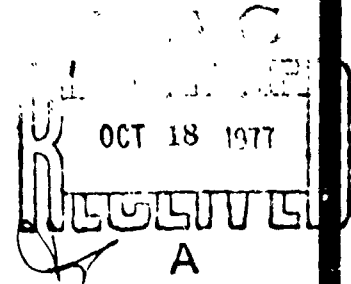AGARD-CP-226

AD A045241

AGARD

ADVISORY GROUP FOR AEROSPACE RESEARCH & DEVELOPMENT

7 RUE ANCELLE 92200 NEUILLY SUR SEINE FRANCE

AGARD CONFERENCE PROCEEDINGS No. 226

Unsteady Airloads in Separated and Transonic Flow

OCT 18 1977

A

NORTH ATLANTIC TREATY ORGANIZATION

AGARD-CP-226

NORTH ATLANTIC TREATY ORGANIZATION

ADVISORY GROUP FOR AEROSPACE RESEARCH AND DEVELOPMENT

(ORGANISATION DU TRAITE DE L'ATLANTIQUE NORD)

AGARD Conference Proceedings No. 226

UNSTEADY AIRLOADS IN

SEPARATED AND TRANSONIC FLOW

THE MISSION OF AGARD

The mission of AGARD is to bring together the leading personalities of the NATO nations in the fields of science and technology relating to aerospace for the following purposes:

— Exchanging of scientific and technical information;

— Continuously stimulating advances in the aerospace sciences relevant to strengthening the common defence posture;

— Improving the co-operation among member nations in aerospace research and development;

— Providing scientific and technical advice and assistance to the North Atlantic Military Committee in the field of aerospace research and development;

— Rendering scientific and technical assistance, as requested, to other NATO bodies and to member nations in connection with research and development problems in the aerospace field;

— Providing assistance to member nations for the purpose of increasing their scientific and technical potential;

— Recommending effective ways for the member nations to use their research and development capabilities for the common benefit of the NATO community.

The highest authority within AGARD is the National Delegates Board consisting of officially appointed senior representatives from each member nation. The mission of AGARD is carried out through the Panels which are composed of experts appointed by the National Delegates, the Consultant and Exchange Program and the Aerospace Applications Studies Program. The results of AGARD work are reported to the member nations and the NATO Authorities through the AGARD series of publications of which this is one.

Participation in AGARD activities is by invitation only and is normally limited to citizens of the NATO nations.

PREFACE

The Specialists' Meeting on "Unsteady Airloads in Separated and Transonic Flow", organized by the Structures and Materials Panel, was held in Lisbon on Tuesday, 19 April and Wednesday, 20 April 1977. It was attended by some hundred Specialists, who took part in the general discussion.
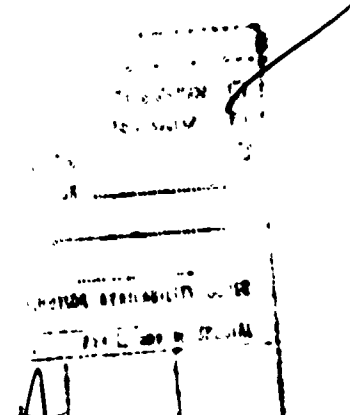
The meeting was divided in two session. Session I, entitled "Airframe Response to Separated Flow", was chaired by Prof B.Laschka, and by W.J.Mykytow; Session II, on "Transonic Unsteady Aerodynamics for Aeroelastic Phenomena", was chaired by Prof H.Försching and Dr J.J.Olsen.

The first session reviewed the prediction and description of the separated flow environment and the essential effects of airframe response on individual aircraft components. This is a special concern for military aircraft where flight operation at extreme manoeuvre conditions associated with flow separation frequently occurs. The scope of the session included analytical approaches, wind tunnel tests, as well as flight test techniques and data evaluation. Session I opened with an evaluation, by C.L.Bore, of papers on loads presented at the FDP Symposium on "Prediction of Aerodynamic Loading", Fall 1976.

The second session dealt with flutter, aeroelastic instabilities, and other static and dynamic aeroelastic problems, for which margins of safety are least in the transonic speed range which is consequently the most critical speed regime. The 8 papers that were delivered covered analytical techniques as well as windtunnel experiments and gave some hope that engineer-type predictions should soon be available.

The general discussion that followed the Specialists' Meeting made it clear that both sessions had covered an urgent need of aerospace industry, and helped the Sub-Committee on "Aeroelasticity and Unsteady Aerodynamics" to decide on a cooperative programme.

G.COUPRY
Chairman, Sub-Committee on
Aeroelasticity and Unsteady Aerodynamics

CONTENTS

UNSTEADY AIRLOADS IN SEPARATED AND TRANSONIC FLOW

by

C.L. BORE

Head of Research, Hawker Siddeley Aviation Ltd., Kingston, Surrey, U.K.

SUMMARY

This paper reviews critically the papers dealing with unsteady loads arising from separated flow that were presented at the AGARD Fluid Dynamics Panel's symposium on Prediction of Aerodynamic Loading (ref. 1). The principal topics discussed include dynamic phenomena arising from aircraft manoeuvres, transient dynamic stall loads and methods for predicting buffet.

INTRODUCTION

For this review, I have chosen to group the topics by the phenomena concerned, rather than the papers reviewed. Thus we will consider dynamic stall, buffet, fin loads in complex manoeuvres, and separation bubbles. This allows observations from various papers and discussions to be brought together around each topic for comparison. For each problem the designer needs an array of methods, suitable for the various phases of design, from concept, through wind tunnel modelling to flight testing.

We will see that the problems of unsteady airloading are now being tackled from various directions and substantial progress is being made, but of course there is still a lot of work to do before they can all be wrapped up.

DYNAMIC STALL

The problems of dynamic stall present themselves in various guises. A wing or helicopter blade pitching rapidly or entering a different flow field rapidly may experience dynamic excursions of lift coefficient far from the curve that is measured by the usual slow traversing of incidence beyond initial stall. Typically, in a fast increase of incidence, the lift may substantially overshoot the quasi-steady stall curve and then drop back rapidly (see fig. 1, taken from ref. 2 — after Ham). The mechanisms that govern such effects are of interest in connection with wing drop and yaw (sometimes leading to spin entry), wing rocking, buffeting and helicopter blade stall flutter: quite a catalogue of problems. Two papers addressed this type of behaviour, from rather different angles.

Ericsson and Reding (2) have observed that on an aerofoil pitching beyond the steady stalling angle, a leading-edge vortex first grows, then detaches from the leading edge and convects downstream (fig. 2). As the vortex convects chordwise (at about 55% of free-stream velocity) it affects the lift and moment on the aerofoil. As it passes 70% chord the normal force on the aerofoil reaches its peak, while just before the trailing edge the pitching moment reaches its peak (fig. 3) Extrapolating from fig 3. to the vicinity of $\bar{\omega} \simeq 1.7$ (buffeting) it seems that a shed vortex would take roughly a quarter of the total cycle time to traverse the aerofoil chord, so the frequency of vibration from this mechanism would be roughly

$$f \simeq 0.14\,\frac{U}{c} \qquad \cdots \cdots \cdots \cdots \cdots (1)$$

This is consistent with the frequencies usually found in buffeting. Of course, not all buffeting is associated with leading-edge separations, but a rather similar vortex-convection mechanism could be envisaged for rear separations, presumably giving higher frequencies. Incidentally, the case quoted by Benepe (4) of buffeting bending moments peaking at 25 hertz (the torsional frequency) raises the question of such a mechanism, and so do the buzz-like phenomena with very little damping in torsion (11, 12).

In order to estimate the magnitude of the vortex-induced effects, Ericsson and Reding extend the leading-edge suction analogy of Polhamus (3) to apply to aerofoils. Thus they argue that both on an aerofoil and on a delta wing the displacement of the vortex with respect to the leading edge is an analogous function of time (fig. 4). Then using Polhamus' equation for the vortex-induced lift on a delta and transforming this into conditions normal to the leading edge, they infer a magnitude for the drop in lift that attends detachment of the vortex from the aerofoil (fig. 5). Using Glauert type terms, they go on to devise compressibility corrections.

Unfortunately, the mathematics of their extension from Polhamus' vortex-lift result to aerofoils seems to have been muddled, although most of the errors cancelled out in the end. For the record, the writer would replace Ericsson and Reding's analysis on page 24—3 of ref. 2 by the following:-

"From Polhamus' leading-edge suction analogy the coefficient of vortex-induced normal force on the leading edge of a delta with apex half-angle θ is given by

$$C_{NV} = \pi\,\sin^2\alpha\,\cos\alpha \qquad \cdots \cdots (i)$$

The angle of attack in the plane perpendicular to the leading edge is

$$\alpha_\perp = \tan^{-1}\left(\frac{\tan\alpha}{\sin\theta}\right) \qquad \cdots \cdots (ii)$$

The corresponding dynamic pressure $q_\perp$ as a fraction of free-stream dynamic pressure q_o is

$$\frac{q_\perp}{q_o} = \sin^2\alpha + \cos^2\alpha\,\sin^2\theta \qquad \cdots \cdots (iii)$$

Combining equations (i), (ii) and (iii) gives the following average loading

$$C_{N\perp} = \frac{N_V}{q_\perp S} = \pi\,\sin^2\alpha_\perp\,\sqrt{1+\sin^2\theta.\tan^2\alpha_\perp} \qquad \cdots \cdots (iv)$$

Here the square root term behaves like $\cos(\theta\alpha_\perp)$ and since the angle θ relates to the deltas from which the inferences were made (i.e. deltas where θ is around 0.5 radian) it is evident that this term is near unity for most practical incidences. It follows that

$$C_{N\perp} \simeq \pi\,\sin^2\alpha_\perp \qquad \cdots \cdots \cdots (v)$$

Incidentally, it was this term that was plotted in fig. 7 of ref. 2 (which is fig. 5 of the present paper) not the function $\pi\,\sin^2\alpha\,\cos\alpha$ as labelled.

It can be concluded that these concepts of transient vortex growth at the leading edge, followed by detachment of the vortex and its subsequent convection over the aerofoil, illuminate mechanisms that are vital in stall flutter and may also be relevant in other problems such as rapid pull-ups, wing rocking and buffet. We will see later that there may also be relevance to the forces induced on the tail.

However dynamic loads effects do not stem only from transient aerodynamic flow fields. Thus Benepe (4) stated that in flight test measurements on two aircraft there was a progressive increase in the wing bending moment at given angle of attack with increasing pitch rate, even below the apparent stall. Much of this increase was accounted for by structural inertia effects, using a 5-degree-of-freedom aircraft dynamic response simulator, in conjunction with quasi-steady aerodynamics. Agreement between flight test and computations was good in some cases but only fair in other respects, and Benepe considers that improved accuracy could be achieved if the dynamic flow phenomena were better understood.

A quite different approach of some dynamic effects near the stall was described by Levinsky (5). This work used a non-linear lifting-line procedure with unsteady wake effects to investigate certain forms of instability when parts of the wing are stalling; notably wing drop, wing rock, and yawing moment at zero yaw. At present, it is limited to wings with low sweep and high aspect ratio

The approach assumed that each element of wing behaves like a two-dimensional aerofoil (even to its stalling lift curve) at the local incidence induced by the time-dependent array of bound vorticity and trailing vorticity. The trailing vorticity was assumed to convect downstream at free-stream velocity (not at 55% of free-stream velocity, as in ref. 2).

The results of these convecting vortex-lattice computations show up a sudden rolling moment asymmetry at zero yaw at incidences above 12^0 for one test case (fig. 6), and show lift hysteresis for aerofoils having large enough negative lift-curve slope after local stalling.

It appears that there is scope for extending the time-dependent-wake notions of this method to compute the loads induced on the tail as well as the wing. For wider applicability it would be desirable to refine the computational methods so that sweep, low aspect ratio, and compressibility, will be embraced.

It would be worthwhile to investigate what is the practical speed of convection for trailing vorticity in the wake. Probably it would be above the 55% of free-stream velocity used by Ericsson and Reding (2) above the aerofoil, but below free-stream velocity. Combining this approach with that of (2) may further illuminate the problems of wing rocking which (as I said in ref. 6) are not adequately predicted by quasi-steady aerodynamics from the known aircraft motion.

BUFFET PREDICTION

As remarked by Benepe in the RTD of ref. 1, the first reason for understanding the mechanisms that cause buffet is to enable the designer to devise a configuration that experiences little or no buffetting, if possible. Usually it will take a substantial time to progress to a stage where wind-tunnel measurements can be made on the chosen configuration. So we need different prediction methods for different stages of design.

Redeker and Proksch (7) presented their computational methods for buffet onset at the early configuration-choosing stage of design. They conclude from calibrations that buffet onset becomes significant on two-dimensional aerofoils corresponds to when boundary layer separation has spread from the trailing edge forwards to 90% chord. For extension to three-dimensional wings they postulate that buffet onset has been reached when the moment of the separated-flow area about the wing root reaches a certain value, and that this corresponds with given rms wing-root bending stress:

$$C_{Bi} = \int_{\eta_R}^{1} \frac{c_s(\eta)}{\bar{c}} (\eta - \eta_R) \, d\eta \qquad \sim \sqrt{\overline{\sigma_M^2}} \quad \ldots \ldots \ldots (2)$$

These assumptions imply that the pressure fluctuations in the separated area are practically constant and synchronised for the extent of separation concerned, and that a given value of this coefficient (equation 2) corresponds with onset or light buffet $(C_{Bi} \approx 0.08 \text{ to } 0.10)$. These assumptions were backed by data such as shown in figs. 7 and 8. The authors recognised that the root bending strain stops being linear against C_{Bi} somewhere near $C_{Bi} = 0.10$ (fig. 7), so the method as it stands will not deal with buffet penetration.

Once the assumptions are accepted, the method uses whatever calculation procedures are considered best at the time for estimating the extent of boundary layer separation on the wing. For the wing pressure distribution the so-called "RAE Standard Method" has been used, together with Murman-Krupp local lift slopes, but transonic methods will be used. For the boundary-layer-separation predictions, the three-dimensional Cumpsty-Head method, with compressibility corrections, has been used. This was found necessary even on yawed infinite-aspect-ratio wings.

This method seems useful for light-buffet prediction, for wings with high enough aspect ratio to result in a simple boundary-layer-separation pattern. The reviewer would argue with the choice of non-dimensional criteria for judging the magnitude of a dimensional response if a similar method were being proposed to predict buffet penetration, but the authors explicitly refrained from making claims for that more difficult problem, and my reservations do not make much practical difference to the buffet onset boundaries at usual altitudes.

As J G. Jones (8) has pointed out, for an experimental assessment of buffet we may either measure the fluctuating pressures and their degree of synchronisation and thus integrate to find the overall fluctuating forces, or we may infer the integrated forces from the response they cause to an elastic model with the right sort of mode shapes. (In parentheses, the reviewer adds, it could happen that the fluctuating forces are not much modified by the structural deformations, so that we may perhaps adopt the most direct method and measure the fluctuating shear force on the buffeted wing) Now the pressure measurement approach requires complex instrumentation and correlation techniques, and special aeroelastic models are expensive and not usually suitable for high Reynolds' number testing, so it is attractive to evaluate the measurements that can be obtained on conventional wind-tunnel models, as recounted by Butler and Spavins (9).

Jones' scheme (8) is based on the idea that at any well-defined mode, the elastic model can be regarded as a linear damped system in forced vibration. Then the response in the simple mode is defined by the differential equation:

$$m\frac{d^2z}{dt^2} + 2m\zeta\omega_o\frac{dz}{dt} + m\omega_o^2 z = X(t) \dots \dots (3)$$

where m is the generalized mass for the mode, $m\omega_o^2$ represents the structural stiffness, and ω_o is the undamped natural frequency (there is a typographical omission in ref. 9). The total damping ratio is the sum of the structural damping and aerodynamic damping. Assuming that the frequency of excitation scales with flow speed U and inversely with mean chord $\bar{c}$, and neglecting Reynolds' number variations so that the mean square exciting force scales with $(qS)^2$, Jones gets:

$$G_x = \frac{E^2\bar{c}}{V}(qS)^2 \dots \dots (4)$$

Power spectral analysis leads to an expression for the dimensionless aerodynamic excitation parameter E as follows:

$$E = 2\sqrt{2}\,n^{-\frac{1}{2}}\frac{m}{S}\left(\frac{\zeta^{\frac{1}{2}}\ddot{\sigma}_z}{q}\right) \dots \dots (5)$$

where $n_o = \frac{\bar{c}\omega_o}{V}$ is the non-dimensional modal frequency. This excitation is then applied to the aircraft, using appropriate aircraft damping, mass and stiffness.

The value of Butler and Spavins' paper resides in their comments on the practical methods of evaluating the various terms in Jones' equation 5. The scheme of (9) is summarized below:

(i)   Determine wing area S and mean chord C for the model and the aircraft

(ii)   Determine modal frequency ω_o, generalized mass m, structural damping ζ_s and mode shape from resonance tests on model and aircraft.

(iii)   Measure rms acceleration or bending moment σ at a point on the model wing, the total damping ζ, flow velocity V, and dynamic pressure q at any given Mach number and incidence in wind-tunnel tests.

(iv)   Relate the bending moment to $\ddot{\sigma}_z$ in generalized co-ordinates for the mode shape.

(v)   Derive E from equation 5.

(vi)   Derive the aerodynamic damping factor K from

$$K = \frac{m\omega_o V\zeta_a}{qS} \dots \dots (6)$$

(vii)   Predict total damping in flight by adding the calculated flight aerodynamic damping (equation 6) to the measured aircraft structural damping.

(viii) Predict rms acceleration or bending moment at a point on the aircraft wing from equation 5 rearranged to give using the mode shape.

The total damping ratio was best obtained by using Cole's random decrement function (10). The evaluation model used was made of alumium alloy to increase the sensitivity of the aerodynamic damping determination relative to what could be obtained from a steel model. Accelerometers were used to deduce the mode displacements both on the model and the aircraft.

Fig. 9 shows comparisons of predicted and flight-measured rms acceleration and damping, which show very encouraging agreement. It was noted that determination of the damping ratio from model tests was somewhat uncertain even with a specially made low-structural-damping model of aluminium alloy, so it may be difficult to determine with denser or more-damped models. Benepe in discussion claimed satisfactory results for a rather similar method. One generalization being explored was the possibility of eliminating mode shape from the process, so that a generalized force distribution may be derived.

It can be concluded that this approach has been demonstrated to have considerable promise when low-damping models of low density are used, and it should be worthwhile to develop the techniques further, particularly in eliminating mode shape from the process. However, it is worth considering briefly some cautionary remarks.

First consider the instances of "buzz" type oscillations remarked on by Benepe (4), Jones (11), and Moss (12), in which torsional oscillations of the wing are associated with strongly correlated pressure disturbances affecting chordwise sections, and the bending response may appear at the torsional frequency. These seem to be a type of limit cycle, where the amplitude of response may remain substantially constant in successive cycles, so that "damping" cannot be determined by any form of logarithmic decrement process based on the concurrent response. Perhaps it will be worthwhile classifying these phenomena within the class of unsteady boundary-layer-separation and closely related to buffet and control-surface buzz.

Secondly there are cautionary remarks to be made on the use of strain gauges to infer the level of unsteady force on a wing. It has been found on full-scale aircraft tests that quite large errors can appear in the bending moment inferred from wing-root strain gauges if the torsion component of the loading is large and the gauges are merely aligned with the constant-fraction-of-chord line (ref 13, 14). What happens is that the nominal bending moment signal contains substantial response to torsion, and quite elaborate calibrations are necessary to evaluate the appropriate regression equations from which the bending moments may be deduced. Now most of the wing root bending moment measurements made in the past on wind-tunnel models, and some of those made in flight, are likely to suffer such errors. These errors were avoided by the use of accelerometers in the paper of Butler and Spavins, and by the use of special load-measurement links in certain other cases, such as the work reported by Kloos (15), but care should be taken to check on this technique in other papers. Perhaps some work on measurement of unsteady shear force on model wings should be done using special load-measurement links. This would also facilitate the distinction between bending moment and torsion fluctuation — bearing in mind the usefulness of rolling-moment measurements in predicting wing-drop and wing-rock phenomena (6).

SEPARATION BUBBLES

There are many circumstances where a boundary-layer separation could be predicted with ease, and even without calculation. It is of greater engineering significance to predict under what conditions the flow will re-attach. In other words, whether the flow will re-attach to form a bubble, or remain separated. Under a separation bubble, there are high-frequency pressure fluctuations, but in general the engineering problems are an order of magnitude greater when the flow fails to re-attach. Two papers at the symposium addressed the problem of separation bubbles.

Lang and Francis (16) reported results of their studies on a separation bubble caused by a smaller s 'oiler oscillating in height, mapping variations in oscillating pressure, bubble size and so on. They found that the size of the bubble lags the movement of the spoiler, but not symmetrically. This was due to the finite time taken for entrainment of free-stream flow into the bubble or out of it — the flow out not being at the same rate as the flow in.

Laruelle and Levart (17) reported investigations of the separation bubble that forms on the outer surface of a sharp-lipped air intake operating with reduced mass flow at subsonic speed. They investigated the pressures under the practically two-dimensional bubble and the re-attachment conditions, and concluded that for this particular intake situation they had arrived at semi-empirical laws that enabled them to calculate the development of the separation bubble.

Taken together, these papers should provide useful material for those investigating the pressure distributions and sizes of other bubbles.

OTHER UNSTEADY LOADS

Kloos (15) showed good agreement between "predicted" loads and flight measurements for a number of transient manoeuvres, such as missile loads during a $M = 0.95$ rolling pull-out. This was based on wind-tunnel load measurements, using an equivalent-angle-of-incidence notion to read across to manoeuvring flight. Incidentally, the effect of a small gap between the missile and its pylon was shown to be substantial. Fin loads in flight were similarly well predicted — the flight load measurements being made with special load-measurement links. However, it should be noted that these "predictions" used flight-measured aircraft attitudes and rates, so there is an element of hindsight here. Against this, the reviewer remarked in (6) that fin loads were not well predicted even with hindsight concerning the aircraft motion when the motion was due to wing rock — hinting that this may be due to unsteady wake flowing past the tail. Note too, that Kloos refers to the use of rudder angle in some wind-tunnel experiments: not a universal practice.

Kloos quoted the large incremental loads that can be experienced by an aircraft entering the vortex wake of a previous aircraft — about equal to the normal force of the previous aircraft.

Finally, there was an account of a very expensive investigation into the magnitude of air-intake surge loadings, in ref. 6. In this work a crucial factor was the transient build-up of pressure both in the ducts of surging air intakes and in the boundary-layer-bleed cavities.

CONCLUDING REMARKS

It is hoped that some idea has been conveyed of the papers on fluctuating loads presented at the AGARD Symposium (1), together with some speculations on where these may usefully lead.

REFERENCES

1.		Prediction of Aerodynamic Loading AGARD–CP–204 1976
2.	L.E. Ericsson, J.P. Reding	Quasi-steady and transient dynamic stall characteristics. paper 24 of ref. 1.
3.	E.C. Polhamus	Prediction of vortex-lift characteristics by a leading-edge suction analogy. J. Aircraft vol. 8 no. 4 April 1971.
4.	D.B. Benepe, Sr.	Aircraft manoeuvres and dynamic phenomena resulting in rapid changes of load distributions or/and fluctuating separation. paper 20 of ref. 1.
5.	E.S. Levinsky	Theory of wing span loading instabilities near stall. paper 25 of ref. 1.
6.	C.L Bore	Examples of load-prediction difficulties. paper 1 of ref. 1.
7.	G. Redeker, H.J. Proksch	The prediction of buffet onset and light buffet by means of computational methods. paper 22 of ref. 1.
8.	J.G. Jones	Modelling of systems with a high level of internal fluctuations. Paper given at AGARD Specialists' meeting on "Methods for aircraft state and parameter identification, NASA Langley, Nov. 1974.
9.	G.F. Butler, G.R. Spavins	Preliminary evaluation of a technique for predicting buffet loads in flight from wind-tunnel models of conventional construction. paper 23 of ref. 1.
10.	H.A. Cole, Jr.	On-line failure detection and damping measurement of aerospace structures by random decrement signatures. NASA CR 2205, 1973
11.	J.G. Jones	Aircraft dynamic response associated with fluctuating flow fields. Paper 5, Aircraft stalling and buffeting, AGARD–LS–74, 1975.
12.	G.F. Moss, D. Pierce	The dynamic response of wings in torsion at high subsonic speeds. RAE Tech. Memo Aero. 1706, March 1977.
13	M.T. White	Optimising strain gauge orientation for load measurement by means of rosette analysis. Strain, October 1973.
14.	E.J. Blackburn, M.T. White	Investigations into errors of load measurement using strain gauge rosettes. Unpublished HSA reports, 1976–1977.
15.	J. Kloos	Comparison of predicted aerodynamic loading with flight test results. Paper 7 of ref. 1.
16.	J.D. Lang, M.S. Francis	Dynamic loading on an airfoil due to a growing separated flow. Paper 26 of ref. 1.
17.	G. Laruelle, P. Levart	Pressions sur une carène de orise d'air a lèvre mince fonctionnant en subsonique a débit réduit. Paper 27 of ref. 1.

NONLINEAR VORTEX—INDUCED LIFT

SHED
VORTEX
EFFECT

HAM'S RESULTS
FOR OSCILLATING
AIRFOIL

$$\frac{c\dot{\alpha}}{U_\infty} = 0; \; Re_c \to \infty$$

$$\frac{c\dot{\alpha}}{U_\infty} = 0, \; Re_c = .35 \times 10^6$$

Fig.1

SPACE—TIME EQUIVALENT VORTEX EFFECTS

$$t_1 - t_o = \frac{x_1}{U}$$

$$t_2 - t_o = \frac{x_2}{U}$$

PITCHING AIRFOIL
SPILLED VORTEX
CONVECTION

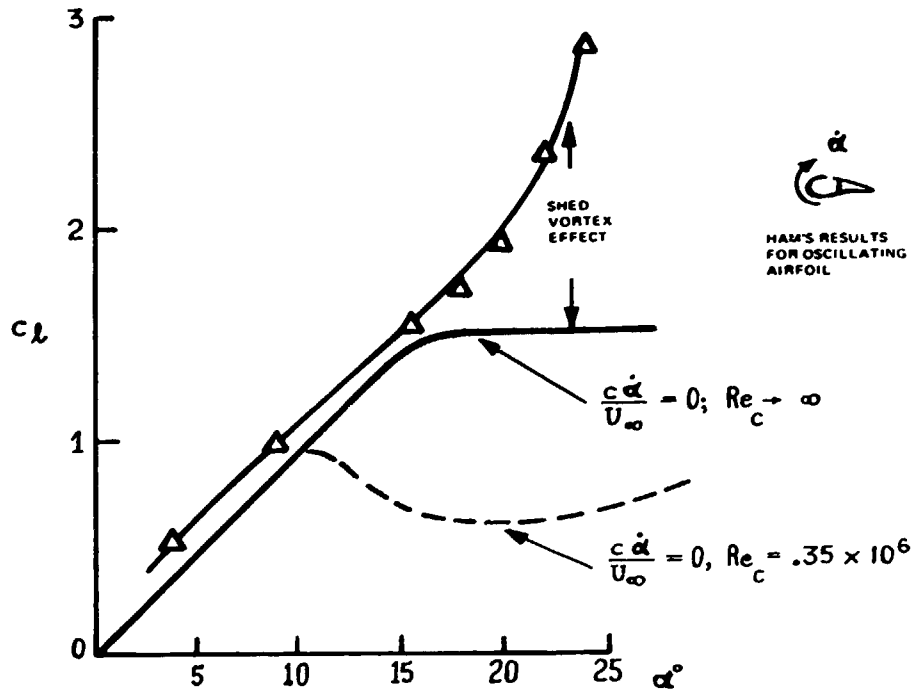**Fig.2**

PREDICTED AND MEASURED DYNAMIC STALL PHASE ANGLES

$$\xi_{CG} = 0.25$$

$$\alpha(t) = 15^\circ + 10^\circ \sin(\omega t)$$

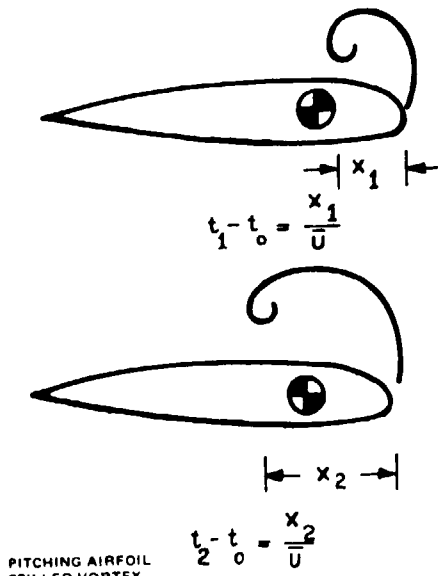| Present Prediction	Experiment
$(\omega t)_{vs}$	O Begin Moment Stall
$(\omega t)_{vs} + (\Delta \omega t)_{vTE}$	$\triangle \; -c_m$ MAX
$(\omega t)_{vs} + 0.7 (\Delta \omega)_{vTE}$	$\square \; c_n$ MAX

Fig.3

SPACE—TIME EQUIVALENT VORTEX EFFECTS

$$t_1 - t_0 = \frac{x_1}{\bar{U}}$$

LEADING EDGE
VORTEX CORE

$$t_2 - t_0 = \frac{x_2}{\bar{U}}$$

DELTA WING
LEADING EDGE
VORTEX CONVECTION

PITCHING AIRFOIL
SPILLED VORTEX
CONVECTION

$$t_1 - t_0 = \frac{x_1}{\bar{U}}$$

$$t_2 - t_0 = \frac{x_2}{\bar{U}}$$
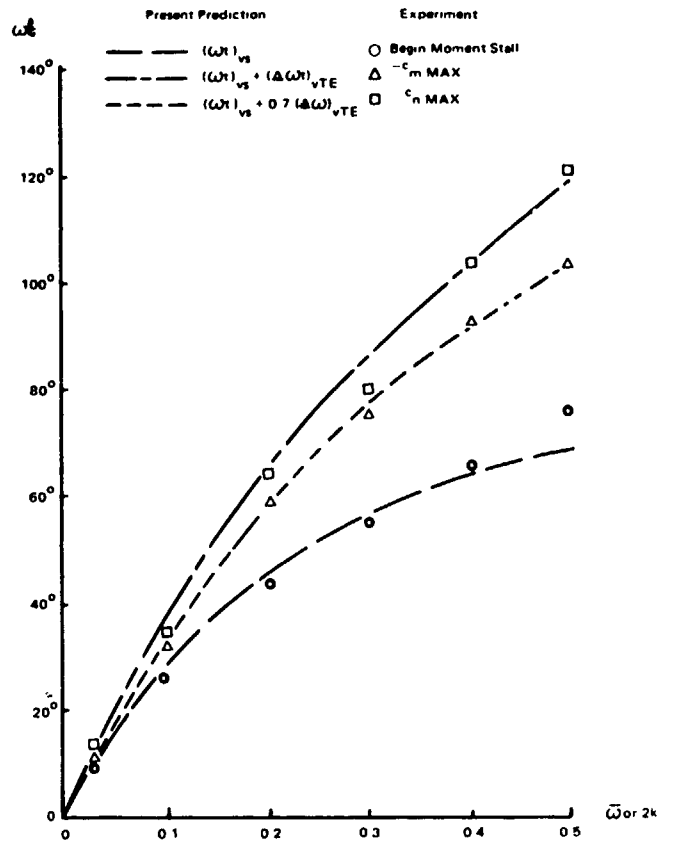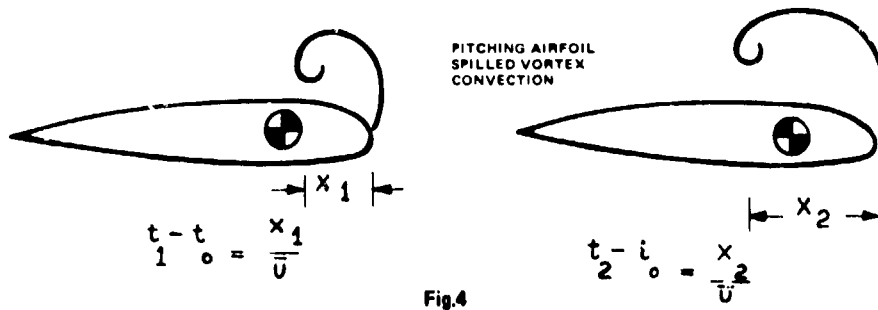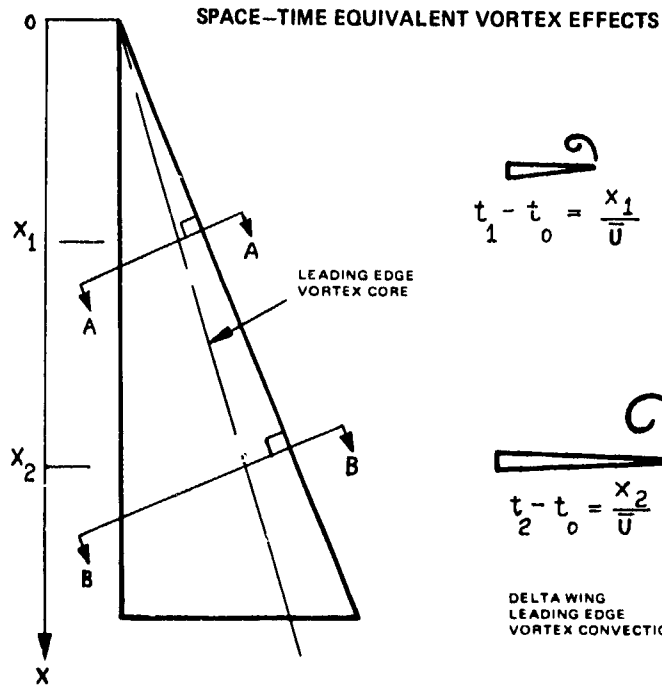
Fig.4

LIFT LOSS DUE TO "SPILLED" LEADING EDGE VORTEX

Experiment

□ NACA-0012
◇ NACA 0012
○ NACA 0009

$\pi \sin^2 \alpha_s$

$\Delta c \ell_v$

$c\ell$

α_s

$\alpha_s°$

Fig. 5
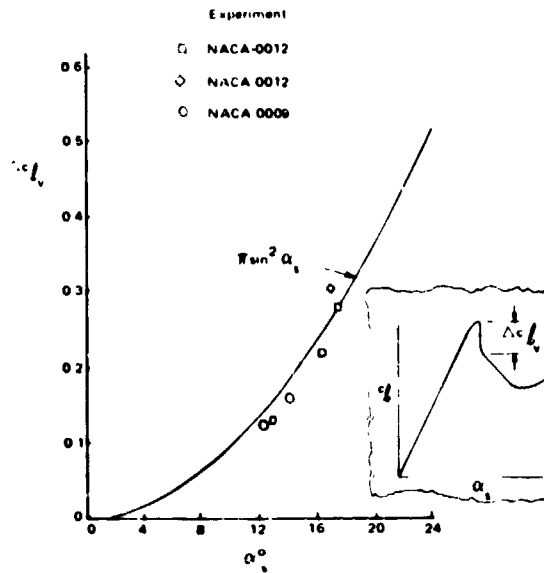
COMPARISON OF PRESENT METHOD WITH T 2C WIND TUNNEL DATA FOR
ROLLING MOMENT AT ZERO YAW ANGLE
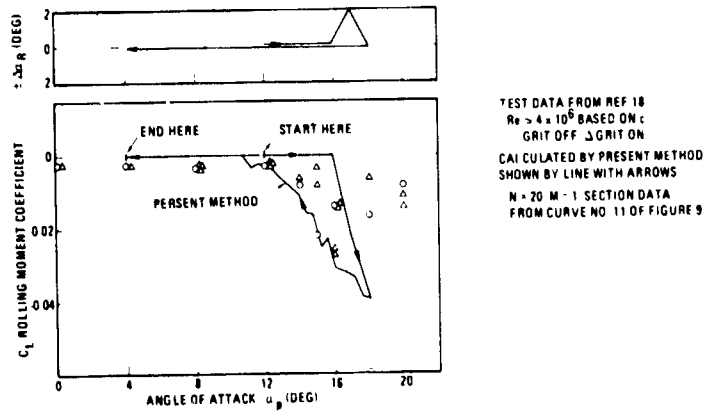
Fig.6

RELATION BETWEEN BUFFETING INTENSITY $\sqrt{\overline{\sigma_M^2}}$ AND
BUFFETING COEFFICIENT c_{Bi} ON A WING MODEL

$(A = 4.8, T/C = 0 12, A = 35^o)$

Fig.7

COMPARISON OF CALCULATED BUFFETING COEFFICIENTS c_{Bi} WITH
LIGHT BUFFETING FROM FLIGHT TEST

Fig.8

PREDICTED AND MEASURED RMS WING TIP ACCELERATION,

σ **AND DAMPING** τ **v NORMAL FORCE COEFFICIENT, C_N : M = 0.7**

Fig.9

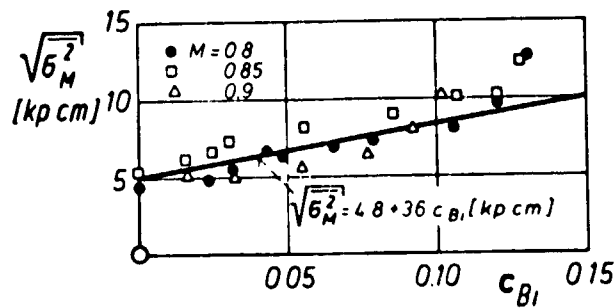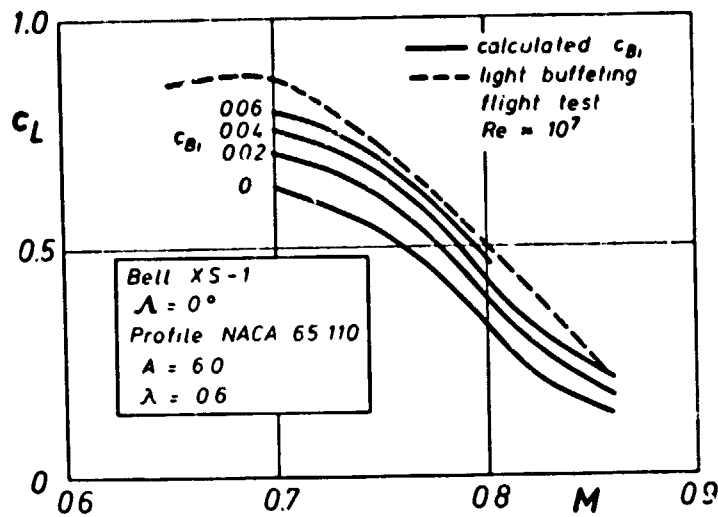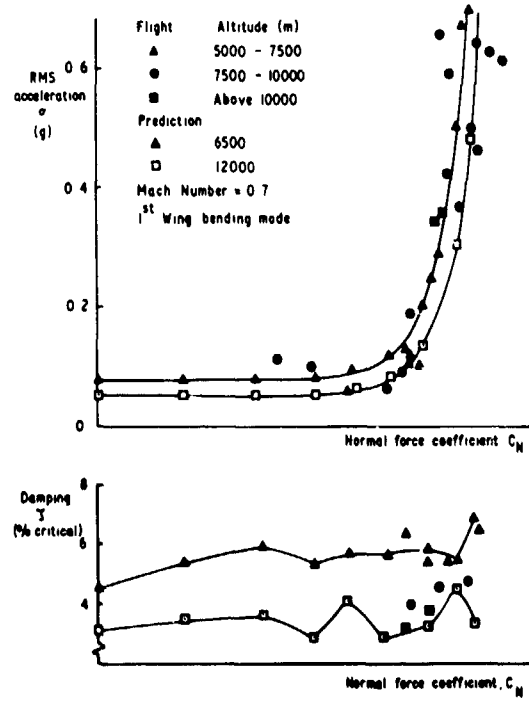# SEPARATED-FLOW UNSTEADY PRESSURES AND FORCES ON ELASTICALLY RESPONDING STRUCTURES

C. F. Coe and D. W. Riddle
Ames Research Center, NASA, Moffett Field, California 94035, USA

and

C. Hwang
Northrop Corp. Aircraft Division, Hawthorne, California 90250, USA

SUMMARY

This paper presents broadband rms, spectral density, and spatial correlation information that characterizes the fluctuating pressures and forces that cause aircraft buffet. The main theme of the paper in describing buffet excitation is to show the effects of elasticity. In order to do so, data are presented that were obtained (1) in regions of separated flow on wings of wind-tunnel models of varying stiffness and (2) on the wing of a full-scale aircraft. Reynolds number effects on the pressure fluctuations are also discussed.

NOMENCLATURE

a_T	acceleration at wing tip	p	pressure, N/m^2 (lb/ft^2)
AR	aspect ratio	PSD	power spectral density
b	semispan length, m(ft)	q	dynamic pressure, N/m^2 (lb/ft^2)
BM	bending moment, N·m (lb·ft)	R	Reynolds number
c	chord length, m (ft)	rms	root mean square
$\bar{c}$	mean aerodynamic chord, m (ft)	RMS	root mean square
C_n	section normal force coefficient	S	area, m^2 (ft^2)
C_N	total normal force coefficient	t	thickness, m (ft)
C_p	pressure coefficient	TR	taper ratio
f	frequency, Hz	V	velocity, m/s (ft/s)
G	power spectral density of pressure, $(N/m^2)^2/Hz$	WS	wing station
		x	chordwise position from LE, m (ft)
G_M	power spectral density of bending moment, $(N-m)^2/Hz$	α	angle of attack (referred to centerline), deg
G_N	power spectral density of normal force, N^2/Hz	α_p	angle of attack (referred to chordline at wing pivot), deg
h	pressure altitude, km		
i	incidence angle (referred to model centerline), deg	Γ	dihedral angle, deg
		γ	coherence function
ℓ	moment arm, m (ft)	η	ratio of span station to semispan
LE	leading edge	Λ	sweep angle, deg
M	Mach number		

INTRODUCTION

It is well known that the pressure fluctuations associated with separated turbulent boundary layers cause buffeting of aircraft and component structures. The occurrence and extent of separated flow on a body is dependent upon the geometry and velocity of the body in a fluid and on the fluid density and temperature. Separation takes place whenever the boundary layer is subjected to intense positive pressure gradients. Such gradients occur because of abrupt changes in the geometry relative to the flow, for example, leading and trailing edges of wings and discontinuities of surfaces, and because of compressibility. The fluid mechanics of separated flow as it relates to the buffet problem is clearly described in Refs. 1-6.

The most significant buffet problem today is associated with transonic maneuvering of high-speed combat aircraft. In the transonic case the occurrence of the shock on the upper surface of a wing and the corresponding severe positive pressure gradient can cause flow separation at cruise and/or at maneuvering angles

of attack that are considerably below subsonic stall angles. As a result, at transonic speeds aircraft can encounter mild to intense buffeting that can limit maneuverability and induce both pilot and structural fatigue.

The effects of buffeting and other transonic phenomena on maneuvering combat aircraft were the subject of a study by an AGARD Working Group (sponsored by the Flight Mechanics Panel) which was reported in Ref. 7. This study, also summarized by Lamar (the Working Group Chairman) in Ref. 8, documented the comprehensive review of the state of the art of buffet test techniques and prediction methods that was carried out by the Working Group. Other noteworthy recent contributions to experimental techniques for predicting buffet loads have been made by John (Ref. 9), Hanson (Ref. 10), and Butler and Spavins (Ref. 11). Three different currently used approaches to testing buffet models in wind tunnels are described. One approach uses a dynamically scaled aeroelastic model to provide a direct measurement of full-scale buffet characteristics (Ref. 10). A second approach involves the measurements of the fluctuating pressures on a nominally rigid model; the measurements are then used to calculate the response of the elastic aircraft (Refs. 12 and 13). The third approach, suggested by Jones of the RAE (Ref. 11), uses measurements of the buffet response of a nominally rigid model of a wing to calculate the aerodynamic excitation and damping; the measurements are then used to calculate the response of the corresponding full-scale wing.

Each of the experimental approaches for obtaining buffet intensity information has its unique technical and cost advantages or disadvantages. From a cost point of view, the dynamically scaled models are the most expensive; and simple, solid metal models with only straingage and accelerometer instrumentation are clearly the least expensive. It is generally expected that dynamically scaled models yield the most accurate prediction of full-scale buffeting. On the other hand, the fluctuating-pressure measurement technique for predicting buffeting has the decided advantage of also revealing local flow-field information that is a necessary adjunct to buffet research. It is for this reason that the buffet research at Ames Research Center has employed the fluctuating-pressure method. A critical question remains to be resolved, however, concerning how well measurements of fluctuating pressures on models represent what really occurs on full-scale vehicles. The main problem is the effect of the different elastic characteristics of the model and flight vehicle. Effects of Reynolds number are also a problem important to all subscale testing.

The purpose of this paper is to describe separated-flow unsteady pressures and forces on elastically responding structures. The main theme here in describing buffet excitation is to make an assessment of the effects of elasticity and Reynolds number. In order to make that assessment, fluctuating pressure data are presented that were measured on several wind tunnel models and aircraft including the F-111A, F-111-TACT and F-5A.

SCOPE OF BUFFET RESEARCH AT AMES RESEARCH CENTER

A systematic buffet study as charted in Fig. 1 is being conducted at Ames Research Center to measure and analyze the aerodynamic excitations that cause aircraft buffet and/or the response of local structure. The data presented in this paper illustrate results from each of the three-dimensional configurations listed. The planned program is not yet complete and the questions posed cannot be entirely resolved at this time; however a significant amount of progress has been made.

The experimental phases of the research encompass the measurements of fluctuating pressures, fluctuating-pressure summations to yield integrated dynamic forces, and structural responses on two- and three-dimensional wind-tunnel models and on aircraft having various geometries appropriate for study. The effects of aerostructural interactions, a main theme of this paper, are being investigated by examination of pressure spectra relative to response modes and by direct comparison of fluctuating-pressure data from two TACT (joint USAF-NASA Transonic Aircraft Technology Research Program) models of different stiffness and from corresponding TACT and F-5A models and aircraft. The end objective of the research is to investigate and evaluate buffet response prediction techniques that are based on the measured aerodynamic excitation. The TACT program, which involves tests of an F-111 configuration with a supercritical wing, and its application to buffet research are described in detail in Refs. 7 and 8. Another joint effort by the USAF, NASA, and the RAE involving the TACT program will provide an evaluation of the Jones method (Ref. 11) of buffet prediction. Wing rock, also listed in Fig. 1, is a related subject of investigation that is part of the Ames buffet research program. The wing-rock research is intended to determine if the onset of wing-rock instability can be predicted from wind-tunnel model tests and also to determine to what extent the severe motions of wing rock effect buffet excitation pressures.

Some of the research on configurations shown in Fig. 1 has been completed and reported. The two-dimensional investigation was undertaken jointly by NASA and McDonnell Douglas Research Laboratories to study surface-pressure and wake-flow fluctuations in a supercritical airfoil flow-field. These results, which disclosed the presence of an aerodynamic frequency not yet identified in data from the three-dimensional models, have been reported by Roos and Riddle (Ref. 14). Riddle also has reported a significant amount of the pressure-fluctuation data from tests of a 1/6-scale semispan model of the F-111A (Ref. 15). A contract effort with General Dynamics Corporation provided F-111A flight buffet-response data from a previous loads flight-test program, as reported by Benepe, et al. (Refs. 16 and 17). These data were used to verify the results of the buffet response prediction technique developed under the same contract and reported by Cunningham, et al. (Ref. 13). Fluctuating-pressure spectral density and spatial correlation data from the F-111A 1/6-scale semispan wind-tunnel tests were used as the aerodynamic excitation for calculating the F-111A responses. A paper, presented by Cunningham at this meeting, describes his prediction technique and assessment of the fluctuating-pressure method for predicting aircraft buffet. Another contract effort (still in progress) with Northrop Corporation provided fluctuating-pressure and response data measured in flight on the thin, low-aspect-ratio wing of the F-5A. The fluctuating pressures and calculations of response and comparisons with the measured buffeting of the F-5A have been reported by Hwang and Pi (Refs. 12 and 18). The F-5A investigation is continuing with analysis of the fluctuating pressures measured on a 1/7-scale model in progress. The F-5A model tests also include the investigation of wing rock.

F-111A Model and Instrumentation

The 1/6-scale model of the F-111A is shown installed in the Ames 11- by 11-Foot Transonic Wind Tunnel in Fig. 2. The F-111A variable-sweep wing configuration was chosen as a means of studying buffet characteristics over a wide range of wing sweep angles using a single instrumented model. This allowed acquisition of buffet data characterized by shock induced separation, leading edge separation, and leading edge vortices. Because the primary study dealt with the surface pressure fluctuations and resultant responses of the wing, the 1/6-scale, semispan configuration was chosen to allow the largest wing consistent with blockage considerations for the Ames 11- by 11-Foot Transonic Wind Tunnel. The benefits of the large solid steel semispan model were volume for the instrumentation, high strength and rigidity for high angle-of-attack and high dynamic-pressure testing, and nearly full-scale Reynolds number capability for more accurate representation of separated flow phenomena. Natural boundary-layer transition occurred at approximately 3% chord; therefore no grit trip was used. A solid floor plate was used to seal the slots in the tunnel floor in the vicinity of the model.

The individual components of the F-111A model are labeled and the geometric parameters are listed on the sketch in Fig. 3. No attempt was made to duplicate the F-111A fuselage and inlets as their contribution to the fluctuating wing flow-field was considered to be negligible. However, the contours of the wing glove of the F-111A were duplicated to allow the inclusion of the glove-induced leading-edge vortex effects on the fluctuating pressure characteristics. At a wing sweep angle of 72°, tests were conducted with the removable horizontal tail both on and off the model; it was concluded that the tail had no significant effect on the wing nonsteady aerodynamics. All data presented in this paper represent the tail-on configuration, with the tail incidence fixed at 0° relative to the model reference centerline.

Figure 4 shows the locations of the mean static pressure orifices, the fluctuating pressure transducers, and the mean and fluctuating bending and torsional moment strain gages. The wing was instrumented with 97 miniature transducers capable of measuring pressure fluctuations with a flat response over a bandpass frequency range of 10 to 5000 Hz. All pressure instrumentation was oriented in rows parallel to the wind-tunnel flow at a wing sweep angle of 26°.

The primary modes and frequencies of the steel, variable-sweep wing panel were determined, prior to the aerodynamic test, with the model installed in the wind-tunnel test section. Mode shapes and locations of node lines were also determined. The frequencies associated with the first four primary wing modes are listed in Table 1. The tests were conducted in the Ames 11- by 11-Foot Transonic Wind Tunnel at Mach numbers of 0.6 through 1.3 at a Reynolds number of 12×10^6, based on mean aerodynamic chord, for wing sweep angles of 16°, 26°, 38°, 50°, and 72°, as measured at the wing leading edge. Additional details of the model, instrumentation, and data reduction are given in Ref. 15.

F-111A Fluctuating Wing Pressures

Root-Mean-Square Pressure Fluctuations. Chordwise distributions of mean static and fluctuating pressures on the wing upper surface at $\eta = 0.602$ are presented for $\Lambda = 26°$ and $M = 0.85$ in Fig. 5 to illustrate the relationship of the mean and fluctuating pressures prior to, and during, various levels of buffet. At $\alpha = 0°$, well below the onset of buffet, the static pressure distribution shows that the normal shock wave was at approximately 65% chord; pressure recovery was complete at the trailing edge, indicating attached flow. The corresponding RMS pressure distribution shows a slight peak at the location of the shock wave, indicative of a small random shock oscillation.

At $\alpha = 3.1°$, approximately at the buffet onset boundary as determined by the wing response measurements, the static pressure distribution shows that the pressure recovery at the trailing edge was weakened with shock-induced separation imminent. The RMS pressure amplitudes under the shock wave and near the trailing edge increased, indicating an increasing shock strength and an apparent increasing amplitude of shock-wave oscillation. At $\alpha = 6.1°$, the pressure distribution shows that the flow was separated from the shock wave to the trailing edge. The fluctuating pressures were still mild, except in the region of the shock wave, at this angle of attack. At $\alpha = 9.1°$, the RMS levels aft of the shock indicate large pressure fluctuations in the shock-induced separation that covered a substantial portion of the section. Based on the wing response measurements, the wing was experiencing heavy buffet. At $\alpha = 12.2°$, the flow at $\eta = 0.602$ was entirely separated aft of the 7% chord, as determined from the fluorescent-oil flow data. The RMS levels were high across the entire section, except for the small region near the leading edge.

The mean static and fluctuating pressure data presented in Fig. 5 have shown distinct relationships for different elements of the flow over the wing. Attached, accelerating flows ahead of the shock wave are indicated by decreasing mean static pressures and low RMS levels. Attached flows aft of the shock wave are indicated by positive mean static pressure recovery at the trailing edge and low RMS levels. The shock-wave location is indicated by a steep, positive slope of the mean static pressures and a sharp RMS peak due to the shock oscillation. Separated flows are indicated by negative mean static pressure recovery at the trailing edge and high RMS levels.

Power Spectra and Coherence of Fluctuating Pressures. Quantitative evaluation of the buffet excitation aerodynamics depends upon the amplitudes and spatial and temporal relationships of the pressure at each point on an aircraft surface. In this section, the power spectra and streamwise cross spectra in terms of coherence are presented for $\Lambda = 26°$, $M = 0.85$, and $\eta = 0.602$. The spectra are presented for the full range of angles of attack to illustrate the changes that take place as the flow separates.

Figure 6 presents the power spectra and coherence of pressures measured at $\alpha = 0°$. Except for the peak due to wind-tunnel-induced noise at 2700 Hz (Ref. 19), the shape and the amplitude of the power spectrum of the fluctuating pressure measured at 5% chord is indicative of attached turbulent flow. The existence of a turbulent boundary layer was substantiated by sublimation tests which showed that natural transition from a

laminar to a turbulent boundary layer occurred at approximately 3% chord. For this angle of attack, below the buffet onset where the structural modes of the wing have not yet been significantly excited, a broad energy peak occurred in the power spectrum of the pressure beneath the wing shock wave (65% chord). This peak, centered at approximately 48 Hz, is not associated with any known frequencies related to model-structure or tunnel-background noise. This same peak is evident to a lesser degree in the power spectra at 95% chord and at 22.5% lower surface chord. This suggests that an oscillation of the circulation around the airfoil is occurring as suggested by Jones (Ref. 20) and Mabey (Ref. 4). Another interesting possi-bility is that instead of the peak at 48 Hz being significant, the valley at lower frequencies may be a negative peak associated with the first bending mode. A hypothesis by Jones (Ref. 20) regarding negative peaks will be further discussed as more data are presented. The coherence between 5% and 10% chord was high for the 10-5000 Hz range of these data. Comparing 65% chord (the shock position) with 70% chord, one notes the high coherence of the pressures in the region of 48 Hz. This same characteristic is repeated in the coherence between the pressures measured at 90% and 95% chord. This tends to support the hypothesis that there was an oscillation of circulation.

Figure 7 presents the power spectra and coherence of fluctuating pressures measured at α = 4.0°. This angle of attack represents data approximately 1° beyond the buffet onset boundary. The power spectra at the shock wave and rearward of the shock wave show increased energy in the region of the wing first torsional mode (189 Hz). The peak in the pressure spectra occurred at 165 Hz. The peak at 48 Hz, which occurred at α = 0°, is no longer predominant. The coherence data in the region of the shock wave and near the trailing edge indicate that a strong correlation existed in the region of the wing first torsional mode. Thus, it is suggested that the circulation oscillation which was being driven by the shock-wave/boundary-layer interaction now has coupled with the torsional mode.

Figure 8 presents the power spectra and coherence of fluctuating pressures measured at α = 9.1°. At this condition, the shock-induced separation affected a large portion of the wing, and the buffet response of the wing was large. The power spectra at 5% chord of the upper surface and 22.5% chord of the lower surface now show small peaks at the wing first bending mode, although larger peaks occurred at the wing first torsional mode. The torsional-mode peak was very significant in the region of the shock and in the separated flow. At 95% chord, the level of the peak was an order of magnitude higher than the level at lower frequencies. The coherence data show high correlation at the torsional-mode frequency in the region of the shock wave and near the trailing edge. This same correlation is evident in the coherence data at the leading edge of the wing, thus tending to substantiate the hypothesis that there is a circulation oscillation coupled with the torsional mode.

Figure 9 presents the power spectra and coherence of pressures measured at α = 12.2°. For this condition, the flow at η = 0.602 was separated aft of 7% chord with high RMS pressure levels across the section as shown in Fig. 5. The increases in the levels of the power spectra at α = 12.2° as compared to α = 9.1°, especially at 5% chord, are evident. At 95% chord, the power spectrum shows that there was a broad energy peak centered at 300 Hz. The coherence between 90% and 95% chord was high in this same frequency band. Since spectral peaks did not occur or were relatively small at modal frequencies, there must be less tendency for the flow to couple with the motion when it is more completely separated.

F-111A Pressure Summations and Responses

Electronic summations of the 97 fluctuating pressure transducer outputs provided fluctuating-section normal force coefficients at each of the five wing sections to show spanwise variations in the buffet excitation and the total fluctuating normal force coefficient and wing-root bending moment for the entire wing panel. Although for this case the summation technique has been applied to the determination of fluctuating normal forces and bending moments, the same approach can be applied to the determination of generalized forces that represent the primary vibration modes of interest.

Root-mean-square Characteristics. Figure 10 presents the RMS of the section and total wing normal-force coefficient fluctuations for Λ = 26° and M = 0.85. At η = 0.273 and 0.438 the flow was characterized by relatively weak fore and aft inboard shock waves and by a wing-glove-induced vortex that crossed the wing root. This vortex appeared to stabilize the inboard flow, thus accounting for the low RMS levels and mild increase with angle of attack. At η = 0.602 the outboard shock wave resulted in substantial shock-induced separation from α = 6° through 10°. At 12°, the flow was separated over most of the section at η = 0.602 but the RMS level was lower due to the lower coherence of the pressures, as previously discussed. At η = 0.768 and 0.932, the flow was characterized by strong shock-induced separation through α = 12°. The total wing normal force coefficient is similar in RMS level and growth rate to the inboard section coefficients and does not reflect the characteristics at the outboard sections. Part of this effect is due to the area weighting of the fluctuating pressure inputs to obtain the total normal force on the high-taper-ratio wing, where the inboard section pressures apply to larger areas. The effective area for the pressures at η = 0.273 is 28.7% of the total wing area and only 11.1% at η = 0.932. The low RMS level of the total wing normal force coefficient is also due to a degrading of the spanwise correlation of the section pressures as the separated area increased with angle of attack. The last statement will be more evident when the spectral and spatial data are discussed in the next section.

Power Spectrum and Coherence Characteristics. Figure 11 presents the PSD and coherence characteristics of the fluctuating section normal force coefficients at Λ = 26°, M = 0.85, and α = 6°, 9°, and 12°. These data correspond to the RMS of the section normal-force coefficient fluctuations presented in Fig. 10 for angles of attack that exceed the buffet boundary. The spectra show the effects of increasing separated flow on the wing with increasing α and the effects of motion on buffet forces.

At α = 6.1°, the shock-induced separation increased at the two outboard sections, η = 0.768 and 0.932, and therefore the corresponding spectra are significantly higher than for other sections. The coherence shows that the dominant correlation between sections occurred at the torsional mode frequency for the outboard wing sections only. At α = 9.2°, the shock-induced separation was substantial at η = 0.602, 0.768, and 0.932. Prominent narrowband peaks occur in the spectra and coherence at the frequency of the first torsional mode, indicating that the coupling observed in the local pressure spectra (Fig. 8) also

influenced the section and overall nonsteady forces. The torsional mode coupling had the largest influence on the energy content of the spectra at $\eta = 0.602$. At $\alpha = 12.3°$, the more extensive separation caused an increase in the spectra at lower frequencies, and there was almost no coupling with structural modes. The coherence between sections was low, and therefore, even though the spectral levels were considerably higher than at $\alpha = 9.2°$, the total fluctuating normal force was only slightly higher. It is significant that coupling occurred only at $\alpha = 9.2°$. More discussion of this point will follow as the results from other configurations are presented.

As previously mentioned, the fluctuating-pressures (voltage time histories) were also summed to yield the nonsteady moments about the wing root. Figure 12 presents a direct comparison of the response spectra of the fluctuating wing-root bending and fluctuating torsional moments and the excitation spectra of the fluctuating bending moment derived from the fluctuating pressure summations. The data are for $\Lambda = 26°$, $M = 0.85$, and $\alpha = 9°$ and $12°$. The primary measured responses (wind-on) were the first bending mode at 26 Hz and the first torsion mode at 208 Hz. There were smaller responses at 100 Hz, corresponding to the second bending mode, and at 165 Hz and 380 Hz, both unidentified modes. The 165-Hz response of the bending moment gage is noteworthy because it corresponds exactly with the frequency peak in the bending moment excitation from the pressure summation at $\alpha = 9.2°$. The coupling was therefore due to this unidentified bending mode or the first torsion mode. Comparison of response frequencies in Fig. 12 with wind-off values in Table 1 show that the bending-mode frequencies were unchanged, but the first torsion mode (189 Hz vs 208 Hz) differed considerably. This result indicates that aerodynamics more strongly influenced the torsional response of the wing at high subsonic speeds than it did the bending response. The fact that the narrowband peak in the excitation spectra at $\alpha = 9.2°$ (Fig. 12) does not agree precisely with the torsional response frequency is consistent with Jones (Ref. 20) who hypothesizes that if aerodynamic stiffness and/or inertia are considered in addition to aerodynamic damping, the total fluctuating aerodynamic force could contain a negative spectral peak at the response resonant frequencies and an adjacent positive spectral peak slightly off the resonant frequencies due to the contribution of the out-of-phase aerodynamic forces. Jones argues that if aerodynamic damping is positive then the total fluctuating aerodynamic force on a structurally responding wing should contain negative spectral peaks at the frequencies of resonance because of cancellation of the aerodynamic excitation at these frequencies by the corresponding in-phase, motion-dependent aerodynamic forces. Such a negative peak appeared at the first bending-mode frequency in the pressure spectra (Figs. 6-9).

Figure 12, and also Figs. 9 and 11, show that when separation was widespread on the wing at $\alpha = 12°$ there was insignificant coupling of the aerodynamic forces that cause buffeting and the motion. It is important, therefore, to keep in mind that the F-111A data show the tendency for the separated-flow nonsteady pressures to be influenced by motion only at certain conditions. Additional data from the TACT and F-5A tests also show tendencies of motion effects on the measured nonsteady pressures only for isolated conditions of M and α.

TACT

The objectives and scope of the joint USAF-NASA TACT program are described in Refs. 7, 8, and 21. The primary buffet research objective of the TACT program is to validate the suitability of measurements of unsteady pressures and forces on wind-tunnel models for prediction of full-scale aircraft buffeting. The investigation includes testing of two 1/6-scale semispan models of different stiffness and corresponding flight tests of the TACT aircraft which is a modified F-111A with a supercritical wing. Because the TACT buffet research is still in progress, none of the flight buffet information is in reduced form. However, a small amount of the TACT scale-model data have been analyzed and can be presented to illustrate some separated flow unsteady pressures and forces and effects of elasticity and Reynolds number on these pressures and forces.

TACT Models and Instrumentation

The 1/6-scale semispan models were constructed of solid steel and aluminum. The installation in the Ames 11- by 11-Foot Transonic Wind Tunnel was similar to the installation of the F-111A model (Figs. 2 and 3). The half-fuselage model used for the TACT model wings was scaled from the aircraft, in contrast with the semicircular shape of the fuselage used for the earlier F-111A model. Pertinent geometric information about the TACT models are listed in Fig. 3 along with the corresponding information for the F-111A model.

The locations of the fluctuating-pressure instrumentation on the models and aircraft are shown in Fig. 13. The steel and aluminum semispan-wing models were left-wing panels. Each model had 50 pressure transducers installed by the technique described for the third-phase tests of the F-111A model (Ref. 15). The aircraft has 25 pressure transducers installed in the right-wing panel. All the fluctuating-pressure instrumentation was oriented in rows parallel to the free-stream flow at a wing-sweep angle of $26°$. Both the models and the aircraft have wing-tip accelerometers and wing-root bending and torsion strain gages.

The test technique used for the TACT steel and aluminum models, the data acquisition system, and data reduction were the same as described in Ref. 15 for the F-111A model. The TACT model tests were conducted over a Mach number range from 0.7 through 0.95 at Reynolds numbers from 7×10^6 to 14×10^6, based on mean aerodynamic chord, for sweep angles of $26°$, $35°$, and $58°$. Vibration-mode frequencies and node lines were determined at each of the sweep angles with the models installed in the wind-tunnel. The frequencies associated with the primary modes for $\Lambda = 26°$ are listed in Table 2.

TACT Fluctuating Pressures

Root-Mean-Square Pressure Fluctuations. Measurements of the RMS values of the pressure fluctuations on the 1/6-scale TACT steel and aluminum models at $\Lambda = 26°$ are illustrated in Fig. 14 for $M = 0.80$ and in Fig. 15 for $M = 0.90$. The results are shown for a mild buffet condition at $\alpha_p = 9°$ which is just above the

buffet boundary, and for moderate to severe buffeting at $\alpha_p = 12°$. The length of each vertical line on the wings and horizontal tail represent the RMS values of the pressure fluctuations at the locations of the measurements. At $\alpha_p = 9°$, the pressure fluctuations that occurred on the wings in the region between the shock wave and trailing edge were relatively small for both M = 0.80 and 0.90; this was because the shock strength was weak and did not induce separation. At $\alpha_p = 12°$ the flow was extensively separated downstream of the shock waves and relatively high pressure fluctuations resulted. It may be noted that the most upstream transducers near the boundary of the disturbed flow on the wings did not always measure the high pressure fluctuations that are characteristic of shock waves. The absence of the shock-wave detection by high corresponding pressure-fluctuation measurements is due to the fact that the shock wave was between transducers for the specific angles of attack shown.

Of special interest in Figs. 14 and 15 is the comparison of the RMS values of the pressure fluctuations on the steel and aluminum wings for the same conditions of Mach number, angle of attack, and Reynolds number. Generally the RMS values and the distributions of the pressure fluctuations are similar. It can be noted, however, that the upstream boundary of the disturbed-flow regions was slightly closer to the leading edge of the steel wing than on the aluminum wing for both $\alpha_p = 9°$ and $12°$. This variation is considered to be due to static-elastic differences in the wings and the consequently greater washout of the aluminum wing than the steel wing under aerodynamic loading. Such effects cannot be ignored with respect to buffet-excitation prediction, although the effects may be small when compared to overall boundaries expected of random data.

Power Spectra and Coherence of Fluctuating Pressures. Figures 16-18 show representative PSDs of the pressure fluctuations on the TACT models from the limited analysis of data that have been completed to date. These spectra further illustrate the characteristics of the pressure fluctuations in separated flow and contribute to the assessment of motion effects. The corresponding PSDs from the steel and aluminum wings are from selected pressure measurements along the chord at $\eta = 0.744$ for the same test conditions shown in Figs. 14 and 15. Figures 16-18 show that the spectra from the steel and aluminum wings were in good agreement except where motion effects have influenced the data.

At M = 0.90 and $\alpha_p = 9°$ (Fig. 16), which represent conditions slightly above the buffet boundary, motion effects were minor with only a slight tendency noticeable for the data to peak at a frequency corresponding to the second bending-mode frequency. The low levels of the spectra at x/c = 0.20 are associated with the attached-flow region ahead of the shock wave. The spectra at x/c = 0.45 for the steel wing and at x/c = 0.54 for the aluminum wing are typical for the shock wave region. The fact that the shock waves were at different chord locations is attributed to a static elastic effect previously shown in connection with the RMS data. The spectra at x/c = 0.63 and x/c = 0.90 are from a region of disturbed flow downstream of the shock wave that was not separated.

Figure 17 shows PSDs of the pressure fluctuations on the TACT models when the flow was extensively separated at M = 0.80 and $\alpha_p = 12°$. The spectra for the steel and aluminum wings are considered to be in very good agreement, and there is no indication by peaks in spectra that the pressure fluctuations were influenced by the motions of the elastically responding wings. In contrast, Fig. 18, containing PSDs for M = 0.90 and $\alpha_p = 12°$, which was also a condition of widespread separation, shows that the pressure fluctuations on the steel wing were affected by motion but not those on the aluminum wing. In this case the apparent coupling was with the second bending mode as opposed to the torsional mode coupling of the F-111A. In Fig. 18, the spectra at x/c = 0.20 are from pressures in the region of the shock wave and the spectra at x/c = 0.32 are strongly influenced by the shock-wave oscillations as indicated by the concentration of energy at low frequencies. The spectra at x/c = 0.63 and 0.90 (Figs. 17 and 18) are typical of separated flow.

The reasons for the coupling of the pressures with the second bending mode of the steel wing but not with that of the aluminum wing are not readily apparent. The second bending mode frequencies were similar (steel, 96 Hz vs aluminum, 99 Hz, Table 2), and the still air vibration tests showed that the second-bending-mode node lines were similar for both wings. Additional analysis will determine the relative response amplitudes of the wings and also whether coupling occurred with the aluminum wing for any of the test conditions.

Some measurements of the coherence of the pressure fluctuations on the 1/6-scale TACT models at $\eta = 0.744$ are shown in Fig. 19 for the same test conditions as the previously discussed spectra at $\alpha_p = 12°$ for M = 0.80 and 0.90. Generally, the trends of the coherence of the pressure fluctuations were similar for the steel and aluminum wings with the exception of the results at M = 0.90, which show a strong coherence of pressures on the steel wing at the second bending-mode frequency. Typical differences in coherence between pressures strongly influenced by a shock wave and pressures in regions of separated flow can be seen. As might be expected, because of the low-frequency content of shock-wave spectra, the coherence of pressures influenced by shock-wave oscillations is concentrated at low frequencies (Fig. 19, M = 0.90, 0.32c/0.46c). The coherence of pressure fluctuations in separated flow regions extends to frequencies approximately 10 times higher than for shock waves. The coherence for the transducer spacings shown is significant, however, more data is needed to establish the spatial decay of coherent pressure fluctuations in separated flow on airfoils. Extensive data analysis, similar to the analysis of Ref. 22, is in progress and will show if the spectral and spatial characteristics of pressure fluctuations in separated flow can be generalized for airfoils and other geometries.

TACT Pressure Summations

Electronic summations of the 50 fluctuating pressure transducer outputs provided fluctuating section normal force coefficients at the four instrumented wing sections of the TACT models and the total fluctuating normal force coefficients for the wing panels.

Reynolds Number Effects on Normal Force Fluctuations. The variations of section normal and total normal force fluctuations with angle of attack for the TACT 1/6-scale steel model at M = 0.80 are shown in Fig. 20 to illustrate effects of Reynolds number. The data are for three test Reynolds numbers of 7.0×10^6,

10.5×10^6, and 14.0×10^6. Reynolds-number effects can only be inferred from these data because, for a given Mach number, dynamic pressure, q, also varies proportionately with Reynolds number changes in the Ames 11- by 11-Foot Transonic Wind Tunnel. Static loads, and hence static elastic effects, and "q" dependent dynamic effects are combined in the data. The results for the three test Reynolds numbers show that normal force fluctuations were in relatively good agreement up to $\alpha_p = 12°$ with the exception of one point at $\alpha_p = 10°$. At angles of attack greater than $12°$ tne normal force fluctuations varied significantly with Reynolds number. The most pronounced effects occurred at the inboard wing sections. The fact that the Reynolds number variations hac very little effect on the data at the most outboard station, $\eta = 0.910$, indicates that static elastic and first-bending and torsion mode dynamic elastic effects were negligible. The discontinuity of points at $\alpha_p = 10°$ and above $\alpha_p = 12°$ are not likely to be due to dynamic elastic effects because inboard wing motions must be small, and also because the normal-force fluctuation coefficients decreased with increasing dynamic pressure. The smaller discontinuities can be caused by the positions of the shock waves relative to the transducer locations on the wing. The larger disagreements in data must be due to Reynolds number effects on leading-edge vortices and separation boundaries. The TACT flight tests will enhance the investigation of Reynolds number effects by providing data at Reynolds numbers up to approximately 35×10^6, based on $\bar{c}$.

Comparison of Normal Force Fluctuations on Steel and Aluminum Wings. The variations of section and total normal force fluctuations on the TACT 1/6-scale steel and aluminum models with angle of attack are shown in Fig. 21 for M = 0.80 and 0.90 and for R = 10.5×10^6. Generally, but with some exceptions, the measurements of $C_{n_{rms}}$ and $C_{N_{rms}}$ from the steel and aluminum models are in good agreement, particularly at M = 0.80. It was surprising, for example, that the $C_{n_{rms}}$ measurements at $\eta = 0.578$, $\alpha_p = 10°$, were the same from both models since the points depart from a smooth variation with angle of attack. The major differences in the normal force fluctuations occurred at M = 0.90 at outboard wing sections $\eta = 0.744$ and $\eta = 0.910$. The higher $C_{n_{rms}}$ measurement on the steel wing at $\eta = 0.744$, $\alpha_p = 12°$, is shown by corresponding PSDs in Fig. 18 to be caused by dynamic elastic effects resulting from some coupling between the pressure fluctuations and the second bending mode of the wing. It is suspected, but confirmation is needed by additional data analysis, that the differences in section normal force fluctuations at $\eta = 0.910$ are also due to dynamic elastic effects.

F-5A

Steady-state and fluctuating pressures were measured on a 1/7-scale model of Northrop F-5A aircraft during two separate tests in the Ames Research Center 11- by 11-Foot Transonic Wind Tunnel (Fig. 22). For the first tests, the model was mounted in the conventional way on the sting support system. Store configurations, flap and control surface settings, Mach numbers, sideslip angles, and angles of attack were varied. The model was constructed of steel. For the second tests a special sting was designed incorporating a torsional spring and damper that allowed the model to oscillate in roll at a natural frequency simulating the Dutch roll motion that occurs during wing rock. The maximum roll angle was 21° single amplitude. The analysis of results from the wing-rock tests, in progress by Northrop Corporation, are not yet sufficiently complete to be included here; however, when they are complete they will show the unsteady pressures associated with wing rock and also whether such a model support with a nominally rigid model can be used for prediction of wing-rock onset.

Previously to the model tests, a buffet flight test program was conducted using a fully instrumented F-5A aircraft. The test results of the flight test were described in Refs. 12 and 18. The scale model tests were conducted using test conditions similar to the flight test conditions so that the dynamic pressure data acquired during the flight test and the scale-model tests may be compared and evaluated, taking into consideration appropriate scaling relationships. Selected comparative results are presented in this paper to illustrate the separated-flow unsteady pressures on the F-5A but mainly to show the static and dynamic elastic effects on buffet excitation.

Basic Dimensions of the F-5A

The F-5A is a single-seat fighter capable of carrying stores at wing fuselage pylon stations. The flight test was conducted with two wing-tip stores (AIM-9B Missiles) with guide rails; otherwise the wing was clean. The scale model tests were conducted with and without the wing-tip missiles. A combination of deflected leading edge and trailing edge flaps as well as the case of completely retracted flaps were used in the test program. A three-view drawing of the F-5A is shown in Fig. 23 with pertinent geometry information. Additional dimensional details are given in Ref. 12.

F-5A Instrumentation

Locations of the static and dynamic instrumentation on the F-5A aircraft and 1/7-scale model are shown in Fig. 24. The F-5A aircraft and model were each equipped with 28 static pressure orifices and 28 adjacent dynamic pressure transducers. In addition, semi-conductor strain gages were installed on both wing root sections to measure the bending and torsion moments of the wing under dynamic loads. There were three accelerometers in the model, one at each wing tip inside the missiles and one at the location of the center of gravity of the aircraft.

In the first model test phase, a six-component balance was installed inside the model fuselage in front of the sting mounting system. The balance was eliminated in the second test phase to make room for the flexible roll and damping device. For this latter phase, dynamic data such as the roll angle, the model pitch and yaw oscillation angles, and the damping coefficient of the damper were recorded. Transition strips were installed on the wing and tail surfaces of the scale model at approximately 10% chordwise positions.

Fluctuating Pressures on F-5A

Root-Mean-Square Pressure Fluctuations. Typical chordwise distributions of static and fluctuating pressures on the right wing upper surface of the 1/7-scale F-5A model are shown in Fig. 25 for M = 0.925 and R = 2.49 x 10^6. The sideslip angle was 0°; the horizontal tail surface and aileron settings were 0°; and the leading edge and trailing edge flap angles were 5° and 12°, respectively. (Note that the termination points of the pressure distributions were arbitrarily drawn to the leading and trailing edges of the wing.) Figure 25 shows the progression and expansion of regions of separated flow with increasing angle of attack. At an angle of attack of 6°, slightly above the buffet boundary, and at M = 0.925 the shock induced separation and pressure fluctuations were near the trailing edge and uniformly distributed over the span. At α = 10°, with moderate to severe buffet conditions, the flow separation and high fluctuating pressures most extensively covered the outboard half of the wing. The inboard attached flow at α = 10° is attributable to the vortex created by the high sweepback of the inboard leading edge. At α = 14° the flow was separated over the whole wing panel. The leading edge vortex no longer delayed separation on the inboard wing sections as evidenced by the measurements of high pressure fluctuations in this region.

The static and fluctuating pressure distributions measured on the F-5A aircraft are not shown (see Refs. 12 and 18); however, the development and expansion of the flow separation regions on the aircraft were similar to the model characteristics noted in Fig. 25, except for slightly higher angles of attack. In general, for a given angle of attack, and at a given spanwise location, the shock tended to stay closer to the trailing edge on the scale model as against the flight test results. The scale model had to be at an angle of attack about 2° higher to develop an identical separated flow pattern on the top wing surfaces. The cause of this problem could not be isolated, but the two most likely contributing factors are: (1) the leading edge flap setting on the model was at 5° vs. 4° on the aircraft; (2) the aeroelastic effect of the full-scale aircraft caused an increase in the local angle of attack in the outer span of the wing. It is known that the wing tips of F-5A aircraft twist (washin) approximately 1.5° to 2° for the load conditions shown in Fig. 25 (M = 0.925, h = 10.668 km, q = 14.36 kN/m²). The transient effect of the transonic maneuver, rate of change of angle of attack, was considered as a candidate cause, but the results of Ericsson and Reding (Ref. 23) show that the maneuver tends to forestall separation for a given angle of attack.

F-5A Model and Aircraft Power Spectral Densities. Comparisons of power spectra of the pressure fluctuations in separated flow on the F-5A 1/7-scale model and on the aircraft are shown in Fig. 26-28 for transducers 2, 5, and 11, respectively. The data are for a Mach number of 0.75 with model and aircraft leading-edge and trailing-edge flaps at 0°. The Reynolds number for the model test conditions was 4.71x10^6 based on $\bar{c}$ and the dynamic pressure was 30.23 kN/m² (631.3 lb/ft²). The Reynolds number for the aircraft flight conditions was 18.90x10^6 at a test altitude of 7,772 km (25,000 ft). The flight test and model data are plotted with reference to the separate scales identified in the figures. The displacement of the scales accounts for the accepted model-flight scaling relationships:

$$\left(\frac{f_{mod.}}{f_{flt.}}\right) = \left(\frac{\bar{c}_{flt.}}{\bar{c}_{mod.}}\right)\left(\frac{V_{mod.}}{V_{flt.}}\right) \; ; \; \left(\frac{G_{mod.}}{G_{flt.}}\right) = \left(\frac{\bar{c}_{mod.}}{\bar{c}_{flt.}}\right)\left(\frac{q^2_{mod.}}{q^2_{flt.}}\right)\left(\frac{V_{flt.}}{V_{mod.}}\right)$$

The flow at each of the three pressure transducers was separated from the leading edge of the wing at M = 0.75. At α = 8°, the flow was separated on the outboard half of the span. At α > 12°, the flow was separated over the complete upper wing surface.

Comparison of the spectra for the 1/7-scale model and the aircraft (Figs. 26-28) generally shows that reasonable agreement exists between the wind tunnel and flight tests, particularly if allowance is made for the marginal statistical accuracy of the flight data. It can be noted that the flight data samples were nonstationary because of the variation of angle of attack. The spectra of the fluctuating pressures on the model tended to always be higher than the corresponding measurements on the aircraft.

A similar comparison was made between power spectra of pressure fluctuation on the model and aircraft at M = 0.925 (now shown). The correlation of results was about the same as for the data shown in Figs. 26-28 with the exception that spectra acquired at a location of a strong shock wave on the aircraft were inconsistent with wind-tunnel data, sometimes by as much as 2 decades. This lack of agreement can be attributed to the sensitivity of the shock wave location to flight condition variations in the maneuver. Because the pressure transducer is at a fixed location and the mean position of the shock wave cannot be followed, the result is a nonstationary pressure-time-history measurement.

In order to consider the effects of the elastically responding structures, the model wing-tip acceleration was analyzed for M = 0.75 and α = 8° yielding the PSD shown in Fig. 29. The principal vibration modes of the model and sting support system have been identified in Fig. 29 and also by arrowheads on the pressure spectra at α = 8° in Figs. 26-28. Examination of the pressure spectra shows some prominent peaks in the spectra, mostly at α = 8°, at frequencies corresponding to the sting and balance bending mode and the wing second symmetrical bending mode. Other modes, including the high-acceleration first bending mode, did not influence the pressure fluctuations. It is significant that coupling occurred at the wing second bending mode on both the F-5A and TACT models. It is not clear why in these cases second bending modes dominated over a torsion mode; however, the response of the F-5A pressures to the sting and balance bending is no doubt caused by angle-of-attack oscillations. The pressure spectra from the flight tests show no peaks that correspond to any of the vibration mode frequencies identified for the aircraft in Table 3.

DISCUSSION OF AEROELASTIC EFFECTS

The foregoing results from tests of models and aircraft of different geometries and elastic properties have illustrated the characteristics of pressure fluctuations that cause buffeting of the complete aircraft

or of local structure. In addition to using pressure-fluctuation measurements from nominally rigid wind tunnel models to investigate the buffet phenomena, such measurements can be used for prediction of buffet response (Refs. 12 and 13), providing they adequately represent the corresponding pressures on the full-scale aircraft. The state of the art for predicting random response characteristics of a structure by any sub-scale test method does not allow precise predictions. Thus the precision required of the pressure fluctuation measurements is not the same as that expected of steady-state aerodynamic measurements. Reynolds number effects, wind tunnel wall and flow quality effects, etc., are important to all sub-scale tests in wind tunnels; however, the main issue of the validity of model pressure fluctuation measurements for buffet prediction is the questionable effect of aeroelasticity.

Static Elastic Effects

In any aerodynamic test of a model, the shape of the model must be the same as that of the full-scale shape or the flow-field will be different. With respect to buffet excitation, static elasticity was shown (Figs. 14 and 15) to slightly alter the chordwise positions of the shock waves on the steel and aluminum TACT models. The amplitudes of the pressure fluctuations in the separated regions were not seriously affected, however; as shown by the good agreement between corresponding power spectra from the TACT models (Figs. 16-18) where dynamic elastic effects were not evident. Static elastic effects also appeared to influence the separation zones on the F-5A (see preceding discussion of root-mean-square pressure fluctuations on the F-5A). Maneuver loads on the aircraft that result in aeroelastic washin of up to 2° at the wing tips was considered a contributing cause of small angle-of-attack differences between model and aircraft for development of equal separation zones. Within the separation zones, as with the TACT models, the wind-tunnel and flight PSDs were comparable (Figs. 26-28).

Dynamic Elastic Effects

The pressure fluctuation measurements on the F-111A, TACT, and F-5A models indicate that buffet excitation can be affected by the dynamic elastic characteristics of a model at certain conditions of M, α and q. Pressure fluctuations on the F-111A model coupled with the first torsion mode at M = 0.85 from $\alpha \geq 4°$ to $\alpha < 12°$ (Figs. 7-9, 11, and 12), as identified by the narrowband peaks in the PSDs at the torsion-mode frequency. On the steel TACT model the pressures coupled with the second bending mode at M = 0.9, $\alpha_n = 9°$ (Fig. 18) but not with a torsion mode. No coupling was observed in the data from the aluminum TACT model; however, only a small amount of data have been analyzed to date. The F-5A model data showed the influence of the sting support and balance bending motion and also the influence of the wing second bending mode (Figs. 26 and 27). No definite dynamic elastic effects were observed in the F-5A flight data.

It is significant that the dynamic elastic effects on the pressure fluctuations measured on nominally rigid scale model wings appeared to occur only at a very limited number of combinations of M, α and q. However, more of the F-111A data needs to be examined and the TACT wind tunnel and flight data analysis needs to be completed before the extent of the effect on buffet excitation measurements can be fully assessed. There are very few flight measurements of buffet excitation pressures available. Possibilities of single-degree-of-freedom aerostructural interactions involving the buffet phenomena have been suspected but not confirmed. A limited amount of data on the F-4 by Mullans and Lemley (Ref. 24) and the F-5A (Figs. 26-28) show reasonable agreement between fluctuating pressure spectra on the corresponding models and aircraft.

As previously mentioned, the dynamic elastic effects of the F-111A, TACT and F-5A model wings on the pressure fluctuations in separated flow appeared as narrowband peaks in the pressure PSDs at the frequencies of the interacting mode. The response of the wings did not appear to affect the power spectra at other frequencies as shown by comparison of PSDs from the TACT steel and aluminum models (Fig. 18) and from the F-5A model and aircraft (Figs. 26-28). If this is true and verified by the TACT data, it is probable that reasonably correct PSDs can be estimated even for those frequencies where model dynamics affect the data, by fairing a curve through the base of the peaks that are identified as being response dependent.

CONCLUDING REMARKS

A large amount of experimental data have been presented that illustrate the characteristics of fluctuating pressures and forces that cause buffeting of aircraft and/or local structure. The data which were obtained on several wind tunnel models and aircraft including the F-111A, TACT and F-5A allow an assessment to be made of the effects of elastically responding structures on the buffet excitation.

The results show that the fluctuating pressures in separated flow may interact with single-degree-of-freedom response modes of wings at certain conditions of Mach number, angle of attack, and dynamic pressure. Such interactions occurred with the first torsion mode on the F-111A model and with the second bending modes on a TACT and the F-5A models. The three models were solid steel. Limited data analyzed from a solid aluminum TACT model for the same conditions did not show evidence of the interaction. Similar aero-structural interactions can be anticipated for full-scale aircraft; however, no evidence of coupling between pressures and response modes was observed in the F-5A data.

Static elastic and Reynolds number differences between wind tunnel models and actual aircraft affect the boundaries of the flow separation on wings and hence the total buffet excitation. These effects do not appear to be large relative to the expected accuracy of total buffet excitation predictions; however, they should not be overlooked.

REFERENCES

1. Monnerie, B., "Flow Separation and Aerodynamic Excitation at Transonic Speeds," AGARD Lecture Series No. 74 on Aircraft Stalling and Buffeting, February 1975.

2. Roos, F. W., "Fluid Mechanics Related to Airfoil Buffeting: A Review," McDonnell Douglas Research Laboratories, Report MDC Q0456, December 1971.

3. Gentry, A. E. and Oliver, W. R., "Investigation of Aerodynamic Analysis Problems in Transonic Maneuvering," McDonnell Douglas Aircraft Co., Report MDC J5264-01, Vol. 1, September 1971.

4. Mabey, D. G., "Beyond the Buffet Boundary," Aeronautical Journal, Vol. 77, No. 748, April 1973.

5. Mabey, D. G., "Pressure Fluctuations Caused by Separated Bubble Flows at Subsonic Speeds," RAE TR 71160, August 1971.

6. Pearcey, H. H., Osborne, J., and Haines, A. B., "The Interaction Between Local Effects at the Shock and Rear Separation," AGARD Conference Proceedings No. 35, September 1968.

7. AGARD Advisory Report No. 82, "Effects of Buffeting and Other Transonic Phenomena on Maneuvering Combat Aircraft," July 1975.

8. Lamar, W. E., "Effects of Buffeting and Other Transonic Phenomena," AGARD Conference Proceedings No. 187 on Flight/Ground Testing Facilities Correlation, April 1976.

9. John, H., "Critical Review of Methods to Predict the Buffet Penetration Capability of Aircraft," AGARD Report 623, September 1974.

10. Hanson, P. W., "Evaluation of an Aeroelastic Technique for Predicting Airplane Buffet Loads," NASA TN D-7066, 1973.

11. Butler, G. F. and Spavins, G. R., "Preliminary Evaluation of a Technique for Predicting Buffet Loads in Flight from Wind-Tunnel Measurements on Models of Conventional Construction," AGARD Conference Preprint No. 204 on Prediction of Aerodynamic Loading, August 1976.

12. Hwang, C. and Pi, W. S., "Investigation of Northrop F-5A Wing Buffet Intensity in Transonic Flight," NASA CR-2484, December 1974.

13. Cunningham, A. M., Jr., Waner, P. G., Jr., Watts, D., Benepe, D. B., and Riddle, D. W., "Development and Evaluation of a New Method for Predicting Aircraft Buffet Response," AIAA Paper No. 75-69, Pasadena, California, January 1975.

14. Roos, F. W. and Riddle, D. W., "Measurements of Surface-Pressure and Wake-Flow Fluctuations in the Flowfield of a Whitcomb Supercritical Airfoil," NASA TN D-8443, 1977.

15. Riddle, D. W., "Wind-Tunnel Investigation of Surface-Pressure Fluctuations Associated with Aircraft Buffet," AIAA Paper No. 75-67, January 1975.

16. Benepe, D. B., Cunningham, A. M., Jr., and Dunmyer, W. D., "A Detailed Investigation of Flight-Buffeting Response at Subsonic and Transonic Speeds," AIAA Paper No. 74-358, Las Vegas, Nevada, April 1974.

17. Benepe, D. B., Cunningham, A. M., Jr., Traylor, S., Jr., and Dunmyer, W. D., "Update on an Investigation of Flight Buffeting Response of a Variable Sweep Aircraft," AIAA Paper No. 75-68, Pasadena, California, January 1975.

18. Hwang, C., and Pi, W. S., "Transonic Buffet Behavior of Northrop F-5A Aircraft," AGARD Report 624, September 1974.

19. Dods, Jules B., Jr., and Hanly, Richard D., "Evaluation of Transonic and Supersonic Wind-Tunnel Background Noise and Effects on Surface Pressure Fluctuation Measurements," AIAA Paper No. 72-1004, Palo Alto, California, September 1972.

20. Jones J. G., "A Survey of the Dynamic Analysis of Buffeting and Related Phenomena," Royal Aircraft Establishment, RAE TR 72197, England, February 1973.

21. Cosenza, C. J. and Kummeth, L. J., "Transonic Aircraft Technology (TACT) Program," AIAA Paper No. 74-620, July 1974.

22. Coe, C. F., Chyu, W. J., and Dods, J. B., Jr., "Pressure Fluctuations Underlying Attached and Separated Supersonic Turbulent Boundary Layers and Shock Waves," AIAA Paper No. 73-996, 1973.

23. Ericsson, L. E. and Reding, J. P., "Dynamic Stall Analysis in Light of Recent Numerical and Experimental Results," AIAA Paper No. 75-26, 1975.

24. Mullans, R. E. and Lemley, C. E., "Buffet Dynamic Loads During Transonic Maneuvers," AFFDL-TR-72-46, September 1972.

Table 1.- Wind-off Frequencies of Primary Vibration
Modes of 1/6-scale F-111A Model at Λ = 26°

Vibration Mode	Frequency, Hz
1st Wing Bending	27
2nd Wing Bending	98
1st Wing Torsion	189
2nd Wing Torsion	284

Table 2.- Wind-off Frequencies of Primary Vibration
Modes of 1/6-scale TACT Models at Λ = 26°

Vibration Mode	Frequency, Hz	
	Steel	Aluminum
1st Wing Bending	20.0	25.3
2nd Wing Bending Coupled with Tail Bending	89.4	*
2nd Wing Bending	95.9	98.9
2nd Wing Bending Coupled with Tail Torsion	116.0	*
1st Wing Torsion	140.0	156.0
3rd Wing Bending	234.0	240.0
2nd Wing Torsion	256.0	*
*Not identified		

Table 3.- Computed and Ground Vibration Test Frequencies of Identified Vibration
Modes on the F-5A Aircraft

Modes	Computed F(Hz)	Ground Vibration Test Frequency (Hz)	Description of Motion
1	4.049	4.45	1st Wing Bending, Fuselage Bending (wingtip and fuselage nose are out of phase)
2	6.522	6.60	1st Wing Torsion
3	8.378	10.2	1st Fuselage Bending, Wing Bending (wingtip and fuselage nose are in phase)
4	16.983	17.20	1st Horizontal Stabilizer Bending
5	18.850	18.40	2nd Wing Bending, Fuselage Bending (wingtip and fuselage nose are out of phase)
6	21.989		2nd Fuselage Bending, Wing Bending, (wingtip and fuselage nose are in phase)
7	31.037		3rd Fuselage (Forward Fuselage) Bending
8	36.620		2nd Wing Torsion, Forward Fuselage Bending
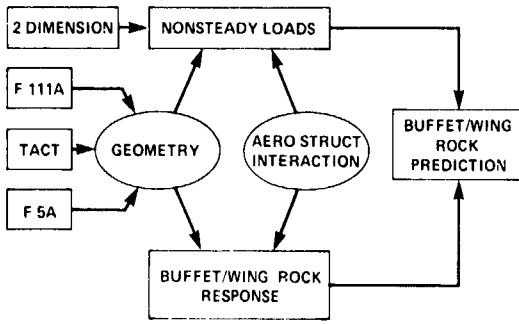
Fig. 1   Scope of buffet research at NASA Ames Research Center.

Fig. 2   1/6-scale semispan model of F-111A.

○ UPPER SURFACE OF WING
◇ LOWER SURFACE OF WING
◇ UPPER AND LOWER SURFACE

SPAN STATION, η	273	438	602	768	932
SPAN AREA, S (M²)	140	117	098	080	054
MOMENT ARM, ι (M)	144	415	685	956	1 227

Fig. 4   Location of mean and dynamic instrumentation on 1/6-scale of F-111A model.
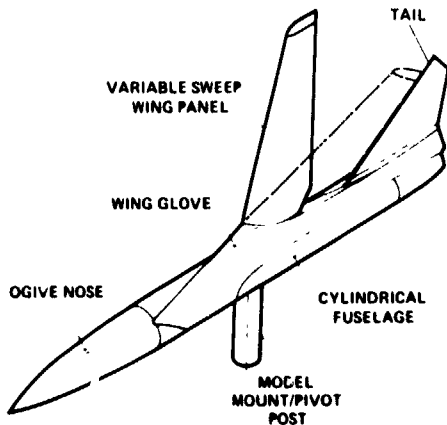
SEMISPAN GEOMETRY	F 111A		F 111 TACT		HORIZONTAL TAIL	
	PIVOT	TIP	PIVOT	TIP	ROOT	TIP
ι	1 0	-3 0	1 0	6 5	0	0
t/c	10 7%	9 8%	10 2%	5.4%	4 0%	3 0%
AIRFOIL	NACA 64.3		SUPERCRITICAL		BICONVEX	
S	0 677 m² (7 29 ft²)		0 779 m² (8 39 ft²)		0 23 m² (2 42 ft²)	
b	1 60 m (5 25 ft)		1 51 m (4 94 ft)		0 42 m (1 38 ft)	
c̄	0 460 m (1 51 ft)		0 532 m (1 75 ft)		0 58 m (1 91 ft)	
AR	7 56		5 83		1 54	
TR	0 325		0 541		0 334	
I	1 0		0		-1 0	
λ_{LE}	16 to 72		16 to 58		57 5	

Fig. 3   Geometry of 1/6-scale semispan F-111A and TACT models.

Fig. 5   Mean and fluctuating pressures on 1/6-scale F-111A model at η = 0.602 for Λ = 26°, M = 0.85.
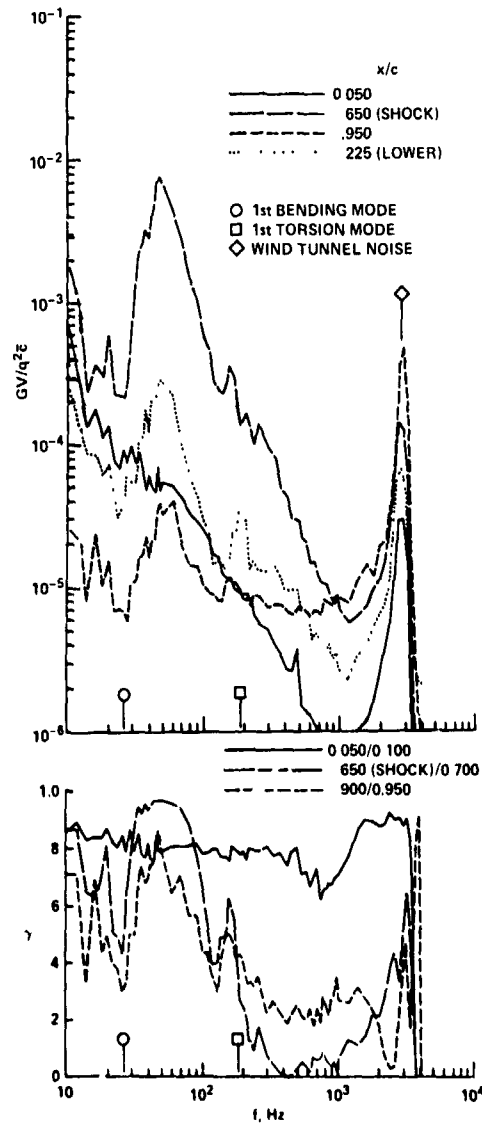
Fig. 6 Power spectra and coherence of pressure fluctuations on 1/6-scale F-111A model at η = 0.602 for Λ = 26°, M = 0.85, α = 0°.
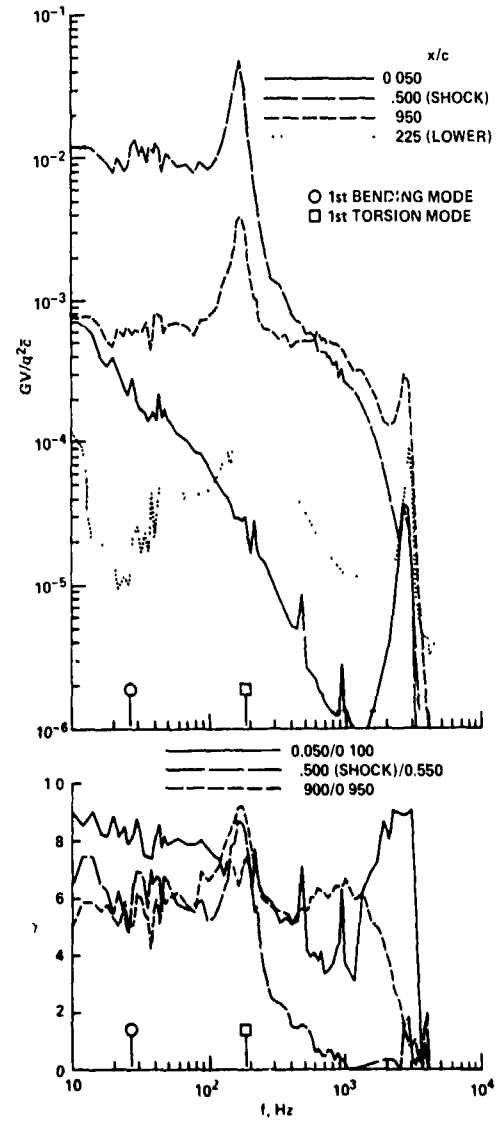
Fig. 7 Power spectra and coherence of pressure fluctuations on 1/6-scale F-111A model at η = 0.602 for Λ = 26°, M = 0.85, α = 4.0°.
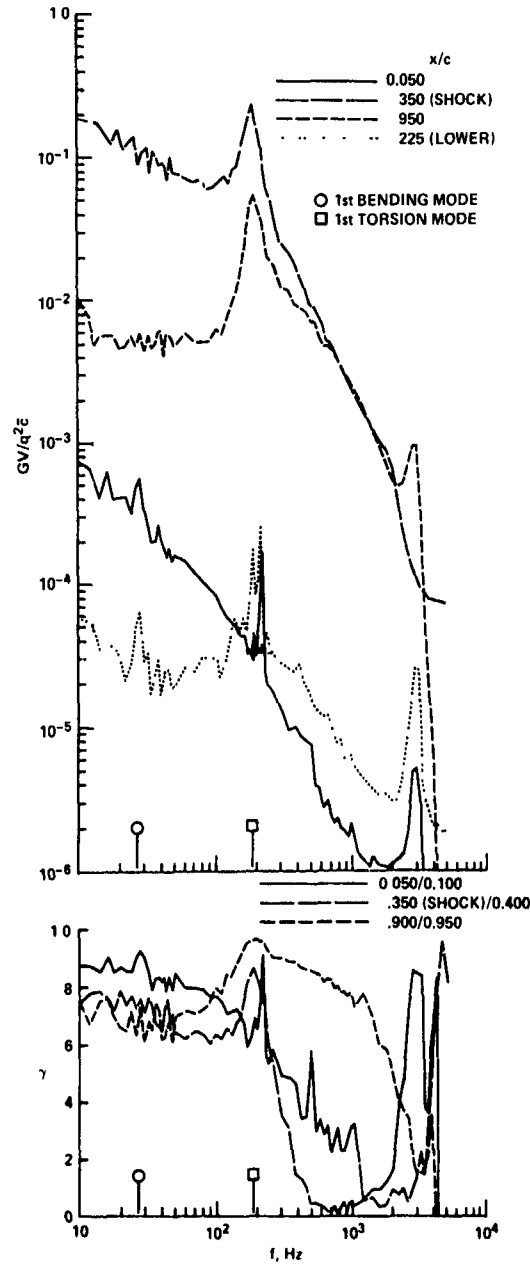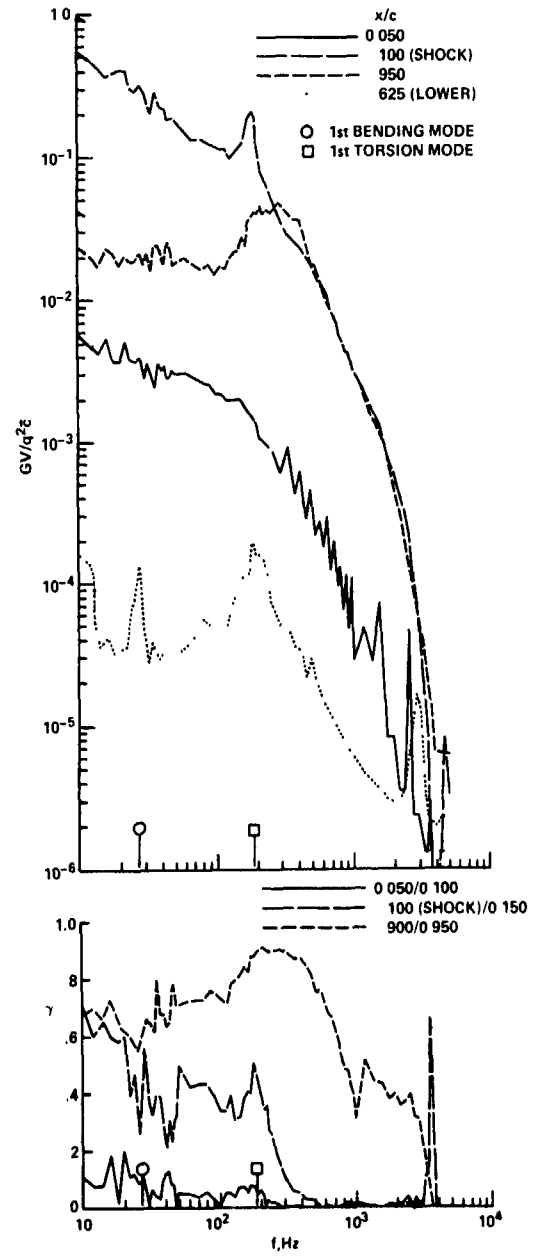
Fig. 8 Power spectra and coherence of pressure fluctuations on 1/6-scale F-111A model at η = 0.602 for Λ = 26°, M = 0.85, α = 9.1°.
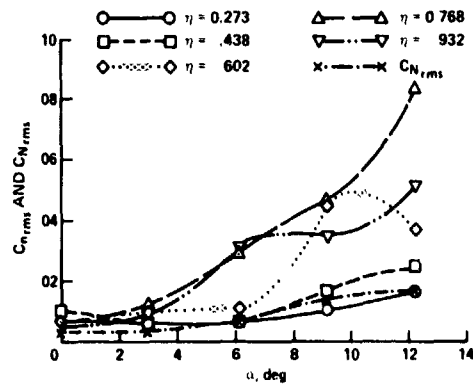

Fig. 9 Power spectra and coherence of pressure fluctuations on 1/6-scale F-111A model at η = 0.602 for Λ = 26°, M = 0.85, α = 12.2°.

Fig. 10 Fluctuations of section and total normal force on 1/6-scale F-111A model for Λ = 26°, M = 0.85.
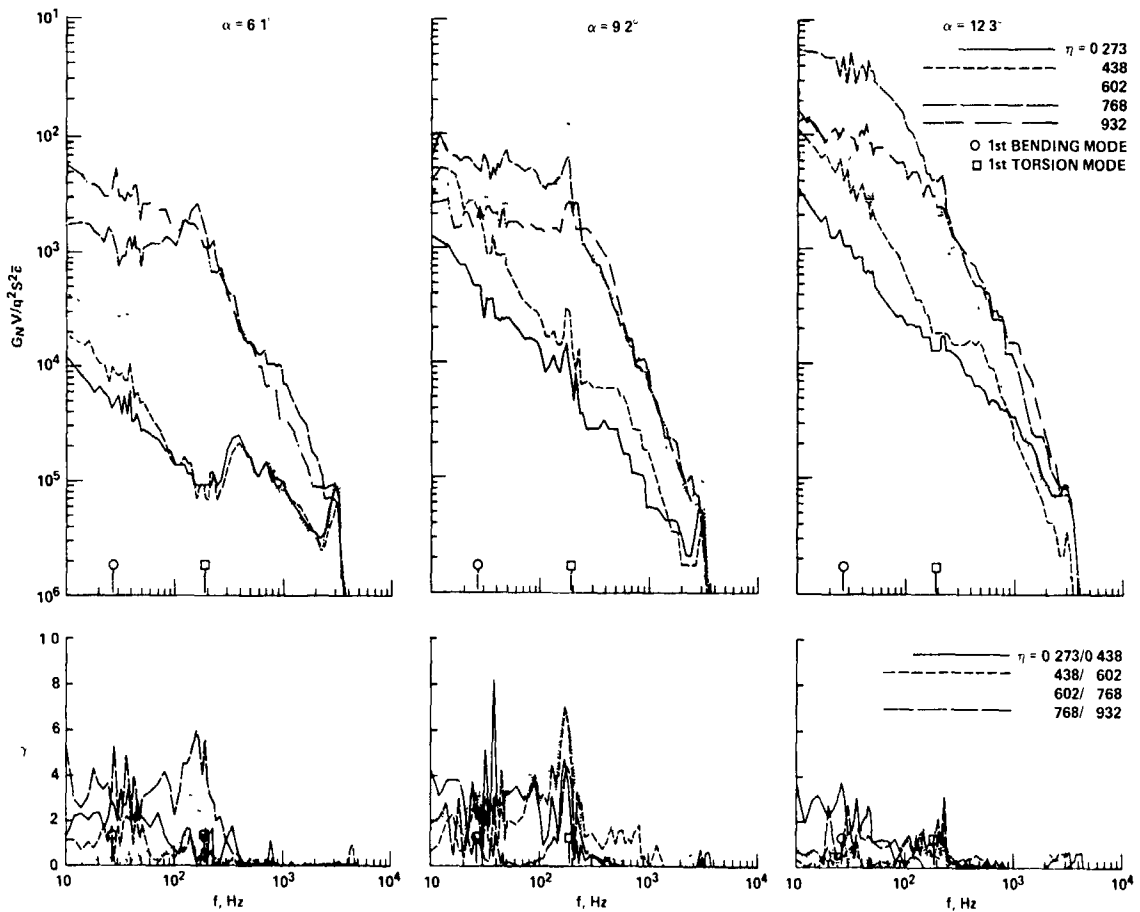
Fig. 11   Power spectra and coherence of section normal-force fluctuations on 1/6-scale
F-111A model for $\Lambda = 26°$, M = 0.85.
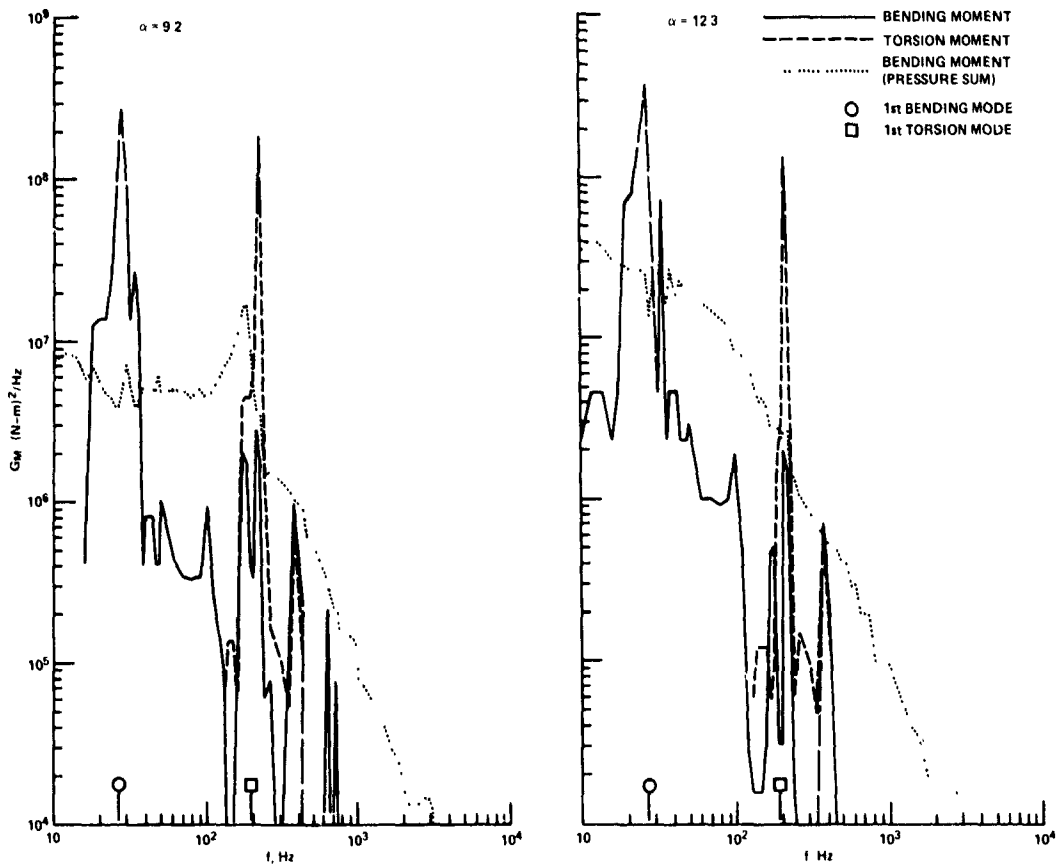
Fig. 12   Power spectra of fluctuating bending and torsional moments and bending moment derived from
fluctuating pressure summations on 1/6-scale F-111A model for $\Lambda = 26°$, M = 0.85.

W T. MODELS — LEFT WING PANEL
50 TRANSDUCERS
ALL SYMBOLS

AIRCRAFT — RIGHT WING PANEL
25 TRANSDUCERS
FILLED SYMBOLS

○ UPPER SURFACE
◇ LOWER SURFACE
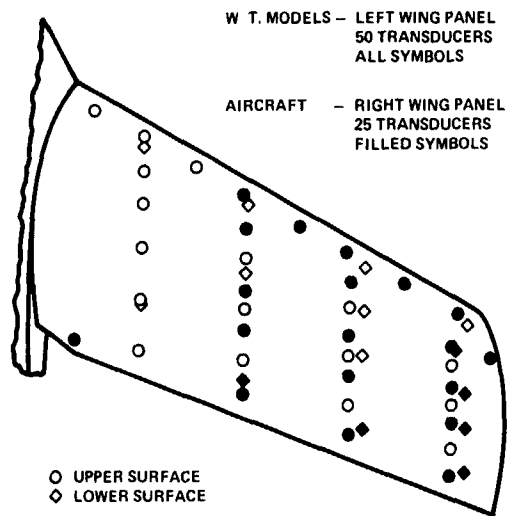
Fig. 13 Locations of TACT dynamic pressure transducers.

STEEL WING
$\alpha_p = 9'$

ALUMINUM WING
$\alpha_p = 9'$

STEEL WING
$\alpha_p = 12$

ALUMINUM WING
$\alpha_p = 12'$
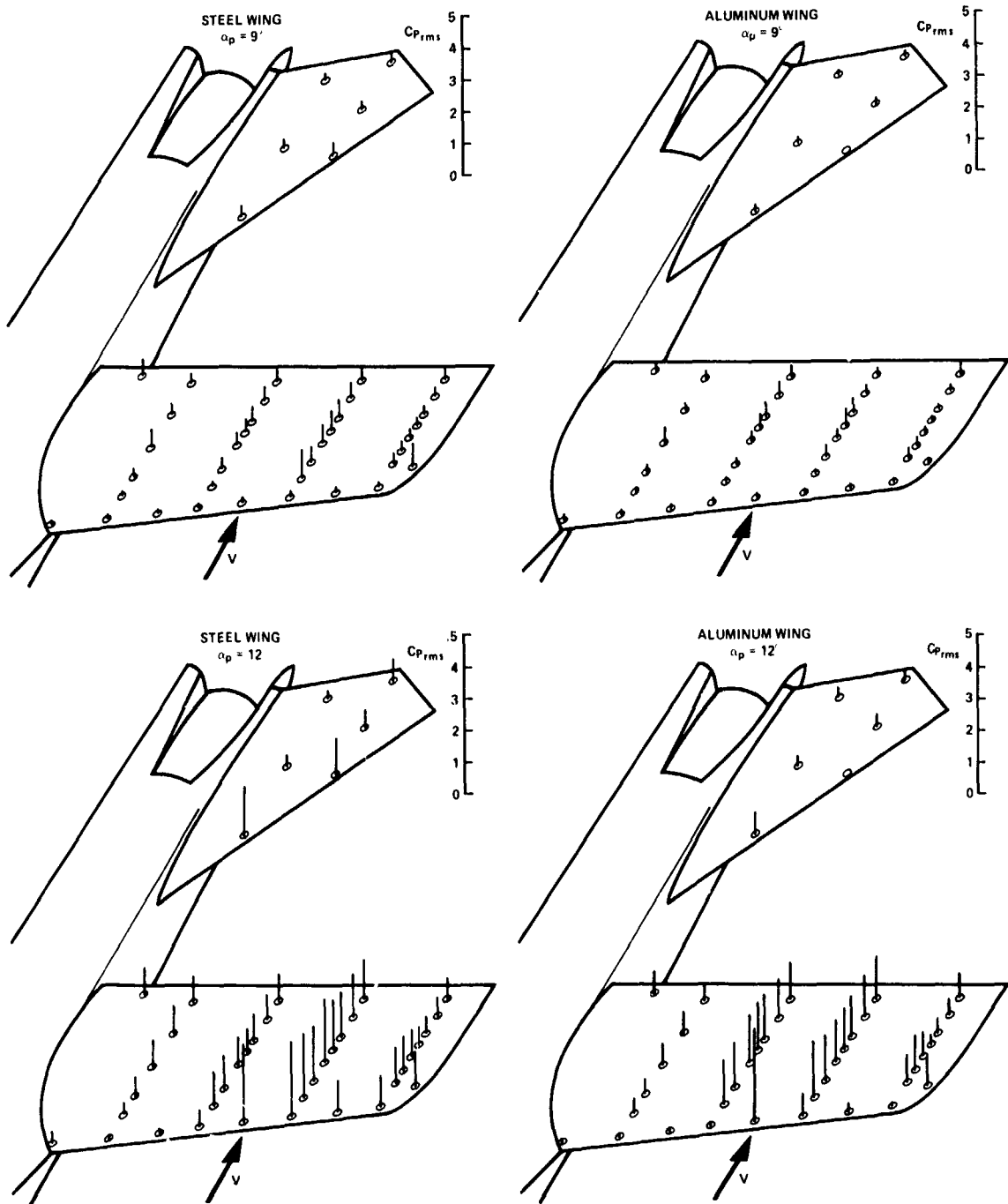
Fig. 14 Fluctuating pressures on 1/6-scale TACT models for $\Lambda = 26°$, M = 0.80, R = 10.5 x 10^6.
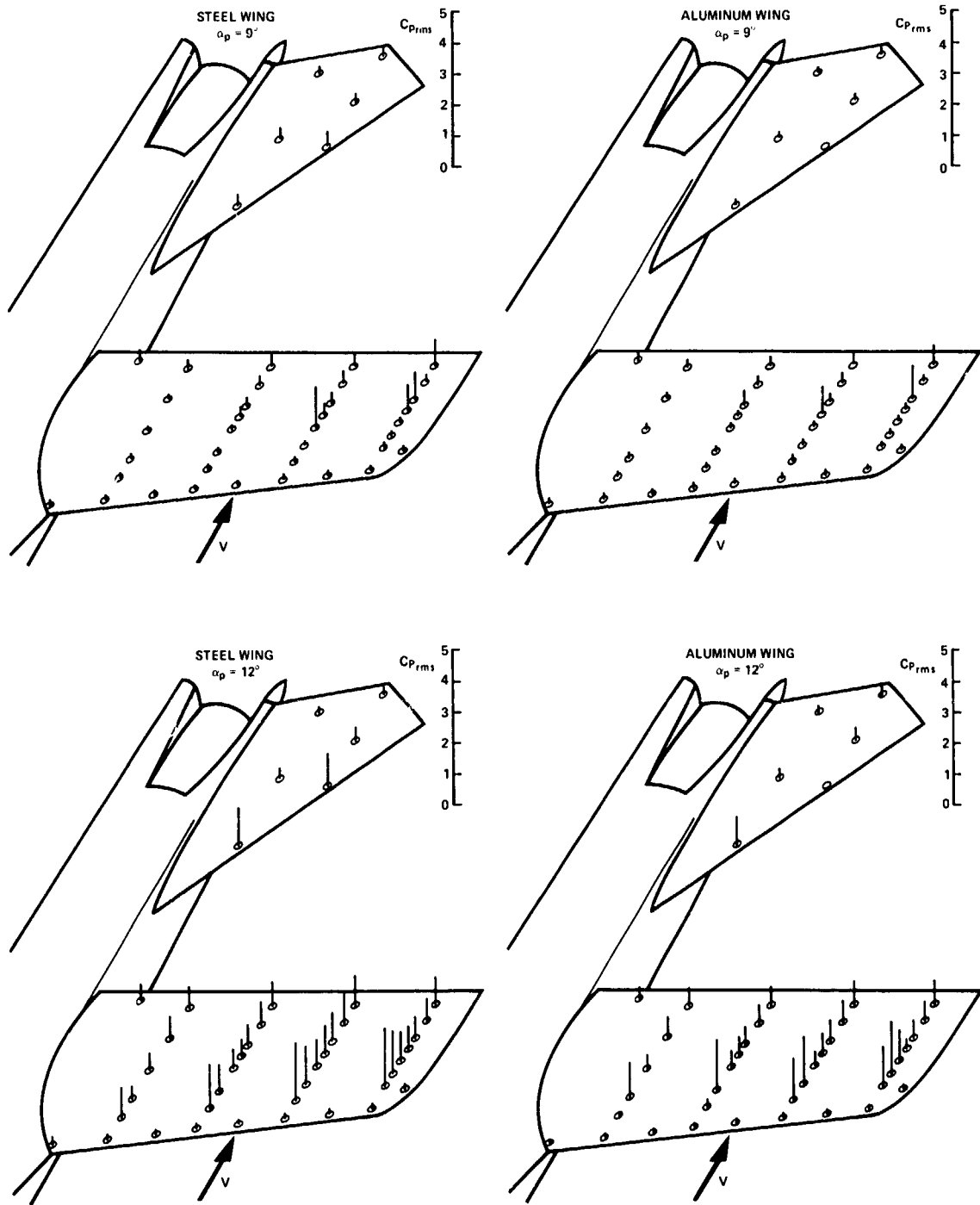
Fig. 15 Fluctuating pressures on 1/6-scale TACT models for $\Lambda = 26°$, M = 0.90, R = 10.5 x 10^6.
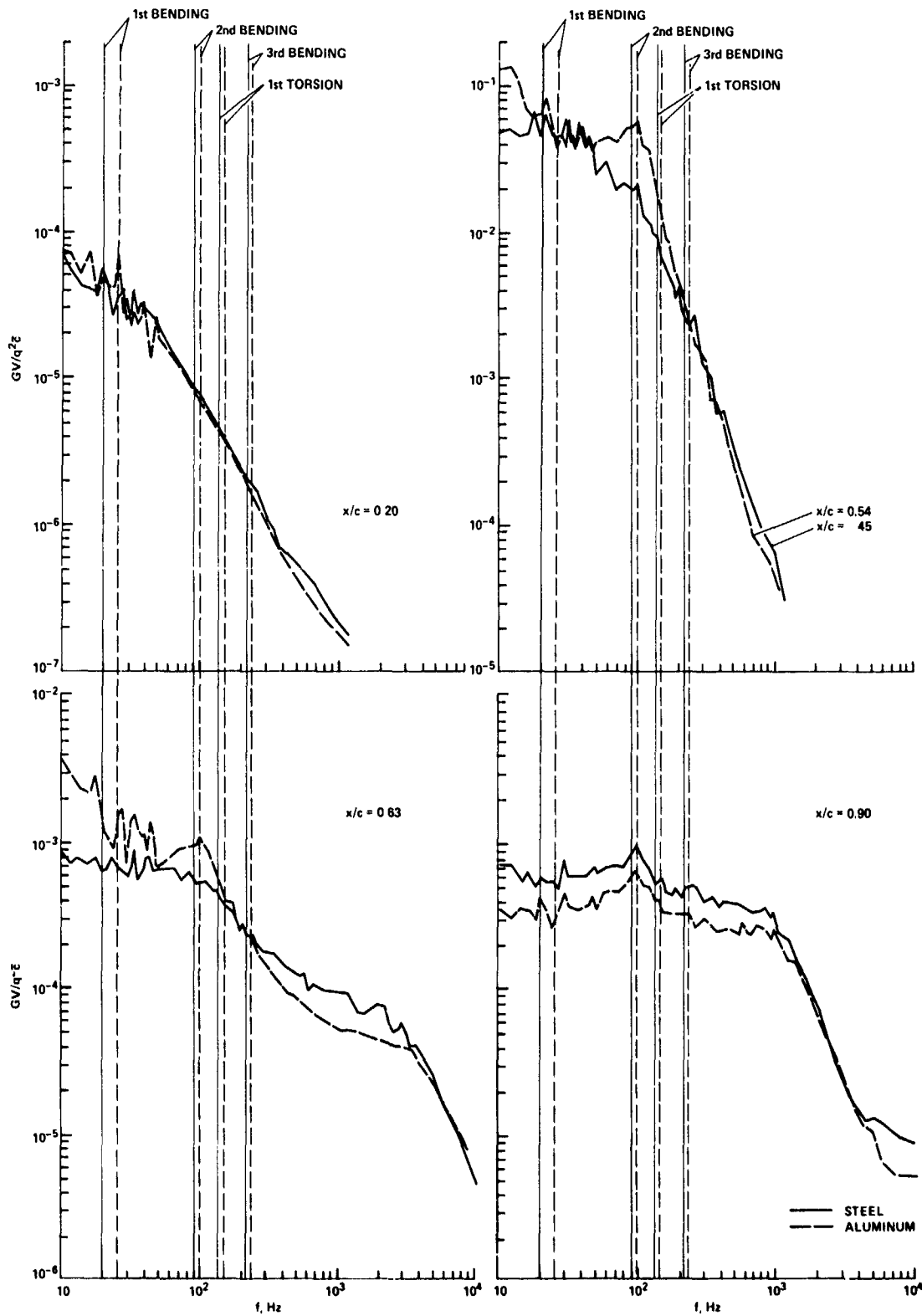
Fig. 16 Power spectra of pressure fluctuations on 1/6-scale TACT models at η = 0.744 for Λ = 26°, R = 10.5 x 10⁶, M = 0.90, α_p = 9°.
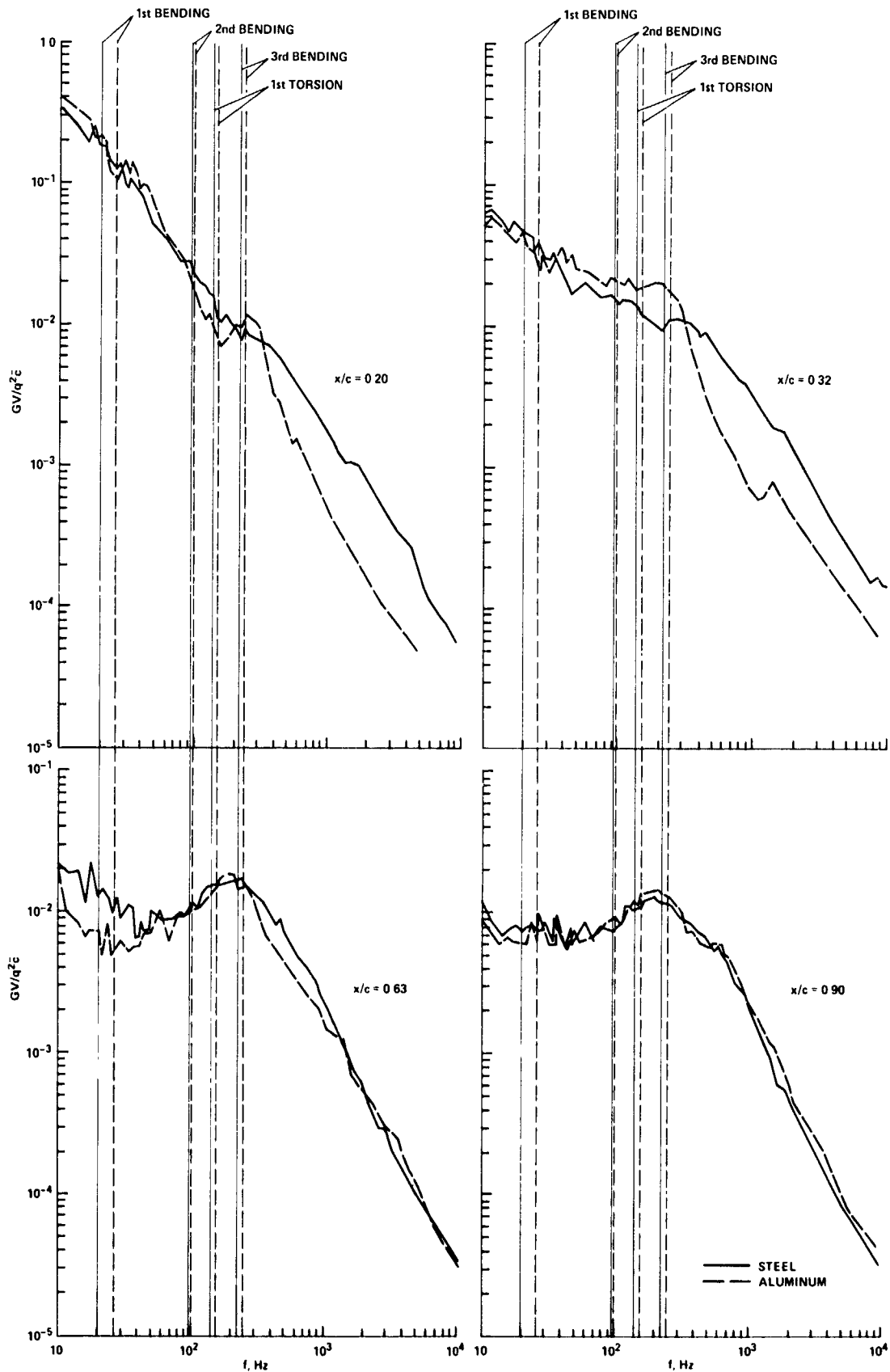
Fig. 17 Power spectra of pressure fluctuations on 1/6-scale TACT models at
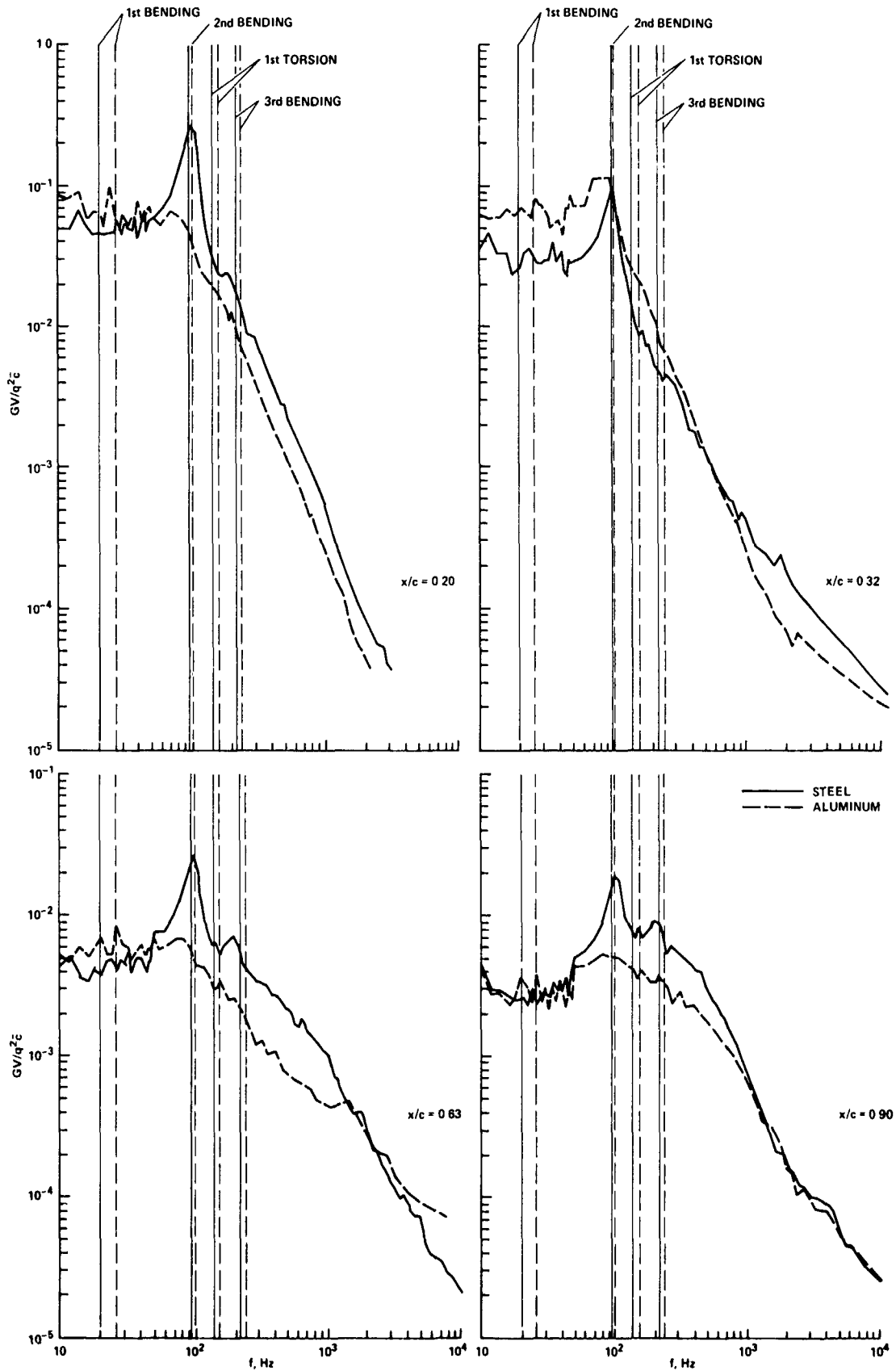$\eta = 0.744$ for $\Lambda = 26°$, $R = 10.5 \times 10^6$, $M = 0.80$, $\alpha_p = 12°$.

Fig. 18   Power spectra of pressure fluctuations on 1/6-scale TACT models at
$\eta = 0.744$ for $\Lambda = 26°$, $R = 10.5 \times 10^6$, $M = 0.90$, $\alpha_p = 12°$.
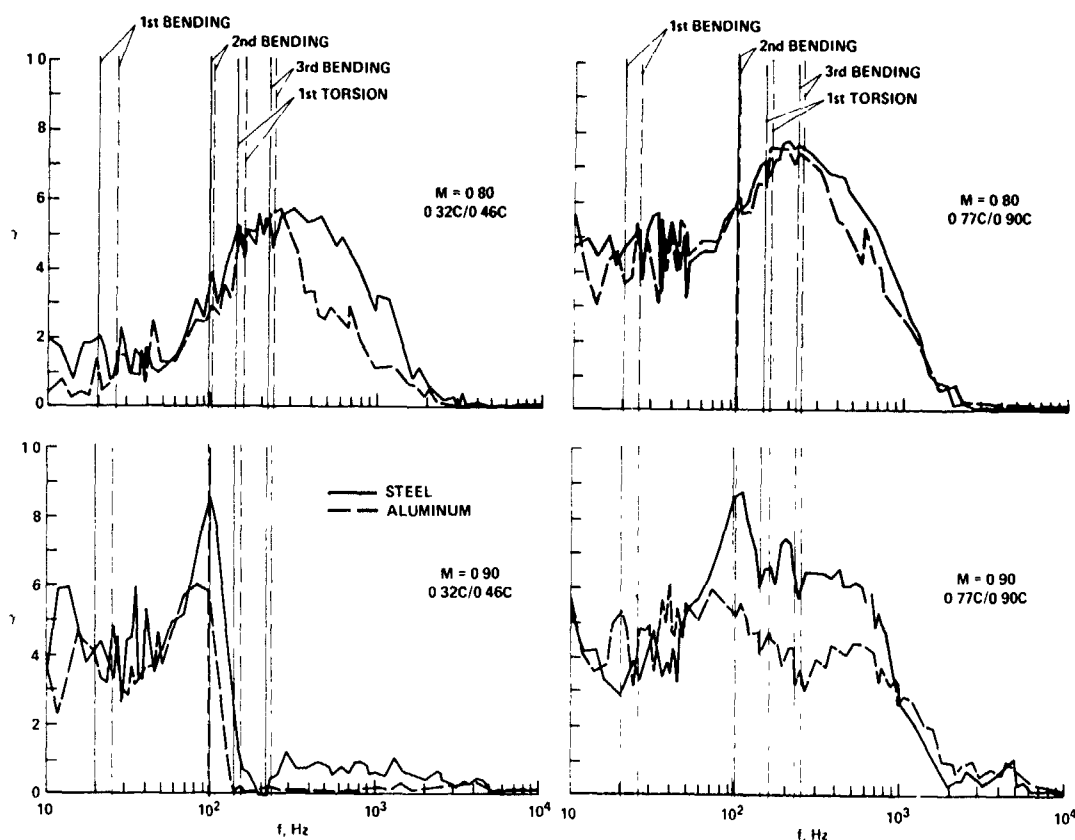
Fig. 19 Coherence of pressure fluctuations on 1/6-scale TACT models at
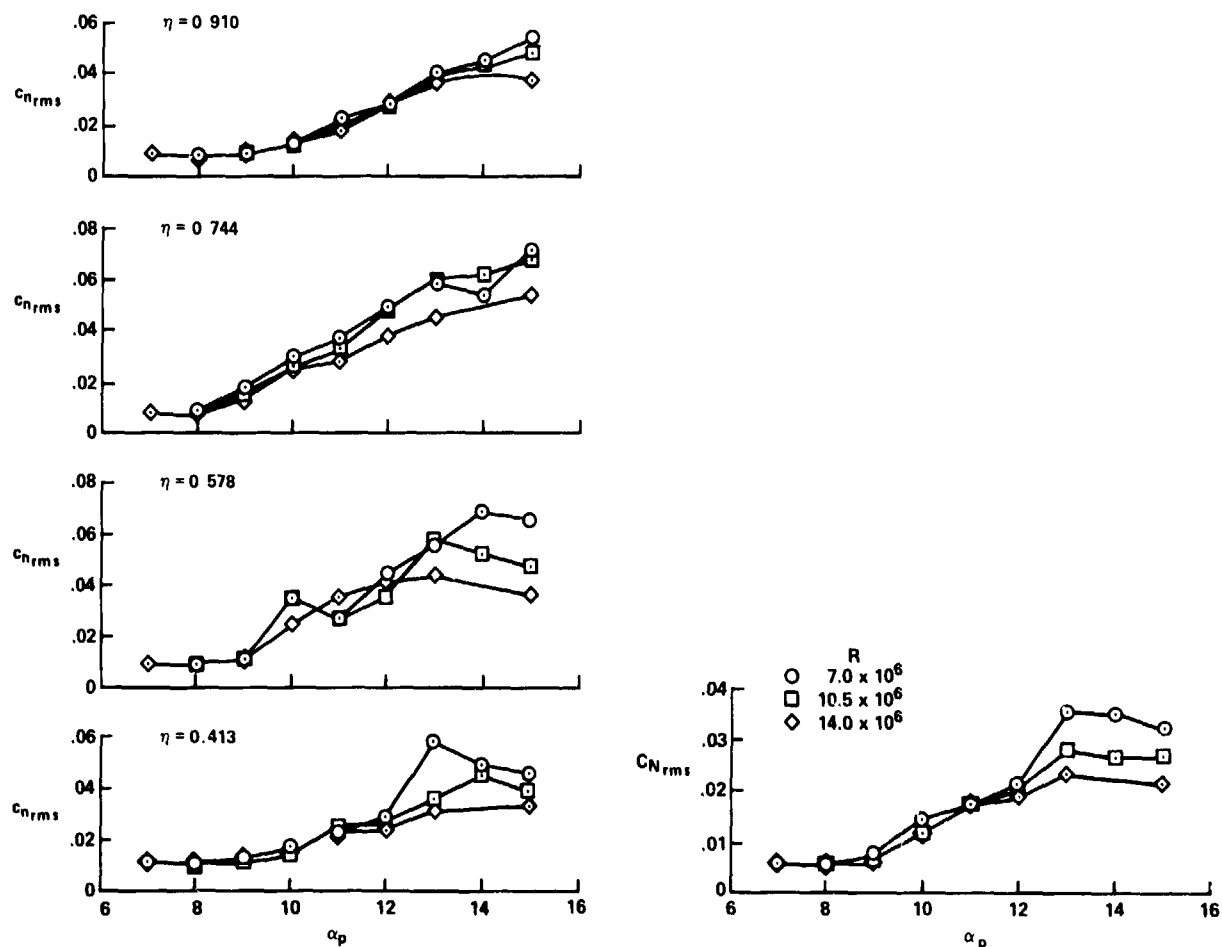$\eta = 0.744$ for $\Lambda = 26°$, $R = 10.5 \times 10^6$, $\alpha_p = 12°$.

Fig. 20 Fluctuations of section and total normal force on 1/6-scale steel TACT model for various Reynolds
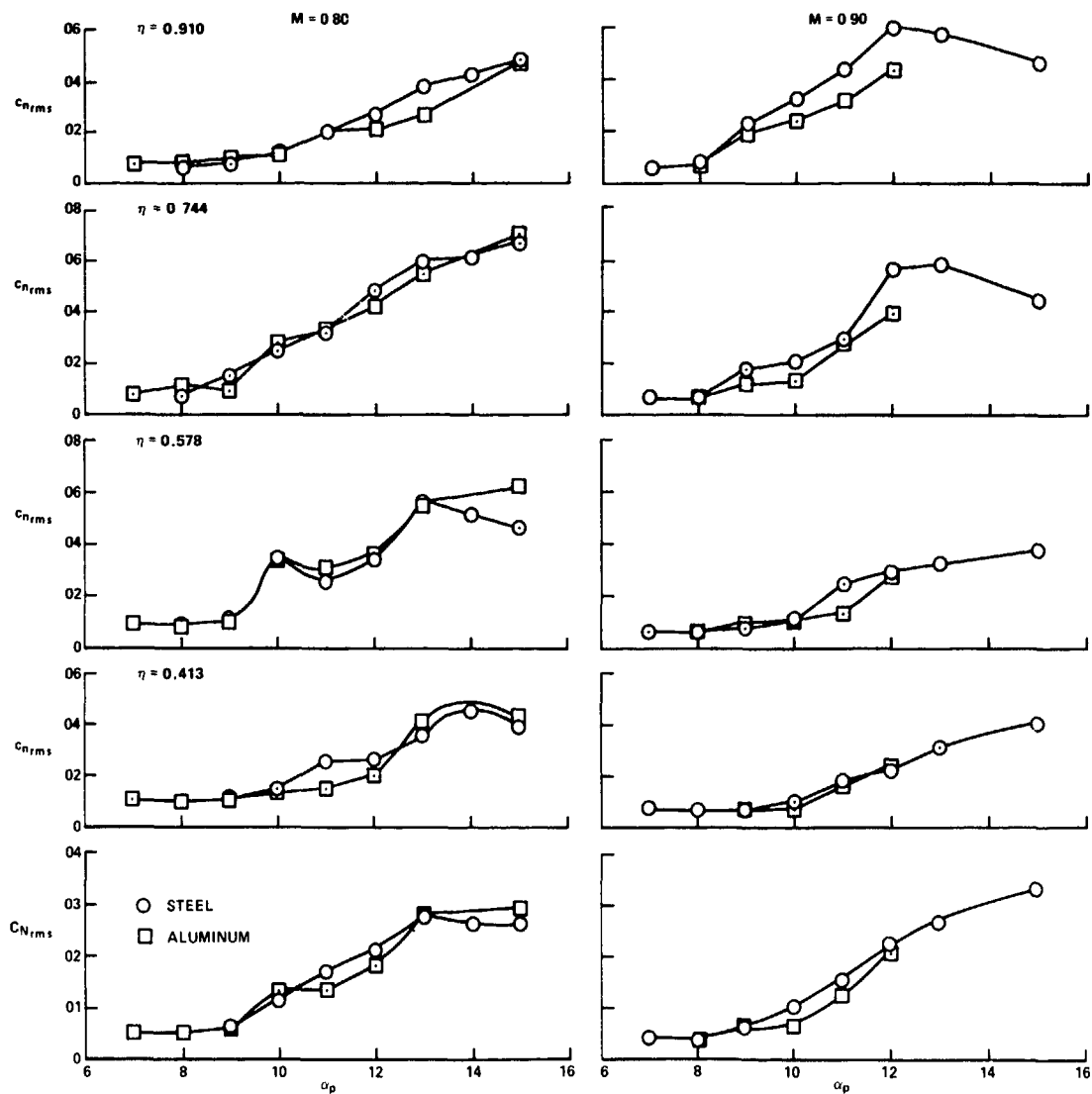numbers at $\Lambda = 26°$, $M = 0.80$.

Fig. 21 Comparison of fluctuations of section and total normal force on 1/6-scale steel and aluminum TACT models at $\Lambda = 26°$, $R = 10.5 \times 10^6$.
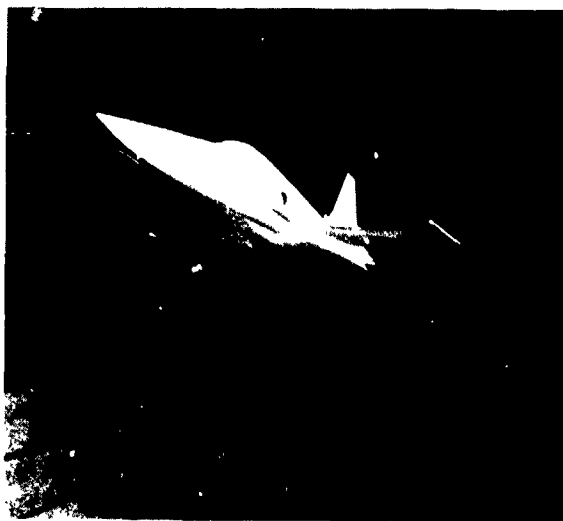

Fig. 22 1/7-scale model of F-5A installed in the Ames 11- by 11-Foot Transonic Wind Tunnel.

AIRFOIL SECTION   NACA 65A004 8 (MODIFIED)
AREA (REFERENCE)   15 79 m^2 (170 00 ft^2)
SPAN (CLEAN TIPS)   7 696 m (25 25 ft)
ASPECT RATIO   3 75
TAPER RATIO   20
SWEEPBACK (25% CHORD)   24
MEAN AERODYNAMIC CHORD   2 356 m (7 73 ft)
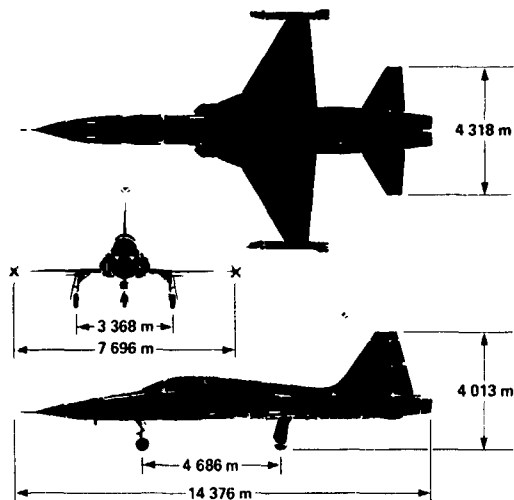DIHEDRAL ANGLE   0
INCIDENCE ANGLE   0

Fig. 23 Basic dimensions of F-5A.
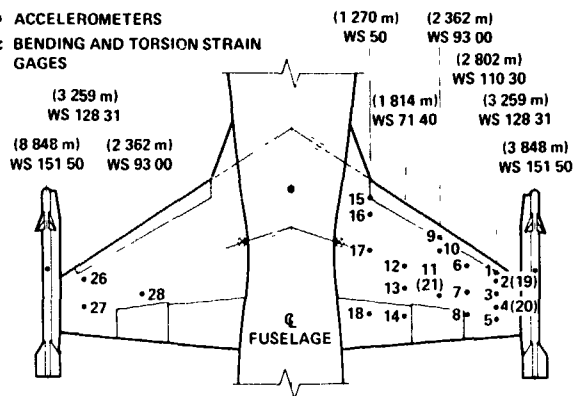
Fig. 24 Locations of dynamic instrumentation on F-5A.
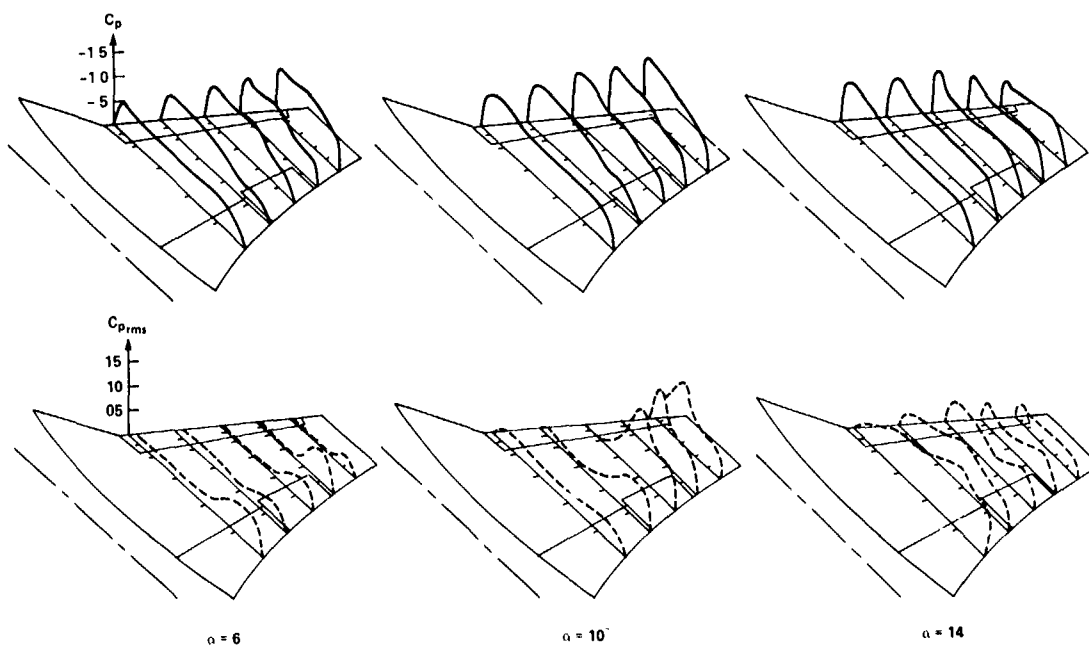
Fig. 25 Mean and fluctuating pressures on 1/7-scale model of F-5A at M = 0.925, R = 2.49 x 10^6.
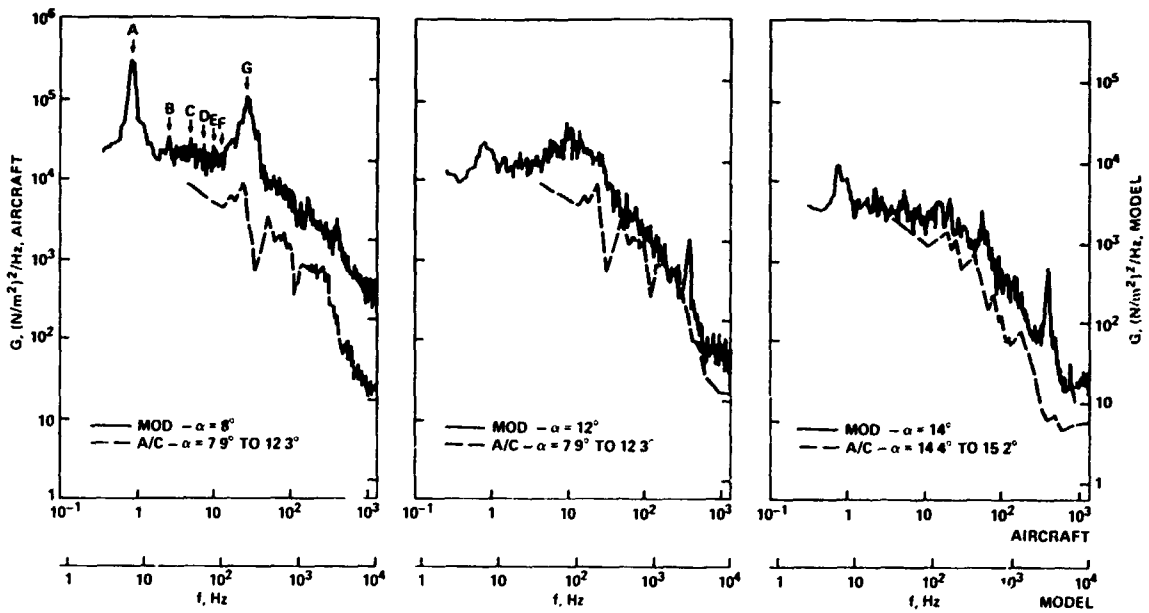
Fig. 26 Comparison of power spectra of pressure fluctuations on F-5A 1/7-scale model and aircraft from transducer 2 at M = 0.75, R_{mod} = 4.71 x 10^6, R_{flt} = 18.9 x 10^6.
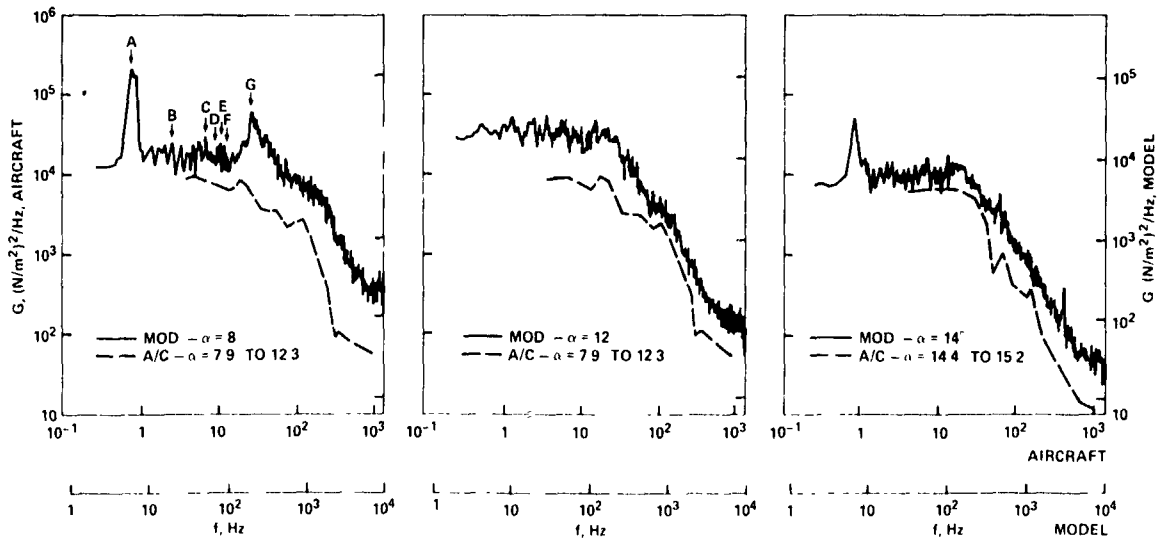
Fig. 27 Comparison of power spectra of pressure fluctuations on F-5A 1/7-scale model and aircraft from transducer 5 at M = 0.75, R_{mod} = 4.71 x 10^6, R_{flt} = 18.9 x 10^6.
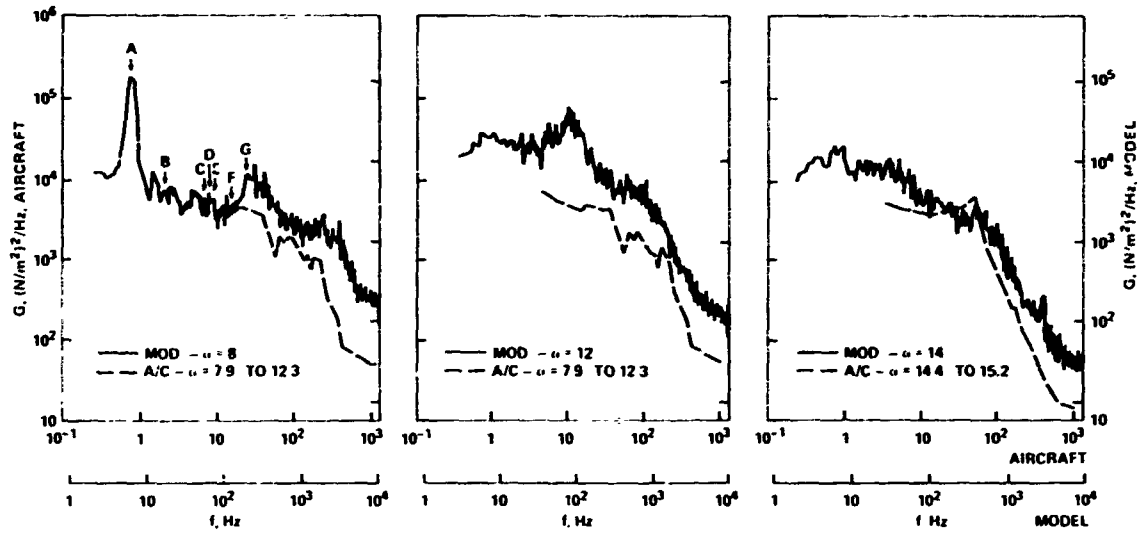
Fig. 28 Comparison of power spectra of pressure fluctuations or F-5A 1/7-scale model and aircraft from transducer 11 at M = 0.75, R_{mod} = 4.71 x 10^6, R_{flt} = 18.9 x 10^6.

A STING AND BALANCE BENDING, 6.6 Hz
B BALANCE ROLL, 13 6 Hz
C MODEL WING 1st SYMMETRICAL BENDING, 53 5 Hz
D RIGID ROLL PLUS WING ANTI SYMMETRICAL BENDING, 62 Hz
E WING ANTI SYMMETRICAL BENDING, 83 7 Hz
F STING AND SUPPORT SYSTEM TORSION, 105 Hz
G WING 2nd SYMMETRICAL BENDING, 170 Hz
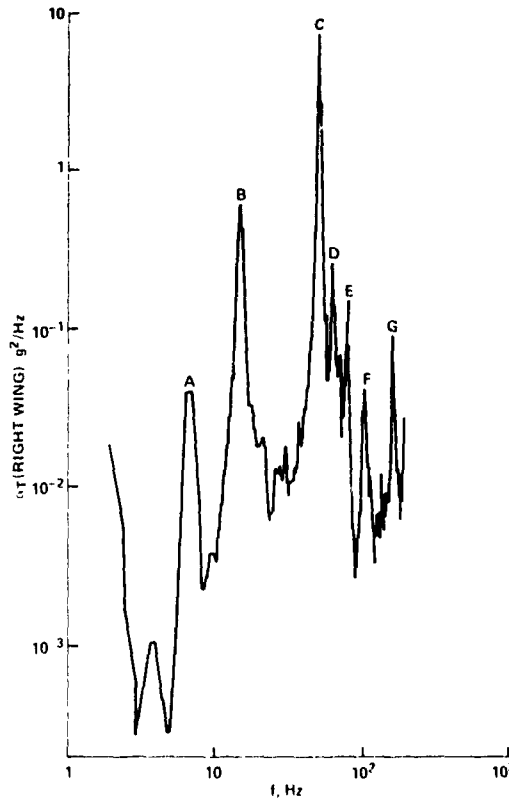
Fig. 29 Power spectral density of right wing tip
acceleration on 1/7-scale F-5A model at
M = 0.75, α = 8°, R = 4.71 x 10^6.

PREDICTION OF TRANSONIC AIRCRAFT BUFFET RESPONSE

Atlee M. Cunningham, Jr., Project Structures Engineer
David B. Benepe, Sr., Design Specialist, Aerodynamics
General Dynamics' Fort Worth Division, Fort Worth, Texas 76101 U.S.A.

SUMMARY

A method for predicting aircraft buffet response is briefly reviewed in this paper. Rigid wind tunnel model fluctuating pressure data are used to form buffet forcing functions to which airplane responses are calculated with a mathematical dynamic model of the airplane. Buffet pressure data on the wing are used to estimate fluctuating loads on the horizontal tail. By including the extremes of phasing and contributions of symmetric and antisymmetric airplane responses, predicted upper and lower bounds are established.

The method is applied to a variable sweep fighter aircraft and predicted results are compared with flight test data. The types of buffeting flow considered for various wing sweep angles include separated and vortex flows as well as oscillating shocks. The current method is compared with three other methods in the correlation with flight test data. The inherent scatter of flight data is discussed as well as probable sources of the scatter. A mechanism is described by which wing torsional motion and shock oscillation couple to produce relatively severe buffeting conditions at a forward wing sweep. The importance of considering buffet fatigue damage on secondary structure is discussed.

SYMBOLS

b_r	reference length
$\overline{F}_r$	aerodynamic loading due to the rth mode
$\overline{F}_B$	aerodynamic loading due to the buffeting pressure field
$h_r(x,y)$	deflection of the rth mode at point x, y
$\sigma_m(x,y)$	mass concentrated at point x, y
M	free stream Mach number
M_{rs}	generalized mass in the modal coordinates for the airplane dynamic model
N_0	characteristic frequency (frequency centroid of the power spectral density distribution)
q	free stream dynamic pressure
$\overline{q}_r$	generalized coordinate
Q_{rs}	generalized force in the rth mode due to aerodynamics in the sth mode
Q_{r_B}	generalized force in the rth mode due to the buffeting pressure field
α	wing angle of attack
$\Delta p(x,y,\omega)$	buffeting pressure amplitude at point x, y and frequency ω
$\theta_{ij}(\omega)$	phase angle between points i and j for the buffeting pressure field at frequency ω
Λ	wing sweep angle
$\phi_i(\omega)$	power spectra of the buffeting pressure field at point i and frequency ω
ω	circular frequency

1. INTRODUCTION

The design of a highly maneuverable fighter aircraft that operates well beyond the buffet onset boundary must take into account the high angle of attack buffet character-istics of that aircraft in order to maximize its effectiveness as a weapons system. These characteristics impose limits in addition to those defined by strength and stability requirements. The limiting factors are varied, as discussed by John[1], and may include vibration levels and frequencies at critical airframe locations where such items as a tracking radar antenna or a gyro might be located. Less quantifiable limits are those established by environmental requirements at the pilot's seat or by structural fatigue of certain structural members. Although buffet does not normally cause fatigue problems with primary structures, secondary structures, especially leading and trailing edge sections of wings, fins, or tails and control surfaces, are highly susceptible to buffet-ing loads. As a result, the designer is faced with "grey area" design constraints caused by buffet that are analogous to ride quality requirements with respect to atmospheric turbulence. More importantly, however, the designer does not have adequate tools avail-able for predicting buffet characteristics without resorting to some sort of wind tunnel experiment. Thus, buffet considerations are difficult to include in preliminary aircraft design. Their impact is not usually felt until the airplane is in the detailed design stage or later, hence the improvement of buffet characteristics is often accomplished with "add-on" fixes such as leading edge slats or vortex generators.

John[1] has presented a survey of the various methods available in Europe for pre-dicting transonic buffet characteristics beyond buffet onset. A more recent European development is the method proposed by Jones[2] and applied by Butler and Spavins[3]. This method makes use of force model test results (which are usually available at an early stage in the design process) to predict the buffet characteristics of a full scale air-plane. All of these methods require wind tunnel model testing of some kind.

Methods which have been developed in the USA are similar to those in Europe in that wind tunnel model testing is required. The testing of a dynamically scaled model was performed by Hanson[4] in order to obtain buffet data which he extrapolated to full scale. The methodology developed by Mullans and Lemley[5] makes use of fluctuating pressure data to form a buffet forcing function to which airplane response is calculated. This method is similar to that outlined by John[1] except that it accounts for aerodynamic forces due to airplane response only through a viscous damping coefficient unique to each natural mode. John's approach correctly considers aerodynamic forces due to displacement, velocity, and acceleration of the lifting surfaces.

The method presented in this paper[6,7] is similar to that of Mullans and Lemley, but is more closely related to that of John. Fluctuating pressure data obtained from a rigid scaled wind-tunnel model[8] is used to predict full scale buffet response. The pre-diction method requires unsteady aerodynamic forces due to airplane response, and natural airplane modes of vibration. A gust response computer program is used to calculate buffet response due to the forcing function which has been obtained from the fluctuating pressure data. A unique feature of the prediction method is the definition of upper and lower bounds on full scale - buffet response. Symmetric and antisymmetric responses are com-bined to form these bounds for both power spectral densities and RMS values of response as a function of angle of attack and Mach-altitude-sweep conditions. The effects of static aeroelasticity and horizontal tail loads are included and discussed.

An extensive comparison of the predicted bounds with flight test results is given in this paper to verify the method's capability. Correlation with flight test is compared with similar results from References 3, 4 and 5. The statistical nature of buffet is examined in order to account for the scatter of flight test data encountered in this and other investigations. A mechanism is described in which wing torsion-motion couples with normal shock oscillation on the wing to produce a relatively severe buffeting condition at a forward wing sweep. Finally, the importance of buffet on the fatigue life of secondary structure is discussed.

2. THE BUFFET PREDICTION METHOD

The prediction method presented in this paper is an outgrowth of a wind-tunnel study conducted at the NASA Ames Research Center to determine the nature of fluctuating pressures during buffeting flow at subsonic and transonic speeds[8]. The wind tunnel model used was a rigid 1/6 scale semi-span model of a variable sweep fighter bomber. The wing could be swept from $16°$ to $72.5°$ and was heavily instrumented with high response pressure trans-ducers. Since it was desired to correlate the model data with flight test results, a supporting study was initiated at the Fort Worth Division of General Dynamics under Contract to the NASA ARC to collect and analyze flight test data and to develop and eval-uate a means for performing the correlations. Some results of the flight test data analysis were presented by the writers in References 9 and 10. These results were

invaluable in the development of the prediction method and are referred to throughout this paper.

2.1 Basic Assumptions

The fundamental assumption in the development of the method was that the buffeting forces are not coupled with airplane motion. Although it was known that torsional motion could couple with shock oscillations to produce very strong buffet, the above assumption was made as a matter of expediency in order to evaluate the importance of this or any other coupling mechanism that might exist under high-angle of attack buffeting conditions. These aspects will be discussed further in a later section of the paper.

Reynold's number effects were assumed negligible by necessity. Until cryogenic wind tunnels or some other form of high Reynold's number facilities are operational and practical, these effects cannot be considered in the prediction of full scale buffet response based on wind tunnel data of any form taken from small scale models. Ignoring these effects should add to the conservatism of the prediction method at high angles of attack. This speculation is based on some Reynold's number effects shown by John[1] and Butler and Spavins[3] as will be discussed later in the paper.

As a result of the above assumptions, the prediction of buffet response reduced to a problem which was identical to the prediction of gust response of a flexible airplane. Hence, the method was developed around an existing dynamic response procedure and its required input. The procedure solves the equations of motion for a total airplane subject to an arbitrary harmonic forcing function[11]. Rigid body as well as elastic modes are used in the model, hence the airplane must be aerodynamically balanced. The equations of motion are expressed in terms of the generalized coordinates, $\bar{q}_r$, in the following matrix form

$$\left| A_{rs} \right| \left| \bar{q}_r \right| = - \left| Q_{rf} \right| \tag{1}$$

where

$$A_{rr} = \left[1 - (\tfrac{\omega_r}{\omega})^2 (1+i\zeta_r) - i2\gamma_r(\tfrac{\omega_r}{\omega}) \right] M_{rr} + Q_{rr}, \ r=s$$

$$A_{rs} = M_{rs} + Q_{rs}, \ r \neq s$$

ω_r = undamped natural frequency of the rth normal mode

ζ_r = structural damping coefficient of the rth mode (assumed as $\zeta_r = 0.03$)

γ_r = ratio of viscous damping to critical damping

M_{rs} = generalized mass

Q_{rs} = generalized aerodynamic force

Q_{rf} = generalized forcing function

i = $\sqrt{-1}$

The M_{rs} and ; terms are defined as

$$M_{rs} = \frac{1}{4\rho b_r^3 \omega^2} \iint_A h_r(x,y)h_s(x,y)\sigma_m(x,y)\,dx\,dy \tag{2}$$

where

ρ = atmospheric density

b_r = reference length

A = configuration area

$h_t(x,y)$ = deflection of the tth mode at point x,y

$\sigma_m(x,y)$ = mass distribution per unit area at point x,y

and

$$Q_{rs} = \frac{-1}{4\rho b_r^3 \omega^2} \iint_A h_r(x,y)\, \Delta p_s(x,y,\omega)\,dx\,dy \tag{3}$$

where

ω = exciting frequency

$\Delta p_s(x,y,\omega)$ = pressure distribution amplitude induced at point x,y by the sth mode oscillating at frequency, ω.

For Q_{rs} terms, the pressure distributions are calculated with either the subsonic doublet lattice[12] or supersonic Mach box[13] method depending on Mach number. The Q_{rf} terms are computed with Equation 3, but the pressure distributions are obtained from the buffet pressure data as will be discussed in the next section. The natural modes of the airplane are calculated with a stiffness matrix method which uses a finite element model of the entire airplane[14]. Figure 1 shows the flow of data from input to final output.

2.2 The Buffet Forcing Function

The buffet forcing function is the unique ingredient in the prediction method which distinguishes it from conventional dynamic response methodology. Referring to Figure 1, the process of converting wind tunnel power spectral densities (PSD's) into a generalized forcing function is a three step process. First, the wind tunnel data is transformed into a complex pressure distribution over the wing for each frequency at which a PSD estimate is made. These pressures are used in conjunction with the doublet lattice unsteady aerodynamic matrices to calculate estimated pressures induced on the horizontal tail by downwash produced by the wing buffet pressures. Finally, the wing and tail pressures are used in the doublet lattice program to calculate the generalized forcing function terms, Q_{rB} and the $\overline{F}_B$ terms for shear, bending moment and torsion on the wing and tail.

The following paragraphs will describe, (1) the means by which static aeroelastic effects are accounted for, (2) the conversion of wind tunnel data, (3) the calculation of horizontal tail buffet pressures, and (4) the calculation of the Q_{rB} and $\overline{F}_B$ terms.

2.3 Calculation of Static Aeroelastic Effects

The wind tunnel buffet pressure data is obtained from a rigid model and hence does not represent the real world flexible airplane in flight. In order to approximately account for static aeroelastic effects, the rigid angle of attack values, α_{rig}, used in the wind tunnel tests are modified with the appropriate ratio of flexible to rigid lift coefficients taken from the theoretical aeroelastic analysis of the airplane being studied. Thus, the buffet response calculated for a given α_{rig} is used to predict airplane response at a value α_{flex} determined according to the Mach-altitude-sweep condition. Since the flexible to rigid wing lift coefficient ratio is always less than unity for this airplane, α_{flex} is always greater than α_{rig}. This technique provides an approximate account for static density effects only and not Reynold's number effects.

The inclusion of static aeroelastic effects adds a degree of realism although it is not exact as is done in the present method. It is assumed that static aeroelastic twist has no effect on the buffet pressures and that they are a function of total normal force on the wing. It is known for the subject airplane that static twist tends to soften the buffeting pressures, in particular those due to strong shock oscillation. Thus, predictions should still be conservative as will be shown by the results when compared to flight test data.

2.4 Conversion of Wind Tunnel Data

The wind tunnel data which are used to generate the buffet forcing functions are received on magnetic tape as collections of PSD's, cross-PSD's, phase angles, coherency functions and convection velocities. The data are available for multiple sets of three pressure transducers which are referred to as x, y and z. A complete coverage of the transducers on the wing is available for each Mach and angle of attack condition. A more complete description of this data and the wind tunnel program is given in Reference 8.

The PSD's, $\phi_m(\omega_i)$, and phase angles, $\theta_{mn}(\omega_i)$, are taken from the tapes and combined to obtain complex pressure distributions as illustrated in the following example. Consider the two-dimensional distribution in Figure 2 where six transducers are located along the chord. Because the data processing used at NASA ARC on the wind tunnel data requires that the data be composed of three items, three sets are used to describe the $\phi_m(\omega_i)$ and $\theta_{mn}(\omega_i)$ for the example. The first set translates to

$$(\phi_x, \phi_y, \phi_z)_1 = (\phi_1, \phi_2, \phi_3)$$
$$(\theta_{xy}, \theta_{xz}, \theta_{yz})_1 = (\theta_{12}, \theta_{13}, \theta_{23})$$

The second set to

$$(\phi_x\ ,\phi_y\ ,\phi_z\ )_2 = (\phi_3\ ,\phi_4\ ,\phi_5\ )$$
$$(\theta_{xy},\theta_{xz},\theta_{yz})_2 = (\theta_{34},\theta_{35},\theta_{45})$$

and so on where each term is a function of frequency. The ϕ_7 may be a repeat of ϕ_6 or some other quantity which is not needed.

The main problem of translating the above data into a complex pressure function is determining the reference point from which the phase angle is measured. Currently, a point is chosen as the "leading edge" point and its phase angle is set at zero. Points which are forward of that location are set to zero in both phase and amplitude. In this manner the effect of partial separation can be simulated. The reference point is determined by scanning the PSD's and the coherency functions. The coherency functions are usually low for points forward of the shock or separation point. Aft of this point, good correlation is indicated particularly for adjacent transducers.

For the example, let the reference be the second transducer. Thus, the amplitudes become

$$\phi_1 = 0 \qquad\qquad \theta_1 = 0$$

$$\phi_2 = \phi_2 \qquad\qquad \theta_2 = 0$$

$$\phi_3 = \phi_3 \qquad\qquad \theta_3 = \theta_{23}$$

$$\phi_4 = \phi_4 \qquad\qquad \theta_4 = \theta_{23} + \theta_{34}$$

$$\phi_5 = \phi_5 \qquad\qquad \theta_5 = \theta_{23} + \theta_{34} + \theta_{45}$$

$$\phi_6 = \phi_6 \qquad\qquad \theta_6 = \theta_{23} + \theta_{34} + \theta_{45} + \theta_{56}$$

$$\phi_7 \text{ ---- IGNORED } \theta_7 \text{ --------------}$$

and the complex pressure distribution is

$$\frac{\Delta p_1(\omega_i)}{q\sqrt{(\Delta\omega)_i}} = 0$$

$$\frac{\Delta p_2(\omega_i)}{q\sqrt{(\Delta\omega)_i}} = \left|\phi_2(\omega_i)\right|^{\frac{1}{2}}$$

$$\frac{\Delta p_3(\omega_i)}{q\sqrt{(\Delta\omega)_i}} = \left|\phi_3(\omega_i)\right|^{\frac{1}{2}} \exp\left|i\theta_3(\omega_i)\right|$$

$$\vdots$$

The $(\Delta\omega)_i$ value is the finite bandwidth used in the NASA ARC spectral analysis. In this scheme, only phase angles between adjacent transducers are used since their coherency is higher, thus, a higher confidence can be placed in the cross correlations. The $(\Delta\omega)_i$ quantity is retained in the pressure distributions since it varies with ω_i in the NASA ARC spectral analysis procedure.

In the treatment of an entire wing as opposed to a two-dimensional case, several chords must be treated and the spanwise phase angle must be accounted for. In each chord a reference point is selected and a set of transducers is assigned. The phase angle construction proceeds for each chord in the manner described above. The spanwise data are used to determine the proper absolute phase angles for each chord. These data are the fluctuating spanwise loadings and are received in the same form of ϕ_m and θ_{mn} as before. Hence, they are processed in the same manner as the chordwise data with the inboard span station designated as the reference point.

The spanwise data are physically calculated as integrals of the chordwise data at each span station. Thus, phase angles of the integral of the processed chordwise pressures must be equal to those of the processed spanwise loadings at each span station. The complex chordwise pressures are processed directly as

$$\left[\frac{\Delta p_{mn}(\omega_i)}{q\sqrt{(\Delta\omega)_i}}\right]_{\theta_S} = \frac{\Delta p_{mn}(\omega_i)}{q\sqrt{(\Delta\omega)_i}} \frac{C_{\ell_m}}{\left|C_{\ell_m}\right|} \frac{\int \Delta p_m^*}{\left|\int \Delta p_m\right|}$$

which yields the complex pressure value at the nth chordwise point on the mth span station with the desired absolute phase angle. The terms on the right hand side are

$\dfrac{\Delta p_{mn}(\omega_i)}{q\sqrt{(\Delta\omega)_i}}$ = complex pressure with phase angle referenced to zero at the leading edge

C_{ℓ_m} = complex span loading at the mth station

$\int \Delta p_m^*$ = complex conjugate of the chordwise integral of

$$\frac{\Delta p_{mn}(\omega_i)}{q\sqrt{(\Delta\omega)_i}}$$

These data are written on a magnetic tape and are valid for a single Mach-α condition since Reynold's number effects cannot be considered and have been minimized as much as possible, as previously discussed.

2.5 Calculation of the Horizontal Tail Buffet Pressures

Horizontal tail buffet pressures were not measured in the wind tunnel test program[8]; however, in the prediction of airplane buffet response, these data were needed for the forcing function. Thus, a method was developed with which the tail pressures could be estimated with linear theory aerodynamic matrices. It was assumed that the wake in the vicinity of the horizontal tail due to buffeting pressures on the wing could be predicted with doublet lattice unsteady aerodynamic influence coefficients from a known wing load distribution. Such an assumption is not unreasonable for distances of several panel chords downstream.

In matrix form, the aerodynamic problem is

$$\begin{bmatrix} A_{ww} & A_{wt} \\ A_{tw} & A_{tt} \end{bmatrix} \begin{Bmatrix} p_w \\ p_t \end{Bmatrix} = \begin{Bmatrix} W_w \\ W_t \end{Bmatrix}$$

where the aerodynamic influence coefficient submatrices are

A_{ww} = wing on wing

A_{wt} = tail on wing

A_{tw} = wing on tail

A_{tt} = tail on tail

and

$\left|p_w\right|$, $\left|W_w\right|$ = pressure and downwash on the wing

$\left|p_t\right|$, $\left|W_t\right|$ = pressure and downwash on the tail

Since the wing is buffeting, p_w is known from the wind-tunnel data as p_{w_B}. The horizontal tail is usually at a negative angle of attack during a high-α maneuver; hence, it is assumed to be in a buffet free condition. Also, the tail upper surface is effectively the only portion feeling the buffeting wake from the wing upper surface; thus,

$$1/2 \left|A_{tw}\right| \left|p_{w_B}\right| + \left|A_{tt}\right| \left|p_{t_B}\right| = \left|W_{tb}\right| = 0$$

which yields

$$\left|p_{t_B}\right| = -\tfrac{1}{2} \left|A_{tt}\right|^{-1} \left|A_{tw}\right| \left|p_{w_B}\right| \tag{4}$$

With this form, all that is necessary to obtain p_{t_B} from p_{w_B} is to calculate the doublet lattice unsteady aerodynamic matrices at the same frequencies for which wind tunnel data PSD estimates are made. In actual practice, the matrices are not calculated

directly at all frequencies but are interpolated from a smaller set since about forty frequencies are used. Otherwise, the cost would be prohibitive.

2.6 Calculation of the Buffet Q_{rB} and $\overline{F}_B$ Terms

Once the horizontal tail pressures are obtained as discussed above, the doublet lattice program is used to combine the buffet pressures with normal modes to obtain the generalized forcing function terms, Q_{rB}. The program is also used to determine the $\overline{F}_B$ terms for shear, bending moment, and torsion on the wing and horizontal tail due to buffet pressures.

The first step in using the doublet lattice program is to interpolate the buffet pressure values at the transducer locations to the load points on the doublet lattice panels. This is done to obtain the actual values of P_{wB} used in Equation 4 above. The values of P_{tB} are already at the panel points on the tail and do not require interpolation. The surface spline technique of Harder and Desmarais[15] is used which simulates the deflected shape of an infinite plate pinned at the points which are being interpolated from. After interpolation, p_{tB} is calculated and then used in conjunction with P_{wB} in the doublet lattice program to obtain the Q_{rB} and $\overline{F}_B$ terms with the same procedure used to calculate the Q_{rS} and $\overline{F}_r$ terms discussed earlier (Equation 3).

2.7 Buffet Response Prediction

With the input data completed for the dynamic response program, the final step in Figure 1 is to calculate the buffet response in terms of accelerations, loads, and moments. Predictions are made for both pure symmetric and antisymmetric airplane motions. Since flight test results[9,10] indicate that the airplane response is usually asymmetric, even in a "pure" symmetric maneuver, both the symmetric and antisymmetric responses are combined to produce an upper and lower bounds on buffet characteristics. These bounds are given as a function of angle of attack at a particular Mach-altitude-sweep-gross weight configuration. Since airplane buffet is subject to many variables other than those already accounted for (such as pilot characteristics and atmospheric conditions) the concept of a predicted bounds seems to be a very attractive means for treating the high intensity buffet problem.

The upper and lower bounds spectra, ϕ_u and ϕ_L, are based on the following assumptions:

1. The maximum response possible is obtained when both symmetric response spectra, ϕ_S, and antisymmetric spectra, ϕ_A, are in phase and 100% active at all frequencies:

$$\phi_u = \left[\phi_S^{\frac{1}{2}} + \phi_A^{\frac{1}{2}} \right]^2 \tag{5}$$

2. The minimum response possible is obtained when (1) ϕ_S and ϕ_A are 100% active and $180°$ out of phase, (2) ϕ_S is active only, or (3) ϕ_A is active only:

$$\phi_L = \text{Min.} \left\{ \begin{array}{c} \left[\phi_S^{\frac{1}{2}} - \phi_A^{\frac{1}{2}} \right]^2 \\ \phi_S \\ \phi_A \end{array} \right\} \tag{6}$$

The ϕ_u and ϕ_L can also be used to obtain upper and lower bounds on the RMS values of response. Examples of both will be presented in the application of the method:

Equations 5 and 6 represent two extremes between which all flight test results should fall. Since 100% excitation is not possible, it would be expected that excursions outside of the bounds would be more frequent for the lower than the upper. Hence, the norm of the flight test data for all cases should be weighted toward the lower bounds.

3. APPLICATION OF THE PREDICTION METHOD

Throughout the development of the prediction method, extensive comparisons with flight test data have been made in order to determine the importance of various phenomenon. This section presents a summary of the more important effects as well as an assessment of the capability of the method for a wide variety of Mach-altitude-wing sweep gross weight configurations. For sake of brevity, most of the results will be given in integrated form rather than PSD's. The wing loads are taken at an inboard span station called "wing station 1" in References 9 and 10, and thus are not exactly the root wing loads.

3.1 Effects of Static Aeroelasticity

Shown in Figure 3 are the predicted upper and lower bounds RMS values for the wing bending moment and the corresponding characteristic frequencies, N_0. Also shown are the flight test results at the same configuration (given in the Figure). The N_0 is the frequency centroid of the PSD curve; hence, its use in conjunction with the RMS provides a much better means for comparing integrated quantities. It is also interesting to note the variation of N_0 with α in the results to be presented.

Figure 3 illustrates the improvement of agreement with flight test results if the predicted α values are shifted according to the flexible to rigid lift coefficient ratio. The plots on the left are shown with the predictions plotted at the rigid values of α from the wind tunnel data. The right hand plots use the flexibilized value of α. In both cases the flight test data are plotted at their actual α values. All of the predictions to be given in the following paragraphs will be shown as functions of the flexible α values.

3.2 Asymmetric Responses

The examination of flight buffet data has clearly shown that in general the airplane responds in an asymmetric manner under high intensity buffet[9,10]. The presence of major response in both symmetric and antisymmetric modes led to the formulation of the upper and lower bounds concept as the only reasonable means by which airplane buffet response could be predicted. Thus, such uncontrollable items as pilot characteristics, atmospheric turbulence, airplane mass and geometric asymmetries, and control system inputs could be covered to a large extent.

An example of an upper and lower bounds PSD plot as defined by Equations 5 and 6 is shown in Figure 4 for the wing tip accelerometer. Comparison is made with both the right and left wing tip results from flight test. It will be noted that even though there is a wide separation between the bounds, there are several points at which the flight test data confirms the difference. At about 12, 21, and 27 Hz, the right and left wing tips indicate such a super-positioning of symmetric and antisymmetric responses. The exceedance of the upper bounds from about 15 to 21 Hz do not occur at the higher angles of attack.

Another example of the upper and lower bounds is shown in Figure 5 to illustrate variation with α. This prediction is for the wing bending moment (same condition as in Figure 4) and a comparison is made with one wing only. These plots are the PSD's for the RMS-N_0 results given in Figure 3. Comparison of Figures 3 and 5 shows how the change in spectral shape toward the first wing bending modes (sym.=4.8 Hz, anti.=7.4 Hz) with increasing buffet intensity is reflected by a steady decrease in N_0. It is also interesting to note that the first symmetric bending mode frequency has increased from 4.8 Hz to about 5.5 Hz as a result of aerodynamic stiffening. The flight test data are well bounded by the predictions.

3.3 Effect of Horizontal Tail Loads

During the prediction method development the effect of adding horizontal tail unsteady aerodynamics and buffet loads were studied. Shortcomings of the initial prediction method which used wing aerodynamics only, led to this investigation. However, measured buffet pressure data were not available for the horizontal tail since the model was not instrumented as such. Thus, the semi-empirical scheme which used the doublet lattice aerodynamic matrices as described in the previous section was developed.

The results shown in Figure 6 illustrate the effect of varying horizontal tail loads on the wing shear. The wing alone results are obtained with wing buffet pressures and wing unsteady aerodynamics. For this simulation, the lower bounds seems to be more representative of the flight data and the N_0 plot does not agree at all. The PSD's for this case verified the disagreement. The second solution with total airplane unsteady aerodynamics and full horizontal tail buffet loads showed a significant improvement, particularly for the N_0 comparison as was reflected by the PSD's. It was apparent, however, from examination of the horizontal tail pivot loads, from both flight test and prediction that the tail buffet pressures were too high. Further thought on the matter led to the conclusion that the estimated tail buffet pressures should be divided by two. This conclusion was based on the fact that at high angle of attack, the buffet wake which leaves primarily from the wing upper surface has very little effect on the tail lower surface. This effect is further emphasized by the tail being at negative incidence relative to the wing. The final solution with 1/2 horizontal tail buffet loads as shown in Figure 6 verifies the reasoning in that the RMS loads are well bounded and the N_0 results show excellent agreement. (This solution has another variation included where the wing first torsion frequencies of the airplane and wind tunnel model were matched which reduced

the frequency limit of the prediction from 38 to 31 Hz. The frequency matching contribution to the improved agreement was insignificant compared to that due to using 1/2 tail buffet loads.)

Figure 7 shows the effect of the same variation of horizontal tail buffet loads on the wing tip accelerometer predictions. For this response item, the final method does not appear to be any more accurate than the wing alone method. Since the wing tip accelerometer is sensitive to all wing modes and the wing root shear is more affected by the lower wing bending modes this is not surprising. Total airplane motion which is affected by the horizontal tail has a greater influence in the lower wing mode responses, hence it would be expected to significantly affect the wing root loads. Likewise, it would not have as great of an influence on the higher wing modes which are equally important for wing tip motion.

Figure 8 shows the results for the C.G. vertical accelerometer. Although the wing alone results show excellent agreement for $\alpha = 6.9^\circ$ and 11.7°, they do not have the decrease in response at $\alpha = 14.1^\circ$ as indicated by the flight test data. Also, since it is felt that it is impossible for the airplane to respond at 100% as the wing alone results show, the final method is more realistic.

From this study it was concluded that the horizontal tail was important in the prediction of airplane buffet characteristics under conditions well beyond buffet onset. It also appeared that the concept for estimating the tail buffet loads was correct; however, even with the 1/2 factor, the predicted tail loads were high as compared with flight test data. It was felt that if the displacement of the wing wake relative to the horizontal tail was accounted for, a large reduction in the tail loads, i.e., a factor of 2 to 4 would result.

4. CAPABILITY ASSESSMENT OF THE METHOD

As a test of the final version of the prediction method, results were calculated for a wide variety of flight conditions and compared with flight test data. The comparisons made in Reference 6 include 218 PSD's as well as RMS-N_0 plots. Also included are the calculated normal modes for both symmetric and antisymmetric motions for all wing sweep-gross weight conditions. Only a portion of the RMS-N_0 results are presented in this paper in Figures 9-13. All predictions shown were obtained with total airplane aerodynamics and 1/2 estimated tail loads as discussed above. The only exception is the last case in Figure 13, M=1.2, which was restricted to a wing alone simulation due to limitations on the supersonic unsteady aerodynamics.

Figures 9 and 10 show the effects of different types of buffeting flow at subsonic speeds and $\backslash = 26^\circ$. In Figure 9, the flow at M=0.7 is primarily of the leading edge separation type for which the response exhibits the peaky characteristic as discussed by Benepe[7]. In Figure 10, the flow at M=0.8 is dominated by shocks on the wing which produces a far more severe buffeting condition. Comparison of Figures 9 and 10 shows that the latter responses are more than double those of former as indicated by both predictions and flight test data. Exceedance of the upper bounds by wing torsion should be noted as the only occurrence in the results presented in this paper.

Figures 10, 11 and 12 show the effects of increasing sweep from 26° to 50° to 72.5° at about M=0.8 to 0.85. Although gross weight and altitude are also changing, the major influence is due to sweep. In these cases, the decrease in buffet intensity with sweep as shown by flight test data, is well predicted with the method.

Figure 13 shows the results for $\backslash = 50^\circ$ and M=1.2 which were obtained with a wing alone simulation. Comparison with Figure 10 for M=0.85 illustrates primarily the changes which take place due to the Mach number changing from subsonic to supersonic. Again, the decrease in buffet intensity with increased Mach number is well predicted by the method. The supersonic results would be improved, however, if a total airplane simulation were used.

Figure 14 shows a frequency plot of the RMS flight test data for the wing tip accelerometer and the wing shear. The data are plotted according to how many points fell between various 10% fractional bands of the upper bounds. For example, 14 points fell between 20% and 30% of the upper bounds for the wing tip accelerometer. Although the sample is small, the results shown in this figure establish the fact that a reasonable relationship does exist between the predictions and flight test. The data points used include all of those shown in Figures 9-13.

5. DISCUSSION

Several items appear in the results just presented that deserve special attention. The over prediction of flight test data by such a large margin as represented by the upper bound in Figure 14 would lead one to conclude that the method is unrealistically conservative. Also, the data are so scattered that it appears impossible to say how well the prediction method works or how could the method be used as a practical tool in the design process. In contradiction, the unconservative prediction of wing torsion in Figure 9, and particularly in Figure 10, would lead to the conclusion that the method is unrealistic, period. Finally, the high frequencies associated with buffet loadings indicate that relatively large fluctuating loads on secondary structure might lead to fatigue problems. Each of these items will be discussed in the following paragraphs.

5.1 Correlation of the Predicted Symmetric Response and Other Methods

First, it should be noted that the predictions for accelerometer responses agree better with flight test results than in the corresponding comparison for the loads. The flight test data used in the comparisons were obtained from a flight loads program in which buffet loadings were a small fraction of the mean loads, i.e., on the order of 2% - 5%. The accelerometer results were obtained from instrumentation which was better suited for the range of measurements obtained. Thus, one would expect less scatter and greater accuracy for the measured accelerations as opposed to loads. As a result, the following discussion will be concerned with accelerometer data only.

The summary of the comparison of predicted upper bounds and flight test results for the wing tip accelerometers in Figure 14 do not necessarily indicate that a gross conservatism exists in the current prediction method. The upper bound as defined in this paper is derived from the assumption that the maximum possible response obtainable is when symmetric and antisymmetric motions are 100% excited and are in phase at all frequencies. Obviously, this could occur on only one side of the airplane. It is highly improbable that both types of motion could be 100% excited at all frequencies; hence, about 50% excitation of both or 100% of one would be more realistic. It is not meant to infer that the total response should be biased, but instead that the upper bound is about twice what should be expected for integrated RMS response results. For some peaks in the response power spectra, the upper bound is reached as has been shown, but for many other peaks it is not. Thus, the integrated RMS response obtained from the upper bound is inherently too large.

In the case of interest, symmetric motion would be more representative of the total response since the maneuvers were primarily symmetric. A log-log correlation plot is shown in Figure 15 for the wing tip accelerometer results for the current method. Also shown are similar results from Butler and Spavins for a second aircraft[3] and Mullans and Lemley for still a third[5]. The current method results are from symmetric predictions only. Butler and Spavins' method makes use of measured aerodynamic damping and response both as a function of angle of attack from a rigid wind tunnel model to predict flight buffet response on the first symmetric wing bending mode. Thus, both predictions and flight test results from Reference 3 are for a single mode only. Mullans and Lemley's method uses all symmetric and antisymmetric modes up to a limiting frequency equally weighted and a constant value of aerodynamic damping individually determined analytically as viscous damping for each mode. The forcing function data for the latter method are determined from fluctuating pressure data on the wing of a rigid wind tunnel model.

A similar plot is shown in Figure 16 for the vertical acceleration at the C.G. Since there is no theoretical contribution to this response item from antisymmetric motions, no argument is necessary for using the symmetric predictions alone. These are the data that are shown in Figures 9-13. Also shown in Figure 16 is the comparison of predictions and flight results as given by Hanson[4]. This method is applied to the same type of aircraft that is used with the current method. Hanson utilized a dynamically scaled elastic model to obtain buffet response data which was scaled up to full scale with a technique similar to Butler and Spavins. The primary difference is that Hanson used a damping ratio for the dominant mode to scale the wide band RMS wind tunnel data as opposed to a single mode. He assumed that the ratio of wind tunnel model to full scale airplane damping remained constant and hence did not have to measure damping as a function of angle of attack. For his method, the dominant mode changed according to the response item of interest.

Not much is revealed in examination of the correlations in Figures 15 and 16 except for some general trends. The current method is more conservative for higher responses on the average for the wing tip accelerometer and about constant for the C.G. accelerometer. Also, the data are more scattered at the lower response levels for both items as might be expected. The results of Butler and Spavins are more scattered and less conservative on the average in comparison to the current method. Mullans and Lemley's

predictions are extremely conservative. Hanson's results are slightly less conservative than the current method but are more scattered.

The results in Figures 15 and 16 are shown as frequency distribution plots in Figures 17 and 18, respectively. The table below summarizes the mean and standard deviation of each distribution.

Table I STATISTICAL ANALYSIS OF THE CORRELATION FREQUENCY DISTRIBUTIONS

Method	Number of Samples	Mean	Standard Deviation	Item
Current	38	.868	.355	Wing Tip Acceleration (Sym)
Butler & Spavins[3]	17	1.138	.489	Wing Tip Acceleration (1st Sym Wing Bending)
Current	19	.701	.243	C.G. Vertical Acceleration
Hanson[4]	21	.861	.388	C.G. Vertical Acceleration

Because of the small sample of data, Mullans and Lemley's predictions are not included, however, the larger conservatism of their results is mainly attributed by the current writers to the equal use of both symmetric and antisymmetric modes in their predictions. The previous discussion in reference to the upper bound in the current method is applicable in this case. It is also felt that use of a simple viscous damping in each mode, ignoring aerodynamic stiffening, and not accounting for static aeroelastic effects further added to the over prediction.

Results in Figures 17 and 18 and the above table show that the current method yields less scatter and is more conservative than the methods of References 3 and 4. In the comparison with Butler and Spavins in Figure 17, the higher scatter of their results is due partly to the concern with the response of a single mode. Because the buffet forcing function is not a smooth function of frequency and is affected by a wide variety of uncontrollable variables, the use of multiple modes will almost always have a smoothing effect on the wide band RMS data. This effect is analogous to the smoothing obtained through longer time samples of random data. The difference in conservatism is felt to be partly due to the use of linear theory aerodynamic damping forces for the current method and measured wind tunnel damping for the Butler and Spavins method. Damping results for wind tunnel data shown for the latter[3] indicate that aerodynamic damping during buffet for the fundamental wing bending mode of their airplane increased by about 30% over the attached flow value. Ignoring this effect in the current method would certainly lead to some conservatism on the order of 10% to 15% if the increase is typical. Comparison of the wind tunnel and flight damping in Reference 3 also indicated that the former was slightly high which would cause their results to be unconservative. Another source of differences between the two methods are Reynold's number effects. Butler and Spavins presented results that indicated that they should not have any appreciable Reynold's number effects in scaling wind tunnel response data to full scale in the response range of interest. Because the current method was applied over a large range of angles of attack and to conditions which involved strong shock boundary layer interaction, Reynold's number effects are quite likely responsible for some conservatism. The effect of pitch rate during maneuvers is also believed to be a source of difference which will be discussed later.

The comparison between the current method and that of Hanson[4] in Figure 18 shows the greatest difference to be in the scatter of data. Since Hanson is effectively using wind tunnel aerodynamic damping forces, it is very likely that this is the primary cause of the greater scatter in the correlation. Hanson's predictions as shown in Reference 4 contain as much, if not more, scatter than the flight test data with which he is comparing. Hence, it is not surprising that the prediction-flight test correlation likewise shows greater scatter than does the current method for the same airplane under similar conditions. Since both methods use models of about the same scale, similar Reynold's number effects should exist in both methods. In addition to pitch rate effects, this is probably one of the main reasons for both methods being conservative. It would be expected, however, that Hanson's method would yield less conservative results due to the use of wind tunnel generated aerodynamic damping forces as opposed to the attached flow theoretical forces used in the current method. The results shown in Table I support this reasoning.

In summary, the current method predicts very realistic RMS values from symmetric motions. Comparison with purely wind tunnel based methods shows it to be conservative by a reasonable amount which is felt to be mainly due to the use of theoretical aerodynamic damping forces as opposed to the slightly greater forces that exist under separated flow conditions. Reynold's number effects are probably more important at higher angles of attack as indicated by an increase in conservatism of the current method

at higher response levels as shown in Figure 15. This is the result that would be expected based on the Reynold's number effects shown by John[1] and Butler and Spavins[3] where the buffet forces are shown to decrease with increasing Reynold's number for high intensity buffet. The current method shows less scatter in the flight test correlation as compared to the other methods. In one case this was attributed to the use of many modes as opposed to one and in the other case the use of theoretical aerodynamic damping as oppsoed to experimental damping for the wind tunnel model.

5.2   The Inherent Scatter of Flight Buffet Data

A well known aspect of flight buffet data analysis is the scatter associated with measured response from supposedly similar conditions. Many factors contribute to this phenomenon ranging from atmospheric conditions to pilot characteristics. One factor of particular interest is the effect of pitch rate on buffeting forces. Since the wind tunnel generated data, either fluctuating pressure or model response data, are taken over relatively long periods of time, pitch rate effects should be nil for such data. Full scale maneuvers, however, are performed over short periods which are of the order of 2 to 10 seconds. Benepe discussed the effects of pitch rate on wing root bending moment for a fighter aircraft in Reference 16. His results showed that for an increasing pitch rate, the maximum obtainable lift coefficient for a given high angle of attack increased by about 40%. Since the lift vs. α curve for the slow pitch rate diverged significantly from that for the higher rate, it would be expected that the separation was likewise de-layed for the higher rate. These results are qualitatively in agreement with those given by Ericsson and Reding[17] for dynamic stall analysis. In Reference 17, a non-dimensional pitch rate, $\bar{\alpha}$, is defined as

$$\bar{\alpha} = \frac{\dot{\alpha} \; \bar{c}}{U_\infty}$$

where $\dot{\alpha}$ is pitch rate in degrees per second, $\bar{c}$ is the airplane MAC in meters and U_∞ is the free stream velocity in meters per second. According to results presented, signifi-cant delays occur in the α value for separation for values of $\bar{\alpha}$ as low as 0.01-0.03. All of the maneuvers considered in the current study are within this range, hence, pitch rate effects certainly appear to contribute to lower values of buffet response encountered in flight.

An interesting observation is that the flight test data used by Butler and Spavins[3] were obtained from very slow maneuvers in which Mach number and α were held nearly con-stant for periods ranging from 10 to 50 seconds. Scatter was still introduced, however, since the airplane had to lose altitude in order to achieve this goal. Refering to Table I and Figures 15-18, the mean of their results were unconservative unlike the other three methods. The methods of References 3 and 4 essentially used the same aerodynamic damping forces but predictions were compared with quasi-steady maneuvers in the first case and more rapid maneuvers (as discussed above) in the second. As a result, it appears that the conservatism in the prediction methods is not so much due to technique as it is due to the dynamic effects of the maneuvers on flight measured buffet response.

The very low values of flight test response for $\alpha = 12.5°$ and $15.6°$ in Figure 9 are most likely a result of a very high pitch rate that took place during the final part of the maneuver. The non-dimensional pitch rate was $\bar{\alpha} = 0.04-0.05$ which should have been sufficient to cause significant changes in the separated flow according to Ericsson and Reding[17]. In constrast, the flight test data obtained for the lower values of α in that maneuver were taken during times at which $\bar{\alpha} \sim 0.01$ or less. Thus, a specific point is illustrated during a single maneuver in which pitch rate could be responsible for signi-ficant scatter in the flight-prediction correlation.

Another phenomenon which introduces scatter in the correlations is the decrease of Mach number and free stream dynamic pressure, q, during a maneuver. The variation of these quantities in the maneuvers considered in the current study is on the order of 5% to 10%. Although this effect can be considered when analyzing a maneuver that has already been performed, it is not a practical consideration for design and prediction purposes. Thus, this type of scatter should be expected and its impact would be more concentrated in the high response portion of a maneuver.

The main point of the above discussions is that flight buffet data is inherently scattered for a wide variety of reasons, many more than those considered. Although the distributions in Figures 17 and 18 are made for two different airplanes, two types of accelerometers, three distinct prediction methods, and different types of maneuvers and flight conditions, they all bear a striking resemblance. Hence, the prediction of full scale buffet response must be made on a statistical basis, not so much because of scatter in the prediction techniques, but because of the scatter due to the uncontrollable vari-ables that affect the flight data. The idea of using upper and lower bounds or mean value

curves with some kind of statistical distributions between the bounds or about the mean is a very practical approach for defining the predicted buffet characteristics for any given airplane. The statistical distributions could be obtained from a wide variety of data since they are more a function of the uncontrollable variables rather than a given aircraft configuration. The distributions would probably be affected by airplane type more than anything else. An extreme example would be fighter vs. transport aircraft. This approach would be applicable to any type of prediction method as demonstrated in Figures 17 and 18.

5.3 The Coupling of Wing Torsion and Shock Oscillation

The exceedance by wing torsion response of the predicted upper bound in both Figures 9 and 10 is attributed to a coupling between wing torsional motion and shock oscillation. This mechanism was not accounted for in the current prediction method due to the state of the art in the theoretical unsteady aerodynamics at the time of its development, 1971-1974. Its existence was known, but in order to evaluate the overall capability of the method the shock-torsion coupling had to be ignored so that the method could be developed. Thus, it was no surprise when the results in Figures 9 and 10 were obtained.

The basic mechanism occurs primarily at low wing sweeps and has been described previously by the writer[18] and Riddle[8] with regard to wind tunnel model data and by Benepe[9,16] for flight test data. John[1] also shows similar results under similar circumstances. Moss[19] has observed the phenomenon on flexible wind tunnel models where shock induced separation appears. In all cases, the observations show either significant or dominant peaks in response spectra at the first wing torsion mode frequency. The response items range from fluctuating pressure data to loads and accelerometer data.

The major ingredient in the shock-torsion coupling is attributed to the unstable nature of the primary wing shock on the upper surface of the wing when it is located near the local crest of the airfoil. The upper shock movement associated with increasing α is toward the trailing edge at low α until separation is induced at which point it begins to move forward with increasing α. The shock moves forward in an "orderly" fashion as α increases until it gets close to the local crest on the upper surface. As it approaches this point, it moves faster with a given increment in α. Since it is not stable on the crest, there is a point at which a small $\Delta\alpha$ will cause it to jump from just aft of the crest to just forward. In unpublished data used in the development of the current method, this distance of abrupt shock movement appears to be on the order of 10% of the chord. Thus, a large forward movement of the shock with a very small increase in α results in a loss in lift due to a larger high pressure area behind the shock without any appreciable increase in lift due to incidence. The loss manifests itself as a momentary decrease in lift curve slope or even a reversal which is a well known anomalous aerodynamic characteristic in transonic flow. This phenomenon occurs long before $C_{L_{max}}$ and is not related directly to stall.

Because the shock can move forward significantly with small α increases, it can likewise move aft with small α decreases. In other words, it can oscillate across the crest for very small torsional movements. Hence, the basic mechanism is established for large shock excursions with small torsional motions when the wing is at α values near the transonic lift curve slope anomoly. The net effect is to produce a forcing function which, if the local crest is near or forward of the elastic axis, is 180° out of phase with the torsion mode. Phase lag will be introduced due to unsteady effects on the shock motion and hence the forcing function. The lag is in part due to the finite time required for the flow to change and the shock to move as shown in the experimental work of Tidjeman[20] for an oscillating flap on a two-dimensional wing. Another contribution to the lag is caused by the pitch rate effects on the shock induced separation. Pitch rate will tend to stabilize separation for increasing α, and hence retard forward motion of the shock from its quasi-steady motion. The resulting lag creates a pitching moment due to shock oscillation that is in opposition to that produced by the aerodynamic damping force for the torsion motion. Thus, for the shock crossing the crest at or forward of the elastic axis of the wing, the aerodynamic damping due to torsional motion should decrease to near zero and torsional response increase accordingly. Due to the limited maximum force available through the shock movement, the response tends to reach a limit cycle and hence is referred to as buffet rather than flutter.

The effects of static aeroelastic deformation are not well understood since the twist that is introduced must be superimposed on that built into the wing. An indication of the effects can be obtained for the airplane considered in this paper by comparing aeroelastic force model results for different altitudes. The effect of a higher q at M=0.8, h=5,000 feet vs. that at M=0.8, h=20,000 feet shows a smoothing of the transonic lift curve anomalies. It also appears that the angle of attack at which the anomalies begin is increased.

The radius of curvature of the local crest is probably very influential on the amplitude of the shock motion and hence the amplitude of the buffeting forces. Greater shock motion should occur for a flatter crest.

It has been determined through extensive analysis of oil flow results and pressure data that the higher responses at $\alpha \approx 11°$ for M=0.7 in Figure 9 are caused by the above mechanism although it is not as well developed as the case shown in Figure 10. In Figure 10, the maximum flight response for wing torsion would probably occur near $\alpha = 10°$ for M=0.8. Note also, that the predicted response in Figure 10 reflects the increase over that in Figure 9 in agreement with the flight test data. The wing tip accelerometer and wing torsion response increased by about a factor of 2 to 3 for both prediction and flight. For these conditions, q increased by a factor of 1.7, which, if no Mach number effects were present, would produce a change in response of about 1.3. Thus, it is apparent that the correct trends due to Mach number are embodied in the wind tunnel data used to form the buffet forcing function for the current prediction method. Since the wind tunnel model had a solid steel wing, the response was much lower than for the airplane which would diminish the importance of the shock-torsion coupling in the model data. In order to properly account for this effect, the unsteady aerodynamic method used to calculate response induced loads would have to include the presence of imbedded shocks in the flow field.

5.4 Buffet Fatigue Damage to Secondary Structure

Because of the high frequencies associated with buffet loads as indicated by the N_0 results in Figures 9-13, one would expect buffet fatigue damage to be a problem in highly maneuverable aircraft. The level of these loads is quite low, as compared with design wing root bending moment for example, thus the damage is usually negligible or for all practical purposes, zero. This is the classical concept which is certainly correct when applied to primary structure that is designed to carry high loadings. Secondary structure, however, is not designed to carry much load and is usually located in areas of high buffet loading. Examples are leading and trailing edge sections of wings, horizontal tails or fins, and control surfaces, as well as various types of fairings.

The writers have previously discussed the relative magnitude of buffet induced wing bending moment as a fraction of the maximum amplitude attained during various maneuvers in flight[16]. The ratio is shown as a function of wing span which varies from about 5% near the root to about 20% near the tip. Although these results do not apply specifically to secondary structure, they are indicative of the desired relationship since the wing tip is usually lightly loaded in a manner similar to the trailing edge section of the wing where there are no control surfaces.

Speed brakes and spoilers are well known victims of buffet fatigue. Both the surfaces and their supports are subject to the problem. Furthermore, the wakes that they create can cause problems on other parts of the airplane. For example, in some unpublished data available to the writers, an electronics pod located just aft of a speed brake was found to experience high frequency fluctuating yawing moments when the brake was extended for which the RMS amplitudes were about 25% of the static design value.

To appreciate the effect of a fluctuating 20% incremental load on fatigue life, a design case will be examined. The example is a piece of secondary structure for which a critical stress point exists in 2024-T851 aluminum (68 KSI ultimate strength) with a geometric stress concentration factor, $K_T=4.0$. For a yield strength of 57.5 KSI and a 15% dynamic factor, the maximum static design stress is 50 KSI. Assuming that a buffet loading of 20% of the static mean exists (40% peak-to-peak) at the maximum load condition, the fatigue life for this material would correspond to 6000 cycles for a cyclic stress of 10 KSI about a mean of 50 KSI. For a stronger design such that the maximum stress is 25 KSI static, the cyclic stress of 20% or 5 KSI would produce a life of 100,000 cycles. An infinite life could be obtained by a stronger design in which the static maximum stress was 15 KSI and the cyclic stress was 3 KSI.

With regard to frequency, the N_0 of the buffet loadings near the wing tip in Reference 16 is typically 35 to 40 Hz. Thus, a single load cycle in the maneuver loads spectrum could produce 70 to 200 cycles of buffet loads for a maneuver time of 2 to 5 seconds. An example has been worked out for a single segment of a typical total airplane maneuver spectrum in which a particular high-g maneuver is made at the rate of 33 times per 4000 hours of service life. Assuming an average time of 3 seconds per maneuver at the high-g condition and an N_0 for the buffet loadings of 35 Hz, a total of 3465 cycles of fluctuating stress at 20% of the mean value would be accumulated. If the critical stress point was assumed to be the first example given in the previous paragraph and the mean stress for this particular high-g maneuver was 50 KSI, the buffet fatigue damage for 4000 hours would be about 58% of the total life of 6000 cycles. Assuming that the maneuver load cycle is produced as a 15 KSI cyclic load about a 35 KSI mean, the fatigue life is

4500 cycles for the critical stress point. The total fatigue damage for the 33 cycles of maneuver loads is only about 0.7%. According to the well known Miner's rule, the total fatigue damage for these 33 cycles would be 58.7% of which almost 99% of this damage is due to buffet.

Since the above segment of the total airplane maneuver spectrum is only a very small fraction of the airplane service life, it is obvious that such a condition would result in a fatigue failure. The fix would be to redesign for infinite life due to buffet damage which would reduce the mean maximum maneuver stress to about 15 KSI as discussed previously.

In many cases, however, stiffness requirements of the design result in much stronger structures than would be obtained with strength requirements. Thus, it would seem reasonable to make simple surveys of the critical stress points in the secondary structure to determine whether or not a 20% cyclic stress applied to the mean stress would produce an infinite life. The relationship will vary according to the stress concentration factor and the material used, however, the most sensitive areas would probably be bonded joints.

6.   CONCLUSIONS

A method has been presented in this paper for predicting the high intensity buffet response characteristics of airplanes in flight. The method contains the major ingredients responsible for airplane buffet. Results were presented in the form of an upper and lower bounds which were verified by extensive comparison with flight test data. The changing spectral characteristics of flight test data were shown to be predictable with the method. Static aeroelastic effects were shown to have a significant impact on the predictions. The horizontal tail was found to have a significant influence on wing and fuselage responses, hence, the total airplane should be considered. The technique for estimating the tail buffet loads from wing data appears to be correct in concept, however, an accounting for the wing wake displacement is felt to be necessary in order to accurately predict these loads.

The correlation of symmetric predicted response from the current method with flight test data has shown results similar to other prediction methods. An analysis of the comparison with other methods resulted in several important conclusions. Reynold's number effects should cause predictions based on wind tunnel data from a small scale model, to be conservative by some as yet indeterminable degree. Aerodynamic damping forces in separated flow as compared with those in attached flow, should reduce predicted response by about 10% to 15%. The use of more modes in the prediction should produce a smoother correlation with flight test data as well as a more realistic picture of total airplane response. The use of experimentally determined aerodynamic damping should result in greater scatter in the correlation with flight test data.

Flight buffet data was shown to be inherently scattered, due primarily to the effects of maneuver transients which consist of varying q, Mach number and pitch rate. It was shown that, in several instances, where the pitch rate was high, the flight buffet data was lower relative to predictions. Thus, a statistical approach was recommended for taking into account the scatter of flight buffet data. Since the scatter is due to many uncontrollable variables, a frequency distribution of occurrences could be established between the upper and lower bounds in order to better define the buffet characteristics for any given airplane. Since these distributions would be more a function of airplane type and usage rather than geometry, they would probably be determined in an almost universal manner.

A mechanism has been described by which wing torsional motion and normal shock oscillation can couple to produce a relatively severe buffeting condition at forward wing sweeps. The mechanism is attributed to the instability of the upper surface wing shock as it reaches the local crest of the airfoil at fairly high angles of attack. The instability was shown to be the source of the transonic lift curve anomaly for the airplane considered in this paper.

A hypothetical example of buffet fatigue damage to secondary structure has been examined to illustrate the impact on structural design. It was shown that if a structure, which was subject to buffet forces on the order of 20% of the mean load, was designed too close to the static mean loads, early failure could occur due to buffet fatigue. A simple method for checking the structure was recommended to determine if potential problems exist.

REFERENCES

1.   John, H.; "Critical Review of Methods to Predict the Buffet Penetration Capability of Aircraft", AGARD Lecture Series No. 74 on Aircraft Stalling and Buffeting. February 1975, pp. 7-1 to 7-29.

2. Jones, J.G.; <u>A Survey of the Dynamic Analysis of Buffeting and Related Phenomena</u>, RAE Tech Report TR 72197, 1973.

3. Butler, G.F. and Spavins, G.R.; "Preliminary Evaluation of a Technique for Predicting Buffet Loads in Flight From Wind-Tunnel Measurements on Models of Conventional Construction", AGARD Conf. preprint No. 204 on Prediction of Aerodynamic Loading, September 1976, pp. 24-1 to 24-11.

4. Hanson, P.W.; <u>Evaluation of an Aeroelastic Model Technique for Predicting Airplane Buffet Loads</u>, NASA TN D-7066, February 1973.

5. Mullans, R.E. and Lemley, C.E.; <u>Buffet Dynamic Loads During Transoric Maneuvers</u>, Air Force Flight Dynamics Laboratory Technical Report AFFDL-TR-72-46, September 1972.

6. Cunningham, A.M., Jr., Benepe, D.B., Watts, D., and Waner, P.G.; <u>A Method for Predicting Full Scale Buffet Response with Rigid Wind Tunnel Model Fluctuating Pressure Data</u>, to be published as a NASA Contract Report, 1977.

7. Cunningham, A.M., Jr., Waner, P.G., Jr., Watts, J.D., Benepe, D.B., and Riddle, D.W.; "Development and Evaluation of a New Method for Predicting Aircraft Buffet Response", AIAA Paper No. 75-69, January 1975.

8. Riddle, D.W.; "Wind Tunnel Investigation of Surface Pressure Fluctuations Associated with Aircraft Buffet", AIAA Paper No. 75-67, January 1975.

9. Benepe, D.B., Cunningham, A.M., Jr., and Dunmyer, W.D.; "A Detailed Investigation of Flight Buffeting Response at Subsonic and Transonic Speeds", AIAA Paper No. 74-358, April 1974.

10. Benepe, D.B., Cunningham, A.M., Jr., Traylor, S., Jr., and Dunmyer, W.D.; "Update on an Investigation of Flight Buffeting of a Variable Sweep Aircraft", AIAA Paper No. 75-68, January 1975.

11. Woods, D.J.; <u>Program to Compute Response to Random or Discrete Excitation</u>, Report No. ERR-FW-921, Fort Worth Division of General Dynamics, November 1969.

12. Albano, E., Perkinson, F., and Rodden, W.P.; <u>Subsonic Lifting Surface Theory Aerodynamics and Flutter Analysis of Interfering Wing/Horizontal-Tail Configurations</u>, Air Force Flight Dynamics Laboratory Technical Report AFFDL-TR-70-59, September 1970.

13. Pines, S. and Dugundji, J.; <u>Application of Aerodynamic Flutter Derivatives to Flexible Wings with Supersonic and Subsonic Edges</u>, Republic Aviation Report E-SAF-2, April 1954.

14. Allen, M.G.; <u>Structures Analysis Digital Procedures C28</u>, (now Digital Procedure BY7), Report No. ERR-FW-751-1, Fort Worth Division of General Dynamics, September 1968.

15. Harder, R.L. and Desmarais, R.N.; "Interpolation Using Surface Splines", <u>Journal of Aircraft</u>, Vol. 9, No. 2, February 1972, pp. 189-191.

16. Benepe, D.B.; "Aircraft Maneuvers and Dynamic Phenomena Resulting in Rapid Changes of Load Distributions or/and Fluctuating Separation", presented at AGARD Fluid Dynamics Panel Symposium on Prediction of Aerodynamic Loading, Moffett Field, California, September 1976.

17. Ericsson, L.E. and Reding, P.J.; "Dynamic Stall Analysis in Light of Recent Numerical and Experimental Results", AIAA Paper No. 75-26, January 1975.

18. Cunningham, A.M., Jr.; <u>The Application of General Aerodynamic Lifting Surface Elements to Problems in Unsteady Transonic Flow</u>, NASA CR-112264, February 1973.

19. Moss, G.F.; Personal Communication to D. B. Benepe, 1976.

20. Tijdeman, H.; <u>On the Motion of Shock Waves on an Airfoil with Oscillating Flap in Two-Dimensional Transonic Flow</u>, NLR TR 75038U, March 1975.
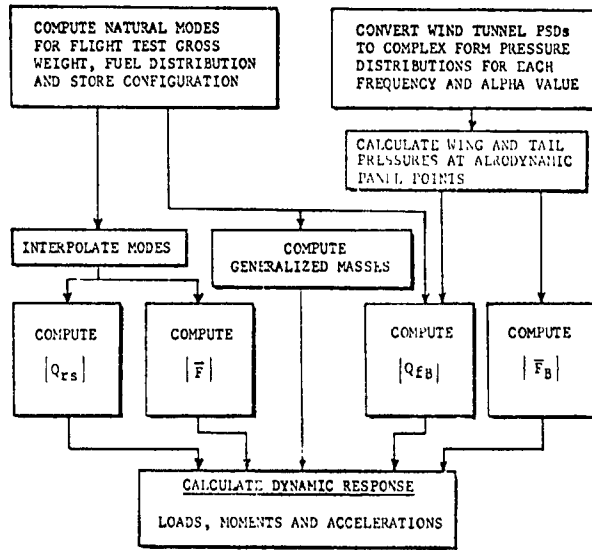
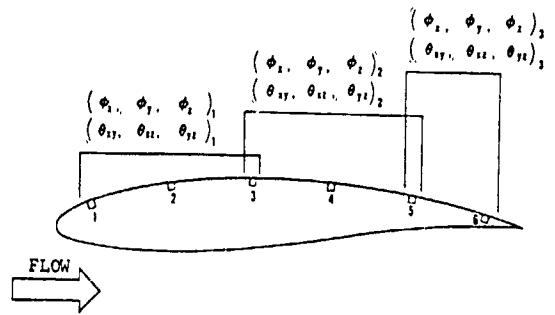Figure 1 BUFFET PREDICTION METHOD FLOW DIAGRAM

Figure 2 RELATIONSHIP BETWEEN THE NASA ARC SPECTRAL DENSITY ANALYSIS AND THE PRESSURE TRANSDUCER LOCATIONS
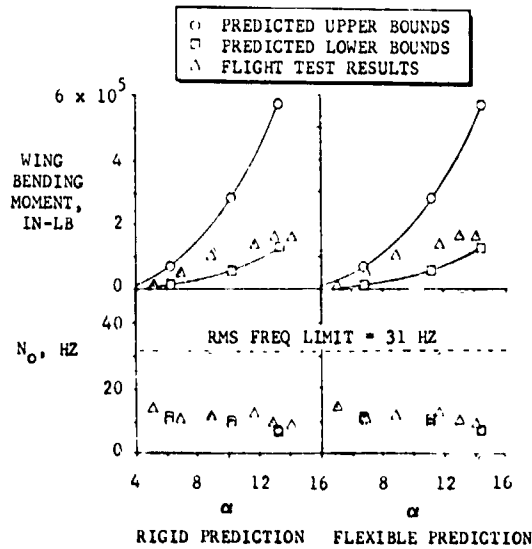

Figure 3 RIGID AND FLEXIBLE WING BENDING FOR $\Lambda = 26^{\circ}$, M = 0.8, ALT = 6035M
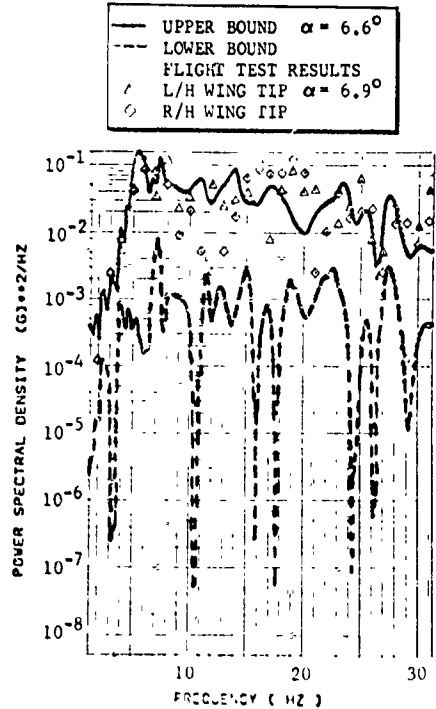

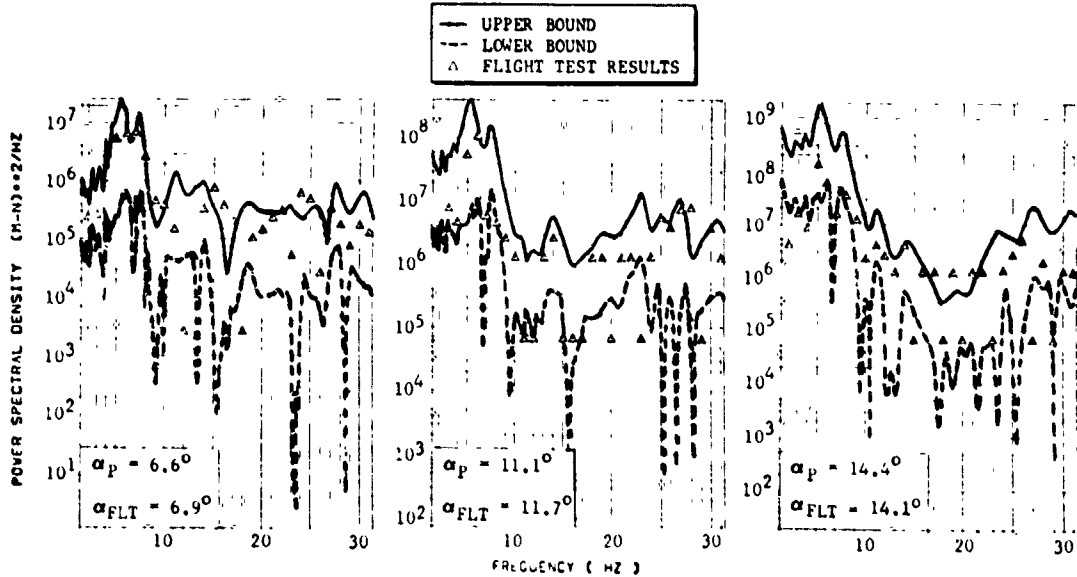Figure 4 PREDICTED BOUNDS ON WING TIP ACCELEROMETER PSD FOR $\Lambda = 26^{\circ}$, M = 0.8, ALT = 6035M

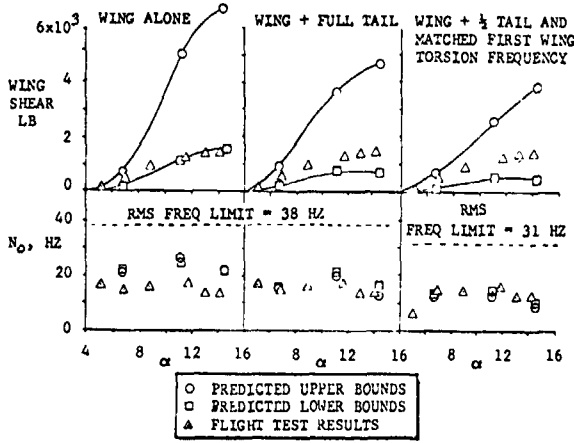Figure 5 PREDICTED BOUNDS ON WING BENDING PSD FOR $\Lambda = 26^{\circ}$, M = 0.8 ALT = 6035 M

Figure 6 EFFECT OF HORIZONTAL TAIL LOADS ON WING
SHEAR FOR λ = 26°, M = 0.8, ALT = 6035 M
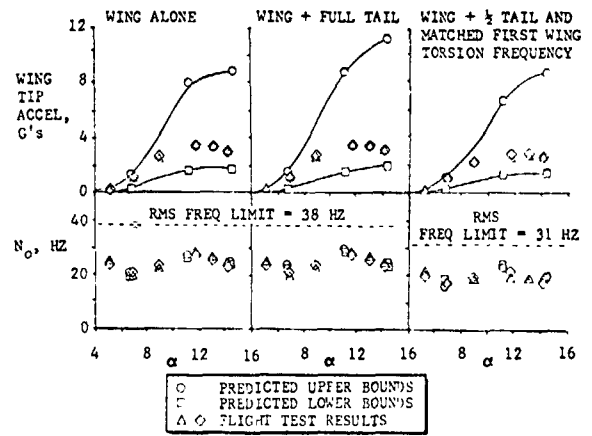
Figure 7 EFFECT OF HORIZONTAL TAIL LOADS ON WING TIP
ACCELEROMETER FOR λ = 26°, M = 0.8, ALT = 6035 M
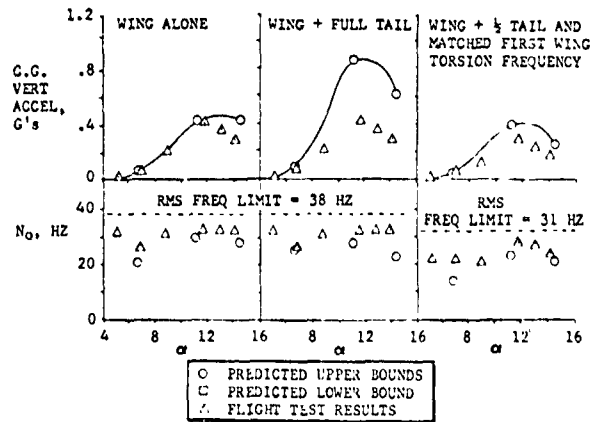
Figure 8 EFFECT OF HORIZONTAL TAIL LOADS ON C.G.
ACCELEROMETER FOR λ = 26°, M = 0.8, ALT = 6035 M
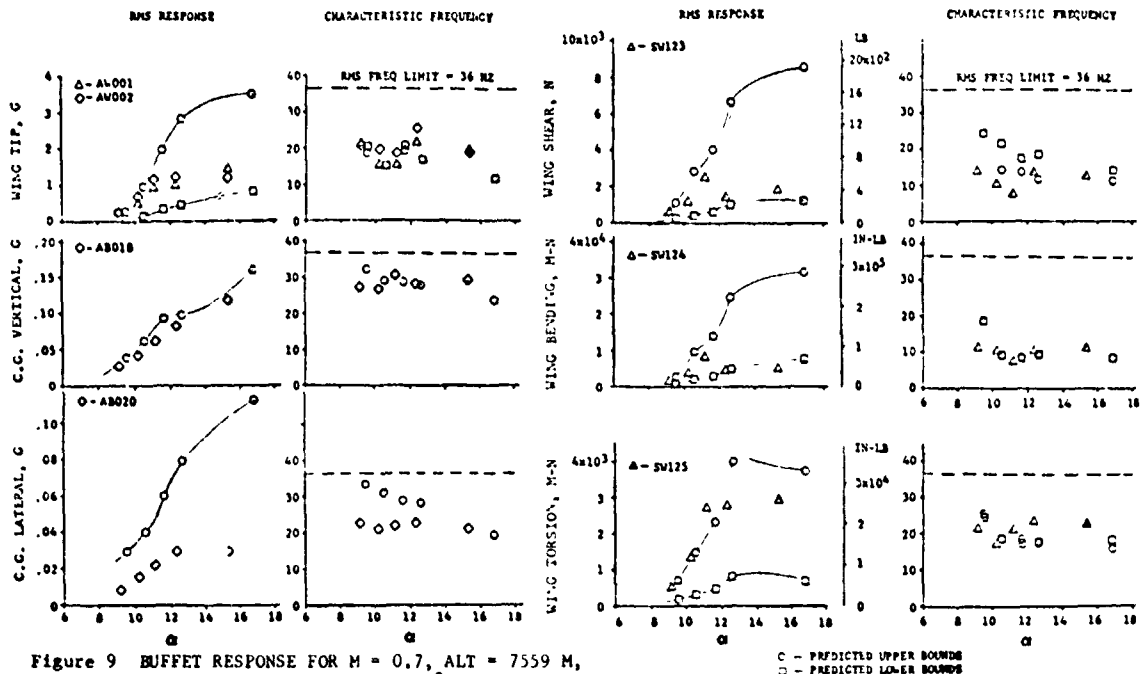
Figure 9 BUFFET RESPONSE FOR M = 0.7, ALT = 7559 M,
G. W. = 293138N, AND λ = 26°

Figure 10 BUFFET RESPONSE FOR M = 0.8, ALT = 6035 M,
G.W. = 266448N, AND Λ = 26°

Figure 11 BUFFET RESPONSE FOR M = 0.85, ALT. = 8382M,
G.W. = 331392 N, AND Λ = 50°
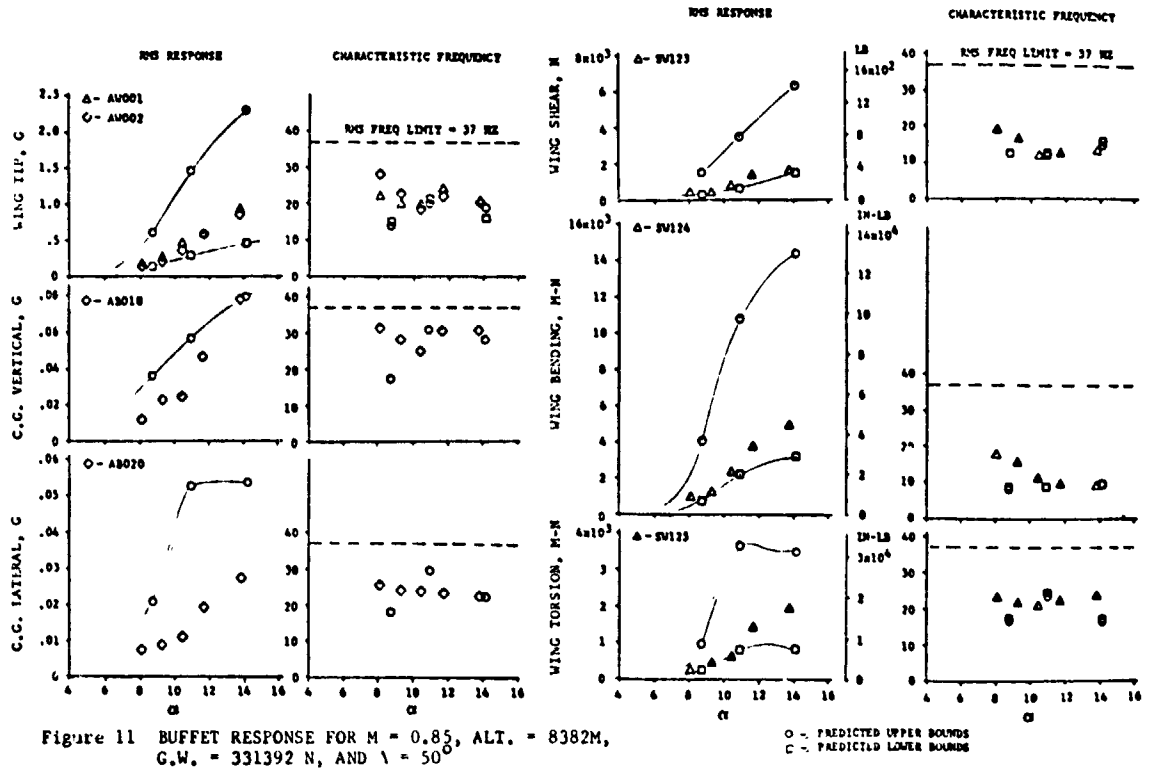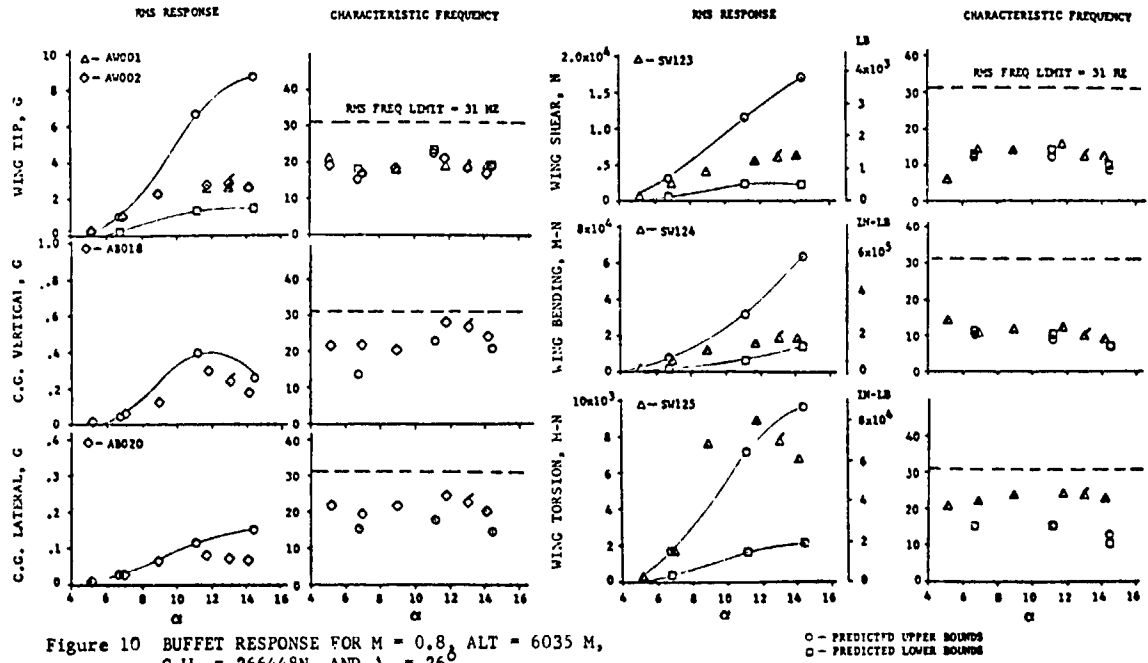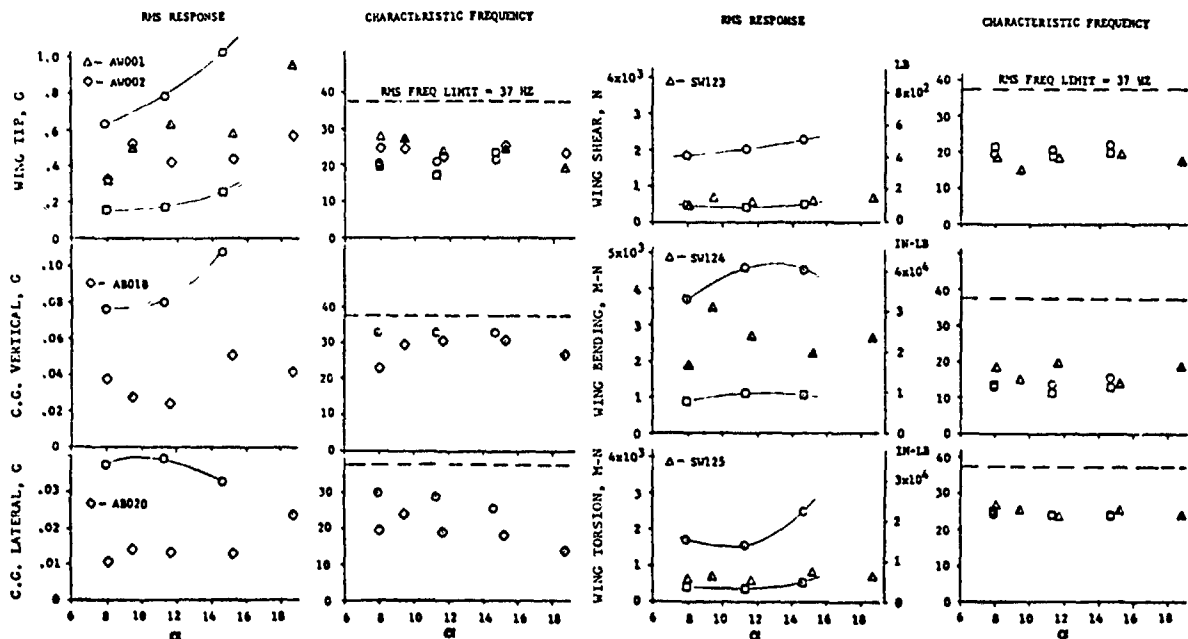
Figure 12 BUFFET RESPONSE FOR M = 0.85, ALT. = 7285 M,
G.W. = 268673 N, AND Λ = 72.5°
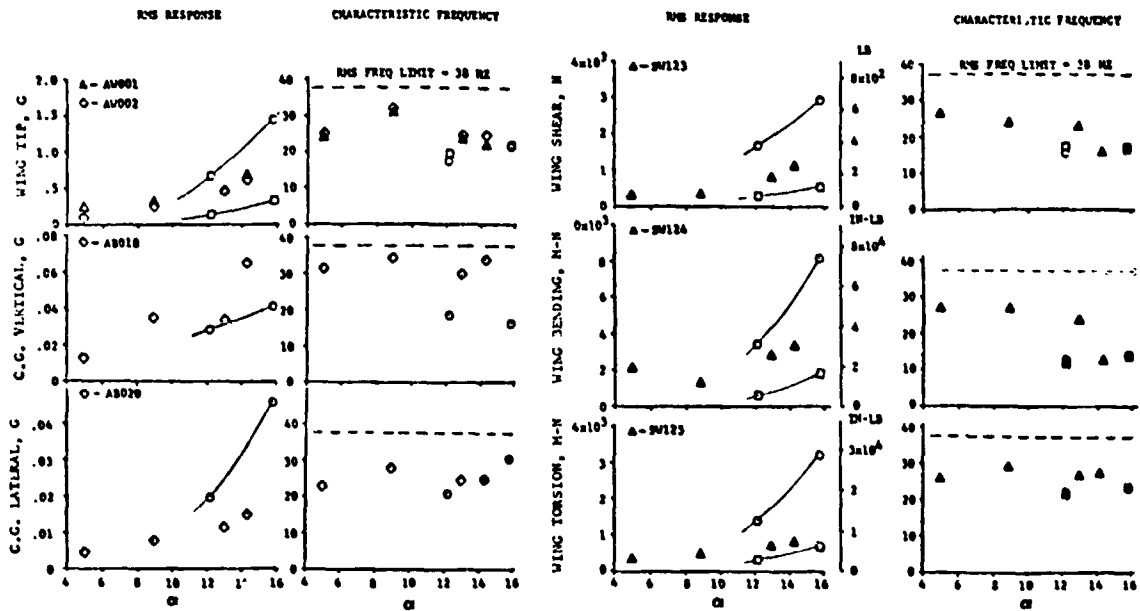
Figure 13 BUFFET RESPONSE FOR M = 1.2, ALT. = 9053 M,
G.W. = 261778 N, AND Λ = 50°
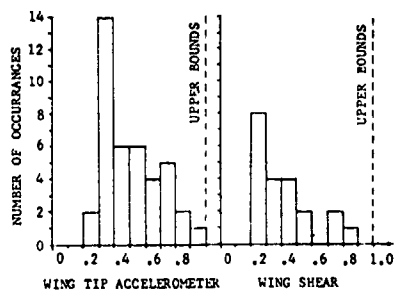
Figure 14 FREQUENCY OF FLIGHT TEST DATA
DISTRIBUTION AS FRACTION OF UPPER BOUNDS
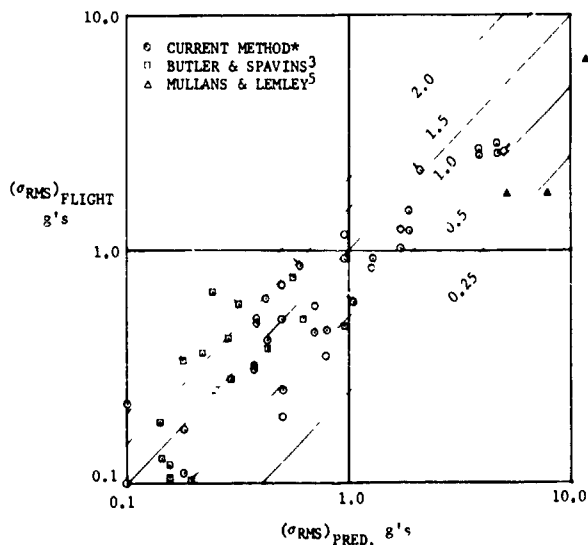
* (ʋ) DENOTES TWO POINTS

Figure 15 CORRELATION OF PREDICTION AND FLIGHT
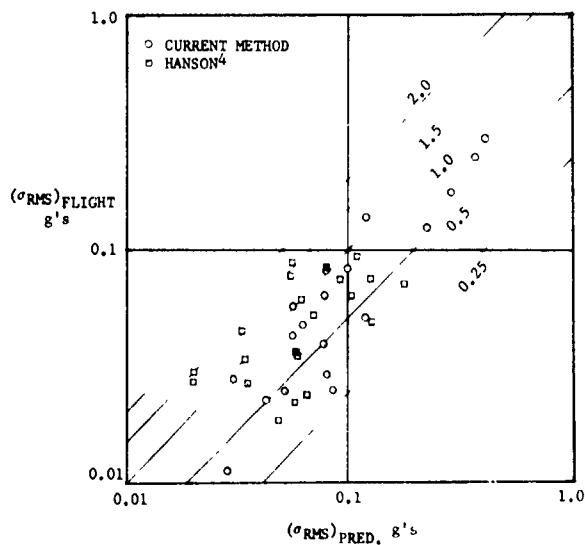TEST DATA FOR WING TIP ACCELEROMETER

Figure 16 CORRELATION OF PREDICTION AND FLIGHT
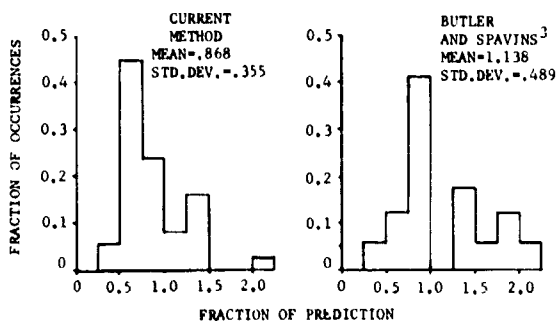TEST DATA FOR CG ACCELEROMETER

Figure 17 FREQUENCY DISTRIBUTIONS FOR WING TIP
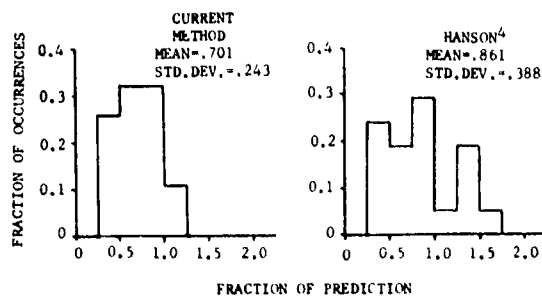ACCELEROMETER CORRELATION IN FIGURE 15

Figure 18 FREQUENCY DISTRIBUTION FOR CG
ACCELEROMETER CORRELATION IN FIGURE 16

THE DYNAMIC RESPONSE OF WINGS IN TORSION AT HIGH SUBSONIC SPEEDS
by
G. F. Moss and D. Pierce
Aerodynamics Department
Royal Aircraft Establishment, Farnborough, Hampshire, UK

SUMMARY

This paper discusses some aspects of the structural response of aircraft wings to aerodynamic excitation at conditions appropriate to manoeuvres at high subsonic speeds. Reference is made to some recent RAE wind-tunnel experiments using models specially designed to deform under test in a realistic way as well as 'rigid' models of conventional construction. The primary torsion mode of vibration of the wings tended to be strongly excited under some aerodynamic-flow conditions on the flexible models used, and in some cases the amplitude was large and similar to single-degree-of-freedom flutter in character. Data from some flight tests is quoted to demonstrate that this type of response may well occur in practice.

NOTATION

AR	aspect ratio	$R_{\bar{c}}$	Reynolds number based on $\bar{c}$
α	incidence, deg	ΔL	change in normal force
x	distance from leading edge	ΔM	change in pitching moment
c	local wing chord	C_L	lift coefficient
$\bar{c}$	geometric wing chord	$C_{N\ell}$	local normal-force coefficient
y	spanwise distance from centre line	$C_{m\ell}$	local pitching-moment coefficient
b	semi-span of wing	C_p	pressure coefficient
η	y/b		
t	wing thickness (maximum)	C_p^*	critical pressure coefficient (local M = 1)
z	vertical deflection	f	frequency, Hz
ϕ	torsional twist angle, deg	ω	$2\pi f$
S	model scale	ζ	apparent damping ratio, % critical
V	velocity	N_z	normal acceleration
M	Mach number		
Λ	leading-edge sweep, deg	T_w	torsion moment
H_0	stagnation pressure	M_w	bending moment
RN	unit Reynolds number		

1. INTRODUCTION

As the buffet boundary is penetrated the structural response of the airframe usually most evident to the pilot is that in the first bending mode of the wing where the frequency is comparatively low, but higher-order responses can occur which may raise problems for the airframe and any associated stores or equipment. Operational limitations as regards aircraft manoeuvre performance can thus arise on this account much in the same way as they can as regards the tolerance of the pilot to low-frequency structural vibration.

The conventional wind-tunnel model of solid-metal construction can usually only be used to predict the dynamic response of an aircraft structure to unsteady aerodynamic excitation (i.e. buffet) in the primary wing-bending mode because this is often the only mode which is reasonably well represented dynamically. The levels of amplitude of the response even so are generally much smaller with such a model construction than those for the aircraft at corresponding conditions in flight. However this can be allowed for by empirical factors, and over the last 20 years or so techniques of prediction using strain gauges[1-3] and dynamic pressure transducers[4,5] on these virtually 'rigid' models have been successfully developed and have been evaluated by many workers in the field[6,7]. Recent critical reviews have stimulated more sophisticated approaches and the consequent development of new more powerful experimental techniques[8-10]. In parallel with this use of 'rigid' models, techniques using aeroelastic models with properly-scaled elastic and inertial characteristics (as normally used for classic flutter clearance) have also been used occasionally for the prediction of buffet response[11,12]. Many more structural modes than the primary bending mode can thus be represented and the amplitudes of response are likely to be much more realistic. However, to make such models strong enough to take the high static loads at elevated incidences in high-speed wind tunnels at normal test stagnation pressures is very difficult. Testing at low stagnation pressure to reduce the chances of what can be a very expensive catastrophy is likely to lead to intractable aerodynamic scale-effect problems which can invalidate the predictions obtained for quite different reasons[13,14].

A higher-order structural vibration of particular importance is that in the primary torsion mode of the wing. At supercritical-flow conditions, which are generally present as the buffet boundary is penetrated at high subsonic speeds, the disposition of shock waves and areas of separated flow over the surface can be such as to excite this particular mode strongly. This kind of structural response has been noted in one or two particular instances in the recent past[15,16]. However, as this paper hopes to show, the intensity of this torsional vibration is much more dependent on the amplitude of the response of the structure and thus may not always be apparent on wind-tunnel models of conventional, solid-metal construction, even when the frequency and mode shape are fairly well represented. Under some circumstances single-degree-of-freedom flutter of comparatively high amplitude can develop out of this torsional response[17]. This usually takes the form of a limit-cycle[18] and is quite distinct from the catastrophic classical-flutter phenomenon. Because of this it is better to call this class of single-mode, sustained response 'torsional buzz' if only to avoid the unfortunate emotive associations of the word 'flutter'. Indeed, there are some indications that the occurrence of this 'buzz' during buffet penetration at high speeds can even be advantageous in some respects as regards the overall manoeuvre performance of an aircraft.

This paper discusses the way torsional buzz can occur on a wing at high subsonic speed and refers to some wind-tunnel tests with 'rigid' and flexible models recently carried out at RAE Farnborough.

2.   AERODYNAMIC EXCITATION AT HIGH SPEEDS

To set the scene, Fig 1 shows diagrammatically some normal modes for a swept wing. The primary bending mode of the wing panel, considered here to be encastré at the body side, usually has a fairly low frequency (f Hz) and that of the corresponding primary torsional mode may be several times this (say, 5f). Then there are a whole series of overtones in bending and torsion, and various other complex modes with less regular patterns of nodal lines across the wing. The relative motion of the surface at any point is shown by the + and - signs on the diagrams, and it is obvious that there can be complicated patterns across the span as regards the variation of the local incidence to the free stream with time. Which of these modes is actually strongly excited in any particular buffeting condition is a matter of the pattern and frequency of the aerodynamic excitation, and of course of the relative levels of total structural and aerodynamic damping. In flight the aerodynamic damping is more important[2] and it is thus probably the first requirement in any corresponding model experiment that the structural damping should be kept as low as possible.

Fig 2 shows a small selection taken from aerofoil test data of the many types of static-pressure distribution which can occur at buffeting conditions on a wing at high subsonic speeds. In each case a change of one degree of incidence is shown after buffet onset, that is after separation of the surface boundary layers has started. The part of the wing chord subject to unsteady loading at the higher incidence in each case is shown with a zig-zag line along the x-axis. This is the main source of aerodynamic excitation in the 'rigid' wing case, but if the local incidence is varying significantly as the wing vibrates elastically in response to the unsteady loading, we will get extra cyclic excitation due to the vibration itself. The oscillation in loading associated with this could be smaller than, but similar to, that between the quasi-steady distribution shown in these diagrams. At the lowest Mach number of 0.65, the change in load due to a shock-induced 'bubble' separation is shown (Wing A) which will result in an increase in the local lift force ($+\Delta L$) and a nose-up couple ($+\Delta M$) about the flexural axis (assumed here to be about 40% chord). However, as the case for Wing C shows, if a flow separation builds from the trailing edge, there can be a dramatic drop in the suction level on the upper surface near the leading edge giving quite the reverse effect, a resultant loss in lift ($-\Delta L$) and a nose down couple ($-\Delta M$). At higher speeds the worsening of the flow separation aft of a strong shock wave due to a small increase in incidence can have either the same effect on the local lift and couple ($-\Delta L$, $-\Delta M$: Wing D at M = 0.70), or completely the opposite effect (Wing B at M = 0.79). In this latter case the shock gets much stronger with a small increase in incidence and moves forward resulting in a rapid transfer of the lift force forward on the chord. However, the shock may be reluctant to move forward at all (Wing A at M = 0.80) as for some 'supercritical' wing designs. Wing B at M = 0.70 shows the special case of an aft flow separation on a 'shockless' type of supercritical wing flow, the load changes due to an increase of incidence being small and in the direction $+\Delta L$ and $-\Delta M$.

The sign of the change in pitching moment, ΔM , with increase of incidence on an aerofoil section is thought to be an important characteristic as regards the possible development of pitching oscillations. Thus if the slope of the local pitching moment/incidence curve becomes negative outboard on a three-dimensional wing with respect to a moment reference point at or near the nodal line of a torsion mode, then single-degree-of-freedom stalling flutter becomes a possibility[18]. It will, of course, be necessary for this sectional aerodynamic characteristic to apply over a large part of the outer span of the wing and for the appropriate type of hysteresis loop to be present during the cycle of the oscillation. Fig 3 shows the appropriate pitching-moment curves for two local stations at 0.6 and 0.9 semi-span for a particular swept wing design, the dynamic characteristics of which are discussed in detail later in this paper. The marked negative slope in the curves at both stations at incidences between 6° and 9° should be noted. Some typical forms of hysteresis loop are also shown diagrammatically. This marked negative slope is mainly due to the shock moving forward between the moment reference point (at 35% chord) and the leading edge in this incidence range. At higher Mach numbers this characteristic does not occur because the corresponding rapid forward movement of the shock is aft of the reference point. The sketches in the lower half of Fig 2 demonstrate this effect.

As may be inferred from the changes in pressure distribution shown in Fig 2, of particular importance is the aerodynamic excitation locally near a strong shock wave where there is a large change of pressure on the surface. Data from some past RAE measurements on a rigid wing section are shown in Fig 4 for the case where the shock has caused a bubble separation. The rms pressure on the surface near the leading edge of the bubble, i.e. near the foot of the shock, was found to be highest in the lower range of frequency parameters, up to (fc/V) = 0.2 . This is the range which will generally include those frequencies typical for the primary bending and torsion modes of an aircraft wing. At higher frequencies, however, the excitation was greatest at the rear of the 'bubble' separation, that is, where reattachment of the flow to the surface was taking place. However, there was no indication in the data of sharp tuning in the frequency spectrum of the excitation; the model was thought to be effectively rigid over this frequency range with no modes of structural response which could interact with the aerodynamic flow.

The whole flow situation over a three-dimensional wing at high subsonic speeds and high incidences near the buffet-penetration boundary is, of course, usually very complex and it is misleading to rely too much on interpretations from two-dimensional data. To make this point, an oil flow visualization study is shown in Fig 5 taken from some recent RAE tests. Areas of calm, organized flow occur alongside strongly perturbed, unsteady flows. Both strong shocks and weak, oblique shocks are present, and it will be seen that leading-edge, trailing-edge, vortex and shock-induced types of flow separation all occur together. We need to remind ourselves, however, that such complex patterns of partly-separated flow over a surface as indicated by such visualization techniques are actually far from steady with respect to time, time measured in terms of tens or hundreds of structural vibrations, that is. Thus the aerodynamic excitation characteristics giving rise to structural response are probably continuously changing at a rate which can have little to do with the response itself. It can be assumed that there is generally a continuous, random 'drifting' process in the whole flow pattern with respect to time which contributes to a corresponding continuous drift in the amplitude of the structural response, and thus presumably in the degree of

interaction between excitation and response in any mode. To give circumstantial evidence for this, Fig 6 shows the rms structural response in the primary bending mode for three wings at limiting buffeting conditions. The 'instantaneous' rms response has been calculated in each case using only a very few cycles at a time and is plotted against an extended timescale for samples as long as 45 s in duration. The zero line has been included and it is clear that variations of 50% or more in the amplitude of the response occur at comparatively low frequencies (of the order of 10 to 100 times smaller than the frequency of the response itself). The record shown at the top is for a large, steel half-model in a wind tunnel, with a very low level of stream turbulence, the second one is for a smaller, aeroelastic complete model, (this is in fact Model 577/Flex 2 of Fig 8) and the third one for a small military aircraft in flight.

In the first two cases, of course, the model attitude was held constant with respect to the free-stream direction. Conditions were not so easily maintained constant in the flight experiment, however, and the aircraft was free to respond as a whole leading inevitably to some small variations in incidence during the recording. Taken as a whole the similarity of these three records may be taken to indicate that there is a natural tendency for comparatively slow, random changes in aerodynamic excitation to occur at separated-flow conditions.

3 MEASUREMENTS WITH FLEXIBLE MODELS

3.1 Models

During some recent tests made at RAE to investigate the static-deformation effects of full-scale aircraft wings[19], tests were carried out with a range of model wings designed with bending and torsional characteristics, scaled such that the three-dimensional static deformation in the wind tunnel would be approximately the same as that for a typical wing structure in flight at pre-determined speeds and altitudes. Fig 7 shows a sample of the comparisons made as regards the static lift-incidence curves between a normal 'rigid' all-metal model wing and one of these 'aeroelastic' wings. It may be noted in passing that representation of the full-scale deformation characteristics in this manner generally resulted in an increase in usable-lift, and that the vertical deflection of the tip of the flexible wing was of the order of 10 times that of the 'rigid' aluminium-alloy wing (and about 30 times that of one made in steel). As was expected, all these 'pseudo' aeroelastic wings had greater amplitudes of buffeting at high incidence than usual, but purely by accident it was noticed that at some conditions there was a considerable structural response in the primary torsion mode of the wing panel superimposed on the normal response in bending. This response in torsion was at a frequency too high for observation by eye and was not even immediately apparent from high-speed cine films. A special investigation into this phenomenon was therefore instituted.

Fig 8 gives some details of the three wings, all of the same aerodynamic design, for which dynamic data are quoted in this paper. The 577/A1 wing was made of solid aluminium-alloy, the 577/Flex 2 had a composite structure of steel sheets and epoxy resin, and the 2070 wing had a skin of carbon-fibre epoxy composite and was foam filled. Relative to the nominally 'rigid' all-metal wing (577/A1), the 577/Flex 2 wing was about 1/10 as stiff in bending and about 1/8 as stiff in torsion (based on tip deflections under a nominal, representative load distribution). The 2070 wing was 50% larger in size than either of the other two, but allowing for scale this was about 1/2 as stiff in bending and about 1/6 as stiff in torsion as the all-metal wing. The nodal line of the primary torsion mode was reasonably straight for all three models and the wind-off frequencies were 760 Hz (577/A1), 275 Hz (577/Flex 2) and 287 Hz (2070). The primary bending-mode frequencies were 77 Hz, 39 Hz and 75 Hz respectively. The nodal lines and frequencies of several higher bending modes are indicated in the diagram together with the positions of the strain gauges, accelerometers and upper-surface pressure transducers used in the experiments.

The aircraft associated with these models was in fact never built and flown, although the structural design had reached an advanced stage at the time of cancellation. The following table summarizes some of the relevant structural features of the above three models, normalized with respect to the nominal full-scale wing:-

LE. sweep : 27.2° M = 0.8 : tunnel T_0 = 45° Aircraft at sea level	Model 577/A1 solid metal	Model 577/Flex 2 steel/resin	Model 2070 carbon fibre/resin	Aircraft (assumed in model design)
Scale, S	1/15	1/15	1/10	1.0
RN per ft	3×10^6	3×10^6	2×10^6	5.9×10^6
RN on mean chord	1.26×10^6	1.26×10^6	1.26×10^6	24.6×10^6
Wing density, lb/ft³	173.1	143.4	66.02	20
Air density, ρ_{air}, lb/ft³	0.0413	0.0413	0.0275	0.0766
Density ratio, wing/air	4191	3472	2383	261
1st bending frequency, Hz	77	39	75	(7½)
1st torsion frequency, Hz	760	275	287	(30)
Relative frequency × S				
1st bending:	0.68	0.35	1.0	1.0
1st torsion:	1.69	0.61	0.96	1.0
Relative mass/S³	8.6	7.2	3.3	1.0
*Relative stiffness/S³				
bending:	10.2	1.0	5.33	1.0
torsion:	8.2	1.0	1.32	1.0
*Relative stiffness/S³ρ_{air}				
bending:	18.9	1.85	14.8	1.0
torsion:	15.2	1.85	3.65	1.0

* Based on the deflection root-to-tip due to a representative loading, summed across the span.

The important point to note in this table is the fact that the scaled frequencies of the primary bending and torsion modes were about correct for the 2070 model wing, but that the stiffnesses were too high (5.33 × too high for bending and 1.32 × too high for torsion). On the other hand the stiffnesses were correct for the 577/Flex 2 wings but the frequencies in bending and torsion were too low relative to full-scale (factors of 0.35 and 0.61 respectively). In no sense were these true 'aeroelastic' models in the context of conventional flutter testing. In the design, no attempt had been made to get the inertial characteristics right: the static strength together with the stiffness (for 577/Flex 2) or the mode-frequency (for 2070) were the primary considerations.

3.2 Buffeting response

The two 577 wings were tested at two angles of sweep (LE, 27.2° and 42°), and at the 42° setting for the most part a traditional type of buffet response was found at all speeds. Fig 9 gives the aerodynamic excitation at the two points P_1 and P_2 (see Fig 8) as measured with upper-surface pressure transducers for a Mach number of 0.85 and a tunnel stagnation pressure adjusted to give static distortion character-istics representative of full-scale flight at sea level. Flow separation on the model occurred first at the trailing edge near P_2 (at $\alpha = 4.3°$) with the main shock lying across the wing just aft of P_1. The linear spectral loading plots show a low level of excitation at each station. By $\alpha = 6.4°$ however, the shock has separated the whole of the flow behind it and has swung round to the leading edge at the tip, positioning itself right over P_1. There is a dramatic increase in local excitation shown here, particu-larly at the lower frequencies (with some slight suggestion of peaks in some high-order bending modes) but no significant increase at P_2, although the trailing-edge static-pressure has risen a little as the extra diagram at the top shows. By $\alpha = 7.5°$ the flow separation has spread to the leading edge at the tip and the shock has moved forward and inwards leaving the point P_1 well inside the separated-flow region. The excitation here drops back to a low level again, but in the separated region near the trailing edge the signal at P_2 now shows a strong increase in excitation, particularly at very low frequencies, associated with a recovery of mean static pressure at this position. At a higher incidence still, with the flow over the whole outer wing thoroughly separated, the excitation at both P_1 and P_2 becomes very even across the frequency range.

This may be regarded as a fairly normal pattern of excitation behaviour in a classic case of buffet response. The corresponding spectra of local acceleration of the wing (normal to the chordal plane) indicate a vigorous response in several of the modes of vibration, including primary torsion. These are not shown here, but at no point is there any apparent significant interaction with the excitation.

3.3 Development of torsional buzz

In contrast to this normal development of buffeting, Fig 10 shows for the same 577/Flex 2 wings set at a lower sweep how a strong, single-mode response in torsion can develop as buffet is penetrated, a state of torsional buzz being achieved at some incidences. At this combination of a leading edge wing sweep of 27.2° and a Mach number of 0.75, the shock moves forward more uniformly across the span as flow separations develop and in fact tends to remain fully swept, lying along the spanwise generators of the wing except at very high incidences. By an incidence of 6.5° the shock has moved forward to a position roughly half way between the nodal line of the primary torsion mode of the wing (shown in Fig 8) and the leading edge, and the flow aft is completely separated to the trailing edge over the whole of the outer half of the wing. A marked response in this particular mode (at about 250 Hz) develops out of the more general mild buffeting response at preceding incidences, as may be seen by the signal from the accelerometer A_1. The pressure at the foot of the shock at P_1 becomes generally very unsteady and also shows a corresponding peak. The shock is thus moving in sympathy with this torsional response of the wing and there is the possibility of a state of incipient buzz. It will be noted that the unsteady pressure at P_1 also contains a peak at 165 Hz, the frequency of a high-order bending mode which has a nodal line outboard near the tip (see Fig 8), but that the structural response as given by A_1 does not show any significant peak associated with this. As incidence is further increased this secondary peak in the spectrum of the pressure disappears and the possibility of torsional buzz at a frequency near 250 Hz becomes stronger because of the marked peaks in the unsteady pressure spectrum from both the transducer at P_1 near the foot of the shock and the trans-ducer at P_2 near the trailing edge. This is shown in the separate spectral plots at the top of the diagram for $\alpha = 7.6°$. At higher incidences still, above 8.7°, the shock moving forward with increase of incidence reaches positions so near to the leading edge that movement in sympathy with torsional vibration of the wing becomes inhibited and the buzz response can no longer be sustained. The peaks in the spectra of unsteady pressure virtually disappear and the response of the structure reverts to what is more properly described as a state of buffeting, although intermittent bursts of buzz are still evident.

Fig 11a gives some samples of the raw signal from the accelerometer at A_1 for this same case. When flow separations first appear at $\alpha = 4.4°$ the response is initially mainly in the first few bending modes, but as incidence is increased this then decreases as the primary torsional mode is excited. A moderate level of buffeting in this higher-frequency mode occurs by $\alpha = 6.0°$ and by $\alpha = 7.6°$ the buzz or sus-tained limit cycle of comparatively large amplitude has developed. As the corresponding filtered signals in Fig 11b show, a buffet response in the primary bending mode is superimposed which persists at the highest incidence when the mean torsional response has become smaller in amplitude and intermittent in character. It should be noted that the torsional buzz response at $\alpha = 7.6°$ is by no means steady in amplitude, but from the remarks made above with the respect to the data of Fig 6 we should not expect this. Generally it was found that any increase in amplitude of the primary torsional mode was accompanied by a reduction in the buffet response in the primary bending mode, or at least by an arrest in its growth with incidence. This moderation of a low frequency response (in bending) by a strong response at a higher frequency (in torsion) will be of benefit full-scale where the former type of response is usually of more concern as regards the ability of the pilot to carry out his tasks and can thus be a criterion for limiting the manoeuvre performance of an aircraft. However the structural implications of too strong a response at a high frequency may well be overriding.

It is interesting at this point to compare the frequency spectra of the structural response of the three model wings shown in Fig 8 at an incidence chosen such that this response is near the maximum achieved over the incidence range in all three cases at this Mach number. Fig 12 shows this comparison

for $\alpha \simeq 7.5^o$, but it must be noted that because of the different static distortion of the three wings, the aerodynamic lift and flow conditions will be somewhat different. For the 577/Flex 2 wing the diagram already shown in Fig 10 at buzz conditions is reproduced, obtained using the signal from the A_1 accelerometer. The 2070 wing never at any time in the whole test range showed such clear indications of a sustained limit cycle, and here at $\alpha = 7.5^o$ the response as indicated by the signal from the A_3 accelerometer is best described as 'single-mode buffeting'. The response is highly tuned, but the mean rms wing-twist amplitude about the nodal line, although still large by normal buffeting standards, was only about 10% of that of the mean rms of the limit cycle of the 577/Flex 2 wing at this incidence. Even at higher incidences the maximum amplitude achieved was only a little over double this. Lastly the corresponding frequency spectrum of the response of the 577/Al wing is shown; with several modes evidently being excited and more background 'noise' present we can identify this as the more traditional type of buffet response. Even here, however, on a much stiffer wing with a much higher frequency primary-torsion mode involved, the structure responds significantly in this same manner. In this instance the signal from strain gauges (S_1) at the wing root was used since no accelerometers were fitted, so interpretation of the analysed signal is not so easy as in the other two cases. Cross checks made comparing the signals from the strain gauges on the other two wings (S_2 and S_3 , see Fig 8), with the corresponding accelerometer signals demonstrated that the same characteristics were being indicated by both types of transducer.

For convenience the values of the stiffness and frequency of these three models in the primary torsion mode, relative to a nominal full-scale aircraft structure, have also been included in Fig 12, taken from the table given previously in section 3.1. Also for interest the values of the frequency parameter $\omega\bar{c}/V$ are quoted, based on wing mean chord; a value of 0.5 for this function is sometimes regarded as a threshold, below which 'stall flutter' may occur[18]. As was mentioned in section 3.1, 577/Flex 2 wing had a torsional stiffness representative of the equivalent aircraft but too low a frequency in the primary torsion mode; the 2070 wing on the other hand had a representative frequency but too high a stifness. It is a moot point which of these characteristics is the more important to get right in a model experiment in order to make the best prediction of full-scale behaviour. It is clear however that response data such as shown here from using either the 577/Flex 2 or 2070 model designs would raise doubts as regards the excitation of the primary torsion mode on a full-scale aircraft. The values of $\omega\bar{c}/V$, although consistent with the relative magnitude of the response from the three models cannot be used in any more direct way. The value of this parameter at corresponding conditions full-scale is about 1.4 for the nominal aircraft at sea level, i.e. about the same as for the 2070 model wing.

One of the conditions for the development of this torsional buzz response, referred to earlier in section 2, is the negative slope of the curve of local sectional pitching moment outboard on a wing with respect to incidence. The appropriate curves for 0.6 and 0.9 semi-span, obtained from static pressure measurements at M = 0.75 with another model of this same wing design, were shown in Fig 3 and it will be noted that for a local moment reference point at 35% chord, i.e. near the primary torsion mode node line of the 577/Flex 2 model, there is a marked negative slope between incidences of 6° and 9°, i.e. just in the range of incidence in which buzz was found to occur. It must be supposed that the hysteresis within the local pitching moment with respect to small oscillations in local incidence must have been such that a significant degree of negative aerodynamic damping was developed in this range.

Summing up at this point the aerodynamic factors which probably contributed to the development of wing torsional buzz in this case, we can note the limited range of sweepback angle, Mach number and incidence at which a strong shock wave on the upper surface lies approximately parallel to, and a reasonable distance from, the nodal line of the structural mode of vibration in question. The shock must be neither too near the nodal line of the motion nor too near the wing leading edge. Such a position of the shock needs to be fairly uniform across the span of the outer wing, as indeed a wing designer might well strive for in order to maximize aerodynamic performance. Secondly, the movement of this shock with incidence under the influence of the separated flow behind it needs to be such that the slope of the characteristic of local pitching moment about the nodal line with respect to incidence is negative. These factors can probably be generalized in principle with respect to any structural mode of vibration, and are the kind of features which can be fairly readily identified from conventional static-test force and pressure data. However, the extent to which aerodynamic damping becomes negative and varies with the amplitude of the motion is a critical factor which is difficult to predict without special test techniques.

Whether this buzz response in torsion at the peak of its development can be properly identified as single-degree-of-freedom flutter is, of course, open to interpretation. The evidence (not all of which is shown here) is mainly circumstantial, but the authors are of the opinion that, taken overall, this is strong enough to make this identification beyond any reasonable doubt.

3.4   Calculation of damping

Fig 13 gives some calculated values of the total apparent damping in the primary bending and torsion modes for the three wings at M = 0.75, the leading-edge sweep being 27.2^o. The values quoted are expressed as a percentage of the critical damping and have been obtained from the signals from the transducers A_1, A_3 and S_1 as appropriate by using an autocorrelation method[20] developed at the RAE for use with a Hewlett-Packard digital Fourier analyser. The signals were pre-filtered at frequencies indicated from the previous spectral analysis and considerable trouble was taken to avoid errors. At each incidence the average of about 40 sequential calculations is plotted in the figure using long recorded samples of about 60 s in duration. From what has been said earlier as regards the inherent, comparatively slow drifting in the separated aerodynamic flows at deep buffeting conditions, this need to take means over long periods of time to obtain consistent results will be appreciated. A continuous check was made for distortion in the logarithmic-decrement characteristics as the analysis proceeded. Since some of the damping ratios were very small, added accuracy was obtained where necessary by adding a known positive value of damping mathematically during the calculation (at the appropriate frequency of the mode in question) and then subtracting this again from the final answer. As will be seen the results appear to be consistent and plausible taken overall.

The damping, wind-off, was obtained in each case by making a separate experiment and checks were made over a wide range of stagnation pressures at low Mach number, attached-flow conditions to demonstrate,

circumstantially at least, that the level of structural damping obtained wind-off was likely to be sensibly constant over the range of aerodynamic loads applied during the main tests. Other subsidiary investigations demonstrated that the still-air damping, wind-off, was negligible and that the temperature effects on structural damping were small enough to be allowed for by means of simple corrections. Because of an unfortunate oversight no value of the wind-off damping for the 2070 wing in bending can be quoted with confidence.

The results shown for the 577/A1 wing of conventional model construction in Fig 13 are as expected, although the tendency for the apparent total damping ratio to fall in both the bending and torsion modes as incidence is increased is not without interest. However, of greater interest is the way the apparent damping ratio in the primary torsion mode falls dramatically as incidence is increased from 2° onwards for both the wings of flexible construction. In the case of the 577/Flex 2 wing, the mean damping becomes zero over the range of incidence at which buzz was observed to occur (7° to $8\frac{1}{2}^o$ at M = 0.75), but that for the 2070 wing always remained positive. Associated with this fall in total damping in the torsion mode there is a rise in that in the primary bending mode. It will be noted that the aerodynamic contribution to the total apparent damping ratio in the torsion mode becomes negative at the higher incidences. The three cases discussed in Fig 12 at an incidence of near 7.5^o are marked with a small arrow in Fig 13.

3.5 Response amplitude

The comparatively high amplitude of the limit cycle developed in a torsional buzz condition is of particular interest, since at full-scale this is a measure of the oscillatory stresses induced in the structure and thus of the effects on fatigue life. The amplitude of the twist about the nodal line at the position of the accelerometer A_1 (i.e. at about 70% semi-span) for model 577/Flex 2 is plotted in Fig 14 at M = 0.75, together with the apparent aerodynamic damping derived from Fig 13. Although scaling to appropriate conditions in flight cannot be done with confidence, the peak value of $\pm 0.56^o$ observed on the model at $\alpha = 7.6^o$ is thought likely to be at least of the same order as that on the aircraft. A smaller ratio of structural damping to aerodynamic damping is likely in flight and this · self could mean that the amplitudes developed full-scale will be somewhat larger than indicated by a mode experiment such as this. The amplitudes at the extreme wing tip on the model are likely to be about 30% higher than those at 70% semi-span, based on the ratio of the static twist deformations. As Fig 14 shows, the corresponding amplitudes for the 2070 model wing were smaller but very similar in character. In both cases the build-up of amplitude in torsion starts abruptly just at that point in the incidence range at which the aerodynamic apparent damping starts to become negative.

It is interesting to note that the rapid growth of amplitude in the primary torsion mode up to buzz coincided with a marked dip in the amplitude of the primary bending mode. Subsequently as the torsional amplitude declined at higher incidences the amplitude in bending increased once again. The full line in Fig 15 shows this amplitude at 70% semi-span for the 577/Flex 2 wing expressed as the vertical oscillatory displacement at the A_1 accelerometer position divided by the mean chord of the wing. Under 'normal' buffeting development this marked reduction in the amplitude of the primary bending mode did not occur. Associated with this reduction, the apparent aerodynamic damping in the bending mode rises sharply, and reference to Fig 13 shows that even in the case of the 2070 model wing with its milder growth of amplitude in torsion, the damping of the bending mode apparently first dips and then rises significantly in a similar fashion to that for the 577/Flex 2 wing as the amplitude in torsion first grows and then declines again through the incidence range. Generally at all conditions it was found that this opposing effect in amplitude in the two modes appeared to be consistent with the variations in the apparent damping ratios obtained independently in the analysis. Thus we may draw the conclusion that the occurrence of buzz in a high-frequency mode, even though this is only incipient or intermittent, can be beneficial full scale. The buzz itself will be of little concern to the pilot but the more disturbing buffet amplitudes at low frequency may be moderated significantly.

One of the main characteristics of single-degree-of-freedom flutter or buzz is that it takes the form of a limit-cycle[18]. The 'limit' of the cycle may vary considerably in amplitude with time because of the random nature of the aerodynamic separated flows present and the interaction with the buffet response in other modes, but the oscillation is usually of nearly constant frequency and is sustained virtually without interruption. However, another characteristic of buzz is that there is usually a lower threshold in amplitude below which the sustained oscillation dies away, only to be restarted when this threshold is exceeded again[18]. Thus with highly unsteady flows present, it is possible to have a state of intermittent buzz, the limit-cycle being triggered by an occasional large-amplitude excursion in the preceding buffet-response and then being cancelled again by a momentary 'low' in the buzz amplitude. An example of this state is shown in the lowest trace in Fig 11b at $\alpha = 9.2^o$; the mean total apparent damping ratio was positive (Fig 13) but in fact was probably switching between zero and a value of about +1%. Thus, not only can the amplitude of the full buzz condition vary considerably with time, but near the onset boundary of buzz very large variations in amplitude can occur. Well clear of the buzz condition, of course, the amplitude of the mode concerned is small, even though the response may be highly-tuned and is best described as 'single-mode buffeting' (Fig 11).

3.6 Differentiation between buffeting and buzz

The analysis of transducer signals in aerodynamic experiments to obtain damping ratios in a reliable and consistent manner is time-consuming and always fraught with many difficulties. Also, long samples are required which are sometimes not available. As the data of Fig 13 shows, to monitor experiments and to make sensible comparisons between cases is not easy using the derived values of apparent damping ratio, particularly when a buzz response grows out of a state of single-mode buffeting. A special technique was used therefore to differentiate between buffeting and buzz in the analysis of the data from the wind-tunnel experiments described here.

If the signal concerned appears to have a sustained oscillation of virtually constant frequency, even though the amplitude is varying with time, the state of buzz is readily identified. On the other hand if the signal takes the form of a series of short-lived batches of oscillations interspersed with null points at zero amplitude, there is little problem in identifying this as a case of buffeting. A simple electronic device was therefore employed to count the number of times in an interval of time that the amplitude of the

signal dropped to zero. As the number of nulls progressively dropped to zero and tne batches of cycles thus became progressively longer, it could be clearly seen that a state of buzz had emerged from a state of buffeting. It was found by experience that the most consistent way of counting the number of such null points was to use as a criterion the fact that a fairly large change of phase-angle usually occurred between the batches of cycles. After some trial-and-error the number of phase changes greater than $\pi/5$, counted per 1000 cycles of the oscillation, was adopted. All that was required to pre-condition the signal was a narrow-band filter to isolate the component of the mode in question before using the counting device.

The numbers of these phase-changes as defined above are plotted in Fig 16 for the primary torsion mode of the three wings used in the dynamic experiments, and the characteristics may be compared with the apparent damping ratios in this mode shown in Fig 13. A log scale is used to increase sensitivity at the lower values of the number of phase changes recorded. Although strictly speaking a zero count is needed to indicate a full buzz condition, a level of 0.1 counts per 1000 cycles was generally found to be associated with a mean apparent damping ratio of zero (as far as this could reasonably be established), and, for the 577/Flex 2 model, a count of 1 per '000 cycles was a clear indication of incipient buzz. The insensitivity of the 'rigid' wings of the 577/A1 model to this criterion and the reluctance of the phase-change count for the 2070 model wings to drop below 5 at any point in the incidence range, should be noted. The appropriate counts for the primary-bending and primary-torsion modes of the 577/Flex 2 are shown compared, also in Fig 16.

For convenience a *'Buzz Number'* has been contrived by taking the inverse of the phase-change count referred to above. Thus as buffeting develops into buzz this number rises in value. Fig 17 shows contours of this buzz number for the 577/Flex 2 wings against Mach number and angle of incidence. The line for the onset of buffeting in the primary torsion mode was obtained by a separate close scrutiny of the individual spectral-density plots and in general the buzz number was found to be in the range 0.03 - 0.05 at and below this boundary. A clear state of buzz was obtained within the contour of a buzz number of 10, and outside this, within the contour of 1.0, an incipient state of buzz was generally apparent. It will be noted that there appear to be both upper and lower bounds in both Mach number and incidence to the onset of buzz. Some partial explanation of this may be found in the way the quasi-steady aerodynamic flows develop locally with respect to these two parameters but no detailed discussion of this is possible here. As has been noted in section 2 with respect to Fig 3, there is a restricted range of Mach number and incidence within which the upper-surface shock moves forward rapidly with increase of incidence between the nodal line of the torsion mode and the wing leading edge. At this wing sweep (27.2°, leading edge) this movement was fairly uniform over the outer wing (see Fig 10).

4   EVIDENCE FROM FLIGHT EXPERIENCE

The onset of vibration in modes of comparatively high frequency, such as the primary torsion mode, is not likely to be noticed by the pilot of an aircraft, particularly when a general level of buffeting at low frequency is present. Even when recordings of signals from accelerometers on the wing are made and analysed to bring out the various frequency components of a vibration, seldom are the samples very long at any one aerodynamic flow condition. It is thus hardly surprising that the development of high frequency buzz is not well documented in the literature.

For an example of the excitation of these higher-frequency structural modes in flight, attention may be drawn in the first instance to some of the data presented by Benepe of General Dynamics at a recent AGARD symposium[21]. The example was given of a variable-sweep aircraft with the wings in a low-sweep position executing a slow, 4g wind-up turn at about 0.8 Mach number (Fig 18). The buffet response of the wing generally increased during this manoeuvre as expected, but over a certain band of incidences in the range there was a marked tendency for the first torsion mode to be strongly excited more than any others. This is shown by the way the measurement of wing torsional moment varied with incidence - in particular the width of the band of recordings made between, say, 19 and 24 s - and the peakiness in the PSD distributions shown for the time interval 18.5 to 20.5 s at 25 Hz, this being the frequency of the first wing-torsion mode. Benepe makes the point that all the signs here point to the occurrence of wing-torsional buzz. The corresponding data obtained from a 1/6 scale wind tunnel model (Fig 19) shows that at the same aerodynamic conditions even with a very stiff structure which has comparatively small amplitudes of structural response, the power spectra of the surface pressure fluctuations exhibit a tendency to peak at the frequency of the primary torsion mode of the model wing. These fluctuations were well correlated chordwise at this frequency, and the pressure-distribution diagram shows that a fairly strong shock wave lies across the span of the wing at this condition, presumably fairly parallel to the flexural axis in torsion. The conditions for buzz are thus very similar to those found in the RAE experiments discussed above and this comparatively 'rigid' model data shows just how prone to this type of response one would expect the corresponding more flexible aircraft wing to be.

As a second example, a limited amount of data can be quoted here from tests with another aircraft, not too different in configuration from the RAE model wing discussed in earlier sections. Some sample records are shown in Fig 20. The records shown in (a) give, at the top, an excerpt from the raw record from a port-side wing-tip, leading-edge accelerometer for a 4g wind-up turn. This appears to be a fairly normal case of buffet response, and subsequent filtering to bring out the first torsion-mode and the first bending-mode separately shows very much what one might expect: short-lived batches of oscillations interspersed with a return to zero and a phase change in each case. The frequencies of these two modes were approximately 28 Hz and 7 Hz respectively during this flight. The record shown in (b) have been included here to demonstrate by reference to another but similar flight with the same aircraft how the two wings can behave rather differently. At time T_1, just after the start of the manoeuvre, the port wing shows a tendency to develop a response in the first-bending mode whereas at the same time the starboard wing responds primarily in the first torsion mode. Soon after this at time T_2, however, both wings respond rather more generally in buffet in a whole range of modes and frequencies. The records shown in (c) for a different flight condition show some hint of what we have been discussing in this paper. The Mach number and the g pulled are both higher than in (a) and (b) and filtering the raw accelerometer signal to show the response in the first torsion-mode demonstrates that in this case longer-than-normal periods of sustained vibration occur. The PSD plot on the right-hand side of the diagram (on a linear scale) shows that the energy is mainly concentrated in this mode. Such low-level vibrations of the wing structure at such

high frequencies raise no problems in this particular case for either pilot or airframe: indeed, as we have seen from the test results from the RAE wing 577/Flex 2, the response to excitation in such higher modes can be associated with a marked reduction of that in lower-frequency modes, such as those in primary bending, which can limit the effectiveness of the pilot if allowed to become too large in amplitude.

5   RESPONSE IN OTHER MODES

As a demonstration that higher-order modes in bending can have the same effect as those in torsion, reference may be made to some transonic tunnel tests made many years ago with a solid steel complete model of a transport-aircraft layout[22]. Some data is quoted here in Fig 21. The model responded to aerodynamic excitation in a whole range of bending modes, for example at 46, 79, 124, 205 and 500 Hz, as the spectral analysis of the wing-root bending-moment signal showed. All these modes were excited by the development of shock waves and associated areas of flow separation on the wing upper-surface at high speeds. At $M = 0.93$, however, there was a sudden increase in the rms bending-moment signal as incidence was increased, (at point b), which on further investigation proved to be almost entirely due to oscillations in the first antisymmetric bending mode at, or very near, 79 Hz. Also, this sudden large increase vibration in this mode was associated with an inhibiting effect on the previous steady increase in amplitude in the other bending modes, particularly the lower-frequency primary-bending mode. The parallel to the behaviour of the 577/Flex 2 wing discussed above is thus quite marked and it is tempting to suggest that this was also a case of single-degree-of-freedom flutter, or 'buzz' in which there was direct interaction between the motion and the aerodynamic excitation. It would be interesting to know whether the tape record of this oscillation showed any of the characteristics of a sustained limit-cycle, perhaps triggered by the amplitude in buffet exceeding a threshold level. It is certainly remarkable to have had such an occurrence with a solid-steel model for which the response amplitudes would have been so very small. The diagrams quoted in Fig 21 show that 'buzz' in bending (if that is what we may call it) only occurs at $M = 0.93$ and only over a narrow range of incidence, presumably when the wing separations are particularly sensitive to the model response amplitude in this particular mode at 79 Hz. The broader peaks at other conditions, eg at $M = 0.90$, $C_L = 0.68$, were always associated primarily with response in the primary bending mode (46 Hz) and rigid-body modes of even lower frequency (eg 19 Hz), which is what we might normally expect for a classic buffet-response. It may also be seen in Fig 21 that when 'wing-bodies' were added to the wing, the characteristics of the aerodynamic flows were so changed that all tendency to 'buzz' disappeared completely.

6   CONCLUDING REMARKS

This paper has discussed the marked response in torsional vibration which can sometimes occur on wings at high subsonic speeds. The types of aerodynamic flow which can develop as the stall develops may provide the necessary excitation for such vibrations, which may not be immediately apparent unless a special investigation is made. In some cases a sustained high-amplitude oscillation or 'buzz' may develop. Ironically, attempts by wing designers to maximize aerodynamic performance by maintaining shock sweep and good sectional characteristics over the outer part of the wing at high incidence may make just such a structural response more likely in flight. High-speed wind-tunnel models of conventional construction are unlikely to show this phenomenon or be useful in making predictions of the onset boundaries and amplitudes involved. However, although a complete inertial and elastic structural representation is not usually possible as a routine, comparatively simple and robust 'pseudo' aeroelastic models can be used, provided a sensible and balanced mismatch of the structural dynamic characteristics can be made. The occurrence of such high-frequency vibrations in flight has been noted in recent years in one or two instances where suitable instrumentation has happened to be in use, but probably many more occurrences have gone by unnoticed. Although unlikely to be a problem for the pilot, if the amplitudes become large such high frequency vibration could become a matter of concern as regards the aircraft structure and equipment carried. However, as regards the buffet-boundary more generally, the effects could be beneficial since the incidence of such high frequency structural responses tends to be accompanied by a reduction, or at least an arrest in the development, of the vibration at low frequency which can affect the efficiency of the pilot directly. What is needed is a well planned flight-tunnel comparison to explore the phenomenon properly and to develop methods of prediction and alleviation based on a better understanding of the aerodynamic and structural characteristics involved.

REFERENCES

1   W.B. Huston, A study of the correlation between flight and wind tunnel buffeting loads. AGARD Report 121 (1957)

2   D.D. Davis, D.E. Wornom, Buffet tests of an attack aeroplane with emphasis on data from wind tunnel tests. NACA RM L57H13 (1958)

3   D.G. Mabey, An hypothesis for the prediction of the flight penetration of wing buffeting from dynamic tests on wind tunnel models. ARC CP 1171 (1971)

4   C.G.B. Mitchell, Calculation of buffeting of slender wing aircraft at low speeds. RAE Technical Report 68169 (1968)

5   R.E. Mullans, C.E. Lemley, Buffet dynamic loads during transonic manoeuvres. AFFDL TR-72-46 (1972)

6   D.G. Mabey, Beyond the buffet boundary. J. Roy. Aero. Soc., April 1973

7   - , Aircraft stalling and buffeting. AGARD LS-74 (1975)

8   J.G. Jones, A survey of the dynamic analysis of buffeting and related phenomena. RAE Technical Report 72197 (1973)

9   D.G. Mabey, G.F. Butler, Measurement of buffeting on two 65° delta wings of different materials. RAE Technical Report 76009 (1976)

10   G.F. Butler, G.R. Spavins, Preliminary evaluation of a technique for predicting buffet loads in flight from wind tunnel measurements on models of conventional construction. AGARD FDP Symposium, CCP-204-Paper 21, September 1976

11   P.W. Hanson, Evaluation of an aeroelastic model technique for predicting airplane buffet loads. NASA TN-7066 (1973)

12   D.G. Mabey, Measurement of buffeting on slender wing models. ARC CP No.917 (1967)

13   H.H. Pearcey, J. Osborne, A.B. Haines, The interaction between local effects at the shock and rear separation. AGARD Paper CP No.35, ARC 30477 (1968)

14   A.B. Haines, Possibilities for scale effects on swept wings at high subsonic speeds. AGARD Paper CP-83-71, No.14 (1971)

15   D.W. Riddle, Wind tunnel investigation of surface pressure fluctuations associated with aircraft buffet. AIAA Paper 75-67 (1975)

16   C. Hwang, W.S. Pi, Transonic buffet behaviour of a Northrop F-5A aircraft. AIAA Paper 75-70 (1975)

17   L.E. Erikson, Transonic single mode flutter and buffet of a low aspect-ratio wing having subsonic airfoil shape. NASA TND 73 46 (1974)

18   N.C. Lambourne, Flutter in one degree of freedom. AGARD Manual on Aeroelasticity, Pt.5 Ch.5, February 1968

19   G.F. Moss, D. Pierce, Some aeroelastic distortion effects on aircraft and wind tunnel models. RAE Technical Report 76107 (1976)

20   J.S. Bendat, A.G. Piersol, Random data: Analysis and measurement procedures. Wiley, New York (1971)

21   D.B. Benepe, Aircraft manoeuvres and dynamic phenomena resulting in rapid changes of load distributions or/and fluctuating separation. AGARD FDP Symposium, CPP-204-Paper 21, September 1976

22   E.S. Cornette, Wind tunnel investigation of the effects of wing bodies, fences, flaps, and a fuselage addition on the wing buffet response of a transonic-transport model. NASA TN D-637, April 1961
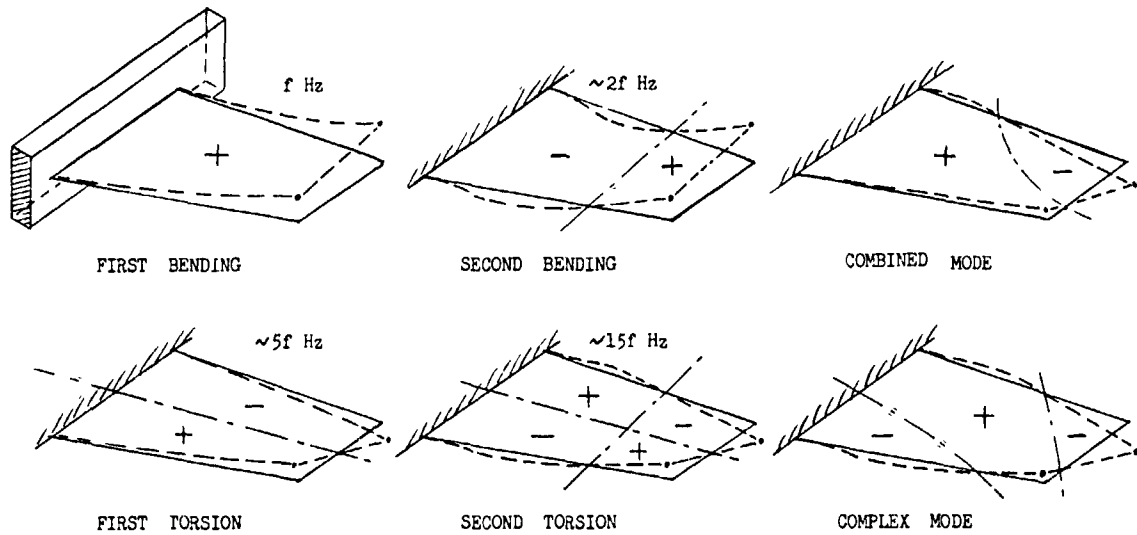
Fig 1 Some normal modes of a swept wing (diagrammatic only)
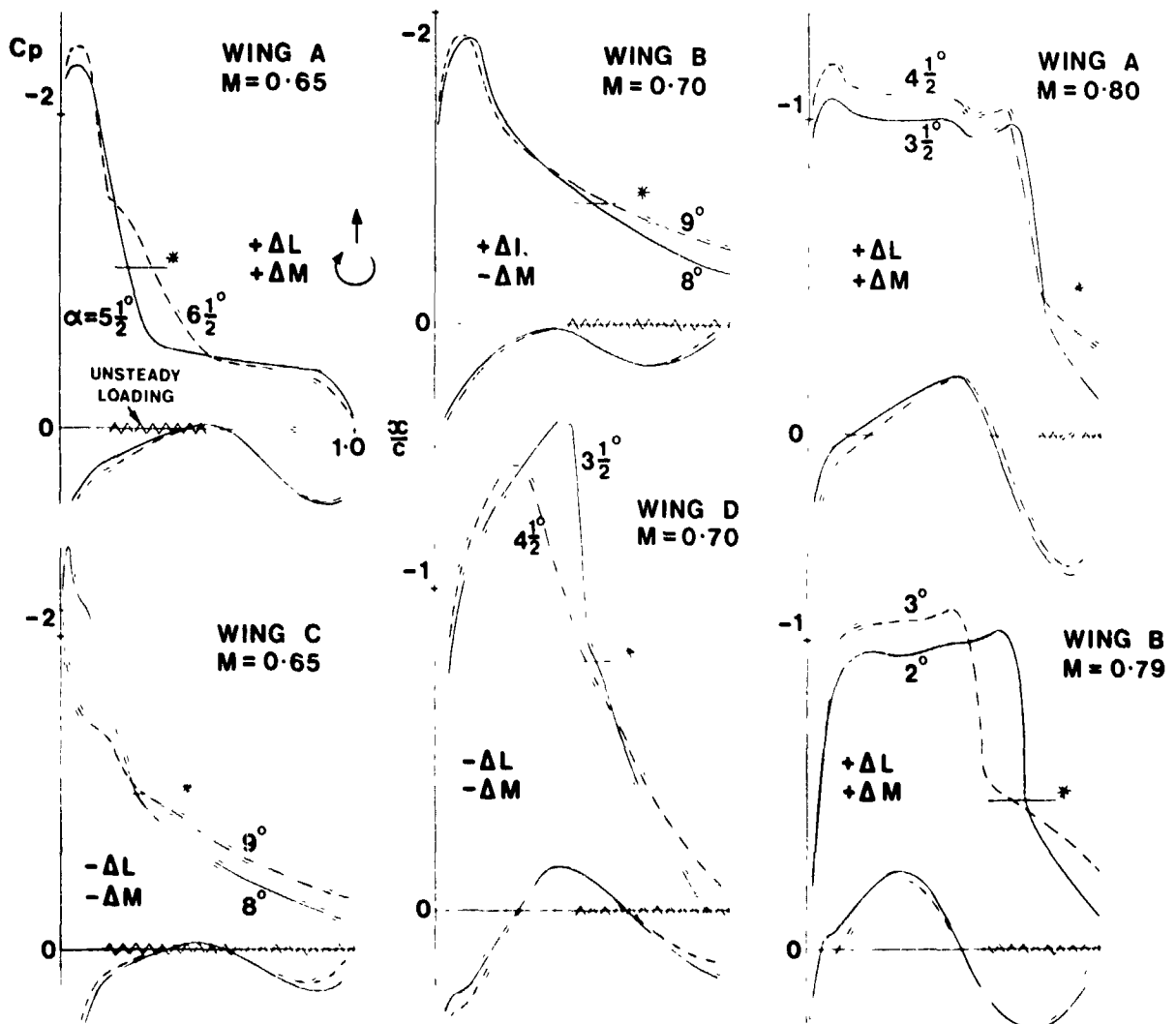
Fig 2 Two-dimensional wing static-pressure distributions with unsteady
flow separations present: change due to 1° of incidence

LOCAL
PITCHING-MOMENT
(35%c)

FOR PRIMARY
TORSION MODE
$\eta = 0.6$
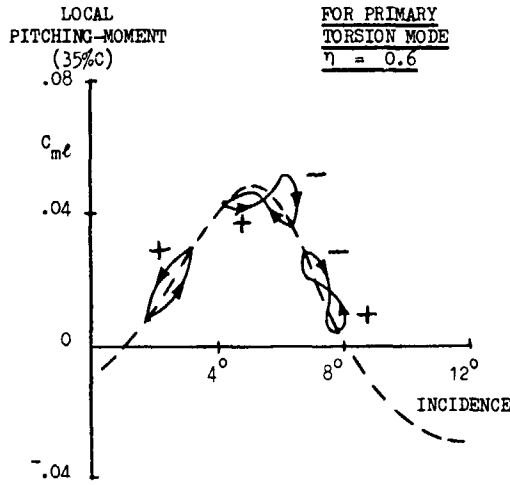
POSSIBLE HYSTERESIS LOOPS IN THE
LOCAL PITCHING-MOMENT FOR
TORSIONAL OSCILLATIONS OF LOCAL
INCIDENCE (DIAGRAMMATIC ONLY)

LOCAL
NORMAL-FORCE

LOCAL
PITCHING-MOMENT
(35% CHORD REF PT)

$M = 0.75$
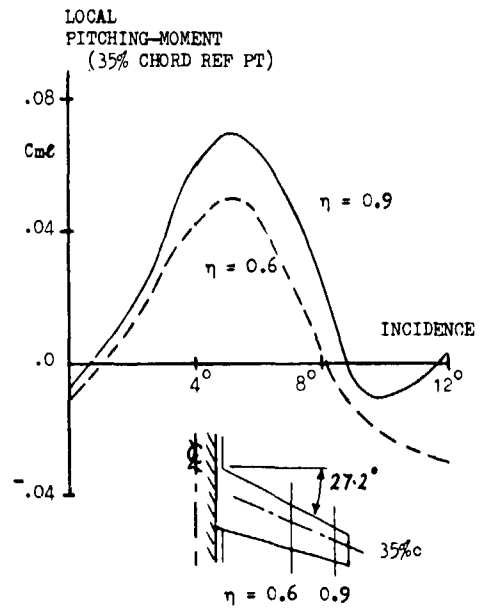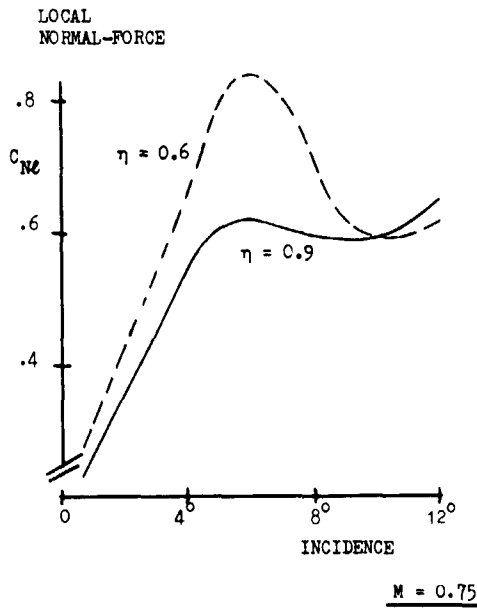
Fig 3   The local variation of static normal-force and pitching-moment
outboard on a swept-wing design (that of models 577 and 2070,
shown in Fig 8)

NACA 16 SECTION
t/c = 11.7%
R_c = 1 x 10^6
M = 0.82
α = 6.7°

UPPER
SURFACE
STATIC
PRESSURE

CLOSED BUBBLE
OF SEPARATED
FLOW

C_p^*

$\frac{Cp_{RMS}}{\sqrt{Band-width}}$

BUBBLE

.80 $\frac{fc}{V}$

FREQUENCY
PARAMETER

.20

($\frac{1}{3}$ OCTAVE
FILTER
USED)

.08

.02
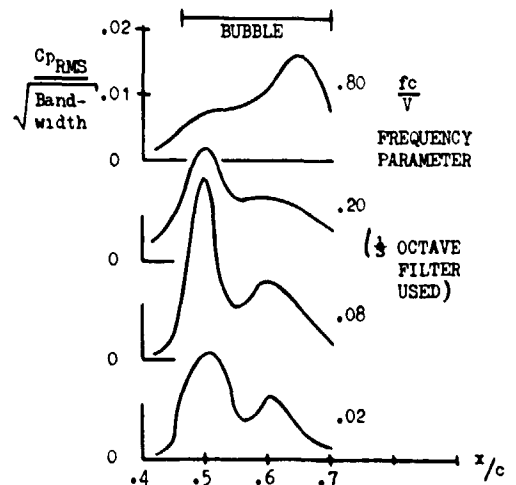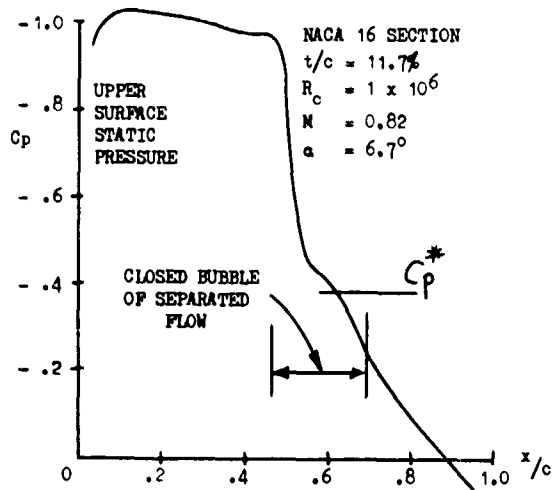
Fig 4   Aerodynamic excitation in a shock-induced bubble separation

ATTACHED FLOWS

WEAK FLOWS IN AREAS
OF FLOW SEPARATION

FLOW LEAVES SURFACE

LEADING—EDGE SEPARATION

TRAILING—EDGE SEPARATION

WEAK SHOCK WAVES

STRONG SHOCK WAVES
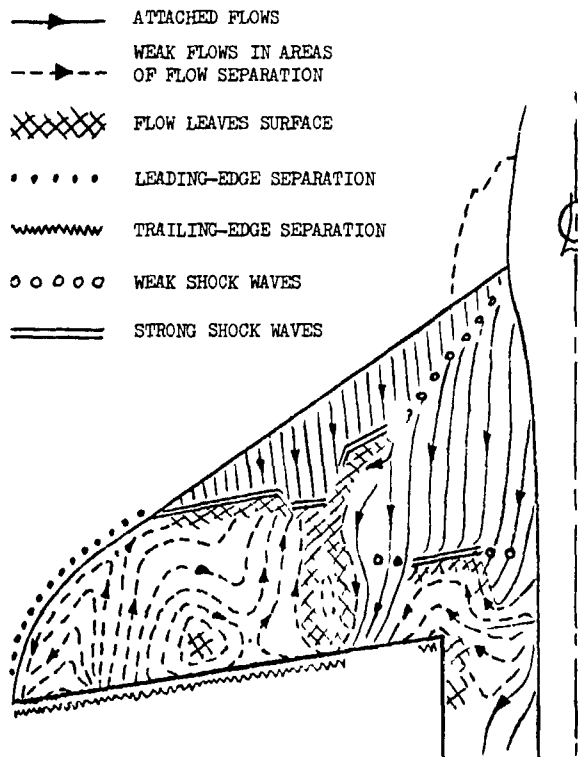
RAE 8' x 6' TUNNEL TESTS:
MODEL 589/1; M = 0.90; α = 8.3°

Fig 5 Example of a complex separated-flow situation at deep buffet-
penetration conditions
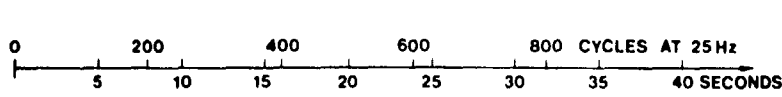
SOLID STEEL HALF-MODEL WITH A
VARIABLE-SWEEP WING IN THE RAE
8ft x 8ft TUNNEL

RMS WING-ROOT STRAIN-GAUGE
SIGNAL, FILTERED AT 25 Hz

AVERAGE OVER 2.5 CYCLES

M = 0.75; $R_{\bar{c}}$ = 11.5 x 10^6;
α ≈ 10°
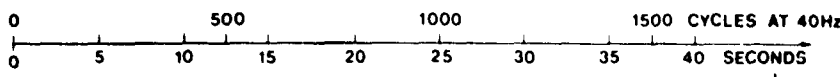
AEROELASTIC COMPLETE-MODEL
WITH A VARIABLE-SWEEP WING IN
THE RAE 8ft x 6ft TUNNEL

RMS ACCELEROMETER SIGNAL 70%
SPAN FILTERED AT 40 Hz

AVERAGE OVER 4 CYCLES

M = 0.80; $R_{\bar{c}}$ = 1.26 x 10^6;
α = 8°
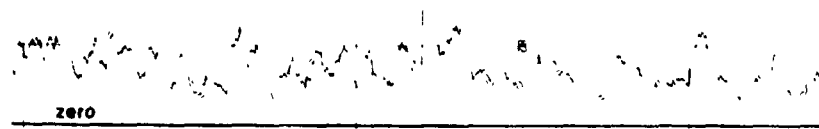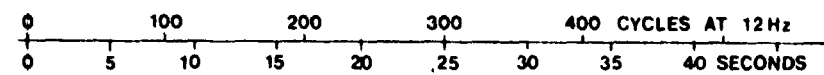
AIRCRAFT 'A' IN FLIGHT

RMS ACCELEROMETER SIGNAL, NEAR
WING TIP, FILTERED AT 12 Hz

AVERAGE OVER 3.5 CYCLES

M ≈ 0.7; 33000ft ALTITUDE:
α ≈ 8½°

Fig 6 Variation of rms structural response with time for three different
cases: first wing-bending mode at moderate buffeting conditions

$M = 0.8 : H_0 = 0.8$ bar

.8

C_L

LIFT

.7

M

THIS LIFT REPRESENTS
A 6g CONDITION AT
SEA LEVEL WITH AN
AIRCRAFT WING-LOADING
OF 5.5 kPa (115 lb/sq ft)

MAX USABLE LIFT

M

.6

BUFFET ONSET

0

.5

.4

'RIGID' WING 577/A1

FLEXIBLE WING 577/FLEX 2

.3

FLEXURAL
AXIS

.08 TIP
z/s

.2

.06

42°

577/FLEX 2
TIP DEFLECTION

S

.04

.1

.02

AR = 5.5 : t/c = 10.5%

0   2°   4°   6°   8°   10°   12°
INCIDENCE
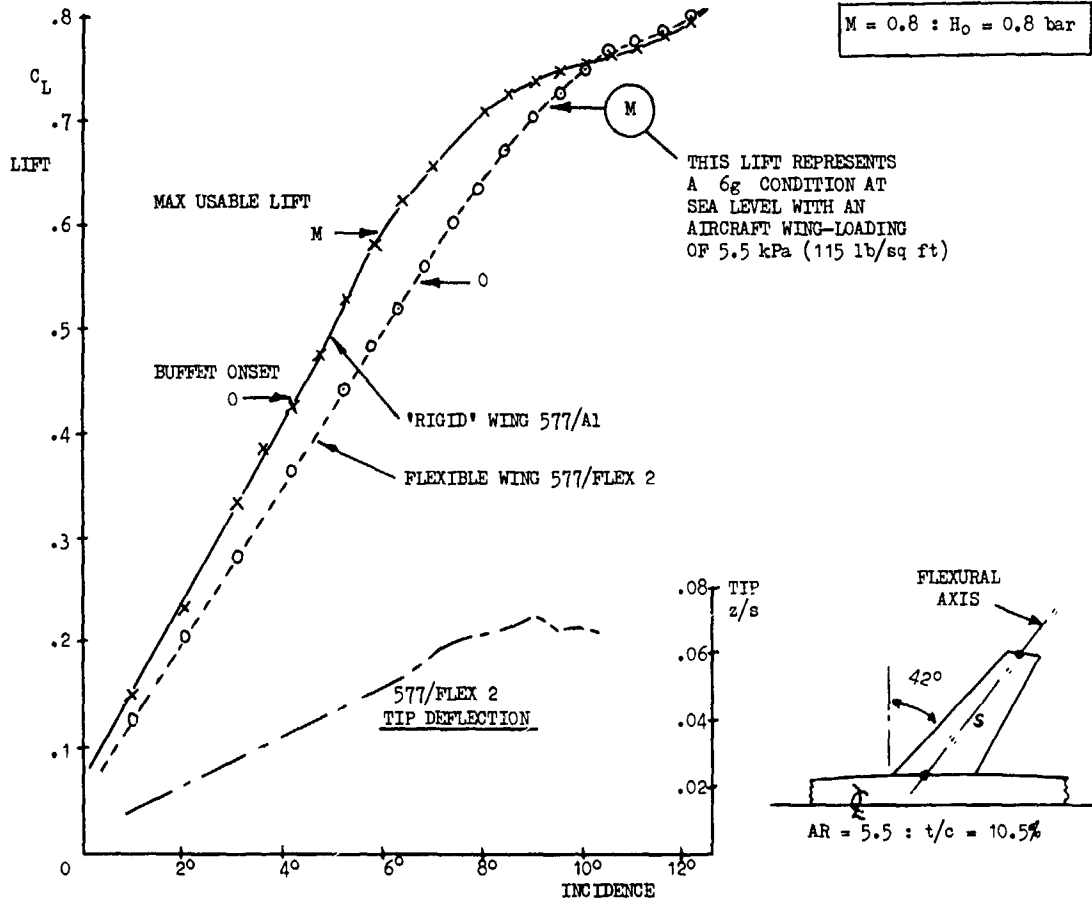
Fig 7   Comparison of static lift-curves: model wings 577

WIND-OFF NODE-LINES
AND FREQUENCIES:-

760 Hz   275   287

494   310   396
294   165
133

	y/b	x/c
ACCELEROMETERS		
A_1	.70	.19
A_2	.66	.72
A_3	.68	.20
PRESSURE-TRANSDUCERS		
P_1	.67	.26
P_2	.64	.86
STRAIN-GAUGES		
S_1	.28	.43
S_2	.34	.66
S_3	.24	.40

494   310   396
294   165
133

A_1
A_2 A_1 A_3
P_2 P_1 310

310

S_1 S_3 S_2
77   39   75

AIRCRAFT BODY   AIRCRAFT BODY   SIMPLE BODY

	577 / A1 COMPLETE MODEL SOLID A1 ALLOY	577 / FLEX 2 COMPLETE MODEL STEEL/RESIN COMPOSITE	2070 HALF MODEL CARBON-FIBRE/RESIN
NOMINAL SCALE, S	1/15	1/15	1/10
RELATIVE MASS / S^3	1.0	.83	.38
" BENDING STIFFNESS / S^3	1.0	.098	.52
" TORSION STIFFNESS / S^3	1.0	.12	.16

Fig 8   Some details of the models used in the dynamic-response tests

UPPER
SURFACE
STATIC
PRESSURE
AT P_2

$-C_{p_2}$

$10 \cdot 6^\circ$

RAE MODEL 577/FLEX 2
LE SWEEP 42°
M = 0·85
RN = 3x10^6/ FT

$4 \cdot 3^\circ$ $6 \cdot 4^\circ$ $7 \cdot 5^\circ$

RMS C_p

$\alpha = 10 \cdot 6^\circ$

$\alpha = 10 \cdot 6^\circ$

$\alpha = 7 \cdot 5^\circ$

$\alpha = 7 \cdot 5^\circ$

$\alpha = 6 \cdot 4^\circ$

$\alpha = 6 \cdot 4^\circ$

SHOCK

SEPARATED
FLOW

$\alpha = 4 \cdot 3^\circ$

$\alpha = 4 \cdot 3^\circ$

P_1

P_2

100   200   300   400   500
FREQUENCY Hz

100   200   300   400   500
FREQUENCY Hz

RMS C_p AT P_1

RMS C_p AT P_2
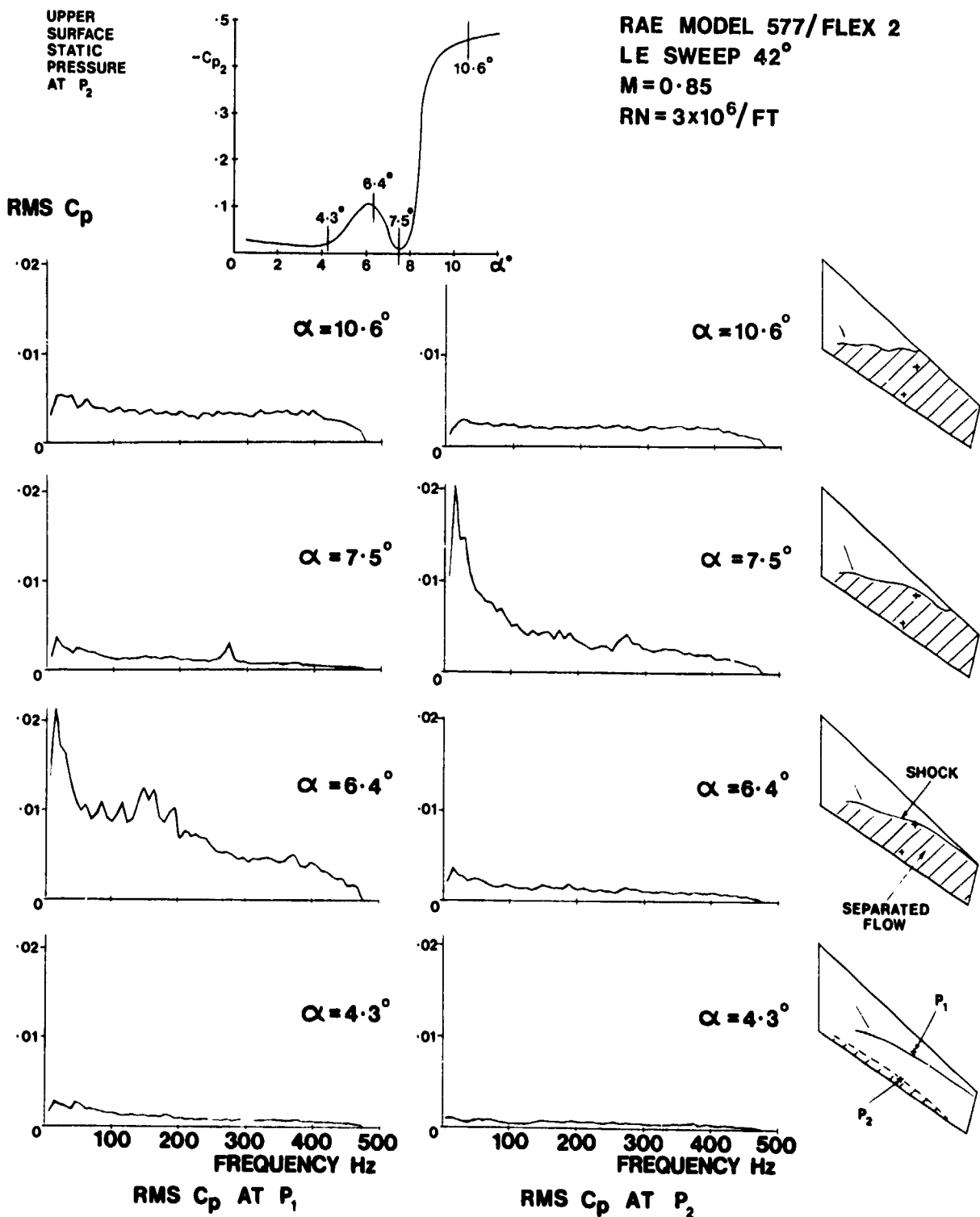
Fig 9   Unsteady aerodynamic pressures on a swept wing at
buffeting conditions
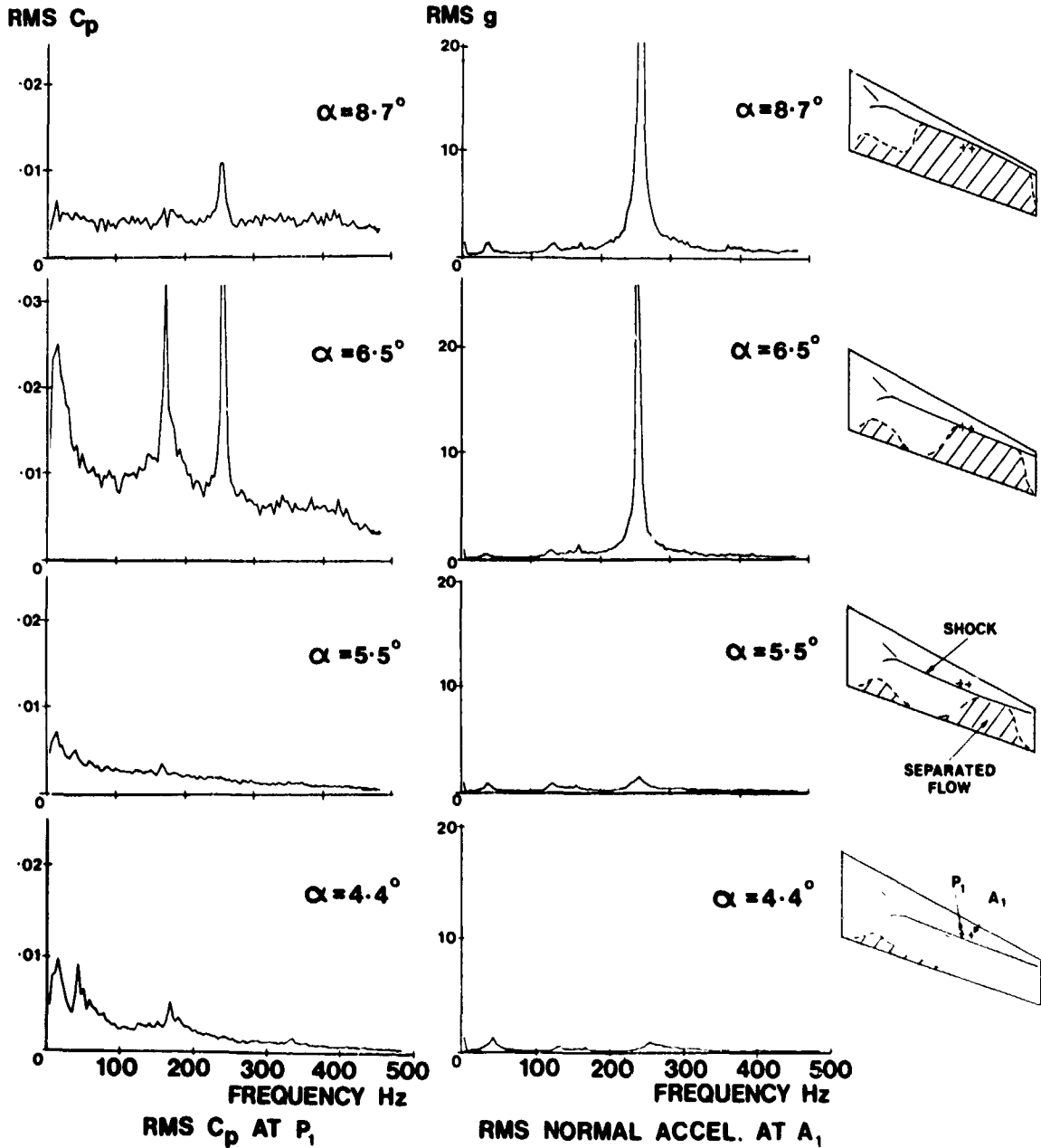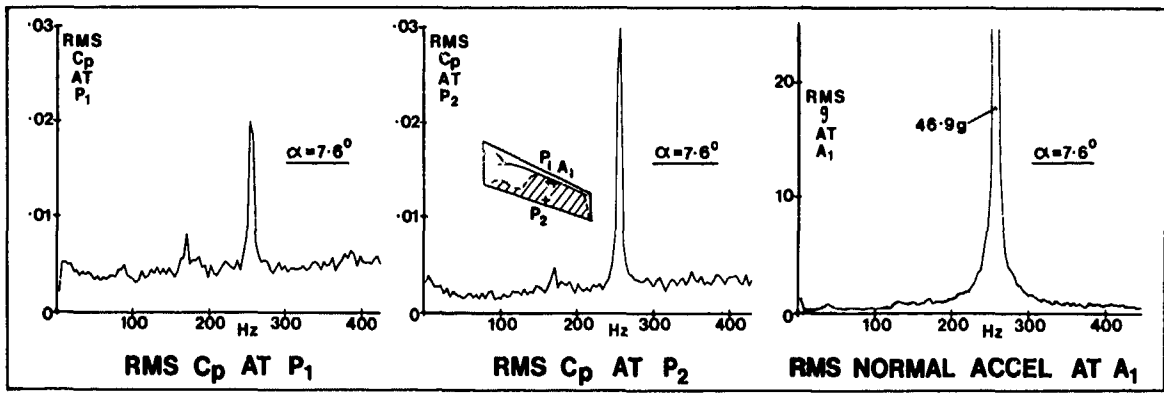
Fig 10 Unsteady aerodynamic pressure and structural response at wing-torsional buzz conditions. Model 577/Flex 2, leading-edge sweep 27.2°, M = 0.75, R_c = 1.25 x 10⁶
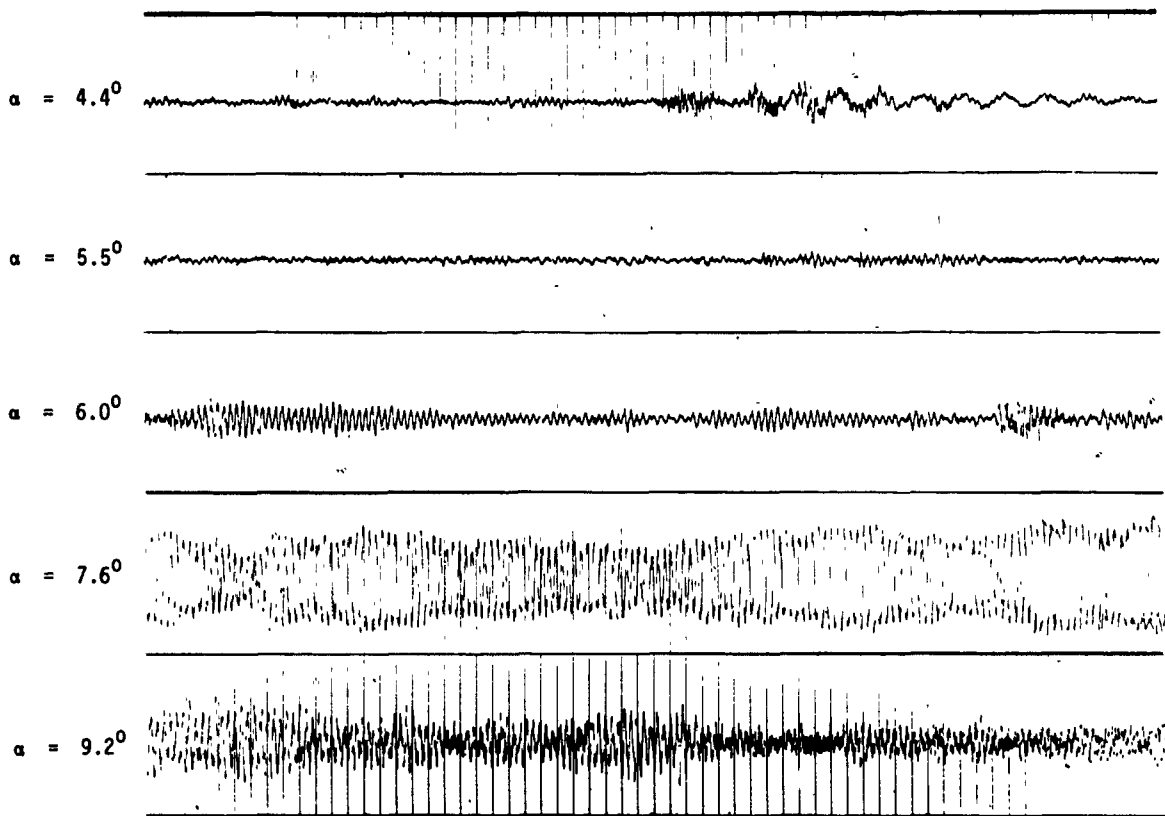
Fig 11a   Some A_1 accelerometer records for model 577/Flex 2:
raw signals: leading-edge sweep 27.2^o, M = 0.75,
R_c = 1.26 x 10^6
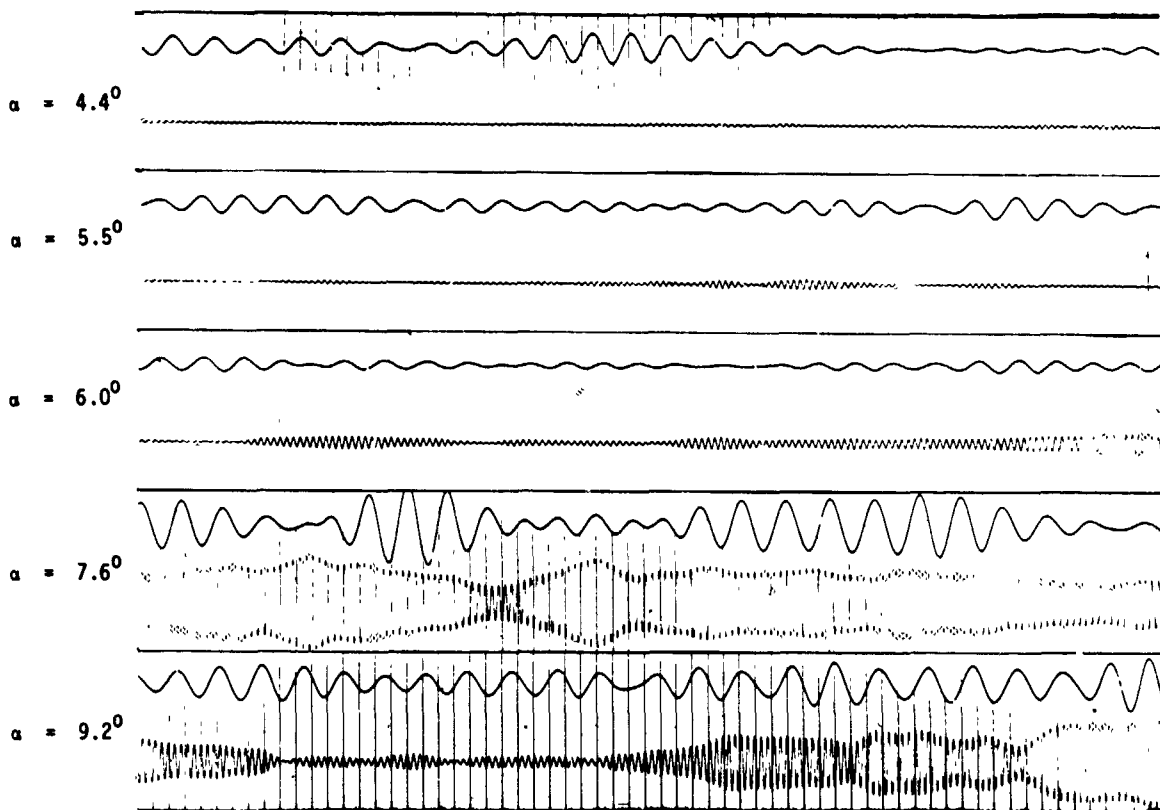
Fig 11b   The signals of Fig 11a filtered at primary bending and
torsion frequencies

FREQUENCY PARAMETER OF PRIMARY TORSION MODE, $\omega\bar{c}/V$

| 0.87 | 1.36 | 2.40 |

FREQUENCY OF PRIMARY TORSION MODE RELATIVE TO NOMINAL AIRCRAFT

| 0.61 | 0.96 | 1.69 |

TORSIONAL STIFFNESS RELATIVE TO NOMINAL AIRCRAFT

| 1.0 | 1.32 | 8.2 |
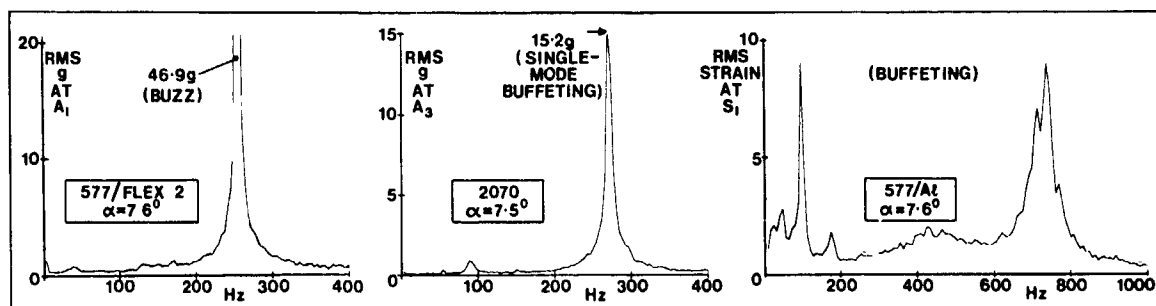
Fig 12   Structural response of the three wings of Fig 8 at a high
incidence; leading-edge sweep 27.2°, M = 0.75,
$R_{\bar{c}}$ = 1.26 x 10⁶
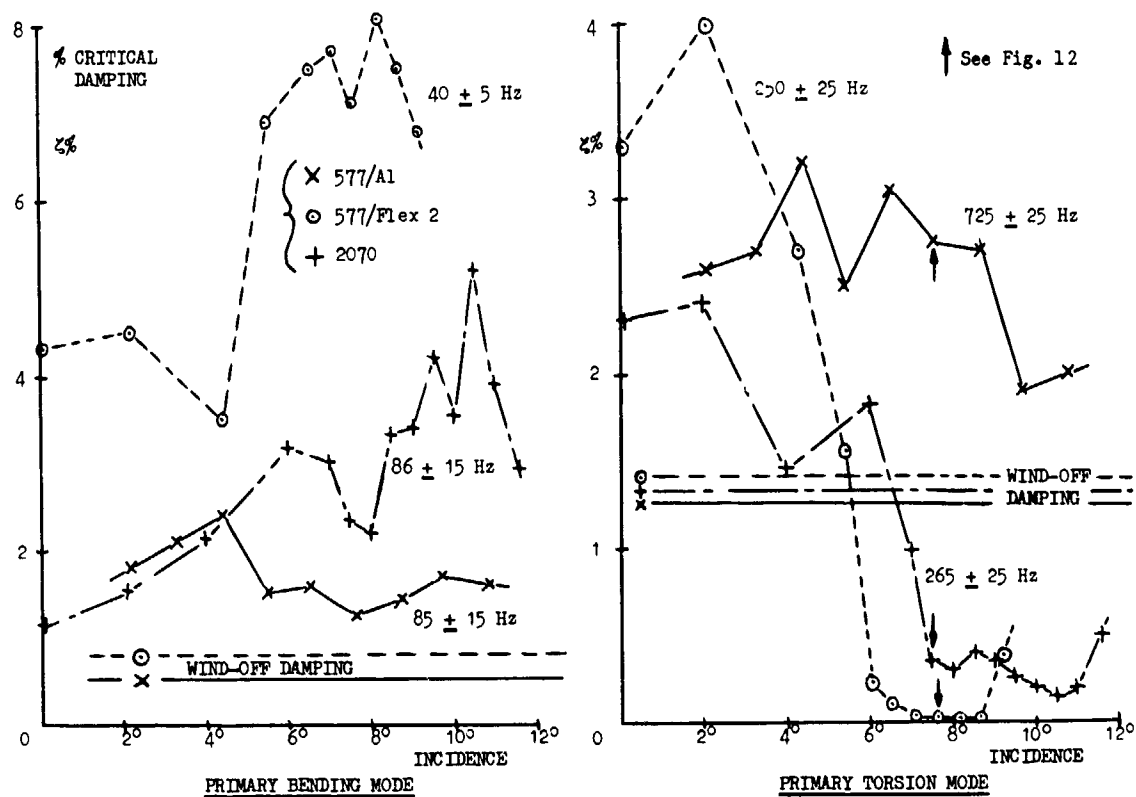
Fig 13   Variation of total apparent damping in primary bending and torsion
modes: leading-edge sweep 27.2°, M = 0.75, $R_{\bar{c}}$ = 1.26 x 10⁶
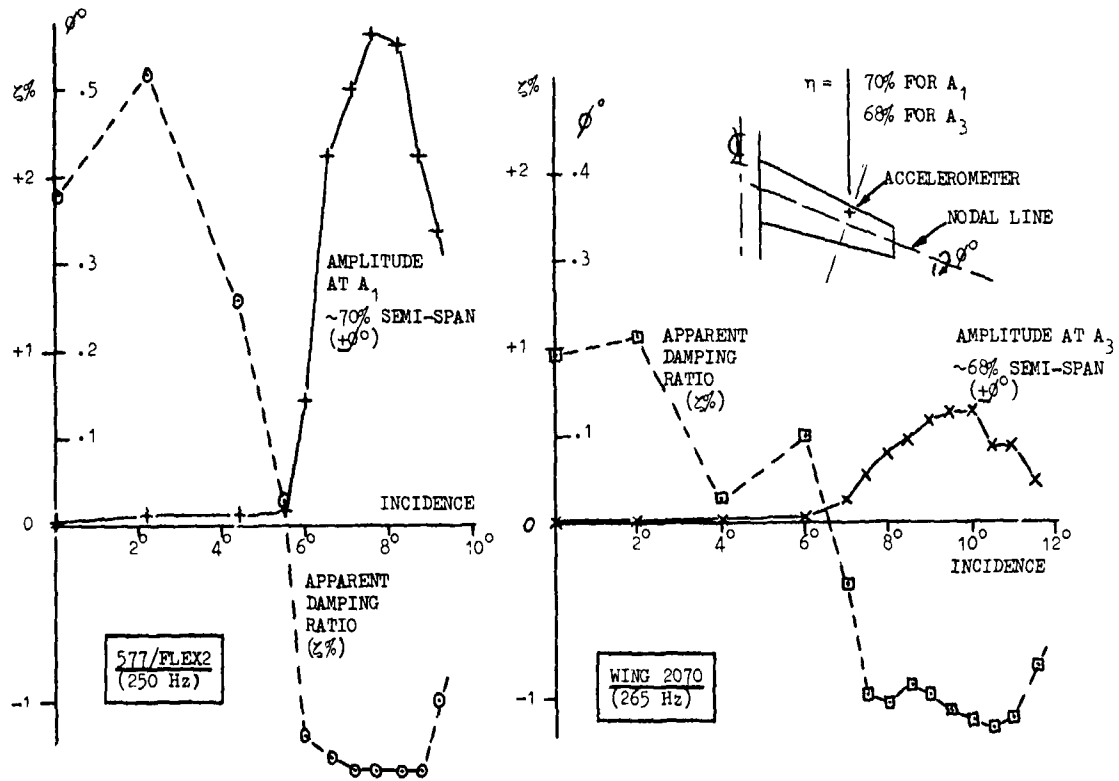
Fig 14 Apparent aerodynamic damping and mean amplitude of response in
primary torsion mode: leading-edge sweep 27.2°, M = 0.75,
$R_{\bar{c}}$ = 1.26 x 10^6
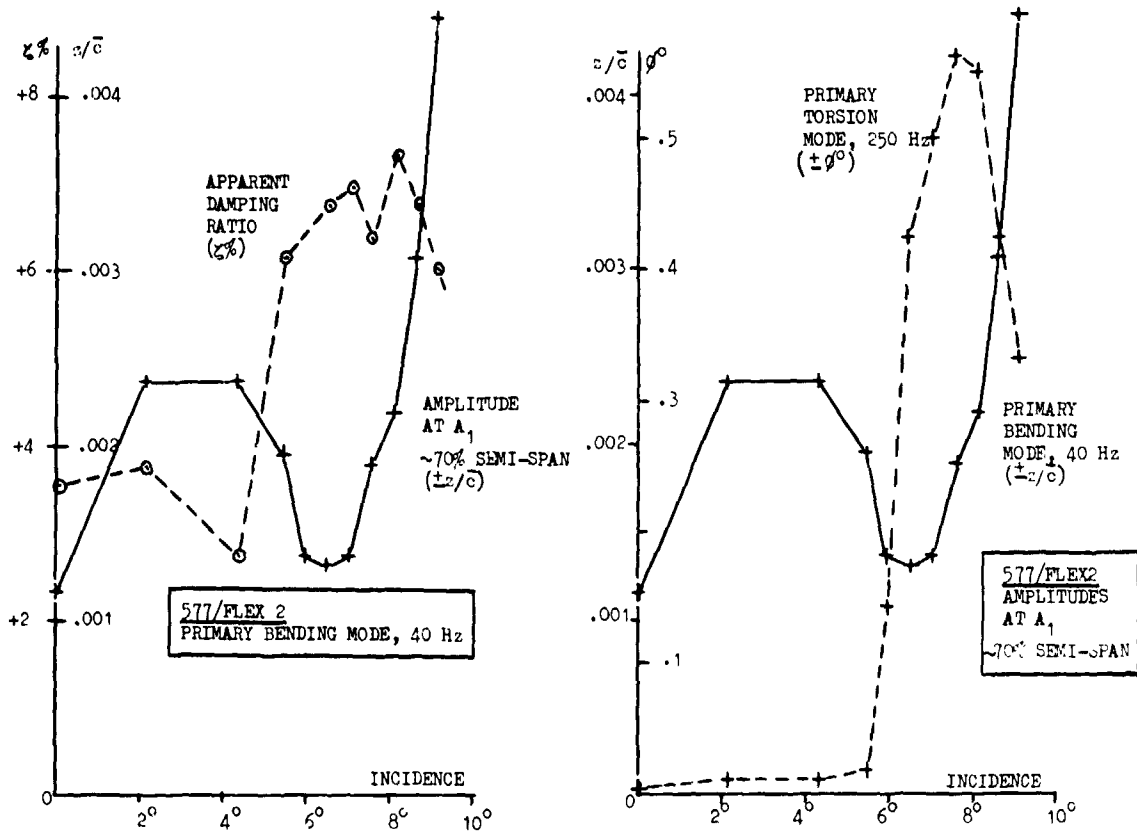
Fig 15 Apparent aerodynamic damping and mean amplitude of response of
577/Flex 2 wing: leading-edge sweep 27.2°, M = 0.75,
$R_{\bar{c}}$ = 1.26 x 10^6

NO OF PHASE CHANGES >π/5 IN A 1000 CYCLES (LOG SCALE)

PRIMARY
BENDING
40 Hz

PRIMARY
TORSION
250 Hz

MODEL
577/FLEX 2

INCIDENCE

NO OF PHASE CHANGES >π/5 IN 1000 CYCLES (LOG SCALE)

577/A1
725 Hz

2070
265 Hz

577/FLEX 2
250 Hz

PRIMARY
TORSION
MODE
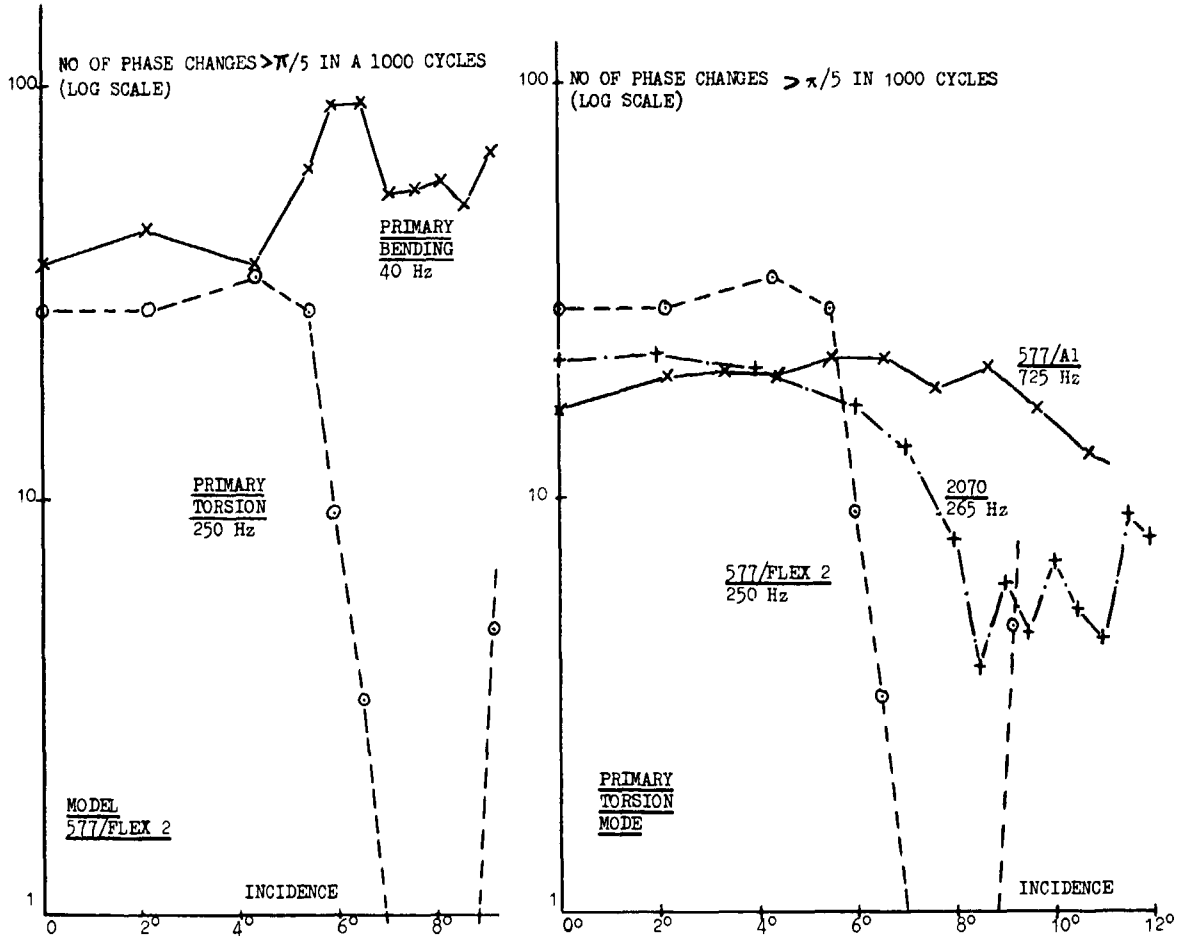
INCIDENCE

Fig 16 Number of phase changes >π/5 in 1000 cycles: leading-edge sweep 27.2°, M = 0.75, $R_{\bar{c}}$ = 1.26 x 10^6

INCIDENCE

WING BUZZ
(Shown hatched)

ONSET OF
TORSIONAL RESPONSE
(BUFFETING)

BUZZ NUMBERS
(See text)
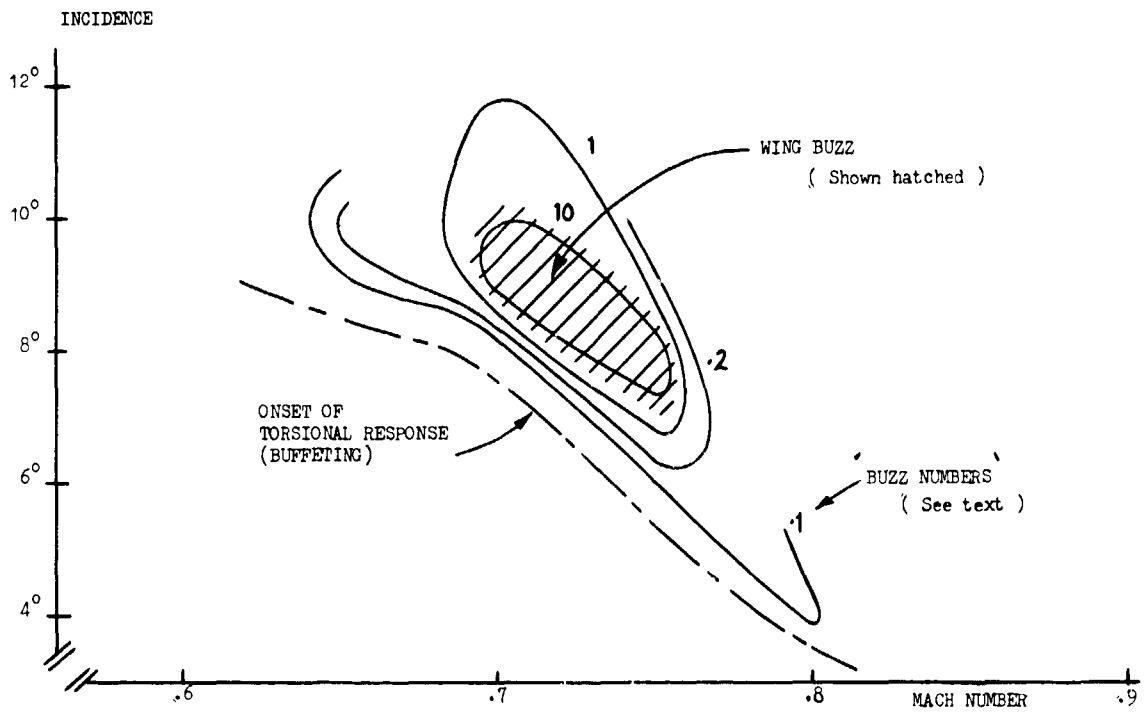
MACH NUMBER

Fig 17 Mach number/incidence boundaries for wing torsional buffeting/buzz model 577/Flex 2, leading-edge sweep 27.2°, $R_{\bar{c}}$ = 1.26 x 10^6

MEAN PRESSURES

$\Lambda = 26^{o}$
$M = 0.80$
$\alpha = 10.18^{o}$
$RN = 8 \times 10^{6}/FT.$

UNSTEADY PRESSURES
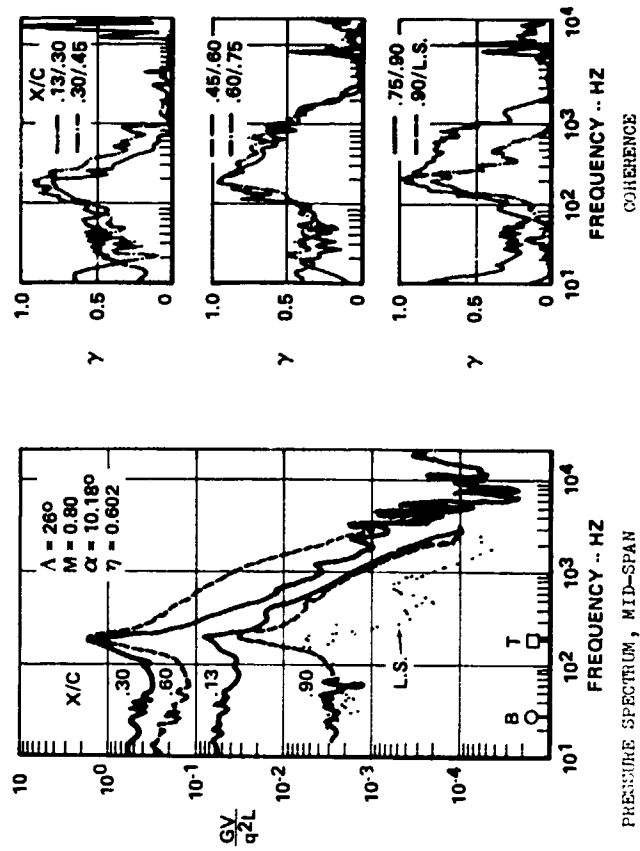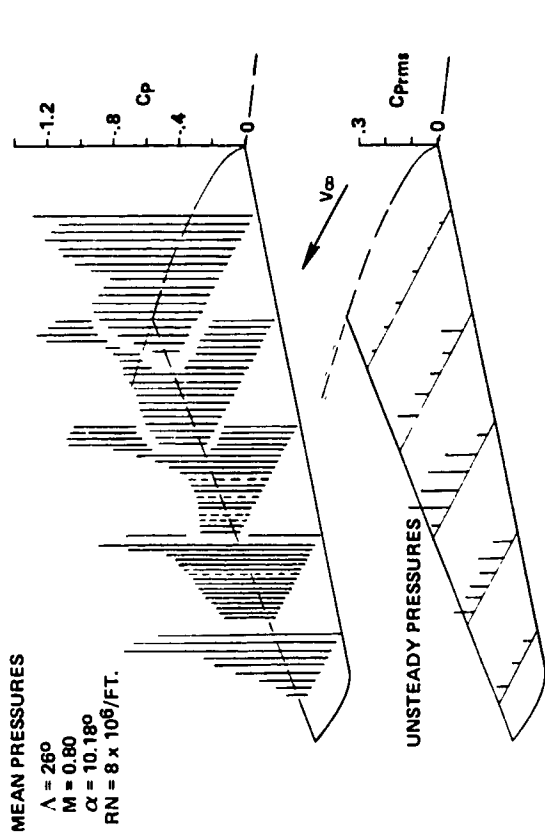
Fig 19 Pressure data from a wind-tunnel model of the aircraft of Fig 18

PRESSURE SPECTRUM, MID-SPAN

$\Lambda = 26^{o}$
$M = 0.80$
$\alpha = 10.18^{o}$
$\eta = 0.602$

FREQUENCY -- HZ

COHERENCE

FREQUENCY -- HZ

TIME HISTORY OF WIND-UP TURN

TIME -- SEC

STRUCTURAL RESPONSE SPECTRA: $\eta = .835$, $x/c = .26$

BENDING   S.F. $= 2.01 \times 10^{8}$ (IN.-LB.)^{2}

TORSION   S.F. $= 1.01 \times 10^{8}$ (IN.-LB.)^{2}

FREQUENCY -- HZ

FREQUENCY -- HZ
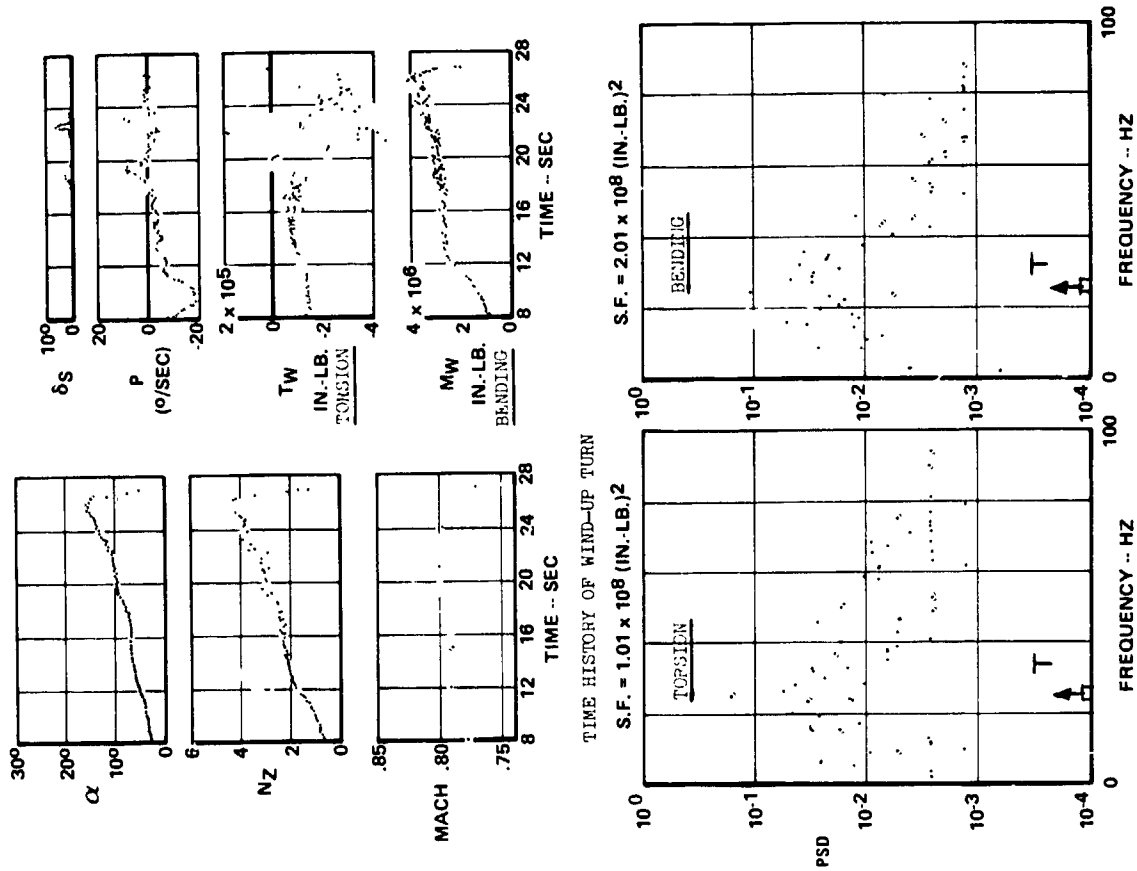
Fig 18 The response of the wing of an aircraft at low wing-sweep at M = 0.8 (from Ref 21)

RAW ACCELEROMETER SIGNAL

(a) SIGNAL FILTERED 25 Hz/35 Hz BAND-PASS

SIGNAL FILTERED 4 Hz/9 Hz BAND-PASS

T_1 T_2 PORT WING

(b) STARBOARD WING

(c) RAW SIGNAL

SIGNAL FILTERED 25Hz/35Hz

PSD

0 10 20 30 40 Hz

INT. PSD
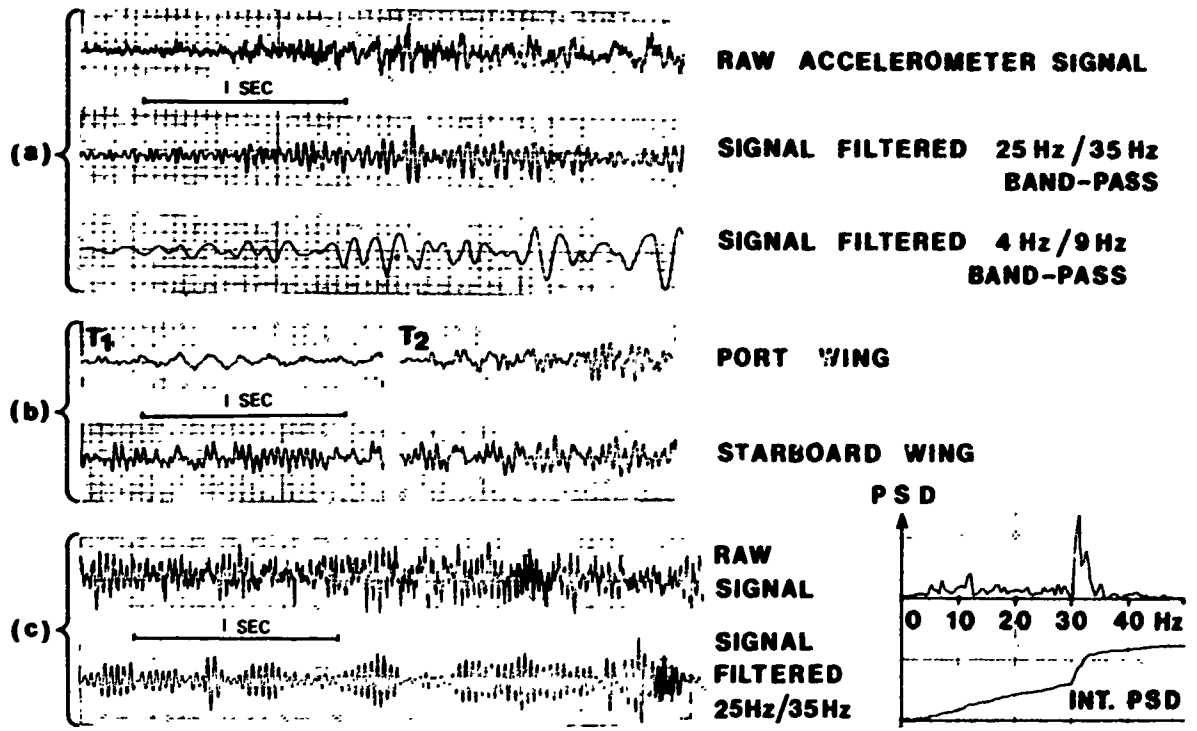
Fig 20 Some records from an accelerometer at the leading-edge wing-tip
of an aircraft at high-subsonic speeds

RMS WING-ROOT BENDING MOMENT

M = 0.80

M = 0.90

B

CLEAN WING

WITH WING-BODIES

M = 0.93

M = 0.96

0   .5   1.0 C_L .5   1.0 C_L

C_L

WITH WING-BODIES

.8

LIFT COEFF

CLEAN WING

.6 B

.4

M = 0.93
$R_c \simeq 0.9 \times 10^6$

.2

0
-5°   0   5°   10°   15°
INCIDENCE

50%c

47.32°

BENDING MOMENT STRAIN-GAUGES

AR = 7

FIRST ANTISYMMETRICAL BENDING MODE 79 Hz

WING BODIES

FROM REF 22 : $H_o = 0.4$ bar
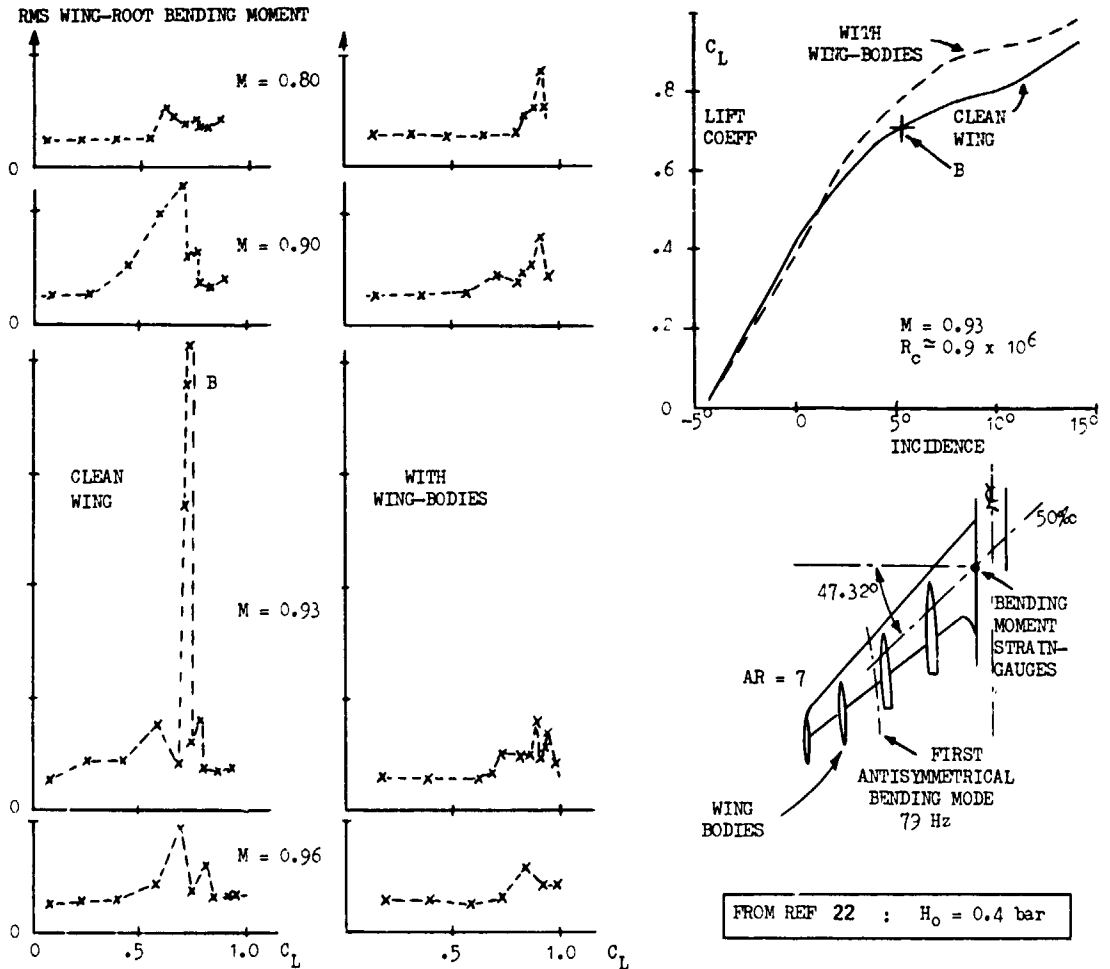
Fig 21 A possible case of transient buzz in a bending mode on a wind-tunnel model

EVALUATION OF VIBRATION LEVELS AT THE PILOT SEAT

CAUSED BY WING FLOW SEPARATION

by

J BECKER

MESSERSCHMITT-BÖLKOW-BLOHM GMBH
—Unternehmensbereich Flugzeuge-
8000 Munchen 80, Postfach 801160

K.DAU

VEREINIGTE FLUGTECHNISCHE
WERKE — FOKKER GmbH
2800 Bremen 1, Postfach 1206
— W.-Germany —

1. INTRODUCTION

The high maneuverability requirements for military aircraft raise the question of how much pilot performance is affected by structural vibrations and the degradation of handling qualities caused by separated wing flow in the low and high speed range and to what extent these vibrations may be used as an indication of stall.

The improvement of buffeting prediction methods is therefore an essential step in the development of configurations which will minimize the problems.
The prediction of structural vibration levels at the pilot seat may be performed by different methods.

In the project phase a qualitative prediction method due to Mabey (Ref. 3) may be used to determine the flight conditions for light, moderate and heavy buffeting for the full-scale aircraft by measurement of the oscillatory wing root bending moment of a wind-tunnel model, without any knowledge of the elastic properties of the full-scale wing. This method is applied to one example of this study.

Another method to predict structural vibrations is based on the dynamic response measurements on dynamically similar models without detailed knowledge of aerodynamic effects, as applied by Hanson (Ref. 6).

Finally a method of the prediction of pilot seat vibration is possible by wind-tunnel measurement of the exciting forces, for example by the determination of fluctuating pressures on rigid models.
In this article two examples of the evaluation of vibration levels on the pilot seat are presented.
The first deals with the results of low speed measurements on a strake wing model with and without flap and slats, including the effect of leading edge blowing, in the incidence region $0 \cdot \alpha \simeq 90°$, Mabey's method is used there.
The second example demonstrates the results obtained by the method based on measurements of fluctuating pressures on rigid models for two configurations with 25 and 45 degree wing sweep in the high subsonic region $(0.7 \leq M \leq 0.85)$.

2. VIBRATIONS AT VERY HIGH INCIDENCES IN THE LOW SUBSONIC REGION CAUSED BY A STRAKE WING

The strake is characterized by a strong steady leading edge vortex which remaines stable up to very high incidences and always creates additional lift, in contrast to the normal swept wing. The strake wing will therefore show a quite different separation behaviour at high incidences compared to a normal swept wing.
Until now it was not known to what extent the vibrations due to separated flow on a wing with strake would lead to problems with respect to pilot fatigue or pilot accelerations at very high incidences in the low subsonic region Buffet investigations have therefore been performed by MBb on a strake wing in the ONE. windtunnel S1 at Modane, and the preliminary results of this study are presented here.

2.1 Test description

Specifically, the aim of the tests was to investigate the effect of blowing, as well as the addition of flaps and slats, on the dynamic response of the strake wing for angles of attack ranging from 0° to 90°.
The model, which had originally been used for static tests, was additionally instrumented with strain gauges at both wing roots, and with two accelerometers at one wing tip. All tests were made in absence of the empennage. Wind tunnel speed was held effectively constant at about 40 m/s.

2.2 Test Results

The analog data of 20 seconds of each test record were digitized using low pass filtering to 600 cps to calculate spectral densities up to 300 cps. Some significant results of the evaluation are presented here. In Figures 2a, 2b the time history of the wing root bending signal of the clean wing with strake and the wing with strake, flap and slat with blowing are shown for several incidences from 0 to 90 degrees. These pictures illustrate the increasing development of an almost harmonical wing bending oscillation up to about 40 degrees which corresponds to the maximum static normal force, and a strong decrease of this signal with a frequency of 18 cps up to 90 degrees.

In contrast to the clean strake wing, the wing with flap and slat shows considerably higher amplitudes at maximum lift conditions. The spectra of the wing torsion and the accelerometer signals (Fig. 3a-3c) reveal the same tendency for the wing root bending signal at 18 cps. Additional smaller but well defined peaks appear at 7,5 cps, the sting frequency and at 31, 63, 120 and 200 cps at higher wing mode frequencies (Fig. 3a-3c), which are caused by random excitation.

Summarising the results, Fig. 3a-3c show that the wing in all test conditions responded mainly in the first wing bending mode up to vortex breakdown, that for the clean strake wing the increase of the bending amplitude is very slow up to 40 degrees. The torsion signal has the same frequency content as the bending signal (Fig. 3). The wing root bending, moment is about five times higher at α = 40° that at α = 0°. A sharp drop of the wing root bending moment is detected above α = 40°, after which it decreases more gradually to a value at 90° corresponding to that of zero incidence. The reason for the very flat slope of the unsteady wing root bending versus angle of at'~ for the clean strake wing is the effect of the strong strake vortex reduces the ene·   ⊥ the randomly fluctuating wake.

2.3 Prediction of pilot vibrations by Mabey's method

In general it is possible to predict with the known values of the wing root bending moment and the windtunnel unsteadiness the intensity of buffeting at the pilot seat using the buffet coefficients for high, moderate and heavy buffeting given by Mabey criteria .
The extrapolation of the wing root bending moments however is a function of the tunnel unsteadiness and consequently the buffet criteria coefficients for other windtunnels are not known. In addition the effect of the elastic behaviour of the aircraft for which the extrapolation is wanted is neglected in Mabey's method, therefore an accurate estimate of the influence for example of the fuselage stiffness and structural damping is not possible. The investigation of the wing root bending moments was therefore only used for trend studies.

3. PILOT SEAT VIBRATIONS OF A VARIABLE WING SWEEP AIRCRAFT IN THE HIGH SUBSONIC REGION

The results of a buffet prediction investigation based on the concept of the evaluation of aircraft buffeting response based on windtunnel measurements of fluctuating pressure will be presented. The intention of the investigation was the development of a method for the evaluation mainly of pilot seat vibrations.

Especially the influence of wing sweep and Machnumber together with the influence of other changes of the configuration, for example the wing with external stores and the empty and fueled wing was studied with this method to get indications of the sensitivity of the buffet intensity.

3.1 The rigid-model pressure method

The central problem in predicting the buffet response of a full-scale aircraft is the difficulty in estimating the excitation due to the separated flow over the wing. In Mabey's method the excitation is estimated by implicitly assuming that the wing responds to buffet pressures in somewhat the same way as to windtunnel turbulence.

Another way of tackling the problem, here referred to as the rigid-model pressure method is to measure the unsteady component of the buffet pressures at a number of points on the wing to get an estimate of the excitation. The measured pressures are then applied to the theoretical transfer function of the full-scale aircraft, with regard to scaling laws, to calculate the response of the full-scale aircraft at various points.

3.2 Mathematical Methods

According to well established practice the small displacement response of an elastic aircraft to a harmonic excitation may be represented by

$$q(\omega) = H(\omega) P(\omega)$$

where $q(\omega)$ = Fouriertransform of the generalized displacement vector of the aircraft

$p(\omega)$ = Fouriertransform of the generalized excitation

$H(\omega)$ = modal transfer matrix.

Local aircraft displacements z are given by the relation

$$z(\omega) = \emptyset\, q(\omega)$$

where $\emptyset$ is the matrix of the mode shapes to which the aircraft motion is restricted.

Since buffet pressures do not in general, have a Fouriertransform owing to their random nature the equations are recast in the form of power spectral densities (PSD's)

$$P_{ij} = \lim_{T \to \infty} \frac{p_i(\omega)\, p_j(\omega)}{T}$$

and

$$Q_{ij} = \lim_{T \to \infty} \frac{q_i(\omega)\, q_j(-\omega)}{T}$$

where p_i and q_i are the Fourier Transforms over a finite time interval T.

It may be shown that the displacement power spectral density Z is then (Fig. 7).

$$Z(\omega) = \emptyset^t\, H^t(\omega)\, P(\omega)\, P(\omega)\, H(-\omega)\, \emptyset$$

3.3 Assumptions and approximations

The use of buffet pressures measured in the windtunnel to calculate the response of a full-scale aircraft implies the assumption, among others, that the full scale flow pattern is roughly similar to the model one.
Because the buffet excitation produced by boundary layer noise, random and periodic vortex shedding and shock oscillation on the wing is in general a function of Reynolds number and vibration amplitude the assumption of flow similarity is not necessarily true. The wind-tunnel and flight Reynolds number differences will give rise to an uncertainty. Another source of error is the fact that the deflections of the full scale wing will be disproportionally larger than those of the stiff model wing and therefore might not only change the buffet pressure pattern, but also introduce motiondependent structural and aerodynamic damping forces not present on the model.

While these errors are difficult to assess, the first one may be estimated by noting that the severity of buffet is a function of the position of the maximum lift coefficient. The uncertainty of predicting the angle of attack at which maximum lift occurs is also exsisting in the determination of the angle of attack for buffeting.

The effects of large elastic wing deflections on the buffet pressure pattern are more difficult to estimate, since the pattern is also a function of the static deflection. This effect could be compensated for to some extent by assigning those buffet pressures to the static angle of attack that corresponds to the rigid model angle of attack of the same magnitude.

Finally, the aerodynamic damping due to the large deflections of the full-scale wing could be represented as a first approximation by aerodynamic forces derived from linear flow equations. This representation is to some extent justified by the fact that most buffet occurs while the flow is still attached to the wing and lift slope is still positive. A correction of the theoretical linear aerodynamic damping by the use of the lift curve slope is proposed.

3.4 Model and Test Description and Resonance Test

The model as shown in Fig. 8 consisted of a half fuselage part without tail and a sweepable wing.
Pressure pickups were loacted at three spanwise sections, at 0.87, 0.67 and 0.47 s in the 25 sweep position on the wing upper side, six at each section. In addition there were six accelerometers installed, to investigate the dynamic response of the model. The test program included the measurement of two sweep positions, 25° and 45°, the Mach numbers M = 0.75 and 0.8 for 25° and M = 0.7, 0.75, 0.8 and 0.825 for 45°. The incidence could be varied stepwise ($\Delta\alpha$ = 0.5°) in the region $4 < \alpha < 13°$. The windtunnel tests were performed in ARA Bedford 8' x 9' transonic windtunnel at 1 atm.

The ground resonance test in the model balance showed mainly vibration modes at 17 and 20 cps of the balance, then the first wing bending at 24 Hz, a second bending at 100 cps and the first torsion mode at 200 Hz.

3.5 Windtunnel Test Results

The summary of the analysed rms pressures and accelerations for the 25 and 45 sweep angle as illustrated in fig. 9, 13, 14 for the different measured Mach numbers, gives important insights into the fluctuating local forces induced by the vortex shedding of mixed attached and separated flow, the dynamic response, and their development with incidence.

25 degree wing sweep results

The 25° wing sweep results at M = 0.75 indicate an attached-flow behaviour up to about 5.5 degree incidence. Then a pronounced strong unsteadiness is produced at the wing leading edge at about 20 % of chord in the spanwise section 0.87 s and 0.67 s which suddenly leads to a strong increase in the acceleration signals, thus indicating a shock wave induced boundary layer separation, a separation bubble in this region. The shock wave location was also determined by flow visualisation pictures. This is the buffet onset condition. With increasing angle of attack and a forward moving shock the fluctuating pressures behind the shock up to the trailing edge grow up to 12 degrees incidence. It is interesting to note, that the amplitudes of the accelerations, which indicate the wing bending oscillation (A2, A4, A6) follow the trend of the fluctuating pressures. The strong increase of the accelerometer signals A3, A5 which will give information about torsion, may be caused by stronger unsteadiness at the leading edge region. This may be concluded from the trend of the results, although there was no information at the leading edge in the chordwise direction from 0 - 25 % chord.

The results of the 25 degree wing sweep at M = 0.8 show the same trends. Buffet onset takes place at a smaller incidence of about 4 5.
The fluctuating rms pressure coeffient Cp = p/q attains values from 0.01 - 0.2 for both Mach numbers.

The spectra of several pressure signals as shown in Fig. 10-12 have broad-band random characteristics, indicating the absence of periodic frequencies.

45 degrees wing sweep results

Compared with the 25 degree wing sweep results, the results of rms pressures, accelerations and significant spectra indicate some remarkable features as demonstrated in the figures 13-16 as functions of Mach numbers and incidence.

Contrary to earlier assumptions, the strength of the excitation force has almost the same order of magnitude in the incidence region 6° α 12° at M = 0.7, as shown in figure 9 and 13 for both wing sweep angles (25 and 45°) on the rms values of the fluctuating pressure at the outer part of the wing area. The magnitude of the wing bending response is also of the same order in both cases (fig. 13, 14). This may be caused by a higher loss of aerodynamic damping in the bending mode, which might be expected, considering the flow separation development as derived from flow visualisation as shown in fig. 17.

Interpreting the remarkable behaviour of the wing torsion response of the wing as shown on the accelerations in fig. 13, 14 and the exciting force for the $\Lambda = 45°$, $M = 0.8$ case at $\alpha = 11°$, it is believed, that in this case, where suddenly a maximum of lift is reached, the aerodynamic damping of the torsion mode is almost zero.

Comparing the results derived for the acceleration of A6, A4, A2 indicating the amplitude of the bending for different Mach numbers and incidence with the wing root bending moment signal (fig. 14), comparable trends can be seen. However the strong increase in the torsion mode response, as illustrated also in the spectrum of the acceleration A5 in fig. 16 at $\Lambda = 45$, $M = 0.8$, is not reflected by the wing root bending signal, that Mabey's method of the extrapolation of wing root bending signals would not be appropriate for the prediction of this high frequency phenomenon.

Stall flutter aspects

Several investigations on swept wings of different geometry at high incidences in high subsonic flow give some indication of an aeroelastic instability of the torsion mode. For example the recent works done by Sruggs and Theisen [8], L.L. Erickson [5], D.W. Riddle and D.P. Benepe, A.M. Cunningham, Jr. and W.D. Dunmeyer [7] show torsion mode instability problems. The instability is know as stall flutter or autobuffet.

Scruggs and Theisen state that the instability is thought to be caused by resonance of the torsion mode with the Strouhal shedding frequency.

N.C. Lambourne 4 remarks in his article of "Flutter in one degree of freedom" in the Chapt. 7.1 Eddy Shedding: "Experiments have shown that self-excited oscillations first occur when the frequency of eddy shedding equals the natural frequency of oscillation of the body."

In connection with the behaviour of Strouhal shedding it is perhaps useful to draw attention to the earlier results derived for circular cylinders. In the flow region characterised by Reynolds number $Re = VD/\nu$ from $300 < Re < 2 \cdot 10^5$ the eddy shedding is almost periodic, the Strouhal number based on the cylinder diameter is almost constant, i.e. $S = f D/V$ 0.2. Above $Re > 2 \cdot 10^5$ the boundary layer on the cylinder becomes turbulent, the wake area becomes narrower, the drag decreases due to increasing mean pressure, the eddy shedding is random in this critical region $(2 \cdot 10^5 < Re \, 5 < 10^6)$. There is no definite Strouhal number, with $S_{min} \simeq 0.08$. Beyond $Re = 5 \cdot 10^6$ a quasi periodic eddy shedding with an almost constant drag coefficient has been observed. The Strouhal numbers in this supercritical region are about $S = f D/V \simeq 0.3$.

This behaviour of eddy shedding on cylinders is principally the same for other obstacles like airfoils at high incidences. The energy content of the eddies and the wake geometry are, however, different [1, 2].

Considering now our windtunnel results derived for the 45° wing sweep case at $M = 0.8$, we derive an equivalent Reynolds number, based on a medium wake width

$$Re = \frac{V \bar{C}}{\nu} = \frac{\rho V C \sin \alpha}{\mu} \simeq 2 \cdot 10^6$$

where C = chord length at 0.75 semispan.

The Strouhal shedding frequency for the stalled aerfoil in the supercritical Reynolds number region

$$Re = \frac{V \bar{C}}{\nu} = 3 \cdot 10^6 \qquad S = \frac{f_n C \sin \alpha}{V}$$

should have a value of $S = 0.26$. This value corresponds to that of a cylinder at supercritical conditions $S = 0.3$.

For the case of the 45° swept wing at $M = 0.8$ in the critical Reynolds number region at an incidence of 11° where the flow is assumed to be totally separated we observe a peak region in the pressure spectra (fig. 15) which is broadband at about 200 - 250 Hz, which corresponds to a Strouhal frequency of about $S = 0.06$ in the critical region $Re \simeq 2 \cdot 10^6$. A quite realistic interpretation of the process is achieved, if we assume that the unsteady pressure at the wing leading edge caused by shock induced boundary layers separation (for example at point K12) is mainly induced by eddy shedding and that the aerodynamic damping at these conditions is becoming zero.

4. COMPARISON OF CALCULATED WITH MEASURED
   ACCELERATIONS OF THE WING MODEL

In attempting to measure the buffet excitation on the wing model one of the problems
is to estimate how well the pressure field over the wing is defined by the pressures mea-
sured at the three chordwise sections of the wing model (wing geometry Fig. 1).
As a check on this potential source of error, and on the method of computation, the acce-
lerations of the location of the six accelerometer were calculated for one sweep angle
and three angles of attack by the method outlined in Section 3, and compared with the
measured values.

Inspection of the PSD's of the measured acceleration (see Fig. 19) showed that the wing
moved predominantly in three modes indicated b three spectral peaks at about 24, 100 and
200 cps, corresponding to the 1st and 2nd bending mode, and the 1st torsion mode. The
shapes of these modes, shown in Fig.   , had been previously measured in ground resonance
tests, and were used to set up the mode shape matrix   . The corresponding
generlized masses were calculated from the known mass distribution of the wing model.

4.1 Calculation of the generalized force

Calculation of the generalized excitation force was determined by the arrangement of
the pressure taps as shown in Fig. 1. The 18 pressure taps were arranged in three groups
of six on chordwise sections at 45 %, 65 % and 85 % half-span, and at 25 %, 35 %, 50 %,
75 %, 80 %, and 95 % chord. For the purpose of integrating the pressure over the wing sur-
face to get the generalized force, a straight-line variation of pressure was assumed bet-
ween two adjacent spanwise sections. In the absence of any other information the pressure
was assumed to be constant from 85 % of half-span to the wing-tip, and also from 45 % of
half-span to the fuselage edge.

These considerations amount to assigning a weighting factor to each measured pressure.
These factors were absorbed into the mode shapes, resulting in a 18 x 3 matrix for three
modes.

1.2 Calculation of the power-spectial density
matrix of the measured pressures

An alternative definition of the PSD matrix of a number of variables $p_i(t)$, i = 1, ..., n
was used

$$P_{ij} = \frac{1}{N} \lim_{N} \sum^{N} p_i(\omega) \, p_j(-\omega)$$

where

$$p_i(\omega) = \int_{-T}^{T} p(t) \, e^{-i \omega t} \, dt$$

and N = number of time records.

The pressures were available in the form of 5 digitized records for each pressure, each
record representing a time interval T = 4 sec , and containing 2048 values.

The maximum frequency that could be extracted from the time record was thus

$$f_{max} = \frac{1}{2} \cdot \frac{2048}{4} = 256 \text{ cps}$$

and the frequency resolution

$$f = \frac{1}{2} = 0.25 \text{ cps}$$

The maximum frequency of interest, 198 cps, of the 1st torsion, was thus well inside the
permissible range.

The PSD matrix P_{ij} of the eighteen measured pressures was calculated, the number of time
records N being 5. Since this is a rather small ensemble, there was a possibility that
the cross spectral densities had not yet attained their limit value, which should be close
to zero, since the pressures looked essentially random.
The PSD's of the accelerations were therefore calculated with the full PSD matrix of the
measured pressures, as well as with a PSD matrix containing only the diagonal terms. The
PSD's of calculated accelerations are shown in Fig.19,20.

4.3 Discussion of results

The measured power spectral density (PSD) of point A5 on the wing tip of the wind tunnel half-wing model is shown plotted against frequency in Fig. 19. The spectrum is seen to be dominated by two large peaks corresponsing to the 1. bending and the 1. torsion mode at 21 Hz and 200 Hz respectively, and a smaller peak due to the 2. bending mode at 95 Hz.

The PSD of the calculated acceleration of the same point for the same test conditions is shown in Fig. 20, with the data points of the measured acceleration superimposed on it. The acceleration was calculated by the method outlined previously, i. e. the measured buffet pressures were used as the excitation, and the aerodynamic forces predicted by linear theory were added to it. The structural damping coefficients were taken from ground vibration tests, being 3 % for all modes. Mode shapes were also taken from ground vibration tests of the model, whereas the generalized masses were calculated from the weight distribution and the measured mode shapes.

Inspection of Fig. 20 shows that the calculation reproduces the peaks for the two bending modes quite well, the ratio of calculated to measured peak values being 1.6 and 0.78 respectively. The peak value of the calculated torsion acceleration, however, is about 20 times smaller than the measured value, indicating that there is practically no damping in torsion due to the aerodynamic forces due to wing motion.

To check this point, the calculation was repeated, with the difference that no linear air forces at all were applied to the torsional mode, and only of the linear airforces to the 2. bending mode. The airforces for the 1. bending mode were left unchanged at 100 %. The result of this calculation is shown in Fig. 21, and it can be seen that the calculated values for the torsion peak match the measured values very well, confirming the assumption that the torsional damping in buffet in this case is en tirely due to structural damping. The ratio R_p of the calculated to measured peak value is now 0.76 for torsion, and 1.1 for the 2. Bending peak, indicating that the assumed reduction by 50 % of the linear air forces for this mode was somewhat too large. The ratio R_p for the 1. bending mode was unchanged.

While the ratio of calculated to measured peak values is a reasonable criterion for the accuracy of the calculation, it should be pointed out here that it is the RMS value of the acceleration that is really relevant to design considerations. Now if g is the damping coefficient, the peak values of the PSD vary as $1/g^2$, and the mean square value of the acceleration, i. e. the integral over the peak varies as $1/g$, so that the ratio of calculated to measured RMS values, R_{rms}, should be approximately equal to the fourth root of the peak value ratio. This was checked by integration of the three resonance peaks, and the ratios R_{rms} of calculated to measured RMS values for each peak turned out to be 1.15, 0.89 and 0.47 for full linear air forces, and 1.14, 1.17 and 0.95 for selectively reduced linear air forces.

Thus if full linear air forces are applied to the bending modes, and none to the torsion mode, the maximum discrepancy in RMS value would be 17 %, which is quite acceptable for design calculations.

Similar calculations were made for another point, A6, at the wing tip, the results of which are shown in Fig. 22. The ratios R_{rms} for this point turned out be 1.14, 1.13, and 0.49 for air forces reduced in the same manner as for point A5.

4.4 Conclusions

The comparison of buffet accelerations measured on a wind tunnel mode wing with accelerations calculated by using air forces predicted by linear theory has shown several things:

(1) The acceleration due to the bending of the wing can be predicted to within 20 % accuracy by applying the aerodynamic loads furnished by linear theory.

(2) Aerodynamic damping is practically absent for the torsion mode of vibration, the damping in torsion being due mainly to structural damping.

In the light of these results it would therefore appear that the torsional motion of the wing is more severely affected by wing buffet than bending. This would, for example, be important in predicting accelerations for wing-mounted stores. It would also indicate that torsional stresses or accelerations are a more sensitive indicator for incipient stall or buffeting. Further calculations should therefore be made to show whether the foregoing conclusions are also valid for other angles of attack and Mach numbers.

5. RESULTS OF THE RIGID PRESSURE MODEL PREDICTION METHOD FOR FULL SCALE AIRCRAFT

In figure 18 the results of the evaluation of vibration levels based on the rigid pressure model technique at the pilot seat are presented for the low sweep configuration $\Lambda = 25°$ and for $\Lambda = 45°$ at M = 0.75 and sea level. The vibration levels (root mean values) are shown at the fuselage axis near the pilot's position and at the elastic axis of the wing in the incidence region 7 - 13°. Both the conditions for the clean wing and the wing with an inboard pylon store are considered.

5.1 Assumptions of the calculation

The general description of the aircraft's forced oscillation would necessitate the introduction of all eigenmodes of the total aircraft in the relevant frequency region. The numerical treatment of the analysis of coupled modes however may only be performed with a limited number of degrees of freedom, due to computer capacity. The choise of proper modes was found through comparision of the order of magnitude of the generalized excitation power spectra derived for 4 and 9 modes. From the comparison of the two results it was concluded, that the introduction of the first wing bending, first and second fuselage bending and the first wing torsion was satisfactory to describe the clean wing configuration both for the wing sweep 25° and 45°. For the external store configuration however introduction of six eigenmodes was necessary (ref. 12).

The structural damping of all modes was assumed to be constant.

The aerodynamic damping of the selected modes was calculated by the use of unsteady linear theory in the whole incidence range where total vortex breakdown did not occur. Several assumptions in connection with the spanwise distribution of the fluctuating force distribution especially towards the wing tip had been considered, since no information was available at outboard stations. No final conclusion of the distribution at the tip can be drawn, but it should not be constant there because flow visualisation indicated attached flow.

5.2 Modal excitation spectra

Nondi-'nsional generalized excitation spectra of the full-scale aircraft's first wing bending mode are presented in fig. 17 for the wing sweep angle 25 and 45 degree. The dimensioned spectrum is related to the nondimensional form by

$$S (\omega) = (1/2 \, \rho \, Vs^3)^2 \, S (k); \quad k = \omega s/_V$$

The frequency content of the spectra and the development with incidience reflects the behaviour of pressure spectra as discussed before.

5.3 Vibrations levels at the pilot seat and at the wing tip

Based on the buffet criteria from ref. 9, 10 which relate vertical g levels in the frequency region 4 - 10 Hz at the pilot seat directly to light, moderate and heavy buffeting, the evaluation of the calculated results fig. 18 indicate moderate to heavy buffet for the 25 degree wing sweep configuration at M = 0.75 in the incidence region $7 \leqslant \alpha \leqslant 11.5°$ at sea level.

The 45 degree wing sweep configuration shows considerably lower g levels in the pilotes seat region (fig. 18). Light to moderate buffeting is predicted from the calculation in the region $7° \leqslant \alpha \leqslant 13°$ at M = 0.75 and sea level.

The comparison of a clean wing and a wing with store configuration shows remarkably higher g level at the levels at the seat, due to the contribution of more modes in the 4 to 10 Hz frequency region in relation to the clean configuration, where mainly the first fuselage bending leads to the pilot acceleration. A strong dependence of the accelerations on the aerodynamic damping is shown by comparison with results gained by introduction of zero aerodynamic damping.

6. CONCLUSIONS

Pilot accelerations at high incidences will reach a maximum value at c_{Lmax}, the condition before an almost totally separated wing flow, both in incompressible and compressible flow.

In incompressible flow a wing with strake shows important reductions of wing root bending signals compared to a wing with strake high liftconfiguration and the effect of a separation delay. Beyond total flow separation the pilot accelerations in the structural frequency domain are negligble at low speeds.

In the transonic flow for the investigated swept wing configuration both at 25 and 45 degree wing sweep, moderate to heavy buffeting situations at $M = 0.75$ are predicted by the rigid-model pressure method. The method was validated by comparison with tunnel results. The rigid pressure model technique moreover allows the prediction of near stall flutter conditions and combined pilot accelerations as well an approximation of the effects of pilot fatigue due to wing with store configurations.

7. LIST OF REFERENCES

1	Y.C. Fung	An Introduction to the theory of aeroelasticity Dover Publications, Inc., New York
2	H. Försching	Zur theoretischen Behandlung aeroelastisch erregter Schwingungen kreiszylindrischer Konstruktionen bei periodischer Wirbelanregung Z. Flugwiss. 18, 1970, Heft 9/10
3	D.G. Mabey	An hypothesis for the prediction of flight penetration of wing buffeting from dynamic tests on wind tunnel models RAE Techn. Report 70189, 1970
4	N.C. Lambourne	Flutter in one degree of freedom AGARD Manual of Aeroelasticity Part V, Chapt. 5
5	L.L. Erickson	Transonic single mode flutter and buffet of a low aspect ratio wing having a subsonic airfoil shape NASA TN D-7346, 1974
6	P.W. Hanson	Structural and aerodynamic quantities of the dynamic system, similarity laws, and model testing AGARD Advisory Report No. 82, 1975
7	D.B. Benepe, A.M. Cumningham, jr., W.D. Dunmeyer	A detailed investigation of flight buffeting response at subsonic and transonic speeds AIAA Paper No. 74-358, 1974
8	R.M. Scruggs, J.G. Theisen	Transonic buffet response testing and control Lockheed-Georgia Company
9	B.I.L. Hamilton	The operational problems encountered during precise maneuvring and tracking AGARD Advisory Report No. 82, 1975
10	R.N. Slarve	Aircrew capabilities and limitations AGARD Advisory Report No. 82, 1975
11	Collmann, Dau	Calculated response of full-scale aircraft to wing buffet VFW Fokker TTD-UPB-013, 1974
12	J. Becker	Buffetvoraussage mit Hilfe der PSD-Analyse MBB UFE 1128, 1974
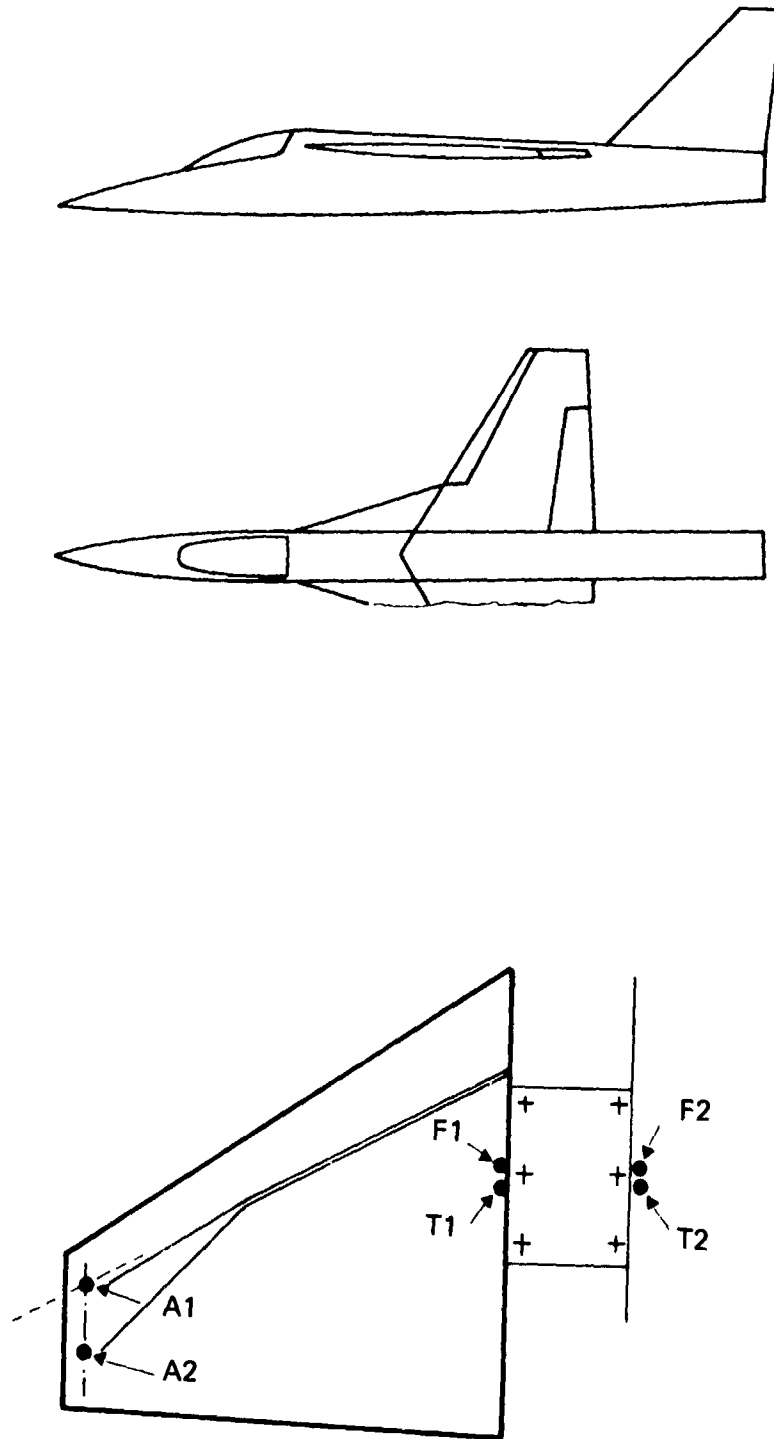
Fig. 1 Geometry of the strake wing model and location of the strain gauges and accelerometers
(F wing root bending gauge, T wing root torsion gauge, A accelerometer)

$\alpha = 12°$

$20°$

$30°$

$33°$

$36°$

$90°$ ← 1 sec →
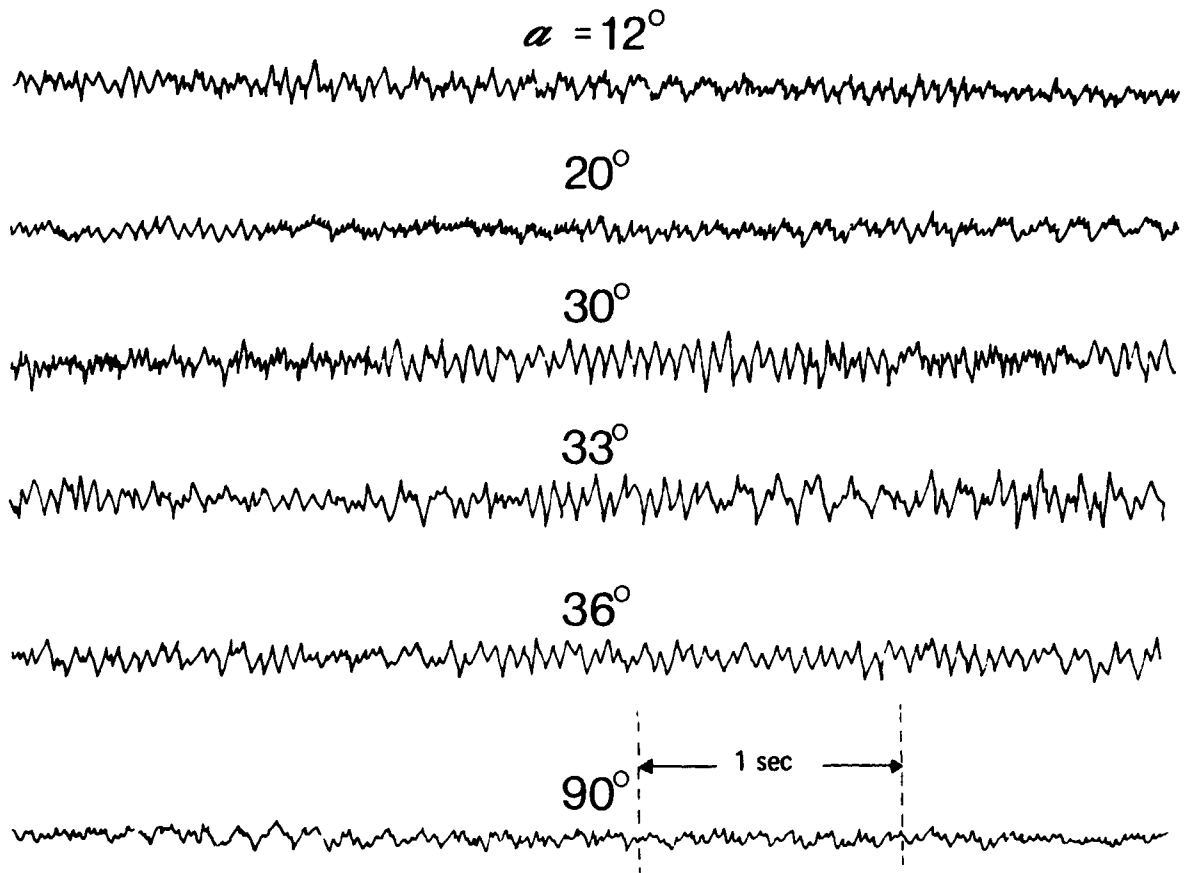
Fig. 2a   Time history of the wing root bending moment F1, clean strake wing

$0°$

$28°$

$35°$

← 1 sec → $90°$
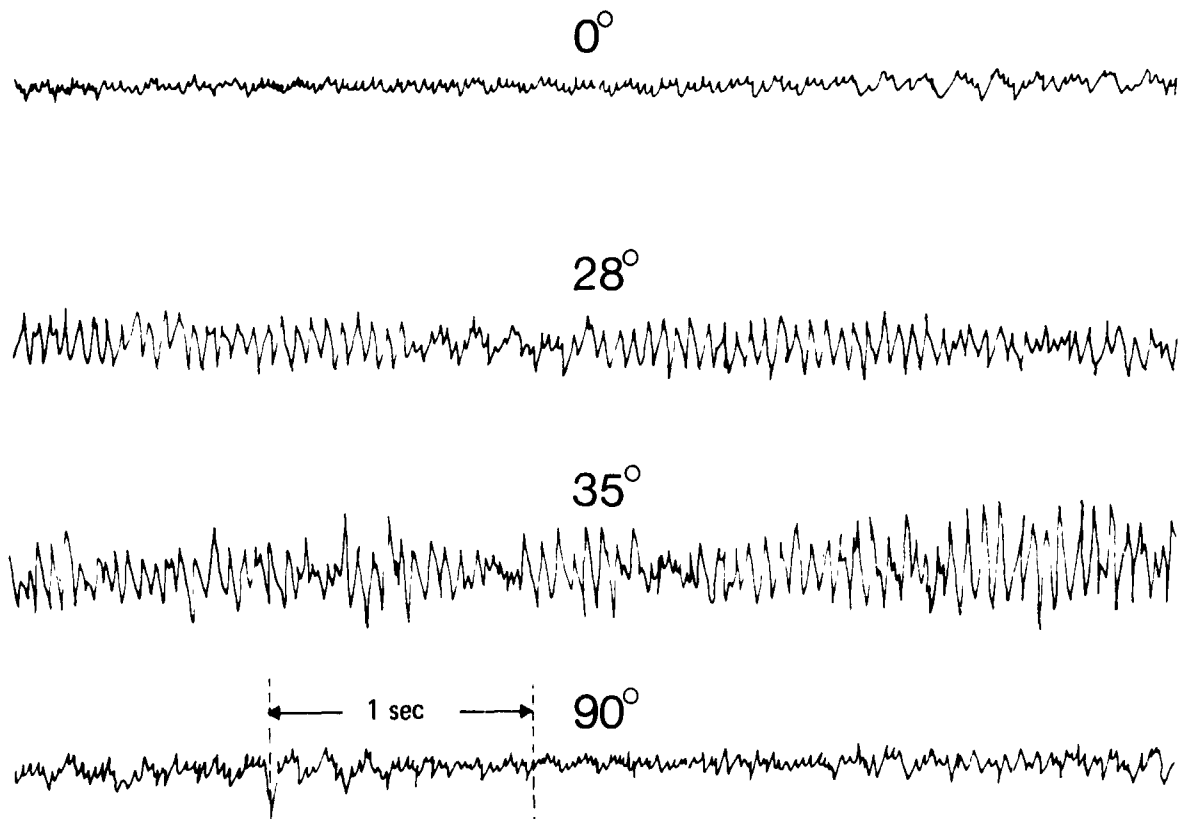
Fig. 2b   Time history of the wing root bending moment F1, strake wing with flap, slat and blowing $\beta = 0°$
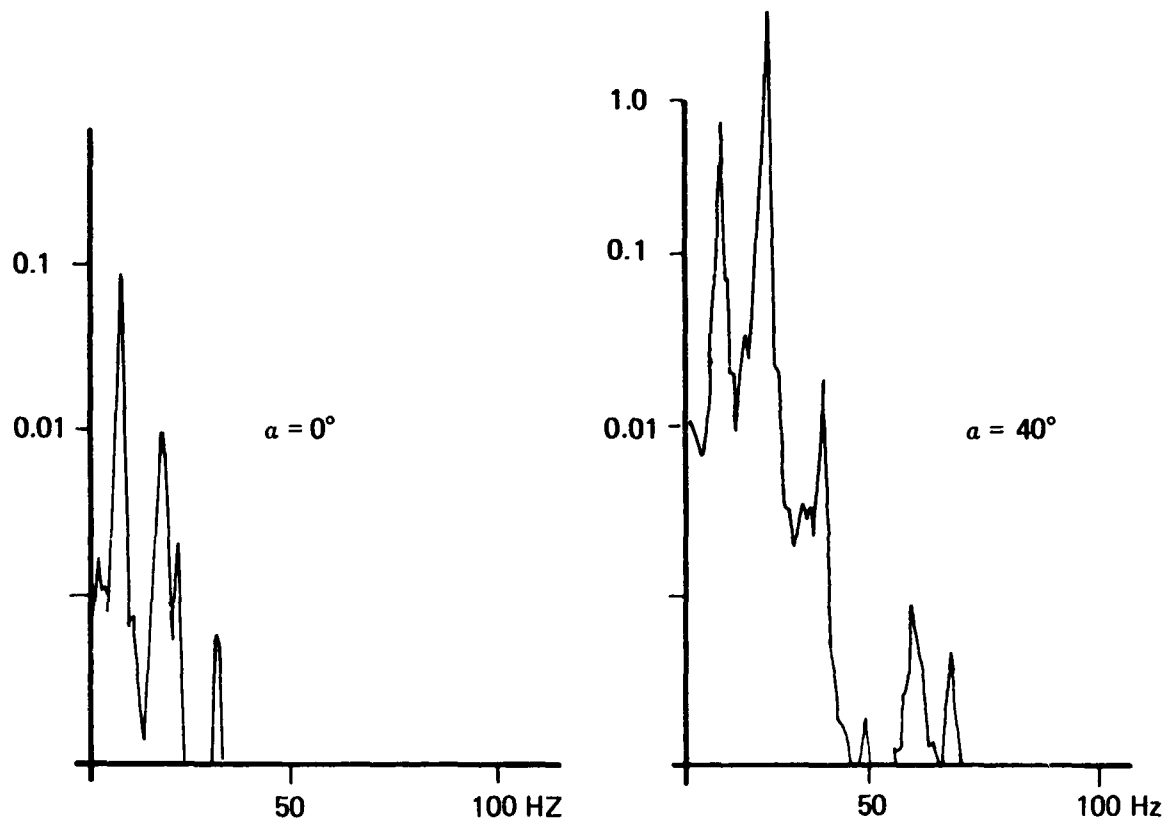
Fig. 3a   Spectrum of the wing root bending moment F1, strake wing with flap, slat and blowing at $\alpha = 0°$; $40°$; $\beta = 0°$
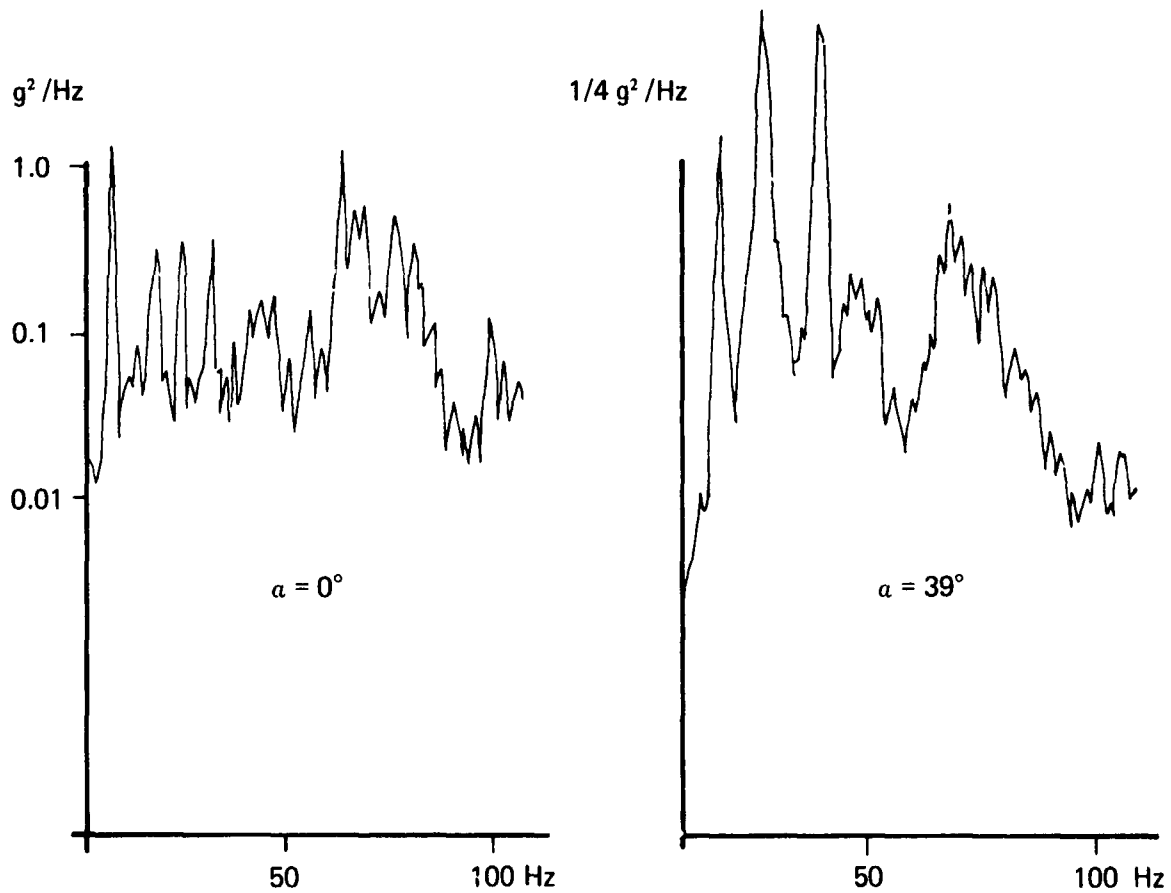
Fig. 3b   Spectrum of the acceleration A1 of configuration fig. 3a $\alpha = 0°$; $39°$; $\beta = 0°$
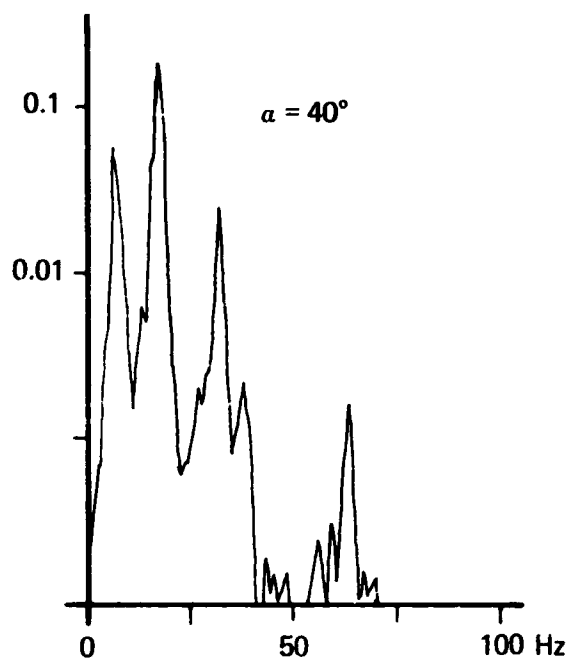
Fig. 3e   Spectrum of the wing root torsion signal of configuration fig. 3a $a = 40°$; $\beta = 0°$
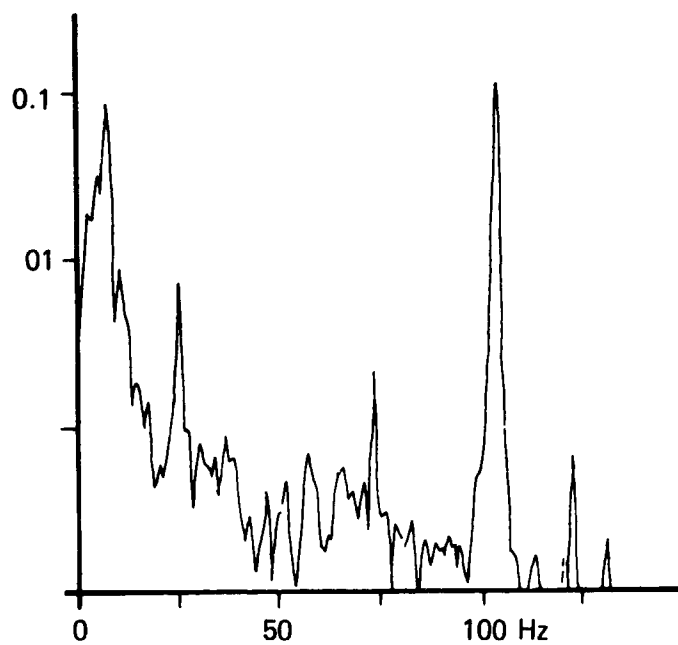
Fig. 4   Spectrum of static tunnel pressure
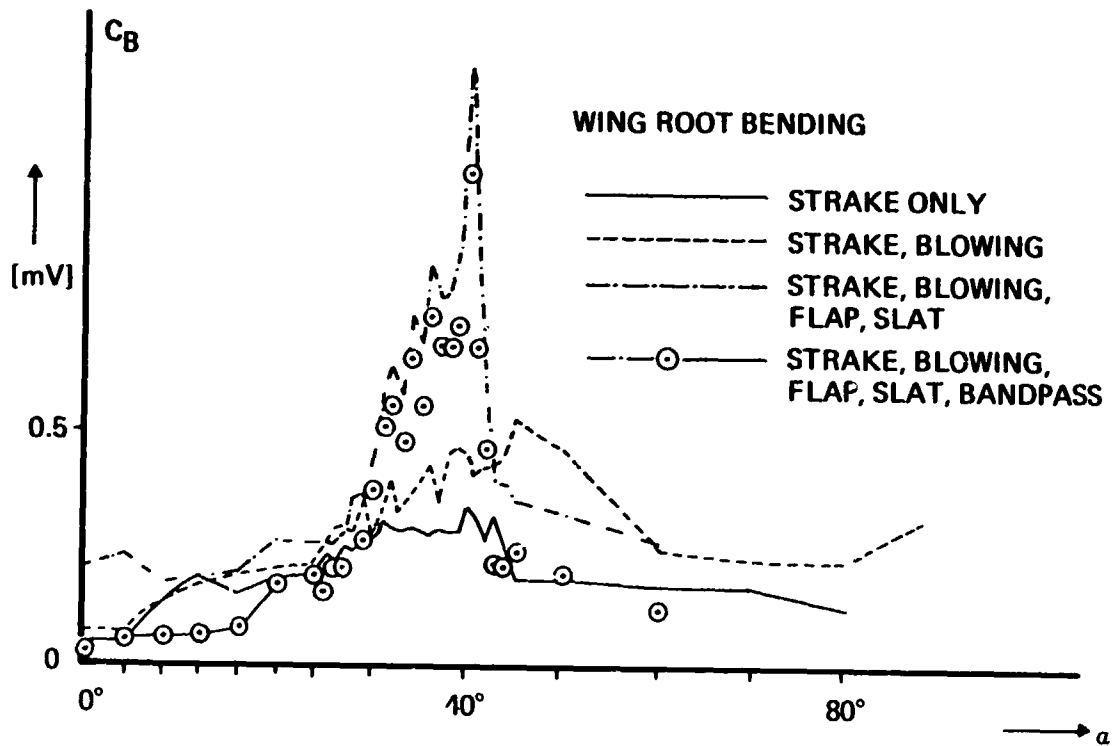
Fig. 5 Filtered and not filtered rms wing root bending moment of the different conditions
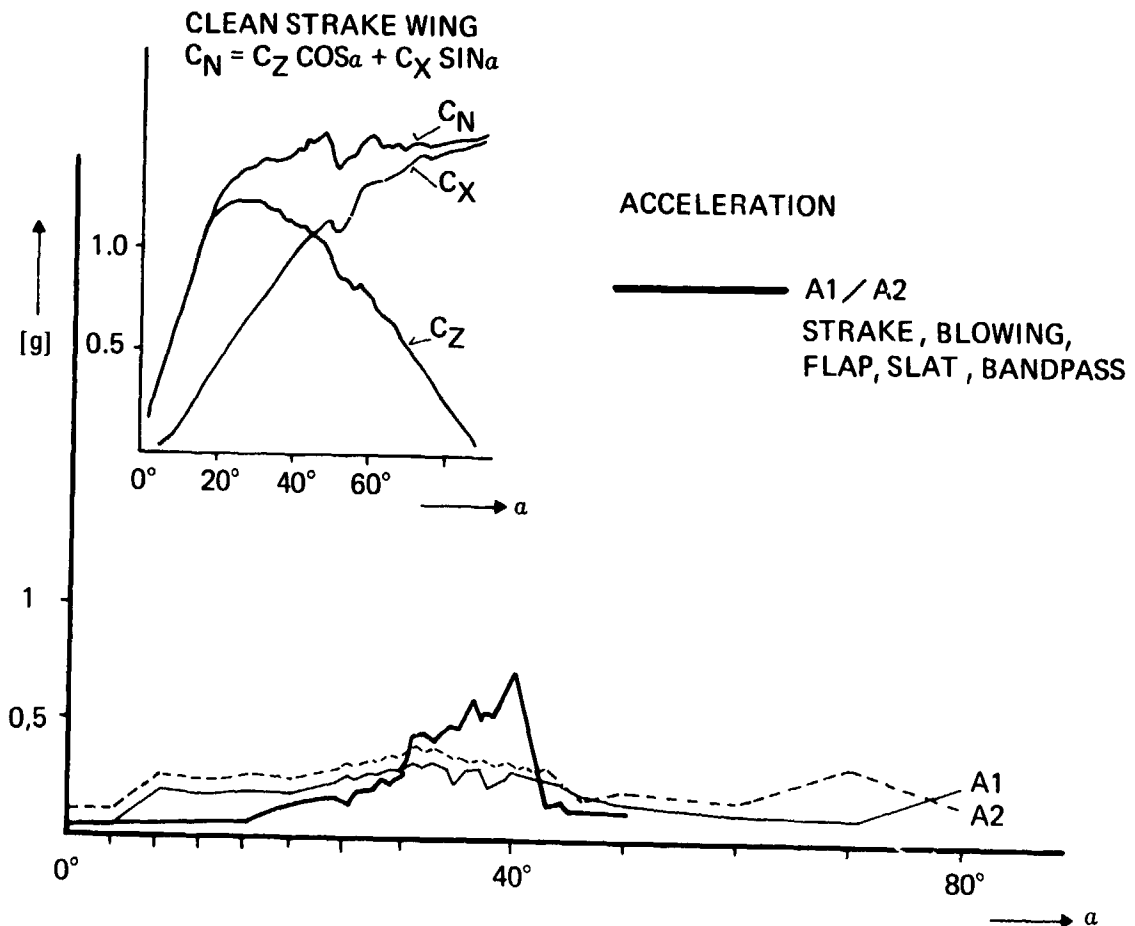
Fig. 6 Filtered and not filtered rms accelerations, of the clean strake wing and the strake wing flap and slat.

BUFFET PREDICTION BASED ON GENERALIZED HARMONIC ANALYSIS

MODAL TRANSFERFUNCTION OF TOTAL AIRCRAFT

$$H(i\omega) = [-\omega^2 M + (1 + ig) K + L (i\omega)]^{-1}$$

M, K, L = generalized inertia, stiffness and aerodynamic stiffness and damping

GENERALIZED SPECTRA OF THE EXCITATION FROM MODEL PRESSURE MEASUREMENTS

$$S_M (i\omega) = \int_{-\infty}^{\infty} R(\tau) e^{-i\omega\tau} d\tau$$

$$R(\tau) \atop mn = \lim \frac{1}{T} \int_0^T [\sum_{j=1}^{J} \phi_{mj} F_{j} \int p_j(t) dF] [\sum_{j=1}^{J} \phi_{nj} \int p_j(t + \tau) dF] dt$$

R_{mn} = generalized cross correlation

CROSS POWER SPECTRA OF THE DYNAMIC RESPONSE

$$S (i\omega) = \phi \, H (-i\omega) \, S_o (i\omega) \, H (i\omega) \, \phi^T$$

$$S_o (i\omega) = (P/P_M)^2 \, (V/V_M)^3 \, (S/\bar{s})^5 \, S_M$$

ϕ_{mj} eigenvector m

F_j panel area j

$p_j(t), F_j, \phi_{mj}$

$\bar{s}$
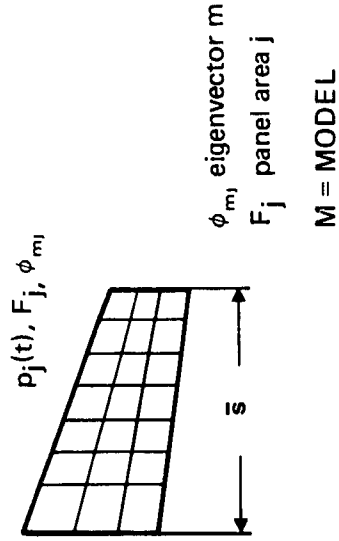
M = MODEL

Fig. 7   Illustration of the buffet prediction analysis
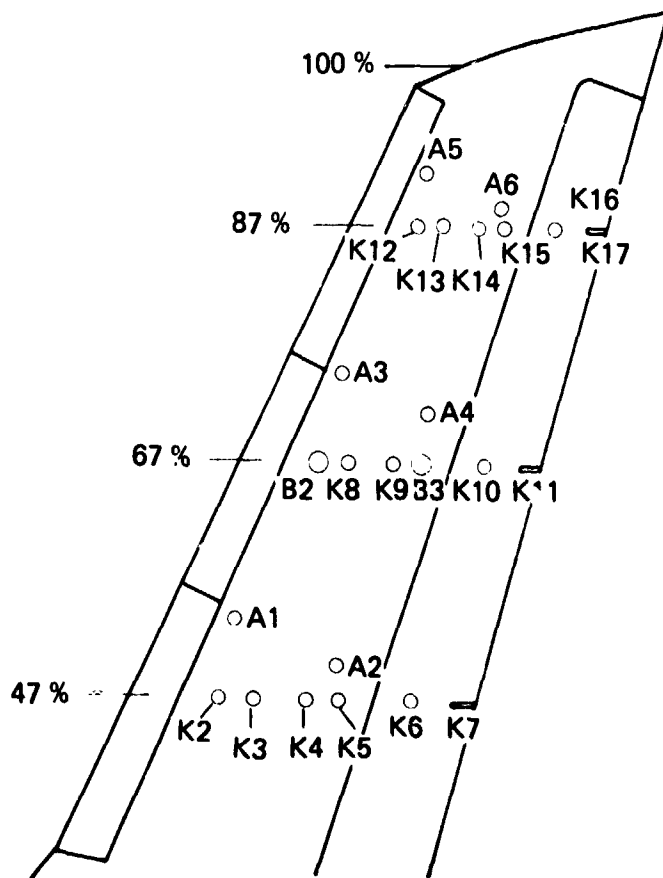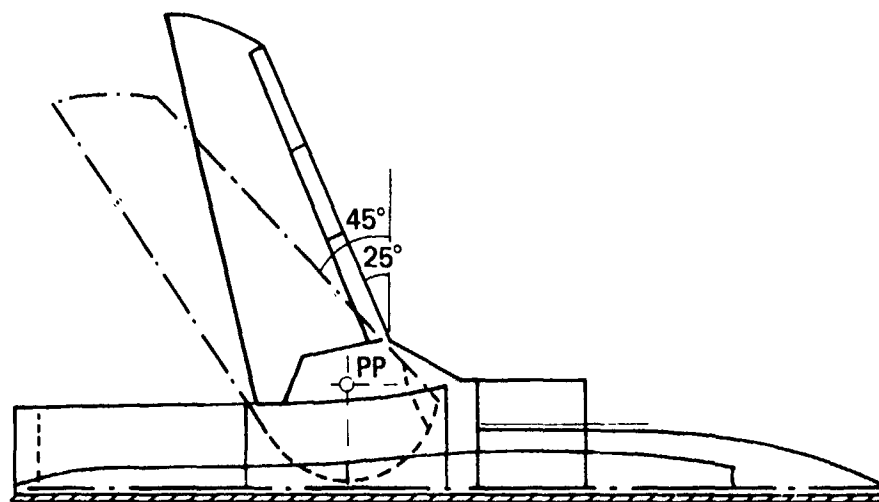
Fig. 8 Geometry of the variable wing sweep model and location of pressure pickups
K, B, and of accelerometers A
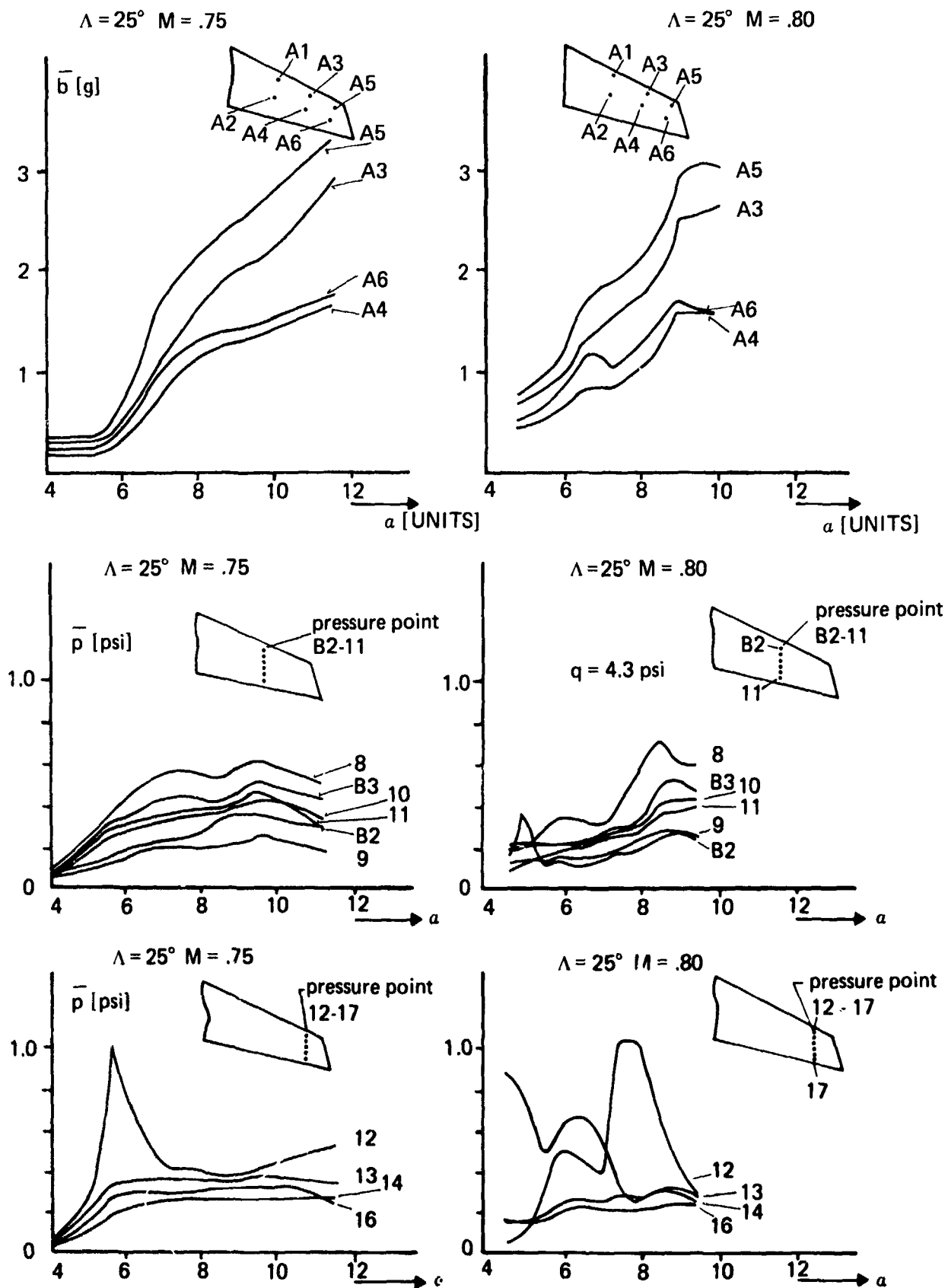
Fig. 9 Influence of incidence and Machnumber on the rms pressures and accelerations on the wing at $\Lambda = 25°$
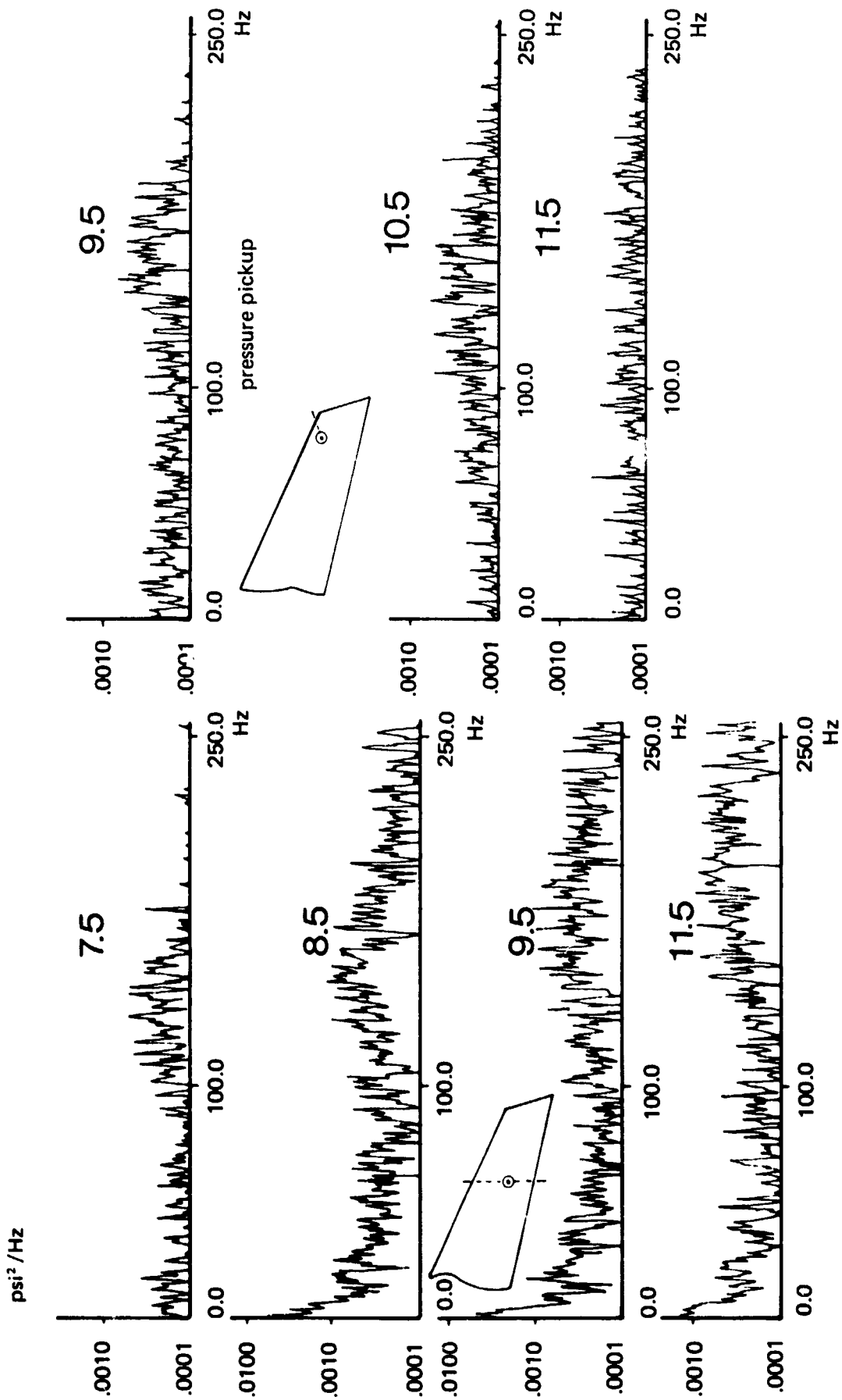
Fig.10(a) Influence of incidence on the spectra of the fluctuating pressures at M = 0.8, Λ = 25°
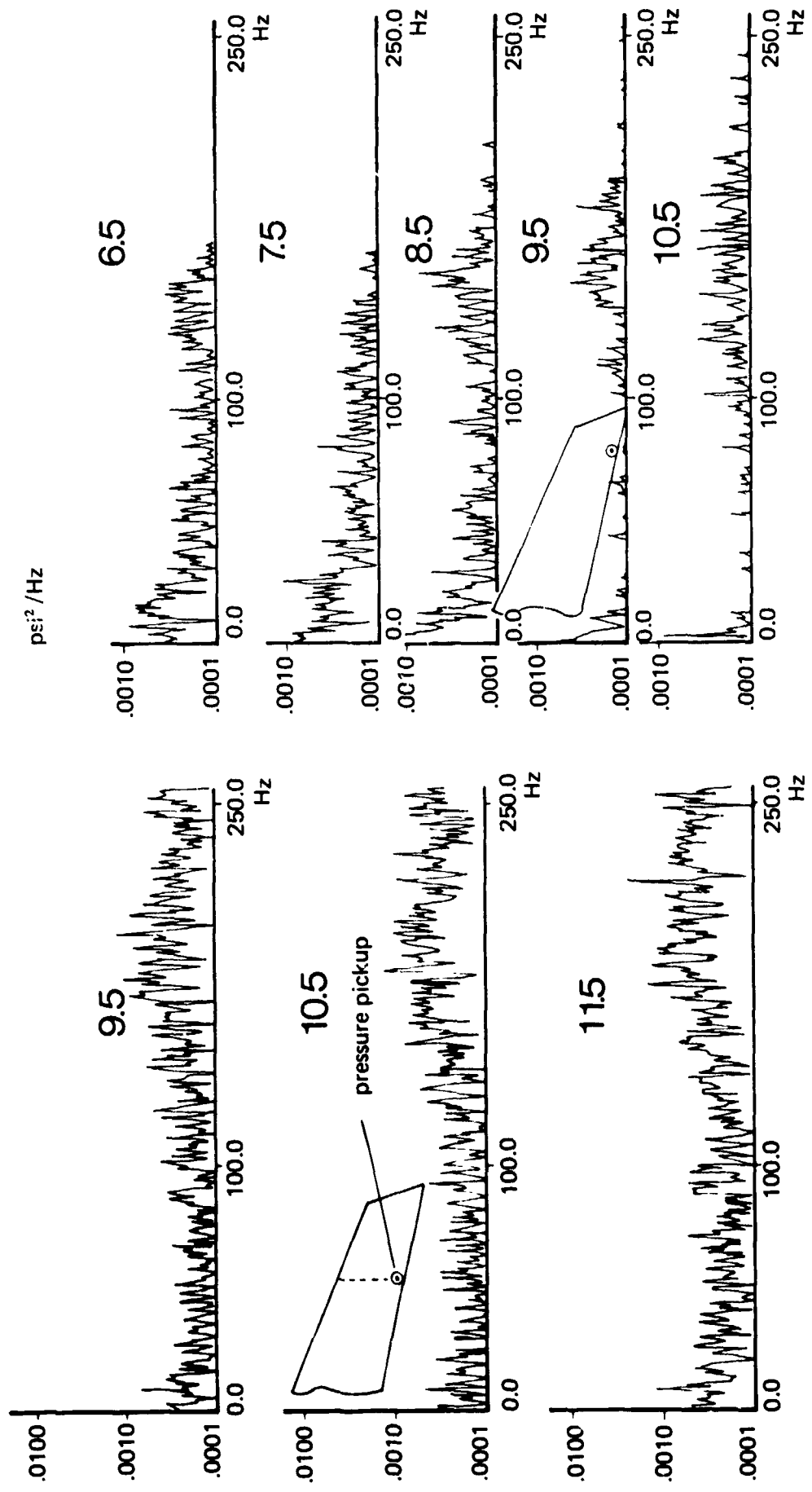
Fig. 10(b) Influence of incidence on the spectra of the fluctuating pressures at two spanwise
stations $\eta = 0.67; 0.87$ s at M = 0.8, $\Lambda = 25°$

g^2/Hz

$\Lambda = 25°$

$M = 0.8$

——— $a = 11.5$

- - - - - 6.5

1.0000

.1000

.0100

.0010

.0001

Hz

0.0   100.0   250.0
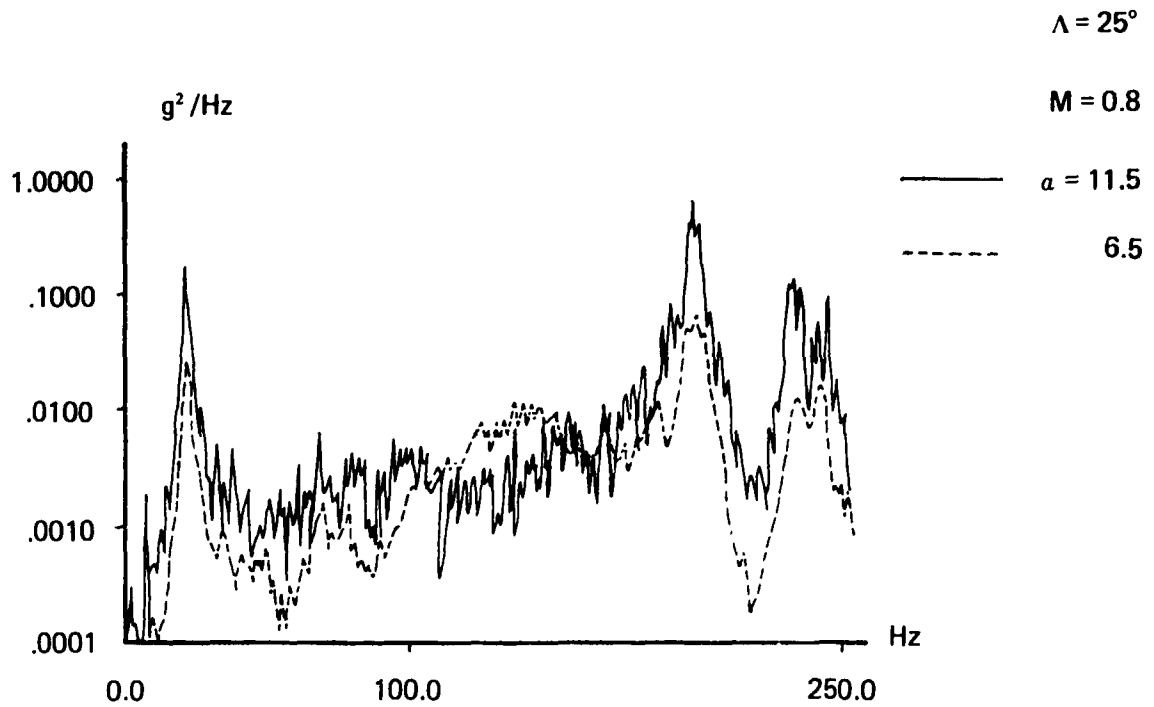
Fig. 11   Influence of incidence on the spectrum of the acceleration A 5 at M = 0.8, Λ = 25°

g^2/Hz

——— A5

- - - - - A6

$M = 0.8$

$a = 8.5$

1.0000

.1000

.0100

.0010

.0001

Hz

0.0   100.0   250.0
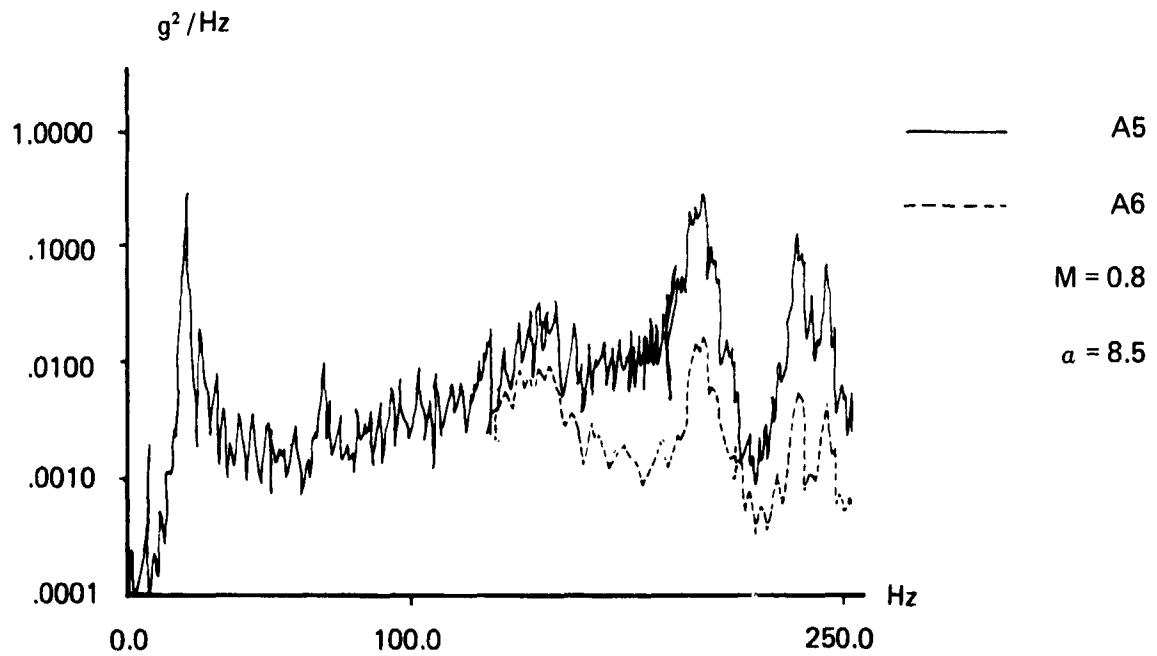
Fig. 12   Comparison of the accelerometer spectra at position A5 and A6 at M = 0.8,
a = 8.5, Λ = 25°
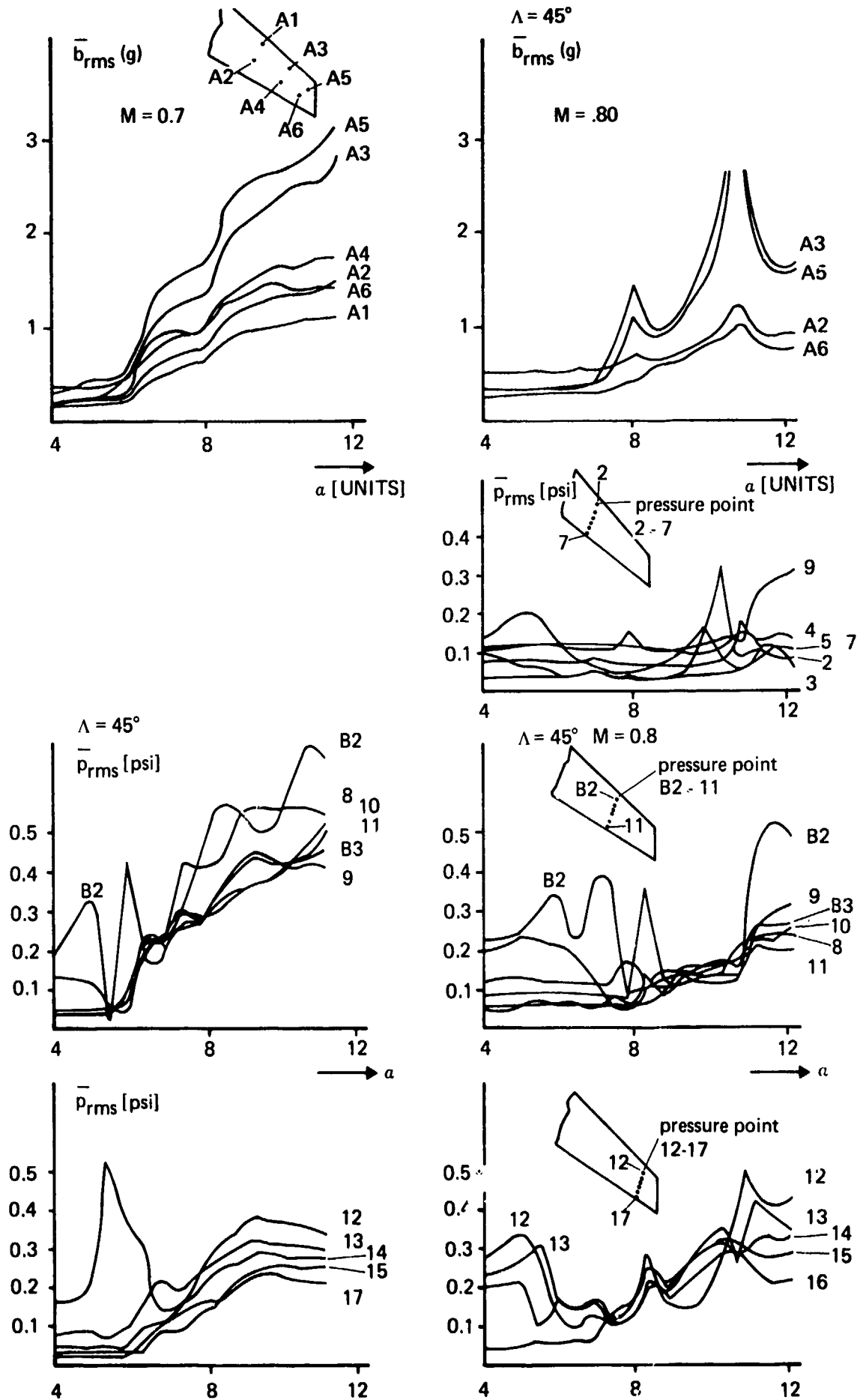
Fig. 13 Influence of incidence and Machnumber on the rms pressures and accelerations on the wing at Λ = 45°
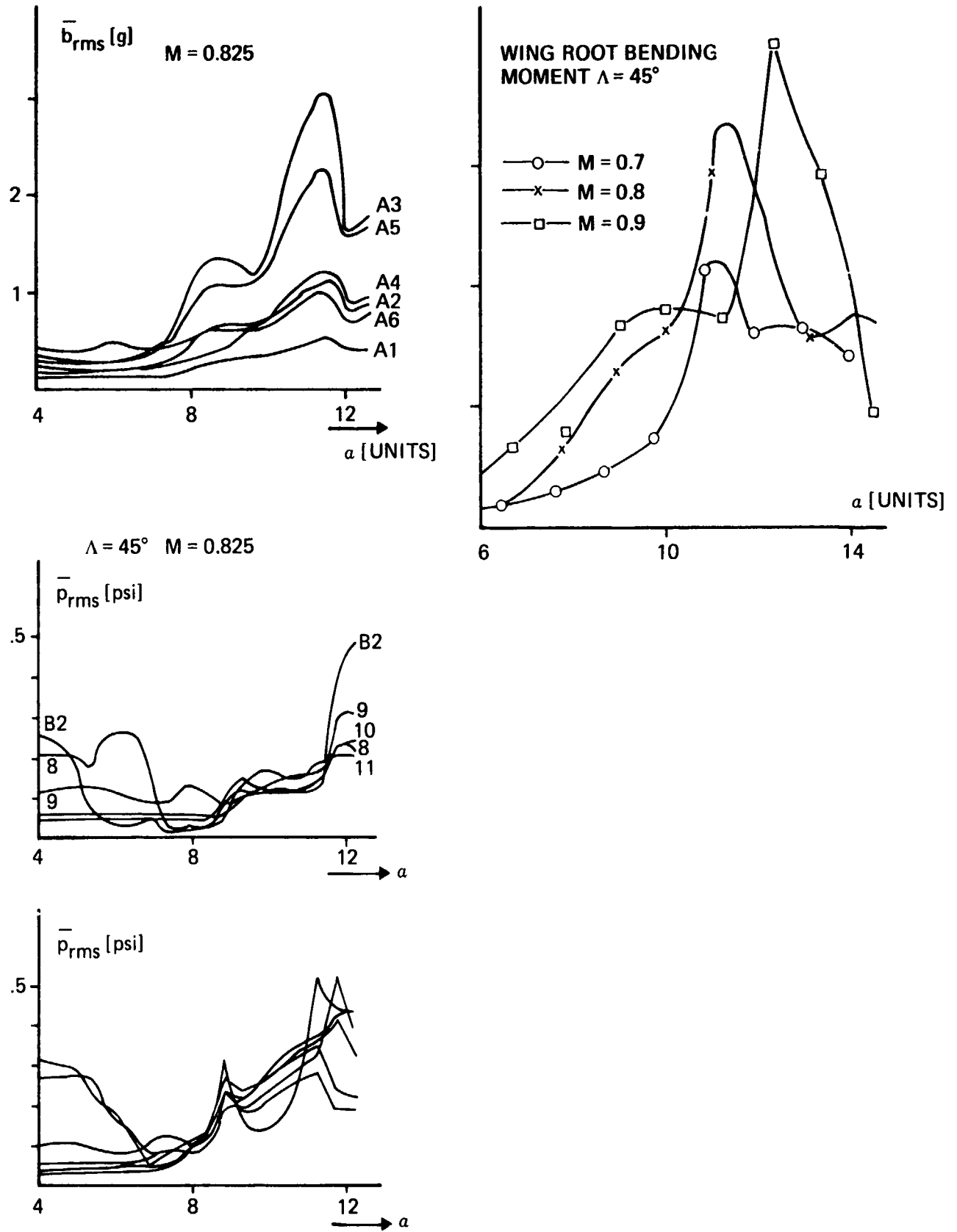
Fig. 14 Influence of incidence and Machnumber on the rms pressures, accelerations
and wing root bending at Λ = 45°
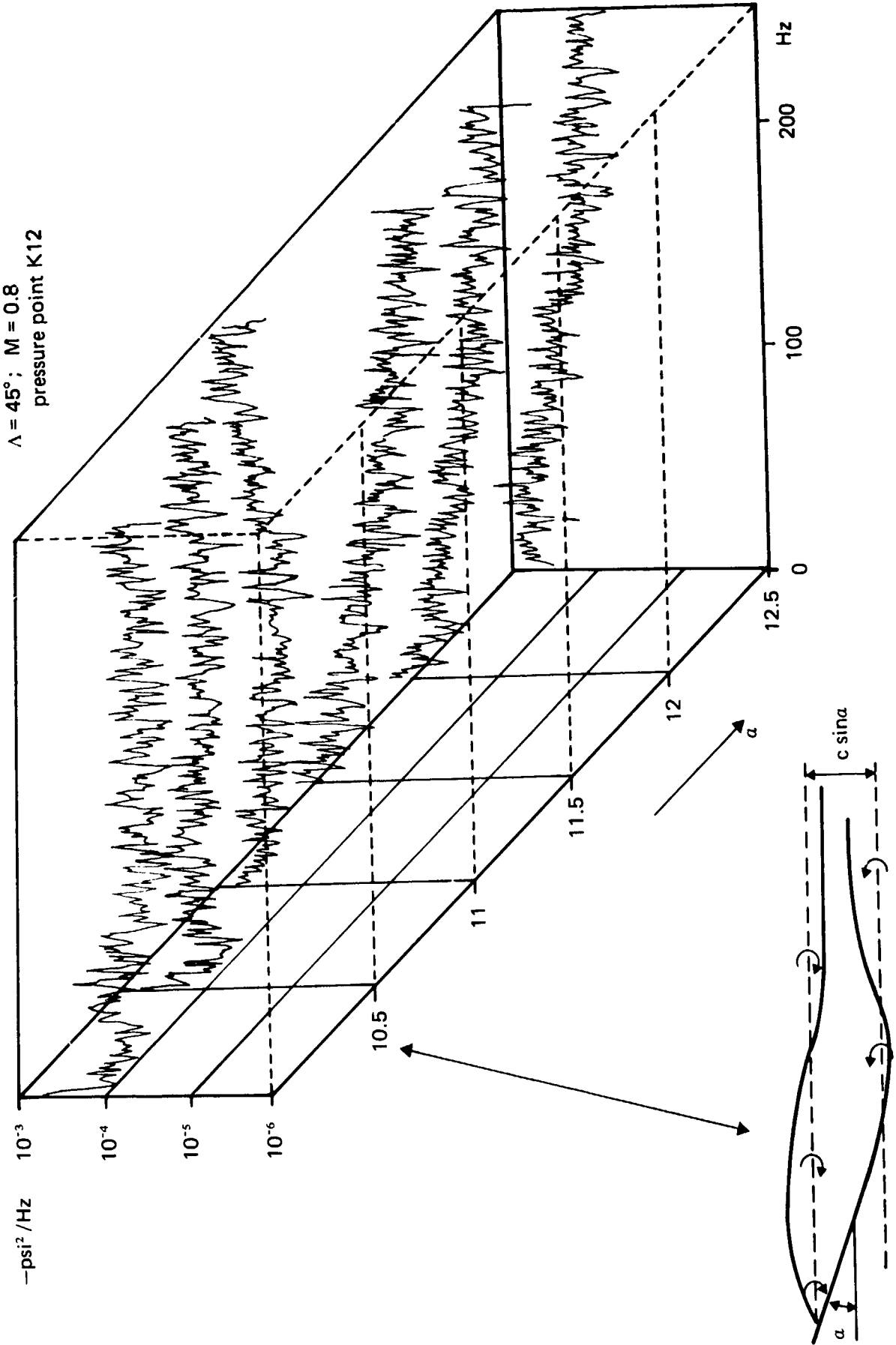
Fig. 15 Influence of incidence on the fluctuating pressure spectra at $\Lambda = 45°$, $M = 0.8$
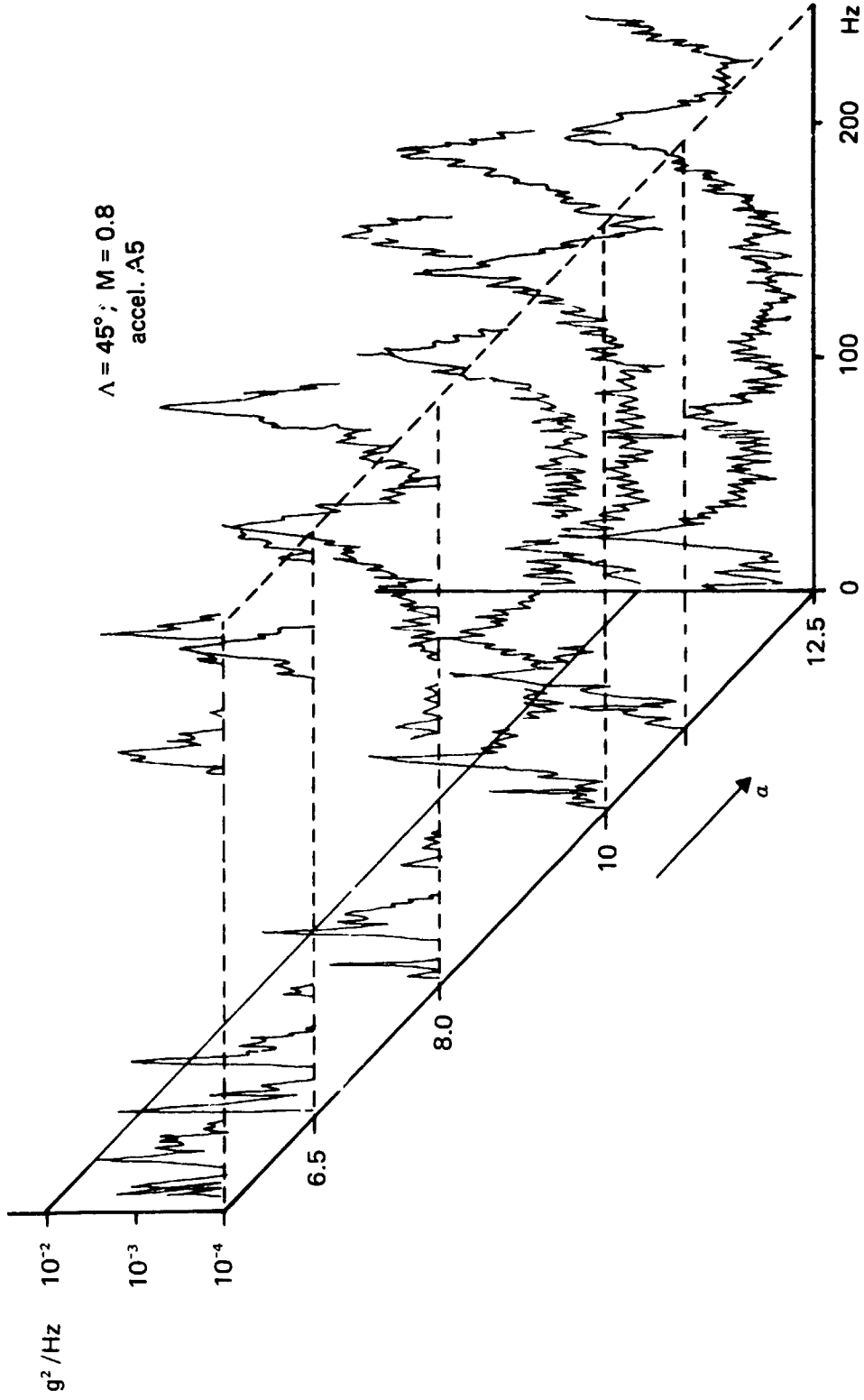
$\Lambda = 45°$; M = 0.8
accel. A5

Fig. 16 Influence of incidence on the acceleration spectra at $\Lambda = 45°$, M = 0.8

SEPARATION DEVELOPMENT

$\Lambda = 25°$

$a = 6.8$ $a = 7.3$ $a = 7.8$ $a = 8.3$

M = 0.7

$a = 11.5$
$a = 9.5$

$a = 7$

AERODYNAMIC DAMPING
FIRST BENDING

DIMENSIONLESS EXCITATION SPECTRA OF WING
FIRST BENDING (MODEL TEST)

SEPARATION DEVELOPMENT

$\Lambda = 45°$

$a = 6$ $a = 8.5$ $a = 10$

M = 0.8

$a = 13$
$a = 9$
$a = 7$

$\omega\, S_1/V$

DIMENSIONLESS EXCITATION SPECTRA OF WING FIRST
BENDING (MODEL TEST)
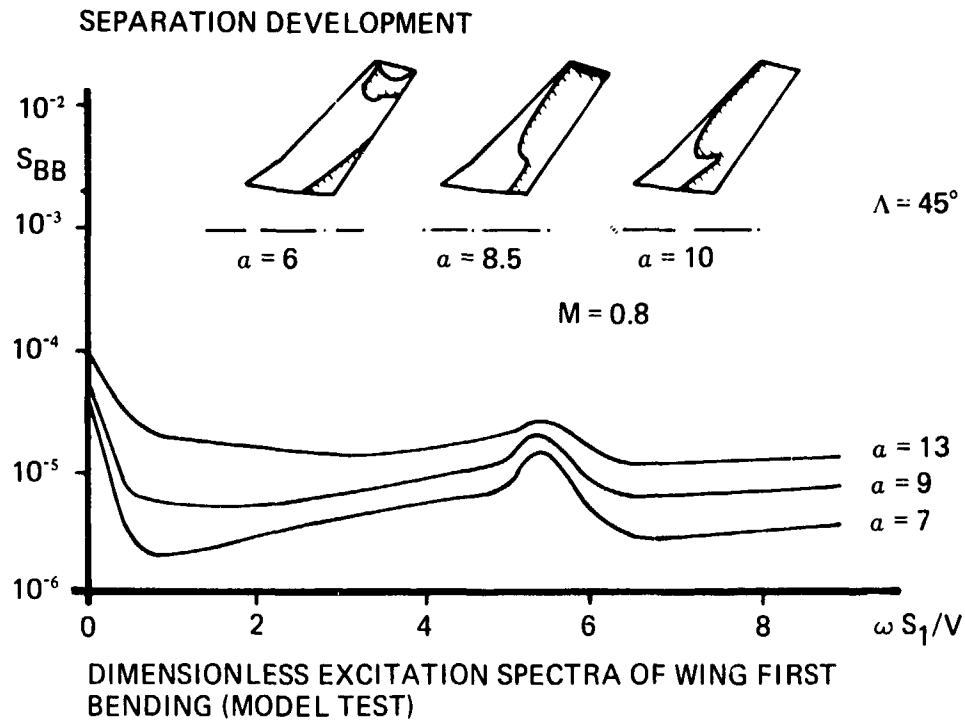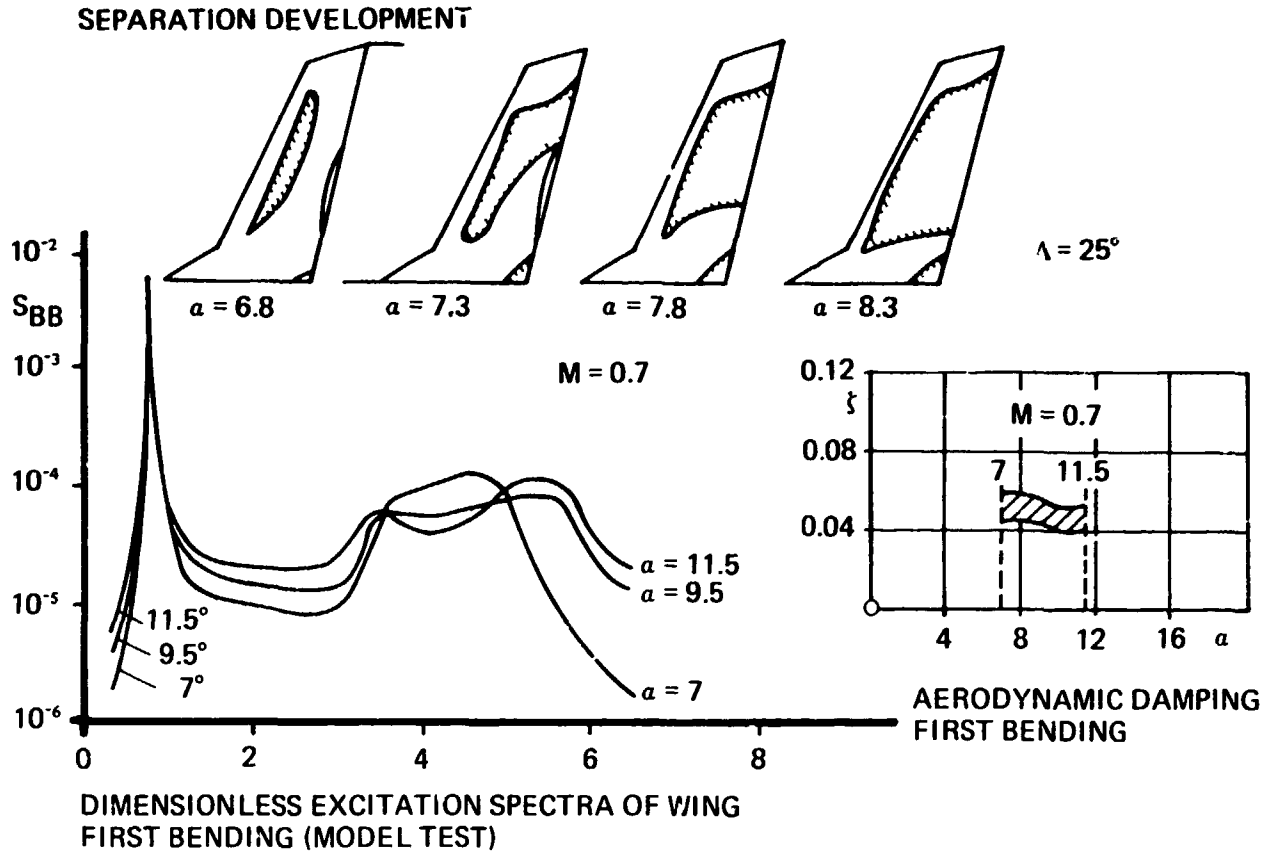
Fig. 17   Dimensionless excitation spectra of the true aircraft at M = 0.7, Λ = 25° and
M = 0.8, Λ = 45°

zero aerodynamic damping

9.5°

$\Lambda = 25°$

11.5
7
9.5

M = 0.75

structural damping 2%
+ aerodynamic damping

[g]

Pilot 1
Pilot 2
FUSELAGE
AXIS

[g]

$\Lambda = 45°$, M= 0.75

structural damping 2%
+ aerodynamic damping

13
9
7

Front Fuselage

Pilot 1
Pilot 2
FUSELAGE
AXIS

[g]

9.5°

zero aerodynamic damping

$\Lambda = 25°$, M = 0.75
structural damping 2%

11.5
9.5
7

PIVOT POINT   WING TIP
wing E.A.

[g]

$\Lambda = 45°$, M = 0.75

structural damping 2%
+ aerodynamic damping

13
9
7

PIVOT POINT   WING TIP
wing E A.

$\Lambda = 25°$, M = 0.75
structural damping 2%
$a = 11.5$

[g]

wing + store

wing only

Pilot 1
Pilot 2
FUSELAGE
AXIS

[g]

M = 0.75

structural damping 2%
+ aerodynamic damping

wing + store

wing only

PIVOT POINT   WING TIP
wing E.A.

BUFFET CRITERIA Ref. 9
onset ± .035 to .1 g_z
light ± .1 to .2 g_z
moderate ± .2 g to .6 g_z
severe ± .6 g to 1.0 g_z
(4÷10 Hz region)

Fig. 18   Results of the rigid pressure model techn   . Predicted pilot seat and wing tip accelerations
for a clean wing and a wing-store configuration
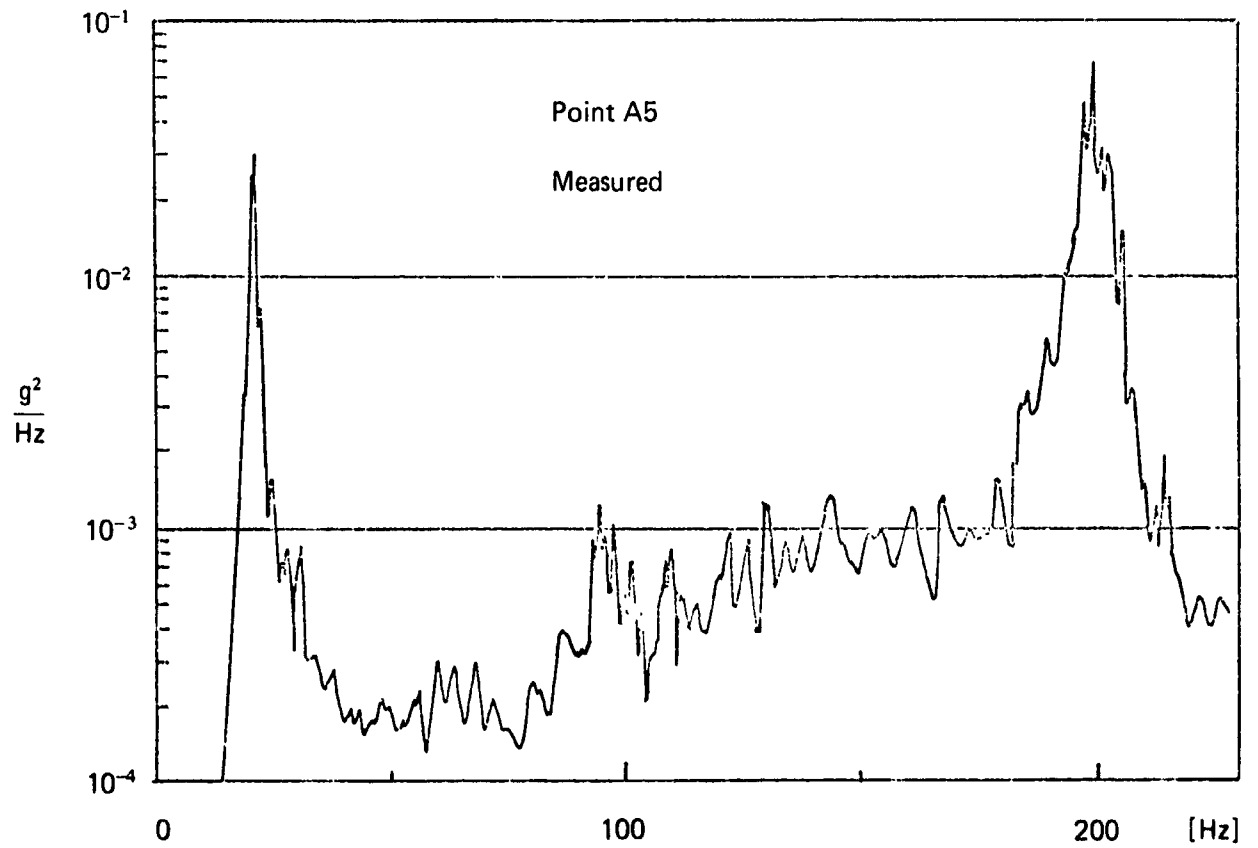
Fig.19   PSD of wing tip acceleration, $\alpha = 12°$, M = 0.7, $\Lambda = 45°$
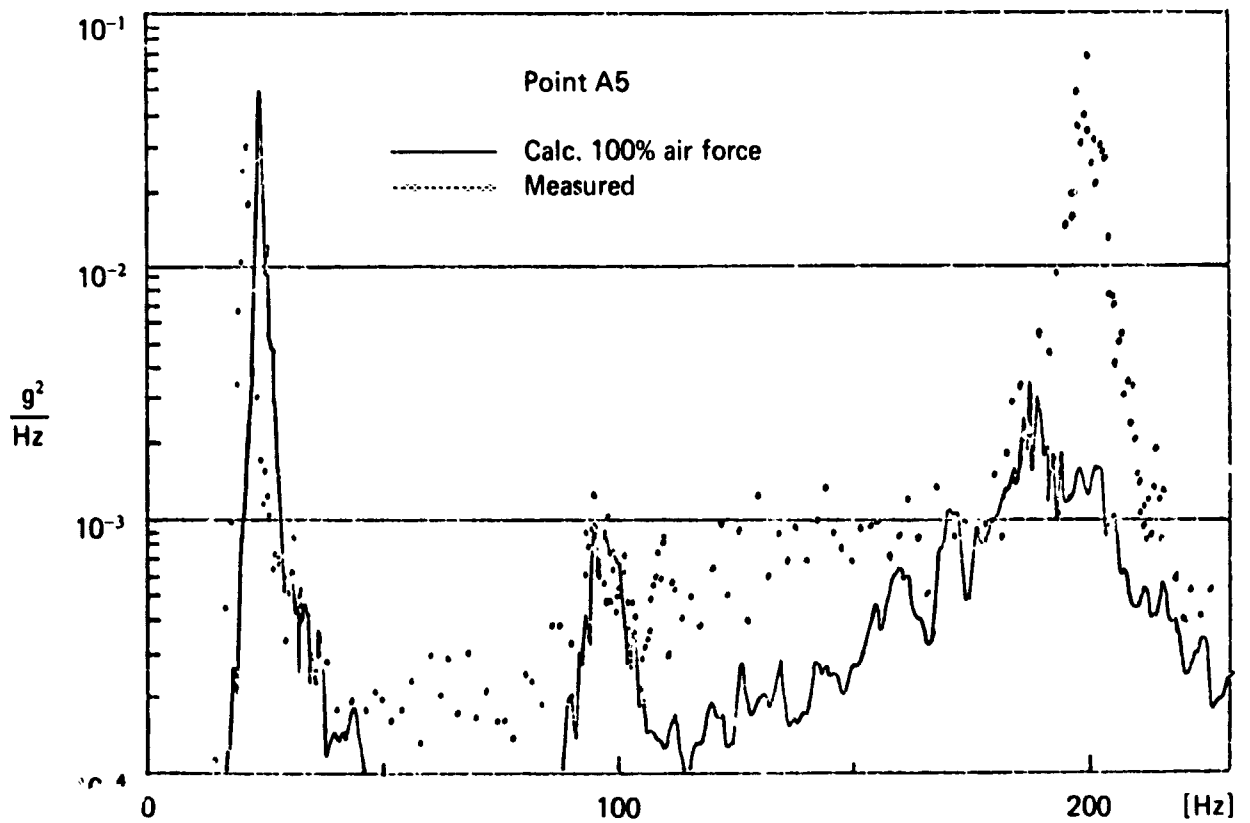
Fig.20
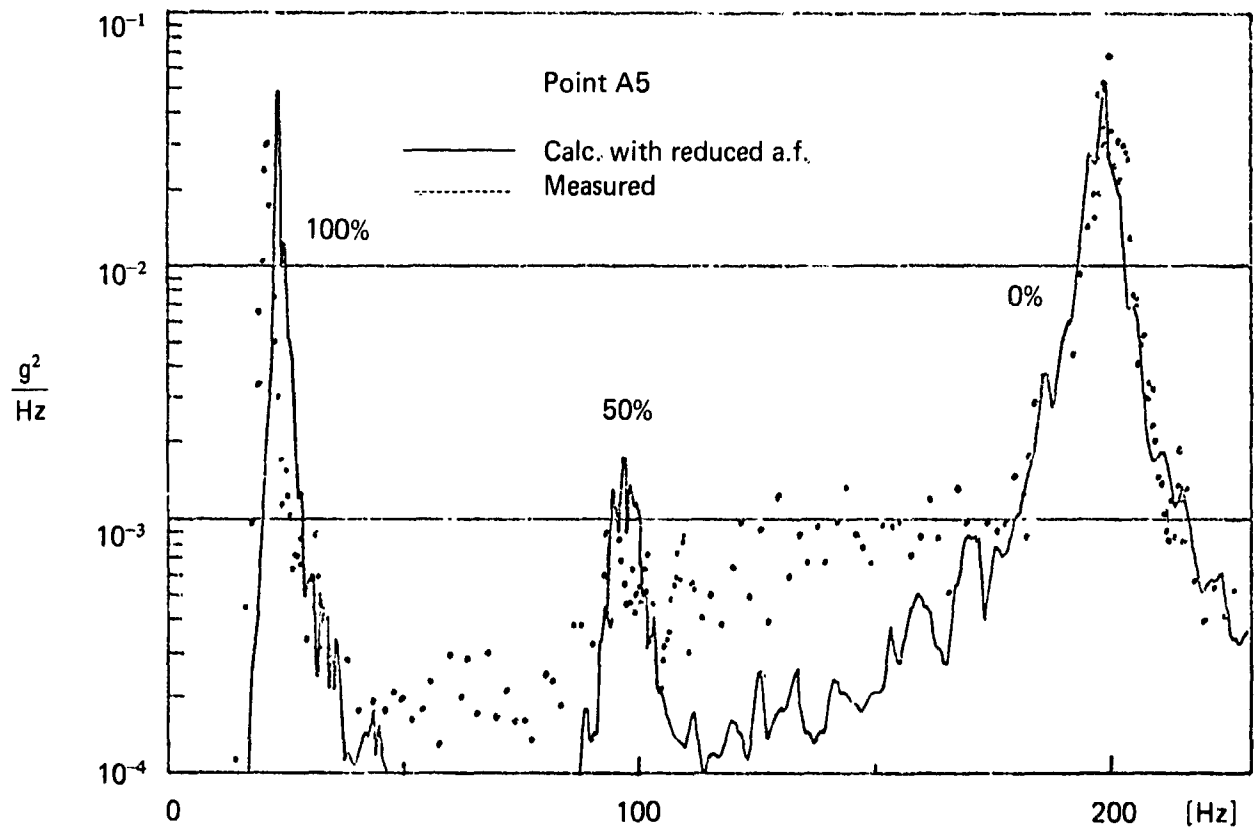
Fig.21   PSD of wing tip acceleration, $\alpha = 12°$, M = 0.7, $\Lambda = 45°$
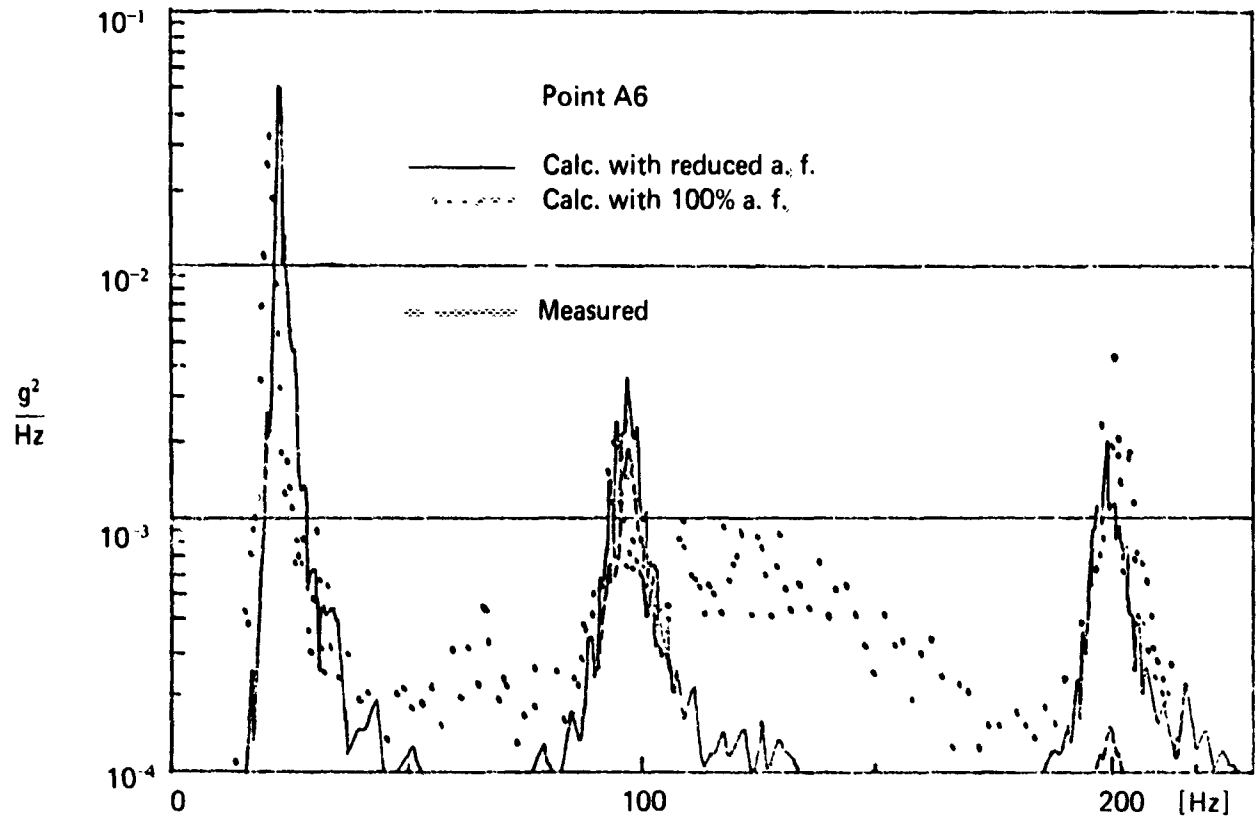
Fig.22

MEASUREMENTS OF BUFFETING ON TWO 65° DELTA WINGS OF DIFFERENT MATERIALS

by
D. G. Mabey and G. F. Butler
Royal Aircraft Establishment, Bedford, England

SUMMARY

Measurements of buffeting were made on two 65° delta wings, one made of steel and the other of magnesium. The objective of the investigation was the derivation of a non-dimensional buffet excitation parameter from measured values of the rms buffeting response and total damping ratio. The materials were selected so that the resonant frequencies of the wings were almost the same, while giving a significant variation of response and damping ratio under identical free stream conditions. The wings were tested at Mach numbers of 0.35, 0.7 and 1.4 and the Reynolds number was varied over a wide range.

The results showed that the buffet excitation parameter for the first bending mode was virtually identical for both wings and was independent of Reynolds number, except at very low Reynolds numbers. A significant level of aerodynamic damping was measured on the magnesium wing, and the experimental values agreed well with estimates made using slender wing theory.

SYMBOLS

A	aspect ratio
C_N	normal force coefficient $= N/qS$
C_L	lift coefficient $= L/qS$
c_0	root chord (533mm)
$\bar{c}$	aerodynamic mean chord (355mm)
E	Young's modulus (N/m^2)
f	frequency (Hz)
$F(n)$	the spectrum function, such that $F(n)\Delta n)$ is the contribution to $\overline{p^2}/q^2$ in a frequency band Δn
$G(n)$	the spectrum function of generalised force, such that $G(n)\Delta n$ is the contribution to $\overline{G^2}/q^2S^2$ in a frequency band Δn
$g/2$	structural damping ratio (% critical)
L	lift force (N)
M	Mach number
m_r	generalised mass in rth mode of vibration
n	frequency parameter $f\bar{c}/U$
N	normal force (N)
$N(n)$	spectrum function of normal force coefficient fluctuations such that $N(n)\Delta n$ is the contribution to N^2/q^2 in frequency band Δn
p	pressure fluctuation in a band Δf at frequency f
P	peak-to-peak wing-tip deflection (mm)
q	$\tfrac{1}{2}\rho U^2$ kinetic pressure (N/m^2)
R	Reynolds number/unit length
r, dr	mean resistance and resistance change
S	wing area $(6.62 \times 10^{-2} m^2)$
S_T	wing semispan ratio
t	wing thickness (mm)
U	free stream velocity (m/s)
v, dv	mean voltage and voltage change
y_a	attachment line of vortex (Fig.18)
y_s	static deflection
$\ddot{y}$	rms wing-tip acceleration
$y(\eta)$	mode shape of vibration of rth mode
α	angle of incidence (degrees)
α_0	angle of incidence for zero normal force (degrees)
β	$y/(S_T x)$
γ	aerodynamic damping ratio (% critical)
ϵ_s	static strain
ϵ	dynamic strain (rms)
ζ	total damping ratio (% critical)
η	spanwise displacement (y/S_T)
Λ	leading-edge sweep angle (degrees)
ρ	free stream density (kg/m^3)
ρ_m	model density (kg/m^3)
σ	gauge factor (about 120 for these semiconductor gauges)
ϕ_x	power spectrum of aerodynamic excitation in given mode (per Hertz)
ω	circular frequency (rad/s)

Subscripts

St	steel
Mg	magnesium

1. INTRODUCTION

There is still considerable interest in the prediction of buffeting in flight from measurements of unsteady wing-root strain on steel or light alloy wind-tunnel models of conventional construction. This

technique, as originally suggested by Huston[1] and elaborated by Davis and Wornom[2], is attractive because of its apparent simplicity and its ability to produce predictions at much higher Reynolds numbers than can generally be achieved with structurally scaled aeroelastic models[3]. However, the method has come under close scrutiny because significant variations in total (structural and aerodynamic) damping ratio in the first wing bending mode with angle of incidence have been observed in some flight[4] and wind-tunnel[5] experiments on swept wings. These variations are difficult to explain or predict but similar variations in total damping ratio have also been observed recently on an aeroelastic model of a low aspect ratio wing with a small angle of leading-edge sweep-back[6].

The variations in total damping must be separated into variations in aerodynamic and structural damping if they are to be correctly incorporated into the buffeting scaling relationships[1,2]. In general the separation of these damping components is still a matter of corsiderable difficulty. The aerodynamic damping should depend on the free stream density and velocity whereas the structural damping can vary with lift on the model (as in Ref.2) or with the level of vibration (as in Ref.7). Analysis of the damping measurements with varying air density may also be prejudiced by associated variations in the wing flow caused by changes in Reynolds number.

Recently, Jones[4] pointed out that the non-dimensional aerodynamic excitation parameter appropriate to a flexible mode of vibration could be derived from measurements of buffeting response and total damping ratio. In the present investigation, the main objective was the derivation of the non-dimensional buffet excitation parameter in the first wing bending mode from measurements made on wings of different materials, to give variations in response and damping, but under nominally identical free stream conditions. To test the scaling relationships implicit in the use of this non-dimensional buffet excitation parameter the flow required to excite the wing buffeting had to be relatively unaffected by a wide variation in Reynolds number and preferably unaltered in general character by a Mach number variation from subsonic to supersonic speeds. These conditions were satisfied by the choice of a slender wing with a well-ordered vortex flow[8], and accordingly a half-model of a delta wing, with a sharp leading-edge swept back 65°, was used (Fig.1). On this simple configuration a variation in the relative proportions of aerodynamic and structural damping at constant Reynolds number was obtained by testing two nominally identical wings, one of mild steel and the other of magnesium alloy. These materials were selected because they had the same ratio of Young's modulus E, to density ρ_m. Hence their natural frequencies were virtually identical and their mode shapes similar. Both wings could be tested over a wide range of free stream air density, ρ, at constant Mach number, giving the same values of the ratio ρ/ρ_m for different combinations of ρ and ρ_m.

The idea of using geometrically similar models of steel and magnesium was suggested by a previous buffeting investigation[7]. However the results of that investigation were inconclusive, possibly because the aerodynamic characteristics of the wing planform and section selected were sensitive to changes in Mach number and Reynolds number. (In that early investigation the kinetic pressure q was varied by changing the Mach number at constant tunnel total pressure, and no tests were included at constant Mach number over a range of Reynolds number.)

The results of the present investigation on the 65° delta wing configuration show that on the steel wing small variations in total damping ratio with free stream density can be detected. On the magnesium wing significantly larger variations in total damping ratio with free stream density are observed. When the total damping ratios are combined with the responses (given by the wing-root strain) a measure of the buffet excitation (or forcing function) is derived, and this is almost the same for both wings and independent of Reynolds number. The measurements extend well into the vortex breakdown region, and thus represent a useful extension of our knowledge of slender wing buffeting. (Earlier measurements of slender wing buffeting were limited by a load restriction on the aeroelastic model[9].)

The wider implication of these tests is that it should be possible to predict the buffet forcing function from tests of ordinary wind-tunnel models, as long as the total damping ratio is derived accurately. However if predictions for buffeting in flight are required, the total damping ratio measured during the model tests must be separated into the aerodynamic and structural components. This condition is somewhat restrictive, and implies that a wide free stream density variation (say 2/1) should be included for several Mach numbers of the model test programme.

2. EXPERIMENTAL DETAILS

2.1 Models

Fig.1 shows some details of the 65° delta wing models. Both wings have a root chord, c_0, of 533mm and nearly identical thicknesses, t, except at the leading-edge. This has a 30° chamfer being applied normal to the leading-edge. Both wings have blunt trailing-edges. There is a clearance of about 2mm between the tunnel sidewall and the centre line of the model to allow the model attitude to vary. No boundary layer fence is provided because the boundary layer thickness varies with Reynolds number and Mach number only from about 8 to 10mm during the tests, compared to the model span of 248mm. Any interference caused by flow through the gap, or the sidewall boundary layer, is common to both models.

The wing root tongue of each model is covered with a thin layer of araldite, and then permanently bolted into a rectangular steel block. This solid method of mounting in the root block is adopted to achieve a low level of structural damping, insensitive to static or dynamic distortion of the model. Each root block has 20 jig-bored bolt holes to ensure positive attachment to the half model balance. Fig.1 includes the nodal lines of the principal modes of vibration for the wings mounted in their root blocks. (These nodal lines, and the corresponding resonant frequencies, were found during a ground resonance test made in a laboratory in Structures Department at RAE Farnborough.) The modal frequencies of the steel wing are about 7% higher than the corresponding modal frequencies of the magnesium wing, because the magnesium wing is 7% thinner. (The difference in thickness occurred because of the difficulties of machining magnesium.) However this small difference in frequency is not considered to be significant because of the flat excitation spectrum associated with the vortex flow[8]. In fact the frequencies excited during the tunnel tests are somewhat different, possibly because of the finite stiffness and mass of the half model balance. (When the wings are mounted on the half model balance it allows small deflections,

i.e. the wings are not 'built in at one end' in the usual sense.) The 'wind on' frequencies are constant over a wide range of kinetic pressure q and angle of incidence α, and are therefore unlikely to be influenced by the aerodynamic stiffness of the wings.

2.2 Instrumentation and analysis

The mean normal force on the wings was measured using the half model balance of the RAE 3ft × 3ft tunnel. The wing angle of incidence was set by the half model turntable incorporated with the balance and no corrections were applied for the small angular deflections of the balance or for tunnel constraint effects, which are small.

The small strains associated with the static and dynamic deflections of the wings were detected by two strain gauge bridges, one at the root and one close to the tip, as shown in Fig.1. The wing-root strain gauge bridge was to measure the vibration in the first wing bending mode, which was of primary interest in the experiment. The tip strain gauge bridge was to measure the response in the fourth mode, which was considered of some interest in the context of previous buffeting tests on aeroelastic models of slender wings[9].

The strain gauge bridges utilised four active semiconductor strain gauges, which were selected because of their high gauge factor $\sigma \simeq 120$ (compared to $\sigma \approx 2$ for wire gauges). Considering first static deflections and strains, for every strain gauge the resistance change dr was related to the unloaded resistance r by the fundamental strain gauge relation

$$dr/r = \epsilon_s \sigma , \tag{1}$$

where ϵ_s = static strain.

Each bridge of four gauges was powered by a direct current voltage v so that the output dv across the bridge was given by

$$dv/v = dr/r , \tag{2}$$

so that

$$\epsilon_s = dv/v\sigma . \tag{3}$$

Values of $\sigma = 120$ (for the steel wing) and $\sigma = 110$ (for the magnesium wing) were derived from a static calibration of the wing-root strain bridge. Some of this difference may be due to misalignment of the strain gauges, rather than a true variation in gauge factor, although temperature effects cannot be excluded. It was assumed that the static and dynamic gauge factors were identical. The tip strain gauge bridge was not calibrated because of the difficulty of applying a sufficient 'point load' between the gauge station and the wing tip.

For the static calibration the dc voltages from the bridges were displayed on digital voltmeters. During the dynamic tests the fluctuating voltages were passed through a pair of Brüel and Kjaer 2107 spectrum analysers which were used as tuneable filters, and then displayed on two DISA type 55D 35 rms meters. The bandwidth selected on the analyser (6.5%) was quite wide relative to the narrow bandwidth of the responses being measured.

The fluctuating voltages from both bridges were recorded on magnetic tape for a number of angles of incidence at typical test conditions. The tape recorder used was a Rapco 4-track FM machine. Recordings of about 30 seconds duration were taken to try to ensure that a sufficiently large number of cycles of buffeting at the first mode (110Hz) were available to give reliable estimates of the damping. The total damping ratios were determined using the random decrement (Randomdec) technique[10], a development of the normal method whereby the damping is calculated from the decay of the autocorrelation function[11].

2.3 Test conditions

The closed 3ft × 3ft working section of the RAE 3ft × 3ft tunnel was selected for these tests because of its low level of flow unsteadiness[12]. With this closed working section and the subsonic liner the maximum Mach number was limited to M = 0.7 to avoid choking, but supersonic speeds from M = 1.3 to 2.0 could be achieved by replacing the top subsonic liner by a contoured supersonic liner. The test Mach numbers selected, M = 0.35, 0.70 and 1.40, allowed comparison with previous measurements on steel and aeroelastic models of slender wings[9] and a significant variation of kinetic pressure q, as well as of free stream density ρ. The test conditions are given in Table 1.

No roughness was applied to fix transition because it was considered that contamination by the side-wall boundary layer would eliminate most of the areas of laminar flow observed during tests of a complete model of a 65° delta wing[13] at low Reynolds numbers.

3. RESULTS

3.1 Normal force measurements and flow visualisation

Fig.2 shows the variation of normal force coefficient C_N, with angle of incidence for both wings at Mach numbers of M = 0.35, 0.70 and 1.40 over the complete range of Reynolds numbers.

At low angles of incidence the lift coefficient given by slender wing theory

$$C_L = \frac{\pi}{2} A\alpha ,$$

where A is the wing aspect ratio and α the angle of incidence, is in good agreement with these normal

force measurements over the whole speed range. At subsonic speeds the normal force coefficient at a given angle of incidence is identical for both wings, and independent of variations in Reynolds number. The agreement between the measurements is particularly impressive at high angles of incidence ($\alpha > 20^\circ$) when the wings move close to the vortex breakdown region, and where some differences caused by scale effects or static aeroelastic distortion might have been anticipated. Hence results from these two subsonic Mach numbers provide an excellent test for the scaling relations appropriate to wing buffeting.

At M = 1.4 the situation is more complex because at angles of incidence greater than 15° differences occur between the normal forces measured at the two Reynolds numbers. The differences could be attributed to aeroelastic distortion and/or scale effects. Thus Fig.2 shows that the steel wing stalls suddenly above $\alpha = 20^\circ$ at the lower Reynolds number, although after the stall, at $\alpha = 25^\circ$, the normal force coefficient reaches the same level at both Reynolds numbers. In contrast, the magnesium wing encountered such a violent low frequency vibration at $\alpha = 18^\circ$ (possibly caused by a shock oscillation enhanced by aeroelastic distortion effects) that the mean normal force coefficient could not be measured by the balance. Hence the measurements at M = 1.4 are of limited value as a test of the buffeting scaling relationships, although they help to establish the relative levels of structural and aerodynamic damping.

Differences between the half-model results and some earlier complete model results[13] are of interest, because the low Reynolds number measurements of the fluctuating normal force given in Ref.13 for this plan-form are relevant to the present experiment. However, the differences observed do not vitiate the main objective of this experiment, the investigation of the buffeting scaling laws in a flow insensitive to variations in Reynolds number. The results shown in Fig.2 for M = 0.35 and 0.70 show clearly that conditions insensitive to Reynolds number were attained, and that slender wing theory should be applicable at low angles of incidence.

Fig.3 shows a sketch of the flow separations based on oil flow photographs. We recognise the primary vortex, with its characteristic 'herring-bone' pattern having a point of inflection in the surface streamlines, and the secondary vortices.

3.2   Dynamic strain measurements

Figs.4 and 5 show the variation of the rms unsteady wing-root strain ε, in the first wing bending mode (110Hz), as a function of the angle of incidence α for both steel and magnesium wings.

For the steel wing Fig.4 shows that at the lowest Mach number, M = 0.35, the rms strain, ε, is small and almost constant over the incidence range from $\alpha = -5^\circ$ to $+5^\circ$ but then increases somewhat to a plateau between $\alpha = 10^\circ$ and 15°. At an angle of incidence of about $\alpha = 18^\circ$ the strain starts to increase steadily, and at about $\alpha = 22^\circ$ when vortex breakdown occurs, the strain increases rapidly. This strain variation closely resembles the buffeting response previously observed in tests on a slender wing at low speeds (e.g. Fig.10 of Ref.9 which shows results up to $\alpha = 25^\circ$ at M = 0.23).

The wing-root strain measurements increase monotonically with Reynolds number (or free stream density ratio ρ/ρ_m) and examination shows that

$$\varepsilon \sim (\rho/\rho_m) \quad . \tag{4}$$

This result is consistent with the total damping in the fundamental mode remaining almost constant, so we may infer that structural damping predominates as in previous tests of small steel models[14]. For the intermediate Mach number, M = 0.70, Fig.4 also shows that the rms wing-root strain has a minimum at $\alpha = 0^\circ$. The measurements thus indicate the light buffeting induced by the vortex on the lower surface of the wing at negative angles of incidence ($-5^\circ < \alpha < 0^\circ$) and by the vortex on the upper surface of the wing at positive angles of incidence ($0 < \alpha < 5^\circ$). The wing-root strain increases steadily from $\alpha = 5^\circ$ to $\alpha = 20^\circ$ without reaching a 'plateau value' as at M = 0.35. This variation resembles the buffeting observed previously on a slender wing at higher subsonic speeds (e.g. Fig.13 of Ref.9 which shows results up to $\alpha = 14^\circ$ at Mach number of 0.50). However between $\alpha = 20^\circ$ and $\alpha = 23^\circ$ there is a much more rapid increase associated with vortex breakdown. Even at this Mach number, the wing-root strain is still almost directly proportional to the density ratio (ρ/ρ_m). At the highest Mach number, M = 1.4, the rms strain, ε, is small and almost constant from $\alpha = -5^\circ$ to $\alpha = 15^\circ$, but increases rapidly at vortex breakdown, at about $\alpha = 20^\circ$ (Fig.4). The variation of the strain with angle of incidence after vortex breakdown is quite different at the two Reynolds numbers and reflects the radically different stalling behaviour shown by the normal force measurements in Fig.2. It is therefore unsuitable as a test of the buffeting scaling relationships.

For the magnesium wing the strain measurements are in many respects similar to those on the steel wing. However, at subsonic speeds two significant differences may be distinguished (Fig.5):

(1)   The rms wing-root strains are generally about two to three times higher on the magnesium wing than they are on the steel wing at the same Reynolds number.

(2)   Although the rms strains still increase monotonically with Reynolds number, or free stream density ratio, the measurements cannot be represented by an approximation of the form

$$\varepsilon \sim (\rho/\rho_m)$$

as for the steel wing. This suggests that the damping of the magnesium wing varies significantly with free stream density, a hypothesis which is confirmed by the damping measurements which follow in section 3.3.

At M = 1.4 and angles of incidence from -5° to $+15^\circ$ the wing-root strain on the magnesium wing (Fig.5) is generally about two to three times higher than on the steel wing (Fig.4). The measurements on the magnesium wing do not extend beyond $\alpha = 15^\circ$ because the wing started to oscillate violently at $\alpha = 18^\circ$.

3.3 Damping measurements

Fig.6 shows the variation of total damping ratio (% critical) with angle of incidence, Mach number and Reynolds number for the steel wing. The variations in damping at constant speed are all comparatively small (less than 0.2% critical). The response relation observed above (equation (4)) is thus broadly consistent with the damping measurements[2]. In marked contrast, Fig.7 shows that for the magnesium wing there are comparatively large variations in total damping ratio with free stream density (about 2.5% critical) which are much larger than the wind-off structural damping ratio (0.45% critical). Hence equation (4) is not applicable to the magnesium wing. At a given density the variation in damping with angle of incidence is small, just as in previous tests on a slender wing model (Fig.21, Ref.9).

Figs.6 and 7 suggest that the variations in total damping ratio with angle of incidence are small over the full range of the tests. Thus even at vortex breakdown, between $\alpha = 23^\circ$ and 25°, when there is a large increase in response (Figs.4 and 5) there is no large change in total damping ratio, either at $M = 0.35$ or 0.70. This implies that the aerodynamic damping at this extreme condition is independent of the amplitude of response. It also indicates that the large local changes in the slope of the overall normal force at vortex breakdown (shown in Fig.2), are not sufficient to influence the aerodynamic damping. This result is rather surprising because the loss of normal force on vortex breakdown will be severe towards the wing-tip, and might thus be expected to have a strong influence on the aerodynamic damping. However, if we restrict our attention to the most reliable set of measurements on the magnesium wing, linked by the dotted curves in Fig.7, a rather different picture emerges. We find that the total damping increases a little as the angle of incidence increases from 0° to about 20°, and then decreases. This variation exhibits the general trend anticipated from the normal force measurements.

Estimation of the relative proportions of aerodynamic and structural damping remains a controversial question and is not strictly germane to the main objective of this paper which is to derive the aerodynamic forcing function. However, the aerodynamic dampings derived under the assumption of constant structural damping are summarised in Fig.8. For the steel wing the aerodynamic damping ratio is generally quite small (less than 0.5% critical) due to the high model density (Fig.8a). For the magnesium wing the aerodynamic damping ratio is higher (up to 3%) because of the lower model density (Fig.8b). These measurements are in good agreement with estimates made using slender wing theory[15], and an approximate mode shape[16].

3.4 Extraction of buffet excitation parameter

In a previous paper Jones[4] pointed out that the non-dimensional aerodynamic excitation appropriate to a mode of vibration could be derived from measurements of buffeting response and total damping ratio. If the power spectrum of the aerodynamic excitation per Hertz is expressed as

$$\phi_x = G(n)(qS)^2 \bar{c}/U \quad , \tag{5}$$

where n is $f\bar{c}/U$, and $G(n)$ is the non-dimensional spectral density, it follows from a single-degree-of-freedom analysis[11] for the mode considered that the buffet excitation parameter, $\sqrt{nG(n)}$, is given by

$$\sqrt{nG(n)} = \frac{2}{\sqrt{\pi}} \left[\frac{m}{q} \frac{\sigma}{S} \ddot{y} \right] (\zeta)^{\frac{1}{2}} \quad . \tag{6}$$

Here m = generalised mass of wing bending mode,
$\quad$ n = the non-dimensional modal frequency,
$\quad$ $\sigma_{\ddot{y}}$ = rms tip acceleration in mode,
$\quad$ q = kinetic pressure
$\quad$ S = wing area
and $\quad$ ζ = total damping ratio (% critical).

The function $\sqrt{nG(n)}$ is a measure of the buffet excitation, analogous to the function $\sqrt{nF(n)}$ associated with fluctuating pressure measurements[8]. For the present tests the total damping ratio measurements in the first wing bending mode for each condition were derived above (section 3.3) and the generalised mass m_1 was estimated from an assumed mode shape.

The derivation of a relationship between the wing-tip acceleration and the measured rms strains was more difficult. The static calibration gave the same relation between static strain, ϵ_s, and static deflections, y_s, for both models (Fig.9a) and also the gauge factors appropriate to each model. To supplement these results a dynamic calibration of the magnesium wing was made with a small exciter. The linear relationship found between the peak-to-peak tip deflection, P, and rms strain, ϵ, (Fig.9b)

$$P \text{ (mm)} = 5.2 \times 10^4 \epsilon \tag{7}$$

was relatively insensitive to the precise mode shape being excited (only 39Hz with a vibration pick-up at the tip compared with 80Hz with the pick-up at the root). Hence the difference between the wind-off frequency (reduced to 80Hz by the additional mass and stiffness of the exciter) and the wind-on frequency (110Hz) should also have had a relatively minor effect in the constant in equation (7). Equation (7) was assumed to be valid for the steel wing as well as the magnesium wing, because their planforms were identical and the wing thicknesses, although not the same, were constant. (With the exciter used, the deflections would have been much smaller for the steel wing, and difficult to measure.)

The peak-to-peak wing-tip deflection and the rms wing-tip acceleration, $\sigma_{\ddot{y}}$, are related by the expression appropriate for simple harmonic motion

$$\sigma_{\ddot{y}} = (2\pi f)^2 \frac{P}{2} \frac{1}{\sqrt{2}} \quad . \tag{8}$$

Hence with equations (6), (7) and (8) and the rms strain and damping measurements given in Figs.6 to 9, the buffet excitation, $\sqrt{nG(n)}$, may be calculated.

Fig.10 shows the buffet excitation parameter as a function of angle of incidence for both models over the full range of Mach number and unit Reynolds number. The general shape of the curves is similar to that of the rms strain curves described previously because the dampings do not vary significantly with angle of incidence. However the $\sqrt{nG(n)}$ curves for the steel and magnesium wings nearly coincide at the higher Reynolds numbers. Looking in more detail, we find that at M = 0.35, and at the higher Reynolds numbers, the results from the steel and magnesium wings are in reasonably good agreement. Slight differences occur at M = 0.70 between $\alpha = 10^\circ$ and 20°. We may not attribute these differences to the effects of either static aeroelastic distortion or amplitude-dependent aerodynamic damping because the $\sqrt{nG(n)}$ curves for the magnesium wing (which have the largest distortions) are independent of Reynolds number and because the curves for both wings coincide again after vortex breakdown. [The $\sqrt{nG(n)}$ curve at M = 0.35 at low Reynolds number (Rc$_0$ = 1.1 × 10^6) on the magnesium wing is appreciably different from the measurements at high Reynolds number. The low level of buffeting after vortex formation is much reduced and vortex breakdown is delayed from about $\alpha = 20^\circ$ to $\alpha = 25^\circ$].

At supersonic speeds (M = 1.4) the level of buffeting at angles of incidence up to $\alpha = 15^\circ$ is much lower, consistent with the reduced strength and size of the leading-edge vortices, just as in previous tests[9]. However, vortex breakdown appears more sharply at supersonic speeds than at subsonic speeds, although the peak level $\sqrt{nG(n)}$ is of the same magnitude as at subsonic speeds. For the steel wing there are apparently strong 'scale effects' on $\sqrt{nG(n)}$ and the mean force after vortex breakdown (see Figs.10 and 2), but these could be caused by some interaction between the wake of the 'burst' vortex and the tunnel normal shock wave. Such an interaction would not, of course occur in flight, and could not be considered a genuine scale effect.

The buffet excitation parameter in the fourth mode can also be obtained from equation (6) if the appropriate damping ratios, generalised masses, and tip deflections are substituted. For the steel wing the response in this mode was too small (Fig.11) to allow the total damping ratios to be derived from the magnetic tape records. However, for the magnesium wing the response was about three times higher (Fig.12), and the total damping ratio in this mode was estimated to be about 0.9% critical, independent of free stream density at M = 0.35. A very similar damping, independent of air density, was found at M = 0.70. We infer that the damping in this mode was predominantly structural, just as in the third symmetric mode of vibration on the slender wing aeroelastic model (Ref.9, Fig.21c).

It was difficult to make a good estimate for the generalised mass of this mode because of the complexity of the nodal lines (Fig.1). However, if we ignore the nodal line close to the apex in Fig.1, mode 4 then corresponds roughly with mode 3 on the 60° delta wings considered in Ref.16. It was found from the tabulated deflections[16] that

$$m_3 \simeq m_1 \quad .$$

Hence for the present 65° delta wings it was assumed that

$$m_4 \simeq m_1 \quad . \tag{9}$$

For this mode it was also difficult to provide an accurate relationship between the small rms strains, ε, measured and the corresponding small tip deflections, P, (peak-to-peak). However the exciter was able to bring up this mode and the dynamic calibration for the magnesium wing (Fig.13) gave the relationship

$$P \text{ (mm)} = 1.25 \times 10^4 \varepsilon \quad . \tag{10}$$

Hence with equations (6), (8), (9) and (10) the buffet excitation parameter in the fourth mode could be estimated for the magnesium wing. Fig.14 shows that at M = 0.35, $\sqrt{nG(n)}$ in the fourth mode is almost identical with that in the first mode (Fig.10) despite the large differences in frequency parameter and mode shape. At M = 0.70, however, $\sqrt{nG(n)}$ in the fourth mode is appreciably smaller than in the first mode at angles of incidence from 5° up to vortex breakdown although after vortex breakdown at $\alpha = 25^\circ$ the levels are nearly identical.

3.5   Prediction of buffet excitation parameter

In this section we make an order of magnitude estimate of the aerodynamic excitation on this planform based on published fluctuating normal force data[13]. In the absence of adequate correlation measurements, we assume that the pressure fluctuations at every point on the wing are perfectly correlated in space and are in phase. Then the non-dimensional fluctuating pressure parameter, $\sqrt{nF(n)}$, and the corresponding normal force parameter, $\sqrt{nN(n)}$, will be identical. Now for a triangular flat plate of semi-span S_T vibrating in the rth bending mode the generalised force of excitation may be written (following Ref.11, p.292, equation (13.32)) as

$$L_r(t) = \int_0^1 W(\eta,t) y_r(\eta) S_T d\eta \quad , \tag{11}$$

where $W(\eta,t)$ = unsteady force/unit span
$S_T d\eta$ = spanwise width of element
and $y_r(\eta)$ = local displacement in the rth mode.

For a triangular wing and under the assumption of perfectly correlated fluctuating pressures, we may replace $W(\eta,t)$ by the appropriate rms level

$$W = \sqrt{nF(n)}(1 - \eta)c_0 q \quad , \tag{12}$$

where c_0 = root chord.

For the first mode we will assume the same mode shape as used to calculate the generalised mass and

the aerodynamic damping, i.e.

$$y_1(n) = n^2 \quad .$$

We find that the rms level L_1 of the generalised force $L_1(t)$ is

$$L_1 = \sqrt{nF(n)}q \, \frac{S_T c_0}{12}$$

so that the buffet excitation parameter in the first mode is

$$\sqrt{nG(n)} = \frac{2L_1}{qS_T c_0} = \frac{\sqrt{nF(n)}}{6} \quad . \tag{13}$$

Fig.15 shows the buffet excitation, $\sqrt{nG(n)}$, in the first mode extracted from the present results at $M = 0.35$ at a frequency parameter $n = f\bar{c}/U = 0.34$; a comparison is made between these measurements and the prediction according to equation (13) based on the fluctuating normal force measurements[13] at $M = 0.09$ at a lower frequency parameter of $n = 0.05$ (and low Reynolds numbers $(Rc_0 = 0.6 \times 10^6)$). The overall agreement between the measurements and the estimates is good (considering the differences in Reynolds number, Mach number, frequency parameter and model geometry), with the slope of the buffet excitation parameter v incidence curve being reasonably well predicted after vortex breakdown.

As observed previously, the measurements at the lowest Reynolds number $(Rc_0 = 1.1 \times 10^6)$ differ considerably from the measurements at the highest Reynolds number $(Rc_0 \geqslant 1.9 \times 10^6)$ in that there is no plateau level of buffeting associated with the establishment of the vortex[9] and that vortex breakdown is deferred to a higher angle of incidence. These two effects bring the measurement at low Reynolds number much closer to the prediction, which is based on fluctuating normal forces measured at even lower Reynolds numbers $(Rc_0 = 0.6 \times 10^6)$.

The good agreement between the measured and predicted forces shown in Fig.15 should be viewed with some caution because of the restrictive assumption made about the degree of correlation of the pressure fluctuations. Before vortex breakdown the pressure fluctuations are restricted primarily to an area under the vortices, and the degree of correlation is relatively small, so that our initial assumption is unlikely to be accurate. However, after vortex breakdown the pressure fluctuations are correlated over relatively large areas of the wing, although there are still significant chordwise and spanwise variations in level (Fig.25, Ref.8). Hence we may expect that our estimate of the excitation force in the first mode, based on the integrated normal force measurement (not upon the measurement of the pressure fluctuations at a single point), should then be reasonably accurate.

It is interesting to note that within the idealised assumption that the pressure fluctuations at different points on the wing are perfectly correlated in space and in phase, the generalised force in the fourth mode can be predicted from equation (11) and the assumed mode shape (i.e. mode 3 of the 60° delta wing) as

$$L_4 = \sqrt{nF(n)}q \, \frac{S_T c_0}{29} \quad ,$$

so that the generalised force coefficient in this mode is

$$\frac{2L_4}{qS_T c_0} = \frac{\sqrt{nF(n)}}{14.5} \quad . \tag{14}$$

However the previous measurements[13] only give the fluctuating normal force coefficient at a frequency parameter $n = 0.05$, whereas equation (14) requires the fluctuating normal force coefficient at $n = 1.72$. Hence we cannot make any fair comparison between measured (Fig.14) and predicted generalised force coefficients for the fourth mode.

4. DISCUSSION

The choice of simple delta wing models for an investigation of the buffeting scaling relationships is justified by the relative simplicity of the results obtained. Thus the buffet excitation parameter in the first mode has been shown to be nearly identical for the steel and magnesium wings (Fig.10), and to be independent of the effects of static aeroelastic distortion or changes of Reynolds number (except at very low Reynolds number).

The present measurements also confirm the important fact, previously inferred from measurements on other models[9], that at vortex breakdown the aerodynamic excitation and the buffeting response become much higher than at low angles of incidence. Hence vortex breakdown, although occurring outside the normal flight envelope of a slender wing transport aircraft, would be accompanied by heavy buffeting (see further discussion of this point in Ref.18). The present measurements, and previous measurements on an aeroelastic model of a typical slender wing aircraft (Ref.9, Appendix A) could be used to estimate the magnitude of the wing-tip deflections caused by vortex breakdown at zero sideslip.

It is possible that vortex breakdown may impose important limitations on other slender wing aircraft. Thus current design studies of a hypersonic research aircraft having a thin 65° swept delta wing[19] assume that this will operate at angles of incidence up to $\alpha = 30^\circ$ (i.e. well above vortex breakdown) for a significant portion of the transonic and subsonic re-entry trajectory, where the kinetic pressures are high. A preliminary assessment of the buffeting problems of this design might be possible with the present measurements of the buffet excitation parameter.

An essential step in the derivation of the buffet excitation parameter is the measurement of the total damping ratio ζ of the mode being considered. For the present tests the total damping ratio, as a percentage of critical damping, was derived by the 'random decrement' process and reasonably consistent values were obtained with the large number of cycles of buffeting available (approximately 3000 and 18000 cycles respectively for the first and fourth modes). However, with a smaller number of cycles the accuracy of the damping measurements would be much reduced, and this could set a limit to the accuracy with which the buffet excitation parameter may be determined in possible future buffeting tests in intermittent transonic facilities. (In Ref.8 it was suggested that 1500 cycles of buffeting would be adequate.)

Extraction of the aerodynamic damping ratio γ, from the total damping ratio, ζ has proved difficult, even for the magnesium wing for which the aerodynamic damping parameter; $\rho/\rho_m U/a^*$, where U = free stream velocity, a^* = critical velocity of sound, attained reasonably high values and for which the wind-off structural damping ratio was small ($g/2 = 0.45\%$ critical). The essential problem is to establish how the structural damping varies during the experiment. Although the structural damping apparently remained constant for the present tests it may not remain constant for tests on sting supported swept wing models of conventional construction or for models incorporating numerous joints and leading-edge and trailing-edge flaps. Hence in future buffeting tests, great care will be required in assessing the relative magnitudes of the structural and aerodynamic components of the total damping. This information is desirable if the measured buffet excitation parameter is to be used to predict the levels of buffeting in flight[4].

For the present tests of slender delta wings it was possible to make accurate theoretical estimates of the aerodynamic damping ratio in the attached flow condition. It is recommended that the attached flow aerodynamic damping be estimated for other models used in buffeting tests. The order of magnitude of the attached flow aerodynamic damping could be estimated for comparison with the total damping measurements, even if the lift-curve slopes are only roughly approximated and the mode shapes are based on those measured for a wide range of planforms by Hanson[16]. The aerodynamic damping ratio for the full scale aircraft might also be estimated by the same method, rather than measured inaccurately on the model (by differing two small, ill-conditioned numbers, ζ and $g/2$) and applying large scaling factors. However the values of aerodynamic damping ratio derived from rigid model tests may indicate the effects of flow separations which develop as the angle of incidence increases. These effects cannot yet be estimated theoretically with confidence, although Lambourne has suggested[20] using measured spanwise load distributions (for uniform incidence) combined with approximate mode shapes.

Fig.2 shows that the differing amounts of static aeroelastic distortion on the steel and magnesium wings did not significantly influence the mean force measurements, at least at M = 0.35 and 0.70. Similarly there is no evidence from Fig.10 that the static aeroelastic distortion influenced the measurements of the buffet excitation parameter. However, for swept wings, static bending and torsion sufficient to influence the mean forces may occur if high static pressures (3 to 5 atmospheres) are used with steel models or if modest static pressures (1 atmosphere) are used with flexible models representing the structure of an aircraft[21]. Hence we must expect that the measurements of the buffet excitation parameter in general will also be influenced by static aeroelastic distortion. It will in general be difficult to determine which changes are caused by aeroelastic distortion and which changes are caused by changes in Reynolds number — unless geometrically similar models of differing stiffness can be tested, or new test techniques are adopted. The proposed high Reynolds number cryogenic wind tunnel is attractive for buffeting tests (see discussion on Fig.13, Ref.22) because, by varying the static temperature, it is possible to operate at constant Mach number with either

(a) varying Reynolds number and constant kinetic pressure (and hence constant aeroelastic distortion) or,

(b) constant Reynolds number and varying kinetic pressure (and hence varying aeroelastic distortion).

There is evidence from recent flight tests[23,24] that significant buffeting occurs in the first torsional mode on swept wing aircraft. The method for measuring the buffet excitation parameter described here for wing bending is equally applicable for the torsional mode. Hence it is advisable to provide a strain gauge bridge to measure wing torsion on the wind-tunnel model, in addition to the bridge provided to measure wing bending.

Despite the difficulties and uncertainties enumerated in this discussion, the measurement of buffeting response on wind-tunnel models of conventional construction provides a relatively simple method to obtain the buffet excitation parameter at reasonably high Reynolds numbers. This method has recently been used to predict the buffet excitation parameter in flight on a typical swept-wing fighter aircraft[25]. An extended version of the present paper is also available[26].

5. CONCLUSIONS

Analysis of measurements of buffeting on two $65°$ delta wings, one made of magnesium and one made of steel, has established two main conclusions.

(1) The non-dimensional buffet excitation parameter, $\sqrt{nG(n)}$, in the first bending mode is almost the same for both wings and increases rapidly at vortex breakdown (Fig.10).

(2) The magnesium wing has a higher damping ratio than the steel wing because of the higher ratio of free stream density to wing density for the same Reynold number. The aerodynamic damping ratios deduced from buffeting measurements on these wings are in good agreement with estimates made using slender wing theory (Fig.8).

Using the techniques described in this paper it should be possible to extract the buffet excitation parameter in the bending and torsional modes on other wind-tunnel models of conventional construction. It will, however, be difficult to establish the contributions of the aerodynamic and structural damping to the total damping measured on the model. If these contributions can be established they can be combined with the buffet excitation parameter to predict the flexible response of the full-scale aircraft.

Table 1

TEST CONDITIONS

Mach number M	Total pressure (kN/m²)	(inHg)	Reynolds number $Rc_0(\times 10^{-6})$	Kinetic pressure q(kN/m²)	Free stream density ρ(kg/m³)	Density ratio of wings Magnesium $\rho/\rho_m(\times 10^3)$	Steel $\rho/\rho_m(\times 10^3)$	Velocity ratio U/a*	Frequency parameter $f\bar{c}/U$(110Hz)
0.35	24.1	7.1	1.0	1.8	0.28	0.15	0.04		
	43.4	12.8	1.9	3.2	0.50	0.28	0.06		
	96.6	28.5	4.3	7.3	1.10	0.61	0.14	0.379	0.34
	193.0	57.0	8.5	14.5	2.21	1.22	0.28		
0.70	24.1	7.1	1.7	6.0	0.23	0.13	0.03		
	48.3	14.2	3.4	12.0	0.46	0.25	0.06	0.732	0.17
	96.6	28.5	6.8	24.0	0.93		0.12		
1.40	28.1	8.3	2.3	12.0	0.15	0.085	0.02	1.300	0.10
	56.2	16.6	4.6	24.0	0.30		0.04		

$$c_0 = 533\text{mm} ; \quad \bar{c} = 355\text{mm} .$$

REFERENCES

1. Huston, W.B., "A study of the correlation between flight and wind tunnel buffeting loads". AGARD Report 121 (ARC 207404) (1957)

2. Davis, D.D., Wornom, D.E., "Buffet tests of an attack airplane model with emphasis on data from wind tunnel tests". NACA RM L57H13 (1958)

3. Hanson, P.W., "Evaluation of an aeroelastic model technique for predicting airplane buffet loads". NASA TND 7066 (1973)

4. Jones, J.G., "Aircraft dynamic response associated with fluctuating flow fields". AGARD Lecture Series 74, Aircraft Stalling and Buffeting, February 1975

5. Cornette, E.S., "Wind tunnel investigation of the effects of wing bodies, fences, flaps and fuselage additions on wing buffet response of a transonic transport model". NASA TND 637 (1961)

6. Erickson, L.E., "Transonic single mode flutter and buffet of a low aspect ratio wing having subsonic airfoil shape". NASA TND 7346 (1974)

7. Rainey, A.G., Byrdsong, T.A., "An examination of methods of buffeting analysis based on experiments with wings of varying stiffness". NASA TND 3 (1959)

8. Mabey, D.G., "Beyond the buffet boundary". J. Roy. Aero. Soc., April 1973

9. Mabey, D.G., "Measurements of buffeting on slender wing models". ARC CP 917 (1966)

10. Cole, Jr., H.A., "On-line failure detection and damping measurement of aerospace structures by random decrement signatures". NASA CR 2205 (1973)

11. Richards, L.J., Mead, D.J., "Noise and acoustic fatigue in aeronautics". John Wiley & Son (1968)

12. Mabey, D.G., "Flow unsteadiness and model vibration in wind tunnels at subsonic and transonic speeds". ARC CP 1155 (1971)

13. Earnshaw, P.B., Lawford, J.A., "Low speed wind tunnel experiments on a series of sharp edged delta wings". R & M 3424 (1964)

14. Mabey, D.G., "Measurements of wing buffeting on a Scimitar model". ARC CP 954 (1967)

15. Squire, L.C., "Some applications of 'not-so-slender' wing theory to wings with curved leading edges". R & M 3278 (1962)

16. Hanson, P.W., Tuovila, W.J., "Experimentally determined natural vibration modes of some cantilever-wing flutter models by using an acceleration method". NACA TN 4010 (1957)

17. Jones, J.G., "The dynamic analysis of buffeting and related phenomena. AGARD CP 102 (1972)

18. Mabey, D.G., "An hypothesis for the prediction of flight penetration of wing buffeting from dynamic tests on wind tunnel models". ARC CP 1171 (1971)

19. Penland, J.A., Creel, T.R., Howard, F.G., "Experimental low speed and calculated high speed aerodynamic characteristics of a hypersonic research airplane concept having a 65° swept delta wing. NASA TND 7633 (1974)

20. Lambourne, N.C., "Some remarks on the aerodynamic damping appropriate to wing buffeting. RAE (unpublished)

21. Moss, G.F., Pierce, D., "Some important aeroelastic distortion effects in experimental aerodynamics".
     Fifth Australasian Conference of Hydraulics and Fluid Mechanics, Christchurch, New Zealand,
     December 1974 or AGARD CP 187, Paper 6b

22. Kilgore, R.A., Adcock, J.B., Ray, E.J., "Flight simulation characteristics of the Langley High
     Reynolds number cryogenic transonic tunnel". AIAA 74-80 (1974)

23. Monaghan, R.G., Friend, E.L., "Effect of flaps on buffet characteristics and wing-rock onset on an
     F-8C airplane at subsonic and transonic speeds". NASA TMX 2878 (1973)

24. Benepe, D.B., Cunningham, A.M., Dunmyer, W.D., "A detailed investigation of flight buffeting response
     at subsonic and transonic speeds". AIAA Paper 74-358 (1974)

25. Butler, G.F., Spavins, G.R., "Preliminary evaluation of a technique for predicting buffet loads in
     flight from wind tunnel measurements on models of conventional construction". AGARD Fluid Dynamics
     Symposium, NASA Ames, September 1976, Paper 24, AGARD CPP 204

26. Mabey, D.G., Butler, G.F., "Measurements of buffeting on two 65° delta wings of different materials".
     RAE TR 76009 (1976)

Mode	Frequency (Hz)	
	Steel	Magnesium
1	121	114
2	330	304
3	523	476
4	595	556
t(mm)	6 30	5 90
c₀(mm)	533	533

30° Section Normal to L.E

Strain gauge bridges

65°

Gap 2 mm

Tunnel sidewall

Wing-root tongue

Attachment to half model balance
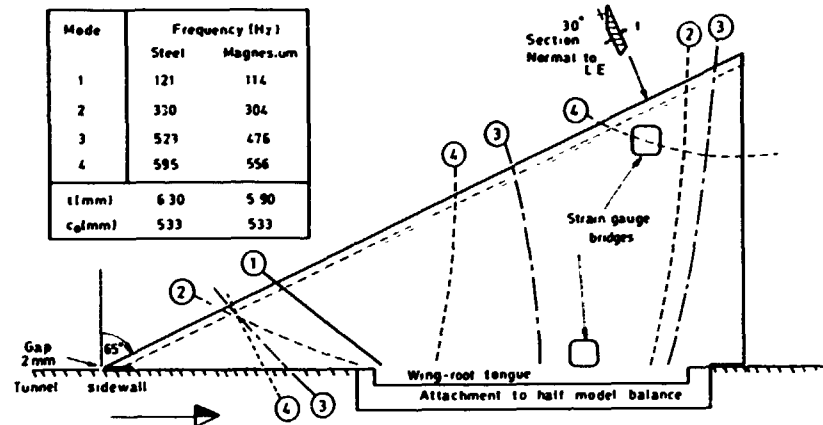
Fig.1 General arrangement and distortion modes of steel and magnesium delta wing models

M	Rc_0 (×10⁻⁶)	Magnesium	Steel
0 35	1 9	□	—
	4 3	□	○
	8 5	△	◇
0 70	1 7	□	—
	3 4	□	○
	6 8	—	◇
1 4	2 3	□	○
	4 6	—	◇

C_N

M = 0 35

Slender wing theory
$$\frac{dC_L}{d\alpha} = \frac{\pi A}{2}$$

M = 0 70

M = 1 40
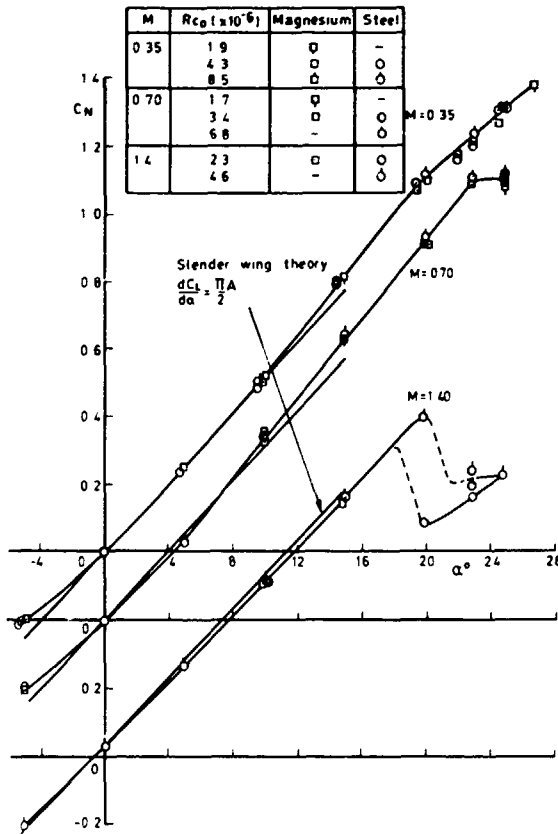
Fig.2 Variation of normal force coefficient with angle of incidence
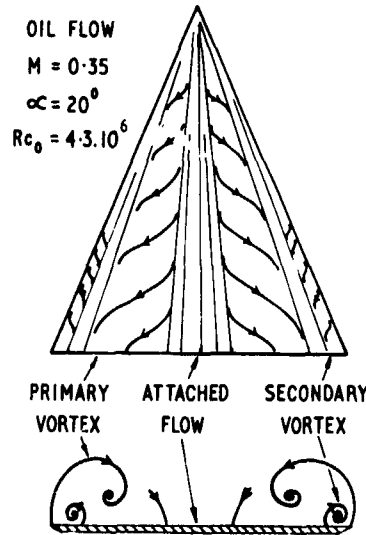
$10^{-5} \times 16$

f = 110 Hz
M = 0 70 $f\bar{c}/U = 0$ 17

ϵ

6 8

3 4

$Rc_0 \times 10^6$

ϵ

M = 0 35 $f\bar{c}/U = 0$ 34

8 5

4 3

Fig.4a Steel wing. Unsteady wing-root strain (rms) v. angle of incidence

OIL FLOW

M = 0·35

∝ = 20°

$Rc_0 = 4·3.10^6$

PRIMARY VORTEX   ATTACHED FLOW   SECONDARY VORTEX

Fig.3 Flow separations

$10^{-5} \times 1$ 4

f = 110 Hz
M=1 4 $f\bar{c}/U = 0$ 10

ϵ

$Rc_0 \times 10^6$

4 6

2 3
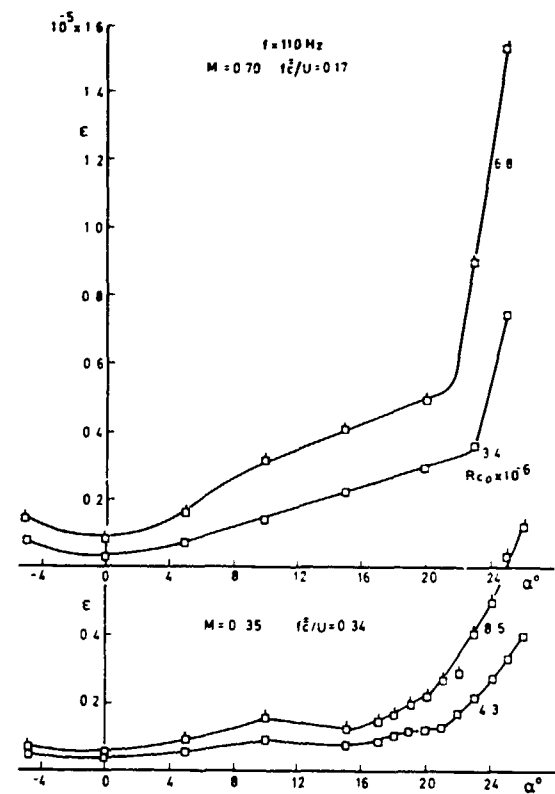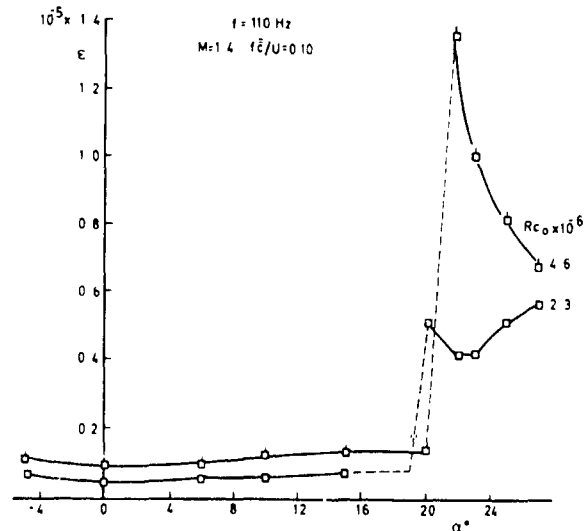
Fig.4b Steel wing. Unsteady wing-root strain (rms) v. angle of incidence
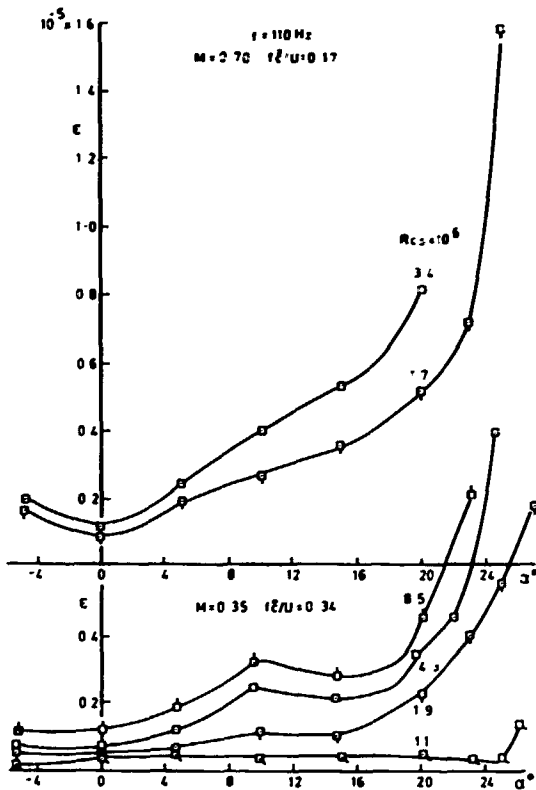
Fig.5a Magnesium wing. Unsteady wing-root
strain (rms) v. angle of incidence
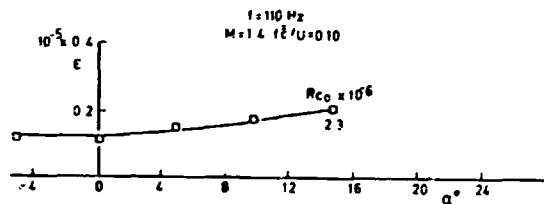
Fig.5b Magnesium wing. Unsteady wing-root
strain (rms) v. angle of incidence
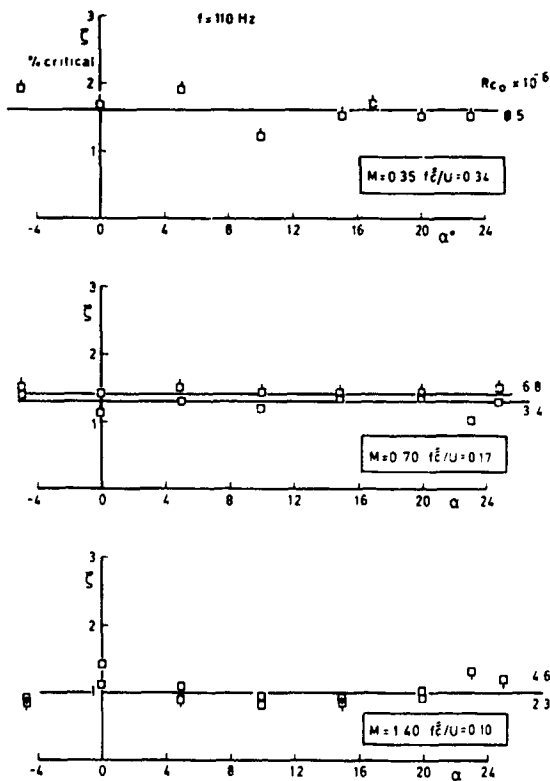
Fig.6 Steel wing-variation of total damping
ratio wing angle of incidence and
Mach number
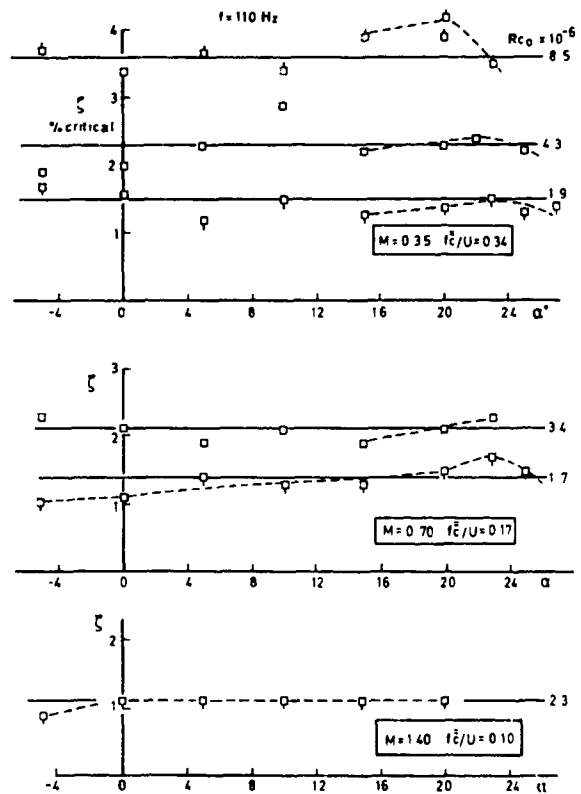
Fig.7 Magnesium wing-variation of total damping
ratio with angle of incidence and Mach
number
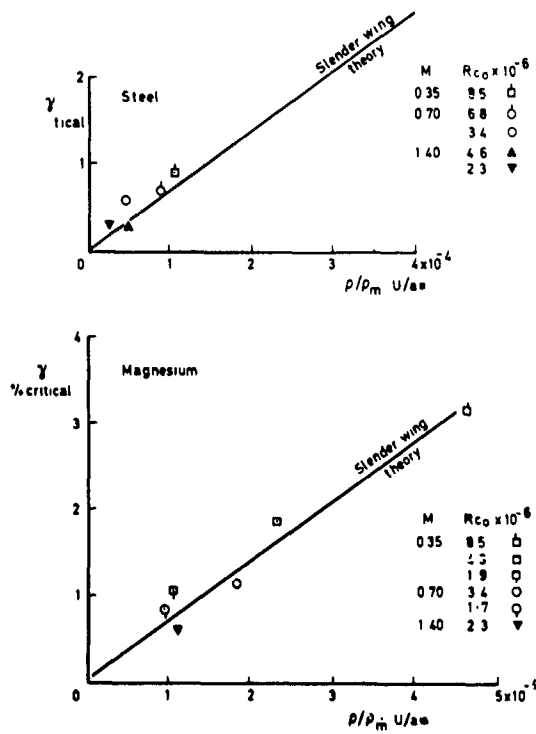
Fig.8 First bending mode: variation of aerodynamic damping ratio with density and velocity ratio
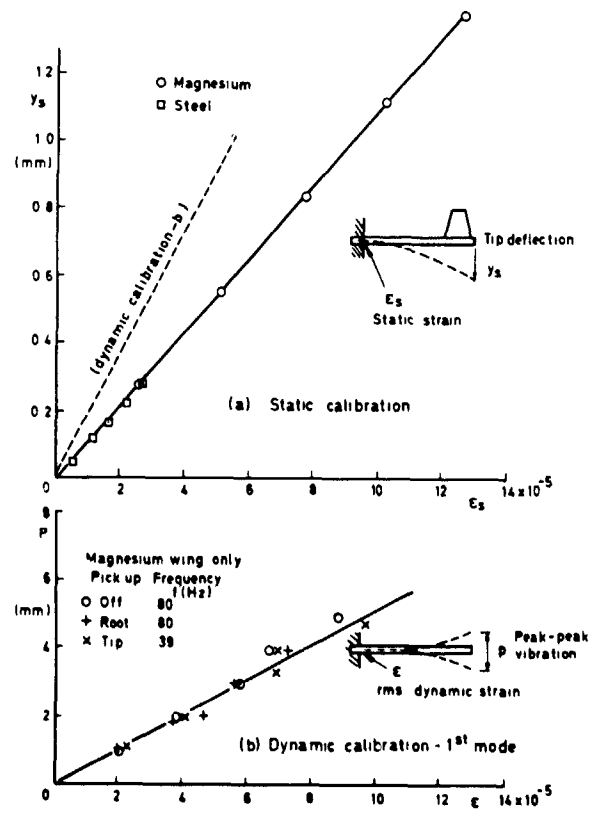
Fig.9a&b Relation between wing tip deflection and wing-root strain

(a) Static calibration

(b) Dynamic calibration - 1st mode
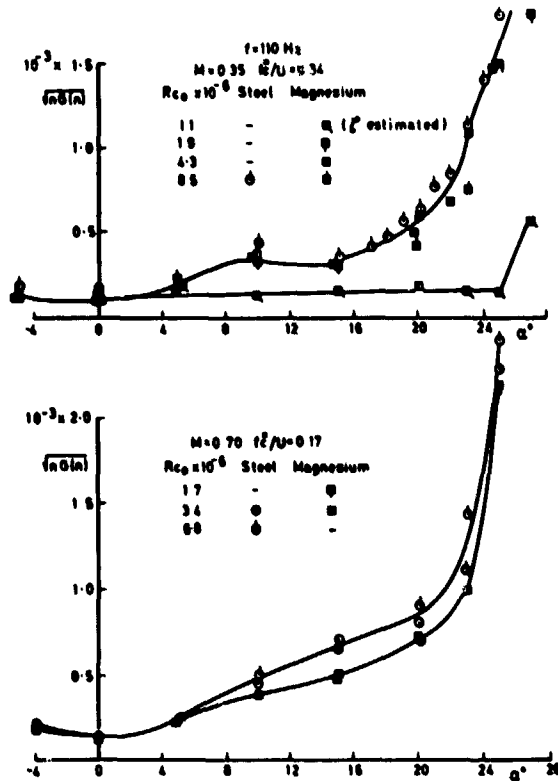
Fig.10a Buffet excitation parameter in first mode for steel and magnesium wings
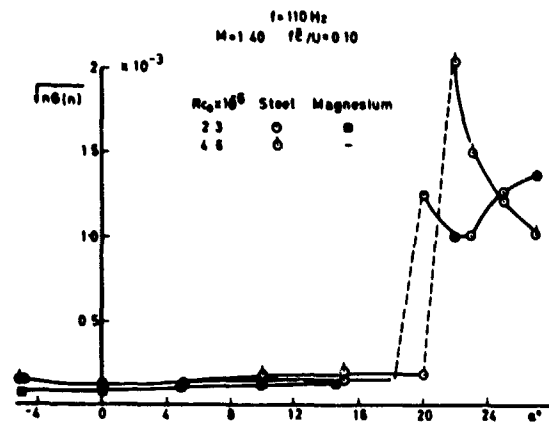
Fig.10b Buffet excitation parameter in first mode for steel and magnesium wings
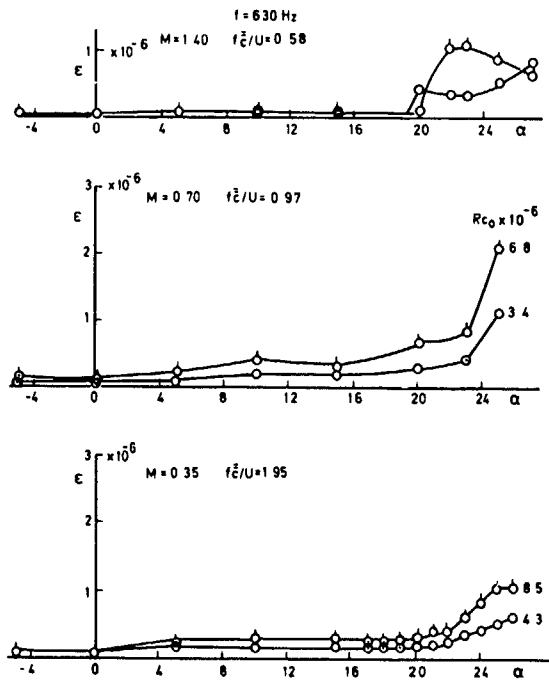
Fig.11 Steel wing-variation of wing-root strain (rms) v. angle of incidence - 4th mode
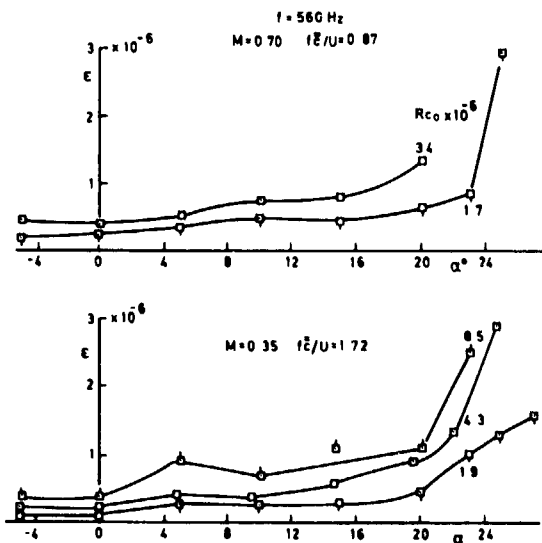
Fig.12 Magnesium wing-variation of wing-root strain v. angle of incidence - 4th mode
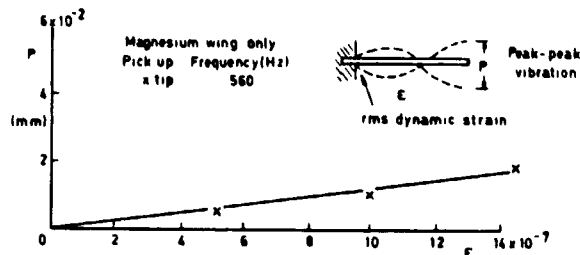
Fig.13 Magnesium wing-dynamic calibration of 4th mode
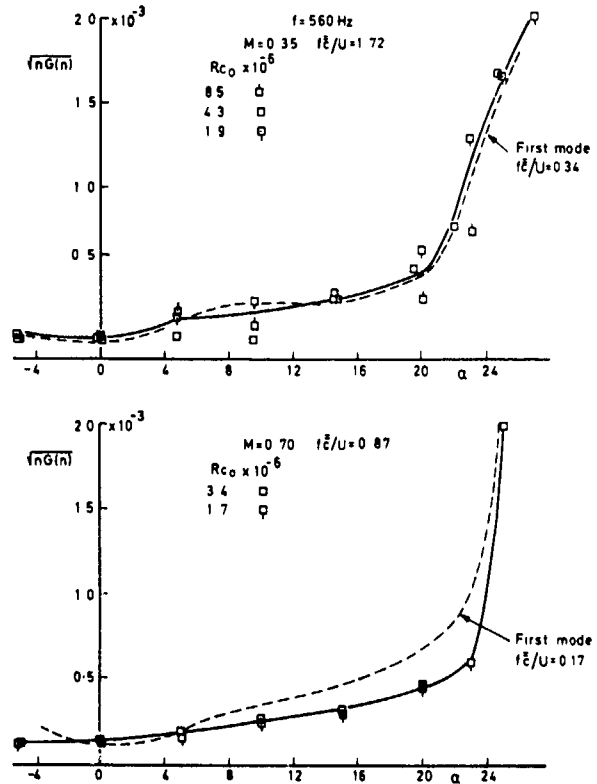
Fig.14 Buffet excitation parameter in 4th mode for magnesium wing
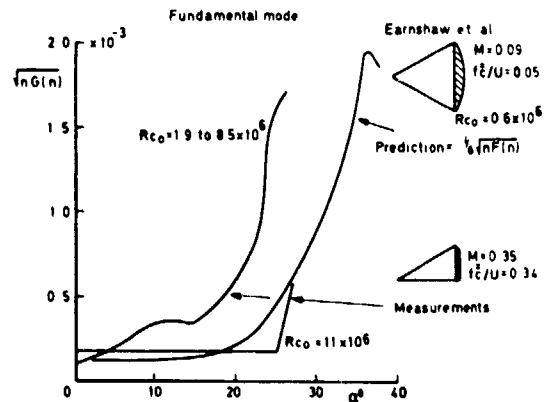
Fig.15 Comparison of measured and predicted buffet excitation parameters

DYNAMIC LOADING OF AIRFRAME COMPONENTS

by:

C.G. LODGE   and   M. RAMSEY
Chief Dynamics Engineer   Dynamics Engineer

British Aircraft Corporation Limited,
Military Aircraft Division,
Warton Aerodrome,
Preston,
Lancashire,
England.
PR4 1AX

SUMMARY

An important aspect of the design of modern combat aircraft is the structural fatigue
life. In particular it is becoming increasingly important to have accurate knowledge
of the unsteady loads due to separated flow conditions in manoeuvring flight.

This paper describes the prediction of dynamic loading on a modern variable sweep wing
combat aircraft, making use of wind tunnel model tests and results from flight testing
of previous aircraft. In addition, the predictions are compared with available
prototype flight measurements.

A.   INTRODUCTION

Fatigue has been a major design consideration on military combat aircraft for many
years, but in the past the critical aerodynamic loading has been associated
primarily with steady flow conditions, for example, during repeated manoeuvres, and
to a lesser extent with unsteady but attached flow conditions, for example, during
flight through turbulence. Unsteady aerodynamic loadings associated with separated
flows have been negligible in the context of structural fatigue margins available
in contemporary strength designs.

More recently, increased manoeuvring capability, higher wing loading and higher
speeds have combined with more refined structural designs which have lower inherent
fatigue margins to highlight a new fatigue problem (Figure 1). The critical
aerodynamic loading for fatigue design of some secondary structures such as slats,
and some features of primary structures (for example, attachments) can be associated
with separated flow conditions. This paper describes some BAC(MAD) experience in
quantifying aerodynamic loadings, where separated flows are inevitable, for aircraft
design purposes.

B.   TYPICAL APPLICATION

First, a systematic review is made of the aircraft layout in order to identify those
sources, which, despite attempts to clean up the installation, will inevitably
produce significant separated flow due to some overriding design consideration.
Second, the region of influence and magnitude of unsteady loadings associated with
these sources are estimated.

Third, fatigue margins are calculated for those components influenced by the
separated flow which previous experience suggests will be fatigue prone. Fourth,
design modifications are introduced and/or prototype flight data requested for
production design purposes on potentially critical items.

Some potential problem areas are summarised in Figure 2, for a modern combat
aircraft. Observe that the associated flight conditions are predominantly
subsonic; the airbrake is exceptional in this respect.

Since the prime concern is for the fatigue life of components there is no immediate
safety problem, the accuracy of predictions required is not high and reliance upon
available data is considered acceptable.

Three main data sources have been used to derive unsteady loading data. These are:-

i)   Flight measurements from earlier BAC(MAD) aircraft.

ii)   Wind tunnel measurements from models of the new design.

iii)   Published literature.

Existing wind tunnel models, particularly of the component loads type, have proved
to be adequate for main surfaces, but problems of representation at model scale have
cast doubt on their value for secondary surfaces and flight data has been used in

these cases. Throughout, the accuracy of predicted magnitudes of unsteady loads is not thought to be better than a factor of about 2, bearing in mind the dependence upon structural damping.

C. EFFECTS OF WING BUFFET

C.1 On Slats and Spoilers

A substantial amount of flight data is available from an earlier BAC(MAD) aircraft on the response of slat and spoiler attachments due to unsteady aerodynamic loading during wing buffet. The dominant feature of these responses is the progressive increase in the intensity and extent of wing flow separation as incidence increases at all subsonic Mach numbers.

The available data are in the form of time-histories and power spectra of strain-gauge responses (Figure 3). By suitable scaling, these can be translated to a new aircraft, and in our application this adjustment is relatively straightforward. Since the wing flow breakdown characteristics for the earlier aircraft and the new prototype were similar, including buffet onset incidence, it is possible to scale the aerodynamic excitations, at the same wing incidence, by the ratio of slat or spoiler area for the two aircraft. The dominant fatigue loading occurs virtually in single degrees of freedom, featuring substantial distortion of the slat attachments and of the spoiler operating mechanism, (Figure 4). Since the natural frequencies and shapes of the associated vibration modes were known from ground resonance tests to be broadly similar, a further scaling on response loads to account for slat and for spoiler inertia ratios between the two aircraft surfaces completes the transformation. Resultant load predictions are presented in Figures 5 and 6.

Figure 5 shows contours of constant percentage unsteady load in the slat attachments for the cases of slat retracted and manoeuvre slat setting. The substantial reduction in unsteady loading when the slat is extended is a manifestation of slat effectiveness.

Figure 6(a) gives contours of constant percentage unsteady load in the spoiler attachments for the fully open spoiler. The variation of unsteady load with spoiler angle is linear for incidences up to that at which the maximum load occurs for each Mach number (e.g. 11° at M = 0.9) as the region of separation produced by the spoiler increases in size and intensity.

Above this incidence the unsteady load is independent of spoiler angle (Figure 6(b)) as the separation produced by the wing spreads over the entire wing and encompasses the spoiler.

C.2 On Wing

Although no wing fatigue problems have been experienced, the discovery of an unexpectedly high unsteady response condition on an earlier BAC(MAD) aircraft during high incidence load measurements led to a specific review. This loading condition featured substantial response in the wing torsion mode under moderate buffet conditions in addition to the expected wing bending mode response, and Fig. 7 shows some typical strain-gauge responses. No fatigue problem was associated with this phenomenon, but its mechanism is not well understood. It might be associated with a single degree of freedom flutter condition, although based on Reference 1, the frequency parameter $\frac{\omega C}{V}$ is high enough to preclude this and there was no tendency for divergent instability in the flight data. The mechanism seems to be associated with a transition between alternative but equally possible steady flow states (Fig. 8) so that any "instability" would be expected to have a limited amplitude.

Flight data from tests on the new prototype confirm the extence of similar torsion mode responses at moderate incidences (Fig. 9). The accelerometer responses show that the lower wing sweep angles are most critical in this respect, and that torsion and bending mode responses increase with incidence in about the same proportions for the lower sweep angles (Figure 10). Specific instrumentation has been introduced on prototypes to provide data for fatigue assessments, and to monitor modal stability. There is no indication of any instability to date, but careful control of Mach number, equivalent airspeed and incidence effects is being maintained as the flight envelope is expanded.

C.3 On Taileron

A more compact layout and variable wing sweep prompted an assessment of wing-buffet-induced taileron response for the new design. Since no appropriate flight measurements were available from earlier aircraft at the extremes of wing sweep required, recourse had to be made to wind tunnel models of the new design.

It is standard practice to use unsteady wing root bending moments from nominally rigid component load wind tunnel models to provide information on buffet onset and on wing attachments loads during buffet. The relatively successful

application of this data to full scale has stemmed from the fact that wing
fundamental mode shapes, and excitation, have been broadly similar on nominally
rigid models and aircraft. The successful application of similar techniques to
buffet load predictions for taileron attachments is probably much less likely,
since even fundamental modes of vibration for a taileron, being relatively high
in frequency, usually include substantial contributions from fuselage and wing
and fin distortions, and these are not all likely to be reproduced on nominally
rigid models. In addition, pre-buffet excitation sources may be different on
model and aircraft (e.g. importance of engine noise on aircraft). Nevertheless
it is tempting to assess the available model data, if only to indicate how
unsteady loads might vary with manoeuvring flight condition and configuration,
as a basis for prototype flight test planning.

A typical variation of model taileron attachment load coefficient with incidence
is shown in Figure 11, and this includes only the root-mean-square contribution
from the fundamental taileron mode (identified from model resonance tests). The
taileron response variation with incidence is characterised by a fairly constant,
but non-zero level up to buffet onset. At the lower subsonic Mach numbers and
lower wing sweep angles, this buffet onset is dictated by the wing, and the
taileron is responding to wing excitation. At the higher subsonic Mach numbers
and higher wing sweep angles, although the buffet onset is dictated by the wing,
the taileron buffeting response is due to a combination of taileron and (very
mild) wing buffet. These features are entirely consistent with the taileron
design concept of operation at relatively low, essentially buffet free lift
coefficient.

Associated taileron attachment unsteady loads variations with manoeuvring flight
condition and configuration are presented in Figure 12. Observe the
insensitivity to wing sweep below about M = 0.6 - 0.7 and the increasing
importance of taileron buffet as wing sweep angle increases, particularly above
M = 0.7 - 0.8.

Figure 13 shows the effect on taileron loads of selecting the manoeuvring wing
slat setting. The dramatic reduction quantifies and mirrors the improvement
in wing buffet characteristics (cf Figure 12(b)).

Available flight measurements from the new prototype are compared in
Figures 12(a) and (c). As yet there is not enough data available under
buffeting conditions to judge the accuracy of predictions.

In order to predict actual unsteady load magnitudes from this model data, it
would be necessary to infer wing and taileron excitation distributions from
measurements of wing and taileron response, and scale these via knowledge of
the model and aircraft transfer function properties. This approach is
practicable if the buffet excitation can be represented by a combination of a
few pressure distribution shapes. This offers a more economic, but probably
less accurate alternative to either direct measurement of pressure distributions
or dynamically-scaled wind tunnel models.

Estimates which have been made can have significant fatigue implications, and
appropriate instrumentation is being monitored on the new prototype.

D. EFFECTS OF STORE BUFFET

D.1 On Store Attachments

Flight data is available from an earlier BAC(MAD) aircraft on unsteady
attachment responses due to store buffet for underfuselage and underwing
installations. The important feature of these responses is the relatively
small Mach number range (typically 0. `< M < 0.95, Fig. 14) within which
significant unsteady loading occurs in nominally straight and level flight.
This loading is associated with shock-induced flow separation. Associated
loads can be alleviated by the introduction of vortex generators mounted
around the store afterbody just upstream of the separated region, but will be
amplified by backlash in pylon/store attachments.

By suitable scaling, these loading data could be translated to a new aircraft,
given similar fuselage/wing-pylon-store geometries. The attachment fatigue
loading is dominated by the fundamental bending modes of the flexible store
and in this respect fuel tanks are especially critical. Since the natural
frequencies and shapes of these modes can be determined from resonance tests
the transformation to account for structural dynamics would be straightforward.

D.2 On Taileron

Underwing store configurations introduce a potential taileron fatigue problem
associated with store wake excitation. Some typical effects are shown in
Figure 15, from flight tests on an earlier aircraft. From this, the dominant
store increment occurs at frequencies which are appropriate to local surface
modal deformations, at least for the airspeeds where magnitudes of incremental
loads are significant.

Component load wind tunnel model tests, on the new design, confirm this and

Figure 16 shows the virtually identical contributions from the taileron fundamental mode to the root-mean-square attachment load, as incidence increases, for a variety of store installations on inboard and/or outboard pylons.

E. EFFECTS OF EXCRESCENCES AND CAVITIES

Excrescences and cavities associated with avionic equipment, for example, can provide a significant source of unsteady loading for internal structure and downstream panels, even when careful consideration is devoted to achieving an aerodynamically clean installation. Two important flow characteristics which can exist in isolation or in combination are a random component associated with any separated flow regions and a periodic component associated with vortex shedding or cavity resonance.

The frequency content of the former is, apparently, sensibly independent of how the separation occurs (from Reference 2) and a ubiquitous spectrum can be defined which can reasonably be applied in most cases for design purposes (Fig. 17). It remains to judge the appropriate scale of the separation region and to estimate appropriate amplitudes of unsteady pressure for each application. Some typical examples are illustrated in Figure 17. These essentially random excitation sources are dominant for shallow excrescences and cavities, and for most applications the associated energy content is concentrated in the local panel frequency range.

Possible exceptions to this general rule are airbrakes and deep bomb bays, where periodic flow effects can dominate and where the important frequencies can be in the range of lifting surface fundamental modes.

E.1 Airbrake

Contours of constant total R.M.S. pressure coefficient in the wake of a 50° airbrake in a subsonic free stream are summarised in Figure 18 (Ref. 3). From this, the airbrake cavity is especially vulnerable. Also shown are the predicted variations with airspeed of the frequency and unsteady pressure levels associated with the vortex shedding contribution for the new design. These results indicate that problems are extremely unlikely so far as the lifting surfaces are concerned, but that the airbrake itself will be influenced.

F. COMMENT

This paper has described the prediction of some dynamic loadings associated with inevitable separated flows on a modern combat aircraft. It is considered that the accuracy of these predictions is not high but that it is probably adequate for all components, with the possible exception of the tailerons. Design modifications which have been introduced to absorb the dynamic loadings described, even with substantial factors, are relatively trivial, except for the taileron. In this case modifications would be relatively extensive but the available predictions are least accurate. No modifications will therefore be introduced unless flight measurements show that they are necessary.

A genuine need is clearly emerging for much more accurate methods of predicting taileron fatigue loadings due to separated flows on compact military combat aircraft, and there is obvious appeal in combining flutter and buffet testing on a single wind tunnel model - given suitable tunnel facilities - to achieve this. A more economic procedure might be to study pressure distributions under buffeting conditions as a means of better utilising data from nominally rigid component load wind tunnel models.

In addition, the torsional response of wings at incidence needs to be better understood. Once more a combined flutter and buffet modelling approach seems more appropriate, although a study of pressure distributions during buffet could offer more insight.

G. REFERENCES

1. N.C. Lambourne   -   "Flutter in one degree of freedom". AGARD Manual on Aeroelasticity Vol. V, Chapter 5   October, 1968

2. D.G. Mabey   -   "Pressure fluctuations caused by separated bubble flows at subsonic speeds". August, 1971   RAE TR 71160

3. T.B. Owen   -   "Low speed static and fluctuating pressure distributions on a cylindrical body with a square flat plate airbrake." January, 1956   RAE T.N. Aero 2396

FIG. 1

FATIGUE DESIGN STATUS

FIG. 2

UNSTEADY AERODYNAMIC LOADING ASSOCIATED WITH SEPARATED FLOW
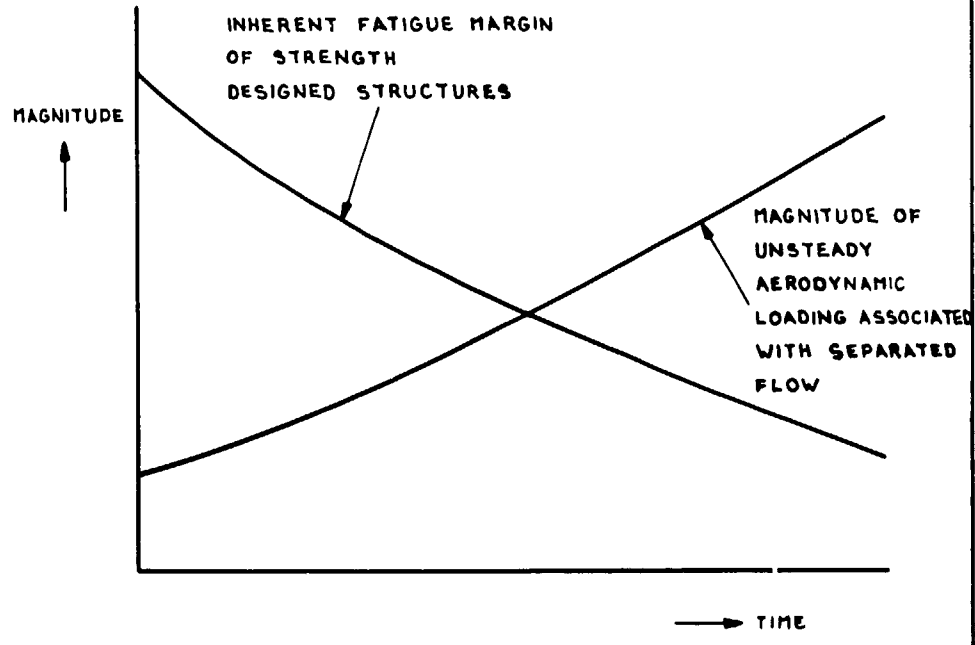
SOURCE OF EXCITATION	EFFECTED ITEM	DATA SOURCE		
		EARLIER A/C FLIGHT DATA	WIND TUNNEL MODELS	LITERATURE
WING BUFFET	SLATS SPOILERS WING	✓		
	TAILERON		✓	
STORE BUFFET	ATTACHMENTS	✓		
	TAILERON		✓	
AIRBRAKE BUFFET	EMPENNAGE			✓
EXCRESCENCES	LOCAL DOWNSTREAM STRUCTURE			✓

FIG. 3

FLIGHT VIBRATION DATA
TYPICAL ATTACHMENT LOAD SPECTRA

20Hz   40Hz   60Hz   80Hz   100 Hz

SPOILER

0Hz   40Hz   80Hz   120Hz
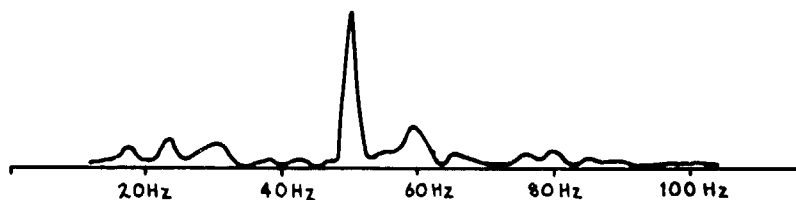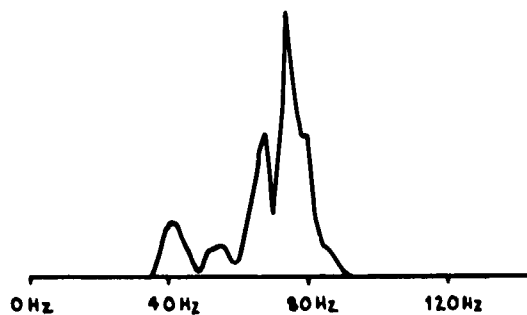
SLAT

FIG 4

FLIGHT VIBRATION DATA
FUNDAMENTAL MODE SHAPES
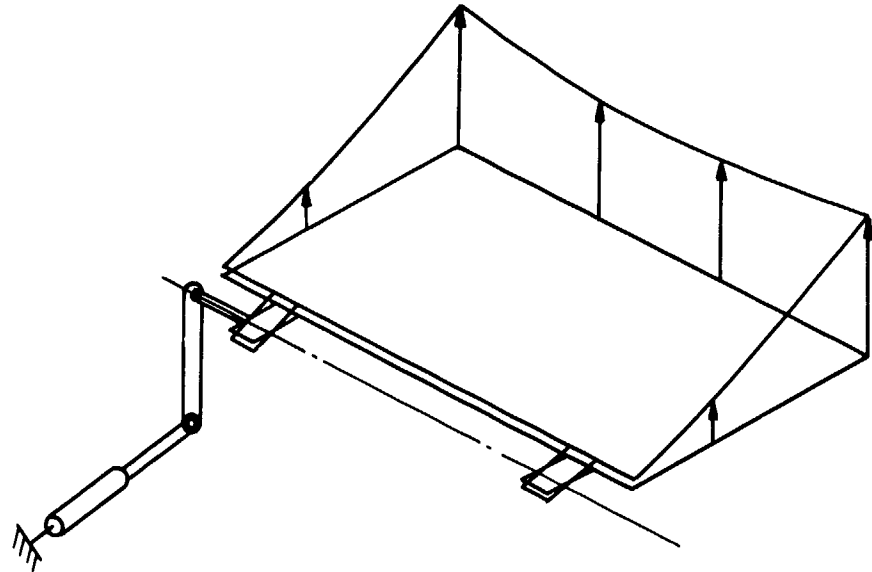
SPOILER
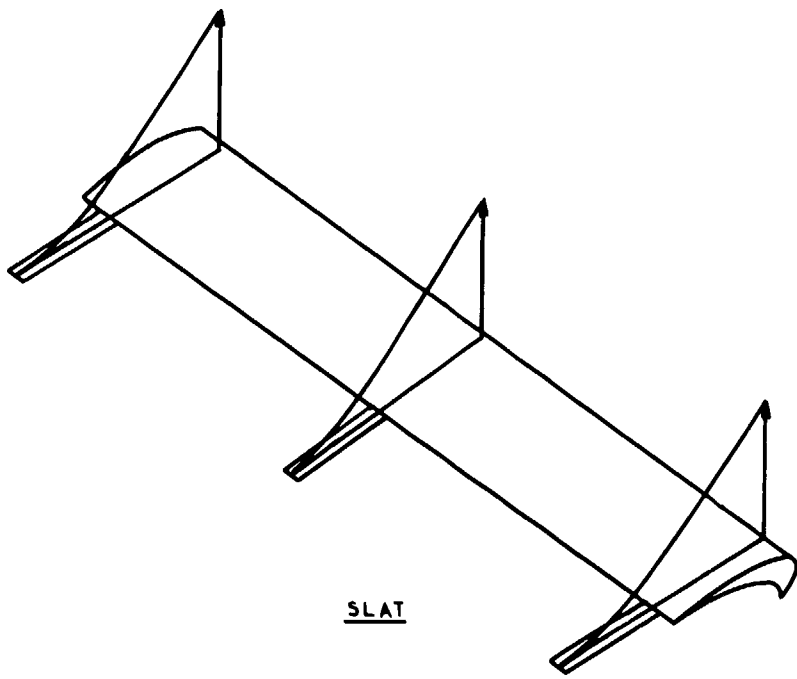
SLAT

FIG 5a

SLAT UNSTEADY LOAD PREDICTION
SLAT RETRACTED
f = 80 Hz
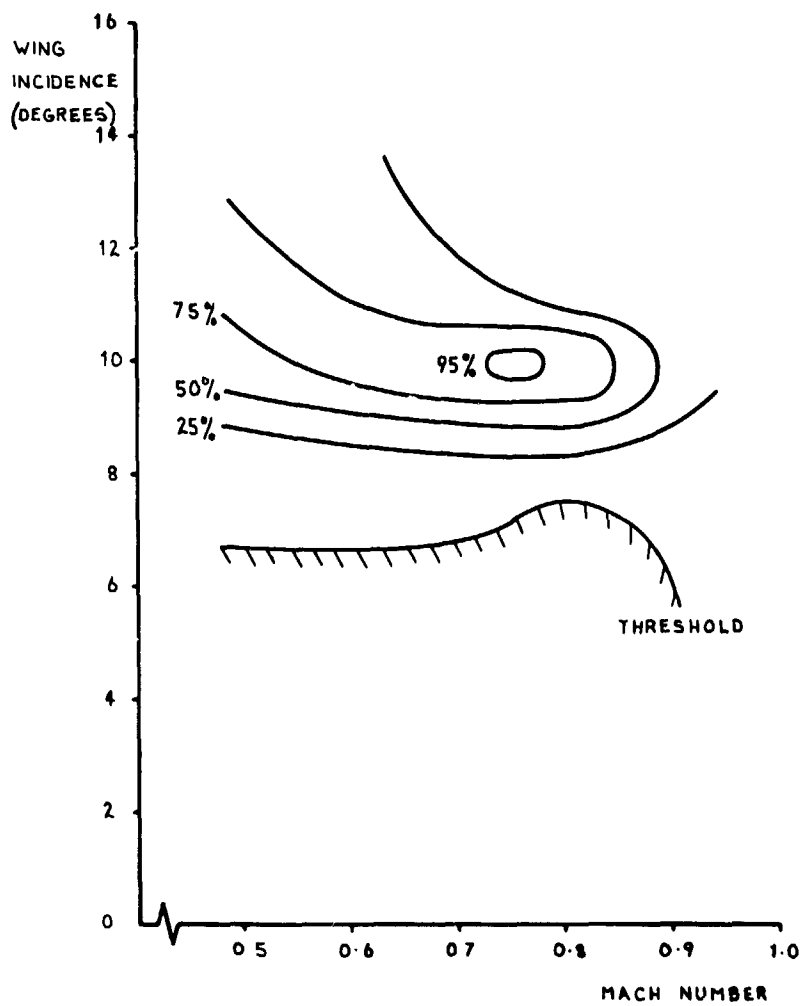
FIG 5b

SLAT UNSTEADY LOAD PREDICTION

MANOEUVRE SLAT

f = 80 Hz
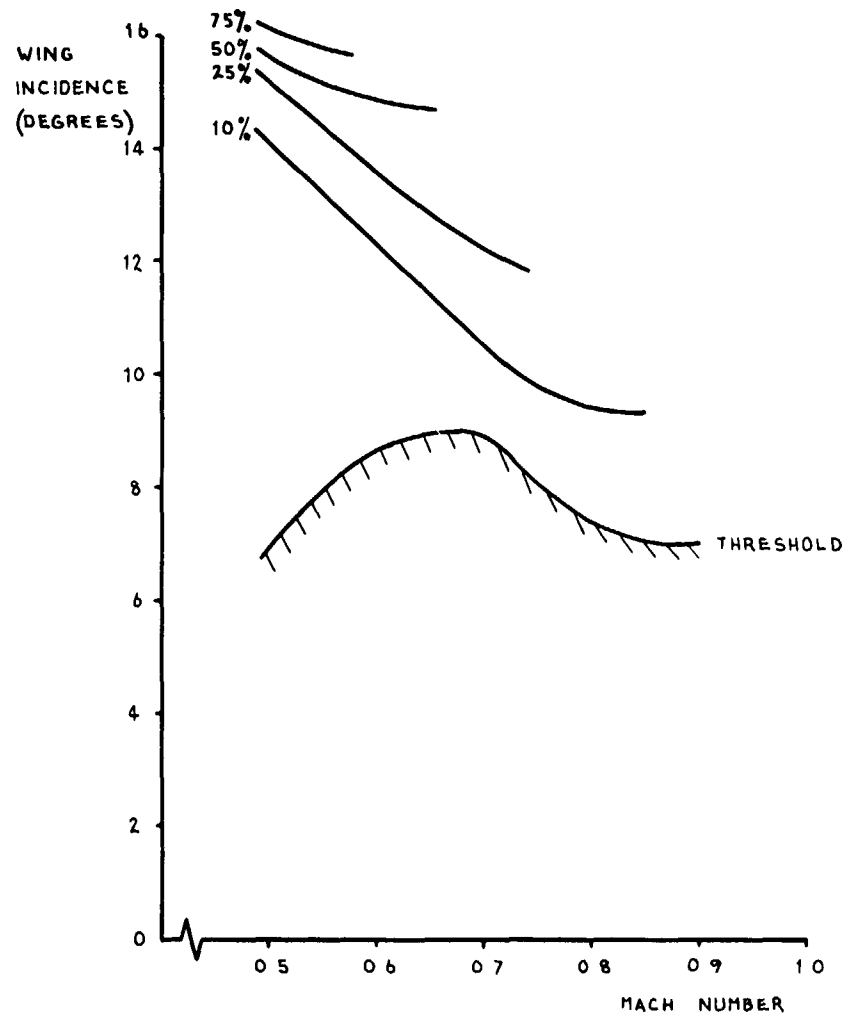
FIG. 6a

SPOILER UNSTEADY LOAD PREDICTION
P=55 Hz
MAXIMUM SPOILER ANGLE
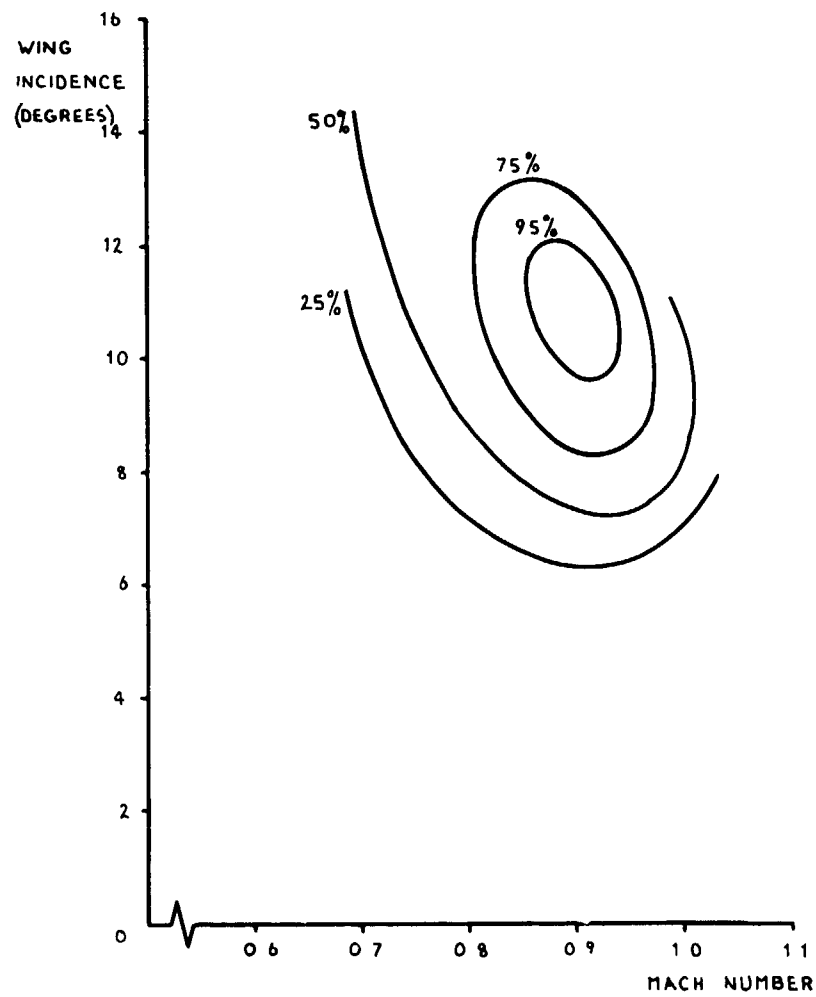
FIG. 6b

PREDICTED EFFECT OF SPOILER ANGLE
M=0·9

SPOILER
UNSTEADY
LOAD

11° INCIDENCE

100%

13° INCIDENCE

10° INCIDENCE

8° INCIDENCE

MAX

SPOILER ANGLE

FIG. 7

WING BUFFET — AIRCRAFT 1

M = 0·9

BENDING GAUGE

33 Hz WING TORSION

8 Hz WING BENDING

C_L INCREASING

TORQUE GAUGE

33 Hz WING TORSION

1 SEC
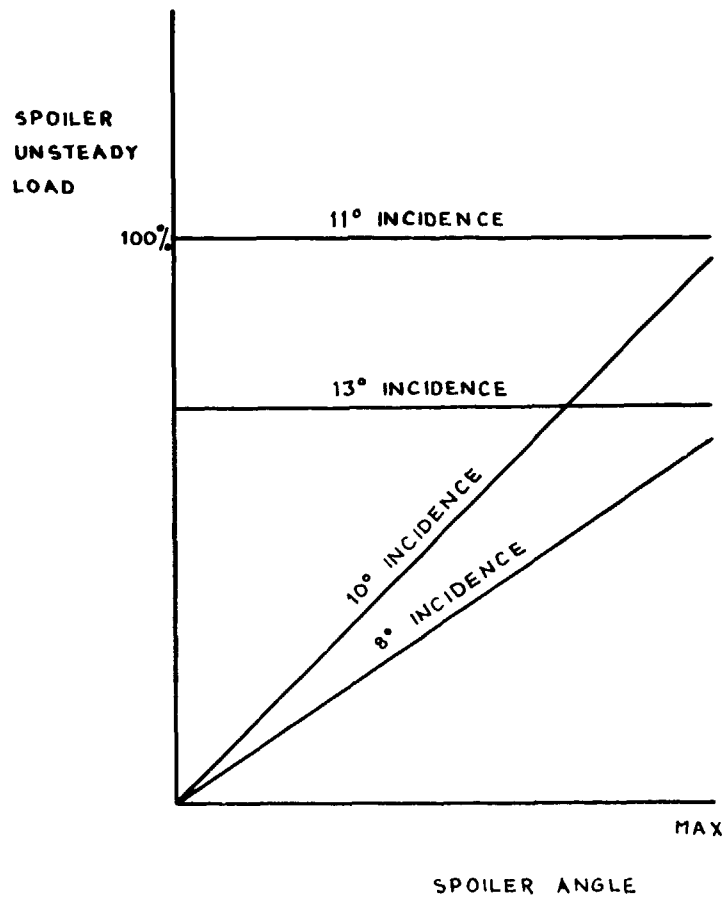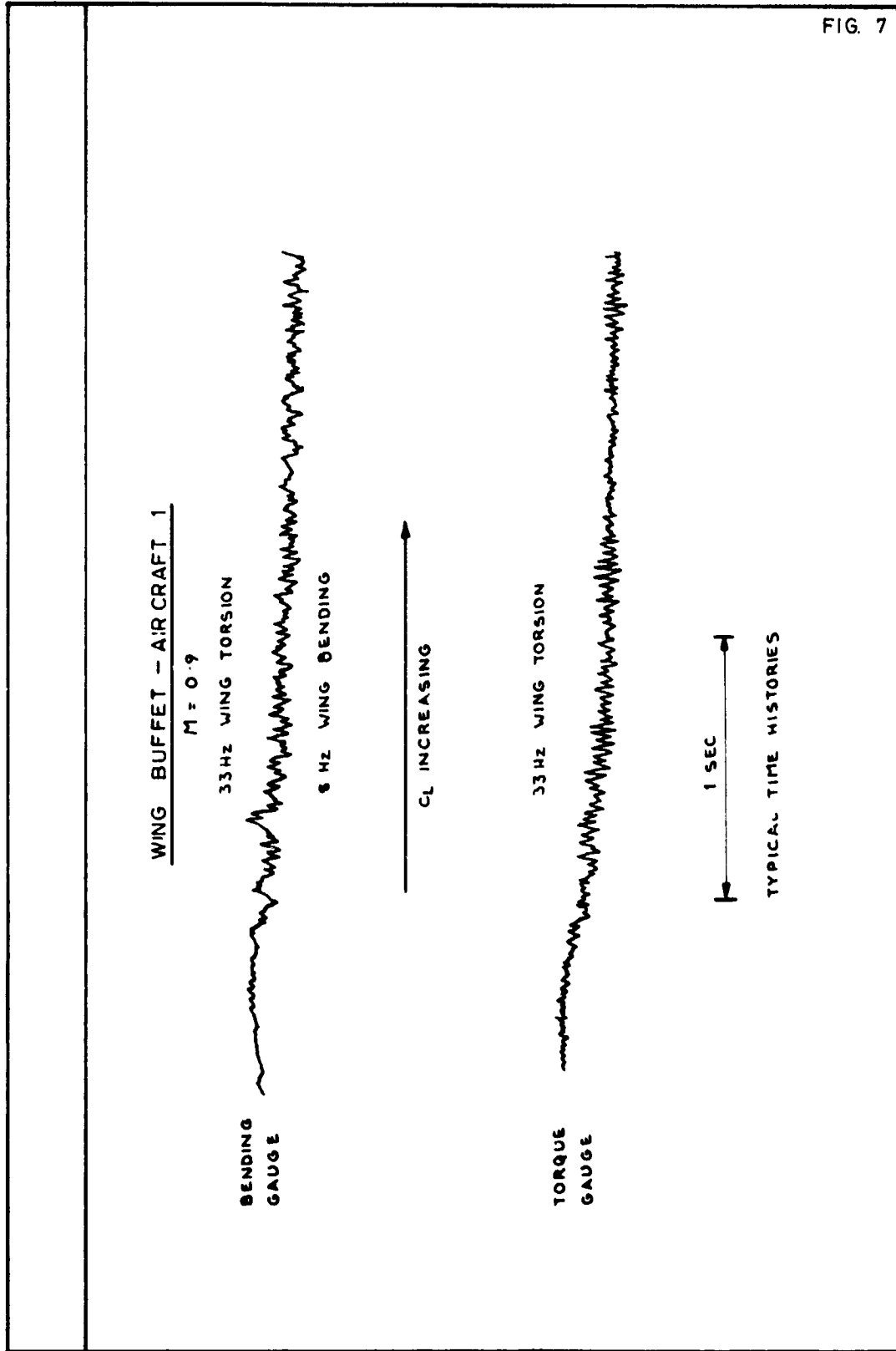
TYPICAL TIME HISTORIES

FIG 8

WING STEADY TORQUE

CLEAN A/C
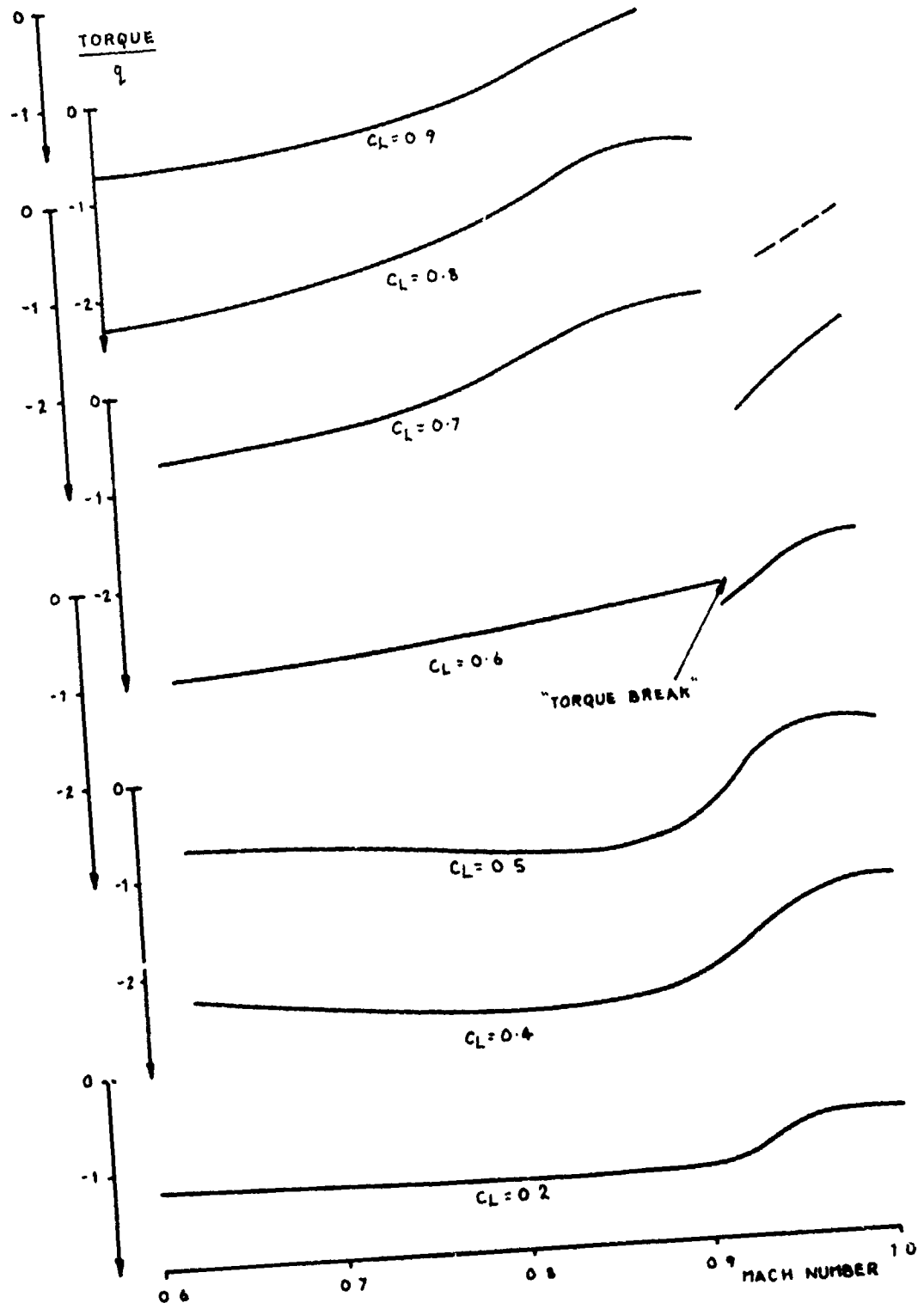
FIG 9

MEASURED WING BUFFET ON A NEW PROTOTYPE

25° SWEEP   M=0.76

WING TIP g

1 SEC

28Hz WING TORSION

68° SWEEP   M=0.75

WING TIP g

1 SEC

28 Hz WING TORSION
6 Hz WING BENDING

TYPICAL TIME HISTORIES

FIG 10

MEASURED WING BUFFET ON A NEW PROTOTYPE
ACCELEROMETER RESPONSE
25° SWEEP M = 0·76

WING
BENDING

WING
TORSION

1
UNIT

0 Hz   50 Hz

INCREASING

INCIDENCE

40
UNITS

0 Hz   50 Hz
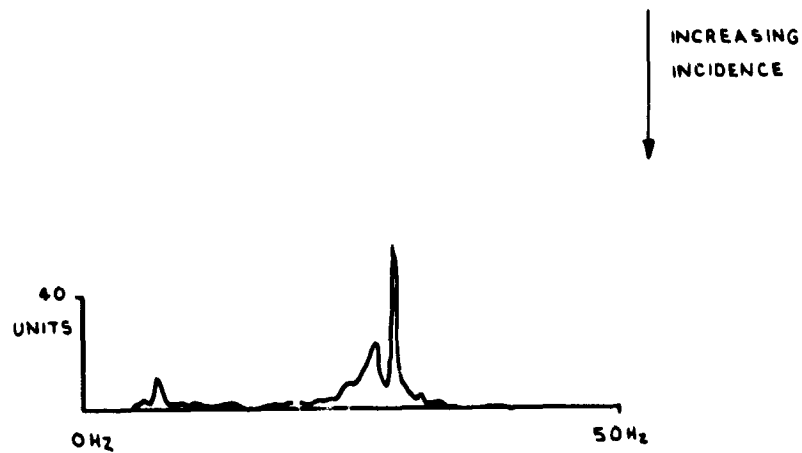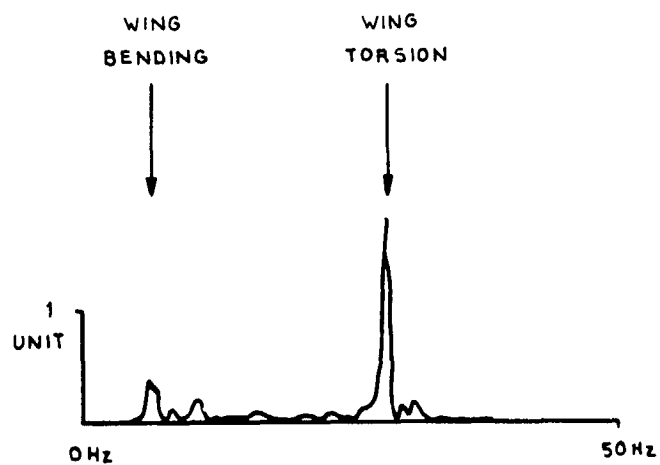
FIG 11

TYPICAL VARIATION OF TAIL ROOT
BENDING MOMENT COEFFICIENT

$$C_{TRB} = \frac{\text{TAILERON ATTACHMENT LOAD}}{\frac{1}{2} P v^2}$$
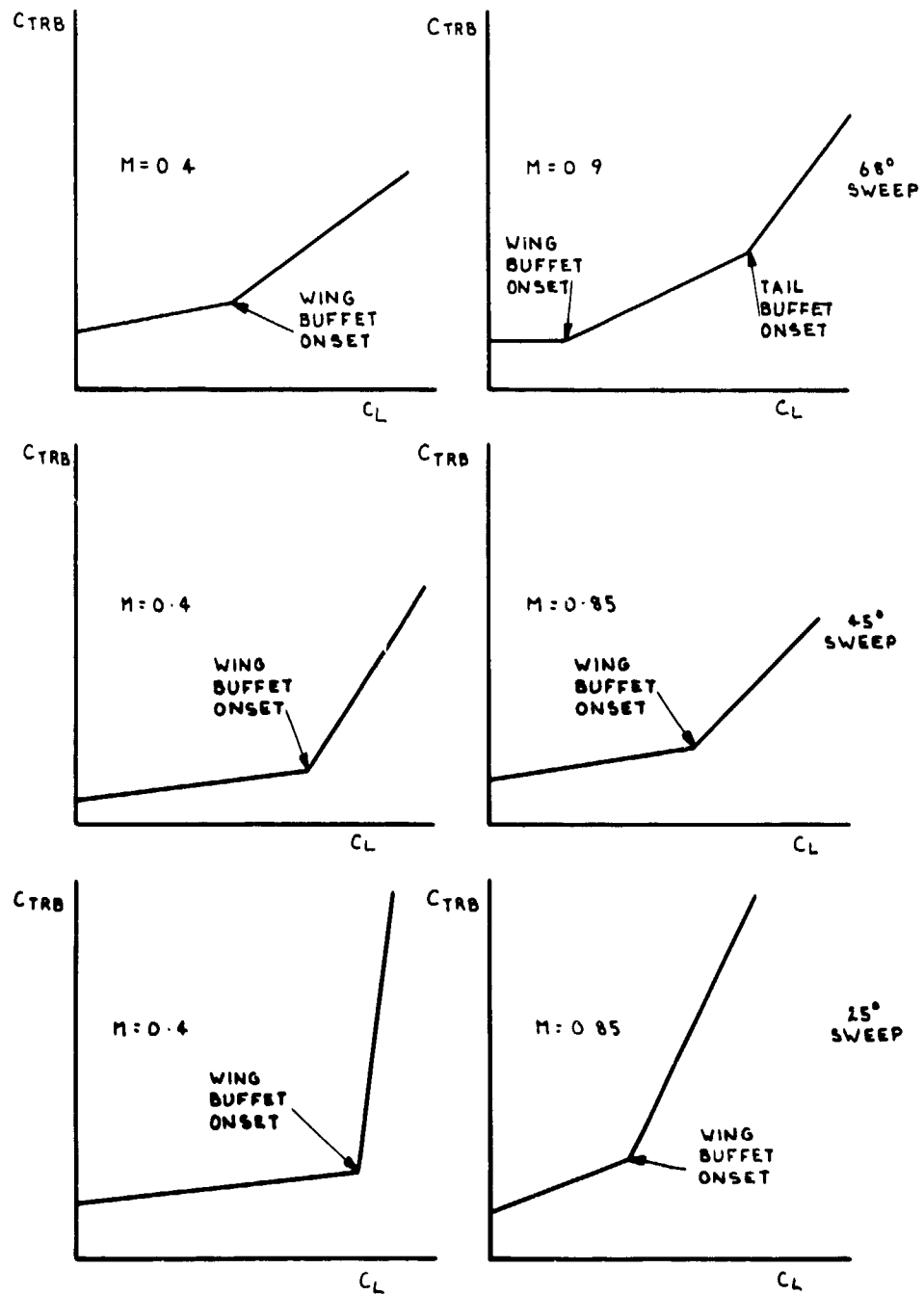
FIG 12a

PREDICTED TAILERON UNSTEADY ATTACHMENT LOADS

25° SWEEP   CLEAN

X FLIGHT MEASUREMENTS
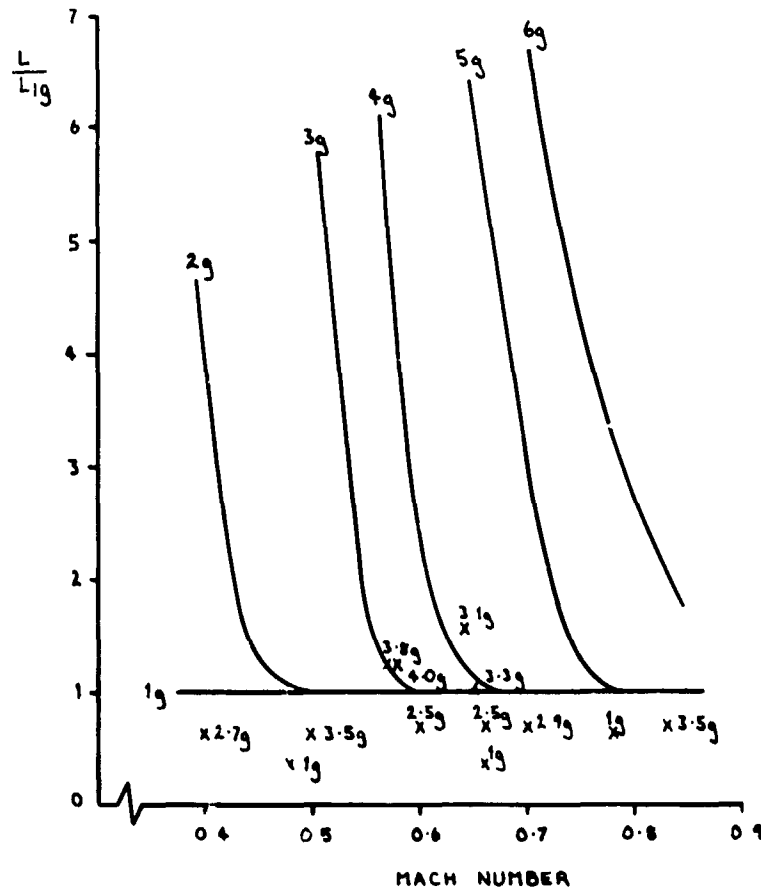
PREDICTED TAILERON UNSTEADY ATTACHMENT LOADS

45° SWEEP   CLEAN

X FLIGHT MEASUREMENTS
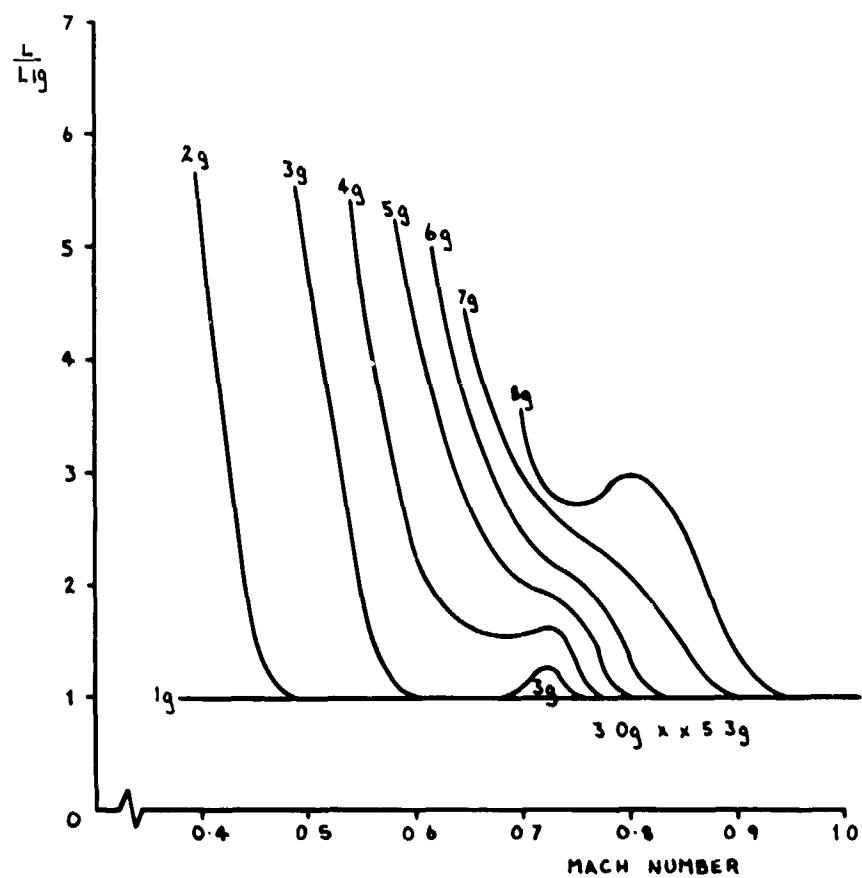
FIG. 12c

PREDICTED TAILERON UNSTEADY ATTACHMENT LOADS

68° SWEEP   CLEAN

X FLIGHT MEASUREMENTS
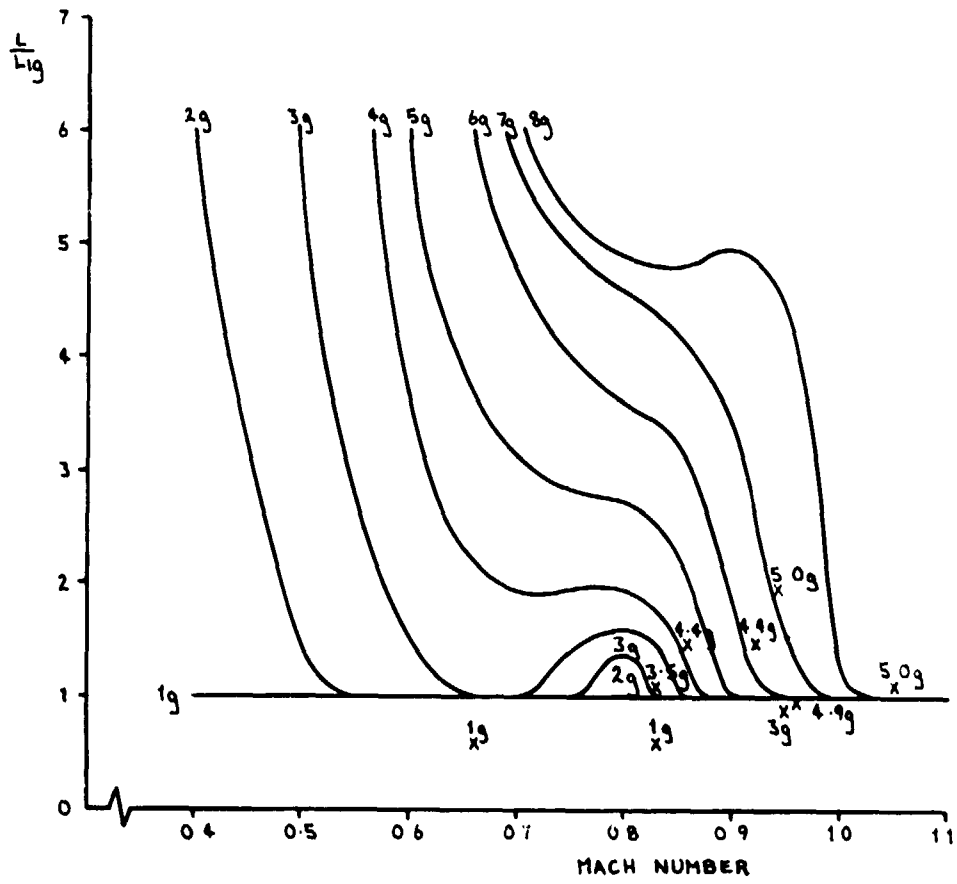
FIG. 13

PREDICTED TAILERON UNSTEADY ATTACHMENT LOADS

45° SWEEP   MANOEUVRE SLAT/FLAP
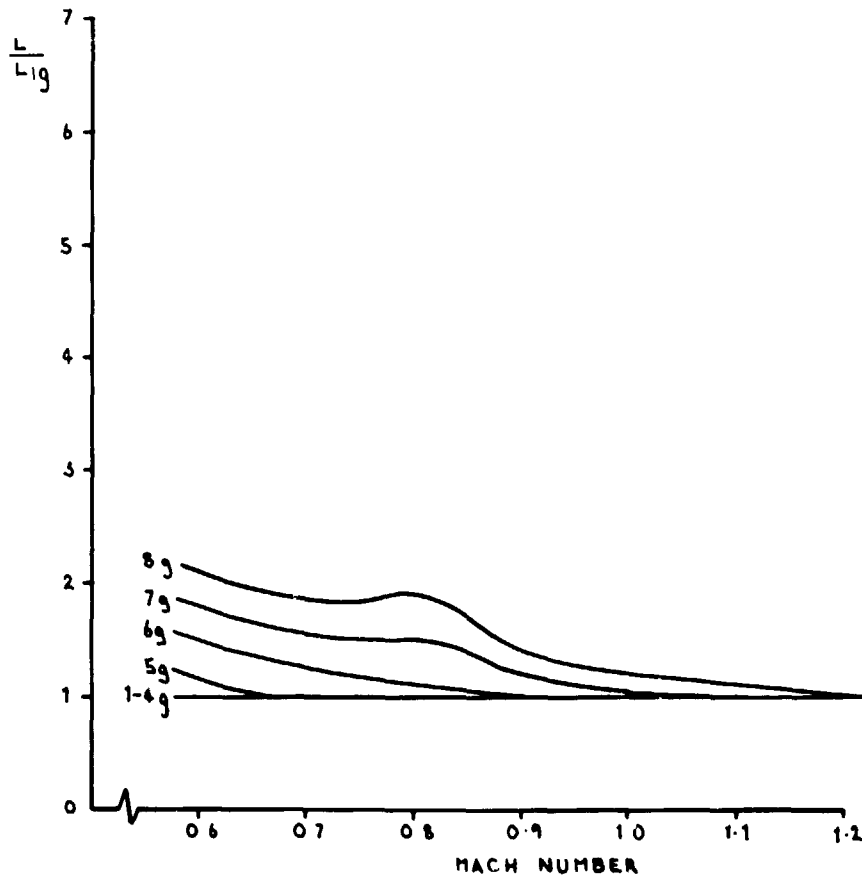
FIG 14

EXTERNAL TANK VIBRATION
MEASURED IN FLIGHT

SEA LEVEL
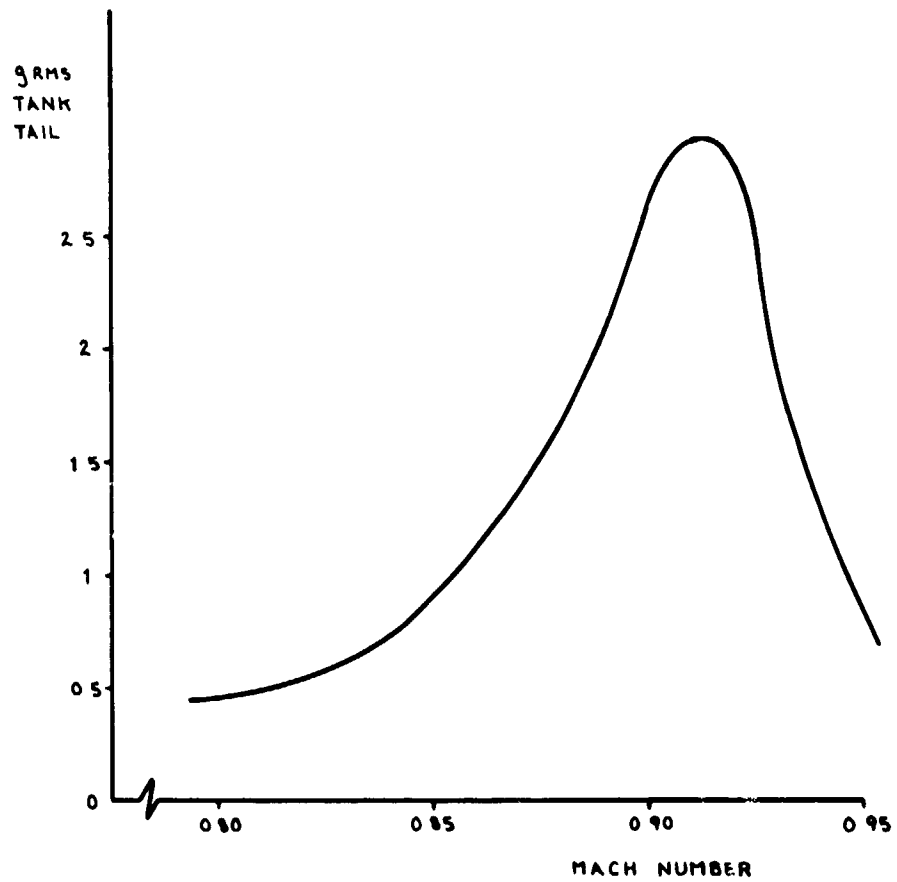
FIG 15

EFFECT OF UNDERWING STORES ON TAILPLANE RESPONSE

TAILERON TIP ACCELERATION

MACH 0·9 SEA LEVEL

CLEAN A/C

TYPICAL STORE
INCREMENT

g^2/Hz

0   1   2

FREQUENCY

TAILERON FUNDAMENTAL

FIG 16
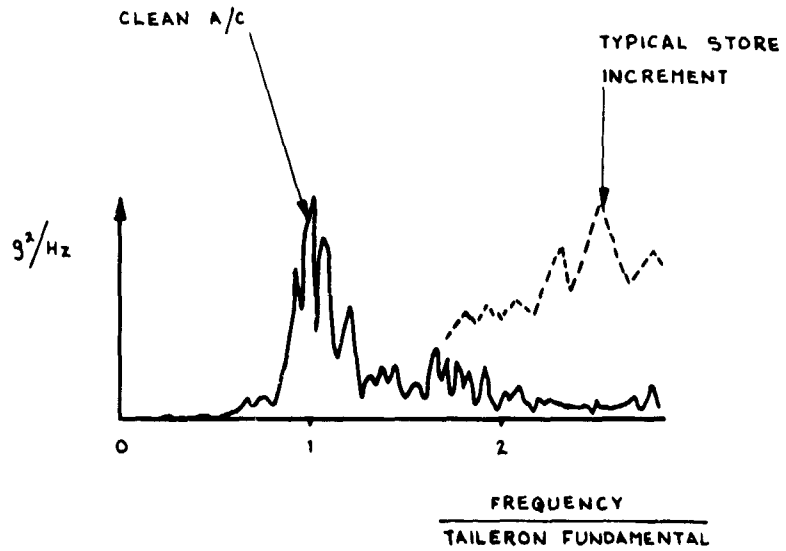
EFFECT OF STORES ON TAIL ROOT BENDING
MOMENT COEFFICIENT
68° SWEEP M = 0·9
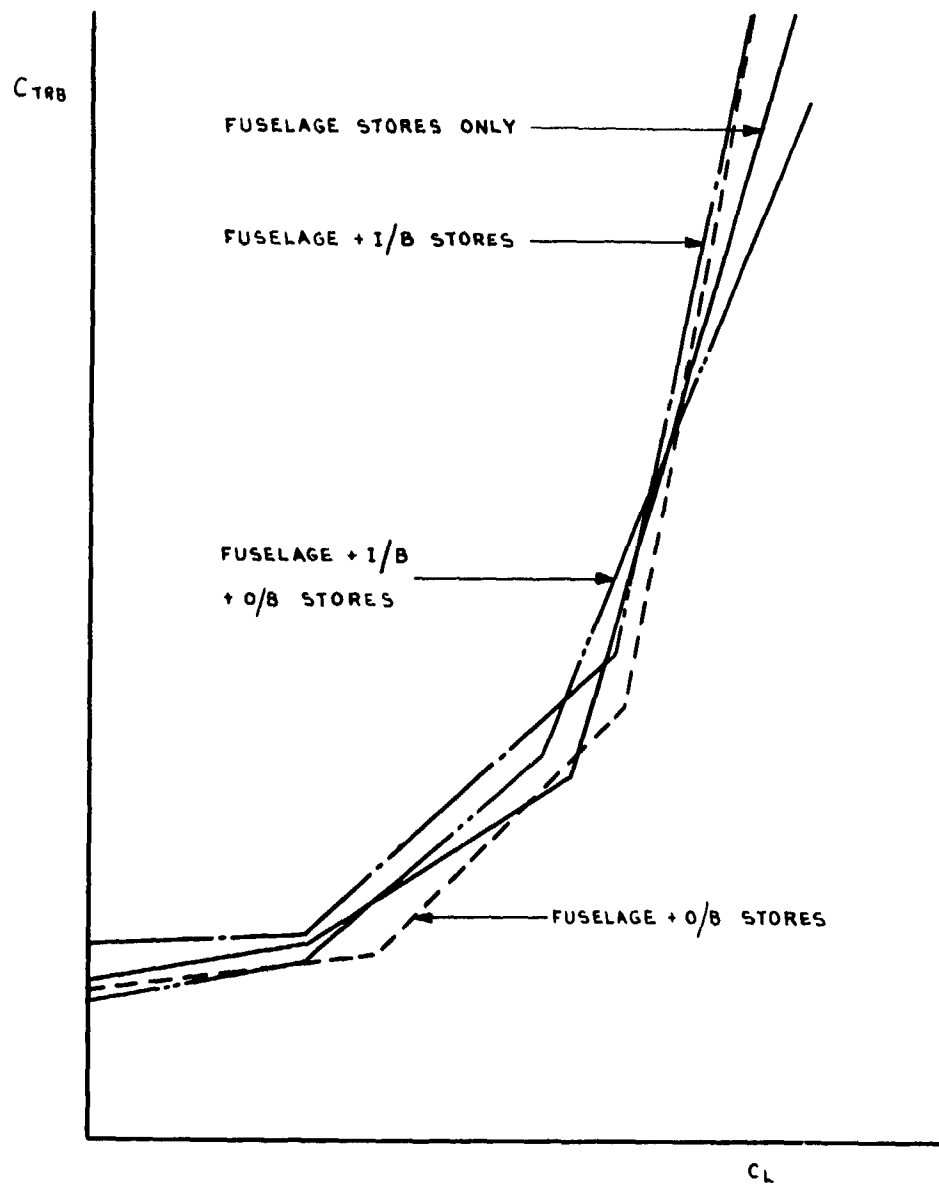
FIG 17

RANDOM PRESSURE FLUCTUATIONS IN SEPARATED
FLOW REGIONS – SUBSONIC FREE STREAM
(REF 2)

$\dfrac{\sqrt{\overline{p^2}}}{\left(\sqrt{\overline{p^2}}\right)_{MAX}}$

UBIQUITOUS
SPECTRUM

$n = \dfrac{fl}{V}$
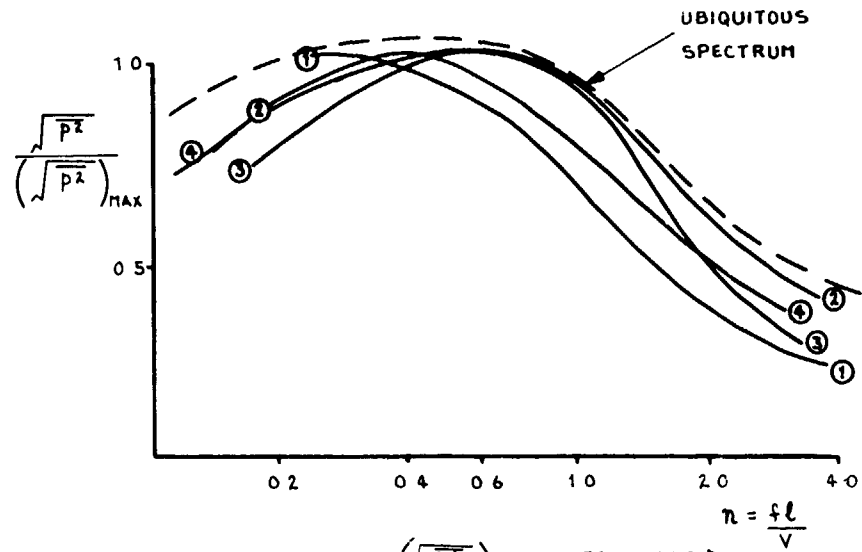
CONFIGURATION	$\left(\dfrac{\sqrt{\overline{p^2}}}{\frac{1}{2}\rho V^2}\right)_{MAX}$	$\dfrac{TOTAL\ RMS\ P}{\frac{1}{2}\rho V^2}$
① FLOW ➔ ⱼ ✗	·022	·08
② ➔ ✗	·010	·06
③ ➔ ✗	·022	10
④ ➔ ✗	·021	$\dfrac{L}{D} = 6$

l IS SCALE OF SEPARATED FLOW REGION

$\sqrt{\overline{p^2}}$ IS RMS PRESSURE IN BANDWIDTH 0·1n

✗ MEASUREMENT POINT

FIG 18

CONTOURS OF TOTAL RMS PRESSURE COEFFICIENT IN WAKE OF AIRBRAKE AT 50° OPENING
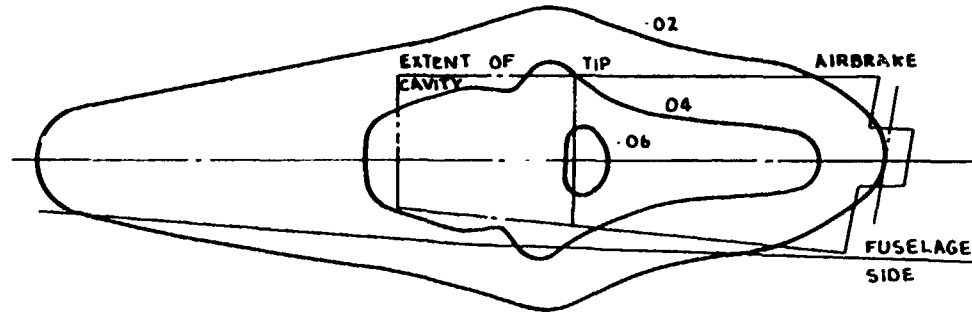
VARIATION OF AIRBRAKE VORTEX SHEDDING FREQUENCY WITH AIRSPEED FOR 50° OPENING
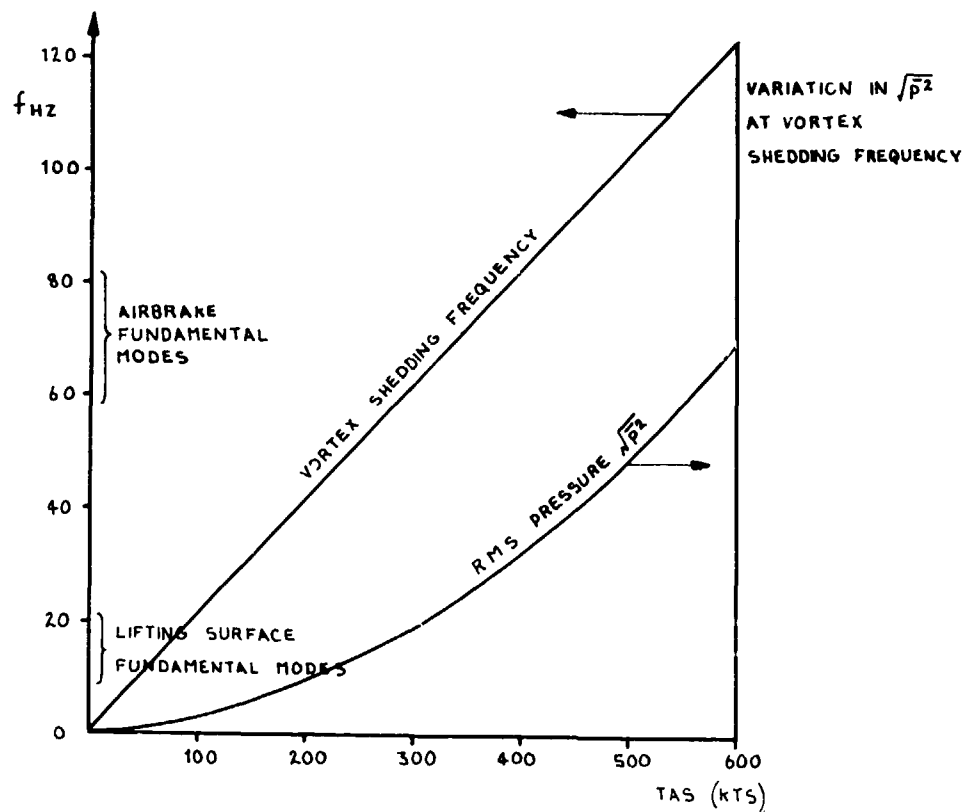
AIRFRAME RESPONSE TO SEPARATED FLOW ON THE SHORT HAUL AIRCRAFT VFW 614

by

Helmut Zimmermann, Günter Krenz

Vereinigte Flugtechnische Werke - Fokker GmbH, D-2800 Bremen

Germany

SUMMARY

The growth of installed engine thrust for combat aircraft, and the rise in by-pass ratio for transport aircraft aggravate the problem of integrating power plant and airframe. The result of this is a growing influence of the engine exhaust flow on the aircraft flight characteristics and structure. Conventional computation and measurement methods are in many cases insufficient to determine jet boundaries and to predict jet-induced structural loads. Using the VFW 614 aircraft as an example the influence of an intermittent jet flow on substructures outside known jet boundaries is illustrated in this paper. Effects comparable to those due to the engine jet are caused also by the wake of movable wing parts such as spoilers and airbrakes. The VFW 614 is used again as an example to illustrate the occurrence of horizontal tail buffet due to flow disturbances for outside the spoiler wake region, and to describe the steps taken to eliminate this type of buffet. The last part of the paper lists several examples of flow separation with ensuing buffeting which, typically occur in the course of flight trials, and measures to combat these disturbances are discussed.

LIST OF SYMBOLS

B.O.	Buffet Onset	n_z	Acceleration in z-axis
D	Nozzle diameter	$n_{z_{wing}}$	Acceleration on wing
H	Altitude	P	Static pressure
$\Delta M_{Hor.Tail}$	Asymmetrical horizontal tail moment	P_0	Static pressure in still air
		P_t	Total pressure
N	Engine r.p.m.	P_{te}	Total pressure at jet exit
M	Mach number	t	Time
RMS	Root mean square of instationary flow function	v_c	Propagation speed
Re	Reynolds number	V	Flight speed
SL	Sea level	V(IAS)	Indicated airspeed
U	Flow velocity in x-axis	V'	Disturbance velocity
$\bar{U}$	Mean value of U	V_j	Jet exit velocity
W/T	Wind tunnel	x, y	Cartesian coordinates
C_L	Lift coefficient		
C_p	Pressure coefficient	α	Angle of attack
C_p^*	Critical pressure coefficient	δx, δy	Distance of anemometer
C_{P_t}	Total pressure coefficient	γ	Intermittency factor
n	Frequency	η	Spanwise wing section

1.0 INTRODUCTION

The paper discusses some structural aspects due to flow separation and engine influence of the shorthaul aircraft VFW 614 [1].The aircraft - shown in Fig. 1 - is a 44 passenger jet airliner with engines mounted on the upper wing side. Some structural aspects are directly connected with this engine position. During flight trials a number of buffeting phenomena were detected on the VFW 614 which were caused by turbulent flows produced somewhere on the aircraft for certain configurations and operating conditions. Among these is the excitation of the horizontal tail by

- Engine exhaust jet on the ground

- Wake of the wing spoilers

- Wing flow separation during stall

The excitation of the horizontal tail are caused by turbulent flow distortions of spoiler wake and engine exit flow respectively. Except for wing wake which always affects the horizontal tail depending on its vertical position for certain angles of attack, the horizontal tail is usually designed to stay clear of the engine exhaust jet and the spoiler wake.

FIG 1   DURING TAKE OFF

The boundaries of turbulent flow distortions are however, not fixed. Intermittent flows alternating between laminar and turbulent flows arise in the jet boundary region, the jet- or wake-boundaries are not stationary, but fluctuate in a random fashion according to a Gaussian distribution. In this paper we attempt to describe these phenomena with the aid of modern statistical methods. Cut-outs in the leading edge of the flaps are used as an example to illustrate that structurally necessary features can lead to flow separations causing unacceptable aircraft flight behaviour. Furthermore the pattern of wing buffet may be changed considerably by reshapement of the wing nose, as shown by tests on the VFW 614.

2.0   FLOW DISTORTION at the BOUNDARIES of JETS and WAKES

2.1   Theoretical Basis and Experiments

Free turbulence occurs in the absence of fixed boundaries, although originating at a fixed boundary, such as an obstacle placed in a free stream. For the flow around an air- craft two main sources of turbulent flow distortion exist:

- movable parts such as airbrakes, spoilers, lift-dumpers

- engine jet

The various theories that have been put forward to describe free turbulence which have gradually come to be considered classical, are purely phenomenological in character. Measurements confirmed the assumption of similarity, or rather, of self-preservation, of these flows, i.e. that the turbulence maintains its structure during its downstream devel- opment. Because of this similarity it is sufficient to consider a single cross-section of the flow with the aid of nondimensional velocities and lateral distances, as follows [2] [3] In the core of the wake and on the jet exit, respectively, the flow is fully turbulent, but becomes increasing intermittent toward the jet boundaries.
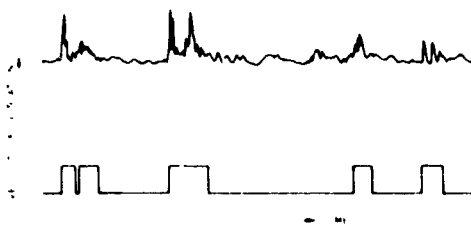
FIG 2   SIGNALS OF TURBULENCE IN INTERMITTENT FLOW
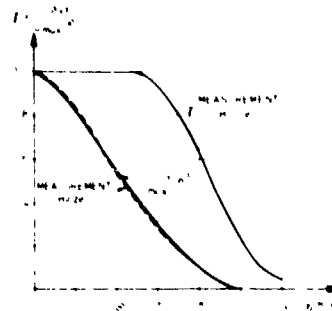
FIG 3   INTERMITTENCY FACTOR AND
VELOCITY PROFIL

Fig. 2 shows in the upper part the velocity fluctuation as a function of time for a point in the boundary region of a free jet, as measured by a hot-wire anemometer. It shows the boundary region flow is intermittent, i.e. alternating between laminar and turbulent. For better illustrating the turbulent signals are converted in the lower part of this figure into impulses of constant unit height, thus the laminar flow can be described by a horizontal line whereas the turbulence is marked by rectangular fields of unit height. The distribution of the velocity fluctuations shown is typical for the flow pattern in the boundary region. Although it was measured in a free jet, it may be also used to describe the turbulence in a wake by phenomenological methods. From the rectangular curve of the lower part of the figure you can determine the so-called intermittency factor that is the ratio of the summation of turbulent flow occurrence to total time.

Fig. 3 shows the intermittency factor and the velocity profile plotted against radial distance in the free jet. The jet boundary R(X) has been determined here by the usual definition. While the mean velocity decreases sharply from the jet axis toward the jet boundary, the intermittency factor is non-zero beyond the boundary, indicating that the intermittent turbulence contributes hardly anything to the mean velocity. Thus the magnitude of the mean velocity is not necessarily a good indicator of the aerodynamic loads to which an elastic structure, such as an empennage, is subjected when immersed in a free-turbulence flow, especially as the velocity fluctuations of the turbulent events in the boundary region are of the same order of magnitude as those in the core of the jet.
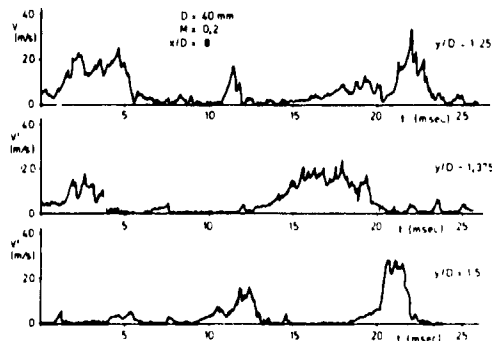
FIG 4 SIGNALS V' AT THE JET BOUNDARY
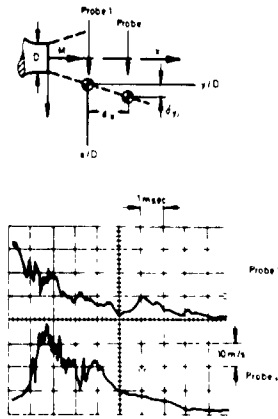
FIG 5 POSITION OF HOT WIRE INSTRUMENTS
AND SIMULTANEOUS MEASUREMENTS

Fig. 4 shows the velocity fluctuation for three distances Y/D at the edge of a model jet. The flow disturbances have a duration of 2 to 8 msec. The disturbance velocities v', occuring in turbulence packets, attain magnitudes of about onehalf of the jet exit speed. The number of high-intensity events decreases with increasing distance from the jet axis. By interpreting the disturbances occurring at the edge of the jet as events in the statistical meaning of the word, we are merely describing test result in a phenomenological sense. These disturbances can be however interpreted, with some justification from other tests, as turbulence packets swept downstream, having a size of up to one tenth of the normal jet radius.

Fig. 5 shows the arrangement of two hot-wire anemometers in the jet and the disturbance signals measured by them simultaneously. Although the signal measured by the downstream anemometer is flatter than that of the upstream one, the two signals may be recognized as being similar. Obviously the disturbance registered here has travelled in time Δt from probe 1 to probe 2. The propagation speed v_c of the disturbance may be calculated from Δt and the probe spacing. The disturbance speed V' of the turbulent event can be read directly from the amplitude of the signal. Fig. 6 shows the probability density distribution of the measured propagation speed of the events, represented as a first approximation by a Maxwell distribution with a slightly shifted maximum. The diagramm was produced by analysing about 40 to 50 single photos, shows that propagation speed scatters around an average value which in this case is about 20 % of jet exit speed. The propagation speeds of the meas.red disturbance signals were also determined by means of the time shift of the peak of the cross correlation function.

A further time-saving method to find the propagation speed is the "stored beam" method. Wherein 100 signals of each probe were displayed simultaneously on a storage oscilloscope. The superposed signals outlined an envelope, and the time shift of the two envelopes together with the probe spacing yielded a mean propagation speed. The results of the methods compare well. Fig. 7 shows the mean propagation speed v_c, the mean jet velocity U, and the RMS value of the disturbance velocity in the edge region of the jet, 8 jet diameters behind
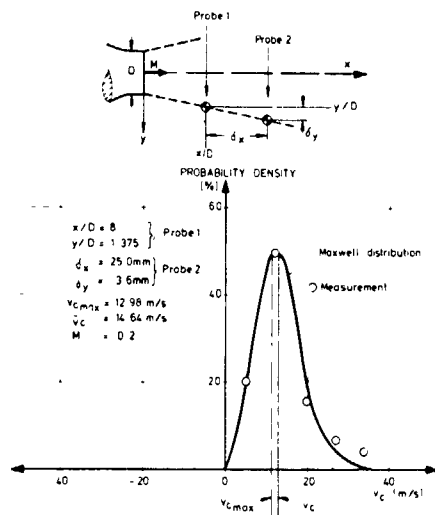
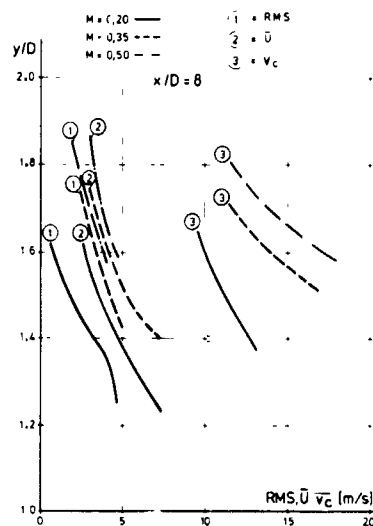FIG 6 PROPAGATION SPEED OF TURBULENT EVENTS

FIG 7 VELOCITY FLUCTUATIONS IN A CIRCULAR JET

the jet exit. The mean propagation speed is 4 to 5 times larger than the RMS velocity, and 2.5 to 4 times larger than the mean jet velocity. This means that there are individual disturbances in the edge region of a jet that move at speeds far above the values measured by ordinary methods (e.g. pitot-tube).

The arguments of the foregoing section therefore indicate that significant disturbances of the air flow exist outside the jet as defined by pitot static surveys, and that therefore any obstacle such as an horizontal tail placed outside the stationary jet could very well experience unstationary forces.

2.2 Jet Influence on the Horizontal Tail

In general engine jets may interfere with the empennage owing to their location. In particular, the effect of the engine jets on the VFW 614 empennage will be considered here, by applying the preceding arguments concerning jet spread. The conclusions drawn from tests on a model jet may not be applied directly to the spreading of the engine jet of the VFW 614 for the following reasons:

- R.R. power plant M 45 H-O1 is a turbo-fan engine, with an interior high-speed hot jet embedded in a low-speed cold jet.

- Crosswind leads to intake distortions causing a deformation of the jet profile at the exit and further downstream.

- The neighborhood of the fuselage affects the spreading of the engine jet, and hence its symmetry.

During the development of the aircraft many tests were done to clarify the interference between the engine jets and the horizontal tailplane. Fig. 8 shows results from W/T-tests where the static pressure fluctuations were measured at the horizontal tail lower side at changing crosswinds. It can be taken from this figure that pressure fluctuations increase with increasing crosswind. P is an average peak to peak value taken when 5 or more peaks arise during one second. Fig. 9 shows the relative locations of wing, engine, empennage and the extention of the stationary jet as measured on the aircraft. The pressure distribution was measured in the engine jet exhaust in front of the horizontal tail by means of a pitot rake, vertical measuring plane being in the spanwise engine position. Jet boundary distance from horizontal tail is about 3/4 engine exit diameter. On the first reviewal of these measurements, it is improbable to expect aerodynamic loads due to jet influence on the horizontal tail. However, buffeting occurred at the horizontal tail and the fuselage with engines running at full power and the aircraft stationary on the ground. The buffeting disappeared at a lowered idle position or when the aircraft started to taxi.

Therefore vibration measurements were made by means of accelerometers on the wing, horizontal tail, and fuselage (flight deck, center of gravity), and by pressure pick-ups in the cold circuit of the engine, and the under side of the horizontal tail in the neighborhood of the jet. The nozzle exit speed increases with engine r.p.m. as illustrated in Fig. 10 for the M 45 H-O1 engine. Fig. 11 shows typical signals of a pressure transducer at the horizontal tail, asymmetrical horizontal tail moment and outer wing acceleration at about 89 % engine r.p.m. with the aircraft grounded.
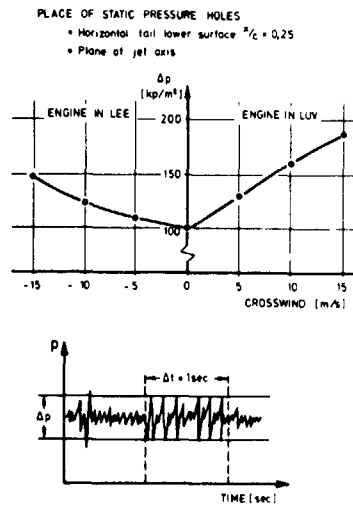
PLACE OF STATIC PRESSURE HOLES
• Horizontal tail lower surface $x/c = 0.25$
• Plane of jet axis

FIG 8 STATIC PRESSURE AT THE HORIZONTAL TAIL
W/T TESTS

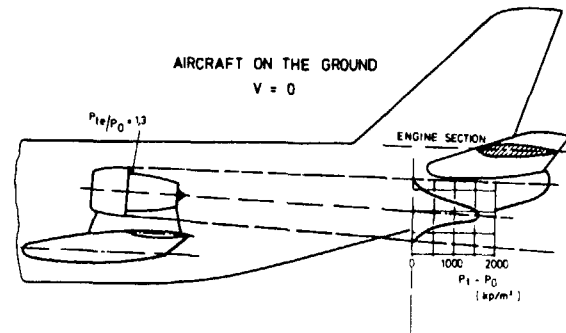AIRCRAFT ON THE GROUND
V = 0

$P_{te}/P_0 = 1.3$

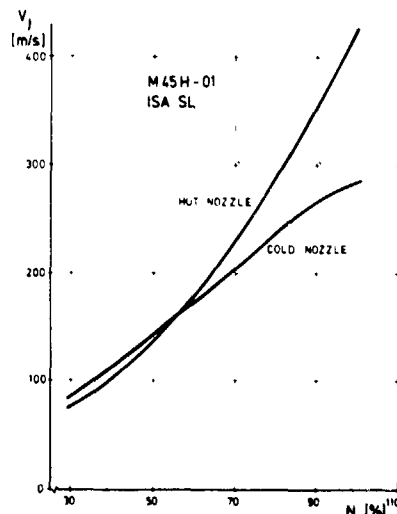FIG 9 ENGINE JET SPREADING UNDERNEATH THE HORIZONTAL TAIL
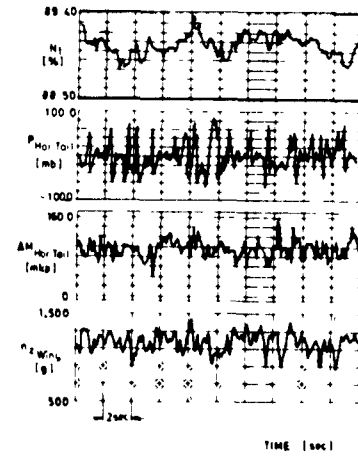
FIG 10 JET EXIT SPEED

FIG 11 JET INFLUENCE ON TAIL AND WING

The investigations were performed for different engine intake and exit conditions and geometries, as well as at different directions of the jet axis towards the tail and the fuselage. The main results show:

- tail vibrations at high engine speeds were caused by the jets and decreased with decreasing engine r.p.m.

- vibrations increased when the engine was tilted to bring the jets closer to the horizontal tail or the fuselage, on the other hand decreased when the jets were moved away from the tai and the fuselage

- neither did the improved intake shapes - used to prevent intake flow separation in heavy crosswinds - nor t e use of different exhaust nozzles alter the vibrations

On the other hand vibrations increased with increasing crosswinds. A crosswind is likely to change the flow spreading in a free jet, and it may by expected to shift the axis or the shape of the jet and thus raise the intensity of the disturbances.

The results of all investigations may be summarized as follows: The vibrations of the horizontal tail is influenced by jet deflections as well as by magnitude and direction of the surrounding flow. These results are in agreement with the phenomenological description of the flow in the edge region of a free jet developed in the previous section. Buffeting dissappeared at a lowered idle position or when the aircraft started to taxi. The vibrations occurring at 100 % engine speed led to minor dynamic loads which affected neither the fatigue life of the substructures concerned, nor their structural dimensions. Passenger comfort, however, was impaired at high engine speeds. This adverse effect was eliminated by lowering the engine idling speed.

2.3 Horizontal Tail Loads Caused by Spoiler Wakes

The VFW 614 is equipped with two flight spoilers on each wing. Fig. 12 shows the geo-
metrical lateral arrangement of the spoilers on the wing respect to the horizontal tail.
It is obvious that the wake of the outer flight spoiler II is outboard of the horizontal
tail, while the wake of the inner flight spoiler I passes beneath the horizontal tail.
This was confirmed by pressure measurements in front of and underneath the horizontal tail
in a vertical measuring plane of the flight spoiler I inboard edge. Fig. 13 shows the
flight spoilers are at a large vertical distance away from the tail; here the tail section
is marked by cross-hatching, which lies in the plane of the inboard edge of flight spoiler
I. The pressure losses of the spoiler wake in the plane of this section were measured for
several incidences with a pitot rake in the wind tunnel. On the basis of these measurements
one would not expect the wake to cause any disturbances at the horizontal tail, because the
distance between tail and wake edge at an incidence of $\alpha = 0$, for example, amounts to more
than a meter, being about equal to the appropriate horizontal tail section.
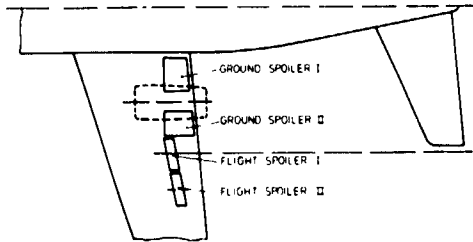
FIG 12 FLIGHT SPOILER POSITION WITH
REFERENCE TO HORIZONTAL TAIL
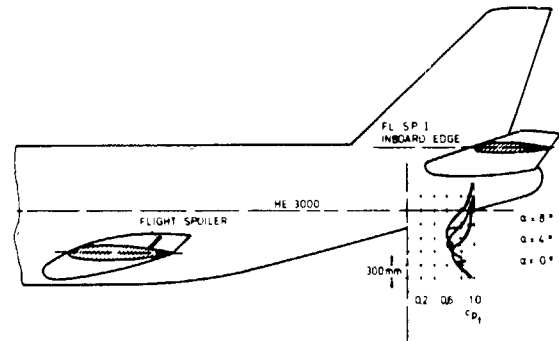
FIG 13 FLIGHT SPOILER WAKE AT HORIZONTAL TAIL

In fact, however, noticeable disturbances occurred at the horizontal tail, as Fig. 14
shows. The pilot affirmed that the vibrations in the passenger compartment were not accept-
able. The display of Fig. 14 shows the growth of the asymmetrical horizontal tail moment,
when both flight spoilers I and II have been extended. The following diagramm, Fig. 15,
shows the asymmetrical horizontal-tail moment vs. flight speed for various spoiler actua-
tions and deflections. The influence of the spoiler angle is interesting. A 10° decrease,
from 50° to 40° reduces the tail moment due to both spoiler by half. Furthermore, the
effect of the outboard spoiler is less than the inner one, and by superposing both indi-
vidual effects one obtains approximately the resultant effect of both spoilers. This
resultant effect is surprisingly large, compared to the wake boundary of total-pressure
deficit shown in Fig. 13. The vertical distribution of the pressure loss below the tail
shows that the intermittent flow in the spoiler wake has a larger vertical extent than
measured by stationary methods. On the basis of these results the inner flight spoilers
are no longer extended in flight and used only as ground spoilers; the outer spoilers cause
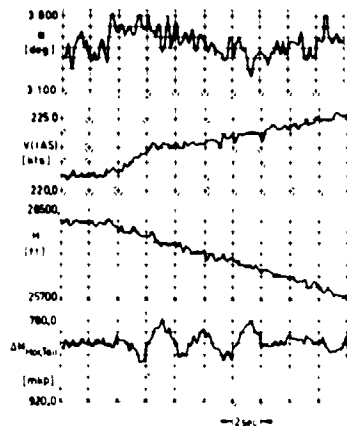no aircraft vibration.

FIG 14 HORIZONTAL TAIL MOMENT DUE TO
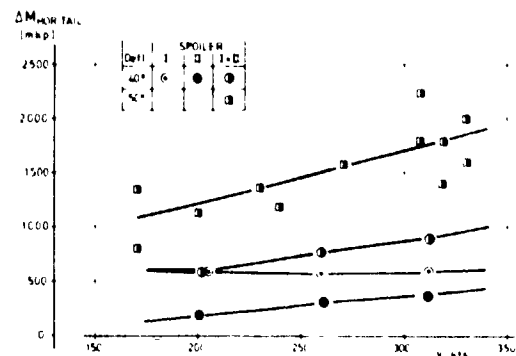EXTENTION OF FLIGHT SPOILER I AND II

FIG 15 HORIZONTAL TAIL LOAD AT SPOILER OPERATION

3.0 AIRCRAFT BUFFET due to FLOW SEPARATION

3.1 Static and Dynamic Antisymmetric Loads on the Horizontal Tail

When applying civilian airworthiness regulations, difficulties often arise in deciding the strength of the horizontal tail connection to cope with asymmetric loads. According to FAR Part 25, maximum antisymmetric loads are calculated by multiplying the maximum horizontal tail load on one side with 1, and on the other with 0,8. The resulting moment is supposed to take care of the moments caused by the following conditions:

- Rolling moments due to vertical-tail in sideslip

- Rolling moments due to horizontal tail dihedral during sideslip

- Asymmetric downwash due to wings, flaps and ailerons

- Unsteady rolling-moments due to the wing wake during the stall

The rolling moment calculated by airworthiness regulations amounted to 1480 mkp. Final flight tests show a maximum rolling moment of 5325 mkp, which was more or less due to aircraft sideslip for high dynamic head. The moments due to a combination of stall and sideslip did not exceed 5325 mkp either. The structural dimensions of the horizontal tail were sufficient to absorb this moment.

During stall the wing wake passes below the horizontal tail up to an angle of attack, where flow separations occur at the wing. This was confirmed by W/T-measurements of pressure losses underneath the horizontal tail. The display on Fig. 16 is taken from stall tests: For decreasing flight speed and increasing incidence a g-break occurs at about $\alpha = 15^\circ$, which has been marked by the pilot at the vertical dotted line. This g-break is the consequence of a noticeable flow separation at the inboard wing, causing simultaneously large accelerations and buffeting at the wing as well as larger instationary asymmetrical horizontal tail moments. The sudden appearance of disturbances at the horizontal tail, and their order of magnitude indicate that the large difference moments at the tail are caused by the wing wake, and not by vibration excitation at the wing. Fig. 17 shows the instationary asymmetric horizontal tail moments expanded further in time. They show that the disturbance at the horizontal tail occur stochastically having a frequency of about 6 Hz. This frequency corresponds to the lowest antisymmetric horizontal tail bending mode.
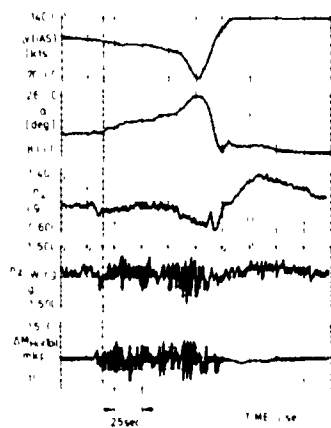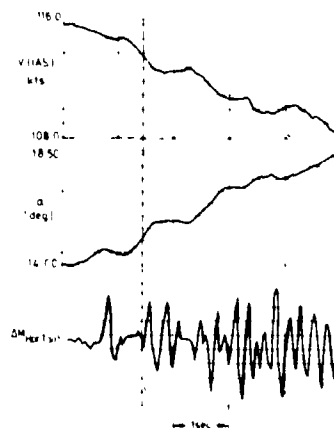

FIG 16 STALL CHARACTERISTICS

FIG 17 HORIZONTAL TAIL MOMENTS DURING A STALL

3.2 Change of Buffet Boundary by Modification of the Wing Leading Edge

During flight testing a change of the wing nose had become necessary to improve stall characteristics. The wing lay-out had to take account of the engine location, but the actual response of the engines to the separated wing flow was unknown until well into the flight trials [4] . Because of these uncertainties the wing flow was imputed to start separating between fuselage and engine, and outboard of the engine during the stall, as shown in Fig. 18. This lay-out was not successful. During stall trials the outboard flow separation spread rapidly giving rise to pitch-up and large unacceptable rolling moments for certification, especially at large aircraft incidences. The engine was completely insensitive to separated wing flow even for extreme flight conditions, during this trial phase. Advantage was taken of this result to improve stall characteristics by modifying the wing leading edge [5] . A low cost nose modification for the outboard wing was done by increasing the nose radius and camber.
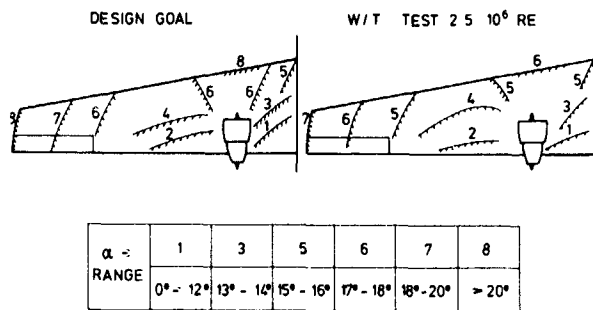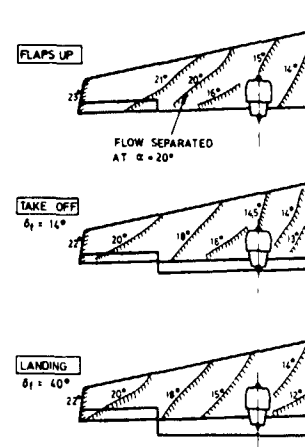
FIG 18 STALL PROPAGATION DESIGN/MODELL TEST

FIG 19 STALL PROPAGATION AFTER L E MODIFICATION

Fig. 19 shows the progression of flow breakdown after the modification taken from tuft studies during the stall tests. Flow separation is conventional resulting in favorable stall characteristics. Care had to be taken, however, by the leading edge modification that the buffet boundaries were not lowered too much by shock separation on the wing pressure side. Fig. 20 shows the geometry before and after the change at an outer wing section with the pressure distributions corresponding to a flight Mach number M = 0,71, and level flight at an altitude of H = 20 000 ft. Pressure distribution-calculated by means of a subsonic panel method - is completely changed at the forward wing part resulting in decreased aircraft buffet boundary. Fig. 21 shows the onset of buffet at the wing as a function of Mach number before and after the leading edge modification. It may be seen that the boundary for buffet onset - here defined by z-accelerations at the outboard wing $n_z \approx \pm 1$ g, which agreed with pilot judgement - has shifted by about M = 0,015 toward smaller Mach numbers. This shift did not signify a limitation of the specified flight regime [6] .
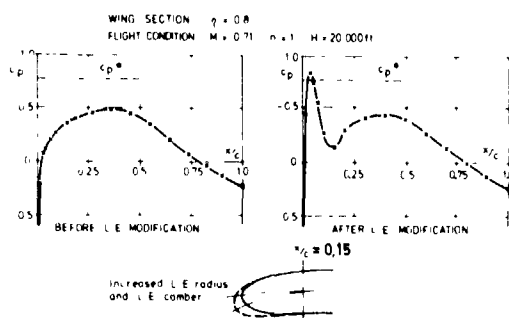

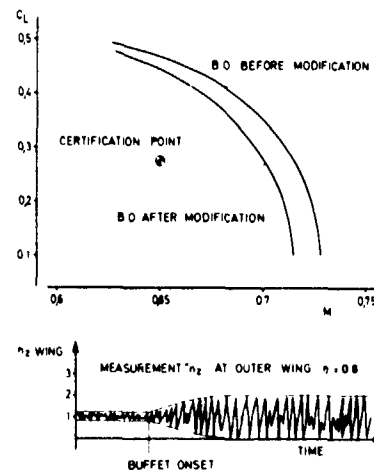FIG 20 CALCULATED PRESSURE DISTRIBUTION AT THE WING LOWER SUREFACE

FIG 21 CHANGE OF B O BOUNDARY DUE TO WING L E MODIFICATION

3.3 Heavy Buffet Produced by Small Cut-Outs at the Flap Leading Edge

The design of the trailing-edge flap tracks of the VFW 614 required small cut-outs of about 15 cm width in the flap nose. A design with a movable mechanism to cover up the three holes at each wing was too elaborate and subject to malfunction so that flight testing was commenced at first with the open cut-outs, as sketched in Fig. 22. During the first-time extension of the flaps into landing position of $\delta f = 40°$, severe buffeting occurred that the pilot had to retract the flaps immediately. In order to reduce the buffeting without having to install any complicated covering mechanism, the cut-outs were

reduced in size, as shown in the lower part of Fig. 22, by a cover plate in the upper flap nose contour. With fully extended flaps the plate leading edge was now situated below the wing trailing edge, forming a well-defined slot, as illustrated in Fig. 22. The cut-outs in the flap nose were only partly covered by a thin plate with a sharp, aerodynamically poor leading edge, resulting in a completely buffet-free wing flap. This concluding case demonstrated how small sources of disturbances can have large effects on the aircraft characteristics.
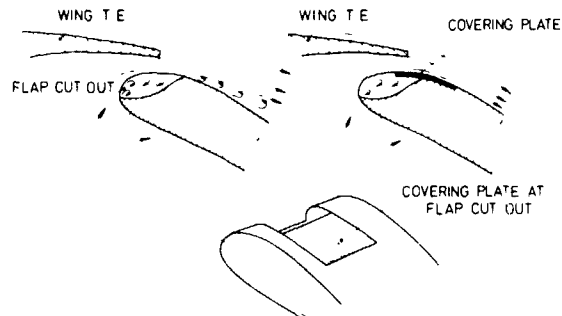
FIG 22 FLOW IMPROVEMENT AT THE FLAP LEADING EDGE

4.0 CONCLUDING REMARKS

Experience with the VFW 614 has shown, that conventional measurement methods, such as pitot static systems are insufficient to detect the boundary region of the flow field of jets and wakes. The intermittent region of the flow field extends considerably beyond the classical boundaries of jets and wakes. This intermittent flow field can cause heavier buffeting and higher dynamic loads on substructures immersed in this flow field than the high-frequency turbulent flow field itself, because the intermittency frequencies lie in the same range as the frequencies of the structural modes of these parts. For future transport aircraft especially the interference of the engine jet with the empennage because of increasing thrust and by pass ratio will become larger. Similar problems exist for the wakes of spoilers, dumps and airbrakes which can influence the empennage. Here new methods have to be found to describe the combined airframe propulsion system. It is also important to get a better insight into the physics of the intermittent flow field with the aim to control the extent and the statistical properties of this flow pattern.

REFERENCES

1. R. Stüssel; Jet bus VFW 614. Flugrevue Heft 5/6 1968

2. A.K. Banerjea, O. Wehrmann; Strahlinduzierte Instationäre Luftkräfte im Nahfeld von Freistrahlen. ZTL-Bericht VFW-Fo 4.06/4/72, BMVg T/Rü Auftragsnr. 425/24100/22012

3. O. Wehrmann, W. Burgsmüller, J. Rohde; Grobstrukturelle Zerfallsphänomene im Freistrahl. RüFo IV - Bericht 75/76, VFW-Fo, RüFo-Auftragsnr. T/RF 42/RF 420/51062

4. J. Barche, H.J. Beisenherz, H. Griem, G. Krenz; Some Low Speed Aspects of the Twin-Engine Short Haul Aircraft VFW 614. AGARD, FMP, Edinburgh 1974, AGARD CP-160

5. G. Krenz; Aerodynamische Auslegung und Flugerprobung der VFW 614. DGLR 9. Jahrestagung 1976 München, Vortrag 76 - 208

6. VFW 614 flight test reports,unpublished.

TAIL RESPONSE TO PROPELLER FLOW ON A TRANSPORT AIRPLANE
by
L. CHESTA
AERITALIA S.p.A.
Corso Marche, 41 - TORINO

INTRODUCTION

Propeller powered Airplanes are, more than jet Airplanes, subject to very strong vibrations.
The reason is that in addition to the usual vibrations induced by buffet or separated flows another vibration source, the propeller (and its gearboxes and accessories) with the associated flow field distortions induced by the rotating blades is acting on the Airplane.
But unlike the buffet that has broadly a random character the excitation forces associated to the propeller are of deterministic type and practically all the power involved is concentrated at certain frequencies, those related to the propeller and gearbox unbalance and those due to the blades number of passes over the airframe, with their harmonics.
Since vibration modes of the Aircraft (mainly the higher wing modes and fuselage and tail modes) are usually in the same range, a dynamic amplification of these forced vibrations may therefore occur.
The problem is well known but still present in modern turboprop Airplanes and Helicopters where, if not completely solved, can yeld to limitations of the A/C performance or fatigue life problems.
In the present paper the main results of a flight investigation on tail vibrations carried on at AERITALIA - TURIN on a medium transport aircraft and the most important measures taken to overcome the problems arisen are described.
The Airplane (see fig. 1) is powered by two turboprop engines each driving a three blades propeller.
The engines are mounted on underwing nacelles and the tailplane lies on a plane slightly above the wing plane.
The elevator is connected to the main surface through four hinges and has two tabs (balance and trim) at the inboard side.
The power plant has a two stage turbine configuration: the first stage drives the compressor and the second stage drives the propeller through a gear box.

VIBRATIONS MEASURED IN FLIGHT

During the initial flights on the Airplanes very large accelerations were monitored on the tailplane that could lead to fatigue problems for the surfaces.
This required an investigation in three directions:
1) Identification of the source of vibrations
2) Identification of the flight conditions in which they occur
3) Identification of the time spent by the airplane in these conditions, during normal operational flights.
The purpose of the first investigation was to identify the possibilities, if any, to cure the vibrations acting on the source.
The second investigation had the purpose to evaluate how necessary are the flight conditions of occurrence of vibrations in the normal A/C mission profiles.
The third investigation is needed in order to know the actual impact of the vibration level on the A/C fatigue life.
The data needed were provided recording during the whole normally scheduled test flights some significant vibration and flight parameters: (fig. 3)
a) Force at the balance tab control rod
b) bending moment on the trim tab between the two hinges
c) accelerations at the tailplane and f. tips (TE and LE)
d) speed, altitude, flap setting, propeller RPM (Np), high pressure turbine shaft RPM (Ng).
The time histories of the recorded vibration signals showed always a very clean oscillation at a frequency equal to three times the propeller speed (3 Np), exactly the number of passes of the blades wake over the tailplane structure.
On fig. 3 a plot of the amplitudes of the vibrations monitored by each pick-up on a single flight versus the propeller speed is shown.
Each diagram clearly shows three peaks at about 75, 87, 100% of the max Np with different relative amplitudes.
The trim tab, balance tab and fin show a peculiar sensitivity to one of the three frequencies ranges identified (respectively 100%, 87% and 74% Np).
The tailplane shows about the same sensitivity to the three ranges. This is in good agreement with the Ground Resonance Test results which showed three tailplane modes in the same ranges.
The conclusion is that the three blades propellers and the associated airscrews are the excitation source of the vibrations monitored on the tail.
In the following analysis the balance tab has been taken as a reference being the most critical item for fatigue life.
Fig. 4 shows in more details the forces measured during many flights on the balance tab control rod at a speed of 110-130 Kts and flap angle of 30°versus the propeller frequency. The envelope of the measured points shows two relevant peaks at 87% and 100% Np arising from negligible amplitude level but it is possible to note inside the peaks a considerable scatter of the forces measured. This leads to the conclu

sion that at least another parameter should affect the problem.

This is shown by fig. 5 in which the points of the peak at 87%-90% Np are plotted versus the high pressure turbine speed (Ng) which is related to the power. The envelope of the points shows a continuous increase of the vibration level with power.

For different speeds (e.g. 100 Kts) the envelope line shows a maximum (see fig. 6).

Therefore the effect of speed was examined in more details for the case of the clean wing (zero flap setting) since a larger scatter of speeds was available for that configuration.

The results appear on fig. 7 which shows that:
1) the vibration level for each speed increases rapidly with Ng up to a maximum and than there is a slow decrease.
2) the absolute maximum has been found at a speed between 150 and 170 Kts.
3) increasing the speed the maxima of the curve shift towards higher Ng.

The explanation of this behaviour may be found correlating the A/C attitude with the flow downwash at the tail for different A/C speeds and flap settings.

Fig. 8 shows this correlation as found during WT tests for different thrust coefficients (C_T).

The crossing of the two curves, occurring at different speeds according to flap setting, means that the flow around the tail is parallel to the tail itself. In these conditions, due to the peculiar geometry of the A/C, the propeller slipstream, being not uniform, but of annular form, gives the maximum interference with the horizontal tail.

Therefore the percentage of the energy generated by the propeller which is transmitted to the tail is maximum whilst the total amount of energy transmitted is affected also by the A/C speed directly correlated with the total generated energy.

Figs. 9 and 10 show these two effects.

On fig. 10 the maximum of the balance tab response found at a certain speed occurs at the flap setting corresponding to an effective incidence α HT of the tail nearly zero which, as previously discussed, in this A/C is the incidence putting the tail in the most effective area of the propeller airscrew annular region.

The fig. 9 shows the same behaviour for the case in which the flap setting is fixed and the speed variable.

The figures 11 and 12 summarize the test results for the balance tab response at 87% of Np correlating respectively the power (Ng) with flap positions and with speed.

The crosses and the unshaded points represent low vibration levels, the shaded points are corresponding to high vibration levels but still acceptable. The x crossed points represent unacceptable vibration levels unless for short periods and the diamonds are the worst conditions, absolutely unacceptable.

As it possible to see the high vibration level points are spread out over a very large area particularly for the intermediate flap condition.

In order to ascertain the possibility of the A/C to withstand this environment during its life it is necessary to analyze in details how connected are the operating conditions of the A/C with these critical areas. The shaded areas and the climb and take off points represent the combinations of propeller torque and rotational speed used normally on the A/C for each specific flight condition (fig. 13).

On the same figure it is possible to see that the lines representing the Np corresponding to the tail plane frequencies are very close to the flight conditions where the full power is required.

The two modes at 84 and 89% Np are very close to the climb and high speed cruise conditions, the mode at 100% Np is just on the high speed climb and at the border of the air dropping and approach conditions with intermediate and max flaps.

As the propeller rotational speed cannot be changed easily this leads to the following considerations:
1) the close proximity of the propeller frequencies and modes causes oscillations dynamically amplified
2) the amplitude of the vibration is necessarily very strong due to the high power involved in the propeller excitation
3) the flight conditions involved last long time in normal operation.

The need of an accurate fatigue life analysis for the tailplane and the associated movable surfaces therefore arises. Starting from the shapes of the vibration modes measured during the Ground Resonance Tests and from the mass distribution of the structure a theoretical evaluation of the fatigue life of each single part of the structure was performed.

PROTOTYPE VIBRATION MODES

The vibration modes of the tail for the prototype A/C are shown on fig. 14.

The mode at 67.2% Np is the torsion mode of the tail involving a large motion of the fin. This mode is not critical since this propeller Np is used only with the gas generator in idle.

The mode at 99.6% Np is a bending of the trim tab and the two modes at 85% and 89% are respectively a bending of the elevator with torsion and the torsion of the elevator with some bending and rotation of the balance tab.

From the theoretical fatigue predictions the most critical items appear to be the two tabs, respectively the trim tab for the mode at 99% Np and the balance tab for the mode at 89% Np.

A fatigue test was therefore set up using a balance tab mounted on a rigid rig and excited through the control rod by an electromagnetic shaker at 50 Hz with a force on the rod nearly corresponding to the maximum found in flight.

After a few hours the first crack appeared on the skin of the tab leading edge.

One of the two hinges was also found cracked at an inspection with nondisruptive controls.

Meanwhile an analysis of the time spent by the tab at each vibration level during the whole flight testing

was carried out, noticing that the test flight profiles were statistically equivalent or even slightly more stressing than the operative flight.

The comparison between these analysis and the fatigue test results showed that the balance tab could not withstand these environmental conditions for the expected A/C life.

A similar situation has been found for the trim tab.

CHANGES ON THE PRODUCTION AIRPLANES

The investigation performed evidenced the following points:

1) the source of vibration has been identified as due to power plant configuration which cannot be changed unless after a major redesiging work

2) the flight conditions in which vibrations occur are the most common in the operative flight and therefore cannot be crossed out

3) the unavoidable stresses are on the other hand unacceptable for fatigue life

The only practicable way to solve the problem is to change frequencies or shapes of the tail modes of vibration and all the following efforts were devoted to found a solution without involving major design changes or significant weight and cost penalties. These requirements lead to reject solutions like: elevator fractioning or stiffening, shifting spanwise of the balance tab control rod position, tab stiffening with consequent rebalancing of the elevator, surface redesign with advanced composite materials.

On the contrary the following measures were easy to take:

1) addition of a third hinge on the tabs

2) reinforcement of the tabs leading edge skin

The first solution was sufficient to solve the problem for the trim tab.

For the balance tab both measures were taken leading to acceptable stresses on the tab itself but, due to the peculiar mode shape, the control rod became the critical item.

This could be explained because the mode shape of the tab turned to an essentialy rotational mode and a large tab inertia was involved. On the other hand the frequency was always the same because the actual mode is the elevator torsion and the motion of the tab is just a consequence of the gear type connection. This leads straight to understand the proper cure of the problem: to increase the frequency of the elevator torsional mode. This could be accomplished in a very simple and easy way just with a change of the elevator mass balance distribution.

PRODUCTION A/C VIBRATION MODES

The GRT performed on the first series airplane, embodying the above mentioned changes, confirmed what expected.

Fig. 17 shows the new mode shapes. The frequency of the mode at 89% shifted to 92.5% Np the one at 85% to 104% and the frequency at 99.6% was shifted out of the range of excitation.

On fig. 16 the new modal situation is compared with the propeller excitation range as previously done on fig. 13.

The frequencies now lie between the main operating aircraft conditions and therefore the effect of the dynamic amplification of the vibrations should be minimized.

Figs. 18 and 19 (to be compared with figs. 11 and 12) show that the vibration level has been considerably reduced as expected to values fully acceptable for confort and fatigue life of the whole tail.

CONCLUDING REMARKS

The analysis performed and the solutions adopted show that an accurate evaluation of the flight tests data and a proper use of the informations available from Ground Resonance and Fatigue Tests may reduce the redesign work during the serialisation of the A/C pointing out very simple and unexpensive solutions.
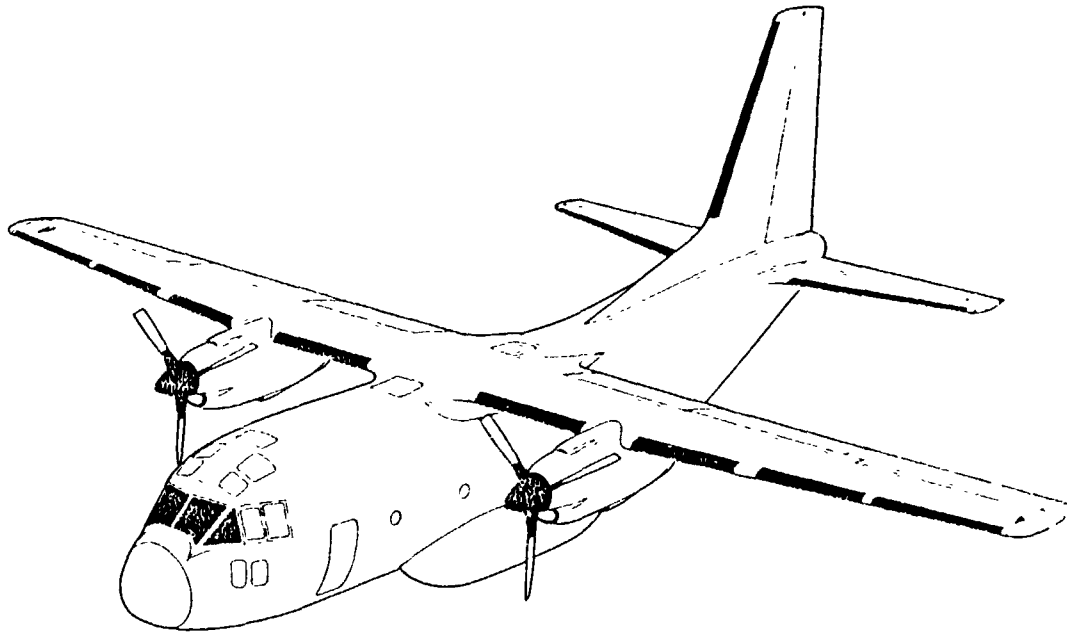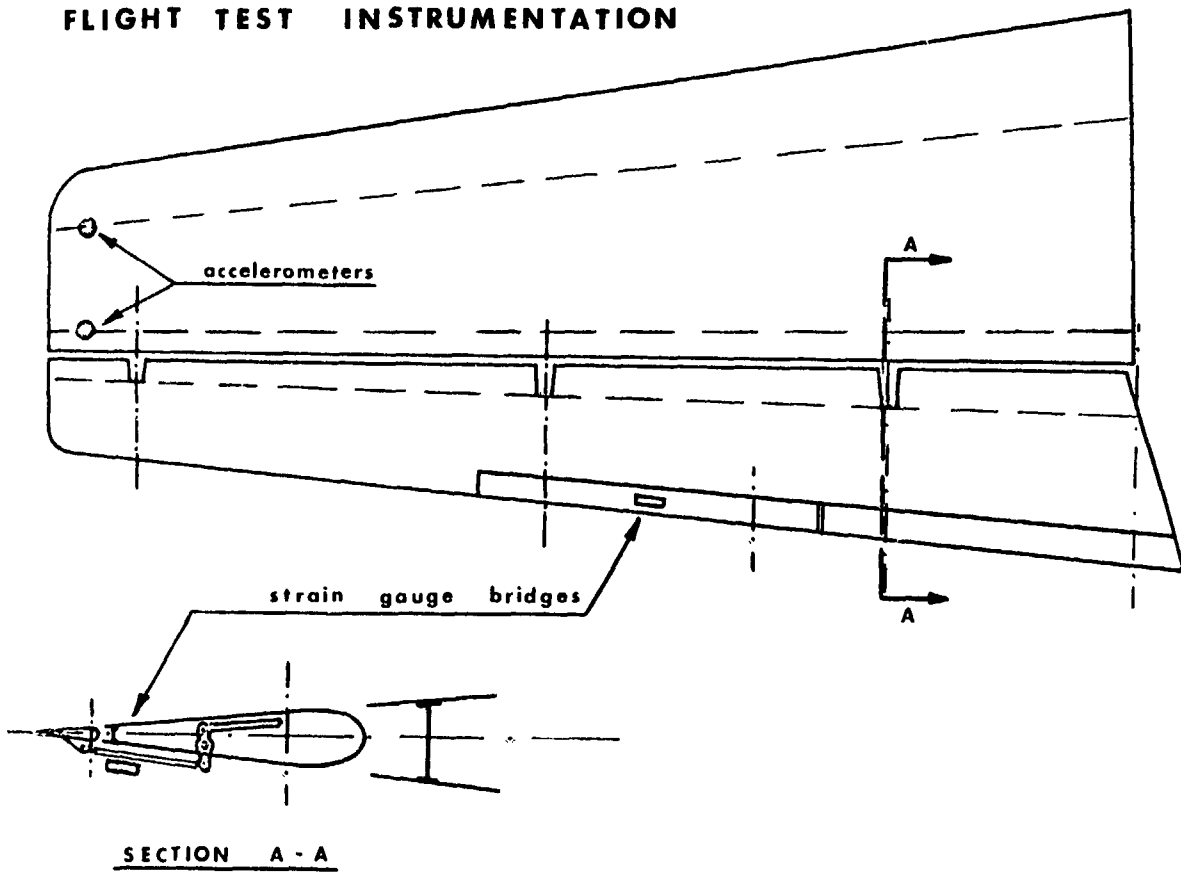
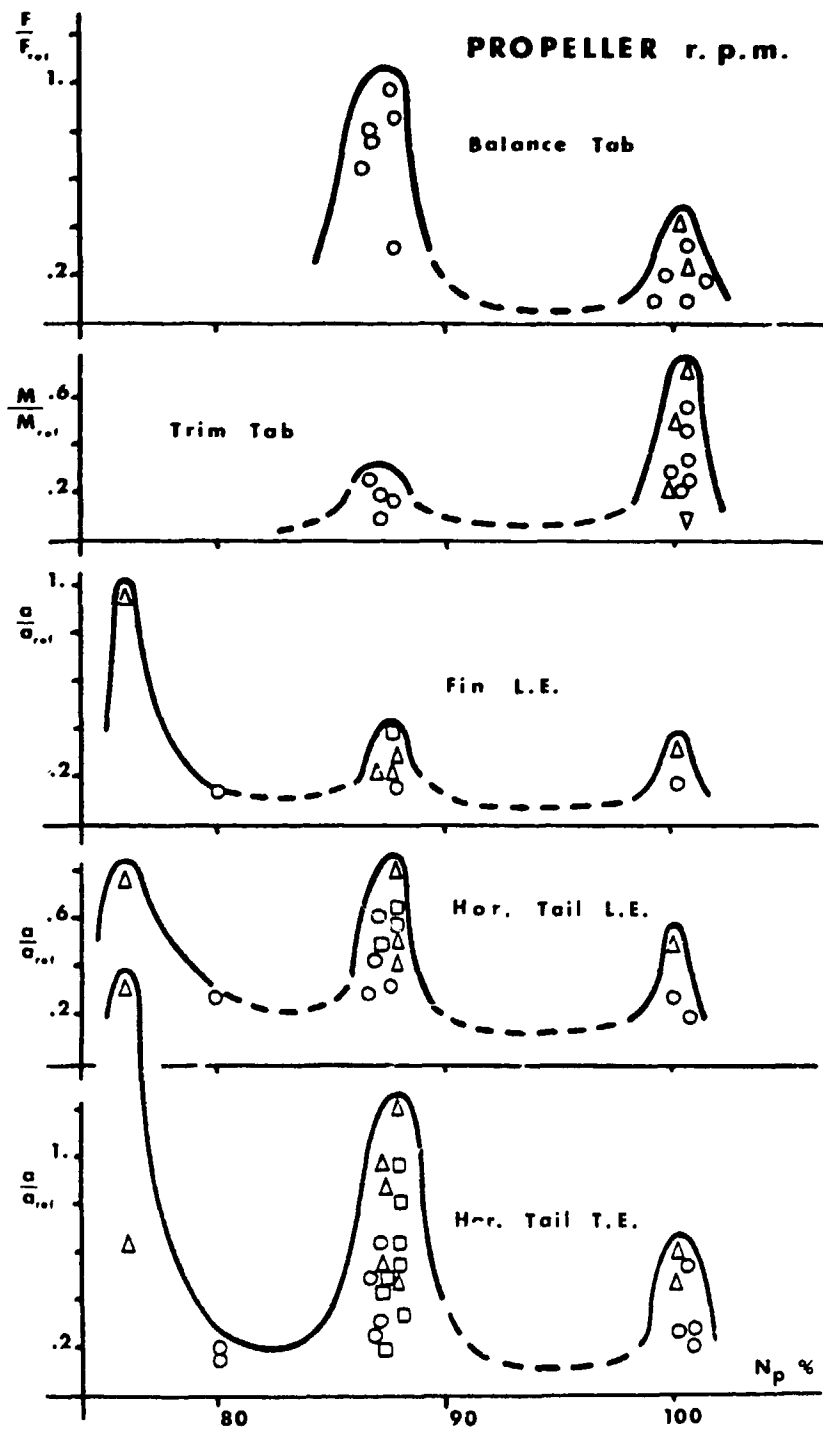FIG. 1

FLIGHT TEST INSTRUMENTATION
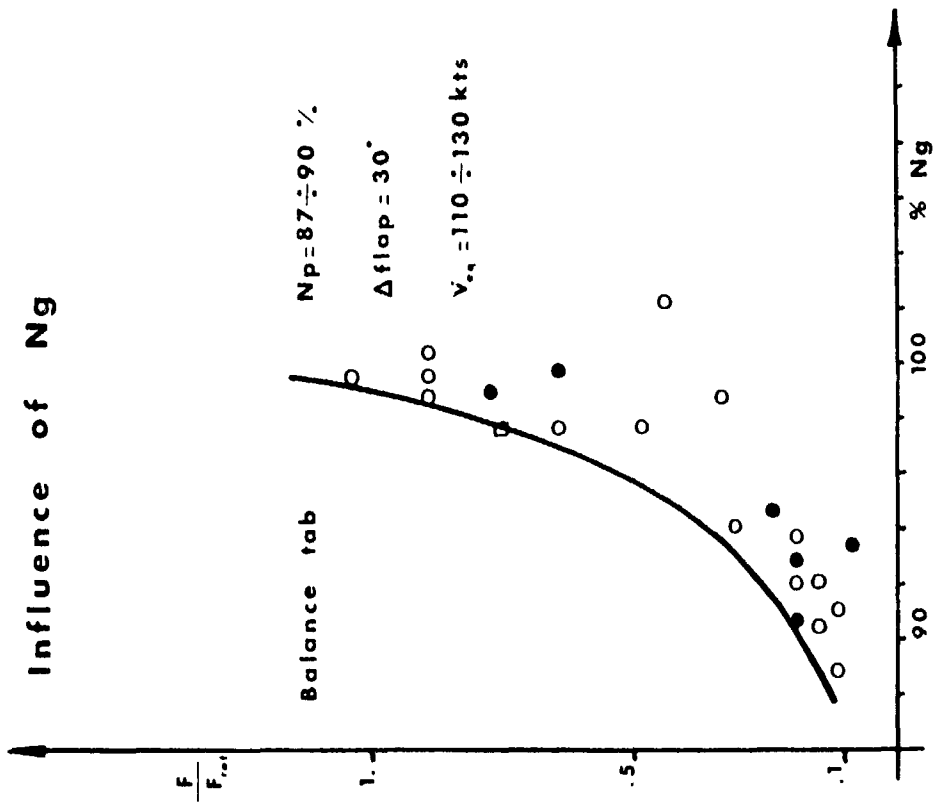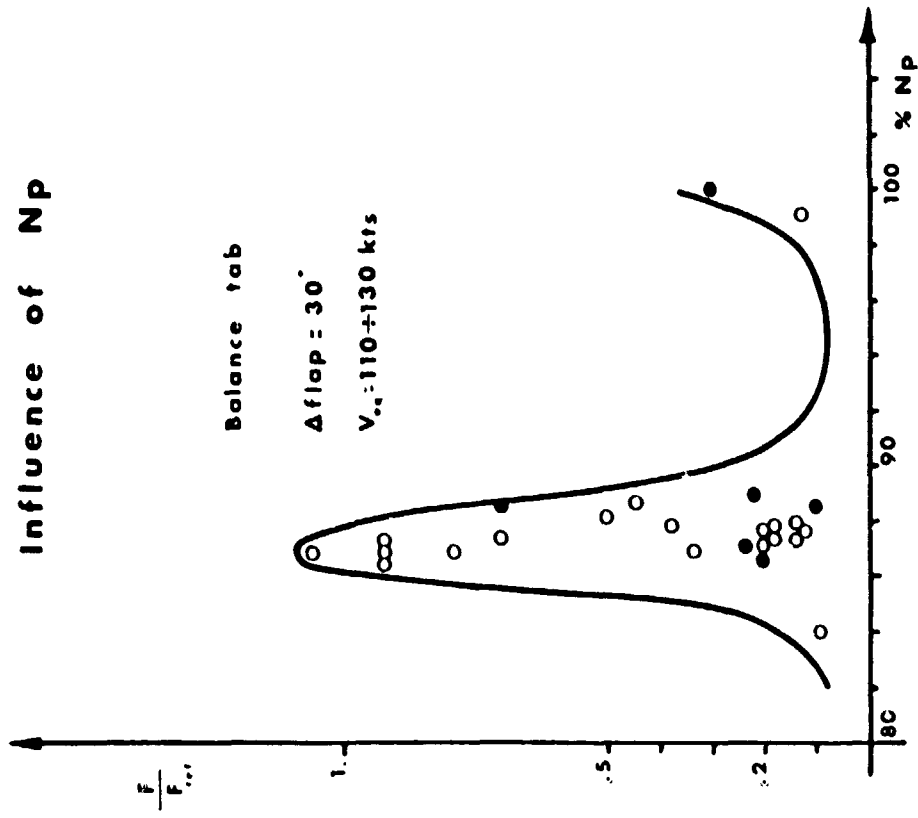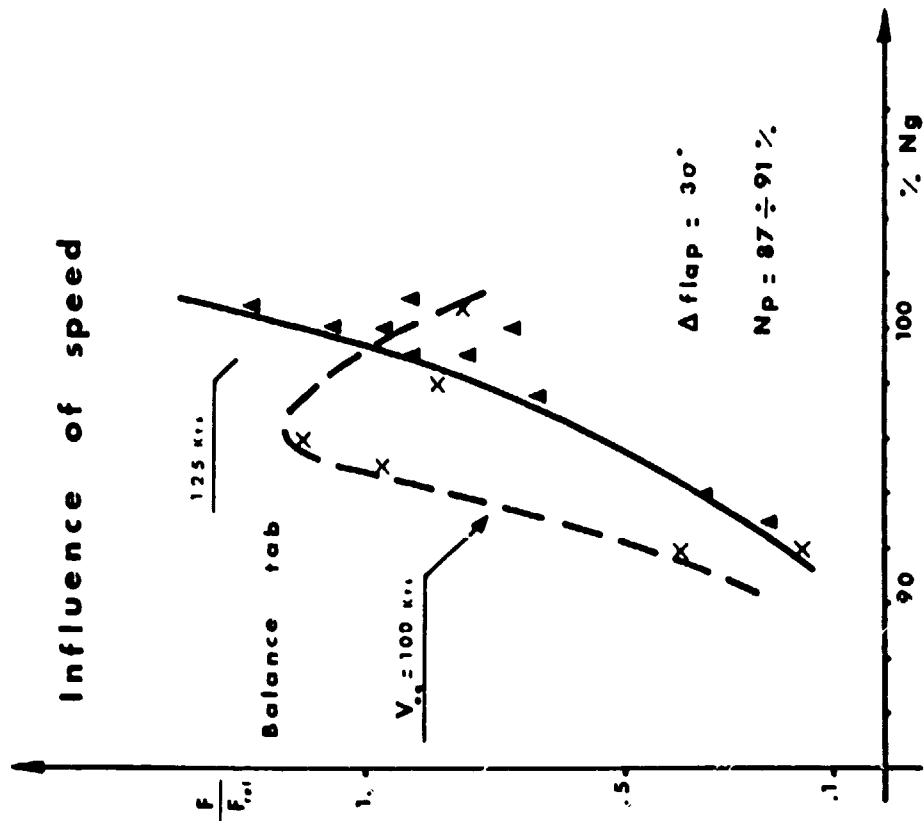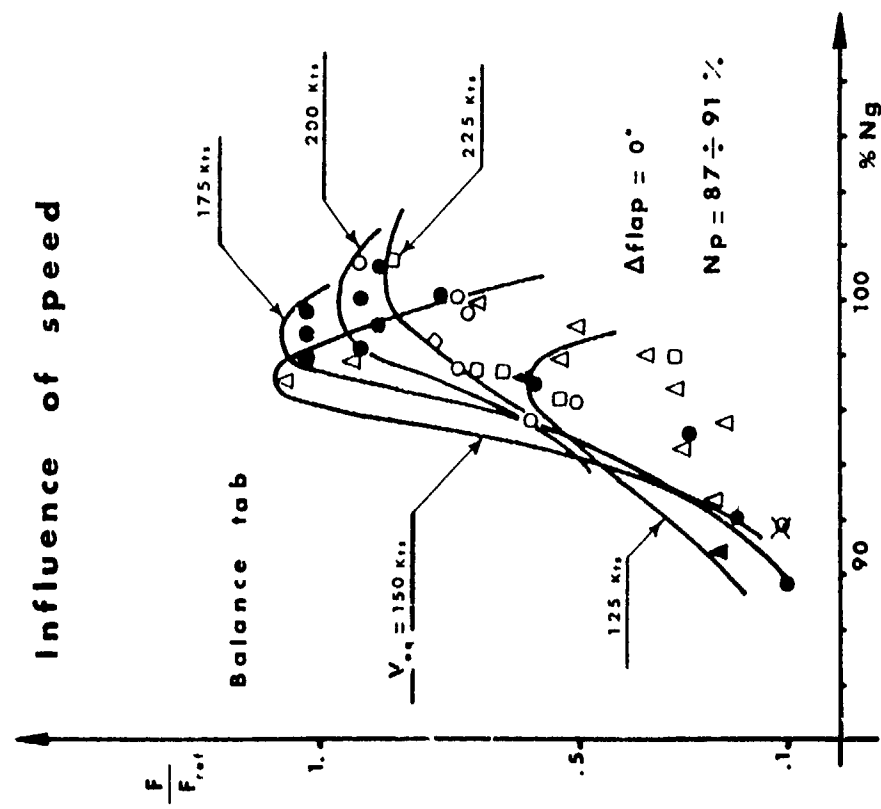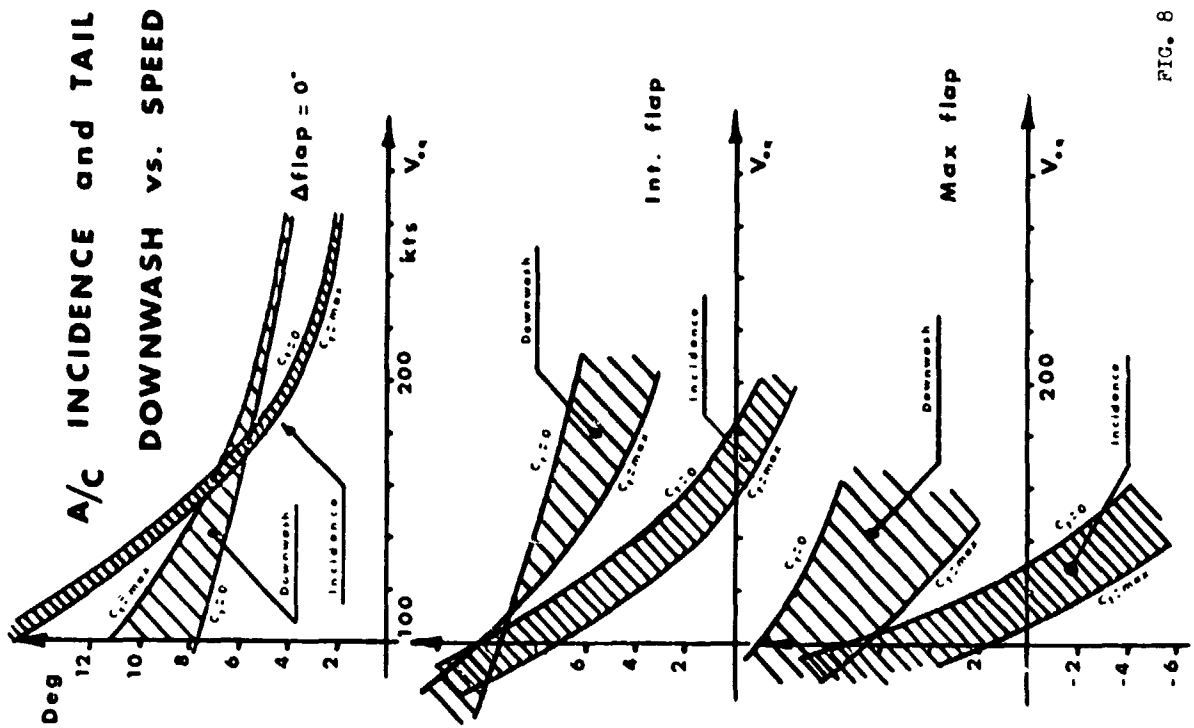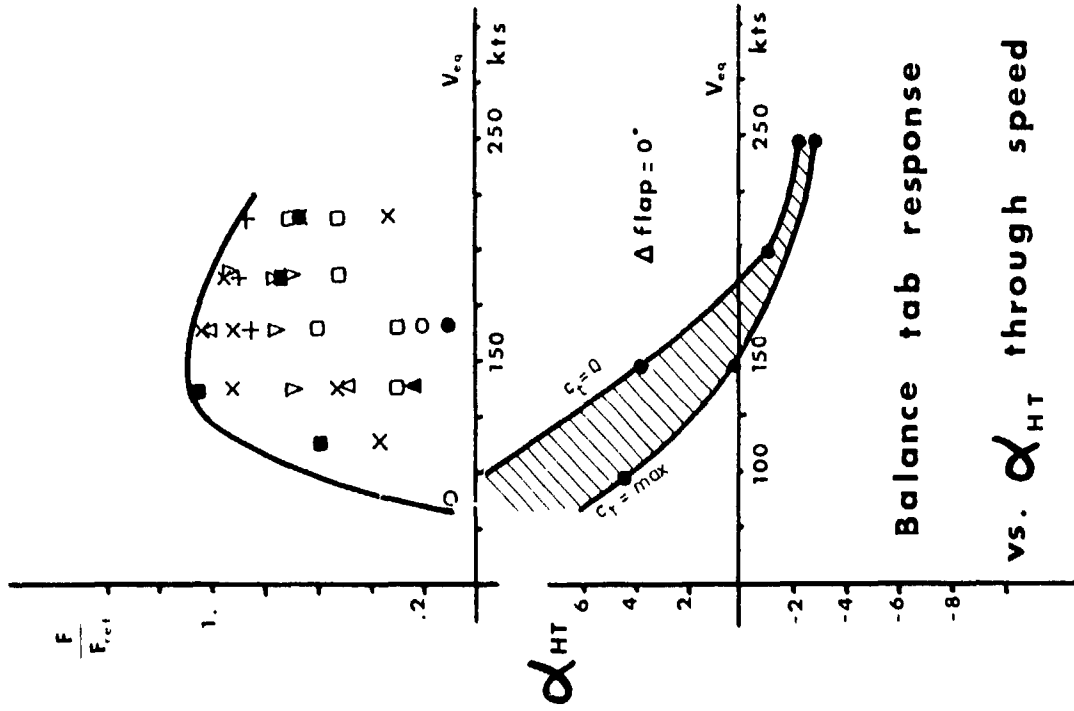
accelerometers

strain gauge bridges

SECTION A - A

FIG. 2

FIG. 3

Influence of Ng

Balance tab

Np = 87 ÷ 90 %.

Δflap = 30°

V_{eq} = 110 ÷ 130 kts

FIG. 5

Influence of Np

Balance tab

Δflap = 30°

V_{eq} = 110 ÷ 130 kts

FIG. 4

Influence of speed

Balance tab

$\frac{F}{F_{ref}}$

$V_{ea} = 150 \, \text{k..}$

175 k..

200 k..

225 k..

125 k..

$\Delta flap = 0°$

$Np = 87 \div 91 \%$

% Ng

FIG. 7

Influence of speed

Balance tab

$\frac{F}{F_{ref}}$

125 k..

$V_{ea} = 100 \, \text{k..}$

$\Delta flap = 30°$

$Np = 87 \div 91 \%$

% Ng

FIG. 6

FIG. 9

Balance tab response

vs. α_{HT} through speed

A/C INCIDENCE and TAIL

DOWNWASH vs. SPEED

FIG. 8

Original distribution

Modified distribution

ELEVATOR   BALLAST   MASSES

FIG. 15

Balance tab response

vs. α_{HT} through flap position

FIG 10

Balance tab response vs. Ng and Flap

PROTOTYPE A/C

$N_p = 87 \div 91$ %

$V_{eq} = 110 \div 150$ kts

FIG 11

Balance tab response vs. Ng and Speed

PROTOTYPE A/C

Δ flap $= 0°$
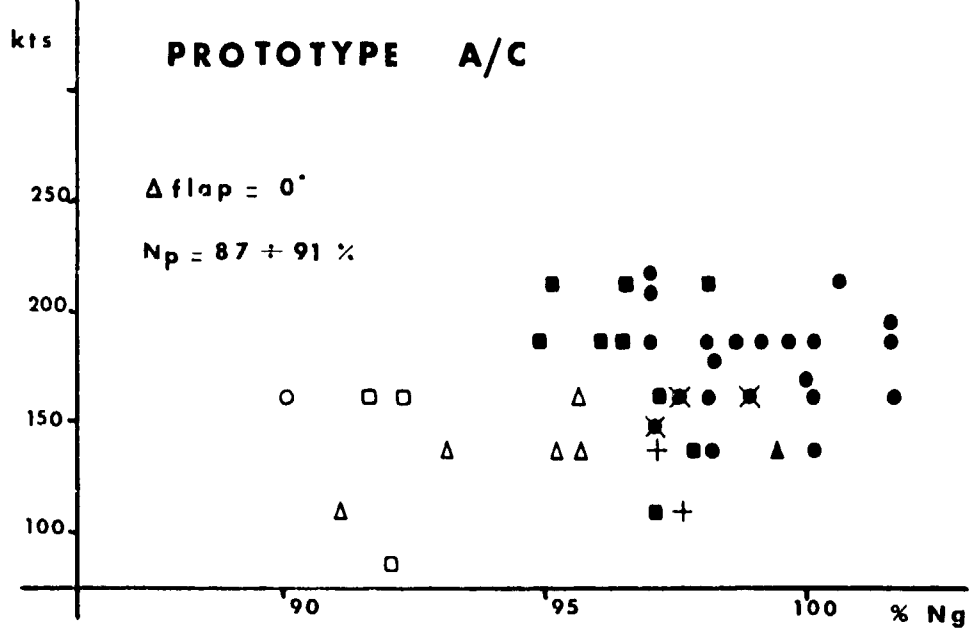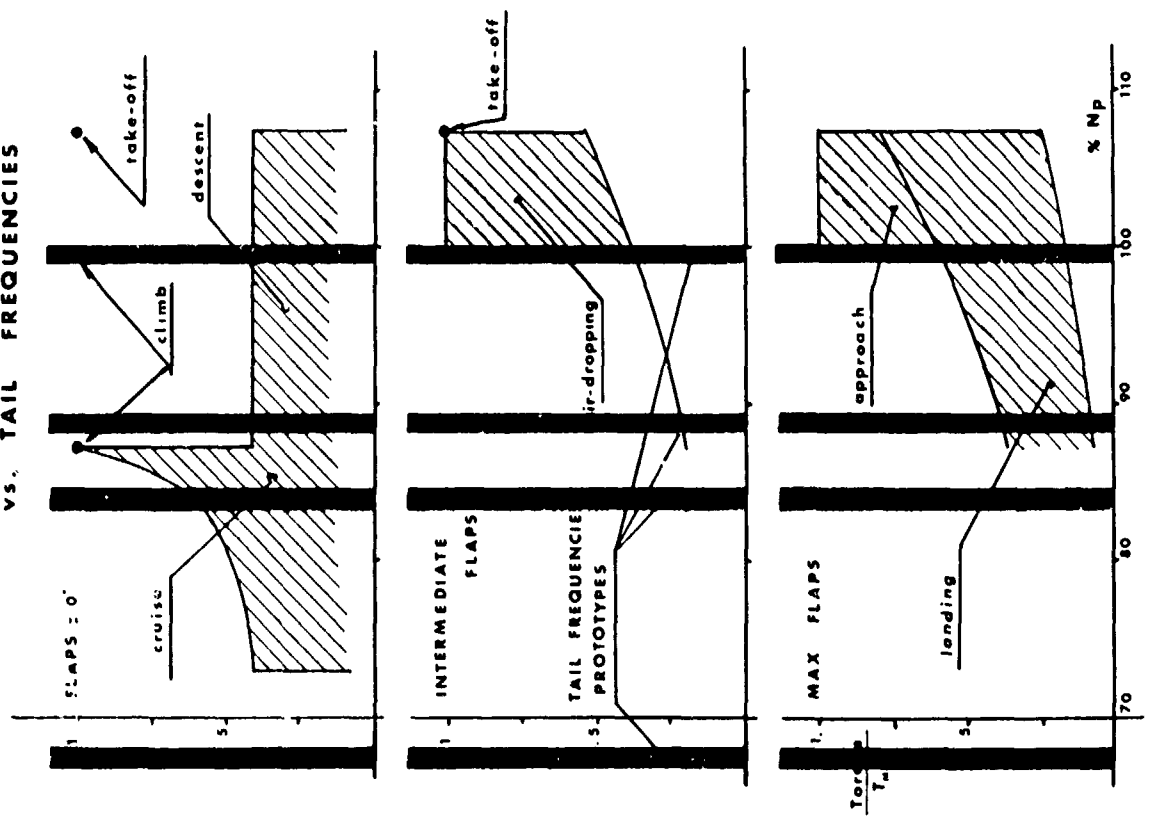
$N_p = 87 \div 91$ %
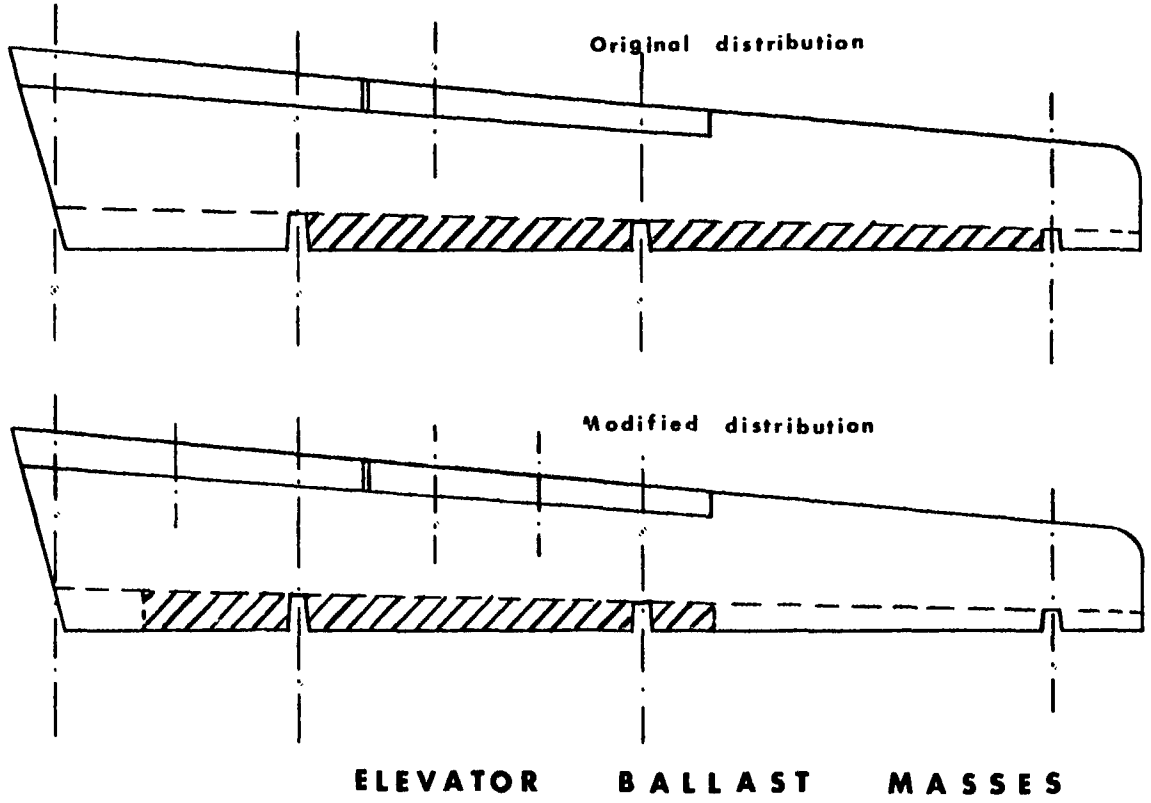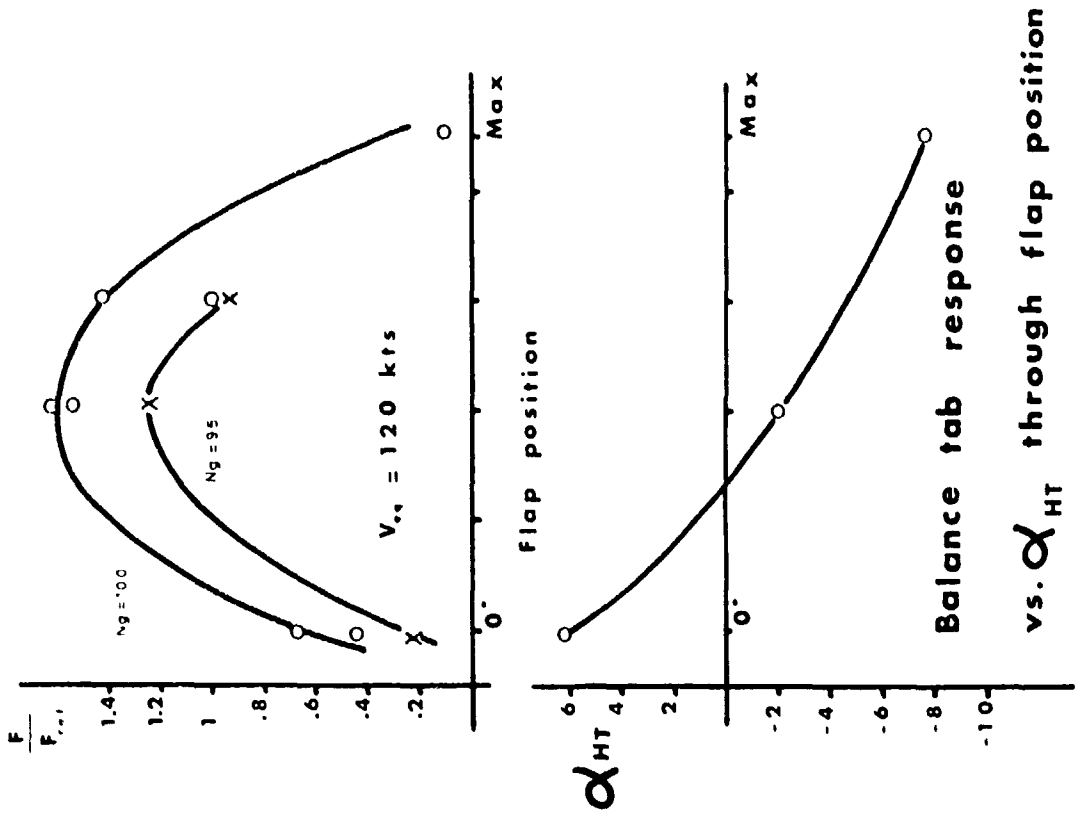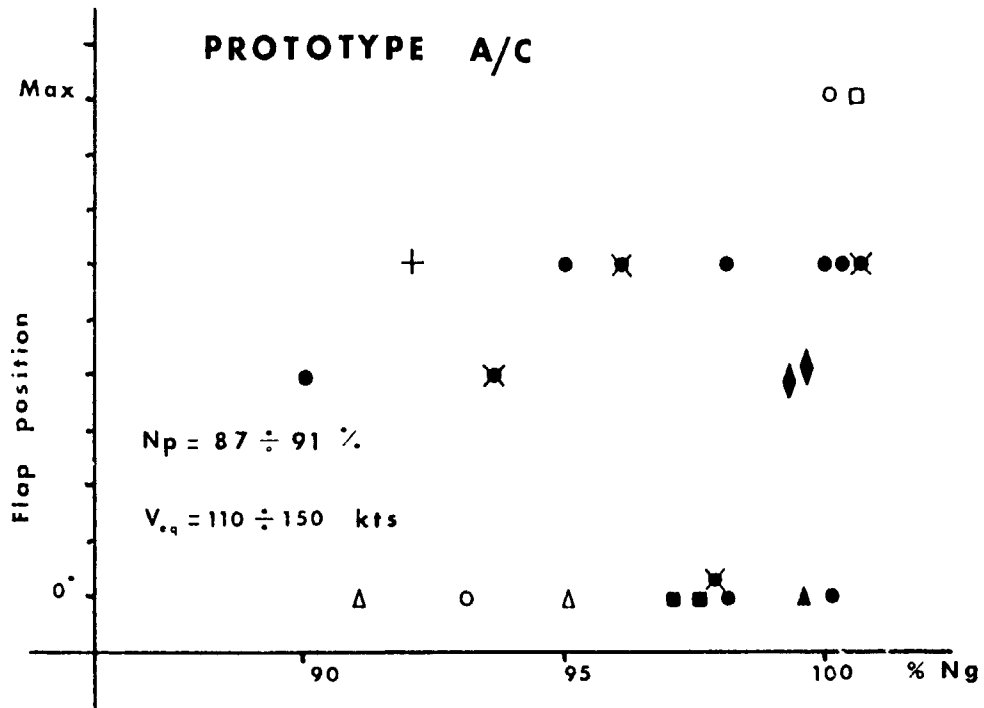
FIG 12

HOR. TAIL MODE SHAPES

PROTOTYPE
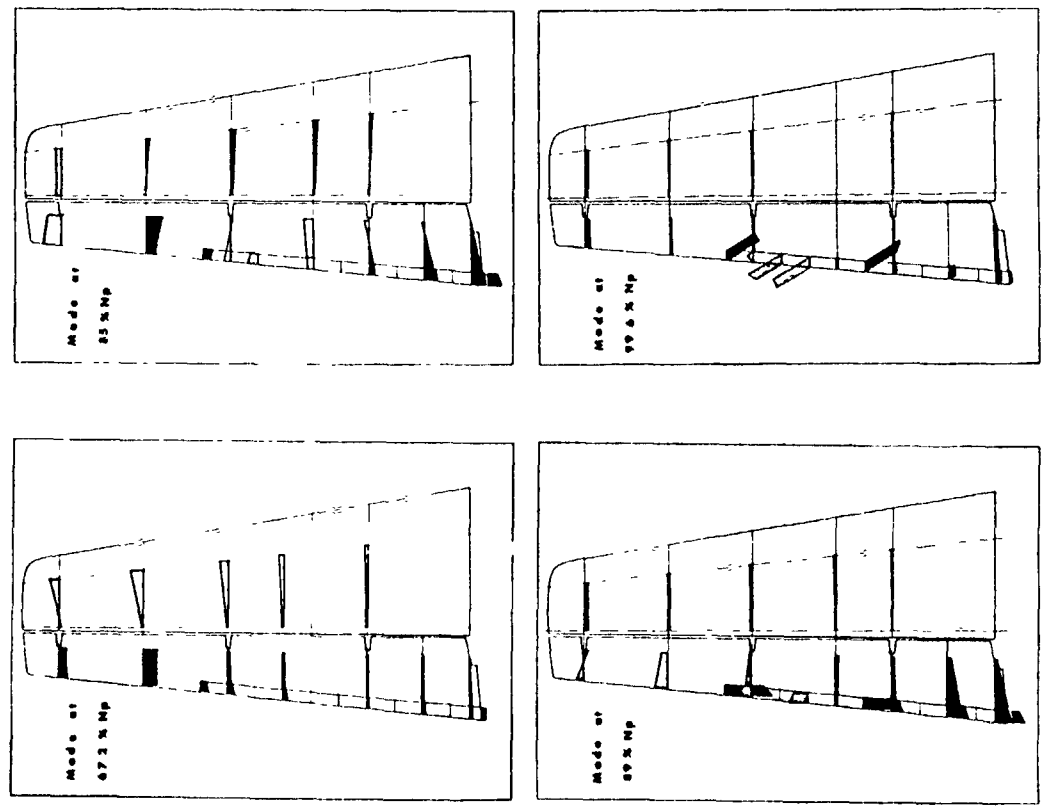
FIG. 14

ENGINE OPERATIVE ENVELOPE
vs. TAIL FREQUENCIES

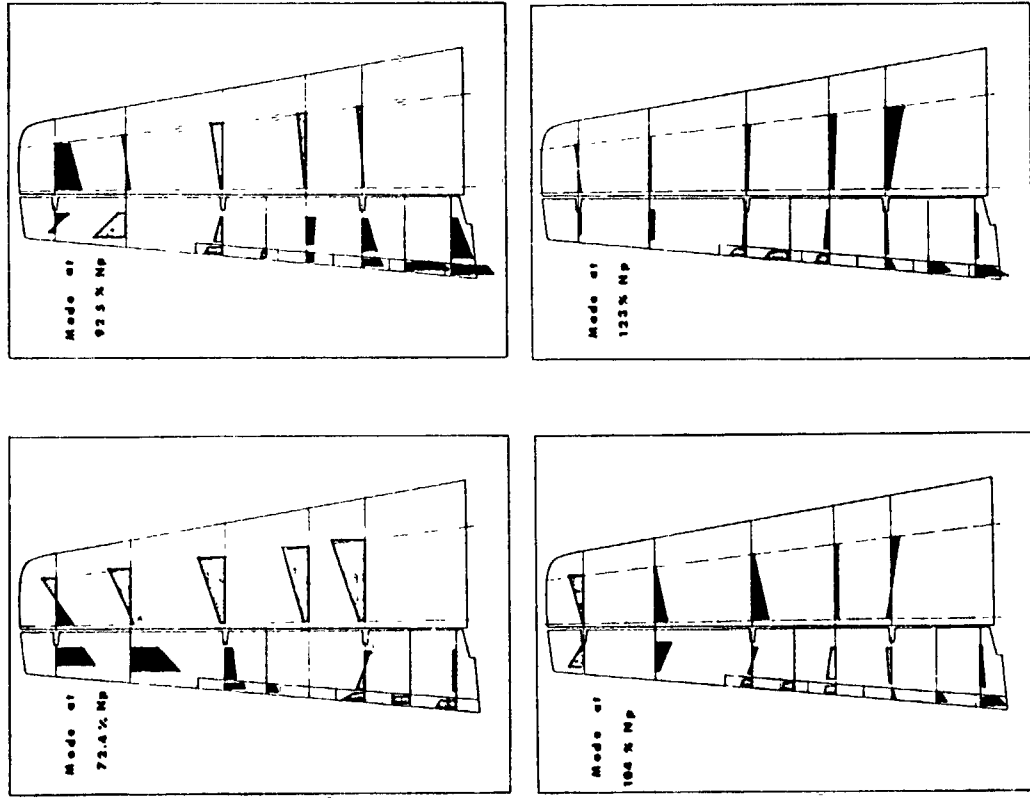FIG. 13

HOR.TAIL MODE SHAPES PRODUCTION A/C

Mode at 72.4 % Np

Mode at 104 % Np

Mode at 92.5 % Np

Mode at 123 % Np

FIG. 17

ENGINE OPERATIVE ENVELOPE

VS. TAIL FREQUENCIES

FLAPS = 0°

cruise

climb

take-off

descent

INTERMEDIATE FLAPS

TAIL FREQUENCIES
PRODUCTION A/C

take-off

air dropping

MAX FLAPS

approach

landing

$\frac{1}{\text{Torque}} T_{max}$

% Np

FIG. 16

Balance tab response vs. Ng and Flap

PRODUCTION   A/C

Max

$N_p = 87 \div 95$ %

$V_{eq} = 110 \div 150$ kts

Flap position

0°

90   95   100   % Ng

FIG. 18

Balance tab response vs. Ng and Speed

PRODUCTION   A/C

V_{eq}

kts

Δ flap = 0°

$N_p = 87 : 95$ %

250

200

150

100

90   95   100   % Ng
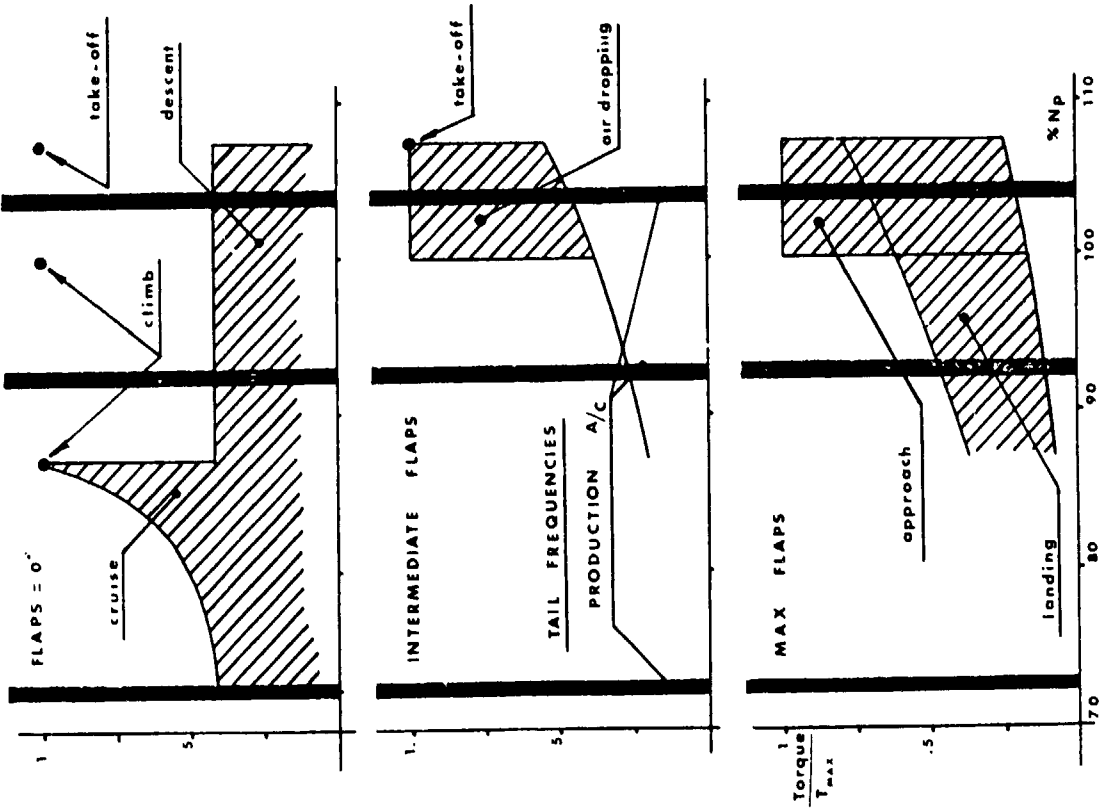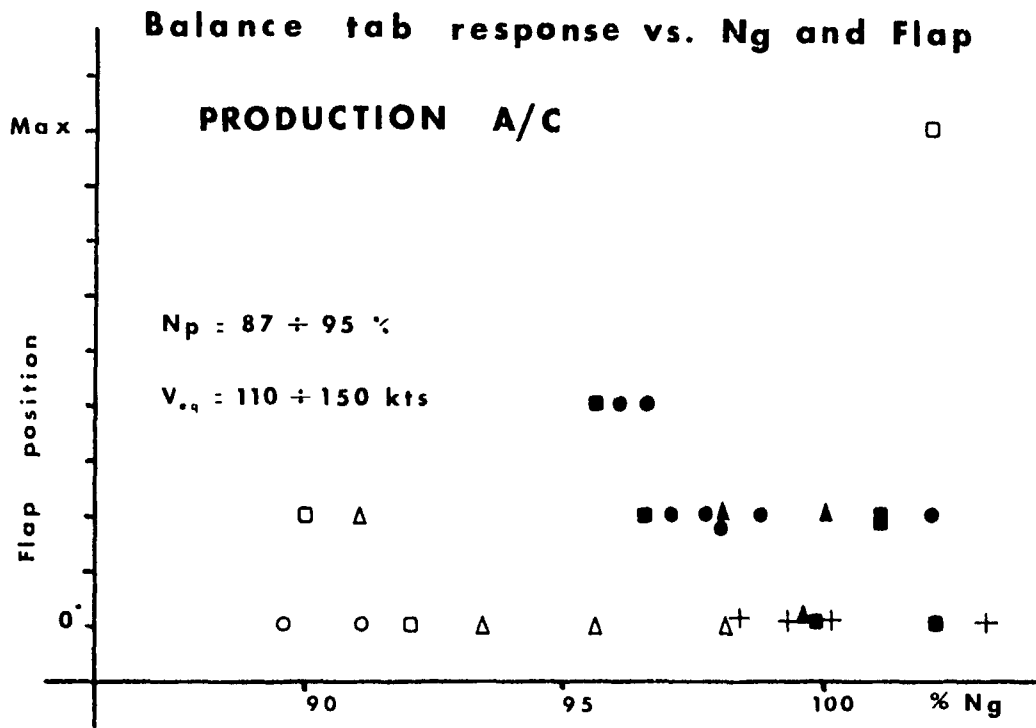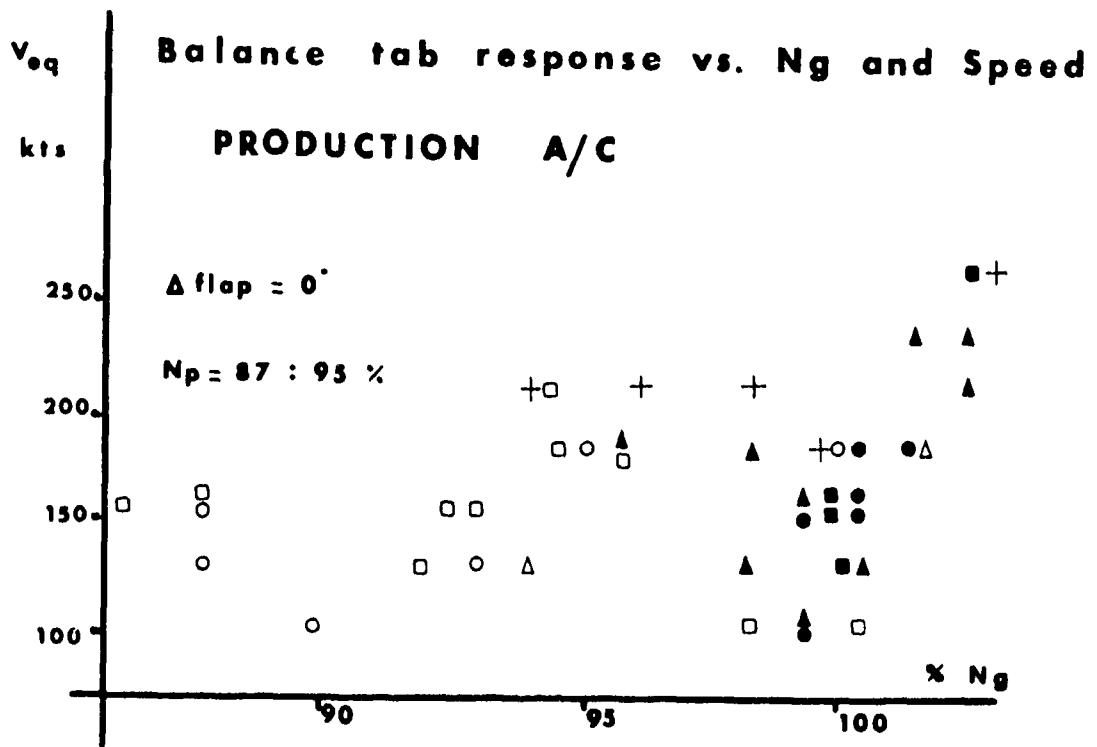
FIG. 19

FLUTTER CALCULATION FOR THE VIGGEN AIRCRAFT WITH ALLOWANCE
FOR LEADING EDGE VORTEX EFFECT

by

Valter J. E. Stark
Research Scientist
Saab-Scania AB, Aerospace Division
Linkoping
Sweden

SUMMARY

An application in a flutter calculation for the Viggen aircraft of a new program system for aero-elastic calculations is briefly described. The result which is checked against an independent calculation shows that a large flutter margin exists. For increasing angle of incidence, however, the margin may decrease due to the effect of the leading edge vortices. An estimate of the decrease was obtained by applying a correction factor based on measured pressure distributions for steady flow to the calculated lift distribution. This estimate may be only slightly erroneous, for it appears that the flutter speed is essentially determined by the stiffness terms of the equations of motion in this case.

SYMBOLS

$\underline{a}$ Aerodynamic matrix; $\underline{a} = \underline{a}(p) = \left[a_{i,j} \right]$

$a_{i,j}$ Dimensionless aerodynamic coefficient; integral of $H_i \Delta c_{pj}$ over the lifting surfaces divided by the reference area S

Δc_{pj} Dimensionless pressure jump; Δc_{pj} corresponds to an oscillation with the amplitude LH_j and is referred to the free-stream dynamic pressure $\rho U^2/2$.

H_j Dimensionless shape function representing the deflection in the normal direction of the surface in the jth deflection mode

L Reference length to be specified in the particular application

M Free-stream Mach number

m Mass ratio; $m = \rho SL/M_{1,1}$

$\underline{m}$ Normalized mass matrix; $\underline{m} = \left[m_{i,j} \right]$, $m_{i,j} = M_{i,j}/M_{1,1}$, $M_{i,j}$ = true generalized mass.

p Dimensionless complex frequency; $p = \mu + i\omega$ and is referred to U/L.

S Reference area to be specified in the particular application

$\underline{s}$ Normalized stiffness matrix; $\underline{s} = \left[s_{i,j} \right]$, $s_{i,j} = S_{i,j}/S_{1,1}$, $S_{i,j}$ = true stiffness matrix element.

U Flight speed

v Velocity ratio; $v = U/(\omega_1^* L)$

v_f Flutter critical value of v or dimensionless flutter speed

x', y', z' Rectangular coordinates with the x'-axis in the free-stream direction

μ Dimensionless damping coefficient; the logarithmic decrement $\Lambda = 2\pi\mu/\omega$.

ρ Free-stream density

ω^* Circular frequency; $\omega = \omega^* L/U$

ω_i^* Natural circular frequency for the ith mode

1. INTRODUCTION

The powerful computers now available permit efficient aeroelastic calculations, but efficient computer programs are also needed. A new program system written in Fortran and running on the CDC 6600 and the UNIVAC 1108 computers has therefore been developed. Some of the numerical methods which are used in this system and an application of the system in a flutter calculation for the Viggen aircraft are simultaneously reviewed in this paper.

It is important to check the system carefully. We therefore show results of the application together with corresponding results of another independent calculation. This was conducted by D. Cooley of the USAF Flight Dynamics Laboratory by courtesy of the U. S. Air Force. He employed the same basic data as we did, but his calculation was made by means of computer programs available to the Flight Dynamics Laboratory.

It is well-known that the lift distribution on a wing with highly swept leading edge exhibits a change when the angle of incidence increases. This change is due to the appearing leading edge vortices. Due to this, the local lift curve slope increases which is particularly pronounced on the outboard part of the wing. Consequently, there is reason to suspect that the unsteady local aerodynamic derivatives likewise increase, and that the flutter speed therefore decreases.

Such a decrease actually exists, for it has been observed in an experimental investigation by D. A. Brown (1963). This investigation, in which a rigid spring-suspended semispan model was used,

has been reviewed by Cooley and Cook (1964).

The leading edge vortex effect could be investigated by measuring unsteady pressure distributions on an oscillating model, but this is expensive. As a substitute, we have therefore utilized steady pressure distributions measured on a rigid model. By means of these data and local lift curve slopes evaluated on the basis of them for some angles of incidence, a correction factor varying along the span was formed and applied to the calculated lift distribution before evaluating the generalized aerodynamic force integrals.

The resulting reduction of the flutter speed represents eventually rather accurately the effect of the leading edge vortices, for it has been found, although only for zero angle of incidence, that it is the stiffness terms which are the important terms in the equations of motion. The damping terms can be deleted, namely, without affecting the flutter speed appreciably in the Viggen case. This simplification was proposed by Pines (1958) and Pines and Newman (1973), and Ferman (1967) found in many examples for primary surfaces that it yielded a quite accurate approximation to the flutter speed. It is therefore possible that the reduction obtained is significant.

2. THE MAIN PROGRAM

The program system consists of a number of subroutines which are grouped in so called subprograms. These are called from a simple main program which essentially consists of the subprogram calls. The subprograms can be executed independently of each other and each of them can read input data from a file generated by another subprogram. The subprograms used in the application are called EIGMOD, HCOEFF, PCP, and STAB. EIGMOD is a simple program which is mainly used for reading ground vibration test data. The basic input data in the Viggen application consist of data of this kind.

3. PROGRAM FOR ANALYTIC DEFLECTION FUNCTION CALCULATION

It is assumed that the aircraft can be modeled as a configuration of thin trapezoidal panels. The model employed in the Viggen application is shown in Fig. 1 and consists of four pairs of panels.
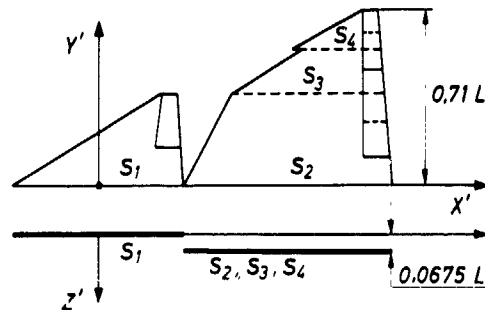

Fig. 1   Idealized Viggen model

HCOEFF defines analytic deflection functions. These are obtained by determining coefficients in linear combinations of given functions by the method of least squares. The given functions are functions of two variables and consist mainly of products of chordwise and spanwise factors as defined by Stark (1973). The factors are orthogonal polynomials which are such that the 2nd and 3rd
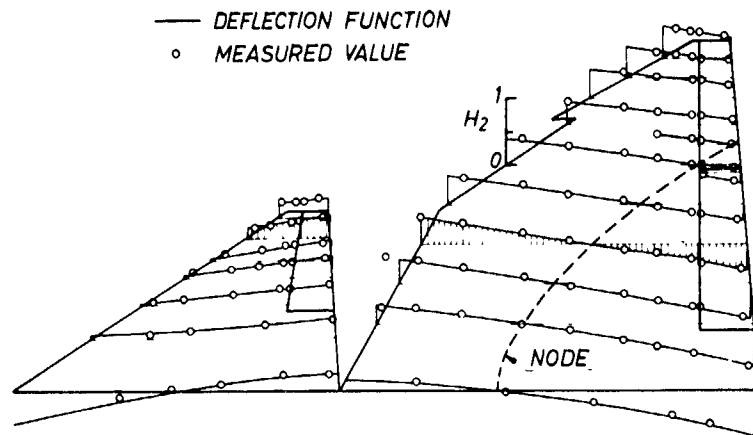

Fig. 2   Analytic representation of the body bending mode

order derivatives at free panel edges can be made to vanish. This yields a favourable behaviour.

Control-surface deflections can be treated by including special control-surface deflection functions in the combination and eventually by dividing the control-surface into parts. Such a division is shown in Fig. 1. The special deflection function for a control-surface part is zero outside the part and a 1st order polynomial inside the part. A typical example was shown by Stark (1973, p. 32).

One of the deflection functions determined in the Viggen case is shown in Fig. 2. Since only low-order modes are considered, control-surface deflections are not significant in this application.

By dividing the panels into small trapezoidal elements and by assigning appropriate elementary masses to the elements, the subprogram HCOEFF can also generate generalized mass matrices. In the Viggen application, however, the generalized masses were obtained from data measured in the ground vibration test. The stiffness matrix elements were obtained by multiplying the generalized masses by the squares of the measured natural frequencies.

4. PROGRAM FOR AERODYNAMIC MATRIX CALCULATION

PCP is a program for calculation of the aerodynamic matrix. It is based on the Polar Coordinate Method described by Stark (1970,1972,1973,1974) and is applicable for subsonic Mach numbers. In the Polar Coordinate Method, the jump in the advanced velocity potential (which was defined by Stark (1968)) is approximated by a linear combination of given potential jumps. Like the functions employed in the combination for the deflection, these jumps are partly products of simple chordwise and spanwise factors (integrals of Birnbaum-Glauert functions) and partly special jumps. The latter correspond to the special control-surface deflection functions and were defined by Stark(1972). The coefficients of the special jumps are known and equal to those of the special control-surface deflection functions, while the coefficients of the simple potential jumps are to be solved from a set of linear equations. The matrix of this set is obtained by considering the velocity field that corresponds to each given potential jump and by calculating the normal component of this field at appropriate control points. This calculation is performed by subtracting the kernel function singularity in a suitable way and by employing polar integration variables for evaluating the resulting double integrals. This formulation implies that the normal velocity component does not ordinarily appear as a d.fference between large numbers and that those integrals, which must be evaluated numerically, receive well-behaved integrands.

The function that is used for subtraction of the kernel function singularity is a first order polynomial in the two surface variables and can at least in the steady case be said to be a tangent plane (See Stark (1970)) to the potential jump at the control point. The procedure can be employed when the singularity is confined to a single point. It is therefore applicable to the relation between the normal velocity and the potential jump, but not to the more often employed relation between the normal velocity and the pressure jump. It is believed that the tangent plane and polar coordinate formulation permits accurate calculation of the normal velocity component.

The velocity field, that corresponds to a given potential jump, is independent of the deflection modes. The matrix of the linear equations can therefore be stored on a file for later use in combination with arbitrary modes.

The pressure jump can easily be calculated when the advanced velocity potential jump has been determined. Fig. 3 shows a dimensionless pressure jump that corresponds to outboard control-surface oscillation with unit angular amplitude.
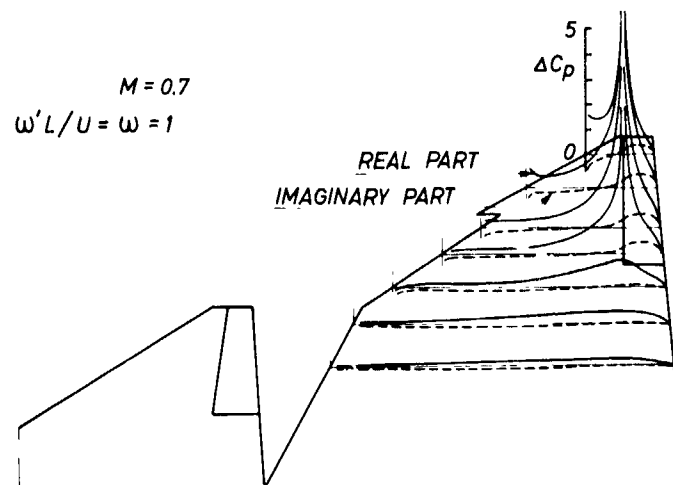

$$M = 0.7$$
$$\omega'L/U = \omega = 1$$

REAL PART
IMAGINARY PART

Fig. 3   Loading due to outboard control-surface rotation

5. PROGRAM FOR FLUTTER CALCULATION

STAB is a program for determination of the flutter speed and the divergence speed and may be used for calculation of frequency and damping of aeroelastic natural modes as functions of the flight

speed. It can operate in accordance with the p method, the p-k method (See Hassig (1971)), the V-g method, or the simplified method of Pines (1958). In case of the p method or the p-k method, the eigenvalue problem is solved by iteration. In each iteration step, an approximate aerodynamic matrix is first calculated by using the eigenvalue obtained in the preceding step. The resulting linear eigenvalue problem is then solved by application of a program for solution of eigenvalues of a general complex matrix. The program developed by Fair (1971) is used for this purpose. Only a few iteration steps (3 or 4) are required which depends on the use of suitable initial values. The eigenvalues are calculated as functions of the flight speed and those determined for one speed are used as initial values for the next speed.

A simple approximate formula

$$\underline{a}(p) = \sum_{r=1}^{r_s} \underline{a}^{(r)} p^{r-1} + \underline{b}\, p\, \ln(p) \tag{1}$$

is used for the dimensionless aerodynamic matrix $\underline{a}(p)$. The quantities $\underline{a}^{(r)}$ and $\underline{b}$ are real matrices and p is the generalized complex reduced frequency, $p = \mu + i\omega$. This is referred to U/L where U is the free-stream velocity and L a reference length (See Fig. 1). The logarithmic term seems to be important only if strip theory is used or if the aspect ratio is large. In the present application, the matrix $\underline{a}(p)$ was calculated for a few imaginary values of p (by the PCP program) and the matrices $\underline{a}^{(r)}$ were then determined by the method of least squares. The result obtained for the aerodynamic matrix element $a_{2,2}(p)$, which corresponds to the mode illustrated in Fig. 2, is shown in Fig. 4. The corresponding reference area $S = 0.84\, L^2$.
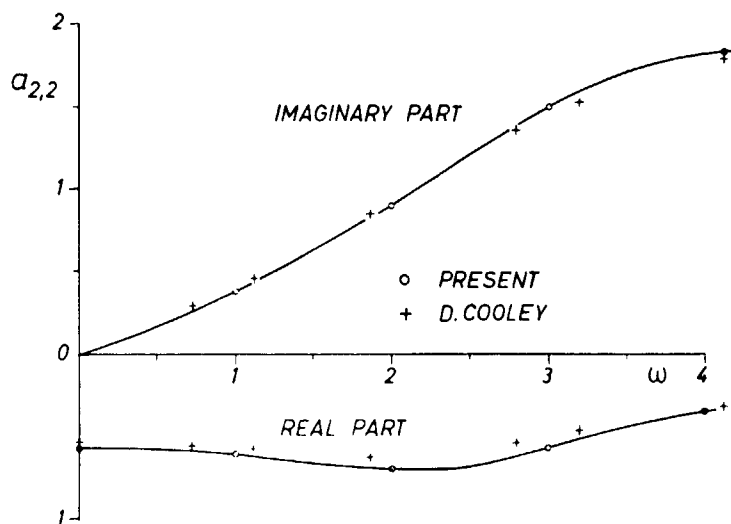

Fig. 4   Dimensionless virtual work in body bending due to body bending

6. COMPARATIVE CALCULATION

As mentioned in the introduction, the Viggen example has also been treated by D. Cooley of the USAF Flight Dynamics Laboratory (FDL). In his treatment, the aerodynamic matrix was calculated by the refined Doublet Lattice algorithm of Giesing, Kalman, and Rodden (1972) which is based on the Lifting Line Element approach that was independently proposed for the unsteady case by Stark (See Landahl and Stark (1968)) and Albano and Rodden (1969) at the AIAA 6th Aerospace Sciences Meeting in 1968. This approach also forms the basis of computer programs early employed in flutter calculations for the Viggen aircraft as mentioned by Stark and Landahl (1968) and Wittmeyer (1968).
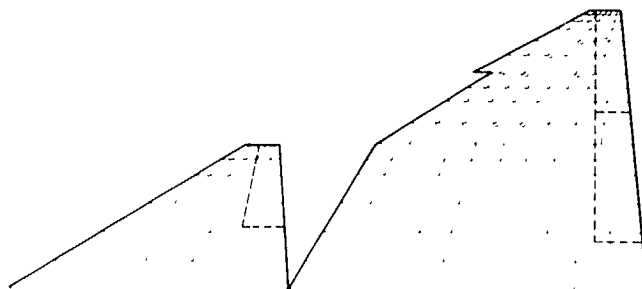

Fig. 5   Lattice employed by D. Cooley

The lifting line elements employed in the Doublet Lattice algorithm are defined by dividing the wing panels into relatively small boxes; each box carries a lifting line and a control point. The boxes employed by D. Cooley are shown in Fig. 5 and amount in number to 158 on one half of the configuration. If control-surface deflections had been significant in the application, a refined lattice would have been required.

Results from Cooley's calculation are included in Fig. 4 and are seen to be in close agreement with those obtained by the PCP program.

7. RESULTS FROM THE FLUTTER CALCULATION

The matrices $\underline{m}$ and $\underline{s}$ in the characteristic equation

$$\left| \underline{m}(vp)^2 + \underline{s} + \frac{1}{2} mv^2 \underline{a}(p) \right| = 0 \tag{2}$$

represent normalized mass and stiffness matrices. These are defined such that the elements $m_{1,1}$ and $s_{1,1}$ are equal to unity. The parameter m is a dimensionless mass ratio which is defined by

$$m = \rho \, SL/M_{1,1} \tag{3}$$

and v a dimensionless velocity ratio defined by

$$v = U/(\omega_1' L) \tag{4}$$

$M_{1,1}$ and ω_1' are the true generalized mass and the natural frequency (in vacuum) that correspond to $m_{1,1}$ and $s_{1,1}$. The matrix $\underline{a}(p)$ is the dimensionless aerodynamic matrix (See SYMBOLS).

The rigid translation and pitch modes plus five natural modes from the vibration test were included in the linear combination for the deflection in the Viggen case. The modes are symmetric and the elastic modes are characterized as follows:

1	Wing bending	with frequency	$\omega_1' = 8.63$ Hz
2	Body bending	"	$1.40\,\omega_1'$
3	Engine mode	"	$1.86\,\omega_1'$
4	Wing torsion	"	$2.48\,\omega_1'$
5	Motion in the wing plane	"	$2.59\,\omega_1'$

The roots of the characteristic equation (2) were solved by the p method. When v increases from zero, the roots move from starting points on the imaginary axis and form loci in the complex vp-plane. The reason for considering vp instead of p is that vp for $m = 0$ is equal to the ratios between the natural frequencies and the first natural frequency; $vp = (U/\omega_1')(p'L/U) = p'/\omega_1'$. If m is small, the starting points are approximately given by these ratios. The loci obtained are shown in the left hand part of Fig. 6 for $M = 0.7$ and standard day sea-level density. For increasing v, the roots first move into the stable left hand half of the vp-plane, but for a sufficiently large value of v one of them turns back and crosses the imaginary axis. The axis is reached for $v = v_f$ which is the flutter critical value of the velocity ratio.

The dimensionless flutter speed v_f has been determined for various Mach numbers and standard-day sea level density. It has been plotted in Fig. 7 where it is represented by the upper solid curve.
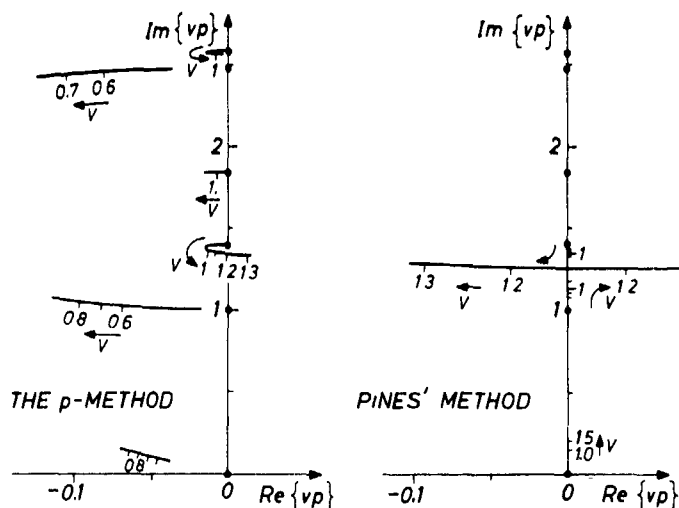

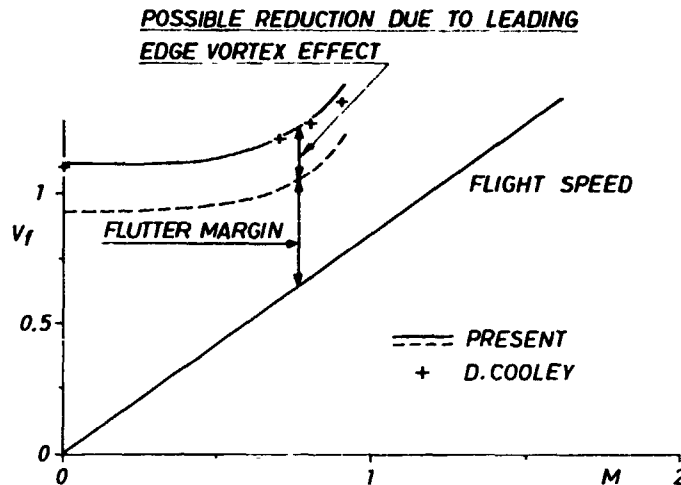Fig. 6   Root locus plot for $M = 0.7$ and sea level density

Fig. 7   Flutter margin for the Viggen aircraft

The comparative calculation of D. Cooley included of course solution of the eigenvalue problem. He employed the p-k method for this purpose. It is seen from Fig. 7 where his results are plotted that the flutter speeds obtained in the two calculations are in good agreement.

8.   TEST OF PINES' APPROXIMATE METHOD

Pines (1958) and Landahl (1964) emphasized long ago that flutter is often associated with a loss of resultant stiffness and that an approximate flutter speed can therefore be calculated by neglecting aerodynamic damping terms. This simplification which Pines and Newman (1973) consider useful for primary surfaces is interesting in the Viggen case for a particular reason.

The simplification has been tested by repeating the flutter calculation and thereby using a modified aerodynamic matrix. The modified matrix consisted of the zero order matrix $\underline{a}(0) = \underline{a}^{(1)}$ instead of the varying matrix $\underline{a}(p)$. The result is shown in the right hand part of Fig. 6.

For small values of v, all the roots obtained by the approximate method lie on the imaginary axis, and three of them are seen to move when v increases. The roots for the wing bending mode and the body bending mode which essentially form the aeroelastic mode that goes unstable move in directions toward each other until they meet. This occurs at a speed which, according to Pines, may be considered an approximation to the flutter speed. For still higher speeds, the two roots leave the imaginary axis in opposite directions and one root thus goes unstable.

From the left hand part and the right hand part of the figure we may read the values 1.20 and 1.15 respectively for the flutter speed. As the latter is only 4 % lower than the former, we conclude that Pines' simplification is useful also in the Viggen case.

9.   LEADING EDGE VORTEX EFFECT ON THE FLUTTER SPEED

The aerodynamic matrices employed in the calculations described above apply only to zero angle of incidence. For increasing angle of incidence, leading edge vortices appear and the lift distribution will therefore change. The local lift curve slope will also change and this indicates that the unsteady local aerodynamic coefficients will change. Their magnitude may increase in particular on the outboard part of the wing which implies that the flutter speed is likely to decrease when the angle of incidence increases. That such a decrease in the flutter speed for wings with a highly swept leading edge actually exists has been shown by Brown (1963).

We have tried to estimate the possible flutter speed reduction due to the vortices by using measured steady pressure distributions for determining a correction factor and by applying this to the calculated lift distribution. This seems to be a rather satisfactory procedure, for the outcome of the above-mentioned test of Pines' approximate method indicates that it is the stiffness terms which are the important terms in the equations of motion.

The correction factor is defined as the ratio between the local lift curve slope at the angle of incidence considered and the slope at zero angle of incidence. It is thus a function of the span-wise coordinate. For an angle of incidence of about 3 degrees, it has been found to increase from a value close to unity on the inboard half of the wing toward a value slightly greater than 2 at the wing tip. It was applied to the calculated unsteady lift distribution through modification of a subroutine in the PCP program.

The result of applying the correction factor appears from Fig. 7. The dashed curve represents the flutter speed that was obtained when using the factor described above. This corresponds roughly to the angle of incidence required for a 4 g pull out at M = 0.8 and sea level and seems to yield

a decrease in the flutter speed of about 17 per cent.

It should be mentioned that this factor is very approximate since the data available were not sufficient for an accurate determination. But it is not unreal. It probably has a different shape for a higher angle of incidence. A complex factor with unit modulus for simulating phase shifts was also applied and varied, but the effect of this was very small.

The straight line in Fig. 7 represents the flight speed for standard-day sea level temperature. By comparing the dashed curve to this, we see that a large flutter margin remains in spite of the reduction that may appear due to the leading edge vortex effect. The minimum value of the margin predicted for 3 degrees angle of incidence is about 50 per cent of the flight speed.

10. CONCLUSIONS

Results for aerodynamic coefficients and flutter speeds from two independent calculations for the Viggen aircraft for zero angle of incidence have been compared and found to be in close agreement. Due to the leading edge vortices which appear for increasing angle of incidence the flutter speed may decrease, however. This decrease has been estimated in a crude way. For an angle of incidence of about 3 degrees, which corresponds to a 4 g pull out at M = 0.8 and sea level, the estimated reduction amounts to 17 per cent. In spite of this, a satisfactory flutter margin seems to remain. It is emphasized that the estimated reduction is approximate and that more detailed investigations are desirable.

REFERENCES

1   Albano, E. and Rodden W. P., "A Doublet-Lattice Method for Calculating Lift Distributions on Oscillating Surfaces in Subsonic Flows', AIAA Journal, Vol. 7. No. 2, 1969, pp. 279-285, and No. 11, 1969, p. 2192.

2   Brown, D. A., "Flutter Model Tests of Advanced Wing Configurations at Initial Angles of Attack", North American Aviation, ASD-TDR-62-498, 1963.

3   Cooley, D. E. and Cook, R. F., "Dynamic Modeling - Its Past and Future", Proceedings of Symposium on Aeroelastic & Dynamic Modeling Technology, Aerospace Industries Association, RTD-TDR-63-4197, March 1964, pp. 15-48.

4   Fair, G., "ALLMAT: A TSS/360 Fortran IV Subroutine for Eigenvalues and Eigenvectors of a General Complex Matrix", NASA, TN D-7032, Jan. 1971.

5   Ferman, M. A., "Conceptual Flutter Analysis Techniques", McDonnell Company, Report F322, Febr. 1967.

6   Giesing, J. P., Kalman, T. F., and Rodden, W. P., "Subsonic Steady and Oscillating Aerodynamics for Multiple Interfering Wings and Bodies", Journal of Aircraft, Vol. 9,   . 10, Oct. 1972, pp. 693-702.

7   Hassig, H. J., "An Approximate True Damping Solution of th Flutter Equation by Determinant Iteration", Journal of Aircraft, Vol. 8, No. 11, Nov. 1971, pp. 885-889.

8   Landahl, M. T., "Graphical Technique for Analyzing Marginally Stable Dynamic Systems", Journal of Aircraft, Vol. 1, No. 5, 1964, pp. 293-299.

9   Landahl, M. T. and Stark, V. J. E., "Numerical Lifting-Surface Theory - Problems and Progress", AIAA Journal, Vol. 6, No. 11, Nov. 1968, pp. 2049-2060.

10   Pines, S., "An Elementary Explanation of the Flutter Mechanism", Proceedings of the National Specialists Meeting on Dynamics and Aeroelasticity, AIAA, Fort Worth, Nov. 1958, pp. 52-58.

11   Pines, S. and Newman, M., "Structural Optimization for Aeroelastic Requirements", AIAA/ASME/SAE 14th Structures, Structural Dynamics, and Materials Conference, March 1973. AIAA Paper No. 73-389.

12   Stark, V. J. E., "Use of Complex Cross-Flow Representation in Nonplanar Oscillating-Surface Theory", AIAA J., Vol. 6, No. 8, Aug. 1968, pp. 1535-1540.

13   Stark, V. J. E., "The Tangent Plane Method and Polar Coordinates - A New Approach in Lifting-Surface Theory", AIAA 8th Aerospace Sciences Meeting, Jan. 1970, AIAA Paper No. 70-78.

14   Stark, V. J. E., "A Subsonic Oscillating-Surface Theory for Wings With Partial-Span Controls", AIAA 10th Aerospace Sciences Meeting, Jan. 1972, AIAA Paper No. 72-61.

15   Stark, V. J. E., "Application of the Polar Coordinate Method to Oscillating Wing Configurations", Saab-Scania AB, TN 69, Dec. 1973.

16   Stark, V. J. E., "Application to the Viggen Aircraft Configuration of the Polar Coordinate Method for Unsteady Subsonic Flow", The 9th Congress of the International Council of the Aeronautical Sciences, Aug. 1974, ICAS Paper No. 74-03.

17   Wittmeyer, H., "Aeroelastomechanische Untersuchungen an dem Flugzeug SAAB 37 Viggen", 12. Ludwig-Prandtl-Gedachtnis-Vorlesung, Munchen, Sept. 1968. Jahrbuch 1968 der WGLR, pp. 11-23.

A BRIEF OVERVIEW OF TRANSONIC FLUTTER PROBLEMS

WALTER J. MYKYTOW
FORMER CONSULTANT, STRUCTURAL MECHANICS DIVISION
AIR FORCE FLIGHT DYNAMICS LABORATORY
WRIGHT-PATTERSON AIR FORCE BASE, OHIO

A BRIEF OVERVIEW OF TRANSONIC FLUTTER PROBLEMS

This introduction to the Specialists' Meeting on Unsteady Aerodynamics in Transonic Flow will provide a framework of industrial flutter problems with particular emphasis on the impact for this speed region.

I will touch briefly on history and present many flutter stability boundaries, re-emphasizing that the transonic flight region presents critical design conditions. This re-emphasis will be accomplished using results from research flutter model tests, aircraft design and development model tests, and aircraft flight damping measurements.

Table One (Ref. 1) shows that, previous to 1952, tab and control surface flutter prevention dominated. These problems were quickly cured by mass balance or small local stiffness changes. One case of autopilot flutter is, perhaps, an early indication of the increased attention that would be later given to aeroservoelastic problems of high-gain feedback systems. Control surface and tab problems were later decreased by use of powered controls. In the 1952-1956 period, high subsonic and transonic speeds and more efficient and flexible aircraft caused wing-store, transonic buzz, T-Tail, all movable surface, and fixed lifting surface flutter. These problems still exist today.

Methods to predict transonic oscillatory loads did not exist, so flutter models were extensively used to provide information. These next data (Refs. 2, 3, 4) were obtained by Cornell Aeronautical Laboratory in 1956-1958 for the U. S. Air Force. The flutter models were relatively large and well defined mechanically. Wall effects and tunnel Reynolds number effects versus conditions in flight are open for discussions, but these models could be used to evaluate analysis methods, and vice versa. The models used different levels of mass and stiffness distributions to obtain flutter at similar wing-air mass ratios. Figure One (Ref. 2) shows that the critical free stream Mach number, defined by a constant-altitude tangency (diagonal) line, is near Mach 1.2 for the low aspect ratio straight wing. The higher aspect ratio wings also approach critical Mach numbers near 0.95. The effect of wing-air mass ratio was not very pronounced.

Figure Two (Ref. 3) shows results for the swept wings. There is a pronounced detrimental effect of mass ratio. The critical Mach number is near 1.05. Other and more recent model tests show a significant increase in flutter dynamic pressure as mass ratio is further decreased from low values. This makes flutter model testing difficult.

Farmer and Hanson (Ref. 5 [Figure Three]) have shown the significant decrease in model flutter speed of a swept wing having a supercritical airfoil compared to conventional airfoil. The drop is about equal to the safety margin required. Overall lift curve slope and center of pressure differences are suspected. Reasons for these differences have not been substantiated since additional studies have not yet been completed.

While we are discussing swept wings, we might mention that Ruhlin and Gregory of NASA and Destuynder of ONERA have investigated tunnel wall effects (Ref. 6) on transonic model tests of an American version of the SST. They show (Figure Four) that inadequate porosity leads to lower flutter speeds. They also discuss tunnel resonance effects at $M = 0.75$ and wall reflected shock waves near $M = 0.9$ on a simplified model.

Returning to the Cornell Aeronautical Laboratory tests, Figure Five presents data for a delta wing flutter model (Ref. 4). The free stream Mach region near 1.0 is critical.

Trends with Mach number, as discussed above, are configuration sensitive and depend on modes, frequencies and separations, and mechanical and aerodynamic couplings.

Flutter models are costly, ranging in price from $5000-$7500 (U.S.) for a small component model, to $200,000 and above for large transonic models. Some dynamic characteristics cannot be completely simulated, so pre- and post-test analyses are essential for both model and aircraft to identify important parameters and their effects. Models are not readily suited for design trade-off studies involving configuration changes and in preliminary design.

In Europe, excellent and wise use of unsteady aerodynamic pressure measurements is made for both research and aircraft development. Perhaps the U. S. state of the art will soon catch up. But this approach, while excellent, also suffers from cost,

Accurate prediction methods would reduce these flutter and pressure model costs, as well as flight flutter test costs.

One exasperating situation the flutter engineer faces is prediction and prevention of external store flutter. He analyzes thousands of wing-store combinations. In many cases, flutter speed restrictions near M = 0.8 or lower are required. These limit mission performance. On large aircraft, engine-nacelle locations are influenced by flutter prevention. Also, sometimes fuel usage sequences must be employed to avoid flutter. Flutter suppression using active controls is being vigorously pursued now in Europe and the U. S., particularly for the wing-store flutter problem.

ONERA is conducting flutter suppression studies on a wing equipped with a large tank. Figure Six shows results obtained by Destuynder (Ref. 7) which indicate the higher velocity local flow induced by the tank on the lower wing surface at M = 0.8. A large portion (1/2) of the lower wing surface is enveloped in Mach 0.9 to 1.05 local flow. ONERA is also making significant progress in development of pure torque miniature actuators for flutter model suppression studies.

Space Shuttle studies investigated interference effects (Ref. 8) on flutter. They were found to be slightly beneficial. Wade (Ref. 9), at a recent AIAA meeting, gave an excellent resume of the impact of structural dynamics on Space Shuttle design. Other authors discussed the impact on various types of aircraft and turbomachinery.

NASA's Langley Research Center Transonic Dynamics Wind Tunnel has been used extensively for many aircraft flutter safety evaluations, including T-Tail tests reported by Ruhlin and Sandford (Ref. 10). Figure Seven shows a sudden drop of 35% in flutter velocity ratio just below Mach 1. A bulbous intersection fairing reduced the drop by about 50%, supposedly by adjusting area distribution. Another T-Tail model shows a 22% drop in flutter velocity ratio at a lower Mach number of 0.7.

The following figures show use of the flutter model (and flutter analyses) for other industrial applications. Perisho and Zimmerman (Ref. 11) - see also Shelton and Tucker (Ref. 12) and Katz-Foppe-Grossman (Ref. 13) - present data for several critical modes of a fighter. About six modes (Ref. 13) were adjusted by mass balance or configuration changes to eliminate possible difficulties and to meet the required 15% velocity margin. The high reliance on model tests is very noticeable. Figure Eight shows that the margin for fin bending-fuselage lateral bending flutter is not quite adequate. Fin tip balance weights were added. Figure Nine shows the frequent all movable surface flutter problem. In this case, the inboard leading edge was removed to provide a snag to save weight, and to help prevent flutter in another mode. Figure Ten demonstrates the wing-external store problem. (The agreements of the g = 0.02 analyses - from strip, doublet and Mach box methods - with experiments are probably fortuitous. Transonic analytical results are faired to follow model trends.)

Mr. C. Lodge (Ref. 14) and the British Aircraft Corporation have kindly offered flight test data showing transonic effects on modal damping levels. The benefits of modifications and the critical effects of transonic flows are clearly evident. Figure Eleven shows the transonic loss in damping of a trailing edge control, and also the possible all movable control flutter problem. Figure Twelve shows the drop in wing-store damping at M = 0.92 and also the need to hold all movable surface rotational backlash to very low values to avoid oscillations at M = 0.99.

In Summary:

- The transonic flutter problem has existed for 20 years.

- Lacking methods to predict transonic loadings, we cannot optimize the structural design early.

- Methods are needed for a wide range of configurations and initial conditions, a quite difficult and lengthy task. These configurations include:

  - Control surfaces for:

    - Servoaeroelasticity
    - Flutter suppression
    - Actuator power requirements

  - Interfering and interacting surfaces and bodies:

    - Wings with stores
    - Wing-horizontal tails
    - T-Tails
    - All movable surfaces-fuselages
    - Fins - fuselages

- The critical range extends from M = 0.8 to 1.2 or higher.

- Many more unsteady aerodynamic pressure and load measurements are

- Standard configurations are needed to evaluate methods.

- Selected flutter model tests and limited unsteady pressure measurements in flight should be included in the evaluation process as soon as appropriate since the engineer has urgent application needs.
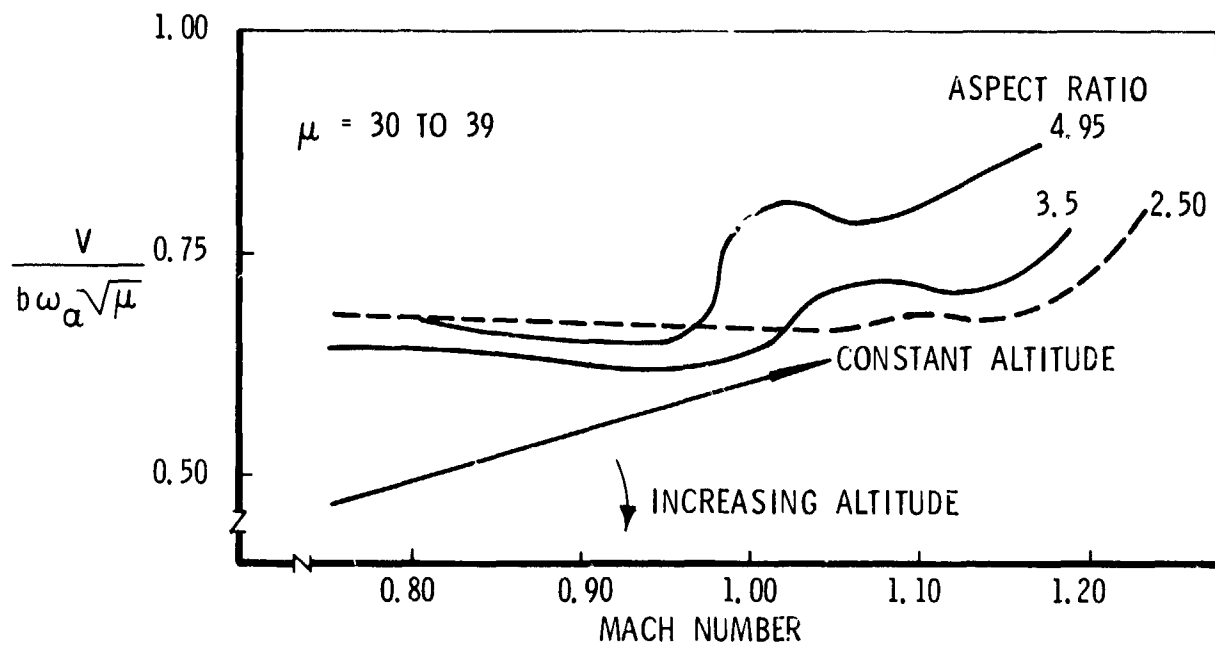
REFERENCES

(1)   NACA Subcommittee on Vibration and Flutter, "A Survey and Evaluation of Flutter Research and Engineering," NACA RM 56I12, Oct 5, 1956

(2) Brady, W.G., King, S.R., and Maier, H.G.   "Transonic Flutter Model Tests. Part II Straight Wings," WADC Technical Report 56-214:Part II. Jan 1958

(3) Maier, H.G. and King, S.R.   "Transonic Flutter Model Tests. Part I: 45 Degree Swept Wings," WADC Technical Report 56-214:Part I. Sep 1957

(4) Balcerak, J.C. and Ostaszewski, N.H.   "Transonic Flutter Model Tests. Part III: Delta Wings," WADC Technical Report 56-214:Part III. Jan 1958

(5) Farmer, M.G. and Hanson, P.W.   "Comparison of Supercritical and Conventional Wing Flutter Characteristics," AIAA/ASME/SAE 17th Structures, Structural Dynamics and Materials Conference, King of Prussia, Penn. 5-7 May 1976

(6) Ruhlin, C., Destuynder, R., and Gregory, R.   "Some Tunnel Wall Effects on Transonic Flutter," AIAA Paper No. 74-406, AIAA/ASME/SAE 15th Structures, Structural Dynamics and Materials Conference, Las Vegas, Nevada, April 1974

(7) Destuynder, R.   "Unsteady Pressure Measurements in Wing-With-Store Configurations," AGARD Report 636, Comments on Transonic and Wing-Store Unsteady Aerodynamics, January 1976

(8) Chipman, R.C. and Rauch, F.J.   "Analytical and Experimental Study of the Effects of Wing Body Interaction On Space Shuttle Subsonic Flutter," NASA CR 2488, January 1975

(9) Wade, D.C.   "Influence of Structural Dynamics on Space Shuttle Design," AIAA/ASME 18th Structures, Structural Dynamics and Materials Conference, San Diego, California, 21-23 March 1977 (See also Volume B, "A Collection of Technical Papers on Dynamics and Structural Dynamics," AIAA Dynamics Specialist Conference, San Diego, California, 24-25 Mar 77)

(10) Ruhlin, C.L. and Sandford, M.C.   "Experimental Studies of Transonic T-Tail Flutter," NASA TN D-8066, December 1975

(11) Perisho, C.H. and Zimmerman, N.H.   "Transonic Flutter Clearance", McDonnell Aircraft Company letter dated 16 December 1976

(12) Shelton, J.D. and Tucker, P.B.   "Minimum Weight Design of the F-15 Empennage for Flutter," AIAA/ASME 16th Structures, Structural Dynamics and Materials Conference, May 1975

(13) Katz, H., Foppe, F.G., and Grossman, D.T.   "F-15 Flight Flutter Test Program," NASA Symposium on Flutter Testing Techniques, Dryden Flight Research Center, October 1975

(14) Lodge, C.G.   "Transonic Effects on Modal Damping Levels," British Aircraft Corporation Ltd letter dated 2 November 1976

TABLE I

Some Past Flutter Incidents

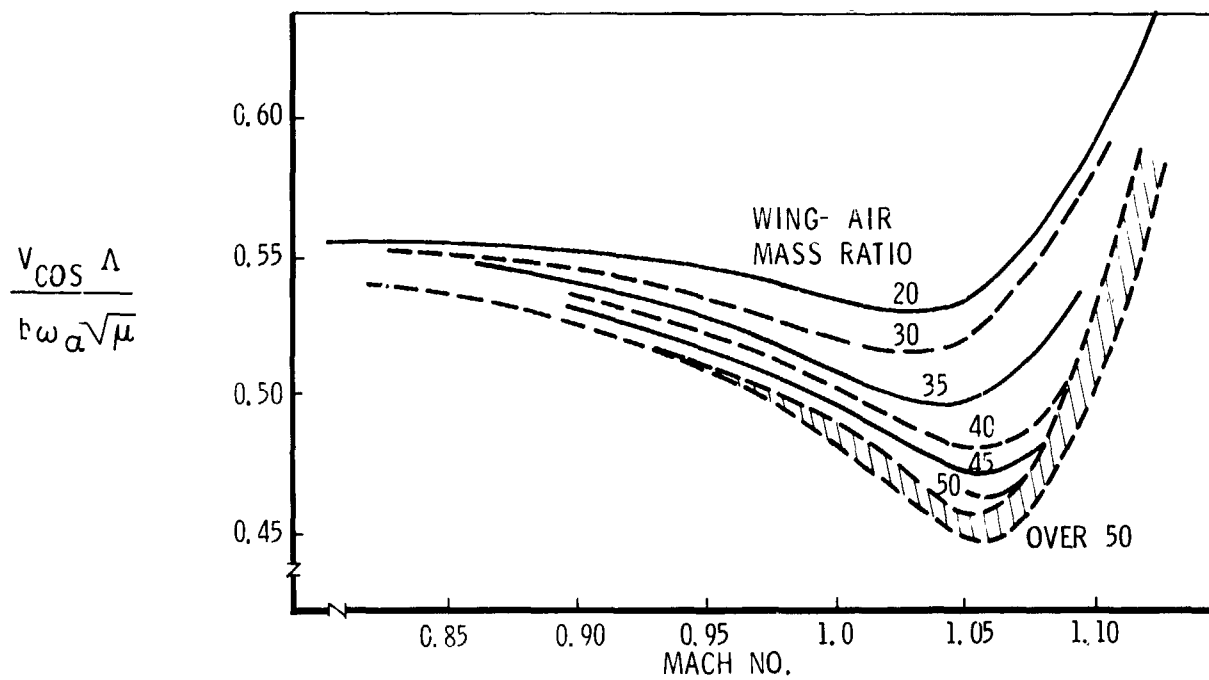|	1947 - 1951	1952 - 1956
TABS; CONTROL SURFACES*	11	8
WING WITH EXTERNAL STORES	1	6
AUTOPILOT COUPLING	1	
TRANSONIC BUZZ RELATED		21
T-TAIL		1
ALL MOVABLE SURFACE		4
FIXED SURFACE - BENDING-TORSION		1

*BALANCED AND UNBALANCED SURFACES

REF: NACA RM 56 I 12

REF: WADC TR 56-21411

Fig 1   Straight cantilevered wings transonic flutter model tests
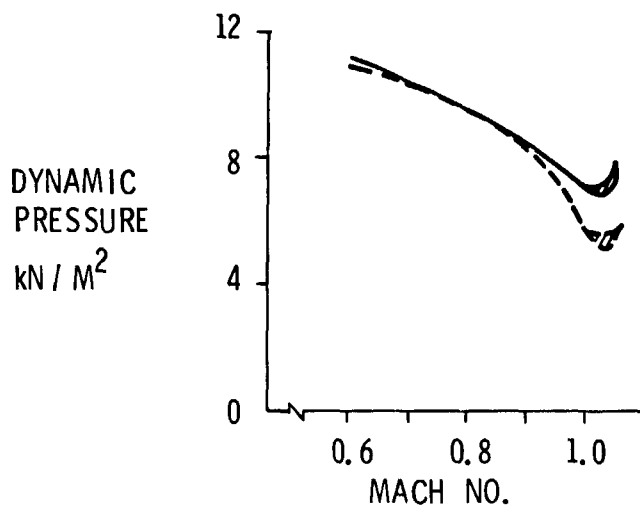
$$\frac{V_{COS} \Lambda}{b\omega_a\sqrt{\mu}}$$

REF: WADC TR 56-214 I

Fig. 2· Swept cantilevered wing transonic flutter model tests
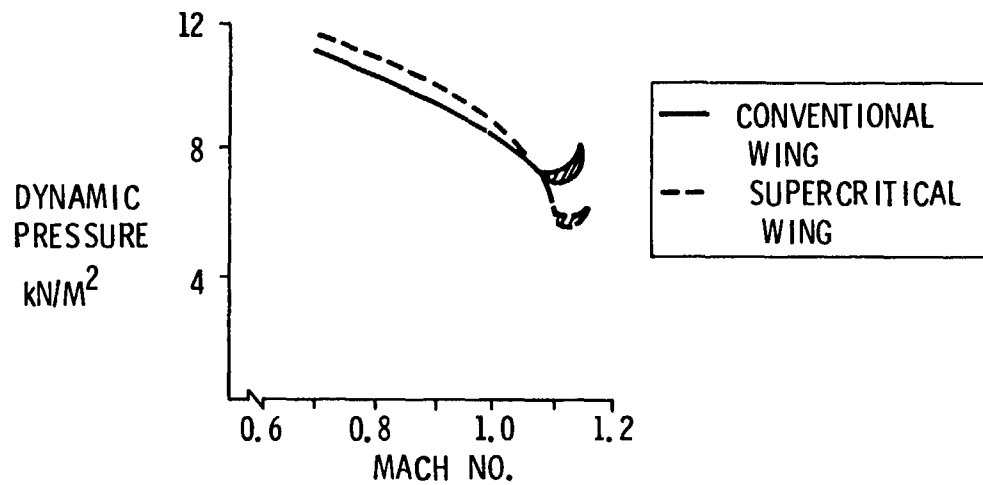
FLUTTER BOUNDARIES ADJUSTED FOR
STRUCTURAL DIFFERENCES

FLUTTER BOUNDARIES WITH ADJUSTED SUPER-
CRITICAL WING BOUNDARY (FROM FARMER
AND HANSON)

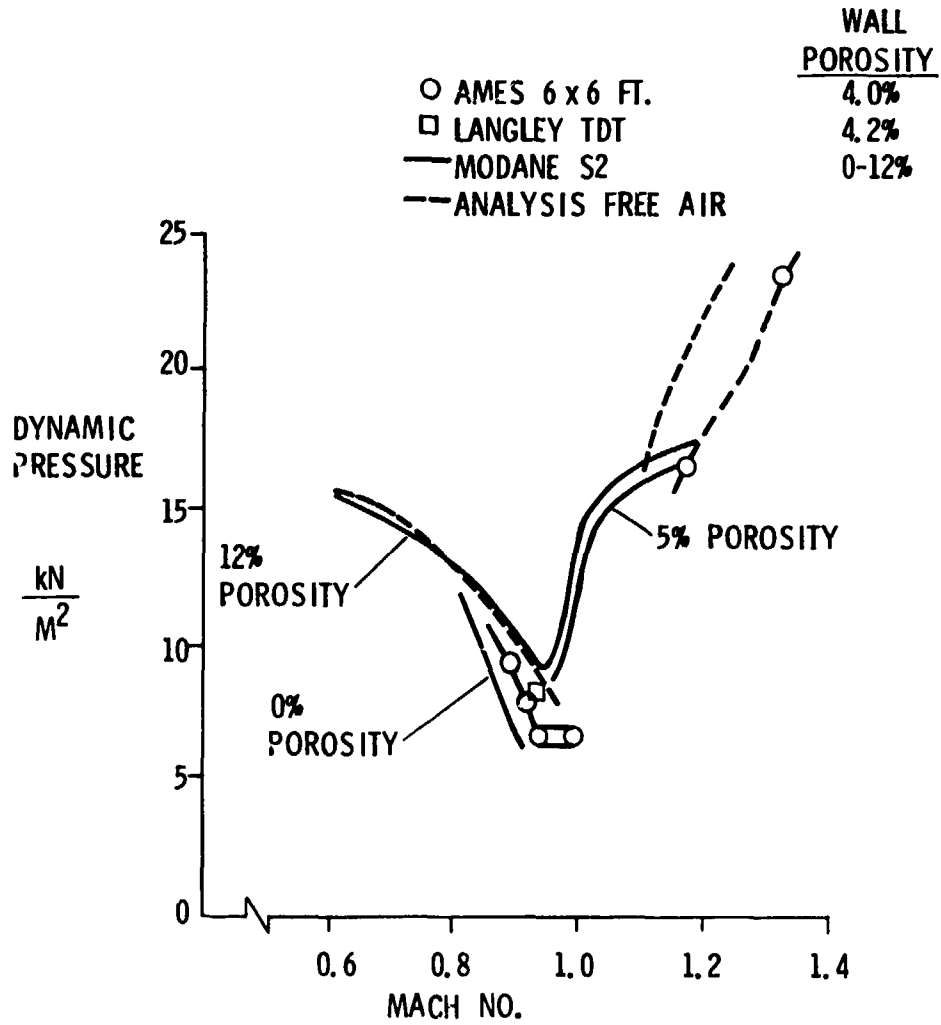Fig. 3.   Supercritical flutter model tests

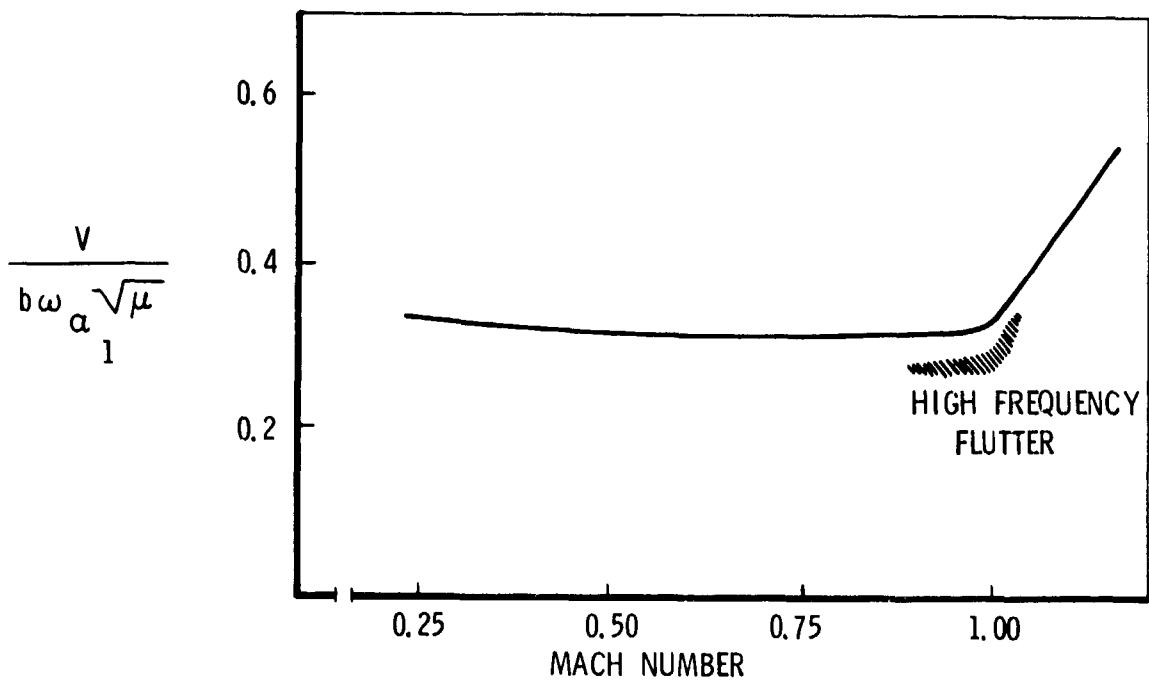|	WALL POROSITY
O AMES 6 x 6 FT.	4.0%
□ LANGLEY TDT	4.2%
── MODANE S2	0-12%
── ANALYSIS FREE AIR	

Fig. 4 Flutter dynamic pressure vs porosity

REF: WADC TR 56-214 III

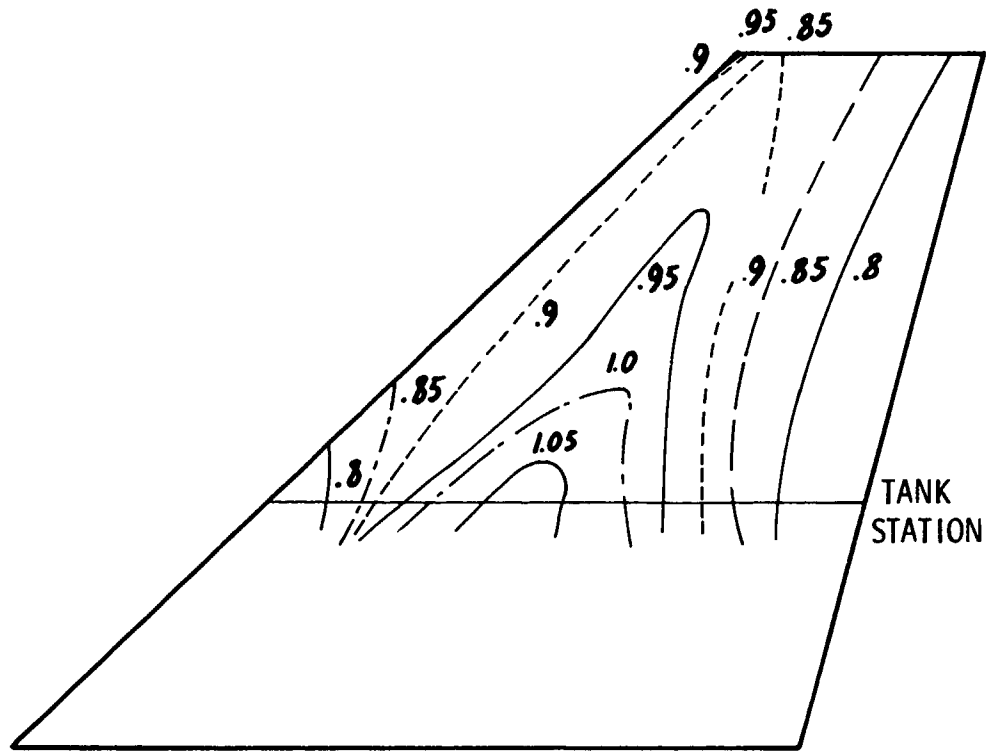Fig. 5 Delta cantilevered wing transonic flutter model tests

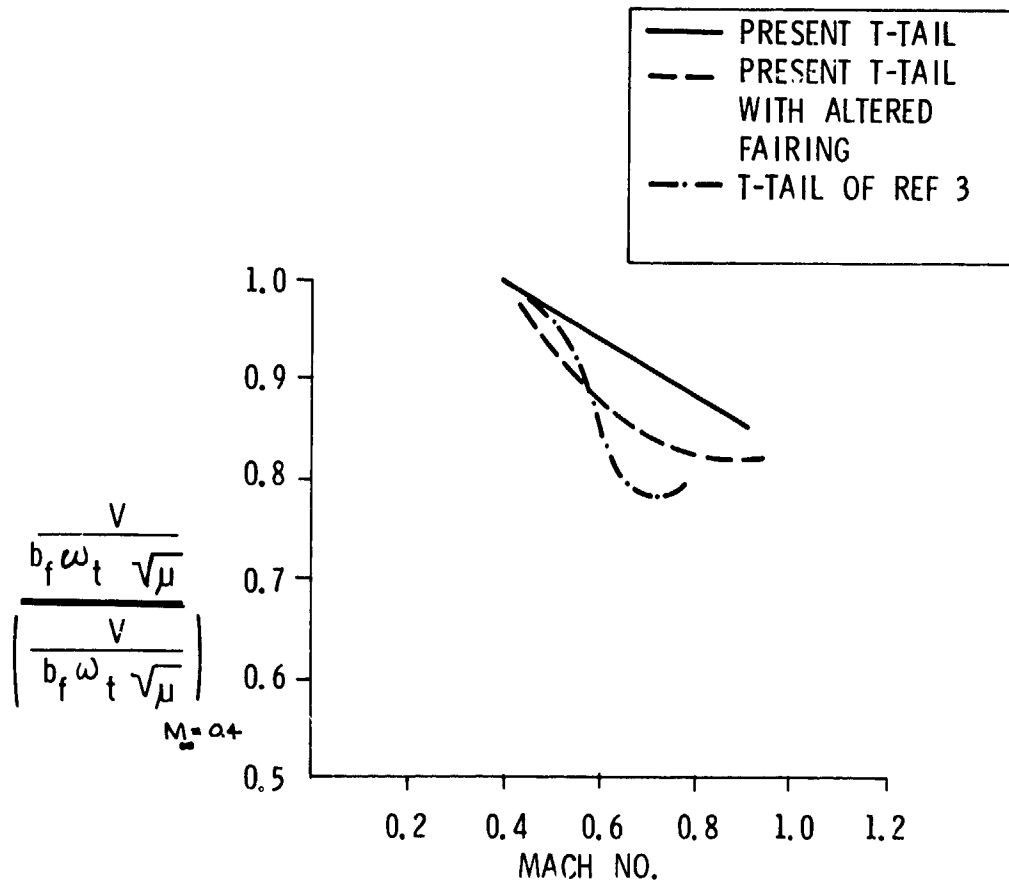Fig. 6:   ISO-Mach lines. Wing plus large tank M = 0.8

PRESENT T-TAIL
PRESENT T-TAIL
WITH ALTERED
FAIRING
T-TAIL OF REF 3

$$\frac{\dfrac{V}{b_f \omega_t \sqrt{\mu}}}{\left(\dfrac{V}{b_f \omega_t \sqrt{\mu}} \right)_{M_\infty = 0+}}$$
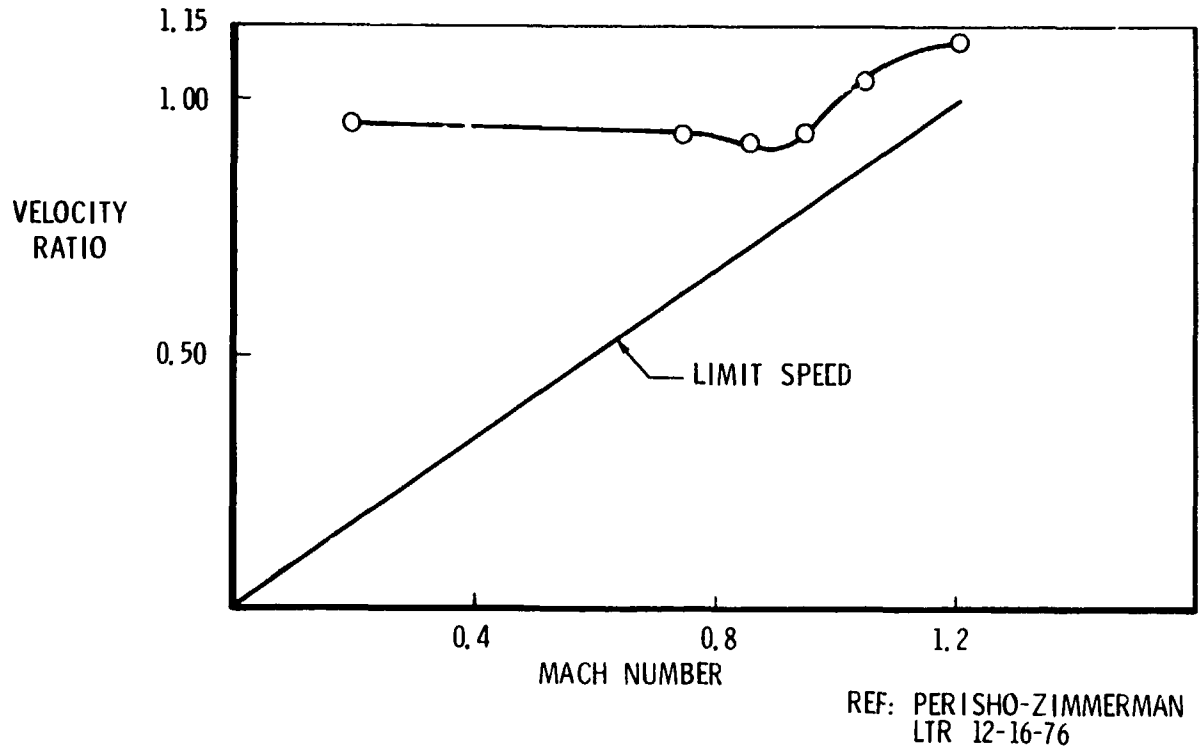
MACH NO.

Fig. 7·   Transonic T-tail model tests
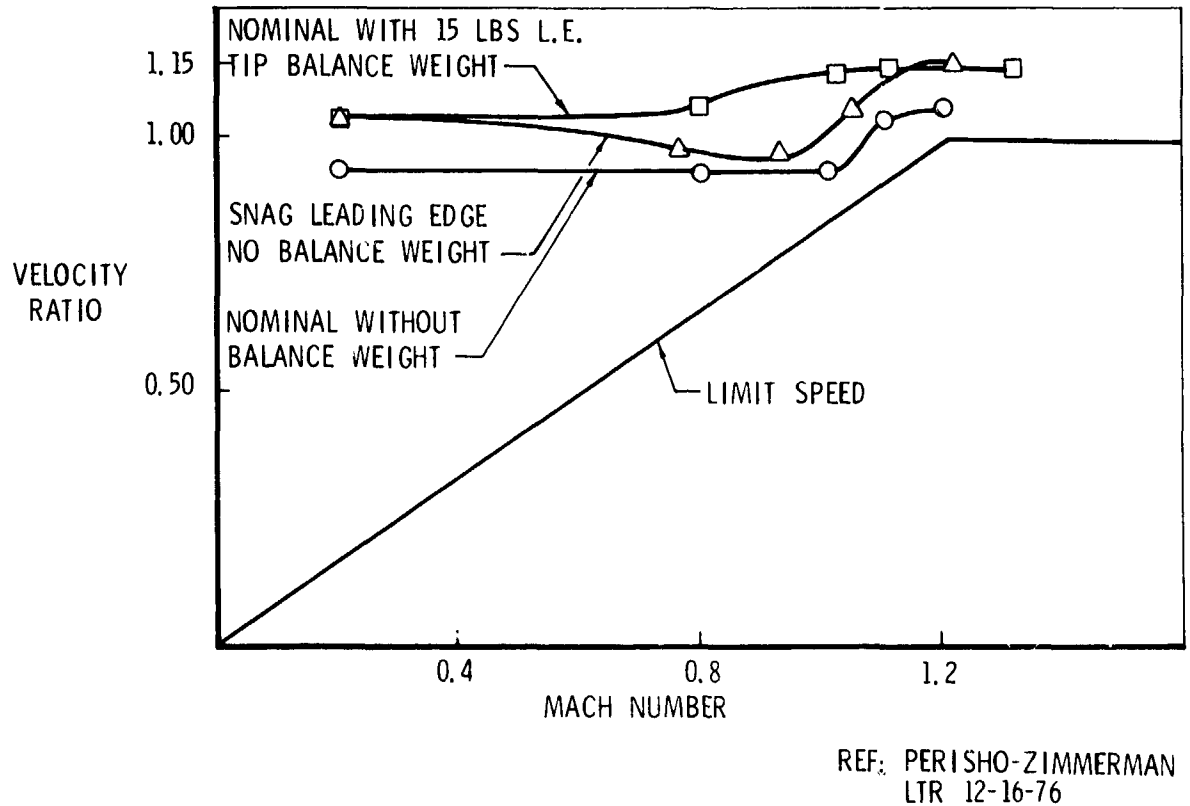
Fig. 8: Model flutter speed fin bending — fuselage lateral bending no fin tip balance weight

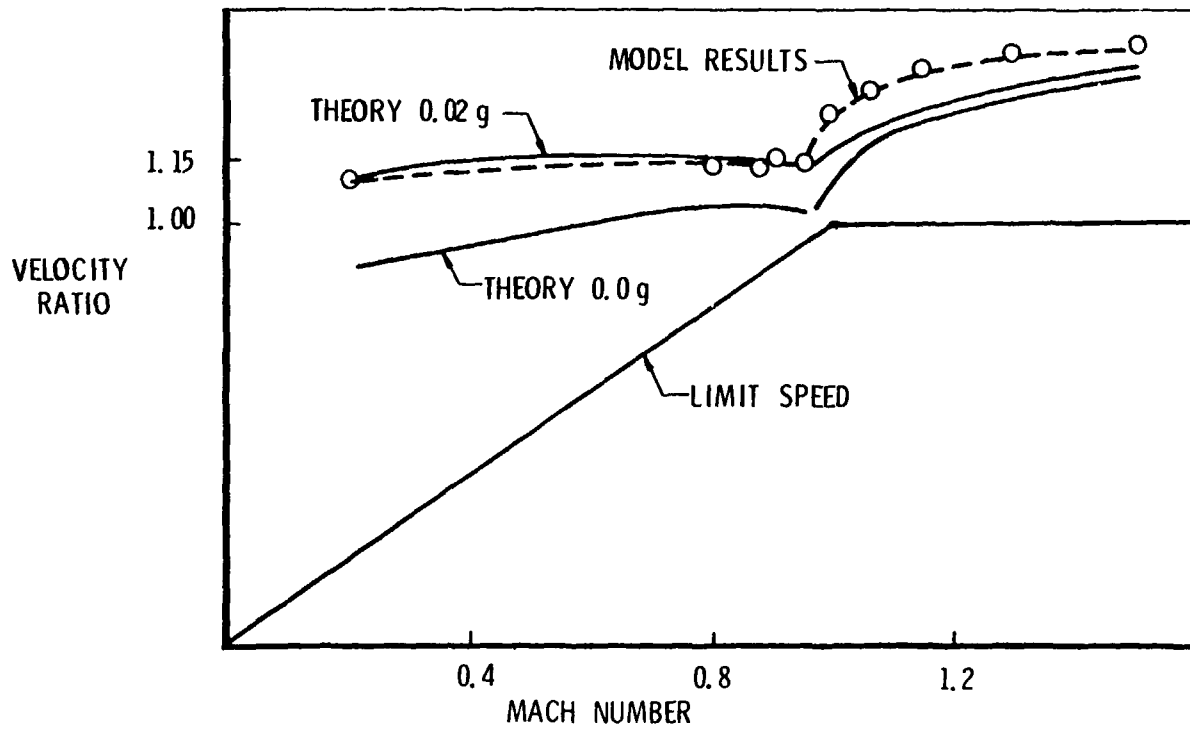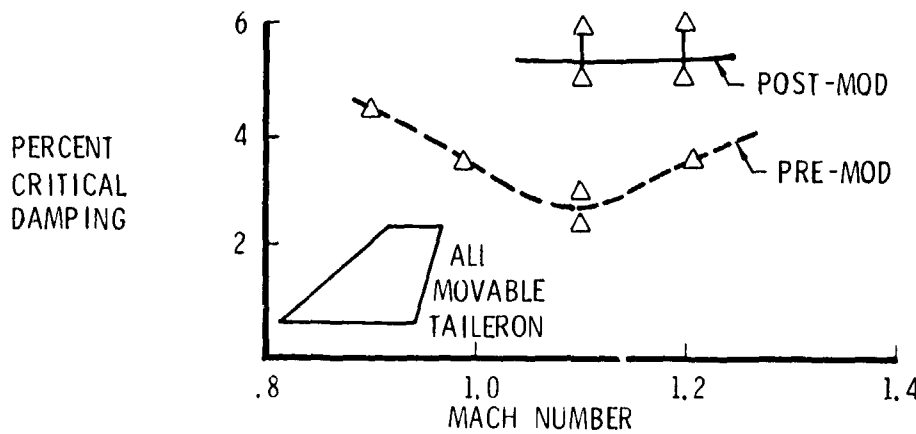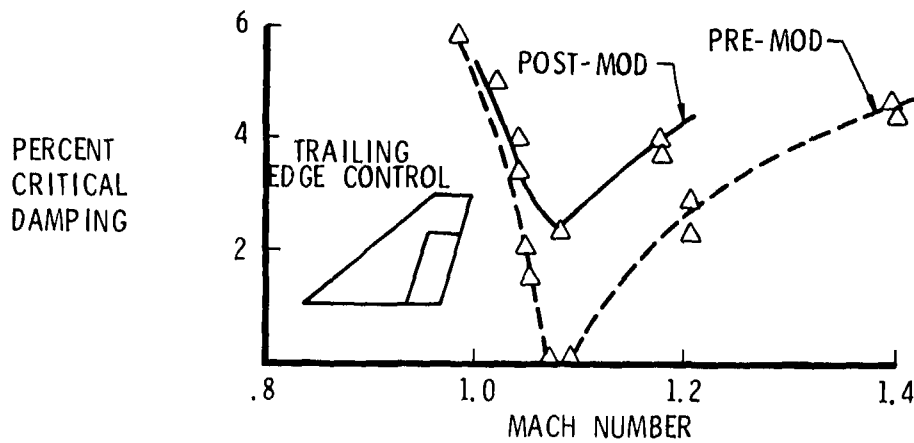Fig. 9. Model flutter speed-stabilator

Fig. 10: Flutter speed — wing with external tank model tests and analyses

REF: PERISHO-ZIMMERMAN
LTR 12-16-76

REF: LODGE (BAC). LTR 11-2-76

Fig. 12   Flight data

UNSTEADY AIRLOADS ON AN OSCILLATING SUPERCRITICAL AIRFOIL

by

H. Tijdeman, P. Schippers and A.J. Persoon
National Aerospace Laboratory NLR
Anthony Fokkerweg 2, Amsterdam,
The Netherlands

SUMMARY

Results are presented of unsteady pressure measurements on a two-dimensional model of the super-critical NLR 7301 airfoil performing pitching oscillations about an axis at 40 per cent of the chord.

CONTENTS

LIST OF SYMBOLS

a	velocity of sound
c	chord
C_ℓ	lift coefficient
C_p	steady pressure coefficient
$\Delta C_p = \dfrac{\Delta p}{q.\Delta\alpha}$	unsteady pressure coefficient
f	frequency of oscillation (Hz)
I	component of unsteady pressure in quadrature with the airfoil motion
$k = \dfrac{\omega U}{2c}$	reduced frequency
k_α	unsteady normal force derivative
m_α	unsteady moment derivative about the 1/4-chord point
M	Mach number
p	pressure
Δp	variation in pressure due to variation in incidence
q	dynamic pressure
R_e	Reynolds number based on the chord
R_e	component of unsteady pressure in phase with the airfoil motion
t	time
t	thickness of airfoil
U	flow velocity
α_o	geometric incidence
α_c	effective incidence (including tunnel wall correction)
$\Delta\alpha$	amplitude of the airfoil motion or change in incidence (quasi-steady conditions)
φ	phase angle
ω	frequency of oscillation

1. INTRODUCTION

Nowadays there is a considerably interest in methods to predict the unsteady airloads on airfoils and wings oscillating in transonic flow, especially in connection with the current interest in the so-called supercritical wing concept. However, in contrast with the steady flow case, exp rimental data, that are sufficiently detailed to verify fundamental theoretical assumption.: or to confirm the validity of calculated results are very scarce and thus a definite need exists.

For this reason recently at NLR an exploratory wind tunnel investigation has been performed on a model of an oscillating supercritical airfoil, of which the geometry has been generated with the hodograph method of Boerstoel (Refs. 1, 2). While the airfoil was oscillating in pitch about an axis at 40 per cent of the chord detailed pressure distributions were determined. In addition time histories of shock wave motions were recorded.

The aim of the present paper is to illustrate some typical high subsonic and transonic effects as observed in the experiments. After a brief description of the test set up, an analysis is given of the pressure distributions and the resulting unsteady airloads as measured 'or some characteristic flow conditions. Further attention is paid to the periodical motions of the shock wave and finally it is tried to assess what can be expected from the new generation of calculation methods for unsteady transonic flow (For details about the various theoretical methods reference is made to the other papers presented during this meeting).

2. MODEL AND TE: . SET UP
2.1 Model and excitation system

The airfoil under consideration, the NLR 7301, was designed for "shock-free" flow under prescribed conditions (Fig. 1) and was tested extensively in steady flow by Rohne and Zwaaneveld (Refs. 3, 4). For the purpose of the present unsteady experiments a new model has been built, which could perform pitching oscillations about an axis at 40 per cent of the chord. This model, made of Dural, has a chord length of 18 cm and spans horizontally the test section of the NLR Pilot tunnel. The pitching motion is generated by means of a hydraulic actuator (For a detailed description of the hydraulic system and the model suspension reference is made to Poestkoke (Ref. 5)). To keep the suspension as simple as possible the model is excited at one side, while the opposite side is supported by a bearing just outside the tunnel wall (Fig. 2). To avoid a compl..cated sealing between model and window, the window closest to the actuator is attached to the model and follows its motion. In addition it results in a clear view on the model surface for the optical flow studies.

Both the upper and lower surface of the model are provided with 20 pressure orifices (Fig. 3), connected with two scanning valves outside the wind tunnel via pressure tubes. In addition 13 miniature Kulite transducers are built in. This number, which is larger than necessary for the dynamic calibration of the pressure tubes, was chosen to create the possibility to arrest the actual time histories (including the higher harmonics) of the chordwise pressure distribution along the upper surface.

To determine the motion of the model use is made of 6 accelerometers, located in three spanwise sections. The mean incidence is controlled by the hydraulic system.

2.2 Optical flow studies

The periodical shock wave motions on the oscillating model were determined from a series of subsequent shadowgraph pictures. These pictures were taken using a stroboscopic light source, triggered by an electrical signal from a displacement pick up. By means of an adjustable phase shift in the electric circuit between the accelerometer and the light source the oscillating model with its instantaneous shock pattern could be photographed in every position desired.

2.3 Wind tunnel

The experiments were performed in the Pilot tunnel of NLR, which is an atmospheric closed circuit tunnel for Mach numbers up to 1. Upper and lower surface of the test section (height: 55 cm; width: 42 cm) are fitted with longitudinal slotted walls. The open area ratio of the walls is 0.1 and the plenum chambers of floor and bottom are not connected. Further details of the Pilot tunnel can be found in reference 6.

3. ANALYSIS OF RESULTS
3.1 Introductory remarks

The main unsteady aerodynamic characteristics of the NLR 7301 airfoil will be discussed using experimental data for three different flow conditions, which can be characterized as follows (see figure 4):

 A: fully subsonic flow
 B: transonic flow with a well developed shock wave
 C: "shock-free" flow

To emphasize the importance of the dynamic effects on the unsteady airloads, for each case the corresponding quasi-steady airloads will be considered first. These quasi-steady airloads can be interpreted as the airloads when the oscillations were taking place infinitely slow. For reference purposes the experimental results will be compared also with results of the thin airfoil theory.

The unsteady pressures are given in terms of the dimensionless coefficients ΔC_p, defined as

$$\Delta C_p = \frac{\Delta p}{q \cdot \Delta \alpha}$$

where $\Delta \alpha$ is the amplitude of the pitching oscillation in radians, p the pressure variation and q the dynamic pressure. The corresponding quasi steady coefficient can be derived from steady tests at two different incidence as follows:

$$\Delta C_p = \frac{C_p(\alpha_o + \Delta\alpha) - C_p(\alpha_o - \Delta\alpha)}{2 \cdot \Delta\alpha}$$

where $C_p = \frac{p-p_\infty}{q}$ denotes the steady pressure coefficient.

3.2 Unsteady pressure distributions

3.2.1 Full subsonic flow (condition A)

The steady pressure distributions measured in subsonic flow (condition A) for two values of the angle of attack and the quasi-steady results derived from that are shown in figure 5. In order to facilitate the comparison between upper and lower surface the quasi-steady pressures at the upper surface are plotted with a reversed sign (Fig. 5.II). The agreement between the measured quasi-steady pressures and the prediction of thin airfoil theory is reasonable. The largest deviations show up over the rear part of the airfoil, where the measured data are below the calculated curve. Near the leading edge the measured pressures on the upper surface are larger than predicted by the theory and also larger than the values measured on the lower surface. As will be discussed later (chapter 4) the differences observed have to be attributed to the combined effect of airfoil thickness (plus incidence) and the boundary layer. The first effect dominates on the front part of the airfoil, while the boundary layer effect is more pronounced on the rear part.

A comparison between the unsteady pressures measured on the upper surface of the oscillating airfoil and the corresponding results of thin airfoil theory (Fig. 6) shows similar differences as observed in quasi-steady flow. In general the agreement between theory and experiment is reasonable. Further it can be noted that there is a very satisfactory agreement between the unsteady pressures measured directly with the in situ transducers and the pressures obtained via the pressure tubes.

3.2.2 Transonic flow with shock (condition B)

The next example concerns oscillations of the airfoil about the off-design condition B (Fig. 4). In this condition, being typical for "classical" transonic flow, the upper surface carries a supersonic region extending to about 50 per cent of the chord, which is terminated by a relatively strong shock wave. As shown in figure 7.I a change in incidence of 1 degree results in a shift of the steady shock position of about 10 per cent of the chord. The flow along the lower surface remains subcritical.

From the corresponding quasi-steady pressure distributions (Fig. 7.II) it can be deduced that along the upper surface the pressure is dominated by the effect of the shock displacement, generating a high pressure peak, which of course cannot be predicted by thin airfoil theory. The quasi-steady pressure distribution on the subsonic lower surface is predicted reasonably well.

Unsteady pressure distributions on the upper surface are presented in figure 8 for three different frequencies. These results also show the dominant effect of the pressure peak due to the moving shock wave. It is noted that this pressure peak shifts from the real part of the pressure distribution to the imaginary part with increasing frequency. This is the result of the increased phase lag of the periodical shock motion relative to the motion of the airfoil, a phenomenon to be discussed in more detail in chapter 3.4.1.

By representing the unsteady pressure distributions in terms of magnitude and phase angle (Fig. 9) it further can be shown that the width and the height of the pressure peak associated with the periodical motion of the shock wave decreases as the frequency is increased. This is caused by the decrease of the amplitude of the shock motion with increasing frequency (see also chapter 3.4.1). Concerning the phase curves in figure 9 it should be noted that the measurements show a jump of about 180 degrees just downstream of the mean position of the shock wave. This jump is present already in quasi-steady flow and thus is not a dynamic effect.

From the comparison of the measured pressure distributions with the distributions calculated with thin airfoil theory (Figs. 8 and 9) it is evident that, as far as the upper surface is concerned, this theory is not applicable.

3.2.3 The "shock-free" design condition (condition C)

Of special interest is the unsteady behaviour of the airfoil near its "shock-free" design condition (condition C in figure 4). As shown in figure 10.I a variation in incidence of 0.5 degree about the design point leads to a considerable change of the steady pressure distribution along the upper surface. In particular in the supersonic region, ranging from about 3 per cent to about 65 per cent of the chord the shape of the pressure distribution changes considerably. Further away from the design condition a (weak) shock wave shows up. At the lower surface the steady pressure distribution changes less drastically. Noteworthy is that along the lower surface the velocity becomes slightly supercritical, but still without shock formation.

The changes in steady distribution result in a quasi-steady distribution as given in figure 10.II. On the upper surface a wide bulge occurs, which is caused by the drastic change of the pressure distribution in the supersonic region. Most probably this wide bulge is a feature typical of this type of "shock-free" airfoil, characterized by a relative blunt nose and an extensive region of supersonic flow. A comparison between the measured quasi-steady distribution and the curve determined with thin airfoil theory shows that the prediction for the upper surface is quite useless. For the lower side, where the flow remains almost subcritical, the differences between theory and experiment is considerably smaller.

A series of fully unsteady pressure distributions along the upper surface in terms of magnitude and phase angle is given in figure 11. One easily recognizes in the magnitude curves the large contributions associated with the changes in the shape of the pressure distribution in the supersonic region on the front part of the airfoil. In addition a small peak occurs at about 65 per cent of the chord, caused by the periodical formation of a weak shock in this region (see figure 12). This peak grows larger with increasing frequency as a result of the increased strength of the shock wave. At the same time the bulge on the front part decreases with frequency and the unsteady pressure distribution shows a tendency to change in a direction towards the pressure distributions found for flow condition B.

The phase curves shown in figure 11 behave very regular up to about 60 per cent of the chord. Then a jump in phase angle of about 180 degrees occurs, which can be attributed to the presence of the shock wave.

Finally a comparison of the measured unsteady pressure distributions with thin airfoil theory confirms what could be concluded already on the basis of the quasi-steady data: for these types of mixed flow one has to rely on other prediction methods.

3.3 Unsteady aerodynamic derivatives

Of prime concern to the aeroelastician of course are the overall unsteady aerodynamic airloads. For this reason the unsteady aerodynamic coefficients, obtained by chordwise integration of the measured unsteady pressure distributions, have been collected in figures 13-15, for the characteristic flow conditions A, B and C, respectively. For reference purposes the results according to thin airfoil theory are given as well.

The agreement between the theoretical and experimental pressure distributions for the subsonic flow condition A (see chapter 3.2.1) is reflected also in the curves of figure 13, representing the unsteady aerodynamic derivatives as a function of reduced frequency. The largest deviations, occuring in the real part of both the normal force and the moment derivative, can be attributed to the differences in the pressure distributions, which do exist already in quasi-steady flow (Fig. 5).

For the transonic flow condition B (see figure 14) the differences between theory and experiment are considerably larger than in the preceding fully subsonic example. This is true also for the unsteady derivatives in the "shock-free" design condition C (Fig. 15). A comparison between figures 14 and 15 learns that for the design condition the deviations from thin airfoil theory are of the same order of magnitude as for the "classical" transonic flow condition B.

The behaviour of the aerodynamic coefficients in a transonic flow with shock wave can be correlated qualitatively with the presence of the dominant pressure peak generated by the oscillation of the shock. As indicated schematically in figure 16 (representing for instance the results of flow condition B), the pressure peak associated with the shock wave is responsible for a shift in unsteady lift and moment indicated by a 1. At small reduced frequencies the real part of the normal force derivative, k_α, is larger than predicted by theory. As the frequency increases, the real part decreases faster than the curve for thin airfoil theory, while the imaginary part becomes much more negative than predicted. This behaviour is correlated with the shift of the pressure peak due to the shock from the real part to the imaginary part of the unsteady pressure distribution, as has been shown in figure 8 (see also section 3.2.2).

The same phenomenon is responsible for the change indicated by 1, in the moment derivative, m_α. The remaining part of the deviation in the moment derivative is caused by the circumstance that the mentioned pressure peak is located downstream of the quarter chord point, thus giving rise to a rearward shift of the aerodynamic centre. For the present example this shift, expressed as

$$\frac{\Delta x}{c} = \frac{1}{2}\frac{\Delta m_\alpha}{k_\alpha}$$

can be estimated roughly at 5 per cent of the chord.

In the figures 13-15 results are given for the airfoil with and without transition strip. For flow conditions A and B no significant difference is observed. However, in the delicate "shock-free" design condition C the flow is more susceptible to disturbances over the front part of the airfoil and thus more sensitive to the presence of the strip. For a more detailed account on this sensivity reference is made to reference 7.

Further it should be remarked here that the measured data are given without tunnel wall correction, since reliable methods to determine this effect in unsteady wind tunnel tests are not yet available. An estimate of the amount of wall interference involved in the present tests will be given in chapter 4 on the basis of some quasi-steady flow calculations.

3.4 Remarks on the unsteady shock wave motion
3.4.1 Effect of frequency

With the help of optical flow studies additional information is obtained about the periodical motion of the shock waves in flow condition B. From figure 17, giving the time histories of the shock displacement for different frequencies, it follows that the shock wave performs nearly sinusoidal motions (similar to the type A motion described in reference 8). Further the phase lag of the shock motion relative to the airfoil motion increases with frequency, while the amplitude of the shock motion decreases. The latter corresponds very well with the observations mentioned earlier concerning the contribution of the moving shock wave to the unsteady pressure distributions (see Figs. 8 and 9).

A closer examination of the phase lag of the shock motion with respect to the airfoil motion (Fig. 18) learns that an almost linear relationship exists between frequency and phase lag. This implies that there is a constant time lag between the motion of the airfoil and the shock wave motion. In relation to this it is of interest to recall the investigation of Erickson and Stephenson (Ref. 9) who have found that a fixed relation seems to exist between the phase lag of the shock motion and the time required for a pressure impulse to travel from the trailing edge to the shock wave. Indeed this travelling time seems to be a logical parameter for an airfoil with a large supersonic region terminated by a shock wave, because this is the time period after which major changes in flow condition, namely changes in flow direction at the trailing edge (Kutta condition) can be felt by the shock wave (Fig. 19).

The time required to forward information from the trailing edge to the shock wave amounts

$$\Delta t = \int_{x=c}^{x_s} \frac{dx}{(1-M_{loc})a_{loc}}$$

with M_{loc} being the local Mach number and a_{loc} the local velocity of sound. Due to the gradient in Mach number normal to the airfoil surface the acoustic waves propagate along paths away from the airfoil. Therefore the propagation speed in upstream direction will be some average between the value of $(1-M_{loc})a_{loc}$ near the airfoil surface and the free stream value. To account for this effect the following value of the local Mach number has been introduced:

$$M_{loc} = ? \left|M_{loc}(\text{at the surface}) - M_x\right| + M_x$$

with R being a relaxation factor, which has a value between 0 and 1.0.

For $R \approx 0.7$ an excellent agreement is obtained between the travel time of the "Kutta waves" and the corresponding phase lag of the shock motion, as is demonstrated in figure 18. This value of R agrees very well with the relaxation factor applied in the modified Doublet lattice method of NLR (see Roos, Ref. 10), in which in a semi-empirical way a local Mach number correction is introduced. In this method also the factor R is used to account for the gradients in Mach number normal to the airfoil surface.

3.4.2 Linearity of the unsteady loads

The local pressures in points of the airfoil located within the trajectory of the oscillating shock wave show a strong nonlinear behaviour, caused by the periodical passage of the shock and the accompanying pressure jump. From the time registrations of the unsteady pressures and the resulting overall loads (see example of figure 20) it can be noted, however, that in spite of these local non linearities the resulting unsteady lift varies almost sinusoidal. The overall moment shows irregularities, but its amplitude is very small and strongly amplified. These findings correlate very well with the experiences of Magnus and Yoshihara (Ref. 11), Laval (Ref. 12) and Krupp and Murman (Ref. 13), who in their calculated examples also observed an almost linear behaviour of the overall aerodynamic derivatives, inspite of the presence of an oscillating shock wave.

This phenomenon can be made plausible as follows. In flow patterns with a well developed shock wave it has been observed that the shock motion takes place almost sinusoidal and that the amplitude of the shock motion is almost proportional to the amplitude of the sinusoidal motion of the airfoil (see for instance figure 21). This makes it possible to introduce the schematized model of figure 22, in which the change in pressure in a fixed point A is considered, while the shock wave performs a sinusoidal motion of amplitude x_0.

As derived in reference 8 the local shock strength in point A, located within the shock trajectory, can be written as:

$$(p_2-p_1)_{x_a} = (p_2-p_1)_{x_s} \cdot u(x_a - x_0 e^{i\omega t}) + \Delta p \left(\omega, M_1, \frac{\delta M_1}{\delta y}\right) \cdot x_0 e^{i\omega t}$$

Here $u(x_a - x_0 e^{i\omega t})$ denotes the unit step function and Δp the variation in shock strenght during the shock wave motion. For strong shock waves and small amplitude motions the last term in the above expression can be discarded relative to $(p_2-p_1)_{x_s}$. When $(p_2-p_1)_{x_s}$ is described as a function of time a block type signal occurs (see figure 22), of which the Fourier decomposition yields:

$$p(x_a) = \left[p_2(x_s) - (p_2-p_1)_{x_s} \frac{1}{\pi} \arccos \frac{x_a}{x_0} \right] - (p_2-p_1)_{x_s} \left[\frac{2}{\pi} \sin(\arccos \frac{x_a}{x_0}) \cos \omega t + \frac{1}{\pi} \sin(2 \arccos \frac{x_a}{x_0}) \cos 2\omega t + \right.$$
$$\left. \frac{2}{3\pi} \sin(3 \arccos \frac{x_a}{x_0}) \cos 3\omega t + \dots \right]$$

The corresponding distribution of the first four Fourier components along the trajectory of the shock motion are shown in figure 23. From the distribution of the mean steady value it follows that, due to the oscillatory motion of the shock wave, the jump in the steady pressure distribution is spread out over the shock trajectory. The distribution of the component with the same frequency as the airfoil motion shows a maximum of $2/\pi$ times the steady pressure jump $(p_2-p_1)_{x_s}$.

Integration of the various components over the shock trajectory to obtain the contribution to the overall unsteady lift and moment learns that the lift contains only a contribution of the fundamental frequency. The resulting unsteady moment also contains a term $(p_2-p_1)_{x_s} \cdot x_0^2 \cdot \cos 2\omega t$. So it can be expected that the second harmonic shows up first in the unsteady moment.

From the considerations given above it follows also that measuring the first Fourier component of the pressure signals, as is done in the present tests via the tubing system, gives by chordwise integration a correct value of the unsteady lift. As far as the moment is concerned the second harmonic of order x_0^2 can not be distinguished.

4 EXPECTED CAPABILITY OF THE NEW CALCULATION METHODS

In the preceding analysis of the experimental data the results of thin airfoil theory have been added as a reference for two reasons. Firstly these results serve as a simple basis for the distinction of the typical transonic phenomena and secondly, linear lifting surface theory is widely used in aeroelastic applications. As long as the flow is moderately subsonic thin airfoil theory has proven to be a rather adequate tool indeed. However, from the preceding discussions it is apparent, that calculation methods for transonic flow should include the effect of airfoil thickness, incidence and - if shock waves are present - also the effects of the periodical shock wave motion.

In recent years considerable progress has been achieved in solving the non linear equations for unsteady transonic flow (reviews on the current status are given in references 14-20). With one exception (Ref. 21) all new calculation methods are dealing with inviscid flow. In order to get an impression about the improvements one might expect from these methods some comparisons will be presented between theory and experiment for the NLR 7301 airfoil. At this moment the comparison is limited to quasi-steady flow, but in the near future comparative studies will be performed also for fully unsteady flow.

Considering first the quasi-steady case has the advantage that a reasonable estimate can be given of the effect of the boundary layer, by using an existing method for steady transonic flow, which includes the displacement effect of the boundary layer (Bauer, Korn, Garabedian and Jameson (Ref. 22)). Further for quasi-steady flow a rather accurate estimate can be given of the severity of interference from the slotted tunnel walls, a situation which is not yet reached for unsteady measurements.

The calculations for the 16.5 per cent thick NLR 7301 airfoil have been performed at the same

Mach number as in the experiments, but for an incidence α_c, which includes the correction for wall interference. For the NLR Pilot tunnel this correction has been established to be (Ref. 23):

$$\Delta\alpha= C. \ C_\ell$$

where C_n is steady lift coefficient and C a coefficient, depending on the free stream Mach number (Fig. 24).

4.1 Fully subsonic flow (condition A)

Calculated and measured results for the airfoil in the subsonic flow condition A are shown in figure 25. Figure 25.I reveals a significant effect of the boundary layer in the steady mean position of the airfoil. The corresponding quasi-steady results (Fig. 25.II) demonstrate that the deviations of the test results from thin airfoil theory, as discussed in chapter 3.2.1, are due to the combined effects of thickness, incidence and viscosity. The effect of thickness and incidence dominates on the front part of the airfoil and the effect of viscosity towards the rear.

For the quasi-steady results the wall correction has been applied on the measured data, since this effect can be translated simply in an additional change of effective incidence due to the change in lift. This additional change has to be substracted from the geometrical change in incidence. From the results in figure 25.II it can be noted that the tunnel walls have a considerable effect.

4.2 Transonic flow with shock wave (condition B)

The second example deals with the transonic flow condition B (Fig. 4). In steady flow (Fig. 26.I) viscosity again has a large effect, in particular on the location of the shock wave. The importance of inserting boundary layer effects is reflected also in the quasi-steady results (Fig. 26.II). On the upper surface a considerably improved prediction is obtained, when thickness and boundary layer effects are considered simultaneously. Especially the location of the high pressure peak resulting from the shift in shock position is predicted much better.

The improvements achieved can be observed also in the quasi-steady aerodynamic coefficients, collected in table 1. For instance these data show that a $M_\infty = 0.7$ thickness and incidence are responsible for an increase of the thin airfoil value of the normal force coefficient, k_α, of more than 50 per cent. The inclusion of the boundary-layer leads to a decrease of the order of 35 per cent, as can be observed by comparing the results with and without boundary layer, both obtained with the non-conservative calculation scheme (the conservative scheme, which guarantees the best numerical solution of the transonic flow equations did not converge for inviscid flow so this value could not be added). From the last two columns it follows that the tunnel wall effect in the present tests is considerable and accounts to about 25 per cent. At $M_\infty = 0.5$ the effects mentioned are less than at transonic speed, but still significant.

TABLE 1

Quasi-steady aerodynamic derivatives (NLR 7301 airfoil)

		Thin airfoil theory		Inviscid theory + thickness		Inviscid theory + thickness + boundary layer				Inviscid theory + thickness + boundary layer + wall interference		Experiment	
				Non-conservative F-D scheme		Non-conservative F-D scheme		Conservative F-D scheme		Conservative F-D scheme			
M_∞	α_o	k_α	m_α	k_α	m_α	k_α	m_α	k_α	m_α	k_α	m_α	k_α	m_α
0.5	0.85°	2.31	0	2.73	0.043	2.53	-0.036	2.53	-0.036	2.22	-0.032	2.18	-0.090
0.7	3.00°	2.80	0	4.24	0.11	3.21	0.00	3.92	-0.22	3.23	-0.18	3.20	-0.34

F-D= Finite difference

From the examples discussed so far a good impression is obtained about the improvements which can be expected at most from the inclusion of thickness and incidence theories. Clearly the inclusion of these effects is an important step forward, which on itself, however, does not lead to improved predictions. A genuine improvement in this respect can be achieved only if the second step is made also, i.e. the inclusion of boundary layer effects.

A weak point in the considerations given above is seemingly that the examples deal with a relatively low Reynolds number ($\sim 2.10^6$). However, similar calculations for higher values of this parameter (up to 30.10^6, with fixed transition point) do not exhibit a significant sensivity to Reynolds number changes. This seems to indicate that under full scale conditions the effect of viscosity remains of the same order of magnitude as shown here.

4.3 The "shock-free" design condition (condition C)

To conclude the evaluation of the capability of advanced theories on the basis of quasi-steady flow the "shock-free flow condition C will be considered. For this purpose a comparison is made between results calculated for the theoretical "shock-free" design condition and results measured for condition at which "shock-free" flow is obtained in the wind tunnel.
In this way the circumstance that the experimental design condition (i.e. Mach number and incidence) differs from the inviscid theoretical design condition can be discarded, assuring that both theory and experiment deal with the carefully balanced condition of "shock-free" flow.

The steady pressure distributions computed for incidences at and around the design condition (Fig. 27.I) exhibit in the supersonic region at the upper surface the same marked changes in the shape of the pressure distribution as observed in the measurements (Fig. 10). The lower surface behaves very regularly. From a comparison between the corresponding quasi-steady pressure distributions, given in figure 27.II, it becomes apparent that there is a considerable improvement with respect to

thin airfoil theory. The typical bulgy character of the distribution on the upper surface is predicted reasonably well and also the prediction for the lower surface is improved. This justifies the expectation that methods based on inviscid theory are able to predict at least qualitatively the main characteristics of the unsteady flow for oscillations around the "shock-free" design condition.

5. CONCLUDING REMARKS

From the preceding evaluation it is apparent that the inclusion of airfoil thickness, incidence and transonic shock motions in inviscid flow calculations leads to an improvement of the theoretical predictions in an at least qualitative sense. In quantitative sense a large discrepancy with the real flow will remain as a result of the boundary layer, which to a large extent determines the final location of the shock and by that the overall unsteady airloads. However, as the modelling of unsteady boundary layers is only in its first phase (for a review of the present status reference is made to Ref. 20) it is unlikely that in the near future sophisticated calculation methods will become available for this purpose. Therefore in the coming period an engineering type of approach has to be followed. In this respect the ideas developed by Magnus and Yoshihara (Ref. 21) deserve attention, since their relatively simple "viscous ramp" model lends itself for easy implementation in inviscid calculation methods.

From a computational point of view small perturbation methods are very attractive. It should be investigated, therefore, what the limits of such methods are, in particular when applied to thick supercritical airfoils of the type as the one considered in this paper. In this respect it should be noted that the impressions given in the preceding chapter about the improvements attainable with the new calculation methods are based on solutions of the full potential equation, without assuming small perturbations.

Further from the considerations of the quasi-steady results of the NLR 7301 airfoil it has become clear that in order to improve the reliability of comparisons between theory and wind tunnel data there is an urgent need for methods to assess the amount of wall interference in unsteady experiments in transonic test sections with slotted or poreus walls. Finally the insight with respect to the effect of Reynolds number, being already a crucial parameter in steady transonic flow, should be increased by performing tests in a high Reynolds number test facility.

6. ACKNOWLEDGEMENT

7. REFERENCES

1 Boerstoel, J.W. and Huizing, G.H.   Transonic shock-free aerofoil design by an analytic hodograph method
Journal of Aircraft, 12 No. 9, pp 730-736, 1975.

2 Boerstoel, J.W.   Review of the application of hodograph theory to transonic aerofoil design and theoretical and experimental analysis of shock-free aerofoils
Symposium Transsonicum II, Göttingen, Sept. 1975.

3 Rohne, B.   Data report of a wind tunnel investigation on airfoil section NLR 7301.
NLR report TR 74049 C, 1974.

4 Zwaaneveld, J.   Aerodynamic characteristics of the supercritical shock-free airfoil section NLR 7301.
NLR report TR 76052 C, 1976.

5 Poestkoke, R.   Hydraulic test rig for oscillating wind tunnel models.
NLR report MP 76020 U, 1976.

6 -   Facilities and Equipment at NLR

7 Tijdeman, H.   Investigations of the transonic flow around oscillating airfoils.
Dissertation Technical University Delft (to be published).

8 Tijdeman, H.   On the motion of shock waves on an airfoil with oscillating flap.
IUTAM Symposium Transsonicum II, Göttingen, Sept. 1975.
eds. Oswatitsch, K and Rues, D Springer Verlag, Berlin 1976.
(see also NLR report TR 75038 U).

9 Erickson, R.L. and Stephenson, J.D.   A suggested method of analyzing for transonic flutter of control surfaces based on experimental evidence.
NACA RM A7F 30, 1947.

10 Roos, R.   Application of Panel Methods for unsteady flow.
NLR report TR 76010 U, 1976.

11 Magnus, R.J. and Yoshihara, H.   Calculations of transonic flow over an oscillating airfoil
AIAA paper 75-98, 13th Aerospace Sciences Meeting Pasadena, 1975.

12 Laval, P.   Calcul de l'écoulement instationair transsonique autour d'un profil oscillant par une methode a pas fractionnaires
ONERA TP No. 1975-115, 1975.

12-8

13 Krupp, J.A. and   Studies in Transonic Flow IV
    Cole, J.D.   Unsteady Transonic Flow
                                 UCLA-Eng-76104, Oct. 1976

14 Bland, S.R.   Recent advances and concepts in unsteady aerodynamic theory.
                                 NASA SP-347: Aerodynamic analysis requiring advanced
                                 computing, March 1975, pp 1305-1326.

15 Tijdeman, H.   High subsonic and transonic effects in unsteady aerodynamics
                                 part of AGARD report No. 636, 1976.

16 Stahara, J.R. and   Unsteady Transonic Aerodynamics - An aeronautical Challenge
    Spreiter, S.S.   Symposium on Unsteady Aerodynamics.
                                 ed. Kinney, R.B., Univ. of Tucson, 1975, pp 553-581.

17 Landahl, M.T.   Some developments in unsteady transonic flow research.
                                 IUTAM Symposium Transsonicum II, Göttingen, Sept. 1975.
                                 eds. Oswatitsch, K and Rues, D; Springer Verlag, Berlin, 1976.

18 Ballhaus, W.F.   Some recent progress in transonic flow computations.
                                 Lecture series No. 87 on Computational Fluid Dynamics, von
                                 Karman institute, Rhode-St-Genese, Belgium, March 1976.

19 Wu, J.M. and   A survey of transonic aerodynamics.
    Moulden, T.H.   AIAA paper 76-326; AIAA 9th Fluid and Plasma Dynamic Confe-
                                 rence, San Diego, Ca., July 1976.

20 Mc Croskey, W.J.   Some current research in Unsteady Fluid Dynamics.
                                 Journal of Fluids Engineering, Vol. 99, No. 1, March 1977.

21 Magnus, R. and   The transonic oscillating flap.
    Yoshihara, H.   AIAA paper 76-327; AIAA 9th Fluid and Plasma Dynamic Confe-
                                 rence, San Diego, July 1976.

22 Bauer, F., Garabedian, P., Supercritical wing sections II.
    Korn, D. and Jameson, A.   Lecture notes on Economics and Math. Systems No. 108.
                                 Springer Verlag, 1975.

23 Smith, J.   Values of the wall interference corrections for the NLR
                                 Pilot tunnel with 10 % open slotted test section.
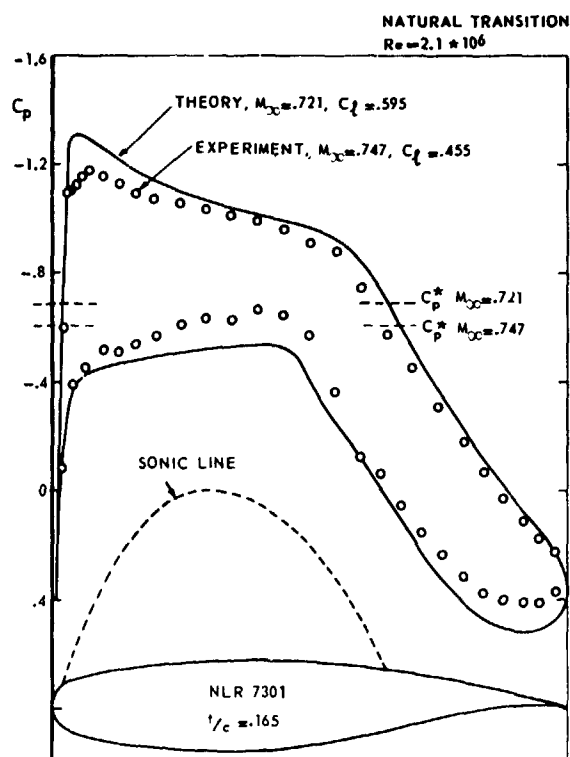   NLR int. report AC 74-01, 1974.

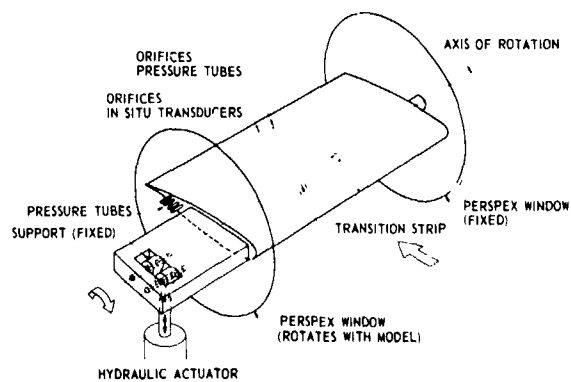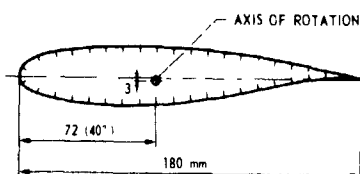Fig. 1 Theoretical and experimental shock — free pressure distributions of the NLR 7301 airfoil (Reproduced from [4])
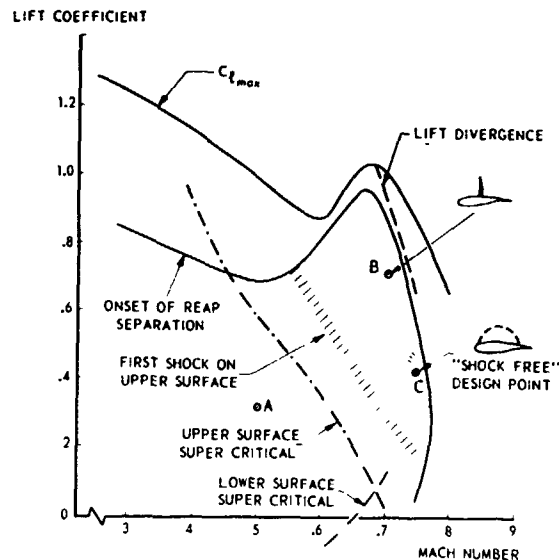

Fig. 2 Schematic view of test set up
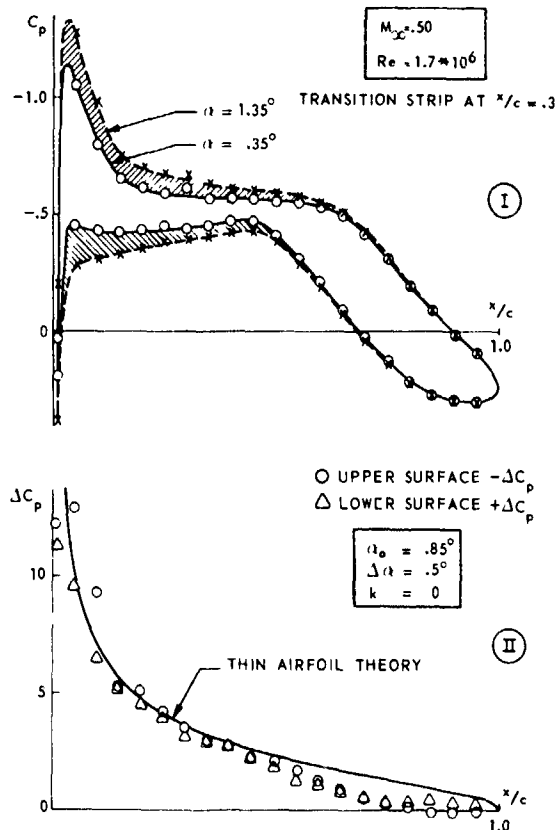

Fig. 4 C_L — M plane for NLR 7301 airfoil (t/c = 16.5%)

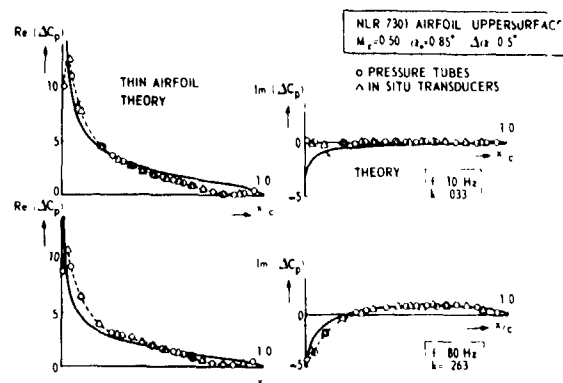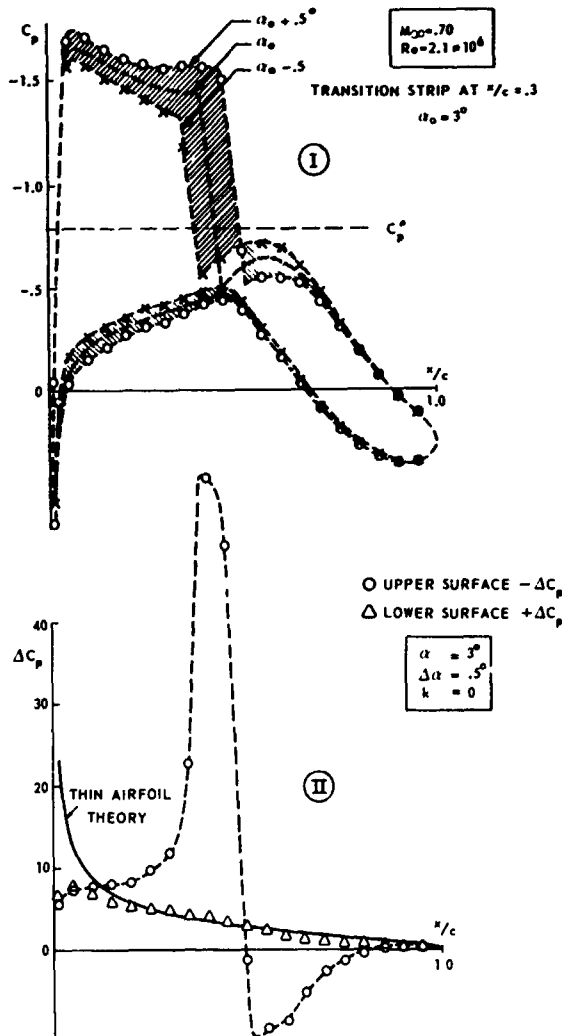Fig. 5 Steady and quasi — steady pressure distributions on NLR 7301 airfoil at subsonic speed (Condition A)

Fig. 7 Steady and quasi — steady pressure distributions on NLR 7301 airfoil in transonic flow with shock wave (Condition B)

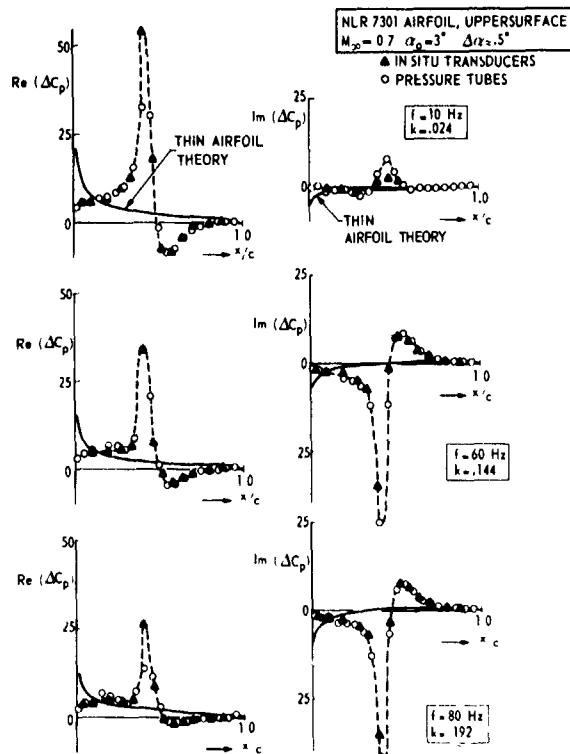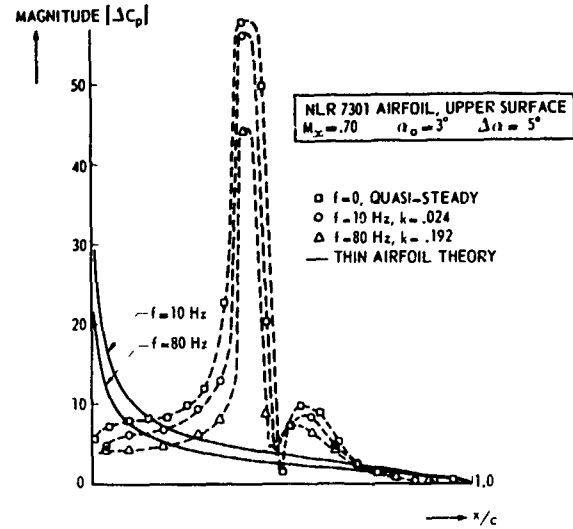Fig. 8 Development of unsteady pressure distributions with frequency in transonic flow with shock wave (Condition B)

Fig. 9 Effect of a shock wave on the unsteady pressure distributions (Condition B)
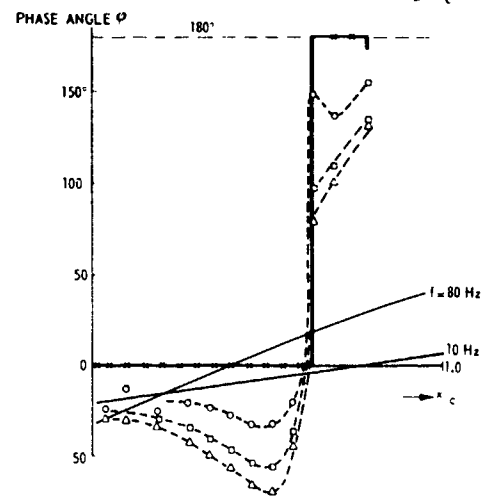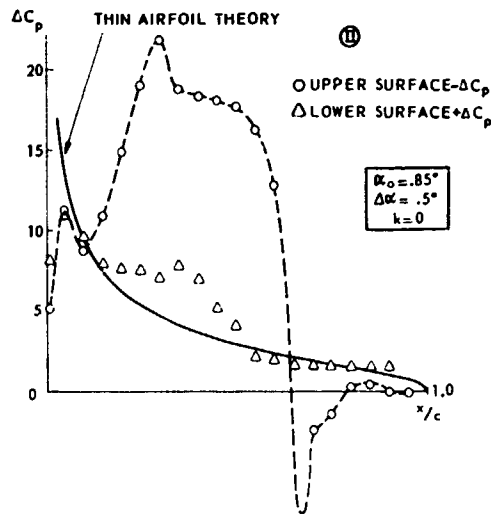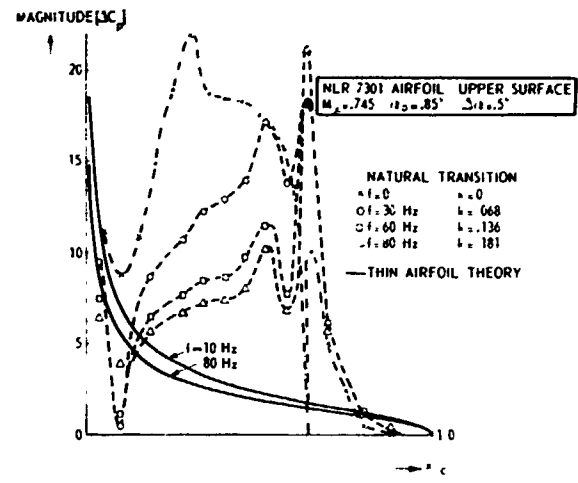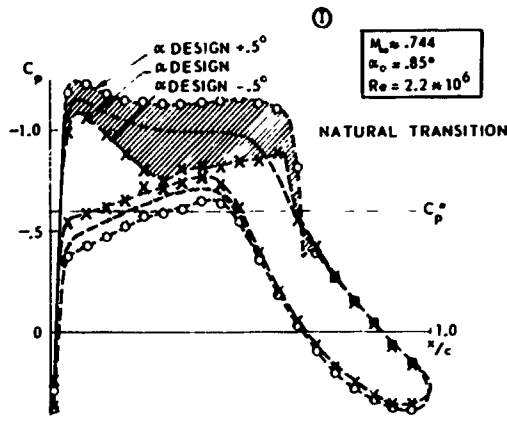
Fig. 10 Steady and quasi-steady pressure distributions on NLR 7301 airfoil around the design point (Condition C)

Fig. 11 Unsteady pressure distributions for the "shock-free" design condition (Condition C)
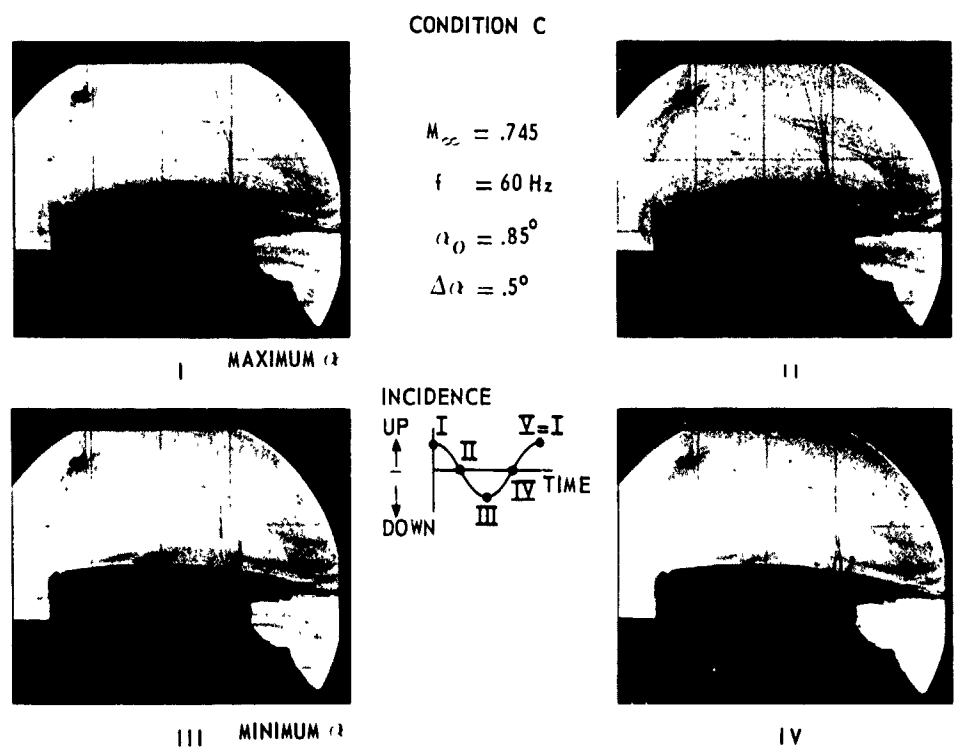
CONDITION C

$M_\infty = .745$

$f = 60 \, Hz$

$\alpha_0 = .85^\circ$

$\Delta\alpha = .5^\circ$

MAXIMUM α

I

II

INCIDENCE

MINIMUM α

III

IV

Fig 12 Time history of the periodical shock wave motion (Condition C)

NLR 7301 AIRFOIL
$M_\infty=0.50$ $\alpha_0=0.85°$ $\Delta\alpha=0.5°$

O TRANSITION STRIP AT x/c .3
△ NATURAL TRANSITION
Re = 1.7 × 10⁶

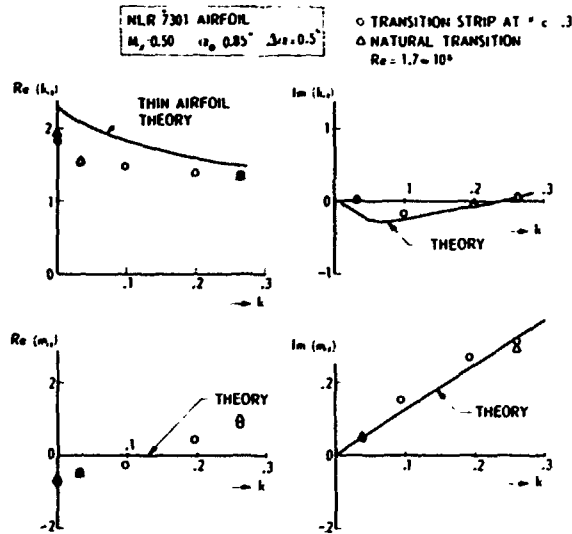Fig. 13 Unsteady normal force and moment coefficients as a function of frequency in subsonic flow (Condition A)
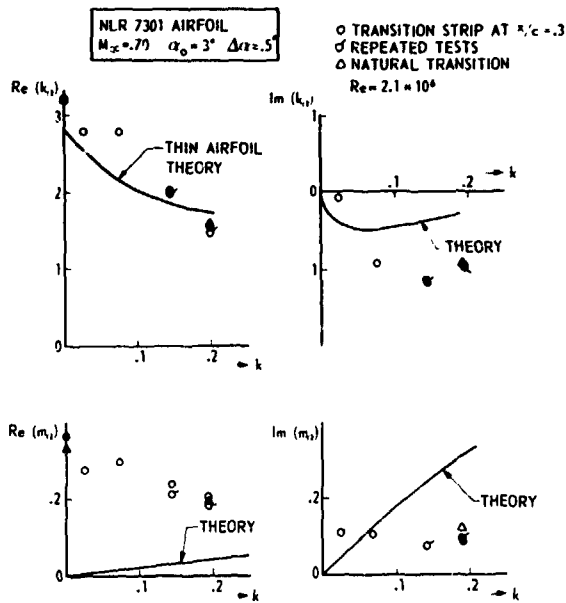
NLR 7301 AIRFOIL
$M_\infty=.70$ $\alpha_0=3°$ $\Delta\alpha=.5°$

O TRANSITION STRIP AT $x/c=.3$
σ REPEATED TESTS
△ NATURAL TRANSITION
Re = 2.1 × 10⁶

Fig. 14 Unsteady normal force and moment coefficients as a function of frequency (Condition B)

NLR 7301 AIRFOIL
$M_\infty=.745$ $\alpha_0=.85°$ $\Delta\alpha=.5°$

O TRANSITION STRIP AT $x/c=3$
△ NATURAL TRANSITION
Re = 2.2 × 10⁶
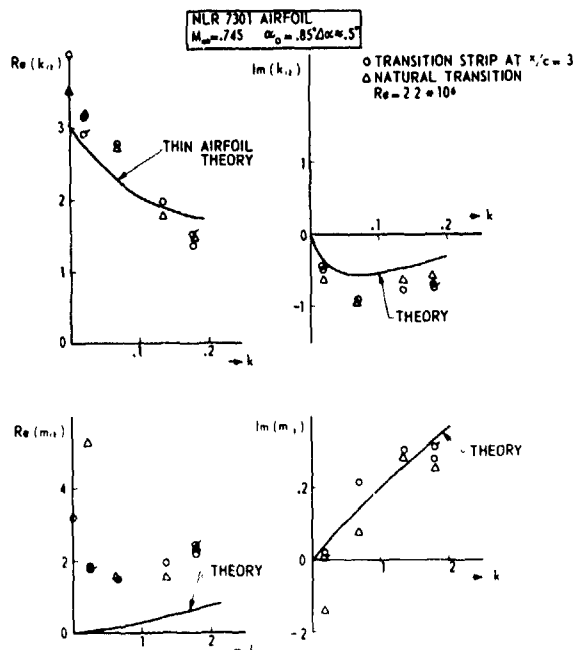
Fig. 15 Unsteady normal force and moment coefficients as a function of frequency (Condition C)

——— THIN AIRFOIL THEORY
– – – EXPERIMENT
—·— EXPERIMENT WITHOUT (ESTIMATED) EFFECT OF SHOCK WAVE

↑1 EFFECT OF PRESSURE PEAK DUE TO MOVING SHOCK WAVE
↑2 SHIFT IN AERODYNAMIC CENTRE
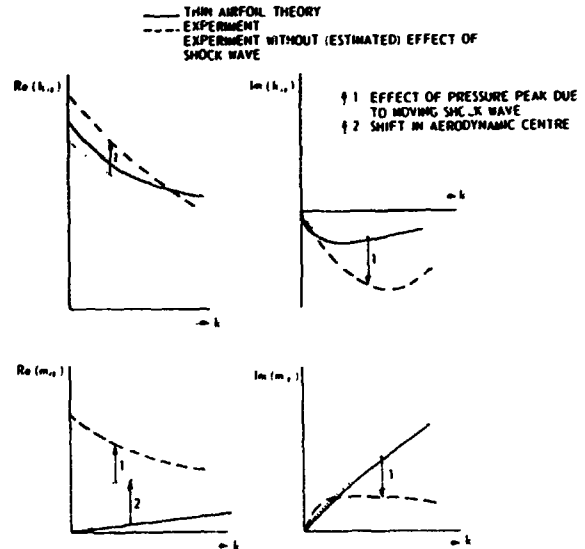
Fig. 16 Qualitative explanation of the effect of the oscillating shock wave on the unsteady aerodynamic coefficients

NLR 7301 AIRFOIL
$M_\infty=0.7$ $\alpha_0=3°$ $\Delta\alpha=1.0°$

AIRFOIL MOTION

SHOCK POSITION

BEST SINE FIT

$f=10$ Hz
$k=.023$

PHASE SHIFT ≈5°

$f=30$ Hz
$k=.072$

≈20°

$f=60$ Hz
$k=.144$

≈35°

BEST SINE FIT

$f=80$ Hz
$k=.192$

≈50°
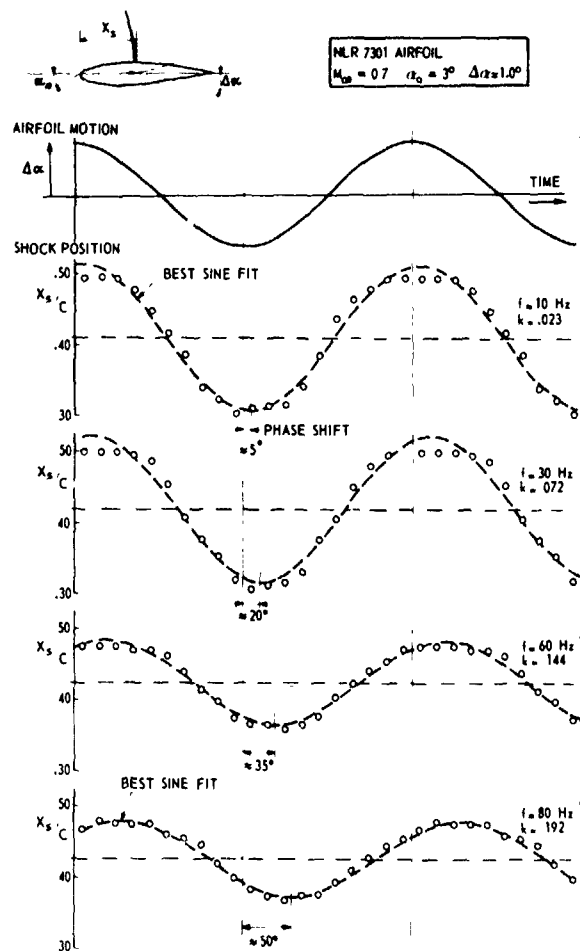
Fig. 17 Periodical shock wave motion in dependence of frequency (Condition B)
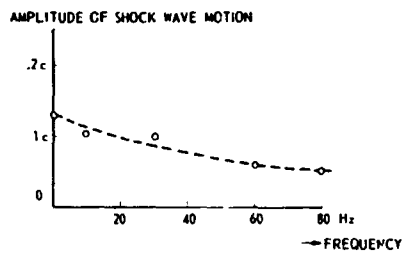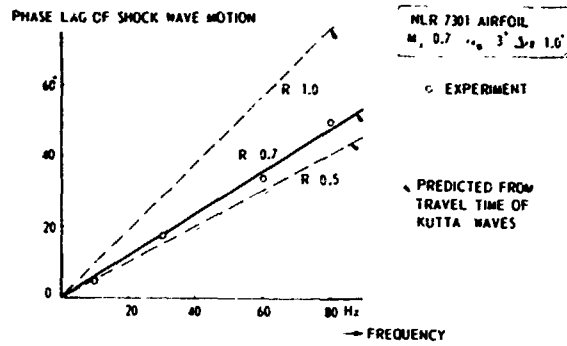
Fig. 18 Effect of frequency on the amplitude and phase lag of the periodical shock wave motion (Condition B)
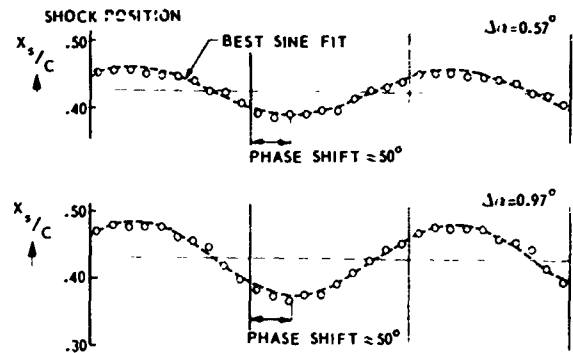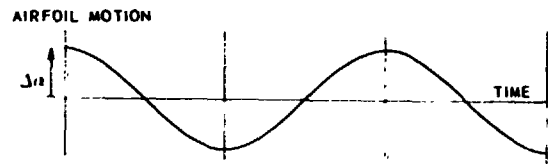
Fig. 21 Influence of amplitude of airfoil oscillation on shock wave motion (Condition B)
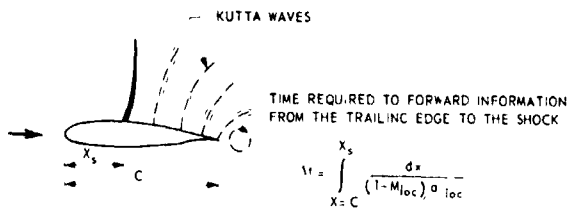
Fig. 19 The propagation of information from the trailing edge to the shock wave
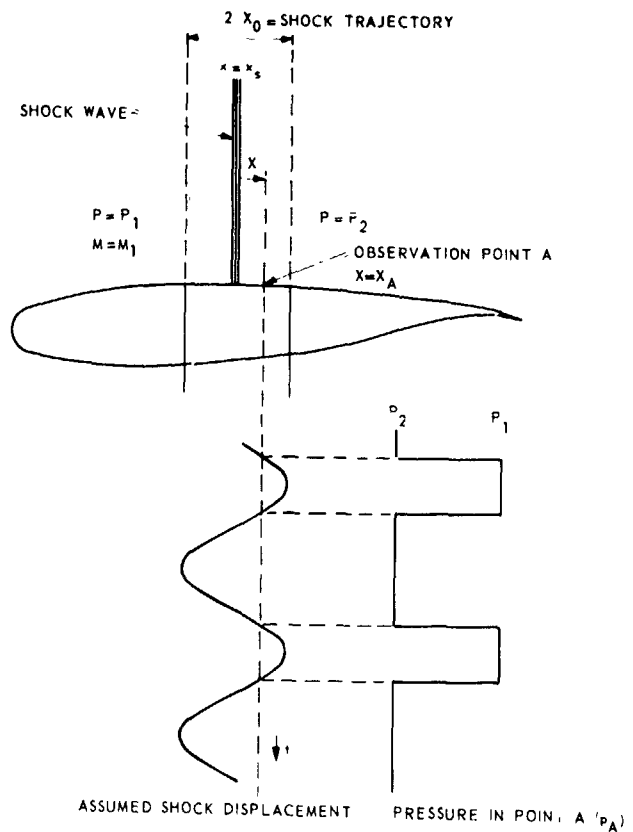
Fig. 22 Contribution of a periodical moving shock wave to the pressure signal in a fixed observation point
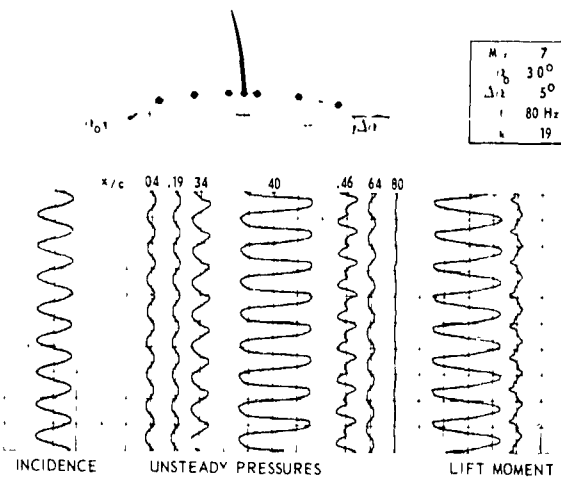
Fig. 20 Example of unsteady pressure signals on an oscillating airfoil in transonic flow with shock wave
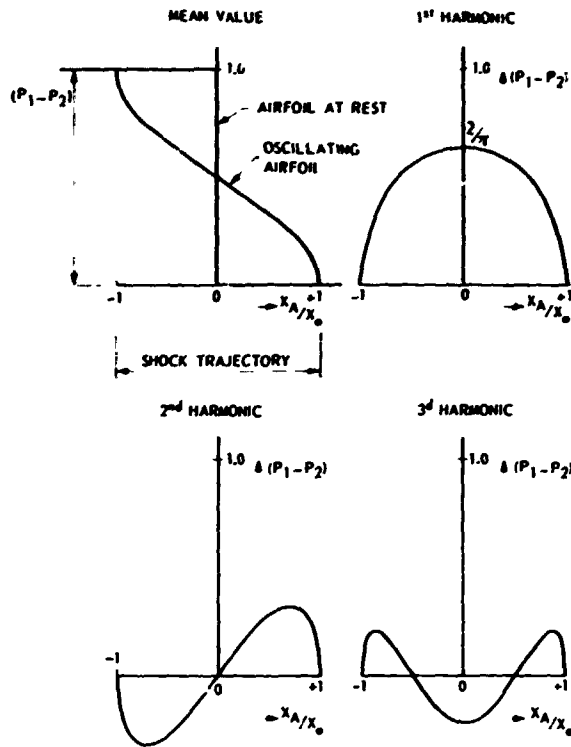
MEAN VALUE

1.0

(P_1-P_2)

— AIRFOIL AT REST

— OSCILLATING AIRFOIL

-1   0 $\rightarrow X_A/X_o$ +1

SHOCK TRAJECTORY

1ˢᵗ HARMONIC

1.0 $\Delta(P_1-P_2)$

$2/\pi$

-1   0 $\rightarrow X_A/X_o$ +1

2ⁿᵈ HARMONIC

1.0 $\Delta(P_1-P_2)$

-1   0   +1 $\rightarrow X_A/X_o$

3ᵈ HARMONIC

1.0 $\Delta(P_1-P_2)$

-1   0   +1 $\rightarrow X_A/X_o$

Fig. 23 Distribution of the first four Fourier components along the trajectory of the shock motion

$a = a_m + \Delta a$

$\Delta i = C.C_{\ell_m}$ (DEG)

(SUBSCRIPT m DENOTES UNCORRECTED, MEASURED VALUES)

$\rightarrow M_\infty$

0   .5   .6   .7   .8   .9

-.5

-1.0

C

-1.5
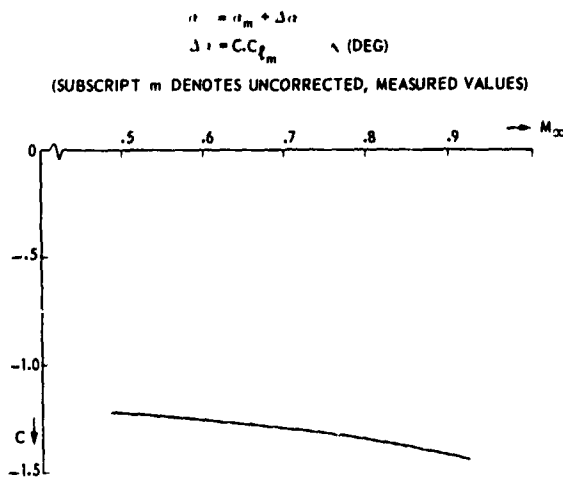
Fig. 24 Wall interference correction for the NLR Pilot tunnel

C_p

I STEADY

NLR 730i AIRFOIL
$M_r = .5$

— INVISCID

WITH BOUNDARY LAYER CORRECTION

1.5

1.0

.5

0   1.0 $\rightarrow x/c$

THEORY [22], $\alpha_c = .4°$
o EXPERIMENT
$\alpha_o = .85°$, $Re = 1.7 \times 10^6$
TRANSITION STRIP AT
$x/c = .3$

$-\Delta C_p$

II QUASI - STEADY (UPPER SURFACE)

25

20

15

10

5

0   1.0 $\rightarrow x/c$

$M_\infty = .5$ $f = 0$
o EXPERIMENT $\alpha_o = .85°, \Delta\alpha = .5°$
• EXPERIMENT CORRECTED FOR WALL INTERFERENCE

THIN AIRFOIL THEORY

INCL. THICKNESS AND INCIDENCE

INCL. THICKNESS, INCIDENCE AND BOUNDARY LAYER
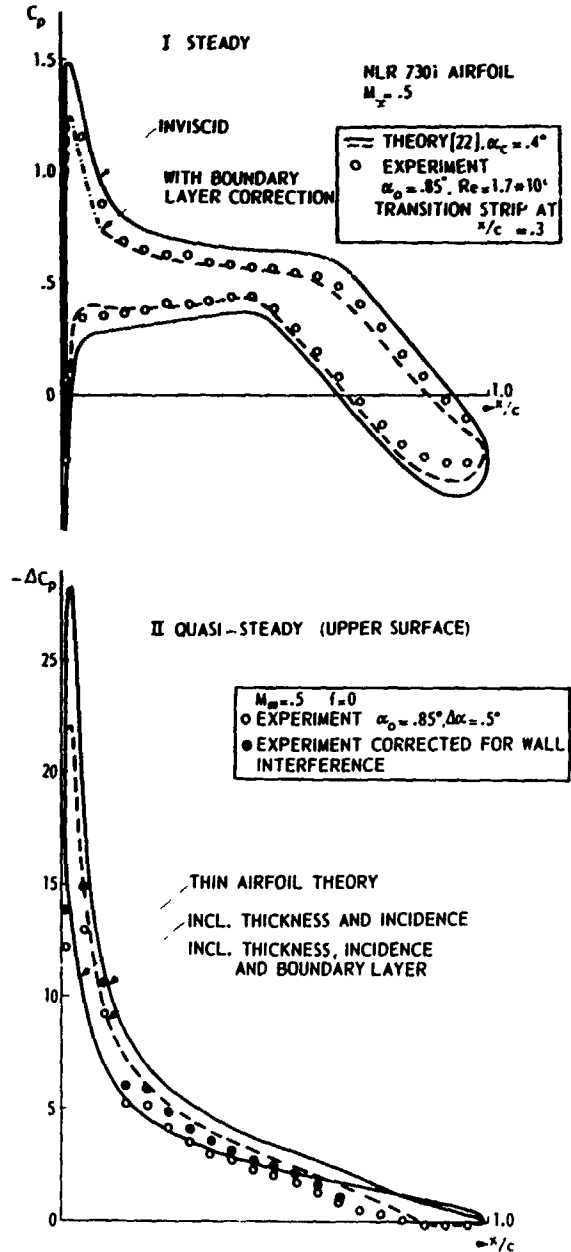
Fig. 25 Effect of thickness, incidence and boundary layer on the steady and quasi − steady pressure distributions in subsonic flow (Condition A)
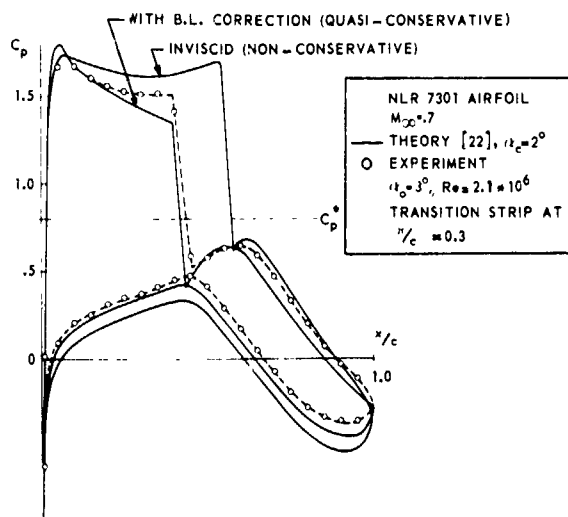
Fig. 26 – I Steady pressure distributions in the mean position (Condition B)
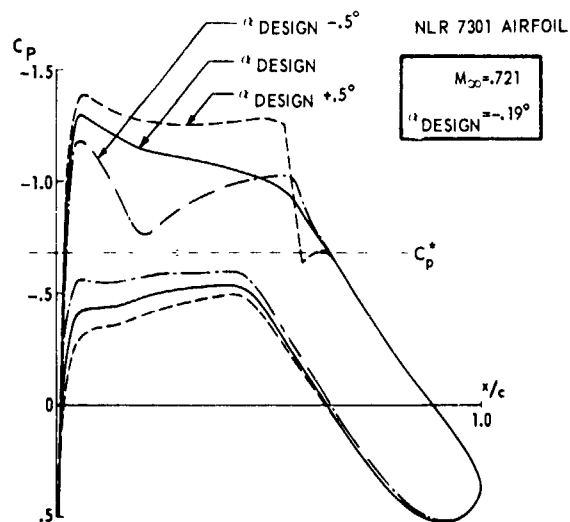
Fig. 27 – I Calculated steady pressure distributions at and about the theoretical "shock–free" design condition (Non conservative scheme)
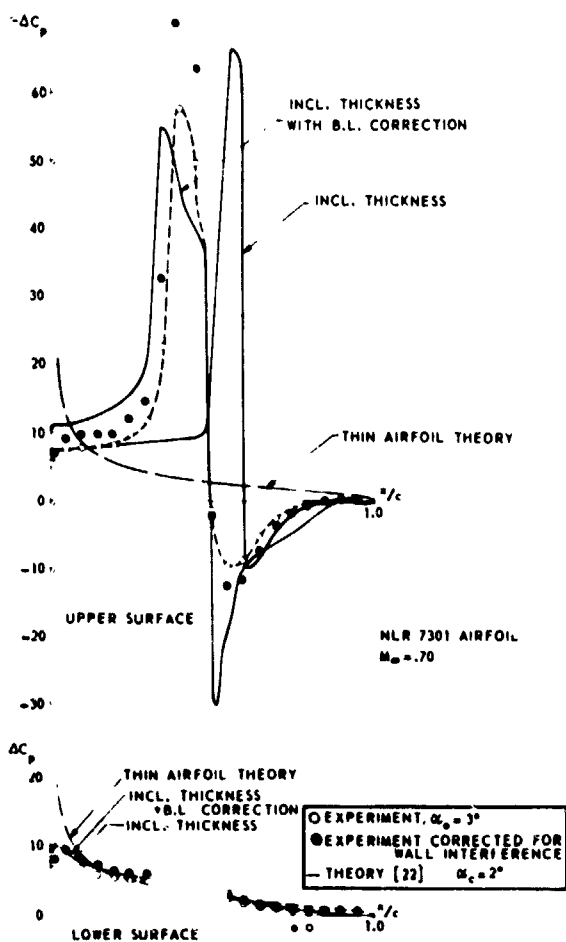
Fig. 26 – II Quasi – steady pressure distributions (Condition B)
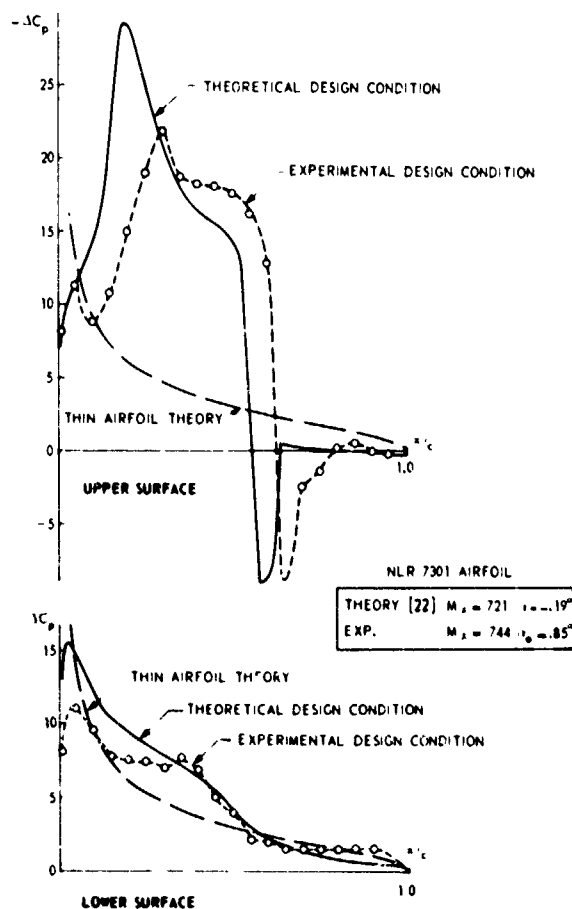
Fig. 27 – II Quasi – steady pressure distributions for the theoretical "shock – free" design condition (Condition C)

THE TRANSONIC OSCILLATING FLAP
A Comparison of Calculations With Experiments*

R. Magnus and H. Yoshihara **

General Dynamics Convair Division
P. O. Box 80847
San Diego, California 92138 USA

SUMMARY

Finite difference calculations based on the exact inviscid equations for an oscillating flap on the NACA 64A-006 airfoil at M = 0.875 are compared to the Tijdeman-Schippers experimental results. Viscous effects were incorporated in a phenomenological manner using viscous displacement ramps. Reasonably good agreement was obtained, but with a significant discrepancy in the shock motions attributable to a mismatch in the surface pressures upstream of the shock. Recalculation at M = 0.854 yielded results in good overall agreement with the experiments at M = 0.875 for both the steady and the unsteady cases. Tentative conjectures as to the cause of the above discrepancy then conclude the paper.

1. INTRODUCTION

In Reference 1 an unsteady finite difference procedure based on the exact inviscid flow equations was used to calculate the flow over the NACA 64A-006 airfoil at M = 0.875 and $\alpha = 0°$ where a quarter-chord flap oscillated sinusoidally. The oscillation amplitude was 1° about $\delta = 0°$, and the frequency was 120 hertz corresponding to a reduced frequency based on the airfoil chord of 0.468.

In the above calculations the important viscous effects were incorporated using a phenomenological procedure. Here airfoil shape modifications, simulating the viscous displacement, were first determined in a steady inviscid calculation in which the measured pressures were prescribed as boundary conditions in lieu of the surface slopes where the viscous displacement effects were significant. The resulting viscous ramps suitably modeled were then inserted into the unsteady problem tying the ramps at the shocks in a quasi-steady fashion to the instantaneous shock strengths, and those on the flap to the instantaneous flap angle.

Thus, in this manner the unsteady viscous effects, modeled from the more readily available steady experimental data, were incorporated as time-varying changes to the airfoil shape which could then be treated by the existing inviscid finite difference procedure.

The above example was chosen because of the existence of the experimental results of Tijdeman and Schippers (Reference 2), which not only furnished the steady pressure distributions to model the viscous ramps, but the unsteady results to assess the final calculations.

A comparison of the calculated and measured unsteady results in Reference 1 showed a reasonably good overall agreement, but there was a significant difference in the behavior of the shocks as seen in Figure 1. Here
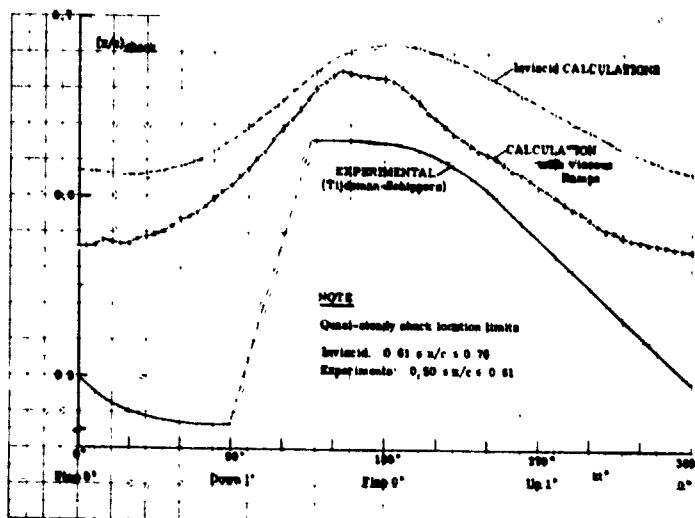

Figure 1. Comparison of the Calculated and Measured Shock Position at M = 0.875

the mean positioning of the shock in the experiments was not only significantly further upstream of the calculated value, but the shock excursion was considerably larger. Moreover in the experiments in contrast to the calculations the shock disappeared during a brief interval in its retreating phase as the shock velocity became sufficient to render the flow upstream of the shock subcritical.

The cause of the above discrepancy in the shock histories can be traced to a mismatch of the pressures upstream of the shock. The lower Mach numbers prevailing here in the experiments led to a weaker shock at a further upstream positioning which then resulted in a more pronounced role of the shock velocity in determining the shock strength. This chain of effects then caused the observed difference in the shock behavior.

Both the calculated and experimental unsteady pressures upstream of the shock and hence their difference remained essentially invariant during the oscillation of the flap at the respective steady values for the mean flap angle of 0°. We can accordingly turn to this steady case to study the cause of the discrepancy in the pressures upstream of the shock.

In Figure 2 we show the steady inviscid pressure distribution at $M = 0.875$ and $\delta = 0°$ compared to the measured distribution. Also shown here is the pressure distribution calculated with the measured pressures prescribed aft of the shocks. In the latter result, assuming the viscous displacements to be properly inputed, the pressures over the entire airfoil should then agree with the experiments. We see in Figure 2 that this is not the case. A mismatch of the calculated and measured pressures upstream of the shock still persists, the addition of the viscous ramps having no effect on the calculated pressures upstream of the shock. We can thus conclude that the modeling of the viscous ramps cannot be blamed for the above pre-shock mismatch.
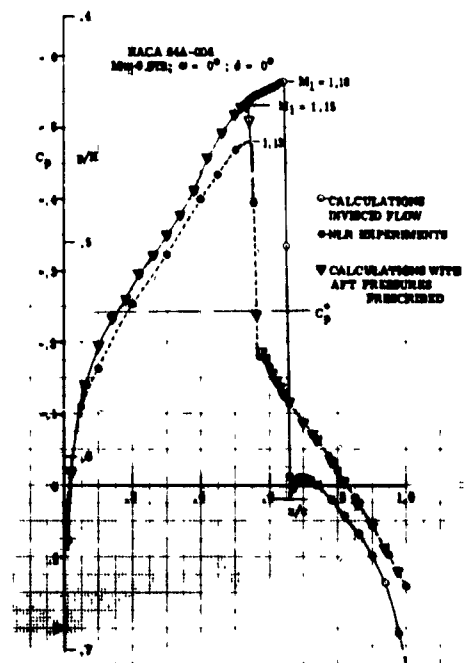
Figure 2. Comparison of the Steady Pressure Distributions for Zero Flap Deflection at $M = 0.875$

In the above calculations we have ignored the viscous displacement occurring upstream of the shock because of the significant prevailing favorable pressure gradients. This omission cannot be the cause of the mismatch since these displacement effects even when included result in a thickening of the airfoil, leading to a lessening rather than a needed enhancement of the pressures upstream of the shock to match the experiments.

The mismatch of the pre-shock pressures must therefore be due either to the inaccuracy of the inviscid calculational procedure itself or to an inadequate flow simulation in the wind tunnel. Past extensive and successful use of the inviscid procedure would suggest tentatively the cause to be the latter, possibly due to an inadequate test section length or to wall interference.

The latter possibility is reinforced by the excellent agreement for $\delta = 0°$ between the steady calculations at $M = 0.854$ and the experimental results at $M = 0.875$ shown in Figure 3 with and without the viscous ramps. Here again prescribing the aft measured pressures or equivalently adding the viscous ramps has not changed the pressures upstream of the shock.

Further evidence of the above correspondence is given in Figure 4 where a comparably good agreement is shown for $\delta = 1°$. Finally in Figure 5 we show the excellent match of the pressures upstream of the shock between the inviscid case for $M = 0.90$ and the measurements from Ref. 2 at $M = 0.875$.
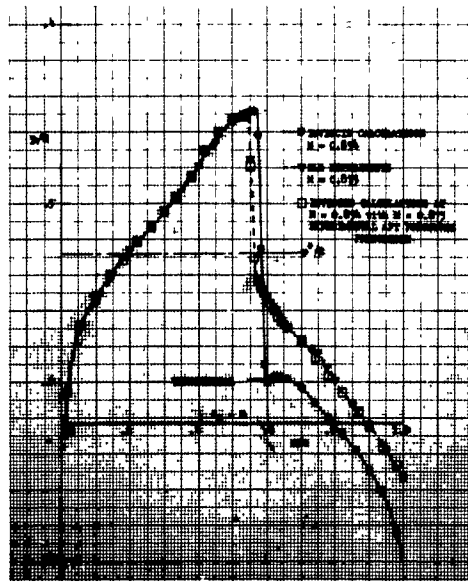
Figure 3. Comparison of the Calculations
at M = 0.854 with the Experiments
at M = 0.875 - Zero Flap
Deflection
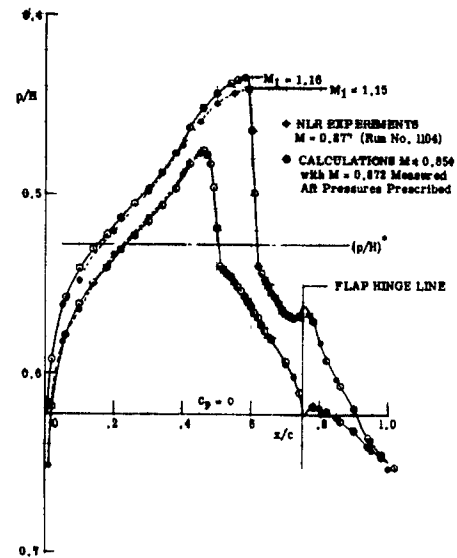
Figure 4. Comparison of the Calculations
at M = 0.854 with the Experiments
at M = 0.875 - 1° Flap Deflection

Figure 6 shows a comparison of the pressure distributions for δ = 1° between the inviscid case at M = 0.854 and the calculations at the same Mach number with the M = 0.875 aft pressures prescribed. In contrast to the upper surface here and to the δ = 0° case of Figure 2, the addition of the viscous ramp on the lower surface has a significant effect on the pressures upstream of the shock.
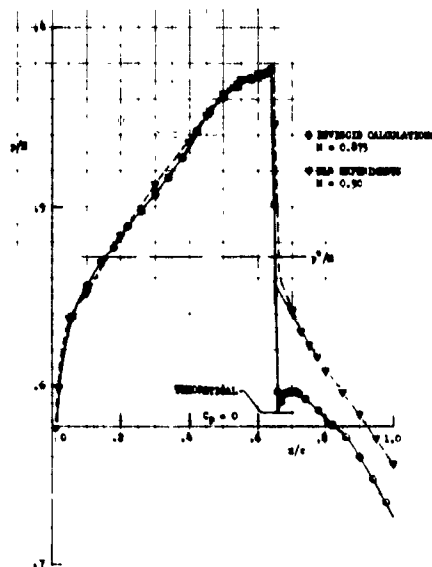
Figure 5. Comparison of the Calculations at
M = 0.875 and the Measurements
at M = 0.900 - Zero Flap
Deflection
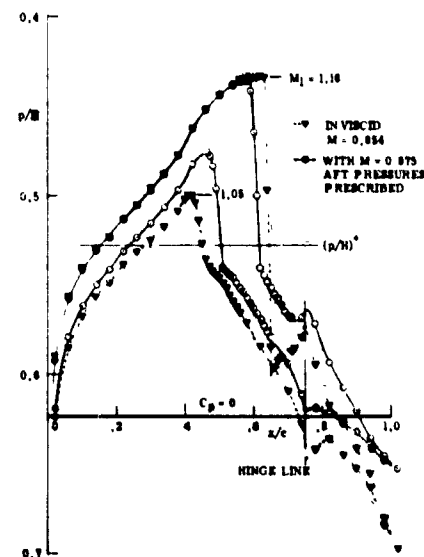
Figure 6. Comparison of the Calculated
Pressure Distributions at
M = 0.854 and 1° Flap Deflection
With and Without the Viscous Ramps

To explain this difference of the upstream influence, we must recall that perturbations originating downstream of the terminating shocks must detour over the intervening embedded supersonic region to arrive at the airfoil surface upstream of the shocks. During this travel the perturbation wave fronts spread geometrically with the bulk of the perturbation energy being swept downstream with the ambient flow. Thus for a given perturbation, its subsequent geometric attenuation and hence its upstream influence arriving at the airfoil surface upstream of the shock will depend on the height of the supersonic barricade. In the case of Figure 2 for δ = 0°, the supersonic barricade is

sufficiently high to block essentially the perturbations due to the viscous ramps, whereas in the case of the lower surface of Figure 6 for $\delta = 1°$, the stronger upstream influence results from the lowering of the barricade.

In the case of the oscillating flap it was found earlier that there was no effect of the moving flap on the pressures upstream of the shock, these pressures assuming the steady pressures corresponding closely to the mean deflection of the flap. On the other hand a sustained flap deflection will clearly change the surface pressures forward of the shock on both the upper and lower surfaces. The difference of the upstream influences here must be clearly due to the temporal difference of the perturbations originating at the flap, as well as on the subsequent phase lags between the "cause and effect" due to the propagation time of the signals between the flap and points on the airfoil surface upstream of the shock.

In summary, the above comparisons in the steady case showed that the calculated cases at M = 0.854 correspond closely with the measurements at M = 0.875. It would therefore be of interest to calculate the unsteady case at M = 0.854, modeling the viscous ramps using the measured steady pressures at M = 0.875 to see whether the measured shock history can be reproduced by such a calculation. An affirmative check here, though not necessarily increasing the creditability of the present phenomenological approach to the viscous interactions, would reinforce the necessity to reexamine the viability of the experiments.

2. OSCILLATING FLAP RESULTS

We shall omit details of the numerical procedure which are covered for example in Reference 1.

The example which we consider here is the inviscid case at M = 0.854 with pitching frequency of 90 hertz. Though this case is not specifically of primary relevance, it nevertheless exhibits features of the shock behavior observed by Tijdeman at M = 0.875.

In Figure 7 we show the resulting pressure distributions at various phases of the oscillation cycle. We see that the shock has degenerated into a weak isentropic compression wave during a portion of the cycle (starting at kt ~ 30°) as in the experiments. We see further that the cause is due to the decrease of the Mach number upstream of the shock by the upstream displacement of the shock followed by the elimination of the remaining flow super-criticality by the downstream motion of the shock. The resulting shock history is next shown in Figure 8, and it is seen that a significant improvement in the match with experiments has been achieved relative to the earlier cases at M = 0.875. The precise point at which a shock ceases to be a shock is blurred by the relative enhancement of the shock profiling by the numerical diffusion as the shock strength weakens, but such blurring is strictly of academic consequence since the pressure distributions are insignificantly affected for such weak shocks.
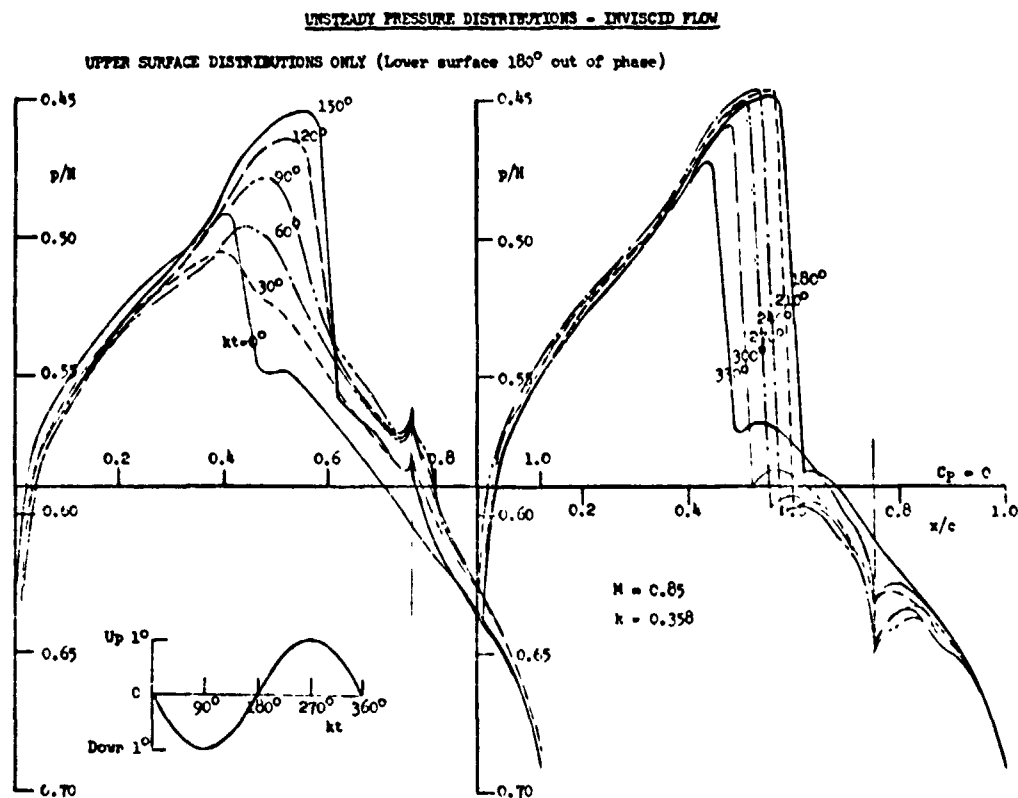
Figure 7. Pressure Distributions for 90 Hertz

Calculations at 120 hertz with the viscous ramps is in process, and the results will be reported at a later time.
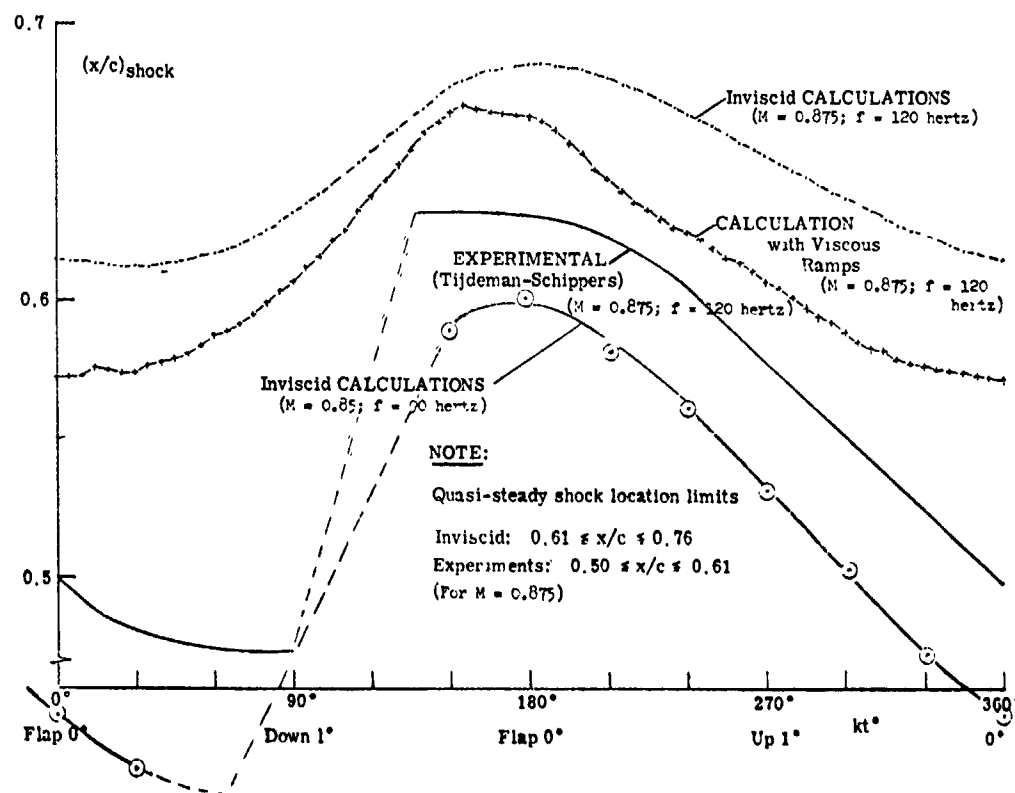
Figure 8. Shock Positioning as a Function of Time

3. CONCLUDING REMARKS

The results of the present calculations showed that the discrepancies found in Reference 1 between the calculated and measured results for the oscillating flap could be eliminated by simply reidentifying the measured results at M = 0.875 as those for M = 0.854. The cause of the discrepancies can be traced directly to the mismatch of the pressures upstream of the shock in the steady case at zero flap deflection between the calculated inviscid case and the measurements. The reliability of the inviscid calculations then suggest the cause of the mismatch to reside in the experiments. The evidence still is circumstantial, and the final resolution must await further test results from a larger wind tunnel than the NLR pilot tunnel using dynamic transducers directly embedded in the airfoil surface.

Finally, one must place in proper perspective the above discrepancy between the measured and calculated unsteady pressure distributions. Though the mismatch of the pre-shock pressures impacted seriously on the shock history, its effect was far less serious so far as the unsteady lift and moments were concerned. The NLR experiments yield results more than adequate for flutter applications.

4. REFERENCES

1. Magnus, R., and Yoshihara, H., the Transonic Oscillating Flap, AIAA Preprint No. 76-327, 1976.
2. Tijdeman, H., and Schippers, P., Results of Pressure Measurements on a Lifting Airfoil with Oscillating Flap in Two-Dimensional High Subsonic and Transonic Flow. NLR Report TR 73018, 1974.

EFFICIENT SOLUTION OF UNSTEADY TRANSONIC FLOWS ABOUT AIRFOILS

W. F. Ballhaus
Research Scientist
Ames Directorate, U.S. Army Air Mobility R&D Laboratory
Ames Research Center, NASA, Moffett Field, California 94035, U.S.A.

and

P. M. Goorjian
Research Scientist
Informatics Corporation
Palo Alto, California 94303, U.S.A.

SUMMARY

An implicit finite-difference procedure has been developed for the efficient solution of unsteady transonic flow fields. Sample computations illustrate applications of this procedure to aerodynamic problems. First, solutions are presented that illustrate three types of shock-wave motion that can result from airfoil control surface oscillations. The significant effect of wind-tunnel wall conditions on these snock-wave motions is demonstrated. Second, solutions are presented for a simple aeroelastic problem in which the flow-field equations and the structural motion equations are integrated simultaneously in time. Both stable and unstable aeroelastic interactions are considered. Finally, the procedure is adapted to compute unsteady aerodynamic force coefficients by the indicial method.

INTRODUCTION

Considerable attention has been directed recently toward the development of numerical methods and codes for the analysis of transonic flow fields resulting from unsteady airfoil motions. Motions of interest can be self-induced, as in the case of aeroelastic instabilities. They can also be externally-driven motions used for propulsion or to generate lift, as in the case of helicopter rotors. In the transonic Mach number range, even simple motions can produce complicated unsteady flow fields. These complications, often associated with the presence of shock waves in the flow, can impose severe limitations on aerodynamic performance. Presently, computational prediction methods are being developed that can provide an understanding of some of the physical phenomena associated with these complicated flows at a cost substantially less than would be required by experimental investigations. Hopefully, methods will eventually be developed that can provide accurate estimations of the aerodynamic loads for a specified design configuration so that performance limitations can be predicted and extended.

Considerations in the development of computational prediction methods for unsteady transonic flows are: (1) flexibility — simple user input for the treatment of arbitrary airfoils and airfoil motions; (2) nonlinearity — including the treatment of moving shock waves; (3) efficiency; and (4) three-dimensional and viscous effects. Let us discuss each one of these considerations keeping in mind the near-term objective, to provide a means for developing an understanding of the physics of unsteady transonic flows, and the long-term objective, to provide precise predictions of aerodynamic loads.

Flexibility

Simple user input for the treatment of arbitrary airfoils and airfoil motions is the principal advantage of a transonic small-disturbance formulation. The boundary condition representing the airfoil and its motion is applied on a flat, mean-surface approximation to the airfoil. An "exact" treatment would require application of the boundary condition on the airfoil surface at its instantaneous location. This is a complicated procedure that could, for example, require coordinate mappings that vary with time. Such complication is unwarranted for our near-term objective, except perhaps for very thick airfoils or airfoils at high angles of attack. In such cases viscous effects would also be important, and a simple treatment of the flow field would be impossible. For the accurate prediction of loads, our long-term objective, detailed treatment of the airfoil surface boundary condition will be required.

Nonlinearity

The Eulerian gasdynamic equations, which govern unsteady transonic flows, are nonlinear and must be integrated in time numerically. Several finite-difference procedures for solving these equations, or approximations to these equations, have been reported (for a review, see Ref. 1). Because these methods all rely on "capturing" techniques to resolve shock waves, the governing equations must be solved in conservation form, which is not always convenient. Failure to maintain proper conservation form can result in shock motions that depend on nonphysical considerations such as mesh spacing. For aerodynamic motions in which shock waves remain essentially fixed, an approximation can be made in which unsteady effects are treated as linear perturbations about some steady-state condition. Such a procedure can be very useful in aeroelastic calculations, for which only infinitesimal amplitude motions need be considered. Two linear perturbation methods have been applied to transonic flows: the harmonic approach and the indicial approach. They will be discussed in greater detail in a subsequent section of this report.

Efficiency

For a time-integration method to be computationally efficient, integration time steps should be chosen on the basis of accuracy. For low-frequency motions, relatively large time steps can be used and adequate flow-field resolution obtained; for high-frequency motions, smaller time steps are required.

Explicit finite-difference schemes (Refs. 2 and 3) are inefficiently applied to low-frequency flows because they have time step restrictions for stability that are substantially more severe than those required for accuracy. This difficulty was partially overcome by the use of semiimplicit schemes (Refs. 4-6), which have less severe time step restrictions. More recently, fully implicit schemes (Refs. 7 and 8) have been developed that permit time-step selection based on accuracy rather than stability considerations. We have chosen to emphasize the treatment of low-frequency flows because shock excursion amplitudes (and hence unsteady aerodynamic force amplitudes) usually increase with decreasing frequency for a fixed airfoil oscillatory motion amplitude. For moderate- to high-frequency motions, shock displacement amplitudes are usually sufficiently small that the fluctuations in the flow field can be treated by a linear unsteady perturbation procedure.

Three-Dimensional and Viscous Effects

Both of these effects are usually important in transonic flow applications. However, their treatment is beyond the scope of the present effort, which is intended to provide a means for studying (inviscid, two-dimensional) nonlinear unsteady influences. The next step would be to develop a small-disturbance procedure for studying three-dimensional unsteady transonic flows. The complete treatment of viscous effects, which is essential for accurately predicting unsteady aerodynamic loads, is a fundamentally more difficult problem.

Reference 9 describes a conservative, implicit finite-difference algorithm to time-accurately integrate the nonlinear, low-frequency, transonic, small-disturbance equation. This procedure is the basis of a computer code, LTRAN2, designed to treat arbitrary combinations of airfoil pitch, plunge, and flap deflections. Unsteady solutions can be computed in about 1 min of CDC 7600 computer time. LTRAN2 can be used to provide solutions by either the time-integration method or the indicial method. The LTRAN2 solution procedure is briefly reviewed here. Computed solutions are then presented that illustrate some of the ways a code like LTRAN2 can be used to treat unsteady aerodynamic problems.

To begin with, solutions for three different free-stream Mach numbers are presented for the flow field about an NACA 64A006 airfoil with a harmonically oscillating trailing-edge control surface. These solutions illustrate the three types of shock-wave motions that have been observed experimentally (Ref. 10) for the same airfoil motion. However, the free-stream Mach numbers at which these different shock motions occurred were all higher in the experiment than in the computations. Additional computations are presented that include wind-tunnel wall simulations. The results indicate that wind-tunnel wall interference could account, at least in part, for this discrepancy in Mach number.

Next, LTRAN2 is used to obtain solutions for a simple aeroelastic problem in which the structural motion equations and flow-field equations are integrated simultaneously; that is, the airfoil motion and the aerodynamic and structural responses to the motion are all free to drive each other. Solutions are presented that illustrate both stable and unstable aeroelastic interactions. Finally, the use of LTRAN2 to obtain solutions by the indicial method is described; lift and moment coefficients computed by the indicial method and by the time-integration approach are compared for the oscillating control surface cases mentioned previously.

GOVERNING EQUATION AND SOLUTION ALGORITHM

A low-frequency, transonic, small-disturbance approximation to the Eulerian gasdynamic equations is the equation

$$2B\phi_{xt} = C\phi_{xx} + \phi_{yy} \tag{1}$$

where

$$B = kM_\infty^2/\delta^{2/3}$$

$$C = (1 - M_\infty^2)/\delta^{2/3} - (\gamma + 1)M_\infty^m \phi$$

and where ϕ is the disturbance velocity potential, M_∞ is the free-stream Mach number, and δ is the airfoil thickness-to-chord ratio. The choice of the exponent m is somewhat arbitrary. Here m is a function of M_∞ chosen to adjust the critical pressure coefficient, C_p^*, for Eq. (1) to match the exact isentropic C_p^* (Ref. 1). The parameter k is the reduced frequency. For an airfoil of chord length c, traveling with speed U_∞, and executing some unsteady oscillatory motion of frequency ω, $k = \omega c/U_\infty$. The reduced frequency is given in units of radians of oscillatory motion per chord length of airfoil travel. The quantities x, y, t, and ϕ in Eq. (1) have been scaled by c, $c/\delta^{1/3}$, ω^{-1}, and $c\delta^{2/3}U_\infty$, respectively. The low-frequency, transonic, small-disturbance equation is a valid approximation to the Euler equations for

$$k \sim 1 - M_\infty^2 \sim \delta^{2/3} << 1 \tag{2}$$

The boundary conditions are enforced in the usual small-disturbance fashion.

The finite difference algorithm used to solve Eq. (1) is an alternating-direction implicit (ADI) scheme first reported in Ref. 7. It was subsequently adapted to lifting cases and used to compute solutions for several types of unsteady airfoil motions in Ref. 9. Since the scheme is implicit, numerical integration time steps are chosen on the basis of accuracy rather than stability. For low-frequency cases, these time steps are many times greater than would be permitted by the stability restrictions associated with explicit schemes. The difference equation is solved in conservation form for the proper treatment of shock waves.

The ADI procedure advances the solution from one time step to the next in two sweeps through the grid. In the first sweep, tridiagonal matrix equations are solved directly treating grid points on y=constant lines implicitly. On the second sweep, tridiagonal matrix equations are solved directly treating grid points on x=constant lines implicitly. Note that no iteration is required to obtain the solution at the new time level.

AIRFOIL WITH OSCILLATING CONTROL SURFACE

Free-Air Computations

Researchers at the National Aerospace Laboratory (The Netherlands) have experimentally observed and classified three types of shock-wave motion produced by an airfoil with a harmonically oscillating trailing-edge control surface (Ref. 10):

1. Type A, sinusoidal shock wave motion: The shock moves nearly sinusoidally but with a phase shift relative to the flap motion. There also exists a phase shift between the shock motion and its strength; that is, the maximum shock strength is not encountered when the shock reaches its maximum downstream location, as in the steady case, but at a later time during its upstream motion.

2. Type B, interrupted shock wave motion: The shock moves as in type A, but now the oscillatory shock strength is of the same magnitude as the mean steady shock strength. Hence, the shock weakens in such a way that it disappears during the downstream-moving portion of its cycle.

3. Type C, upstream-propagating shock waves: A slightly supercritical conditions, shock waves are formed that do not oscillate in displacement but continue to propagate upstream as the embedded supersonic region vanishes during the flap motion cycle.

Computations illustrating these three types of shock-wave motion were reported in Ref. 9 and are also shown here. Results for motion types A and B have also been obtained by Magnus and Yoshihara (Ref. 3) and made available to us for comparison. These computations are solutions to the Eulerian gas dynamic equations, and the airfoil and flap motion boundary conditions are enforced on the airfoil surface at its mean location. The Magnus-Yoshihara procedure therefore provides a more accurate treatment of the problem than the present method.

The computed results for type A motion, at a free-stream Mach number (M_∞) of 0.875, are compared in Fig. 1. They are qualitatively similar to the experimental NLR results for $M_\infty = 0.90$. Note the phase shift between the computed shock wave location and the flap motion. The maximum downstream shock excursion does not occur when the flap reaches its maximum downward deflection, as in the steady case. Note also that the shock strength is not in phase with the shock displacement. The maximum shock strength corresponds to a time between E and F, while the maximum downstream displacement corresponds to a time near D. The maximum downward flap deflection corresponds to a time between B and C.

The computed results for type B motion, at $M_\infty = 0.854$, are compared in Fig. 2. These results are qualitatively similar to the experimental NLR results for $M_\infty = 0.875$. In this case the shock reaches its maximum downstream displacement at time D, increases in strength at time E, and then weakens at times F and A such that it totally disappears at time B. The shock reappears at time C and strengthens as it moves again downstream to its location at time D. LTRAN2 and Magnus-Yoshihara results agree reasonably well throughout the cycle. Detailed comparisons at the points where the shock is strongest ($\omega t = 230°$) and weakest ($\omega t = 50°$) are shown in Fig. 3.

Type C motion computed using LTRAN2 for $M_\infty = 0.822$ is illustrated in Fig. 4. (Magnus-Yoshihara solutions have not been computed for this case.) The shock motion is qualitatively similar to that of the NLR experimental results at $M_\infty = 0.85$. A shock wave forms at some time between C and D, then strengthens and propagates upstream. The forward motion of the shock wave completely eliminates the embedded supersonic region at some time between E and F. The upper surface flow is entirely subsonic from this time until some time just before C. The shock wave continues to propagate upstream as shown at times G, H, and I. At time J, it has disappeared, probably dissipated by numerical viscosity.

The comparisons in Figs. 1-3 of the LTRAN2 and Magnus-Yoshihara results indicate unexpectedly good agreement for the high reduced frequencies involved ($k = \frac{\omega c}{U_\infty} = 0.468, 0.358$). A possible explanation is the following: there are two length scales in the oscillating control surface problem — the chord length, c, and the control surface length, c/4. The question, then, is which length scale should be used in the expression for reduced frequency, k. Fluctuations in the flow field occur primarily in the region between the shock wave and the trailing edge, a distance that is more nearly equal to c/4 than to c. Including c/4 as the proper length scale in the expression for reduced frequency gives $k = \omega c/4U_\infty = 0.117$ and 0.0895 for the cases shown in Figs. 1 and 2, respectively. Both of these values are well within the low reduced frequency range.

LTRAN2, which uses an implicit algorithm to solve the low frequency transonic equation, Eq. (1), required 8 sec of CDC 7600 computer time per oscillation cycle to generate the type B motion solution shown in Fig. 2. The Magnus-Yoshihara procedure, an explicit algorithm applied to the Eulerian equations, required 1500 sec per cycle on the same machine. (A larger number of grid points were used in the LTRAN2 computations (7900) than in the Magnus-Yoshihara computations (5484). However, Magnus and Yoshihara distributed a larger percentage of points on the airfoil surface, especially near the shock, as shown in Fig. 3). Some of this difference is attributable to the difference in the governing equations — the Magnus-Yoshihara procedure solves a system of four first-order partial differential equations (PDE's) as opposed to one second-order PDE for the LTRAN2 procedure. However, the most significant contribution to the substantial difference in run time is the difference in computational efficiency between an implicit

and explicit method. Furthermore, halving the reduced frequency would double the computer time required per cycle for the explicit scheme, since the time-step restriction would remain essentially the same but the cycle would be twice as long. On the other hand, the time step could probably be increased with the implicit scheme because the unsteady gradients would be smaller and the time step is based on accuracy rather than stability. So the implicit approach would become relatively more efficient with decreasing frequency.

Wind-Tunnel Wall Simulations

Discrepancies in comparisons of experimental and computational data for transonic flows are most frequently attributed to viscous and wind-tunnel-wall-interference effects. Recall that in both the Magnus-Yoshihara and the LTRAN2 computations, shock-wave motions were obtained that qualitatively agreed with those observed experimentally at NLR; but the corresponding values of M_∞ in the computations were all lower than the experimental ones. In an attempt to account for the disagreement and thereby reproduce the experimental results computationally, Magnus and Yoshihara (Ref. 3) repeated their computations with a viscosity model included. This failed to produce the desired result, which led them to conclude that the disagreement between the computational and experimental results was probably a wind-tunnel-wall-interference effect. In what follows, evidence is presented that indicates that this is a plausible explanation.

The object here is to demonstrate that wind-tunnel walls can significantly affect airfoil surface pressures, and hence shock-wave motions, for Mach numbers, reduced frequencies, control-surface motions, and tunnel half-height-to-chord ratios equivalent to those in the NLR experiments. (We make no attempt to precisely model the experimental conditions. For such a computation detailed information about the test section geometry and unsteady tunnel wall pressures would be required.) In the computed simulations, the test section was assumed to be infinitely long, and the walls were located a distance of 1.528 chord lengths from the airfoil mean surface, as in the NLR experiment. A 99-point smoothly-stretched grid was used in the free-stream direction. The upstream and downstream boundary conditions were $\phi = 0$ (equivalent to $\phi_y = 0$, i.e., parallel flow) and $\phi_x = 0$ (free-stream pressure), respectively. Because we have no way of accurately simulating the experimental wall conditions, we consider the two extreme cases: the solid wall case, for which $\phi_y = 0$ at the wall, and the free-jet case, for which $\phi = 0$ at the wall. For both of these cases a uniform grid of 67 points was used in the y (stream-normal) direction. Free-air computations were also computed for comparison, and for this case the same y grid was used except that 32 smoothly varying grid points were added beyond $|y| > 1.528$ to remove the vertical boundaries to a distance of 271 chord lengths from the airfoil mean surface location.

Computed steady surface pressures for $M_\infty = 0.845$ and zero control-surface deflection are shown in Fig. 5. Pressures at the location of the tunnel walls are also shown. Note that the solid-wall shock wave is stronger than the free-air shock wave, and the free-jet shock wave is weaker. Since the NLR experimental shock motions were observed for higher Mach numbers than in the computations, the wind-tunnel-wall influence must be one that weakens shock waves. From the comparison shown in Fig. 5, it is clear that the free-jet wall simulation produces such an effect.

Computed free-air and free-jet unsteady surface pressures are compared in Fig. 6 for $M_\infty = 0.865$, $k = 0.468$, and a flap deflection amplitude of 1° (the solid wall flow field for this case was choked). Note that the free-air shock motion is type A, and the free-jet shock motion is type B. The shock-weakening effect of the tunnel walls is such that a type B motion is observed for a value of M_∞ at which a type A motion would occur if the walls were not present.

EXAMPLE OF A SIMPLE AEROELASTIC PROBLEM

In transonic flight, small-amplitude oscillations of a body can produce large variations in the aerodynamic forces and moments acting on that body. Furthermore, phase differences between the motion and the resulting forces and moments can be large. These characteristics tend to increase the probability of encountering aeroelastic instabilities, making the transonic regime a sensitive one for aircraft flutter.

Flutter boundaries are usually calculated using the following system of equations:

$$[M]\ddot{q} + [C]\dot{q} + [K]q = F(t) \tag{3}$$

where M, C, and K are mass, damping, and stiffness matrices, respectively; q is a vector that is a measure of the structural response; and F(t) is a vector of applied forces. The aerodynamic response to the motion, F(t), can be computed in several different ways. For example, Eq. (3) could be integrated in time simultaneously with the governing equations for transonic flow. The airfoil motion and aerodynamic forces would then be free to drive each other. Such an approach is investigated in this section for a one-dimensional aeroelastic problem. An alternative approach, valid for small amplitude oscillations, is described in the next section.

Consider an NACA 64A006 airfoil with moment of inertia I free to pitch about midchord. The pitching motion is resisted by a torsion spring of stiffness K and structural damping g. The governing equation is

$$I\ddot{\alpha} + g\alpha + K\alpha = M(t) \tag{4}$$

where M(t) is the aerodynamic moment I, g, and K are all positive constants.

A neutrally stable system (one that will flutter) can be constructed by choosing the structural constants to balance the effect of the aerodynamic moment. For example, for small-amplitude pitching

oscillations about midchord of an NACA 64A006 airfoil at $M_\infty = 0.88$ and $k = 0.1$, LTRAN2 gives $|C_{m_\alpha}| = 0.8617$ and $\phi = -68.87°$, where $|C_{m_\alpha}|$ is the pitching moment amplitude, normalized by the oscillation amplitude in radians, and ϕ is the pitching moment phase relative to the motion (i.e., $C_m = \alpha_0|C_{m_\alpha}|\sin(t-\phi)$). Assuming the airfoil pitching motion is harmonic, $\alpha = \alpha_0 e^{i\omega t}$, and substituting into Eq. (4) results in two expressions (the real and imaginary parts of Eq. (4)) relating the aerodynamic and structural constants:

$$A_1 = A_3|C_{m_\alpha}|\sin\phi$$

$$A_2 = 1 + A_3|C_{m_\alpha}|\cos\phi \qquad (5)$$

where

$$A_1 = g/I\omega = 1.072$$

$$A_2 = K/I\omega' = 1.414$$

$$A_3 = Qc^2/I\omega^2 = 1.333$$

$$Q = \text{dynamic pressure}$$

The equations are satisfied for the values shown.

Having constructed an aeroelastic system that will flutter, let us now consider a series of computations for this system in which the structural damping is varied parametrically. The computed results are shown in Fig. 7; they were obtained using LTRAN2 coupled with a simple ordinary differential equation integration procedure for Eq. (4). The aerodynamic and airfoil motion equations were integrated simultaneously. The motion was forced for the first few cycles until the pitching moment became periodic, after which the airfoil motion and aerodynamic response were left free to drive each other. The first cycle shown in Fig. 7 is forced for all cases. The initial motion amplitude is $\alpha_0 = 0.5°$. For $A_1 = 1.072$, that is, the neutral stability point obtained using $|C_{m_\alpha}| = 0.8617$ and $\phi = -68.87°$ in Eq. (4), the motion is very nearly sinusoidal. The small deviations from sinusoidal behavior can be attributed primarily to nonlinear effects and truncation errors in the numerical integration schemes. For other choices of A_1, the motion is either damped or unstable for values greater or less than the value corresponding to the neutral stability (flutter) point. For this system to flutter, it is necessary that the moment variation lead the motion, which it does in the nonlinear case for $M_\infty \geq 0.88$. Linear (flat-plate) theory does not predict a phase lead and thus could not be used in this case to predict the flutter point.

A similar calculation is shown in Fig. 8. The initial amplitude in this case is considerably larger, $\alpha_0 = 1\text{-}1/2°$, and the Mach number is smaller, $M_\infty = 0.87$; the structural constants differ from those in the previous case. This example is an extreme case that illustrates the nonsinusoidal pitching-moment behavior that can result from the large shock-wave excursions encountered at relatively large airfoil motion amplitudes.

AN EFFICIENT LINEAR UNSTEADY PERTURBATION APPROACH: THE INDICIAL METHOD

In the introduction it was stated that for aerodynamic motions in which shock waves remain essentially fixed, an approximation can be made in which unsteady effects are treated as linear perturbations about some steady-state condition. Since in many aeroelastic calculations one need only consider infinitesimal amplitude motions, time-linearized methods can be very useful. To begin with, assume that the motion and force response of some simple aeroelastic system are simple harmonic. Substituting the expressions $q(t) = \bar{q}e^{i\omega t}$ and $F(t) = [A]q$ into Eq. (3) leaves

$$[K + i\omega c - \omega^2 M]\bar{q} = [A]\bar{q} \qquad (6)$$

The matrix $[A]$ represents the dependence of the aerodynamic forces on the motion of the body. In what follows, two linear perturbation methods, for determining this dependence, the harmonic method and the indicial method, are described.

The harmonic method assumes that the flow field for some harmonic aerodynamic motion of frequency ω can be expressed in the form

$$\phi(x,y,t) = \phi_0(x,y) + \varepsilon\phi_1(x,y)e^{i\omega t} \qquad (7)$$

where ϕ is the disturbance velocity potential and ε is related to the amplitude of the motion. For transonic flows, the unsteady solution, ϕ_1, depends on the mean steady-state solution, ϕ_0, and on the motion frequency, ω. The mean steady-state solution, ϕ_0, is the solution to a nonlinear equation, whereas ϕ_1 is the solution to a linear equation obtained by substituting Eq. (7) into Eq. (1) and neglecting terms in ε^2. Since the unsteady perturbation is linear, multiple degree-of-freedom aeroelastic systems can be treated by considering each degree of freedom independently and superposing solutions.

The harmonic approach (Refs. 11-14) has the advantage that the unsteady solution, ϕ_1, can be obtained using the same transonic relaxation procedure used to compute the steady-state solution. It has the disadvantage that a complete finite-difference flow-field computation must be performed for each motion frequency of interest.

The indicial method (Refs. 15 and 16) has the advantage that from a single flow-field computation, the indicial response, solutions can be obtained for all frequencies with the aid of Duhamel's integral. For example, consider some arbitrary variation of angle-of-attack α as a function of time and suppose that the indicial lift coefficient response to a unit change in α, C_{ℓ_α} (t), is known. Then the lift coefficient response to the arbitrary variation of α is

$$C_\ell(t) = C_{\ell_\alpha}\alpha(0) + \int_0^t C_{\ell_\alpha}(\tau) \frac{d}{dt} \alpha(t - \tau) \, d\tau \qquad (8)$$

That is, once the indicial response to a given motion mode is known, then the lift coefficient response to an arbitrary variation of that type of motion is given by Eq. (8). Multiple-motion mode problems can be treated by considering each mode separately and then superposing solutions, as for the harmonic approach. For a given mode, the integral in Eq. (8) must be evaluated for each motion frequency of interest. The cost is negligible compared with the cost of the complete finite-difference flow-field computation required by the harmonic method.

Indicial responses were computed using LTRAN2 for the control-surface deflection problem that produced the three types of shock wave motion discussed previously. Lift and moment coefficients were then computed using Duhamel's principle and the results compared with results obtained by the LTRAN2 time-integration procedure that produced the surface pressures shown in Figs. 1-4. This comparison, shown in Fig. 9, indicates that the linear perturbation assumption is valid in the cases with weak shock waves, corresponding here to shock motion types B and C, even though the shock-wave motions are irregular. However, the assumption breaks down in the type A case, because of the presence of a relatively strong moving shock wave.

CONCLUDING REMARKS

An alternating-direction implicit algorithm for solving the low-frequency transonic equation forms the basis of a computer code, LTRAN2, which is a computational tool designed to assist aerodynamicists in developing an understanding of unsteady transonic flow phenomena. LTRAN2 is efficient, flexible, and capable of correctly simulating inviscid, nonlinear unsteady effects, including shock-wave motions. Computer run times for typical cases are usually less than 1 min on a CDC 7600 computer. The code can be easily applied to a wide class of airfoils and airfoil motions because of the simplified treatment of boundary conditions offered by small-disturbance theory. However, LTRAN2 cannot be used to provide precise predictions of aerodynamic loads. Such a capability is beyond the present state of the art and will remain so until methods are developed for the proper treatment of viscous effects.

Sample computations have been presented here for three sample problems to illustrate some of the ways a code like LTRAN2 can be used to solve unsteady transonic flow problems. The first problem is the computation of the unsteady transonic flow field produced by an airfoil with an oscillating control surface. Solutions have been obtained that illustrate the three types of shock-wave motion that have been observed experimentally for this airfoil motion. However, the free-stream Mach numbers at which these three motions occurred were all lower than in the experiment. Additional computations that include wind-tunnel-wall simulations were also obtained; they indicate that wind-tunnel-wall interference could have produced this discrepancy.

The second problem is a simple aeroelastic one in which the structural motion equations and flow-field equations were integrated simultaneously in LTRAN2; that is, the airfoil motion and the aerodynamic and structural responses to the motion were all free to drive each other. Solutions presented illustrate both stable and unstable aeroelastic interactions.

Finally, the use of LTRAN2 to obtain solutions by the indicial method has been described. This approach can be efficiently applied to aeroelastic computations because solutions for many reduced frequencies can be obtained from a single finite-difference flow-field computation.

REFERENCES

1. Ballhaus, W. F., "Some Recent Progress in Transonic Flow Computations," VKI Lecture Series: Computational Fluid Dynamics, von Kármán Institute for Fluid Dynamics, Rhode-St-Genese, Belgium, March 15-19, 1976.

2. Magnus, R. J. and Yoshihara, H., "Calculations of Transonic Flow over an Oscillating Airfoil," AIAA Paper 75-98, Jan. 1975

3. Magnus, R. and Yoshihara, H., "The Transonic Oscillating Flap," AIAA Paper 76-327, July 1976.

4. Ballhaus, W. F. and Lomax, H., "The Numerical Simulation of Low Frequency Unsteady Transonic Flow Fields," *Lecture Notes in Physics*, Vol. 35, Springer-Verlag, 1975, pp. 57-63.

5. Beam, R. M. and Ballhaus, W. F., "Numerical Integration of the Small-Disturbance Potential and Euler Equations for Unsteady Transonic Flow," NASA SP-347, Part II, March 1975, pp. 789-809.

6. Ballhaus, W. F., Magnus, R., and Yoshihara, H., "Some Examples of Unsteady Transonic Flows over Airfoils," *Proceedings of the Symposium on Unsteady Aerodynamics*, Vol. II, 1975, pp. 769-791.

7. Ballhaus, W. F. and Steger, J. L., "Implicit Approximate-Factorization Schemes for the Low-Frequency Transonic Equation," NASA TM X-73,082, Nov. 1975.

8. Beam, R. M., and Warming, R. F., "An Implicit Finite-Difference Algorithm for Hyberbolic Systems in Conservation-Law Form," *Journal of Computational Physics*, Vol. 22, No. 1, 1976, pp. 87-110.

9. Ballhaus, W. F. and Goorjian, P. M., "Implicit Finite-Difference Computations of Unsteady Transonic Flows About Airfoils, Including the Treatment of Irregular Shock-Wave Motions," AIAA Paper 77-205, Jan. 1977.

10. Tijdeman, H., "On the Motion of Shock Waves on an Airfoil with Oscillating Flap," *Symposium Transsonicum II*, Springer-Verlag, 1975, pp. 49-56.

11. Ehlers, F. E., "A Finite Difference Method for the Solution of the Transonic Flow Around Harmonically Oscillating Wings," NASA CR-2257, 1974.

12. Weatherill, W. H., Sabastian, J. D., and Ehlers, F. E., "On the Computation of the Transonic Perturbation Flow Fields Around Two- and Three-Dimensional Oscillating Wings," AIAA Paper 76-99, Jan. 1976.

13. Traci, R. M., Farr, J. L., and Albano, E., "Perturbation Method for Transonic Flow About Oscillating Airfoils," AIAA Paper 75-877, June 1975.

14. Traci, R. M., Albano, E. D., and Farr, J. L., "Small-Disturbance Transonic Flows About Oscillating Airfoils and Planar Wings," AFFDL-TR-75-10, June 1975.

15. Beam, R. M., and Warming, R. F., "Numerical Calculations of Two-Dimensional, Unsteady Transonic Flows with Circulation," NASA TN D-7605, 1974.

16. Ballhaus, W. F. and Goorjian, P. M., "Computation of Unsteady Transonic Flows by the Indicial Method," AIAA Paper 77-447, March 1977.
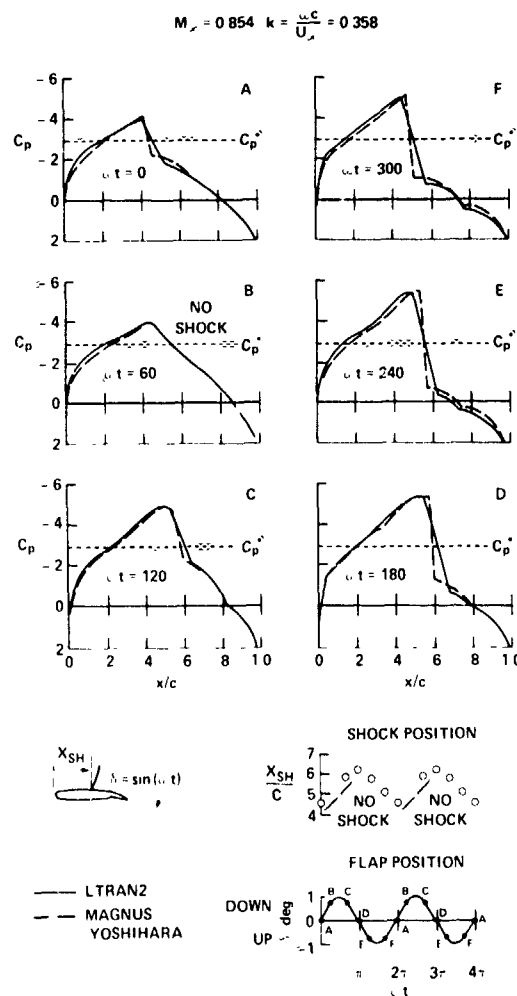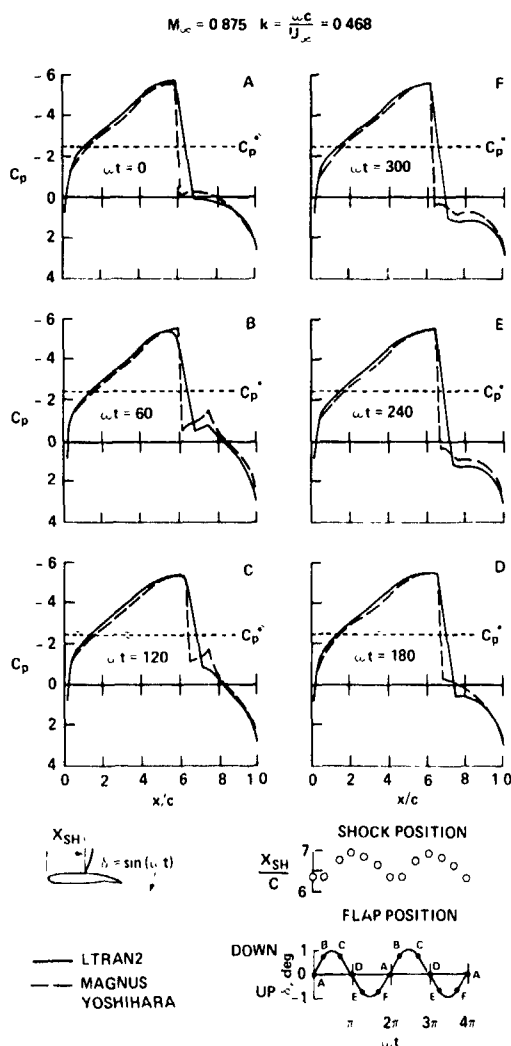
Fig. 1 Unsteady upper surface pressure coefficients for an NACA 64A006 airfoil with oscillating trailing-edge flap: type A motion

Fig. 2 Unsteady upper surface pressure coefficients for an NACA 64A006 airfoil with oscillating trailing-edge flap: type B motion

M∞ · 0.854   k · 0.358
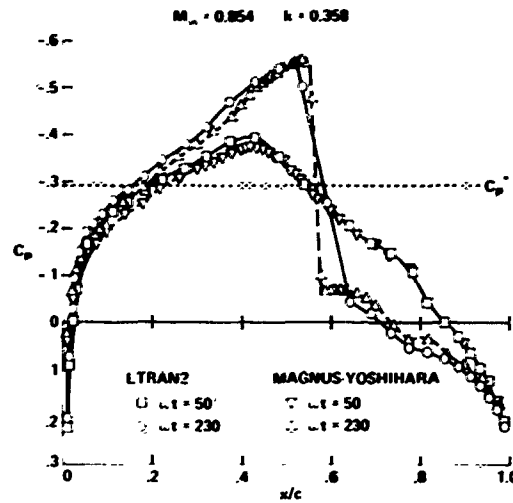
Fig. 3 Detailed comparison of computed unsteady
pressure coefficients for type B motion.

M∞ = 0 822   k = $\frac{\omega c}{U_\infty}$ = 0 496

M∞ - 0 822   k = $\frac{\omega c}{U_\infty}$ = 0 496

SHOCK POSITION

$h = 1 5 \sin (\omega t)$

FLAP POSITION

FLAP POSITION
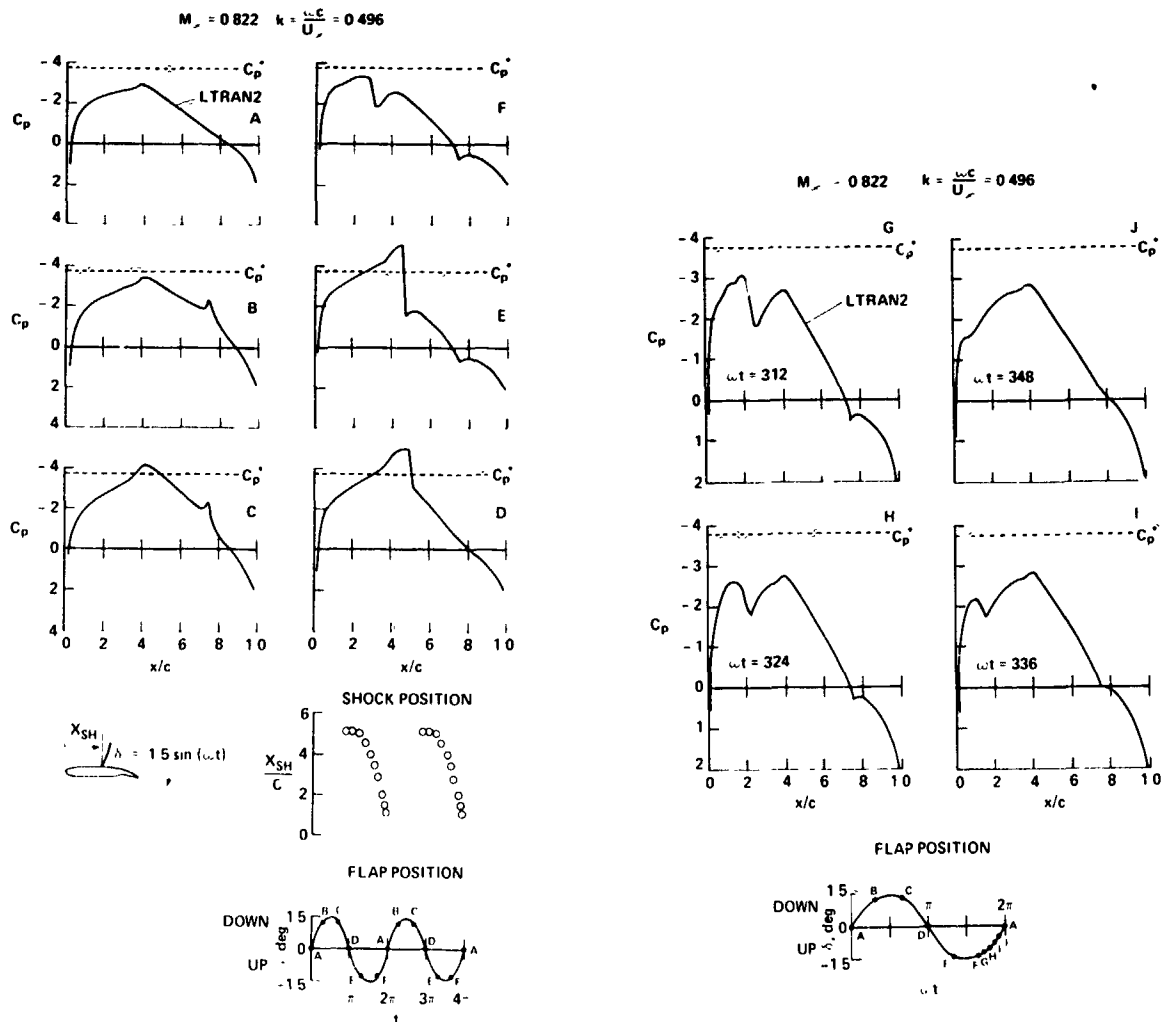
Fig. 4 Unsteady upper surface pressure coefficients for a NACA 64A006 airfoil with oscillating
trailing edge flap; type C motion.

(a) Airfoil surface.
(b) Wind tunnel wall.
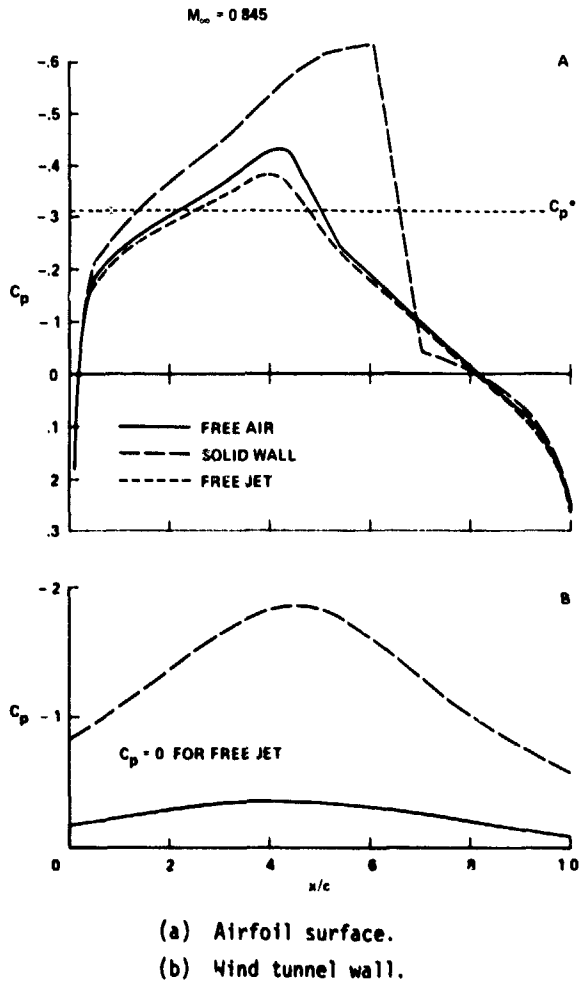
Fig. 5 Steady-state pressure coefficients.
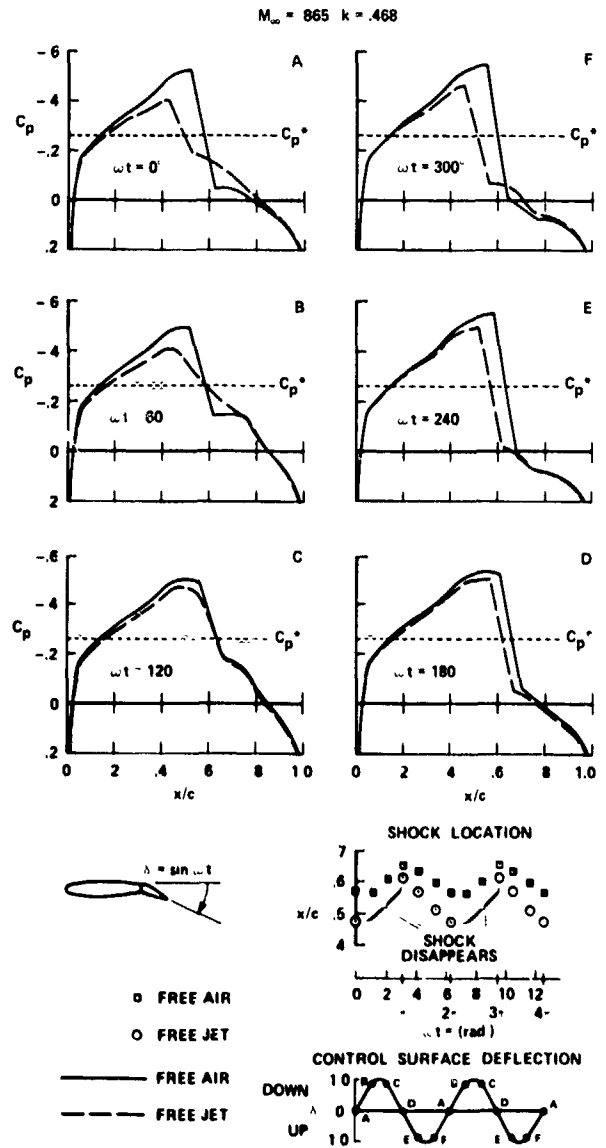
Fig. 6 Unsteady airfoil surface pressure coefficients.
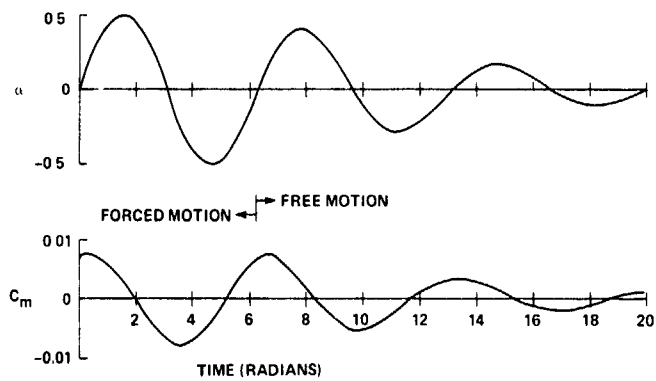
(a) Highly damped case, $A_1 = 1.50$.
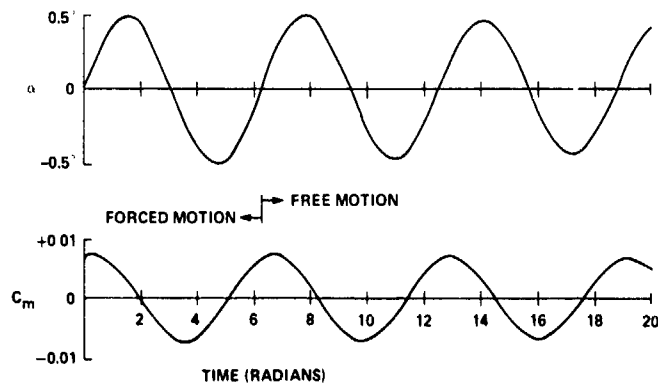
(b) Neutral stability (flutter) case, $A_1 = 1.072$.
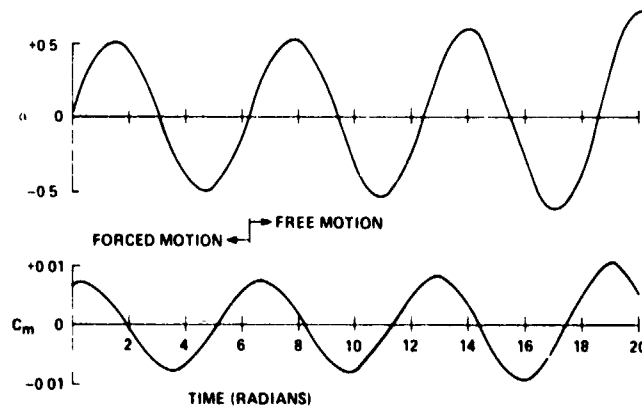
(c) Slightly divergent case, $A_1 = 0.95$.
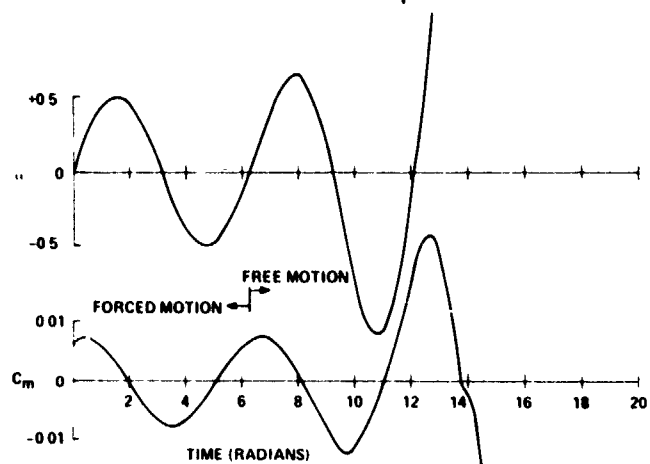
(d) Highly divergent case, $A_1 = 0.50$.

Fig. 7 Constrained pitching oscillations, $M_\infty = 0.88$.
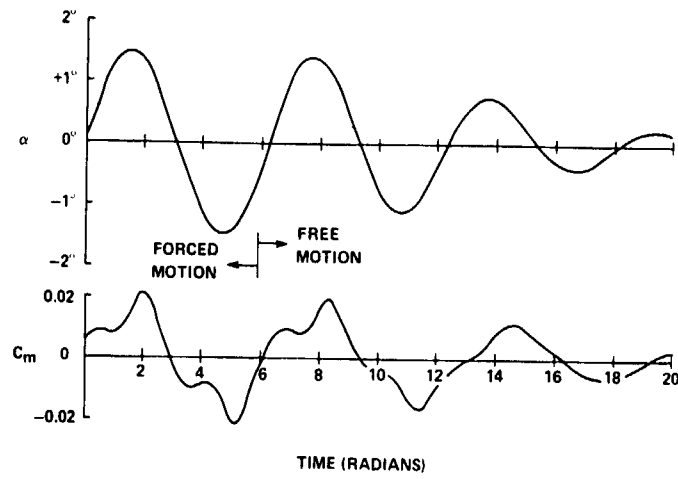
Fig. 8 Constrained pitching oscillations, $M_\infty = 0.87$.
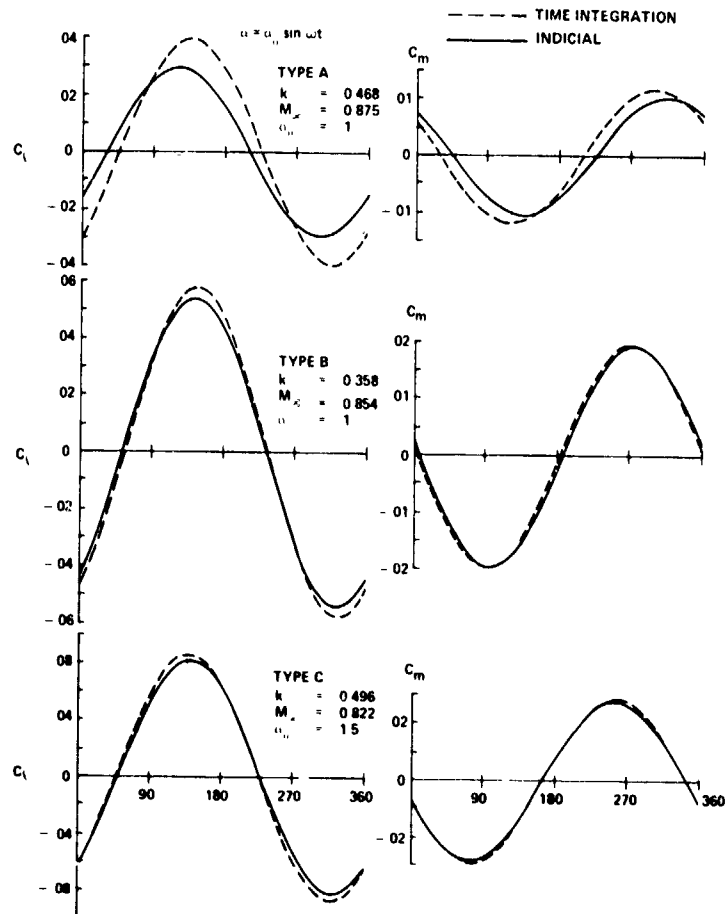
Fig. 9 Comparison of indicial and time integration solutions for an airfoil with oscillating trailing-edge flap.

CALCUL NUMÉRIQUE D'ÉCOULEMENTS TRANSSONIQUES INSTATIONNAIRES

par Alain LERAT* et Jacques SIDÈS

Office National d'Etudes et de Recherches Aérospatiales (ONERA)
92320 Châtillon · France

Résumé

On présente une méthode aux différences finies pour calculer des écoulements transsoniques d'un fluide parfait autour d'un profil animé d'un mouvement quelconque de corps solide. Les équations bidimensionnelles instationnaires d'Euler sont résolues sous forme conservative, dans un plan transformé défini par un changement de coordonnées dépendant du temps. Le schéma numérique utilise, dans le domaine d'espace, plusieurs variantes du schéma de MacCormack convenablement raccordées. Le maillage est raffiné au voisinage des ondes de choc. La condition de glissement est satisfaite sur la surface exacte du profil et la condition à l'infini-aval prend en compte le fait que l'écoulement n'est pas homentropique. La méthode est appliquée au calcul de l'écoulement instationnaire autour du profil NACA 0012 en oscillation d'incidence à Mach 0,8.

NUMERICAL CALCULATION OF UNSTEADY TRANSONIC FLOWS

Abstract

A finite difference method is presented for the calculation of inviscid transonic flows over an airfoil in arbitrary rigid body motion. The two-dimensional unsteady Euler equations in conservation-law form are solved in a transformed plane defined through a time-dependent mapping The numerical scheme makes use of several variants of MacCormack scheme in the space domain with suitable matchings. A mesh refinement is used in the vicinity of shock waves. The slip condition is satisfied on the exact airfoil surface and the boundary condition at downstream infinity takes into account the non-homentropy of the flow. Calculations are made of the unsteady flow over the NACA 0012 airfoil oscillating in pitch at Mach 0.8.

An English translation of this paper is available as TP ONERA n° 1977-19E.

1 - INTRODUCTION -

Il est bien connu que les écoulements transsoniques instationnaires ne peuvent en général être calculés avec une précision suffisante à partir de la théorie linéaire, dans laquelle ils sont considérés comme une petite perturbation d'un écoulement stationnaire uniforme. La théorie linéaire peut être améliorée par une linéarisation des équations instationnaires autour d'un état stationnaire non uniforme. Cette approche a été utilisée de différentes manières par Ehlers [1], Traci, Albano et Farr[2], Chan et Brashears [3] et Kimble [4] pour calculer l'écoulement transsonique autour d'un profil en oscillation harmonique de faible amplitude. Dans ces travaux, on détermine d'abord une solution stationnaire de l'équation du potentiel de petites perturbations, puis on résout la forme instationnaire linéarisée de cette équation, dont les coefficients dépendent de la solution stationnaire *. La méthode numérique est celle

des différences finies dans [1], [2] et celle des éléments finis dans [3] et [4]. Beam et Warming [5] ont une approche quelque peu différente, car ils résolv t les équations d'Euler complètes pour un chang ent brusque d'incidence et en déduisent la "réponse" de l'écoulement à des oscillations harmoniques du profil à l'aide de la méthode indicielle, ce qui n'est valable que pour des amplitudes faibles. D'autre part, l'équation non linéaire instationnaire du potentiel de petites perturbations a été résolue grâce à des extensions de la méthode de Murman et Cole par Ballhaus et Lomax [6] et également par Caradonna et Isom [7]. Les premiers ont calculé l'écoulement autour d'un profil mis instantanément en translation et aussi autour d'un profil d'épaisseur croissante. Les seconds ont déterminé et résolu une équation approchée régissant l'écoulement tridimensionnel s'établissant au voisinage de l'extrémité d'une pale de rotor d'hélicoptère en vol d'avancement.

Les équations instationnaires d'Euler ont été résolues par Laval [8], Beam et Warming [9], Magnus et Yoshihara [10],[11]. Dans le travail [8], l'écoulement autour d'un profil symétrique en oscillation dans une tuyère est obtenu à l'aide d'un schéma aux différences à pas fractionnaires ; certaines propriétés approchées de

---

* Une méthode semblable a été développée à l'ONERA par Fenain et Guiraud-Vallée pour les écoulements subsoniques instationnaires, mais en linéarisant, autour d'une solution stationnaire, l'équation complète du potentiel.

---

* Ecole Nationale Supérieure d'Arts et Métiers, 75640 Paris Cédex 13 et Laboratoire de Mécanique Théorique, Université Paris VI Collaborateur extérieur de l'ONERA

symétrie et d'antisymétrie de l'écoulement sont utilisées de façon à ne calculer la solution que dans une moitié du domaine d'espace. Dans le travail [9] , l'écoulement autour d'un profil oscillant est calculé en tant qu'exemple d'application d'un nouveau schéma implicite imaginé par les auteurs et la condition limite sur le profil est imposée sur la ligne moyenne, ce qui suppose que le profil est mince. Le travail [10] fournit de nombreux résultats numériques relatifs à l'écoulement instationnaire,autour d'un profil, dû à un changement brusque de l'angle d'inc'ience ou de sa vitesse de variation,ou encore dû à une évolution sinusoïdale de l'angle d'incidence. Dans ce travail comme dans [8] , la condition limite est satisfaite sur un contour fixe ayant la form≏ du profil. Le travail [11] est une extension de [10] tenant compte d'effets de déplacement visqueux pour le problème de l'écoulement autour d'un profil muni d'une gouverne oscillante. On pourra trouver une discussion des diverses méthodes dans la référence [12] .

Dans le présent article, nous décrivons une méthode de calcul d'écoulements transsoniques instationnaires autour d'un profil animé d'un mouvement quelconque d corps solide. Les équations d'Euler bidimensionnelle⁻ sont résolues sous forme conservative à l'aide d'une méthode aux différences finies, dans un plan transformé défini par un changement de coordonnées dépendant du temps. Le schéma numérique utilise, dans le domaine d'espace, plusieurs variantes du schéma de MacCormack convenablement raccordées. Le maillage est raffiné au voisinage des ondes de choc. La condition de glissement est satisfaite sur la surface exacte du profil. Au bord de fuite, on impose seulement la continuité de la pression. La condition à l'infini-aval prend en compte le fait que l'écoulement n'est pas homentropique en aval des chocs. La méthode est appliquée ici au calcul de l'écoulement autour du profil NACA0012 en oscillation d'indicence.

2 - EQUATIONS REGISSANT L'ECOULEMENT -

On considère un écoulement transsonique plan autour d'un profil animé d'un mouvement quelconque de corps solide par rapport au courant non perturbé. On admet que le fluide est parfait mais, dans le but de calculer précisément les ondes de choc, on ne suppose pas que l'écoulement est isentropique . L'écoulement est donc régi par les équations d'Euler complètes. Dans un système de coordonnées cartésiennes absolues x, y , au repos par rapport au courant non perturbé, ces équations peuvent s'écrire sous forme conservative :

$$(1) \qquad \frac{\partial w}{\partial t} + \frac{\partial f(w)}{\partial x} + \frac{\partial g(w)}{\partial y} = 0 ,$$

où t est le temps et $w , f(w) , g(w)$ s⊔t les vecteurs :

$$w = \begin{bmatrix} \varrho \\ \varrho u \\ \varrho v \\ \varrho E \end{bmatrix} ,$$

$$(2)$$

$$f(w) = \begin{bmatrix} \varrho u \\ \varrho u^2 + p \\ \varrho u v \\ (\varrho E + p) u \end{bmatrix} , \qquad g(w) = \begin{bmatrix} \varrho v \\ \varrho u v \\ \varrho v^2 + p \\ (\varrho E + p) v \end{bmatrix} ,$$

ϱ désignant la masse volumique, p la pression u et v les composantes de la vitesse absolue, et $E = e + \frac{1}{2}(u^2 + v^2)$ l'énergie totale spécifique. L'énergie interne spécifique e est reliée à p et à ϱ par l'équation d'état :

$$(3) \qquad e = e(p, \varrho) .$$

Dans les équations précédentes, u et v sont normalisés par la vitesse V_∞ du courant non perturbé, ϱ par la masse volumique ϱ_∞ du courant non perturbé, p par $\varrho_\infty V_\infty^2$, E par V_∞^2 , x et y par la corde c du profil et le temps par c / V_∞ .

3 - CHANGEMENT DE COORDONNEES DEPENDANT DU TEMPS -

On cherche une solution faible du système hyperbolique (1) associé à des conditions initiales et des conditions aux limites. Le domaine d'espace est la partie non bornée, extérieure au profil ; ce domaine évolue dans le temps. Pour pouvoir imposer correctement la condition limite sur le profil, on transforme le domaine d'espace en un domaine fixe et simple au moyen d'un changement de coordonnées $T(t)$ dépendant du temps, composé des deux applications :

$$\begin{bmatrix} x \\ y \end{bmatrix} \xrightarrow{T_1(t)} \begin{bmatrix} \xi = \xi(x,y;t) \\ \eta = \eta(x,y;t) \end{bmatrix} \xrightarrow{T_2} \begin{bmatrix} X = X(\xi,\eta) \\ Y = Y(\xi,\eta) \end{bmatrix}$$
$$\underbrace{\qquad\qquad\qquad\qquad}_{T(t)}$$
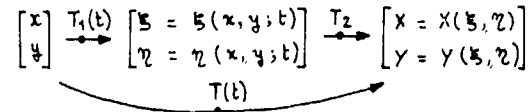
L'application $T_1(t)$ dépendant du temps, associe aux coordonnées absolues x, y d'un point M, ses coordonnées cartésiennes ξ , η dans un repère lié au profil, coïncidant avec le repère absolu au temps initial t = 0 . Par conséquent, $T_1(t)$ est une fonction donnée décrivant le mouvement de solide du profil et elle est telle que $T_1(0)$ est l'identité. L'application T_2 transforme l'extérieur du profil (fixe dans le repère relatif) en un rectangle, comme l'indique la figure 1. Par suite, T_2 est une transformation géométrique du type de celles utilisées dans les calculs d'écoulements autour d'un profil fixe.

Fig 1 — Changement de coordonnées

Avec les nouvelles coordonnées, le système (1) s'écrit :

$$
(4) \quad \frac{\partial w}{\partial t} + \frac{\partial X}{\partial t}\frac{\partial w}{\partial X} + \frac{\partial Y}{\partial t}\frac{\partial w}{\partial Y} + \frac{\partial X}{\partial x}\frac{\partial f(w)}{\pa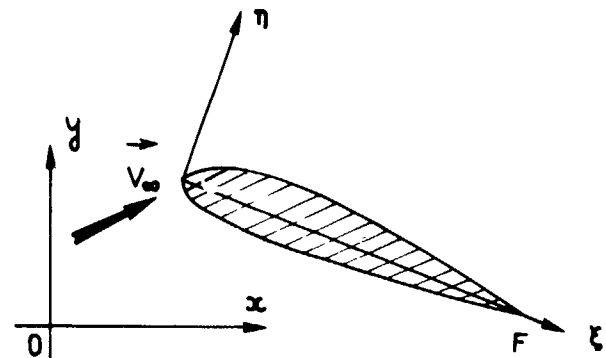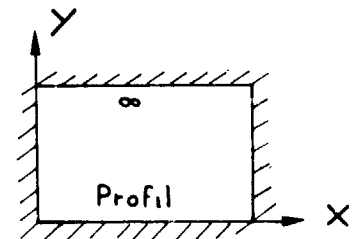rtial X} + \frac{\partial Y}{\partial x}\frac{\partial f(w)}{\partial Y} + \frac{\partial X}{\partial y}\frac{\partial g(w)}{\partial X} + \frac{\partial Y}{\partial y}\frac{\partial g(w)}{\partial Y} = 0
$$

Viviand [13] a montré que (4) peut aussi s'exprimer sous la forme d'une divergence, comme dans le cas classique d'un changement de coordonnées indépendant du temps :

$$
(5) \quad \frac{\partial W}{\partial t} + \frac{\partial F(W)}{\partial X} + \frac{\partial G(W)}{\partial Y} = 0
$$

avec

$$
(6) \quad W = \frac{1}{\mathcal{D}} w , \quad
\begin{aligned}
F(W) &= \frac{\partial X}{\partial t} W + \frac{1}{\mathcal{D}}\left[\frac{\partial X}{\partial x} f(\mathcal{D}W) + \frac{\partial X}{\partial y} g(\mathcal{D}W)\right]\\
G(W) &= \frac{\partial Y}{\partial t} W + \frac{1}{\mathcal{D}}\left[\frac{\partial Y}{\partial x} f(\mathcal{D}W) + \frac{\partial Y}{\partial y} g(\mathcal{D}W)\right]
\end{aligned}
$$

où $\mathcal{D} = \dfrac{\partial(X,Y)}{\partial(x,y)}$ est le Jacobien de la transformation $T(t)$.

On peut faire les remarques suivantes :

a) Bien que les équations (5) soient écrites dans un repère relatif lié au profil, les inconnues de base (composantes de W) restent exprimées à l'aide des composantes cartésiennes u, v de la vitesse absolue.

b) Le jacobien $\mathcal{D}$ est indépendant du temps. En effet, c'est le produit du jacobien $\mathcal{D}_1$ de $T_1(t)$ et du jacobien $\mathcal{D}_2$ de T_2 ; or $\mathcal{D}_1$ est toujours égal à 1, car il correspond à un mouvement de solide, et $\mathcal{D}_2$ ne dépend pas du temps comme T_2.

c) Les expressions (6) peuvent se simplifier [14] si l'équation d'état est une fonction homogène de degré zéro en p et ρ, c'est-à-dire si :
$(7)\quad e(\lambda p, \lambda \rho) = e(p,\rho)$, pour tout scalaire λ.

Dans ce cas, on a :

$$
f(\lambda w) = \lambda f(w) , \quad g(\lambda w) = \lambda g(w)
$$

d'où :

$$
(8) \quad
\begin{aligned}
F(W) &= \frac{\partial X}{\partial t} W + \frac{\partial X}{\partial x} f(W) + \frac{\partial X}{\partial y} g(W)\\
G(W) &= \frac{\partial Y}{\partial t} W + \frac{\partial Y}{\partial x} f(W) + \frac{\partial Y}{\partial y} g(W)
\end{aligned}
$$

Par exemple, les formules (8) s'appliquent dans le cas d'un gaz parfait à chaleurs spécifiques constantes $\left(e = \frac{1}{\gamma-1}\frac{p}{\rho}\right)$.

4 - METHODE AUX DIFFERENCES FINIES -

On résout le système (5) en utilisant, dans le plan X, Y, plusieurs des quatres variantes du schéma de MacCormack [15]. Ces variantes peuvent s'écrire :

$$
(9.a) \quad
\begin{cases}
\widetilde{W}_{i,j}^{n+1} = W_{i,j}^{n} - \frac{\Delta t}{\Delta X}\left(F_{i+1-\varepsilon_X,j}^{n} - F_{i-\varepsilon_X,j}^{n}\right)\\
\qquad\qquad - \frac{\Delta t}{\Delta Y}\left(G_{i,j+1-\varepsilon_Y}^{n} - G_{i,j-\varepsilon_Y}^{n}\right)
\end{cases}
$$

$$
(9.b) \quad
\begin{cases}
W_{i,j}^{n+1} = \frac{1}{2}\left[W_{i,j}^{n} + \widetilde{W}_{i,j}^{n+1} - \frac{\Delta t}{\Delta X}\left(\widetilde{F}_{i+\varepsilon_X,j}^{n+1} - \widetilde{F}_{i-1+\varepsilon_X,j}^{n+1}\right)\right.\\
\qquad\qquad\left. - \frac{\Delta t}{\Delta Y}\left(\widetilde{G}_{i,j+\varepsilon_Y}^{n+1} - \widetilde{G}_{i,j-1+\varepsilon_Y}^{n+1}\right)\right]
\end{cases}
$$

Les indices supérieurs se réfèrent aux temps t^n et $t^{n+1} = t^n + \Delta t$, où Δt est le pas de temps (qui peut dépendre de n). Les indices inférieurs sont relatifs aux points d'un maillage spatial rectangulaire $X_i = i\,\Delta X$, $Y_j = j\,\Delta Y$, où ΔX et ΔY sont des pas d'espace constants ; ε_X et ε_Y sont des paramètres prenant les valeurs 0 ou 1. Une variante du schéma correspond à un choix de ces paramètres. Les vecteurs $F_{i,j}^{n} = F(W_{i,j}^{n})$ et $G_{i,j}^{n} = G(W_{i,j}^{n})$ sont calculés à l'aide des formules (6) ou (8) dans lesquelles les dérivées de X et Y sont prises au point X_i, Y_j et à l'instant t^n. Le calcul des vecteurs $\widetilde{F}_{i,j}^{n+1} = F(\widetilde{W}_{i,j}^{n+1})$ et $\widetilde{G}_{i,j}^{n+1} = G(\widetilde{W}_{i,j}^{n+1})$ s'effectue de même en prenant les dérivées de X et Y au temps t^{n+1} .

Les dérivées de X par rapport à t, x et y peuvent s'exprimer en fonction des dérivées des transformations $T_1(t)$ et T_2 :

$$
(10) \quad
\begin{aligned}
\frac{\partial X}{\partial t} &= \frac{\partial X}{\partial \xi}\frac{\partial \xi}{\partial t} + \frac{\partial X}{\partial \eta}\frac{\partial \eta}{\partial t} ,\\
\frac{\partial X}{\partial x} &= \frac{\partial X}{\partial \xi}\frac{\partial \xi}{\partial x} + \frac{\partial X}{\partial \eta}\frac{\partial \eta}{\partial x} ,\\
\frac{\partial X}{\partial y} &= \frac{\partial X}{\partial \xi}\frac{\partial \xi}{\partial y} + \frac{\partial X}{\partial \eta}\frac{\partial \eta}{\partial y} ,
\end{aligned}
$$

et on a des relations analogues pour les dérivées de Y. Les dérivées de ξ et η par rapport à t , x et y sont calculables à partir de la donnée du mouvement du profil. Les dérivées de la transformation T_2 peuvent s'écrire en fonction des dérivées de la transformation inverse T_2^{-1} :

$$
(11) \quad
\begin{aligned}
\frac{\partial X}{\partial \xi} &= \mathcal{D}_2\frac{\partial \eta}{\partial y} , & \frac{\partial X}{\partial \eta} &= -\mathcal{D}_2\frac{\partial \xi}{\partial y} ,\\
\frac{\partial Y}{\partial \xi} &= -\mathcal{D}_2\frac{\partial \eta}{\partial x} , & \frac{\partial Y}{\partial \eta} &= \mathcal{D}_2\frac{\partial \xi}{\partial x} ,
\end{aligned}
$$

$$
\text{avec}\quad \mathcal{D}_2 = \left(\frac{\partial \xi}{\partial x}\frac{\partial \eta}{\partial y} - \frac{\partial \xi}{\partial y}\frac{\partial \eta}{\partial x}\right)^{-1}.
$$

On peut alors approcher les dérivées de T_2^{-1} par des différences centrées dans le maillage régulier des points (X_i, Y_j). On obtient par exemple :

$$
(12) \quad \left(\frac{\partial \xi}{\partial X}\right)_{i,j} = \frac{\xi_{i+1,j} - \xi_{i-1,j}}{2\,\Delta X} + O(\Delta X^2)
$$

Comme la transformation T_2 ne dépend pas du temps, le calcul décrit par les formules (11) et (12) peut n'être effectué qu'une seule fois. Il est intéressant de remarquer qu'il n'est pas nécessaire d'utiliser une expression analytique de la transformation géométrique T_2 . Il faut simplement se donner les points :

$$\left(\xi_{\lambda_{i\downarrow}}, \eta_{\lambda_{i\downarrow}}\right) = T_2^{-1}\left(X_\lambda, Y_\downarrow\right) \text{ avec } \left(\mathcal{D}_2\right)^{-1}_{\lambda_{i\downarrow}} \neq 0.$$

La méthode aux différences (9) associée à (6), (10), (11), (12) est précise au second ordre dans le plan de calcul, X, Y. Dans le plan physique x, y, la précision dépend de la régularité de la transformation T_2 . Le pas de temps est limité par une condition de stabilité du type Courant-Friedrichs-Lewy, comme pour tout schéma explicite.

On sait que les propriétés dissipatives du schéma de MacCormack dépendent du choix de la variante. Ceci a pu être expliqué dans [16] pour le système unidimensionnel de la dynamique des gaz. Pour le système (5) à deux dimensions d'espace, nous avons constaté dans le cas stationnaire que les meilleurs résultats numériques sont obtenus lorsque les différences finies intervenant dans le correcteur (9.b) sont décentrées vers l'amont. Pour satisfaire au mieux cette condition, on partage le domaine d'espace en plusieurs régions $\mathcal{R}_p$ et dans chacune d'elles, on utilise une variante V_p du schéma (9). On peut réaliser facilement le raccord entre deux variantes V_p et V_{p+1} associées à des régions voisines $\mathcal{R}_p$ et $\mathcal{R}_{p+1}$, sans abaisser l'ordre de précision. Il suffit pour cela de bien exprimer les prédicteurs $\widetilde{W}^{n+1}$ intervenant dans le calcul d'un point $M_{\lambda_{i\downarrow}} = (X_\lambda, Y_\downarrow)$ voisin de la frontière Γ_p entre $\mathcal{R}_p$ et $\mathcal{R}_{p+1}$ .Par exemple, si le calcul de $W^{n+1}_{\lambda_{i\downarrow}}$ au point $M_{\lambda_{i\downarrow}}$ voisin de Γ_p et situé dans $\mathcal{R}_p$ fait intervenir un prédicteur $\widetilde{W}^{m+1}_{\lambda+1,\downarrow}$ en un point $M_{\lambda+1,\downarrow}$ situé dans $\mathcal{R}_{p+1}$, ce prédicteur doit être évidemment déterminé à l'aide de V_p et non de V_{p+1} .

5 - CALCUL DES CHOCS -

Puisque nous avons choisi la forme conservative correcte des équations d'Euler, le schéma aux différences finies approche les solutions faibles des équations aux dérivées partielles et permet de calculer des chocs satisfaisant les bonnes relations de saut. Il est toutefois nécessaire d'ajouter un terme dissipatif au schéma de MacCormack (9) pour amortir les oscillations parasites apparaissant dans le profil numérique des chocs. On peut étendre l'utilisation du terme de viscosité artificielle de Lax-Wendroff au cas du schéma de MacCormack comme dans [14]. Mais, ce type de viscosité artificielle est très coûteux en temps de calcul. Nous utilisons ici une viscosité artificielle plus simple qui revient à remplacer dans l'équation (9.b), les composantes $W^{(k)}$ du vecteur $W^m_{\lambda_{i\downarrow}}$ par :

$$(13) \quad W^{(k)} + \frac{\Delta t}{\Delta x}\frac{\chi_x}{\mathcal{D}}\left(|\Delta_x w^{(k)}|\,\Delta_x w^{(k)} - |\nabla_x w^{(k)}|\,\nabla_x w^{(k)}\right)$$
$$+ \frac{\Delta t}{\Delta y}\frac{\chi_y}{\mathcal{D}}\left(|\Delta_y w^{(k)}|\,\Delta_y w^{(k)} - |\nabla_y w^{(k)}|\,\nabla_y w^{(k)}\right)$$

où Δ_x et ∇_x (respectivement Δ_y et ∇_y) sont les opérateurs aux différences décentrés avancé et retardé dans la direction X(resp.Y), $w^{(k)}$ est une composante du vecteur $w^m_{\lambda_{i\downarrow}} = \mathcal{D}_{\lambda_{i\downarrow}} W^m_{\lambda_{i\downarrow}}$, χ_x et χ_y sont des coefficients positifs pouvant dépendre de λ et $\downarrow$. Par exemple :

$$\Delta_x w^{(k)} = \left(w^m_{\lambda+1,\downarrow}\right)^{(k)} - \left(w^m_{\lambda,\downarrow}\right)^{(k)}$$

L'équation équivalente (au 3ème ordre près) au schéma (9) avec la viscosité artificielle (13) peut s'écrire :

$$(14) \quad \frac{\partial W^{(k)}}{\partial t} + \frac{\partial F^{(k)}(w)}{\partial X} + \frac{\partial G^{(k)}(W)}{\partial Y} = E^{(k)}$$
$$+ \frac{\Delta x^2}{2}\frac{\chi_x}{\mathcal{D}}\frac{\partial}{\partial X}\left(\left|\frac{\partial w^{(k)}}{\partial X}\right|\frac{\partial w^{(k)}}{\partial X}\right)$$
$$+ \frac{\Delta y^2}{2}\frac{\chi_y}{\mathcal{D}}\frac{\partial}{\partial Y}\left(\left|\frac{\partial w^{(k)}}{\partial Y}\right|\frac{\partial w^{(k)}}{\partial Y}\right).$$

où k = 1, 2, 3, 4 et $E^{(k)}$ est la somme de tous les termes du second-ordre venant du schéma sans viscosité artificielle. Le schéma avec viscosité artificielle reste donc précis au second ordre. Le terme non linéaire(13) est particulièrement efficace dans les zones de choc, où les gradients des quantités physiques $w^{(k)}$ sont grands.

On améliore aussi la représentation numérique des chocs en raffinant le maillage dans les zones de choc. Ceci est réalisé en modifiant la transformation T_2 de sorte que le maillage reste uniforme dans le plan de calcul X, Y . Cette modification ne requiert que quelques interpolations et quelques calculs de certaines dérivées de la transformation définies au § 4. Si le choc se déplace peu par rapport au profil, on peut n'effectuer qu'une seule fois le raffinement du maillage autour de la position moyenne du choc, sinon il faut l'effectuer de temps en temps pour que la région de maillage fin suive l'onde de choc.

6 - CONDITIONS INITIALES ET AUX LIMITES -

a) Au temps t = 0, on se donne comme écoulement initial, l'écoulement stationnaire autour du profil au repos dans sa position de départ ($\xi = x$, $\eta = y$) . Lorsqu'on s'intéresse à un mouvement périodique du profil, on choisit l'écoulement initial correspondant à l'incidence moyenne du profil. Dans tous les cas, l'écoulement stationnaire initial peut être calculé par la présente méthode, en l'utilisant comme une méthode instationnaire permettant d'atteindre un état stationnaire à partir de données initiales arbitraires.

b) Sur le profil, la condition de glissement impose que la vitesse absolue du fluide et celle du profil aient les mêmes composantes normales, c'est-à-dire :

$$(15) \qquad V_m = s ,$$

où $V_m = \vec{V}.\frac{\overrightarrow{grad}\,Y}{|\overrightarrow{grad}\,Y|}$ et $s = -\frac{\partial Y}{\partial t}\frac{1}{|\overrightarrow{grad}\,Y|}$,

puisque l'équation du profil est $Y(x, y ; t) = 0$.

L'algorithme de calcul, pour un point du maillage situé sur le profil, est alors le suivant :

On calcule d'abord des composantes provisoires $\bar{u}$ et $\bar{v}$ de la vitesse absolue du fluide, à l'aide d'un schéma n'utilisant que des différences décentrées dans la direction Y. On détermine ensuite la vitesse tangentielle absolue

$$(16) \qquad \bar{V}_t = \left(\bar{u} \frac{\partial y}{\partial y} - \bar{v} \frac{\partial y}{\partial x} \right) \Big| \operatorname{grad} y \Big|^{-1}$$

et on remplace la vitesse normale absolue $\bar{V}_n$ par λ de sorte que les valeurs finales des composantes de la vitesse absolue s'écrivent :

$$(17) \qquad u = \left(s \frac{\partial y}{\partial x} + \bar{V}_t \frac{\partial y}{\partial y} \right) \Big| \operatorname{grad} y \Big|^{-1}$$

$$(18) \qquad v = \left(s \frac{\partial y}{\partial y} - \bar{V}_t \frac{\partial y}{\partial x} \right) \Big| \operatorname{grad} y \Big|^{-1}.$$

Dans ces formules, les dérivées $\partial y/\partial t$, $\partial y/\partial x$ et $\partial y/\partial y$ doivent être exprimées en fonction des dérivées des transformations $T_1(t)$ et T_2 comme au §4.

On remarquera que ce procédé de calcul ne fait pas intervenir les courbes X (ξ, η)= cte; en particulier, il ne nécessite pas l'utilisation d'un maillage curviligne orthogonal dans le plan ξ, η .

c) Au bord de fuite, on satisfait la condition de Kutta-Joukowski en imposant la continuité de la pression. Pour cela, on choisit au voisinage du bord de fuite, les points du maillage ($\xi_{\ldots}$, $\eta_{\ldots}$) comme il est indiqué sur la figure 2. On note A_+ et A_- les points du maillage les plus près du bord de fuite. On calcule d'abord des vecteurs provisoires $\bar{W}_+$ en A_+ et $\bar{W}_-$ en A_- à l'aide du schéma (9). On détermine ensuite la moyenne $\bar{p}$ des pressions $\bar{p}_+$ et $\bar{p}_-$ déduites de $\bar{W}_+$ et $\bar{W}_-$. On construit alors des vecteurs définitifs W_+ et W_- à partir de la pression moyenne $\bar{p}$ et aussi des masse volumique et quantités de mouvement volumique données par les vecteurs provisoires respectifs. Les vecteurs $W_\pm$ ne diffèrent donc des vecteurs $\bar{W}_\pm$ que par leur quatrième composante dans laquelle l'énergie interne a été recalculée avec la pression moyenne $\bar{p}$.
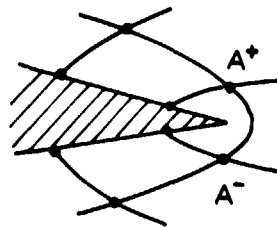

Fig. 2 – Allure du maillage au voisinage du bord de fuite dans le plan ξ, η

d) A l'infini, l'écoulement initial n'est pas perturbé car les perturbations se propagent à vitesse finie et la solution numérique ne peut être calculée que pendant un intervalle de temps fini. Pratiquement, on introduit une frontière lointaine (Γ) sur laquelle on maintient l'écoulement stationnaire initial. En étirant le maillage à mesure que l'on s'écarte du profil, on place la frontière (Γ) suffisamment loin pour que les perturbations ne l'atteignent pas durant l'intervalle de temps considéré.

Dans le calcul de l'écoulement stationnaire initial, on impose les conditions de l'écoulement non perturbé sur la frontière lointaine (Γ) sauf sur sa partie aval (Σ) - voir figure 3 -. Plus précisément, les conditions limites sur (Γ) sont les suivantes :

$$(19) \qquad p = p_\infty , \ \vec{V} \, / \! / \, \vec{z}_\infty , \ |V| = V_\infty , \ s = s_\infty \ \text{sur} \ \Gamma - \Sigma$$

où $\vec{z}_\infty$ est la direction de l'écoulement non perturbé, et

$$(20) \qquad p = p_\infty , \ \vec{V} \, / \! / \, \vec{z}_\infty , \ \frac{\partial |V|}{\partial z_\infty} = 0 , \ \frac{\partial p}{\partial z_\infty} = 0 \ \text{sur} \ \Sigma :$$
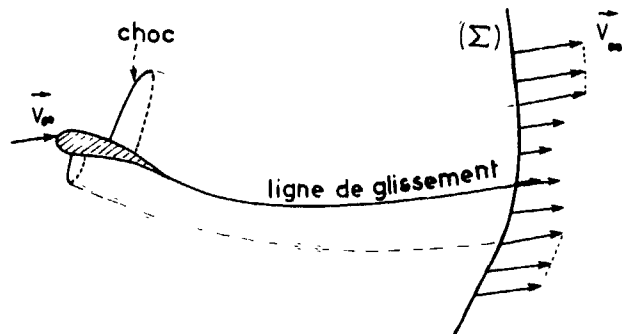

Fig. 3 – Aspect de l'écoulement initial stationnaire à l'aval

7 - RESULTATS NUMERIQUES -

La méthode a été appliquée au calcul de l'écoulement autour du profil NACA 0012 en oscillation d'incidence autour d'un xe situé au quart de la corde, à partir du bord d'attaque. Le fluide est supposé être un gaz parfait à chaleurs spécifiques constantes de rapport $\gamma = 1,4$. Le nombre de Mach de l'écoulement non perturbé est 0,8 et l'angle d'incidence varie selon la loi:

$$(21) \qquad \alpha(t) = \alpha_0 + a \sin(kt)$$

où $\alpha_0 = (\vec{x}, \vec{V}_\infty) = 1°25$, $a = \alpha_0$ et la pulsation réduite $k = \omega c / V_\infty = 10$ (t est le temps réduit).

La transformation $T_1(t)$ est donc définie par:

$$(22) \qquad \begin{aligned} \xi &= \xi_0 + (x - \xi_0) \cos(\alpha - \alpha_0) - y \sin(\alpha - \alpha_0) \\ \eta &= (x - \xi_0) \sin(\alpha - \alpha_0) + y \cos(\alpha - \alpha_0) \end{aligned}$$

avec $\xi_0 = 1/4$.

La transformation T_2 est déduite de la transformation conforme de l'extérieur du profil en l'intérieur d'un cercle [17] *. Le maillage obtenu dans le plan physique est montré partiellement sur la figure 4. La frontière extérieure (Γ), non visible sur cette figure, est placée approximativement à une distance de 6 cordes du profil. Le maillage est raffiné autour des positions moyennes des deux ondes de choc apparaissant dans l'écoulement. Les deux zones de maillage fin peuvent être choisies fixes dans le plan ξ, η , car le déplacement des ondes de choc est faible, en raison de la fréquence élevée des oscillations du profil. Le maillage comporte un nombre total de 144 x 20

---

points. Le schéma aux différences (9) a été utilisé avec $\varepsilon_y = 1$ et ε_x égal à 0 du côté extrados et à 1 du côté intrados.
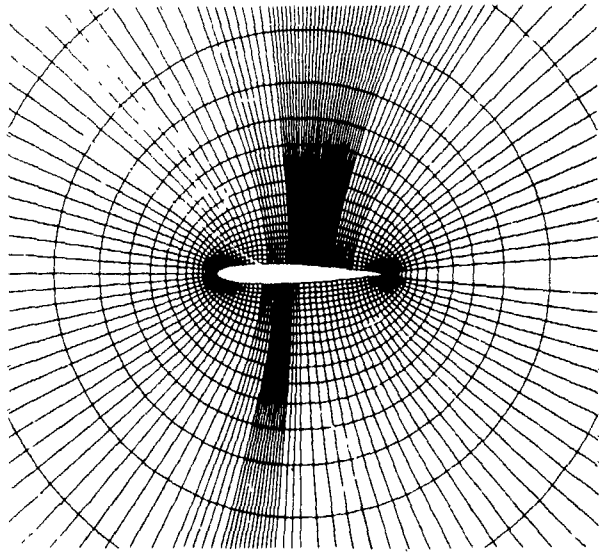
L'état stationnaire initial a été déterminé par la présente méthode pour l'angle d'incidence moyen $\alpha_0 = 1°25$ et un nombre de Mach à l'infini amont de 0,8. La distribution stationnaire de pression sur le profil est montrée sur la figure 5 comparativement à celle fournie par la méthode de Garabedian et Korn [17]. On voit que le choc calculé par la présente méthode satisfait aux relations de Rankine-Hugoniot avec une bonne précision. Les lignes isobares et iso-Mach stationnaires sont visualisées sur les figures 6 et 7. La ligne de glissement existant, dans la solution théorique exacte, en aval du bord de fuite est mise en évidence par la méthode numérique ; elle apparaît comme une rapide variation du nombre de Mach à travers les deux lignes X = cte issues des deux points du maillage sur le profil les plus proches du bord de fuite. On peut déduire du calcul numérique des chocs, la perte de pression génératrice à travers les chocs à l'extrados et à l'intrados du profil et par suite, les valeurs théoriques du nombre de Mach à l'infini-aval de chaque côté de la ligne de glissement ; on trouve pour ces valeurs 0,777 au-dessus de la ligne et 0,798 au-dessous. Le comportement des lignes iso-Mach qui s'éloignent vers l'aval sur la figure 7 est en assez bon accord avec ces valeurs et avec l'existence d'un sillage entropique.

Fig. 4 – Vue partielle du maillage

Fig. 5 – Distribution stationnaire de pression sur le profil

LLL MÉTHODE PRÉSENTE

· · · BAUER-GARABEDIAN-KORN

RELATIONS DE RANKINE-HUGONIOT
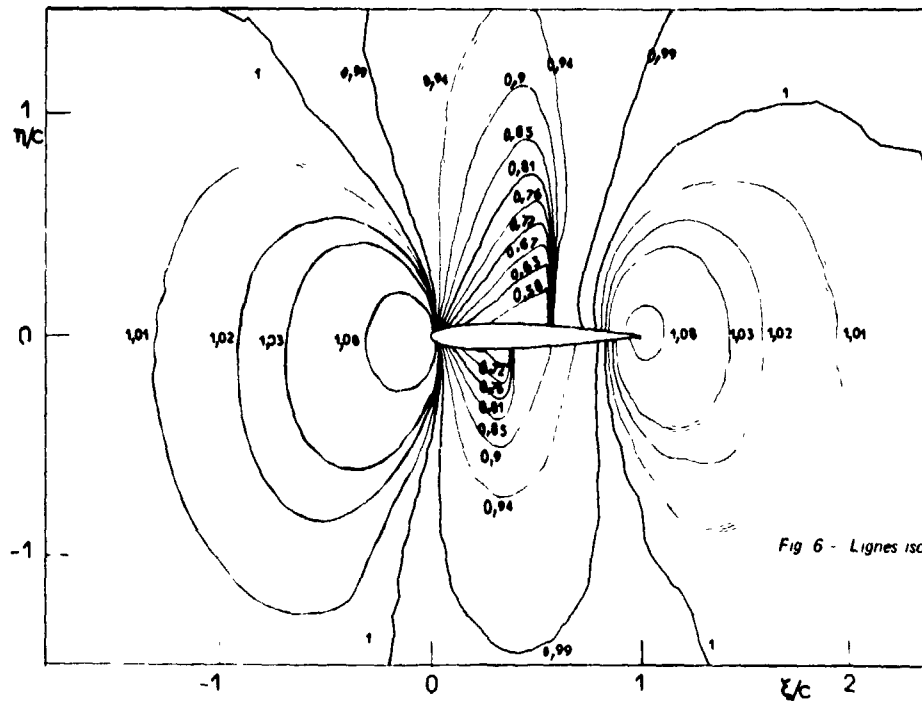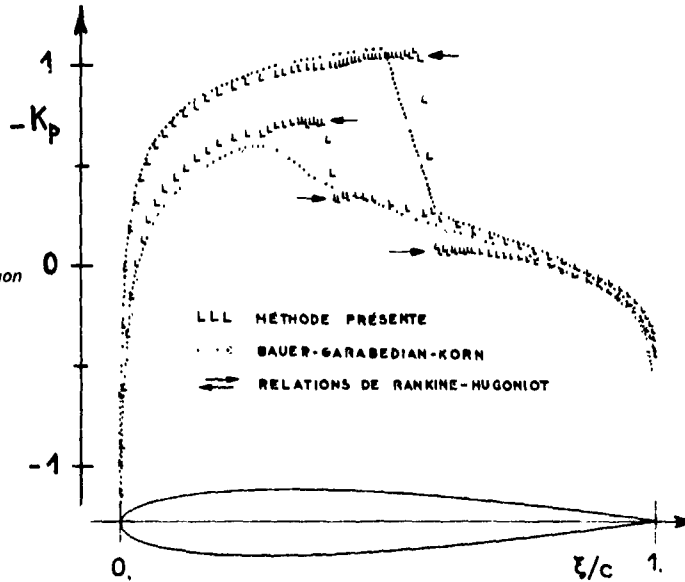
Fig 6 - Lignes isobares stationnaires
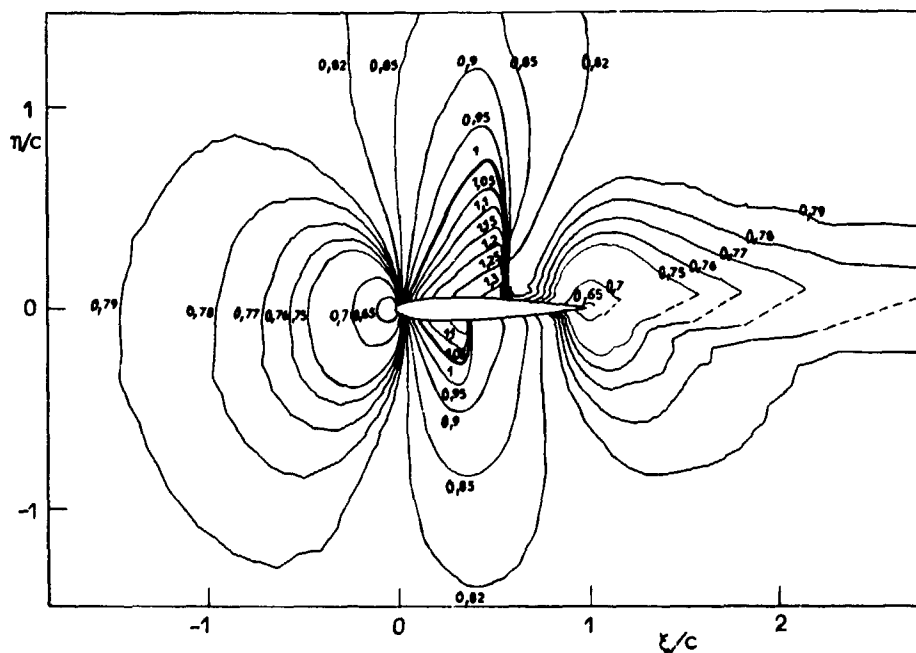
Fig. 7 — Lignes iso-Mach stationnaires.

Considéro s maintenant l'évolution instation-
naire. Les résultats de calcul au voisinage du
profil sont pratiquement périodiques après deux
périodes de la loi oscillatoire (21). La figure 8
montre la distribution instationnaire de pression
sur le profil aux temps t_1 = 2,25 T,
t_2 = 2,50 T, t_3 = 2,75 T
et t_4 = 3 T, ou $T = 2\pi/k$.

kt/2 π = 2,25, α°(t) = 2,50

kt/2 π = 2,50, α°(t) = 1,25

kt/2 π = 2,75, α°(t) = 0

kt/2 π = 3, α°(t) = 1,25
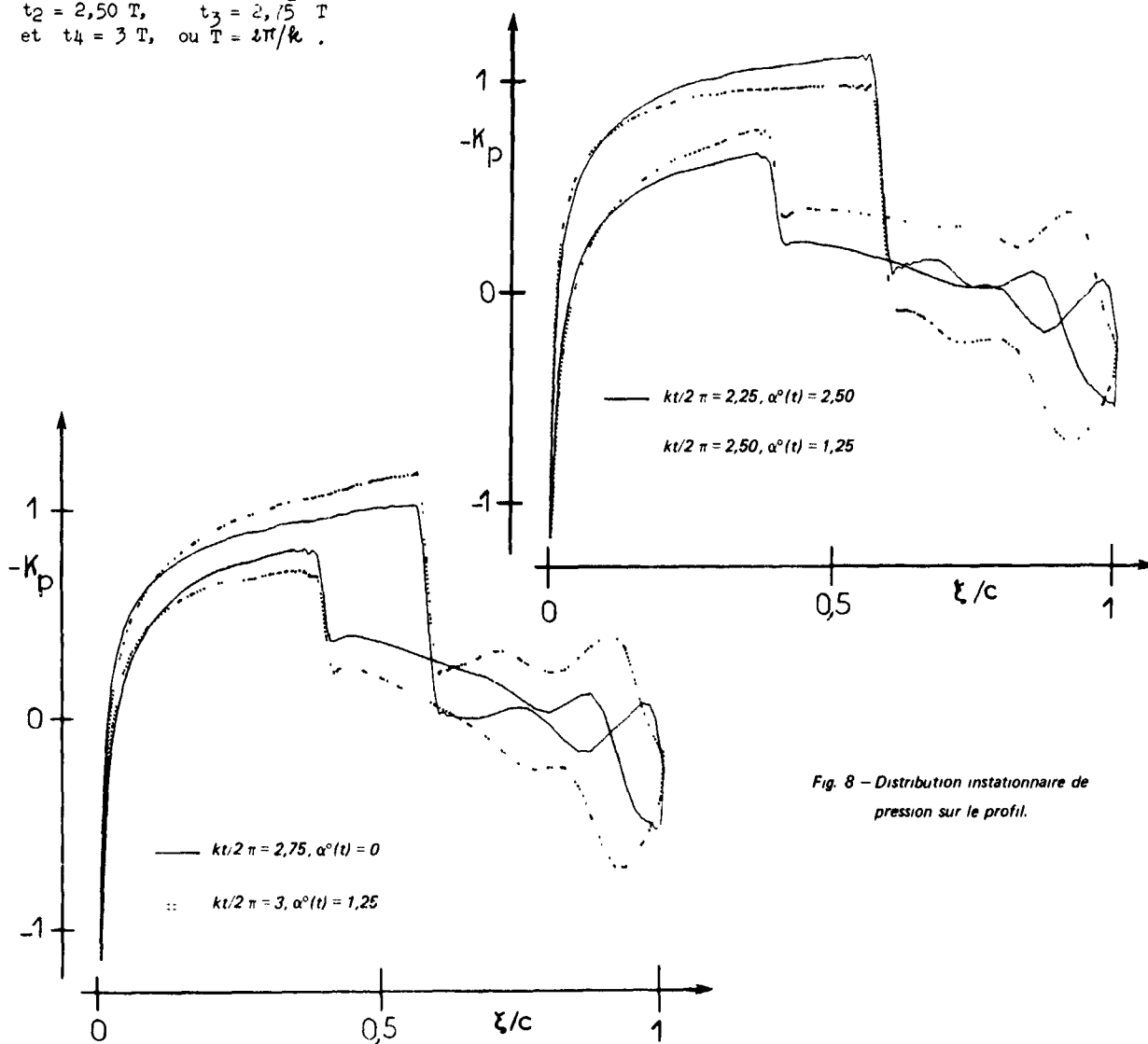
Fig. 8 — Distribution instationnaire de
pression sur le profil.

Les lignes isobares instationnaires sont visua-
lisées sur la figure 9 aux temps t_1, t_2, t_3 et t_4.
La variation dans le temps du coefficient de
portance C_z est montrée sur la figure 10 pour les
trois premières périodes de la loi oscillatoire
(21). On a vérifié numériquement que les pertur-
bations produites par le mouvement du profil
n'atteignent pas la frontière extérieure du
domaine d'espace au cours de ces trois périodes.

La fréquence élevée des oscillations du profil
a pour conséquence un déphasage important entre
la portance et l'incidence ainsi qu'un déplacement
pratiquement nul des ondes de choc, bien que les
états de part et d'autre des chocs varient de
façon appréciable au cours du mouvement.
Précisons enfin que le temps de calcul est infé-
rieur à une demi-heure par période sur un
ordinateur UNIVAC 1110.

$kt/2\pi = 2,25$, $\alpha°(t) = 2,50$

$kt/2\pi = 2,50$, $\alpha°(t) = 1,25$

$kt/2\pi = 2{,}75, \; \alpha°(t) = 0$
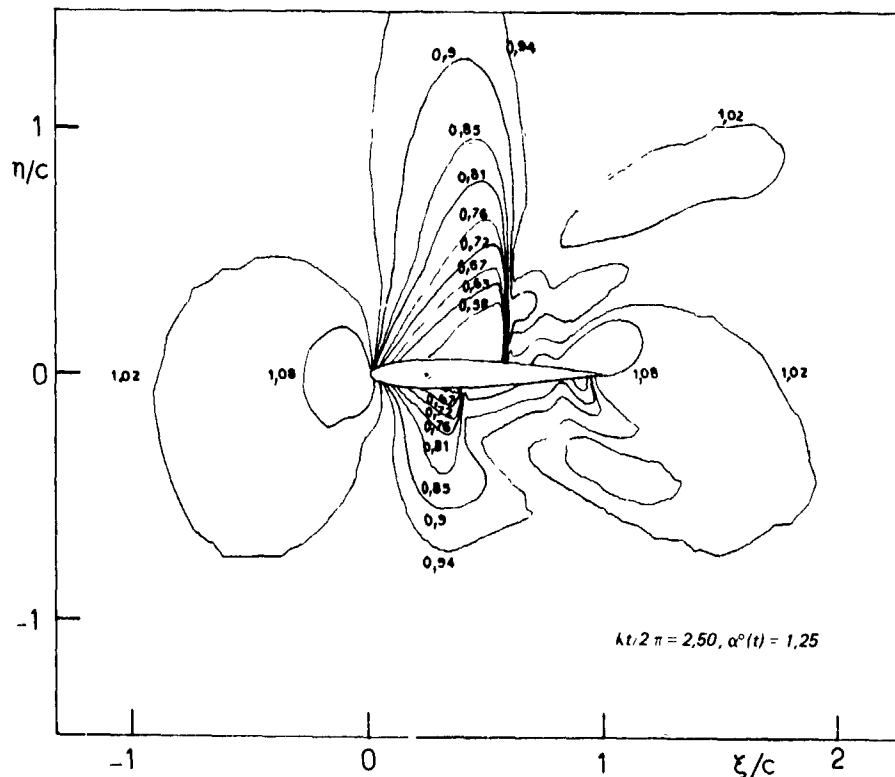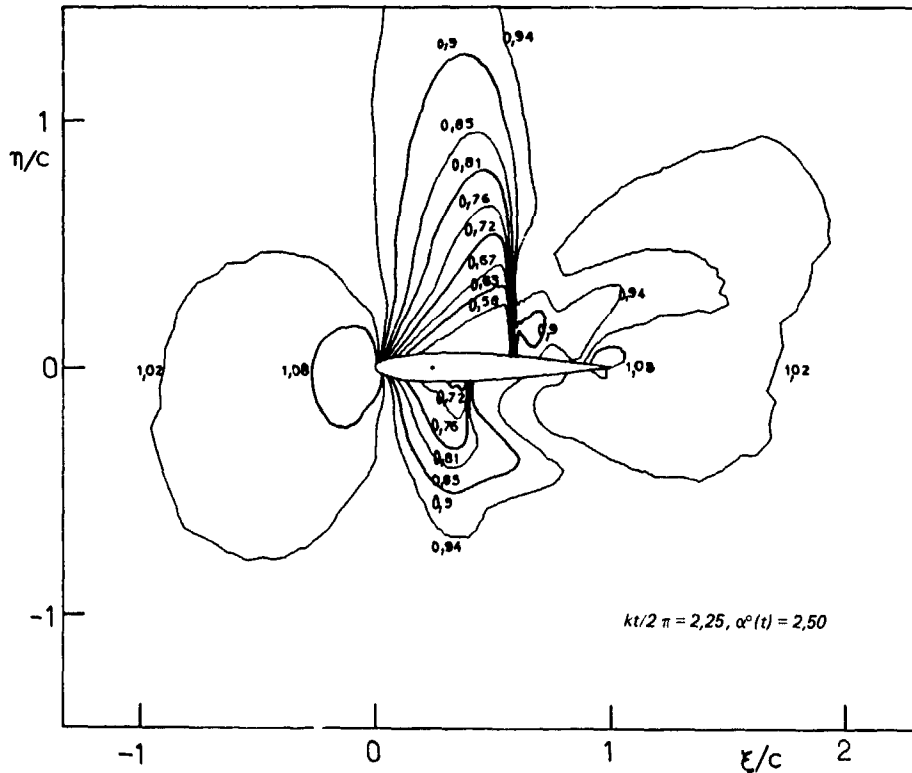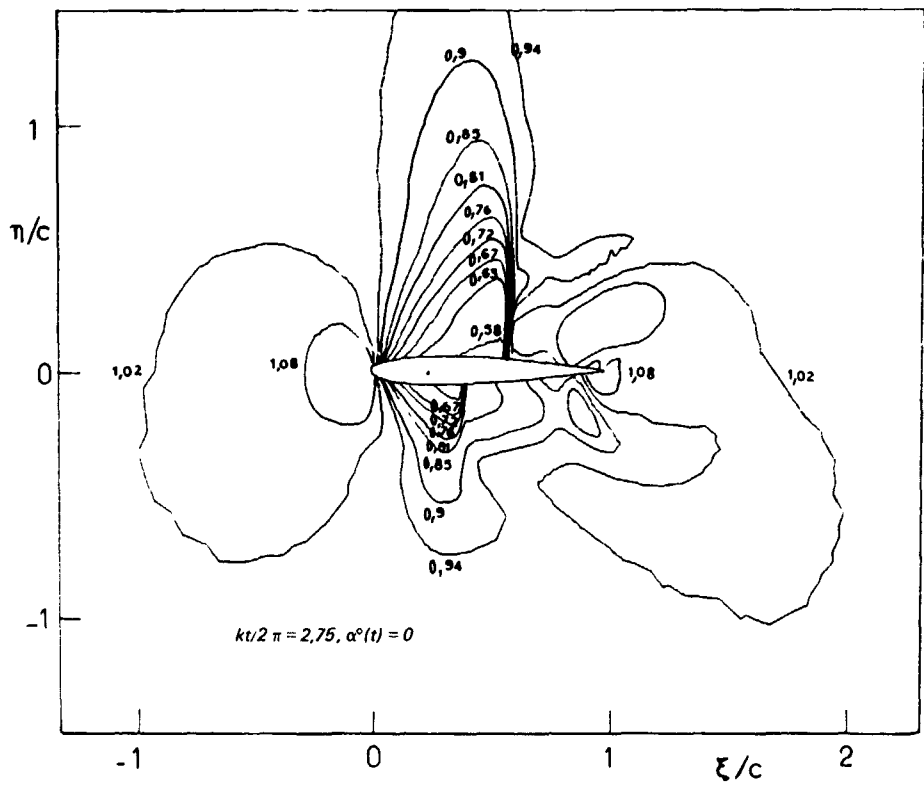
Fig 9 – Lignes isobares instationnaires.

$kt/2\pi = 3, \; \alpha°(t) = 1{,}25$
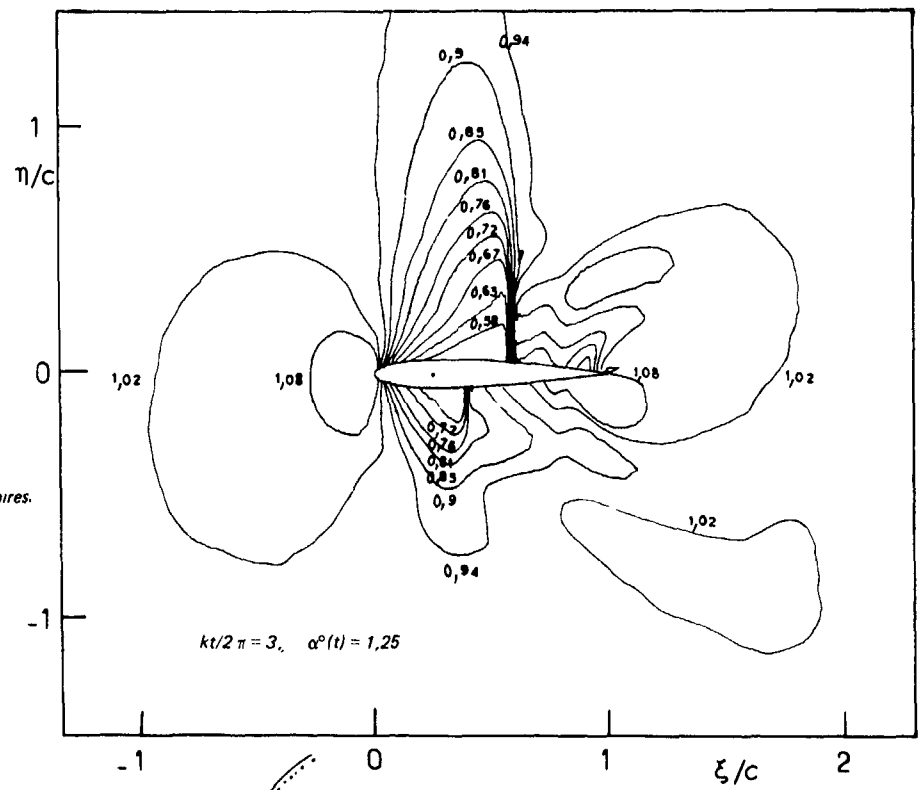
Fig. 10 – Variation dans le temps du coefficient de portance C_z

$0 \leqslant kt/2\pi \leqslant 1$

$1 \leqslant kt/2\pi \leqslant 2$

$2 \leqslant kt/2\pi \leqslant 3$
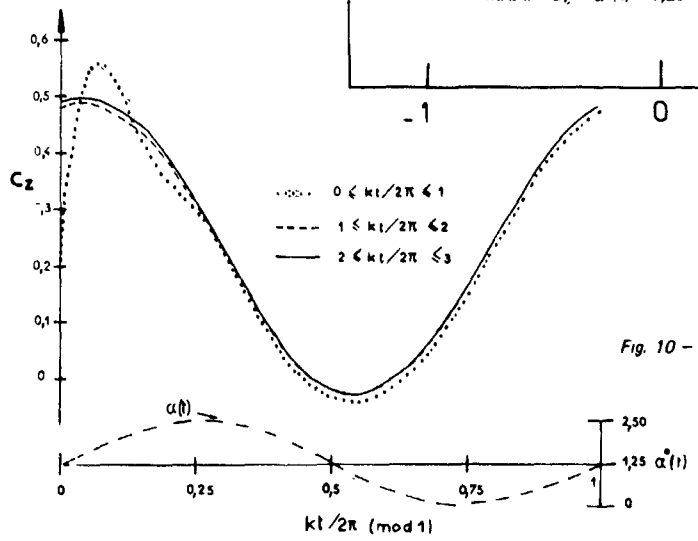
8 - CONCLUSION

Dans cet article, nous avons présenté une méthode de calcul d'écoulements transsoniques instationnaires d'un fluide parfait autour d'un profil rigide en mouvement. Grâce à l'utilisation de la forme conservative des équations d'Euler complètes et à l'application de la condition de glissement sur la surface exacte du profil, la méthode permet d'obtenir des résultats précis y compris au voisinage des ondes de choc et des lignes de glissement. Etant valable pour un mouvement quelconque du profil, elle peut être utilisée pour étudier des phénomènes complexes tels que le flottement d'un profil, l'oscillation d'une gouverne ou encore la rotation d'une section de pale d'hélicoptère. Toutefois, la présente méthode est plus coûteuse en temps de calcul que les méthodes moins précises basées sur l'équation instationnaire du potentiel de petites perturbations. Elle est cependant utile pour déterminer des solutions de référence à des problèmes stationnaires ou instationnaires. Elle peut aussi être indispensable pour calculer certains écoulements autour de profils animés de mouvements de grande amplitude.

RÉFÉRENCES

[1] EHLERS, F.E. - A Finite Difference Method for the Solution of Transonic Flow Around Harmonically Oscillating Wings. 7 th Fluid and Plasma Dyn. Conf., Palo Alto, juin 1974. AIAA Paper n° 74-543.

[2] TRACI, R.M., ALBANO, E.D. et FARR, J.L. - Perturbation Method for Transonic Flows About Oscillating Airfoils. 8 th Fluid and Plasma Dyn. Conf., Hartford, juin 1975. AIAA Journal 14, n° 9, p. 1258-1265 (1976).

[3] CHAN, S.T.K. et BRASHEARS, M.R. - Finite Element Analysis of Unsteady Transonic Flow. 8 th Fluid and Plasma Dyn. Conf., Hartford Juin 1975. AIAA Paper n° 75-875.

[4] KIMBLE, K.R. - A Finite Element Solution of Unsteady Transonic Flow Problems for Three-dimensional Wings and Bodies. 9 th Fluid and Plasma Dyn. Conf., San Diego, juillet 1976. AIAA Paper n° 76-328.

[5] BEAM, R.M. et WARMING, R.F. - Numerical Calculations of Two-dimensional, Unsteady Transonic Flows with Circulation. NASA Techn. Note D-7605, février 1974.

[6] BALLHAUS, W.F. et LOMAX, H. - The Numerical Simulation of Low Frequency Unsteady Transonic Flow Fields. 4 th Intern. Conf. on Numerical Meth. in Fluid Dyn., Boulder, juin 1974. Lecture Notes in Physics 35, p. 57-63 (1975).

[7] CARADONNA, F.X. et ISOM, M.P. - Numerical Calculation of Unsteady Transonic Potential Flow over Helicopter Blades. 13 th Aerospace Sc. Meeting, Pasadena, janvier 1975. AIAA Journal 14, n° 4, p. 482-488 (1976).

[8] LAVAL, P. - Calcul de l'écoulement instationnaire autour d'un profil oscillant par une méthode à pas fractionnaires. 12 th Biennal Fluid Dyn. Symp. on Advanced Probl. and Meth. in Fluid Dyn., Bialowieza, sept. 1975. A paraître dans Archives of Mechanics.

[9] BEAM, R.M. et WARMING, R.F. - An Implicit Finite-Difference Algorithm for Hyperbolic Systems in Conservation-Law Form. J. Comput. Phys. 22, n° 1, p. 87-110 (1976).

[10] MAGNUS, R et YOSHIHARA H - Unsteady Transonic Flows over an Airfoil. 13 th Aerospace Sc. Meeting, Pasadena, janvier 1975. AIAA Journal 13, n° 12, p. 1622-1628 (1975).

[11] MAGNUS, R. et YOSHIHARA, H. - Calculation of the Transonic Oscillating Flap with "viscous" displacement effects. 9 th Fluid and Plasma Dyn. Conf., San Diego, Juillet 1976. AIAA Paper n° 76-327.

[12] BALLHAUS, W.F - Some Recent Progress in Transonic Flow Computation. Lecture Series 87. Von Karman Institute for Fluid Dynamics, mars 1976.

[13] VIVIAND, H. - Formes conservatives des équations de la dynamique des gaz. La Recherche Aérospatiale n° 1974-1, p. 65-68 (1974).

[14] LERAT, A. et PEYRET, R - Noncentered Schemes and Shock Propagation Problems. Computers and Fluids 2, p. 35-52 (1974).

[15] MacCORMACK, R.W. - Numerical Solution of the Interaction of a Shock Wave with a Laminar Boundary Layer. 2 th Intern. Conf. on Numerical Meth. in Fluid Dyn., Berkeley, juin 1970. Lecture Notes in Physics 8, p. 151-163 (1971).

[16] LERAT, A. et PEYRET, R - Propriétés dispersives et dissipatives d'une classe de schémas aux différences pour les systèmes hyperboliques non linéaires. La Recherche Aérospatiale n° 1975-2, p. 61-79 (1975).

[17] BAUER, F., GARABEDIAN, P.R. et KORN, D.G. - Supercritical Wing Sections. Lecture Notes in Economics and Math. Systems n° 66, Springer (1972).

A PRACTICAL FRAMEWORK FOR THE EVALUATION OF OSCILLATORY AERODYNAMIC LOADING
ON WINGS IN SUPERCRITICAL FLOW

by

H. C. Garner
Royal Aircraft Establishment, Structures Department
Farnborough, Hampshire, GU14 6TD, England

SUMMARY

Current approaches to the prediction of unsteady wing loading in mixed subsonic and supersonic flow show a wide variety of method and a clear need for economy in transonic aerodynamic calculations for flutter clearance in subsonic flight. An approximate theoretical treatment is devised in terms of non-linear steady surface pressures and linear oscillatory loading. The steady data are taken either from transonic small-perturbation theory or from static measurements of surface pressure. The resulting theoretical or semi-empirical method can take account of stream Mach number, mean incidence, mode of oscillation, frequency and amplitude. The calculations are organized into a computer program, the scope and broad details of which are outlined.

Its first application is in support of a wind-tunnel study of a rigid half-wing with freedom to rotate about a swept axis. The experiment provides measurements of steady and oscillatory pressure distributions over the range of Mach number from 0.60 to 0.86. The oscillatory results are compared with calculations from linearized theory and from the present method in its theoretical and semi-empirical forms. Like the dynamic experiments, the calculations show large differences between oscillatory chordwise load distributions under subcritical and supercritical conditions. In particular, the region surrounding a shockwave exhibits large and rapid changes in both amplitude and phase of the measured loading, which are reproduced qualitatively in the calculations. The resulting generalized aerodynamic forces are found to depend significantly on the development of supercritical flow. The method should provide an economical indication of the influence of mean flow on the flutter aerodynamics in the lower transonic regime.

Finally there is a forward-looking appraisal of the method, which pinpoints the evidence of a particular need for improvement. The effects of boundary layers are considered to be important in future work on flutter aerodynamics. There should be a concerted plan to compare results from unsteady three-dimensional transonic theories as they are developed.

LIST OF SYMBOLS

a	integer explained below Eq.(9)
$c(\eta)$	local chord of wing
$\bar{c}$	geometric mean chord; reference length in Fig.1
C_1, C_2	output control parameters in Fig.8
C_{LL}	$C_{LLO} + \Re\{(C'_{LL} + iC''_{LL})e^{i\omega t}\}$; local lift coefficient
$C_p(\alpha)$	$(p - p_\infty)/(\frac{1}{2}\rho_\infty U_\infty^2)$; steady pressure coefficient
$\bar{C}_p$	$C'_p + iC''_p$; oscillatory pressure coefficient in Eqs.(2) and (19)
C_{p0}	$C_p(\alpha_0)$; mean pressure coefficient
C'_{p0}	$(\partial C_p/\partial\alpha)_{\alpha=\alpha_0}$
C'_{p1}	equivalent of C'_{p0} at amplitude $\alpha = \alpha_1$ in Eq.(29)
F	ratio in Eq.(17)
$\bar{G}$	local mean flow parameter in Eq.(4)
$\bar{K}$	complex function in Eq.(20)
ℓ	steady non-dimensional loading ΔC_p from linearized theory
$\bar{\ell}$	complex loading coefficient from linearized theory in Eq.(8)
m	number of terms in linearized spanwise loading
M	Mach number
N	number of terms in linearized chordwise loading
p	air pressure
q	integer denoting term in chordwise loading
Q_{ij}	$Q'_{ij} + iQ''_{ij}$; generalized force coefficient in Eq.(30)
$\Re$	real part of
s	semi-span of wing
S	area of wing planform
t	time
U	air speed
x	ordinate in streamwise direction
x_0	location of pitching axis
x_a	local ordinate of swept axis in Fig.1
$x_L(\eta)$	local ordinate of leading edge

y	spanwise distance from centre line
z	upward vertical displacement
α	incidence of wing at crank station $\eta = 0.319$
α_0	mean value of α (degrees or radians)
α_1	amplitude of oscillation in Eq.(22) (radians)
γ	ratio of specific heats of air (= 1.4)
$\Gamma_q(\eta)$	steady loading function in Eq.(18)
$\bar{\Gamma}_q(\eta)$	complex loading function in Eq.(8)
ΔC_p	$C_{p\ell} - C_{pu}$; steady local loading coefficient
$\Delta\bar{C}_p$	$\Delta C'_p + i\Delta C''_p$; oscillatory local loading coefficient
$|\Delta\bar{C}_p|$	amplitude of $\Delta\bar{C}_p$ in Eq.(24)
ϵ_Δ	phase lead of $\Delta\bar{C}_p$ in Eq.(25)
η	y/s ; non-dimensional spanwise distance
$\bar{\nu}$	$\omega\bar{c}/U_\infty$; frequency parameter
ζ	non-dimensional chordwise distance in Eq.(9)
ξ_{CPO}	centre of pressure of chordwise loading ΔC_{p0}
$\bar{\xi}_{CP}$	centre of pressure of chordwise loading $|\Delta\bar{C}_p|$
ρ	air density
ϕ	angular chordwise parameter in Eq.(9)
$\pm\bar{\Phi}$	complex oscillatory velocity potential on upper or lower surface
ψ	ωt ; periodic variable
ω	circular frequency of oscillation
0	subscript denoting mean steady flow at $\alpha = \alpha_0$
∞	subscript denoting undisturbed stream
i	subscript denoting force mode
j	subscript denoting mode of oscillation
ℓ	subscript denoting lower surface
u	subscript denoting upper surface
lin	subscript denoting linearized theory
$\bar{\nu}=0$	subscript denoting steady flow

1   INTRODUCTION

On both theoretical and experimental grounds the achievement of satisfactory flutter characteristics for transonic aircraft is a subject of current concern. The theoretician is mindful that design against flutter relies as much upon aeroelastic calculation as upon experimental validation. He realises that it is inexpedient to estimate transonic flutter conditions from faired curves between reliable predictions based on linearized subsonic and supersonic aerodynamics. The experimentalist is aware of the high cost in time and money of flutter model manufacture and transonic wind-tunnel testing; moreover, he recognizes the uncertainties of tunnel-wall interference and the fact that measurements at zero mean lift may be in-conclusive. The essential dependence of the unsteady flow field of a given configuration upon the mean flow around it, as well as upon the frequency and mode of oscillation and the Mach number, raises severe problems in both disciplines.

The increasing scale of current effort being devoted to the problem of unsteady supercritical flow is evidence, not only of concern among flutter specialists, but of confidence in the progress of this research. Indeed, great strides are being made in the theoretical treatment of two-dimensional unsteady transonic flow. Nevertheless, it will be some while before definitive solutions of the three-dimensional problem become available, and longer still before there is an economical routine of guaranteed accuracy for general use. In the meantime the quest for semi-empirical or other approximate methods of aerodynamic calculation may shed light on what is needed.

The aim of the present paper is to describe the results of a combined theoretical and experimental study of oscillatory pressure distributions on a typical civil-aircraft wing (Fig.1) over the range of Mach number from 0.60 to 0.86, which covers the development of supercritical flow. Ref.1 provides an approximate theoretical treatment of the oscillating wing, while in Ref.2 Lambourne and Welsh report on the experiments and the inherent physical processes. There follows a digest of Ref.1 with an account of some subsequent calculations; finally, after an appraisal of the work to date, some proposals are made for future consideration.

2   THEORETICAL BACKGROUND

Under conditions of subcritical flow there are satisfactory methods of representing the unsteady aerodynamics in aeroelastic calculations, which neglect the wing thickness and the squares of wing dis-placement from a streamwise plane. Such linearized theories are too numerous to mention, but it is import-ant to distinguish between the kernel-functions methods such as Ref.3 and the doublet-lattice methods such as Ref.4. Whereas in calculations of steady pressure distributions for the purpose of wing design it is imperative to incorporate the influence of aerofoil thickness and to make allowance for the boundary layer and wake, in most flutter calculations these complications are either ignored or treated by empirical modifications to linearized theory. For example, the corrective matrix method of Ref.5 is sometimes used in accord with oscillatory experimental data for one single mode to adjust the results of linearized theory for the required modes of a flutter analysis. While this technique has succeeded in subcritical flow, its applicability under supercritical conditions is unassured.

Many attacks on the problem of transonic unsteady aerodynamics are reported in the recent literature, which includes a wide variety of methods. Tijdeman and Zwaan[6] discuss the requirements of such methods in some detail, and in a later review Tijdeman[7] considers different categories of solution. He concludes that, vital as it is, the effect of wing thickness in inviscid flow does not give the required improvement in the prediction of wing loading; since the effects of wing thickness and the boundary layer are of the same order of magnitude, real improvements necessitate the inclusion of both. The other crucial consideration is that not only the mean location of the shockwaves but their time-dependent behaviour should be adequately represented. Much of the published work is restricted either to two-dimensional flow or to near-sonic flow everywhere. We shall focus on three-dimensional theories suitable for a typical supercritical flow when the stream Mach number is below 0.9 and the local Mach number may range from 0.7 to 1.3.

At the Royal Aircraft Establishment, Albone et al.[8] have developed a finite-difference method for two-dimensional steady flow, which has recently been extended to wings of arbitrary planform[9]; results from this latter method are used in some of the present calculations. In the USA, considerable progress has been achieved in the development of finite-difference methods for three-dimensional unsteady flow. The analysis of Ehlers[10] has been incorporated by Weatherill et al.[11] into a pilot program, which has been run for a rectangular wing in pitching oscillation. From the comparisons between the two- and three-dimensional solutions in Fig.21a of Ref.11, it would appear that the difference equations have been linearized so as to suppress the influence of shockwave motion. However, in their method for helicopter rotor blades Isom[12] and Caradonna[13] use the non-linear transonic small-perturbation equations with complete time dependence. They calculate the appearance and disappearance of shockwaves during the cycle of a non-lifting advancing rotor. The method is most promising, and its application to a lifting wing would seem to be a distinct possibility. Nevertheless, it must be anticipated that a general finite-difference method for unsteady flow would be very expensive in routine use.

The lifting-surface element methods provide solutions at lower cost. The general approach is to modify linearized theory by subdivision of the wing surface into regions associated with different stream Mach numbers derived from the mean flow. In one such method under development Cunningham[14] obtains a qualitative improvement in the solution with a linearized kernel-function method and a constant supersonic stream Mach number ahead of the shockwave and a constant subsonic one behind it. Tijdeman and Zwaan[6] have successfully adapted a doublet-lattice method for use under subcritical conditions; the downwash field of each lattice panel corresponds to its own prescribed stream Mach number equal to the average of the local Mach number and the true stream Mach number. Some other techniques for improving linearized lifting-surface element solutions have been tried by Giesing et al.[15]. All these approaches require the same order of computational effort as the linearized theoretical methods, and they deserve further development for mixed subsonic and supersonic flow.

3 PRACTICAL APPROACH

The immediate theoretical requirement is for an approximate method that can be applied with economy and generality to the aerodynamics of oscillating wings when the mean flow may be supercritical. Like the lifting-surface-element methods just described, the method of Ref.1 has been developed in the knowledge that its limitations will eventually be exposed by more elaborate theories, but that its validation as an approximate method could be established by experimental means. The method rests on three basic assumptions, which provide the simplification necessary to give economical calculation and general applicability to a wing-flutter problem.

The first of these assumptions lies in the use of a one-dimensional form of Bernoulli's equation. For a given frequency of oscillation ω, the velocity is written as

$$U(x,t) = U_0(x) + \frac{\partial}{\partial x}\left[\mathcal{R}\{\bar{\Phi}(x)e^{i\omega t}\}\right] , \tag{1}$$

where the subscript 0 denotes a value for the mean flow, $\mathcal{R}$ denotes the real part, and $\bar{\Phi}$ denotes a complex velocity potential. The pressure coefficient is similarly expressed as

$$C_p = (p - p_\infty)/(\tfrac{1}{2}\rho_\infty U_\infty^2) = C_{p0} + \mathcal{R}\{\bar{C}_p e^{i\omega t}\} , \tag{2}$$

where p_∞, ρ_∞ and U_∞ are the pressure, density and velocity of the undisturbed stream. Then to first order in the time-dependent quantities it is shown in Section 3.1 of Ref.1 that under isentropic conditions Bernoulli's equation takes the form

$$\bar{C}_p(x) = -\frac{2G}{U_\infty^2}\left(U_0 \frac{d\bar{\Phi}}{dx} + i\omega\bar{\Phi}\right) , \tag{3}$$

where

$$G = \left(1 + \tfrac{1}{2}\gamma M_\infty^2 C_{p0}\right)^{1/\gamma} , \tag{4}$$

$$U_0 = U_\infty\left[1 - \frac{2}{(\gamma-1)M_\infty^2}\left\{\left(1 + \tfrac{1}{2}\gamma M_\infty^2 C_{p0}\right)^{\frac{\gamma-1}{\gamma}} - 1\right\}\right]^{\frac{1}{2}} , \tag{5}$$

M_∞ is the Mach number of the undisturbed stream and $\gamma(= 1.4)$ is the ratio of the specific heats of air. The first basic assumption is that Eq.(3) holds in three-dimensional flow, when the total derivative is replaced by the partial derivative. Thus the oscillatory component of surface pressure is given by

$$\bar{C}_p(x,y) = -\frac{2G}{U_\infty}\left(U_0(x,y) \frac{\partial\bar{\Phi}}{\partial x} + i\omega\bar{\Phi}\right) , \tag{6}$$

where U_0 and $\bar{\Phi}$ are regarded as surface distributions. This approximation ignores any influence of the lateral component of U_0. Eq.(6) would have greater precision if the differentiation were carried out in the local flow direction. The expediency of integrating chordwise to obtain $\bar{\Phi}$ is thought to have led to a violation of the condition of zero loading at the trailing edge, but this is regarded as a local defect that can be compensated by fairing the amplitude of the calculated oscillatory loading smoothly to zero aft of 80 per cent chord [see Eq.(26)].

The second basic assumption is more sweeping and, perhaps, more successful than it deserves to be. It states that the ratio of the local oscillatory chordwise component of velocity to its value in the quasi-steady case of zero frequency is the same as the corresponding ratio according to linearized theory. This leads to generality in frequency parameter $\bar{\nu}$ and implies that the ratio of the real and imaginary parts of the chordwise component of velocity may be taken from linearized theory. We write

$$\frac{\partial\bar{\Phi}/\partial x}{(\partial\bar{\Phi}/\partial x)_{\bar{\nu}=0}} = \left[\frac{\partial\bar{\Phi}/\partial x}{(\partial\bar{\Phi}/\partial x)_{\bar{\nu}=0}}\right]_{lin} , \tag{7}$$

and an appraisal of this approximation will be made in Sections 6.2 and 6.3.

Any linearized lifting-surface method may be used to implement Eq.(7), but Ref.3 is especially convenient for the purpose because $\partial\bar{\Phi}/\partial x$ is obtainable in analytical form. Ref.3 yields the oscillatory wing loading

$$(\bar{C}_{p\ell} - \bar{C}_{pu})_{lin} = \bar{\ell} = \frac{8s}{\pi c(\eta)} e^{-i\bar{\nu}x/\bar{c}} \sum_{q=1}^{N} \bar{F}_q(\eta) \frac{\cos (q-1)\phi + \cos q\phi}{\sin \phi} , \tag{8}$$

where s denotes the wing semi-span, $\eta = y/s$, $c(\eta)$ denotes the local wing chord, the frequency parameter $\bar{\nu} = \omega\bar{c}/U_\infty$ where $\bar{c}$ is the geometric mean chord, and ϕ is the angular chordwise parameter such that with a leading edge $x_L(\eta)$

$$\frac{x - x_L(\eta)}{c(\eta)} = \zeta = \tfrac{1}{2}(1 - \cos \phi) . \tag{9}$$

16-4

Ref.3 is a coll cation method in which there are N chordwise terms, m spanwise terms and $a(m + 1) - 1$ spanwise integr.ion stations between the wing tips; in the present applications $(N,m,a) = (4,23,4)$. The solutions are obtained as values of the complex functions $\bar{\Gamma}_q(\eta)(q = 1$ to $N)$ at spanwise positions $\eta = - \cos\left[r\pi/(m + 1)\right]$ $(r = 1$ to $m)$, from which $\bar{\Gamma}_q(\eta)$ is expressible as the double Fourier series in Eq.(11) of Ref.3. The linearized form of Eq.(6) is

$$\frac{\partial \bar{\Phi}_{1in}}{\partial x} + \frac{i\omega}{U_\infty} \bar{\Phi}_{1in} = \pm \tfrac{1}{4} U_\infty \bar{\ell}(x,\eta) \quad , \tag{10}$$

where the symbol $\pm$ denotes positive for the upper surface and negative for the lower surface. This linear differential equation is readily solved to give

$$\bar{\Phi}_{1in} = \pm \frac{U_\infty s}{\pi} e^{-i\bar{\nu}x/\bar{c}} \left\{ \bar{\Gamma}_1(\eta)(\phi + \sin \phi) + \sum_{q=2}^{N} \bar{\Gamma}_q(\eta) \left(\frac{\sin (q - 1)\phi}{q - 1} + \frac{\sin q\phi}{q} \right) \right\} \quad . \tag{11}$$

The constituents of Eq.(7) are

$$\partial \bar{\Phi}_{1in}/\partial x = \pm \tfrac{1}{4} U_\infty \bar{K} \tag{12}$$

where $\bar{K}$ is deduced from Eqs.(8), (10) and (11),

$$(\partial \bar{\Phi}/\partial x)_{\bar{\nu}=0} = - \frac{U_\infty^2}{2GU_0} (\bar{C}_p)_{\bar{\nu}=0} \tag{13}$$

and

$$\left(\partial \bar{\Phi}_{1in}/\partial x \right)_{\bar{\nu}=0} = \pm \tfrac{1}{4} U_\infty (\bar{\ell})_{\bar{\nu}=0} \tag{14}$$

from Eqs.(6) and (10) respectively. Hence

$$\frac{\partial \bar{\Phi}}{\partial x} = - \frac{U_\infty^2 \bar{K}}{2GU_0} \left(\frac{\bar{C}_p}{\bar{\ell}} \right)_{\bar{\nu}=0} \tag{15}$$

Eqs.(6) and (15) combine to determine $\bar{C}_p$ for any section $y = \eta s$, and the oscillatory chordwise pressure distribution on the upper or lower surface is given by

$$\bar{C}_p(\xi) = \bar{K}(\xi) \left(\frac{\bar{C}_p(\xi)}{\bar{\ell}(\xi)} \right)_{\bar{\nu}=0} + \frac{i\bar{\nu}c G(\xi)}{\bar{c}} \int_0^{\xi} \frac{\bar{K}(\xi')U_\infty}{G(\xi')U_0(\xi')} \left(\frac{\bar{C}_p(\xi')}{\bar{\ell}(\xi')} \right)_{\bar{\nu}=0} d\xi' \quad , \tag{16}$$

where $G(\xi)$ and $U_0(\xi)$ are defined in Eqs.(4), (5) and (9) in terms of the mean local pressure coefficient $C_{p0}(\xi)$.

The third basic assumption is that the ratio of the quasi-steady rate of change of surface pressure to its linearized theoretical rate of change is the same for all modes of deformation or displacement. By considering the ratio for an infinitesimal change of incidence we write

$$F = \left(\frac{\bar{C}_p}{\bar{\ell}} \right)_{\bar{\nu}=0} = \frac{(\partial C_p/\partial \alpha)_{\alpha=\alpha_0}}{\partial \ell/\partial \alpha} \quad \text{or} \quad \frac{C_{p0}'}{\partial \ell/\partial \alpha} \quad , \tag{17}$$

where $\alpha = \alpha_0$ denotes the mean flow condition and $\partial \ell/\partial \alpha$ is obtained from the linearized steady-state solution for a change of incidence; Eq.(8) reduces to

$$\frac{\partial \ell}{\partial \alpha} = \frac{8s}{\pi c(\eta)} \sum_{q=1}^{N} \Gamma_q(\eta) \frac{\cos (q - 1)\phi + \cos q\phi}{\sin \phi} \quad , \tag{18}$$

where $\Gamma_q(\eta)$ is a real function defined like $\bar{\Gamma}_q(\eta)$ as a double Fourier series. The selection of α as the independent variable of differentiation in Eq.(17) is influenced by the considerations that the steady pressure distributions $C_p(x,y,\alpha)$ will often be available and that the theoretical quantity $\partial \ell/\partial \alpha$ is unlikely to vanish locally. The approximation in Eq.(17) is akin to the corrective matrix method of Ref.5, which is admittedly untried for supercritical flow.

By Eqs.(16) and (17) the final expression for the oscillatory part of the pressure coefficient is

$$\bar{C}_p(\xi) = F(\xi)\bar{K}(\xi) + \frac{i\bar{\nu}c G(\xi)}{\bar{c}} \int_0^{\xi} \frac{F(\xi')\bar{K}(\xi')U_\infty}{G(\xi')U_0(\xi')} d\xi' \quad , \tag{19}$$

where in accord with Eqs.(8), (10), (11) and (12)

$$\bar{K}(\xi) = \frac{8s}{\pi\bar{c}} e^{-i\bar{\nu}x/\bar{c}} \left[\frac{\bar{c}}{c(\eta)} \sum_{q=1}^{N} \bar{\Gamma}_q(\eta) \frac{\cos(q-1)\phi + \cos q\phi}{\sin\phi} \right.$$

$$\left. - \frac{i\bar{\nu}}{2} \left\{ \bar{\Gamma}_1(\eta)(\phi + \sin\phi) + \sum_{q=2}^{N} \bar{\Gamma}_q(\eta) \left(\frac{\sin(q-1)\phi}{q-1} + \frac{\sin q\phi}{q} \right) \right\} \right] , \qquad (20)$$

where x and ϕ are related to ξ in Eq.(9). Besides the quantities $\partial\ell/\partial\alpha$ and $\bar{K}$ from linearized theory, the chordwise distributions of C_{p0} and C'_{p0} are required to obtain $G(\xi)$, $U_0(\xi)$ and $F(\xi)$ before Eq.(19) can be evaluated. While the role of C_{p0} is to modify through Eqs.(4) and (5) the values $G = 1$ and $U_0 = U_\infty$ implicit in linearized theory, the quantity C'_{p0} is of paramount importance, especially in the first term of Eq.(19); the procurement of its surface distribution is discussed in Section 4.

4   ALTERNATIVE METHODS

Just as any oscillatory lifting-surface method can in principle provide values of $\bar{K}$, so can any steady-state technique provide the pressure distributions $C_p(x,y,\alpha)$. These will be required at sufficient values of α to define C_{p0} and C'_{p0} over the desired range of mean incidence α_0. In the present investigation the alternative sources of 'static data' are the theoretical transonic small-perturbation (TSP) method of Albone et al.[8,9] and the wind-tunnel measurements of steady pressure reported by Lambourne and Welsh[2].

There are conflicting arguments for preferring the use of either TSP or experimental static data. The first concerns the number of data points (x,y), which may be limited in pressure plotting tests to the extent that the chordwise behaviour of the integrand in Eq.(19) is ill-defined and there is insufficient spanwise coverage in the integral for the generalized forces; in the present applications an average of ten experimental data points at each of five sections contrasts with 35 TSP data points available at each of 18 sections. Another consideration is the problem of differentiating C_p to obtain C'_{p0}; again the theoretical approach is preferable, because the differentiation of experimental values of C_p with respect to α may be blurred by scatter. The most important argument concerns Reynolds number or boundary layers, and this is two-edged. Since the validation of the present practical approach is through comparison with experiment, the omission of boundary-layer effects in TSP data defeats this objective, especially as experimental evidence points to the increasing importance of viscosity under supercritical conditions. At the same time the experimental wind-tunnel data are for much too low a Reynolds number to be representative of full scale, in which respect the alternative methods can be regarded as two extremes.

The present calculations are for a wing of current design with the planform defined in Fig.1. The measurements of steady and oscillatory pressures at the five sections (I to V) are described in Ref.2. The half-model has camber and twist and a streamwise thickness-to-chord ratio of approximately 0.10. The incidence α is defined as that of the crank section $y = 0.319s$, relative to which the root and tip incidences are $+3.93^\circ$ and -0.57° respectively. In the dynamic experiments of Ref.2 the wing has fairly high stiffness, so that in the present calculations it may be assumed to oscillate rigidly about the axis

$$x = x_a = 0.709\bar{c} + s|\eta| \tan 25^\circ . \qquad (21)$$

The motion is expressed in terms of the instantaneous incidence

$$\alpha = \alpha_0 + \Re\{\alpha_1 e^{i\omega t}\} \qquad (22)$$

where the frequency is 120Hz, so that at model scale $\bar{c} = 139.5$mm the frequency parameter $\bar{\nu}$ ranges from 0.534 at $M_\infty = 0.60$ to 0.385 at $M_\infty = 0.86$.

The approximate theoretical calculations with TSP static data cover the ranges of incidence $-1.93^\circ \le \alpha \le 2.07^\circ$ and $-1.13^\circ \le \alpha_0 \le 1.27^\circ$ with $M_\infty = 0.84$, and the results in Section 4.1 provide a good qualitative indication of the performance of Eq.(19). The present calculations by the semi-empirical version of the method are for restricted incidences $1.57^\circ \le \alpha \le 2.57^\circ$ and $1.90^\circ \le \alpha_0 \le 2.24^\circ$ but cover the whole experimental range of M_∞; these results in Section 4.2 are appraised quantitatively against the measured oscillatory pressures.

4.1   Approximate theoretical method

The three-dimensional TSP method of Albone et al., which is featured in a survey by Lock[9], has undergone some refinement since its application to the present problem, but not so as to affect the qualitative story of the calculations. The computer program for the relaxation solution of the finite-difference equations over a $60 \times 24 \times 40$ grid is expensive to run but, once a solution at one incidence for the given $M_\infty = 0.84$ is obtained, it is relatively quick to get further solutions as α is increased in small steps of 0.40 from -1.93 to 2.07 degrees.

The approximate theoretical calculations of Ref.1 are restricted to $\eta = 0.750$, a grid line close to station IV of Fig.1. Given the values of the upper and lower surface pressure coefficients $C_{pu}(\alpha)$ and $C_{p\ell}(\alpha)$, their gradients C'_{pu0} and $C'_{p\ell0}$ have been calculated at $\alpha_0 = -1.13, -0.33, 0.47$ and 1.27 degrees from quartic polynomial fits to the data points at $\alpha = \alpha_0, \alpha_0 \pm 0.4$ and $\alpha_0 \pm 0.8$ degrees. As indicated after Eq.(9), the lifting-surface method of Ref.3 is applied to the wing motion defined in Eqs.(21) and (22) to provide $\bar{\Gamma}_q/\alpha_1$ from which to evaluate $\bar{K}/\alpha_1$ in Eq.(20), and to the steady change of incidence to

provide Γ_q from which to evaluate $\partial\ell/\partial\alpha$ in Eq.(18). The ratio F is calculated from Eq.(17) for both upper and lower surfaces at the 35 grid points on the chord at $\eta = 0.750$, whereupon Eq.(19) can be evaluated. This process is greatly facilitated in that, after spanwise interpolation in $\bar{\Gamma}_q$, Eq.(20) yields $\bar{K}(\xi)/\alpha_1$ at any required set of positions ξ. Given $\bar{C}_{pu}/\alpha_1$ and $\bar{C}_{p\ell}/\alpha_1$, the oscillatory chordwise loading is split into its real and imaginary parts so that

$$\frac{\bar{C}_{p\ell}(\xi) - \bar{C}_{pu}(\xi)}{\alpha_1} = \frac{\Delta\bar{C}_p(\xi)}{\alpha_1} = \frac{\Delta C_p'}{\alpha_1} + i\bar{\nu}\left(\frac{\Delta C_p''}{\alpha_1\bar{\nu}}\right) , \tag{23}$$

or in terms of its amplitude and phase

$$\frac{|\Delta\bar{C}_p|}{\alpha_1} = \left[\left(\frac{\Delta C_p'}{\alpha_1}\right)^2 + \left(\frac{\Delta C_p''}{\alpha_1}\right)^2\right]^{\frac{1}{2}} \tag{24}$$

and

$$\varepsilon_\Delta = \tan^{-1}(\Delta C_p''/\Delta C_p') . \tag{25}$$

The results from Ref.1 are illustrated in Figs.2 and 3.

The chordwise distributions of the calculated amplitude and phase for the four values of α_0(deg) are shown in Fig.2 where $|\Delta\bar{C}_p|/\alpha_1$(rad^{-1}) is seen to be markedly different from the linearized theoretical curve in the range $0.05 < \xi < 0.50$. As would be expected from the first term of Eq.(19), the broad pattern of behaviour is consistent with that of the quasi-steady gradient $(C_{p\ell 0}' - C_{pu0}')$. The high peak near the leading edge at $\alpha_0 = -1.13^\circ$ is associated with supercritical effects on the lower surface. The next mean incidence $\alpha_0 = -0.33^\circ$ has relatively mild supercritical flow on both surfaces, but there is a significant influence of aerofoil thickness. At the higher incidences there are two marked peaks in each distribution; while the leading-edge peak still dominates at $\alpha_0 = 0.47^\circ$, the peak at mid-chord is the salient feature at $\alpha_0 = 1.27^\circ$. According to linearized theory ε_Δ is almost linear in ξ, and relative to the wing motion it shows a phase lag for $\xi < 0.4$ and a phase lead for $\xi > 0.4$. The calculated influence of transonic flow is to delay the change-over from phase lag to phase lead and to increase the phase lead downstream of about mid-chord. The curve for $\alpha_0 = -0.33^\circ$ is omitted from Fig.2 as it is practically indistinguishable from that for $\alpha_0 = -1.13^\circ$. At $\alpha_0 = 0.47^\circ$ and 1.27° the region of greatest interest is close to the downstream end of the embedded supersonic flow where, as $|\Delta\bar{C}_p|/\alpha_1$ falls from its peak and the real part $\Delta C_p'/\alpha_1$ becomes negative, ε_Δ increases rapidly to give a phase lead in excess of a quarter cycle.

The real and imaginary parts of the individual surface pressures $\bar{C}_{pu}$ and $\bar{C}_{p\ell}$ are plotted against ξ in Fig.3 for $\alpha_0 = 0.47^\circ$ and 1.27°. The interesting effects of supercritical flow are confined to the upper surface. At $\alpha_0 = 0.47^\circ$ there is a forward peak in local mean Mach number $M_{u0} = 1.32$ at $\xi = 0.04$ which is associated with local peaks in $-C_{pu}'/\alpha_1$ and C_{pu}''/α_1 of about 1.8 times the local value from linearized theory, while the recompression from $_{u0} = 1.20$ to 1.05 near $\xi = 0.4$ causes local chordwise jumps of 21 and 17 in $-C_{pu}'/\alpha_1$ and $-C_{pu}''/\alpha_1\bar{\nu}$ respectively. These dominant effects are intensified at $\alpha_0 = 1.27^\circ$, when the peaks at $\xi = 0.04$ reach $M_{u0} = 1.50$ and $\bar{C}_{pu}/\alpha_1$ of about 2.5 times the local value from linearized theory, while recompression from $M_{u0} = 1.32$ to 1.00 near $\xi = 0.5$ causes chordwise jumps as high as 38 and 25 in $-C_{pu}'/\alpha_1$ and $-C_{pu}''/\alpha_1\bar{\nu}$ respectively. It would be surprising if effects of this order of magnitude were not vital in regard to the generalized aerodynamic forces.

It is seen in Fig.2 that the oscillatory loading from the approximate theoretical method fails to reach zero at the trailing edge. As discussed after Eq.(6), a possible contributory fact is that this derivation from Bernoulli's equation does not represent the influence of cross flow which must grow as the trailing edge is approached. Accordingly the behaviour of the loading $\Delta\bar{C}_p$ will be modified by forcing it smoothly to zero with the factor

$$1 - 25(\xi - 0.8)^2 \quad \text{when } \xi \geq 0.8 . \tag{26}$$

The effect of this will be to bring the amplitude $|\Delta\bar{C}_p|/\alpha_1$ much closer to the linearized theoretical curve in this region.

These calculations with TSP static data have enough points to avoid ambiguity in drawing the chordwise distributions. Clearly the method is not restricted to supercritical flow, but its most important application is where M_∞ is below 0.9, say, and the mean flow contains a substantial supersonic region. The results are qualitative in the two senses, that no realistic comparisons with experiment can be expected from considerations of inviscid transonic flow, and that there are no reliable solutions of the full oscillatory three-dimensional equations of motion from which to evaluate the approximations of Eqs.(6), (7) and (17), and in particular to verify the use of Eq.(7) up to flutter frequencies. Whatever shortcomings the present calculations may have, the inadequacy of linearized theory in this flow regime is not in doubt.

4.2 Semi-empirical method

With experiment instead of TSP theory as the source of static data the method becomes semi-empirical. The outline of the computational procedure in Section 4.1 may still suffice, but there are two new facets on the determination of the pressure gradient C_{p0}' with respect to incidence. One possibility, not used in the present investigation, is to obtain C_{p0}' directly from the experiments as the amplitude of the oscillatory pressure when the simple harmonic motion of the model is reduced in frequency to 1Hz, say. However, we consider a quasi-steady analysis of the measured pressure through the finite cycle of incidence in Eq.(22) and evaluate its fundamental term as described in Section 5.1 of Ref.1. Thus C_{p0}' is replaced by

$$C'_{p1} = \frac{1}{\pi \alpha_1} \int_0^{2\pi} C_p(\alpha) \cos \psi \, d\psi \quad , \tag{27}$$

where
$$\alpha = \alpha_0 + \alpha_1 \cos \psi \quad . \tag{28}$$

An alternative expression for Eq.(27) is

$$C'_{p1} = \frac{2}{\pi} \int_0^{\pi} \frac{\partial C_p}{\partial \alpha} \sin^2 \psi \, d\psi \quad , \tag{29}$$

which is suitable for computation whether the amplitude of oscillation α_1 is finite or infinitesimal.

Most of the present calculations are based on $\alpha = 1.74$, 1.90, 2.07, 2.24 and 2.40 degrees with $\alpha_0 = 2.07$ degrees and $\alpha_1 = 0.33\text{deg} = 0.0058\text{rad}$ as in the dynamic experiments, but the influence of small variations in α_0 and α_1 has been examined. Selected results from Ref.1 to illustrate the effects of separate wing surfaces, stream Mach number, mean incidence and spanwise location are given in Figs.4 to 7 respectively, which include comparisons with the chordwise distributions of measured oscillatory pressure at a frequency of 120Hz.

The main consideration in Fig.4 for $M_\infty = 0.82$ and $\eta = 0.766$ is that, while both real and imaginary parts of $\bar{C}_{p\ell}$ for the lower surface from semi-empirical calculation and experiment lie fairly close to their linearized theoretical curves, the departures from these same curves for the oscillatory pressure $-\bar{C}_{pu}$ on the upper surface are large and encouragingly consistent. The purpose of Fig.5 for $\eta = 0.535$ is twofold, to contrast the results for subcritical and supercritical flow and to illustrate the effect of frequency. Whereas at $M_\infty = 0.60$ both the real and imaginary parts of the loading $\Delta \bar{C}_p$ from semi-empirical calculation and experiment are acceptably close to the results of linearized theory, large effects of supercritical flow are calculated and measured at $M_\infty = 0.82$. The comparisons of the real part $\Delta C'_p/\alpha_1$ show the same order of discrepancy between semi-empirical calculation and measurement as at $M_\infty = 0.60$; the quasi-steady and semi-empirical curves for $M_\infty = 0.82$ for which $\bar{\nu} = 0.402$ offer a convincing demonstration that the effect of frequency is adequately represented in the calculations. On the other hand, the imaginary part plotted as $\Delta C''_p/\alpha_1 \bar{\nu}$ shows the correct trends at $M_\infty = 0.82$, but the magnitude of the supercritical-flow effects is underestimated. In Fig.6 the semi-empirical effect of mean incidence is shown by plotting the loading amplitude and phase for $M_\infty = 0.84$ and $\eta = 0.766$ when α_0 is 0.17° above and below that of the experiments. The main differences are associated with the rearward movement of the recompression region as incidence increases. In Fig.7 it is perhaps surprising that at $M_\infty = 0.86$ the peaks and troughs in the measured chordwise distributions of oscillatory loading have weakened by comparison with the results at $M_\infty = 0.82$ and 0.84. Nevertheless at both $\eta = 0.535$ and 0.882 the semi-empirical calculations, unlike linearized theory, give a fair representation of the quantities $\Delta C'_p/\alpha_1$ and $\Delta C''_p/\alpha_1 \bar{\nu}$ from experiment.

A more detailed account of these comparisons is found in Ref.1. The main deficiency of the present method is its failure to reproduce the increases in phase lag over the forward part and the phase lead over the rear part of the chord in sufficient measure to bridge the differences between linearized theory and experiment. The increased phase lead is associated with small measured values of $\Delta C'_p/\alpha_1$ of changeable sign, but the increased phase lag is of much greater importance as it occurs where $\Delta C''_p/\alpha_1$ is relatively large and reasonably well predicted. We shall consider this matter further in Section 6.2, observing here that the semi-empirical method offers great improvement on the linearized theoretical method.

5   COMPUTER PROGRAMS

So far the numerical material has been drawn from desk calculations. The alternative methods are seen to have equal generality. Planform and Mach number are basic to most aspects of the calculations. Frequency and mode of oscillation enter through the linearized theoretical data, while aerofoil section, camber and twist, mean incidence and oscillatory amplitude all feature in the equations relating to the non-linear static data from whichever source. With application to flutter as the prime objective, the approximate aerodynamic equations have now been programmed in FORTRAN language by Computer Analysts & Programmers Ltd. There are three sets of input data for the program:

(a)   CARDDATA, a file prepared by hand to define the planform geometry, the points where the static data (WINGDATA) are to be given and $\Delta \bar{C}_p$ is to be evaluated, the values of α and α_0 , the required force modes, the number of frequency parameters and oscillation modes, the value of M_∞ and some output control data;

(b)   PLATEDATA, a file containing the results of previous calculations for the thin-plate wing from linearized theory at uniform incidence (l_q) and in oscillation $(\bar{\Gamma}_q)$ for the appropriate frequencies, modes and Mach number;

(c)   WINGDATA, a file containing the steady-state data, either theoretical or experimental, for the wing with thickness, camber and twist at the appropriate incidences and Mach number.

The running time is a trivial proportion of that required to produce the PLATEDATA by means of Ref.3 or the WINGDATA by means of Albone's finite-difference ISP method.

The procedure from input to output is summarized in Fig.8. There is some intentional duplication of the initial data so as to cross-check the validity of the CARDDATA file; for example, the 'input parameters' N and m must correspond to the numbers of values of q and n for which l_q and $\bar{\Gamma}_q$ are specified in the PLATEDATA file, and similarly the number of 'data points' (ξ, η) at each section must be consistent with the contents of the WINGDATA file. The standard output of results includes planform data, force mode data,

individual surface pressures $\bar{C}_p(\xi,\eta)$, the corresponding loading $\Delta\bar{C}_p(\xi,\eta)$ with its amplitude and phase, the integrated generalized forces

$$Q_{ij} = Q'_{ij} + iQ''_{ij} = \frac{1}{2S\bar{c}} \iint z_i (\Delta\bar{C}_p)_j \, dS \qquad (30)$$

where z_i is the displacement in the ith force mode and $(\Delta\bar{C}_p)_j$ is the loading in the jth oscillation mode, and finally $\bar{\ell}(\xi,\eta)$ and the corresponding generalized forces as computed from the PLATEDATA. This amount of printout is obtained when the control parameters (C_1,C_2) are set to $(0,0)$. Many other printing options are indicated in Fig.8. But $(3,0)$ gives the minimum printing of just the first row of output quantities, while $(C_1,C_2) = (0,3)$ produces maximum printing including values of C_{p0}, C'_{p0} , spanwise interpolations of Γ_q and $\bar{\Gamma}_q$, $\partial\ell/\partial\alpha$, the chordwise integrals from Eq.(30) prior to spanwise integration, and the corresponding mean forces when $\Delta\bar{C}_{p0}$ replaces $(\Delta\bar{C}_p)_j$ in Eq.(30).

The numerical procedures only depart from those of Ref.1 in matters of detail. In the first place the modifying factor of Eq.(26) is applied to $\Delta\bar{C}_p$. Secondly, an identifier CODEA is used to define how the program accepts the steady-state WINGDATA:

> CODEA = 1 denotes theoretical data fitted exactly by a cubic spline;
> CODEA = 2 denotes measured data fitted by a least-squares cubic spline;
> CODEA = 3 denotes computed data already interpolated at $\alpha = \alpha_0$.

The option CODEA = 3 is used in connection with amplitude effect as expressed in Eq.(29); a subsidiary program has been written to convert a WINGDATA file from its standard format with values of C_{pu} and $C_{p\ell}$ as required when CODEA = 1 or 2 to one with the quantities C_{p0} and C'_{p1} ready for use with CODEA = 3. Thirdly, cubic splines are fitted between the first and last data points in the chordwise and spanwise directions in the evaluation of Eq.(30); between these points and the perimeter of the planform the required edge conditions are applied with continuity in the integrands and their first derivatives at the extreme data points.

The main program has been applied satisfactorily in support of an experimental flutter investigation, but the results are not yet available. However, the calculations of Ref.1 have been extended by means of this program, and the new results in Figs.9 to 14 will now be discussed.

6   DISCUSSION AND APPRAISAL

The additional calculations for the wing of Fig.1 at $M_\infty = 0.84$ are intended to fill two gaps in the content of Ref.1. While Figs.2 and 3 have shown large local effects of supercritical mean flow at $\eta = 0.750$, the global consequences to the integrated forces can now be evaluated and are discussed in Section 6.1. Moreover, there are results from the alternative versions of the present approach to provide more extensive comparisons in Section 6.2, and to emphasise the important influence of viscosity. Finally Section 6.3 gives a forward-looking appraisal of this research.

6.1   Generalized forces

To simulate the application of the method to flutter aerodynamics, the wing of Fig.1 is considered in heaving and pitching motion at $M_\infty = 0.84$ and $\bar{\nu} = 0.393$. The pitching axis is taken at the aerodynamic centre $x_0 = 1.234\bar{c}$ as calculated by the linearized theory of Ref.3 in steady flow. The non-dimensional lift and pitching moment corresponding to force modes

$$\left.\begin{array}{l} z_1 = \bar{c} \\[2ex] z_2 = x_0 - x \end{array}\right\} \qquad (31)$$

are calculated in accord with Eq.(30). The three force matrices

$$(Q_{ij}) = (Q'_{ij}) + i(Q''_{ij}) \qquad (32)$$

in Fig.9 are derived respectively from the linearized theory, the approximate theoretical method of Section 4.1 with $\alpha_0 = 1.27°$, and the semi-empirical method of Section 4.1 with $\alpha_0 = 2.07°$. As for a flutter calculation, the limiting case of small amplitude $\alpha_1 \to 0$ has been taken throughout.

The evaluation of generalized forces from linearized theory within the program of Ref.3 is carried out by Gaussian integration, but the procedure just outlined near the end of Section 5 loses accuracy when the static data points become sparse. This inaccuracy in integration is aggravated if, as may happen with the semi-empirical method, the chordwise distributions of $\Delta\bar{C}_p$ are irregular and poorly defined by the cubic spline fit. Thus the elements of the third matrix equation in Fig.9 are unreliable in the second significant figure. Nevertheless, the results in Fig.9 demonstrate how sensitive the total lift and pitching moment can be to the method of calculation when the influence of supercritical flow is at its peak.

The matrix elements fall into two broad categories, larger ones whose behaviour follows a clear pattern and smaller ones whose order of magnitude is uncertain. Thus the five elements Q'_{11}, Q'_{12}, Q''_{11}, Q''_{12}, Q''_{22} , as calculated by the approximate theoretical and semi-empirical methods, lie on opposite sides of their linearized theoretical values. That the same statement is true of Q'_{21}, Q'_{22} and Q''_{21} is probably fortuitous. Perhaps the large changes from matrix to matrix give an exaggerated idea of the likely effect of the boundary layers, because the tests are at the low Reynolds number of about 10^6 based on $\bar{c}$ at $M_\infty = 0.84$ whereas the TSP data neglect the residual viscous effects at full-scale Reynolds number. On the hypotheses that at full-scale the steady-state results would lie between the predictions of the linearized and TSP theories and that the semi-empirical method is representative of the wind tunnel,

it could be deduced that experimentally determined oscillatory aerodynamic forces would differ from their full-scale values by as much as 50 per cent.

6.2   Theoretical and semi-empirical predictions

In a quest for further clarification of the predicted oscillatory aerodynamics at $M_\infty = 0.84$ with and without viscous effects in the static data, we consider the results from linearized theory, from both versions of the present method and from experiment at all five pressure stations (Fig.1). The results with inviscid static data from TSP theory have been interpolated in η . For the oscillations about the axis $x = x_a$ with $\bar{v} = 0.393$ the chordwise distributions of the amplitude $|\Delta\bar{C}_p|/\alpha_1$ in Fig.10 show how the supercritical flow effects weaken inboard of $\eta = 0.535$. Experiment and semi-empirical calculation give a progressive forward movement of the peak amplitude as η decreases; but at all sections the inviscid transonic approximation leads to twin peaks, the second of which moves gently aft as η decreases. With the choice of mean incidence $\alpha_0 = 0.87^\circ$ the experimental conditions are matched by the calculations over the outer part of the span, but further inboard the results with TSP data retain the features associated with a shockwave near mid-chord.

The corresponding plots of phase angle in Fig.11 show that both versions of the present method usually depart from the linearized theoretical curves towards the experimental data. But at all five sections there is the persistent failure to reproduce the increased phase lag that is measured in the region $\xi < 0.4$. A physical explanation is that the large area of surface flow with local Mach number $M > M_\infty$ impedes the upstream propagation of disturbances from the main periodic-lift-producing region just ahead of the recompression or shockwave. Of the three basic assumptions in Eqs.(6), (7) and (17), it is that of Eq.(7) whose inadequacy must be questioned; near the leading edge where $\bar{\phi}$ is small, Eqs.(6) and (7) force ϵ_Δ towards its linearized theoretical curve. If Eq.(7) is to be re-modelled to meet this criticism, a secondary consideration is that the same area of flow with $M > M_\infty$ must assist the down-stream propagation of disturbances with a tendency to increase the phase lead further aft. There is experimental evidence in Fig.11 from the outer part of the span to bear out this argument.

Fig.12 gives the spanwise distributions of oscillatory lift and the mean-flow coefficient C_{LL0} whose semi-empirical and experimental values are identical. The integrations to obtain the experimental values of $cC'_{LL}/\bar{c}\alpha$ and $cC''_{LL}/\bar{c}\alpha\bar{v}$ are very approximate, and failure of the pressure transducer at $\xi = 0.3$ has made the values at $\eta = 0.309$ too unreliable to be worth plotting. The higher lift curve slope from TSP theory accounts for the higher mean lift coefficients and in-phase spanwise loading. The imaginary or in-quadrature part of the spanwise loading includes the opposing effects of forward phase lag and rearward phase lead, and the consistently more negative experimental values of $cC''_{LL}/\bar{c}\alpha\bar{v}$ reflects the larger phase lags in Fig.11. The chordwise centres of pressure of both the mean loading and the amplitude of the oscillatory loading are plotted similarly in Fig.13, which features in both cases the aft displacement from the experimental or semi-empirical positions to those obtained with TSP data. Such a shift in the aerodynamic centre is considered to have a favourable influence on the critical flutter speed, and there is perhaps a danger that the predictions based on inviscid supercritical flow may be over-optimistic; how-ever, by the same token those based on tests at low Reynolds number may be too conservative.

The two final illustrations give the same experimental data at $\eta = 0.766$ and highlight some further aspects of the calculations. Fig.14 first compares the steady pressure distributions from TSP theory at $\alpha = 0.87^\circ$ and 1.07° with that measured at $\alpha = 2.07^\circ$. The two theoretical distributions match the measured lower-surface pressures and the strength, if not quite the position, of the upper-surface recom-pression. It is worth observing that the small difference between these two theoretical loadings has a primary influence on the calculated distributions of loading amplitude plotted below them. Curves of both $|\Delta\bar{C}_p|/\alpha_1$ and ϵ_Δ are drawn for $\alpha_0 = 0.87^\circ$ and 1.07° in the limit as α_1 tends to zero. In this narrow range of α_0 the neglected viscous effects and the other various approximations are judged from the com-parisons to be more significant than the effects of α_0 . Fig.15 shows the semi-empirical curves of load-ing amplitude and phase for $\alpha_0 = 2.07^\circ$ when, with the aid of Eq.(29), the calculations are made for $\alpha_1 = 0.003$ and 0.009 instead of the experimental value of 0.006 radians. While it is encouraging that the differences in $|\Delta\bar{C}_p|/\alpha_1$ between calculation and experiment are only of the same order as the effects of α_1 , its trivial influence on ϵ_Δ does not obscure the tendency to underestimate the magnitude of the phase angle.

6.3   Future framework

From the outset of the work in Ref.1 the philosophy has been to keep the basic approximations simple with a view to the re-modelling of the equations in the light of experience. The primary need for a fuller appreciation of the physics of unsteady viscous transonic flow remains. But one characteristic of the inviscid aerodynamics, namely the influence of the mean flow on the rate of propagation of time-dependent disturbances, has been identified as the basis of a new building block. It is necessary to distinguish between the attenuation of upstream influence as a steady phenomenon and the time delay in upstream influence as an unsteady phenomenon. Both of these principles are implicit in linearized theory to a limited degree, and the need to intensify the process is expressed in many promising non-linear studies as an effective increase in stream Mach number related to local flow conditions. In the present approach Eq.(7) has taken account of the attenuation within the mean flow, but its apparent failing is to ignore the consequences of the increased time delay due to supercritical flow.

It is desirable to extend the present theoretical treatment to oscillating control surfaces, and this has been attempted for a plain trailing-edge flap with little success in the leading-edge region. Again, the basic assumption of Eq.(7) has proved inadequate; in the case of the oscillating flap, moreover, there is evidence to suggest that the semi-empirical method underestimates both amplitude and phase lag near the leading edge. Since the mechanism of upstream propagation under supercritical conditions should be much clearer when the forward part of the wing is stationary, any re-modelling of Eq.(7) should take the steady and oscillatory evidence for control surfaces into account.

Another road to progress that can be foreseen is the possibility to include Reynolds number as a parameter in the approximate theoretical method. At the Royal Aircraft Establishment, Mr. M.C.P. Firmin

is in the process of incorporating the three-dimensional boundary-layer growth into Albone's finite-difference technique for solving the transonic small-perturbation equations in steady flow. This new source of static data should eventually remove the problems raised in the second paragraph of Section 4. The difficulties of chordwise integration and differentiation with sparse and scattered experimental data would no longer arise. Moreover, the restriction to wind-tunnel Reynolds numbers on the one hand or to infinite Reynolds number on the other would be lifted, so that the calculated flutter aerodynamics would become representative of the full-scale aircraft.

Beyond this foreseeable stage of development there remains the task of assessing the inherent approximations. One should look to more rigorous theoretical attacks on the problem of inviscid unsteady three-dimensional transonic flow, to basic research on unsteady boundary-layer and shockwave interaction, and to detailed wind-tunnel investigations of oscillatory surface pressures on rigid and flexible models. Essential new features of flutter aerodynamics are likely to be revealed in each case. The best that can be hoped from attempts to short-cut the process, such as the present method and Refs.6, 14 and 15, is that they will be pursued with realism and economy.

7   CONCLUDING REMARKS

The present method has achieved a measure of success, which is ample to justify an attempt to incorporate the delay in upstream propagation through a supercritical mean flow as a new building block. Such a refinement must be representative of experience with both oscillating wings and oscillating control surfaces.

There is danger in adopting a complacent attitude to flutter because the onset of inviscid super-critical flow can bring a theoretical increase in critical flutter speed. This trend is probably associated with a rearward shift of the aerodynamic centre, which would, however, be reduced by viscous effects.

It is important that the influence of Reynolds number should be incorporated into the present method as soon as possible by means of the input from steady-state data. The semi-empirical calculations have suffered through an insufficiency of pressure data points, and there is some prospect of replacing such experimental data by more closely-spaced values from finite-difference solutions with the boundary layer included.

The growing current effort and interest in unsteady three-dimensional transonic flow is creating a demand for a concerted plan to bring about direct comparisons between the results of the various theories that are in the course of development. The introduction of some standard examples is recommended as a first step.

REFERENCES

1   H.C. Garner, A practical approach to the prediction of oscillatory pressure distributions on wings in supercritical flow. RAE Technical Report 74181 (ARC CP No.1358) (1975)

2   N.C. Lambourne, B.L. Welsh, Pressure measurements on a wing oscillating in supercritical flow. RAE Technical Report to be issued

3   Doris E. Lehrian, H.C. Garner, Theoretical calculation of generalized forces and load distribution on wings oscillating at general frequency in a subsonic stream. RAE Technical Report 71147 (ARC R & M 3710) (1971)

4   E. Albano, W.P. Rodden, A doublet-lattice method for calculating lift distributions on oscillating surfaces in subsonic flows. AIAA Journal, Vol.7, No.2, pp.279-285 (1969)

5   H. Bergh, R.J. Zwaan, A method for estimating unsteady pressure distributions for arbitrary vibration modes from theory and from measured distributions for one single mode. NLR Report TR F.250 (1966)

6   H. Tijdeman, R.J. Zwaan, On the prediction of aerodynamic loads on oscillating wings in transonic flow. NLR MP 73026U (AGARD Report 612) (1973)

7   H. Tijdeman, High subsonic and transonic effects in unsteady aerodynamics. NLR TR 75079U (1975)

8   C.M. Albone, D. Catherall, M.G. Hall, M.G. Joyce, An improved numerical method for solving the transonic small-perturbation equation for the flow past a lifting aerofoil. RAE Technical Report 74056 (1974)

9   R.C. Lock, Research in the UK on finite difference methods for computing steady transonic flows. Symposium Transsonicum II, Göttingen, 8-13 September, 1975, pp.457-486, Springer-Verlag (1976)

10   F.E. Ehlers, A finite difference method for the solution of the transonic flow around harmonically oscillating wings. NASA CR-2257 (1974)

11   W.H. Weatherill, F.E. Ehlers, J.D. Sebastian, Computation of the transonic perturbation flow fields around two- and three-dimensional oscillating wings. NASA CR-2599 (1975)

12   M.P. Isom, Unsteady subsonic and transonic potential flow over helicopter rotor blades. NASA CR-2463 (1974)

13   F.X. Caradonna, M.P. Isom, Numerical calculation of unsteady transonic potential flow over helicopter rotor blades. AIAA Paper 75-168, AIAA 13th Aerospace Sciences Meeting, Pasadena, 20-22 January 1975 (1975)

14   A.M. Cunningham, The application of general aerodynamic lifting surface elements to problems in unsteady transonic flow. NASA CR-112264 (1973)

15   J.P. Giesing, T.P. Kalman, W.P. Rodden, Correction factor techniques for improving aerodynamic prediction methods. NASA CR-144967 (1976)
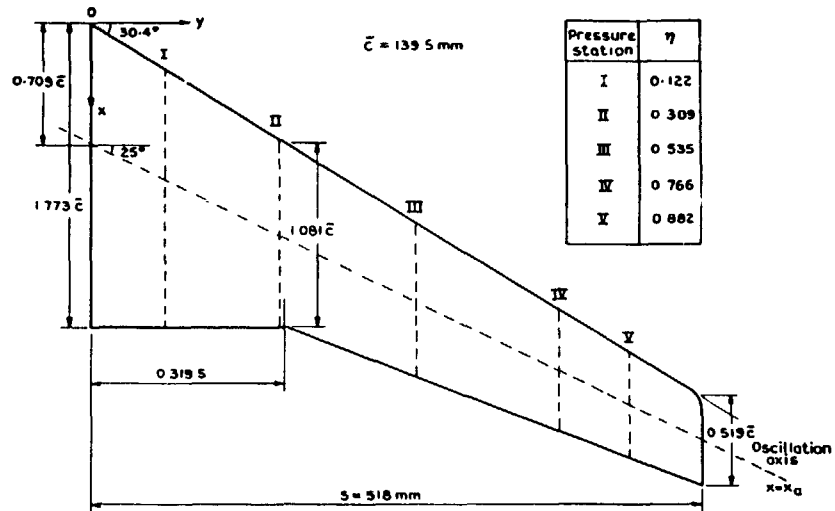
ACKNOWLEDGEMENT

Fig 1 Details of model planform, pressure stations and oscillation axis
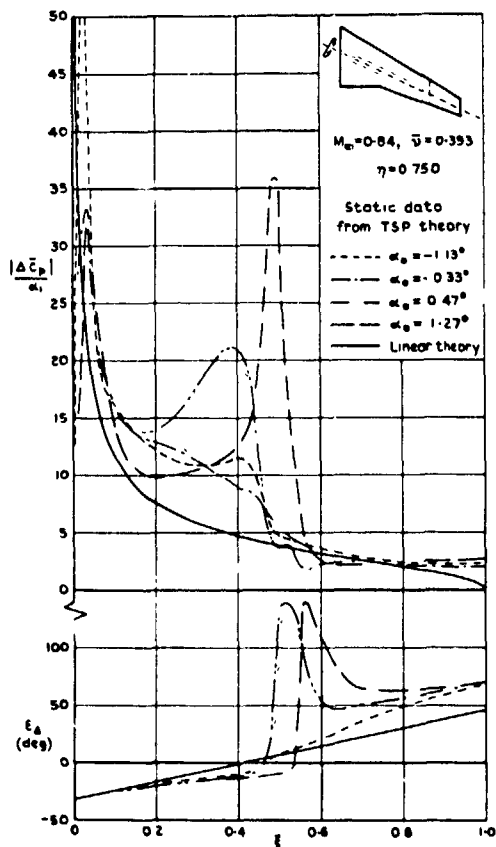
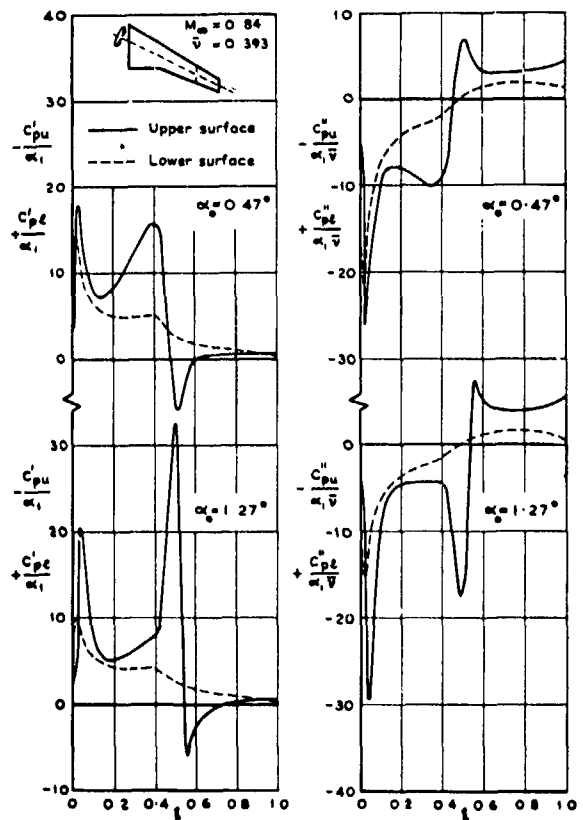Fig 2 Effect of mean incidence on amplitude and phase of oscillatory loading

Fig 3 Calculated oscillatory pressures on upper and lower surfaces at $\eta = 0.750$
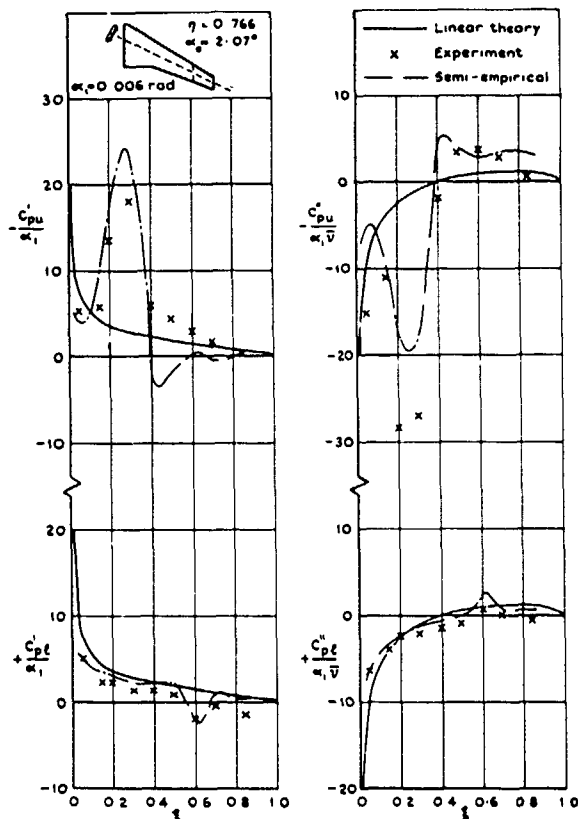
Fig 4 Measured and calculated oscillatory surface pressures ($M_\infty = 0.82$, $\bar{v} = 0.402$)
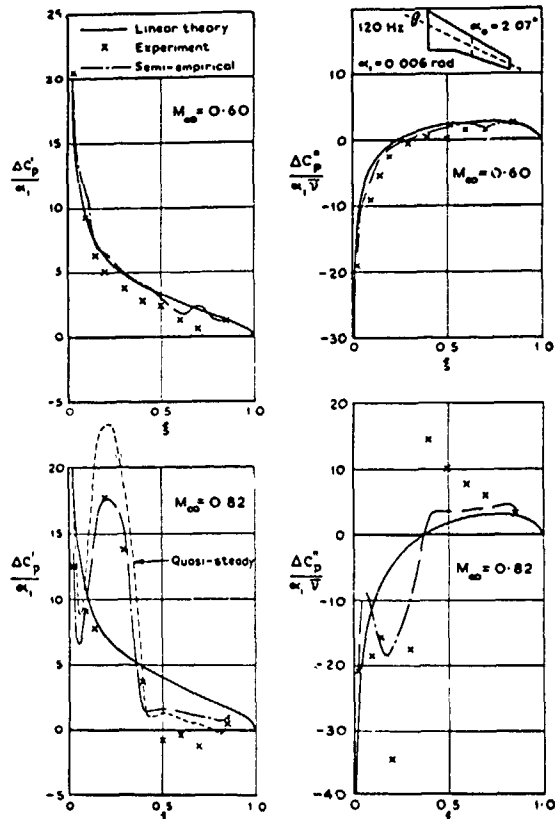
Fig 5 Measured and calculated oscillatory loading at $\eta = 0.535$ in subcritical and supercritical flow
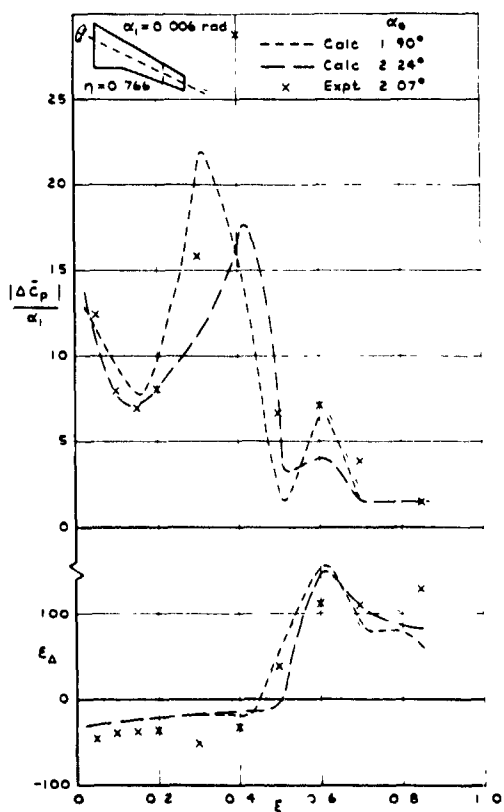
Fig 6 Semi-empirical effects of mean incidence on oscillatory loading ($M_\infty = 0.84$, $\bar{v} = 0.393$)
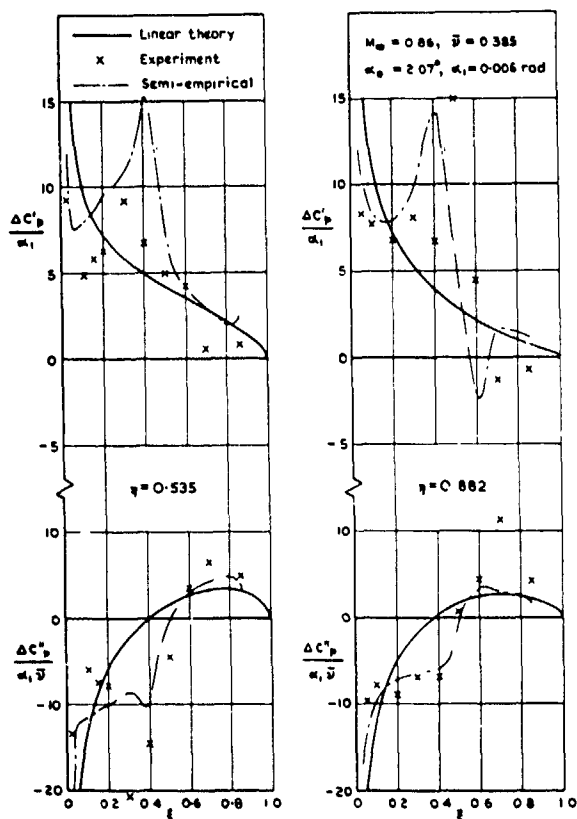
Fig 7 Calculated and measured oscillatory loading at two sections
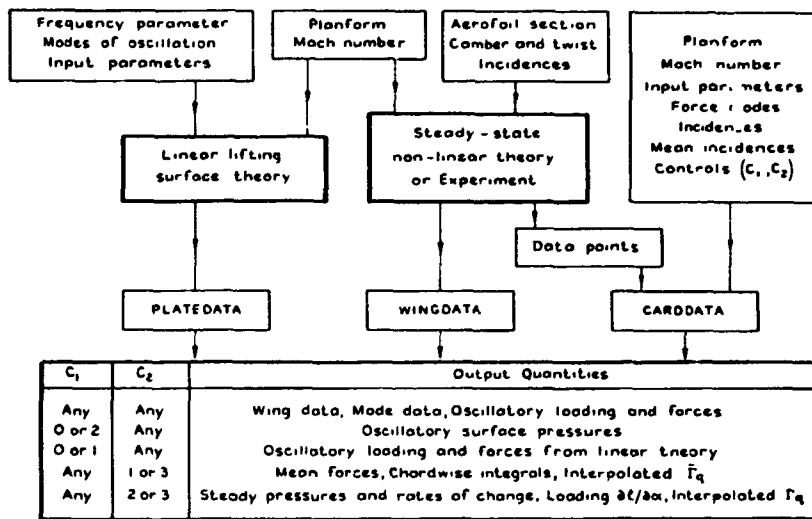
Fig 9   Schematic procedure for input and output data

Fig. 9   Predicted aerodynamic forces for heaving and pitching motion
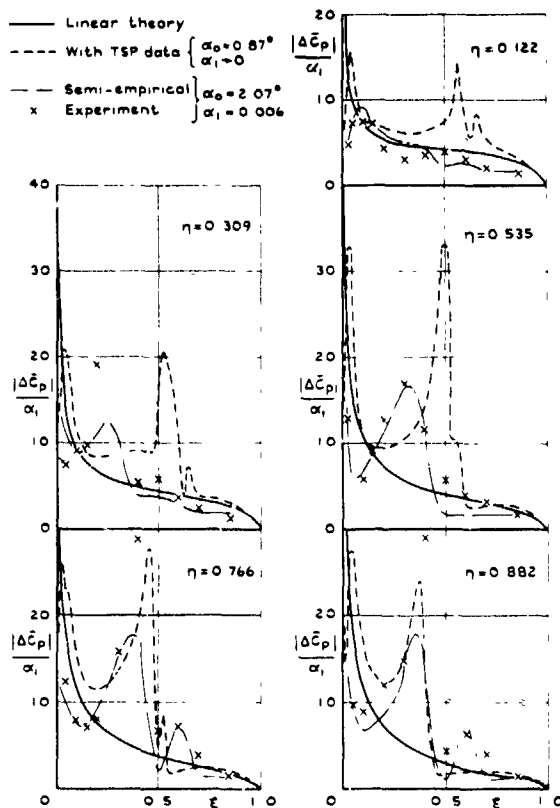

Fig 10   Comparative distributions of loading amplitude
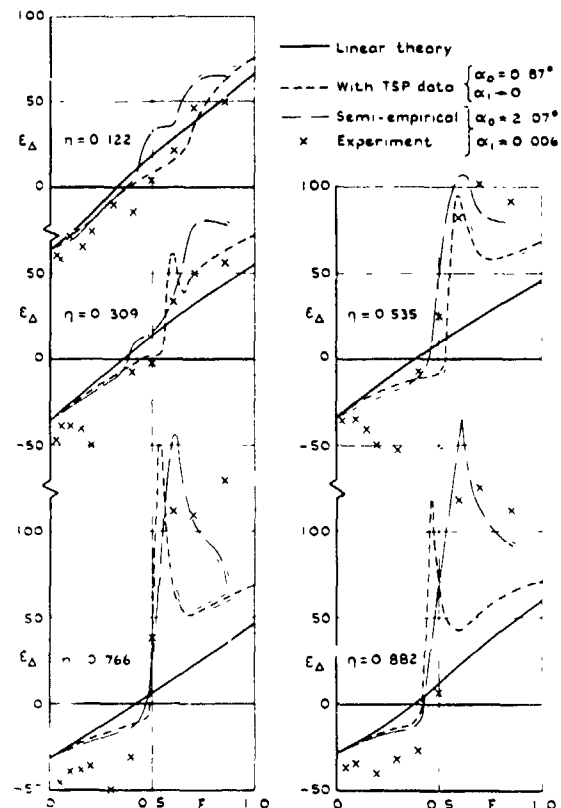$(M_\infty = 0.84, \bar{v} = 0.393)$

Fig 11   Comparative distributions of loading phase
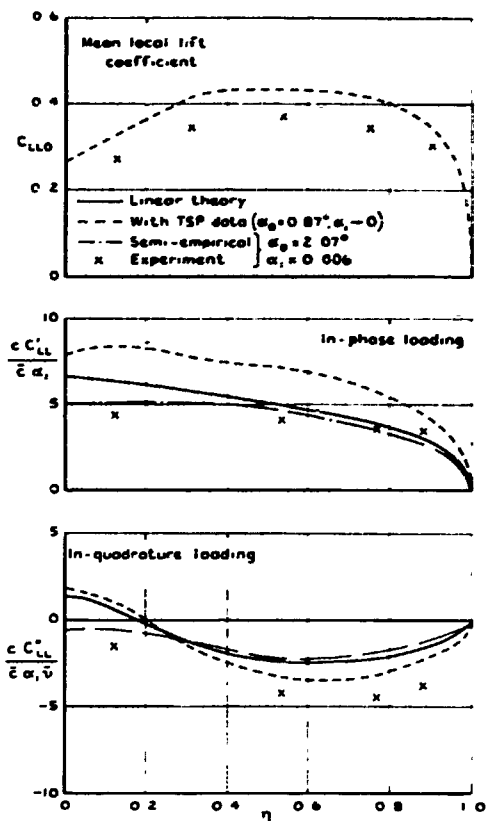$(M_\infty = 0.84, \bar{v} = 0.393)$

Fig 12 Spanwise distributions of mean and oscillatory lift
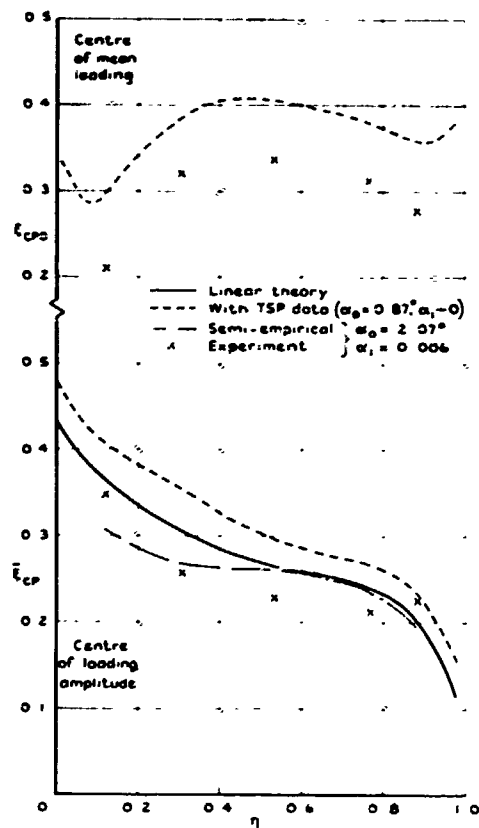$(M_\infty = 0\ 84, \bar{v} = 0\ 393)$

Fig. 13 Spanwise distributions of mean and oscillatory
chordwise centres of pressure $(M_\infty = 0\ 84, \bar{v} = 0\ 393)$
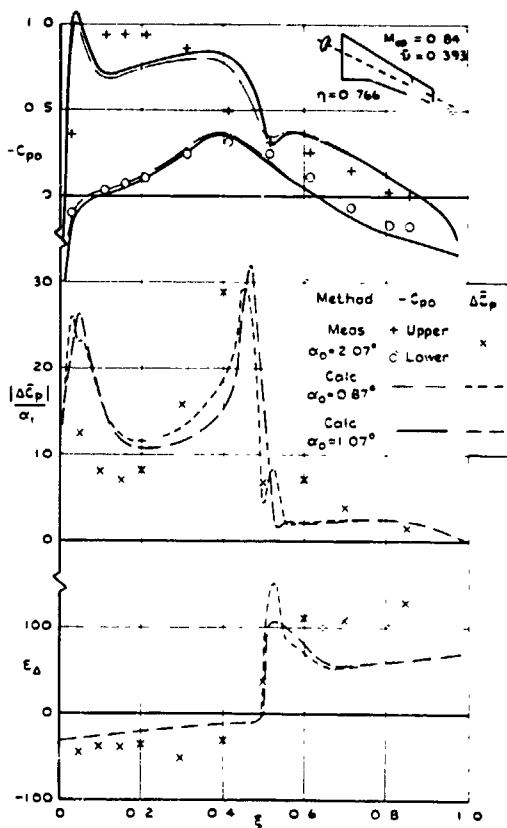

Fig 14 Chordwise distributions of mean pressure and oscillatory
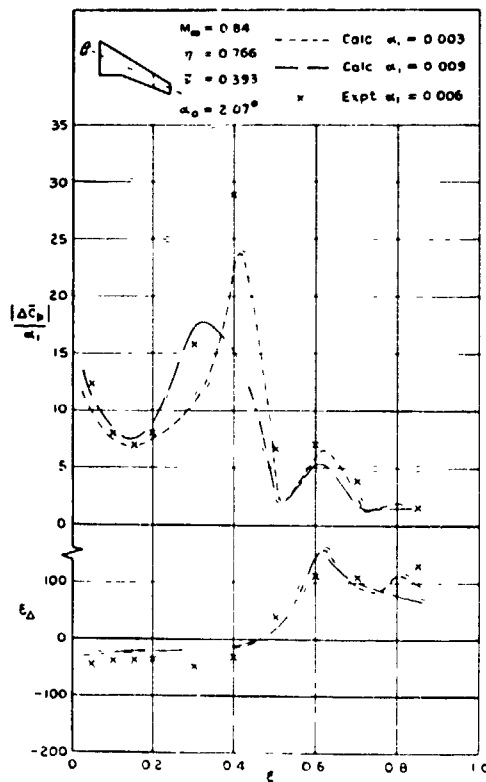loading as measured and calculated with TSP data

Fig 15 Semi-empirical effects of amplitude on oscillatory loading

APPLICATION OF A FINITE DIFFERENCE METHOD TO THE ANALYSIS
OF TRANSONIC FLOW OVER OSCILLATING AIRFOILS AND WINGS*

Warren H Weatherill
Flutter Research Group
Boeing Commercial Airplane Company
P O Box 3707
Seattle, Washington 98124

James D Sebastian
Applied Mathematics Group
Boeing Computer Services, Inc
P O Box 24346
Seattle, Washington 98124

F Edward Ehlers
Aero Research Group
Boeing Commercial Airplane Company
P O Box 3707
Seattle, Washington 98124

SUMMARY

A finite difference method for solving the unsteady flow about harmonically oscillating wings is investigated The procedure is based on separating the velocity potential into steady and unsteady parts and linearizing the resulting unsteady differential equation for small disturbances Solutions are obtained using relaxation procedures

The means for improving the solution stability characteristics of the relaxation process are explored A direct procedure is formulated which permits obtaining solutions for combinations of Mach number and reduced frequency for which the relaxation process has proved unstable The pressure distribution for an aspect ratio 5 rectangular wing oscillating in pitch is presented

1. INTRODUCTION

The purpose of the work presented in this paper is to develop a means for calculating air forces for use in flutter analyses of three-dimensional lifting surfaces in the transonic flight regime Not only is flutter a significant problem at transonic speeds, but it has also proved difficult to predict analytically These difficulties result not only from the mathematical complexities of the equations but also from computer resources required by the repetitive nature of flutter analyses performed during vehicle design

A variety of methods are currently under study for predicting unsteady transonic air forces, ranging from the relatively expensive finite difference models including time integrations to economical approximate procedures based on linear theory The procedure of this paper is intended to be intermediate in terms of computer machine resource usage and is based on a finite difference method developed by Ehlers in reference 1 The assumption of small perturbations from a uniform stream near the speed of sound retains the necessary complexity for describing flows with local supersonic regions The application of the perturbation velocity potential restricts the solution to weak shocks, which for thin wings of reasonably good design, is not too limiting an assumption When the flow is steady the resulting nonlinear differential equation reduces to the well-known transonic small perturbation equation studied by Murman, Cole and Krupp (refs 2, 3, and 4) The unsteady differential equation is simplified by considering the flow as consisting of the sum of two separate potentials representing the steady and unsteady effects The assumption of small amplitudes of harmonic oscillation leads to a linear differential equation for the unsteady potential with variable coefficients depending on the steady flow The resulting air forces are thus superposable and may be directly used in conventional flutter analysis formulations

The effect of thickness is included in the steady flow analysis The unsteady analysis is carried out for a wing of vanishing thickness but submerged in a velocity potential distribution resulting from the steady analysis As formulated the shock is fixed by the steady flow and it does not move with the wing motion It is noted that shock motion could be included in a linear fashion

Generally the results of applying this procedure (as reported in refs 5 through 9) have been encouraging First correlation of finite difference solutions for flat plate configurations with corresponding results from linear theory has been good for both two- and three-dimensional configurations For mixed flow where the solutions for a NACA 64A006 airfoil were compared with experimental data from Tijdeman and Schippers (ref 10) the pattern of the pressure distribution closely follows that observed experimentally, however the analytical pressure levels were generally higher than the measured levels The reason for the discrepancy between theory and experiment is not known but may be due to boundary layer or separation effects or both or to unknown problems associated with the theory or with the pressure measurements Thus as of this time the correlation studies for the two dimensional case have been inconclusive because of the lack of knowledge of viscous effects and for the three dimensional case because of a total lack of experimental pressure data

A significant cause for concern in the practical application of this procedure has been stability problems with the relaxation procedures used to solve the sets of finite difference equations These stability problems which are a function of reduced frequency Mach number and the size of the finite difference region severely limit the use of this method in flow regimes of most interest Solution stability thus is a major topic of this paper

A second section is devoted to a discussion of the accuracy of solutions from the finite difference model in comparison with subsonic solutions for the flat plate. This appears to be important because of the wave phenomenon resulting from the time dependence.

In addition, results are presented for a moderate aspect ratio rectangular wing oscillating in pitch.

A parallel study using finite difference methods on the unsteady transonic flow problem has been conducted by Traci, Albano, and Farr (refs 7, 8, and 9). The resulting procedure concentrates in a consistent manner on the low-frequency regime. Their derived equations do not include the cross product term consisting of the derivative of the unsteady velocity potential ϕ_1 with respect to time and of the second derivative of the steady velocity potential ϕ_0 with respect to the flow-wise coordinate. In most of their applications, the second derivative with respect to time is left out. However, the formulation of the finite difference equations, the handling of the boundary conditions, and the use of a column line relaxation solution procedure appear very similar to the procedure used here.

2. FORMULATION AND SOLUTION

A detailed mathematical derivation of the method used in this paper for the solution of the unsteady velocity potential for the flow about a harmonically oscillating wing is presented in reference 1. The discussion here will be limited to a brief outline of the procedure for the two-dimensional situation.

The complete nonlinear differential equation was simplified by assuming the flow to be a small perturbation from a uniform stream near the speed of sound. The resulting equation for unsteady flow is

$$\left[K \cdot (\gamma - 1)\, \phi_t - (\gamma + 1)\, \phi_x\right] \phi_{xx} + \phi_{yy} \cdot (2\phi_{xt} + \phi_{tt})/\epsilon = 0 \tag{1}$$

where $K = (1 \cdot M^2)/M^2\epsilon$, M is the freestream Mach number of velocity U_0 in the x-direction, x and y are made dimensionless to the semichord b of the airfoil, and the time t to the ratio b/U_0. With the airfoil shape as a function of time defined by the relation,

$$y_0 = \delta f(x,t)$$

the linearized boundary condition becomes

$$\phi_y = f_x(x,t) + f_t(x,t) \tag{2}$$

The quantity δ is associated with properties of the airfoil, such as maximum thickness ratio, camber, or maximum angle of attack, and is assumed small. The coordinate y is scaled to the dimensionless physical coordinate y_0 according to

$$y = \delta^{1\ 3} M^{2\ 3} y_0$$

and ϵ is given in terms of δ by

$$\epsilon = (\delta\, M)^{2/3}$$

The pressure coefficient is found from the relation

$$C_p = -2\epsilon(\phi_x + \phi_t)$$

The preceding differential equation is simplified by assuming harmonic motion and by assuming the velocity potential to be separable into a steady-state potential and a potential representing the unsteady effects. We write for a perturbation velocity potential

$$\phi = \phi_0(x,y) + \phi_1(x,y)e^{i\omega t} \tag{3}$$

and for the body shape

$$y_0 = \delta f(x,t) = \delta\left[f_0(x) + f_1(x)e^{i\omega t}\right]$$

Since the steady-state terms must satisfy the boundary conditions and the differential equation in the absence of oscillations, we obtain

$$\left[K \cdot (\gamma + 1)\phi_{0_x}\right] \cdot \phi_{0_{xx}} + \phi_{0_{yy}} = 0 \tag{4}$$

with

$$\phi_{0_y} = f_{0_x}(x), \quad y = 0 \quad -1 < x < 1 \tag{5}$$

On the assumption that the oscillations are small and products of ϕ_1 may be neglected, Eqs (1) and (2) with the aid of Eqs (3) and (4) yield

$$\left[[K \cdot (\gamma - 1)\phi_{0_x}]\phi_{1_x}\right]_x \cdot \phi_{1_{yy}} \cdot (2i\omega + \phi_{1_x}) \cdot q\phi_1 = 0 \tag{6}$$

where

$$q = \omega^2 \epsilon + i\omega(\gamma - 1)\phi_{0_{xx}}$$

subject to the wing boundary conditions

$$\phi_{1_y} = f_{1_x}(x) + i\omega f_1(x), \quad y = 0, \quad -1 \le x \le 1 \tag{7}$$

A computer program for solving the steady-state transonic flow about lifting airfoils based on Eqs (4) and (5) was developed by Krupp and Murman (refs 3 and 4) The output of this program or a similar program can be used in computing the coefficients for the differential equation of the unsteady potential The similarity of the unsteady differential equation to the steady-state equation suggests that the method of column relaxation used by Krupp for the nonlinear steady-state problem should be an effective way to solve Eq (6) for the unsteady potential ϕ_1 Note that Eq (6) is of mixed type, being elliptic or hyperbolic whenever Eq (4) is elliptic or hyperbolic Central differencing was used at all points for the y derivative and at all subsonic or elliptic points for the x derivatives Backward (or upstream) differences were used for the x derivatives at all hyperbolic points

The boundary condition that the pressure be continuous across the wake from the trailing edge was found in terms of the jump in potential $\Delta\phi_1$ to be

$$\Delta\phi_1 = \Delta\phi_{1_t} e^{-i\omega(x \cdot x_t)} \tag{8}$$

where $\Delta\phi_1$ is the jump in the potential at $x = x_t$ just downstream of the trailing edge and is determined to satisfy the Kutta condition that the jump in pressure vanish at the trailing edge The quantity $\Delta\phi_1$ is also used in the difference formulation for the derivative $\phi_{1_{yy}}$ to satisfy continuity of normal flow across the trailing-edge wake

For the set of difference equations to be determinate, the value of ϕ_1 or its derivative must be prescribed on the mesh boundary Following Klunker (ref 11), we found an asymptotic integral representation for the far-field ϕ_1 potential and for the related pressure potential $\phi_{1_x} + i\omega\phi_1$ Because of the difficulty with convergence of the integral over the wake for the integral equation of the velocity potential, upstream and downstream boundary conditions for the mesh were given in terms of the pressure potential $\phi_{1_x} + i\omega\phi_1$ for which the wake integral can be integrated in closed form The value of ϕ_1 was computed at one point on the upper boundary and one point on the lower boundary–points that were conveniently chosen to facilitate rapid convergence of the wake integral The values of ϕ_1 at other points on the upper and lower boundaries were found by numerically integrating the quantity $\phi_{1_x} + i\omega\phi_1$ with respect to x

The numerical solution to the resulting large order set of difference equations may be obtained using a relaxation procedure The initial solutions were obtained using a line relaxation procedure Convergence is determined by monitoring ERROR, the maximum change in the velocity potential between iteration steps ERROR is defined as the maximum value over all i and j of

$$\text{(i)} \qquad \text{(j)} \qquad \frac{\phi_{1_{ij}}^{(n)} - \phi_{1_{ij}}^{(n-1)}}{r} \tag{9}$$

where $\phi_{1_{ij}}^{(n)}$ is the unsteady velocity potential for the nth iteration, $\phi_1^{(n-1)}$ is the corresponding potential for the preceding iteration, and r is the relaxation factor The solution was considered converged when ERROR $< 10^{-5}$ In some cases, particularly for finer meshes and for the pitch mode convergence was considered complete when ERROR $< 10^{-4}$

3. RELAXATION SOLUTION STABILITY

As has been discussed in a preceding NASA report by the authors (ref 5), significant stability problems were encountered with the relaxation procedures used to solve the finite difference equations Generally, these procedures paralleled those successfully used for the steady-state problem In essence this meant sweeping through the mesh with a line relaxation procedure When the line of points was parallel to the free stream, it was called row relaxation, when the line was perpendicular to the flow it was called column relaxation

The characteristics of the solution instability are as follows

1 It occurs when the flow is purely subsonic as well as mixed with locally supersonic regions Thus the instability is not involved with the presence or absence of transonic shock flow

2 It appears to be a function of $\lambda_1 = \omega M(1-M^2)$ and the size of the finite difference area for the two dimensional problem or volume for the three-dimensional problem An analysis of the flat plate with a uniform mesh yields for the critical value of λ_1 the value of λ_1 above which the relaxation solution is unstable

$$\lambda_{1_{CRITICAL}} = \pi\left[\frac{1}{a^2} + \frac{1}{Kb^2}\right]^{1/2} \tag{10}$$

where a is the streamwise dimension of the mesh region b is the height and K is the transonic parameter

3 For a given condition (say a fixed Mach number and finite difference point setup) as λ_1 was increased the rate of convergence decreased until the solution started to diverge Thus the actual value of λ_1 for which the solution first diverges is ill-defined although it is generally in the neighborhood of the value given by the preceding formula

Some insight into the causes of the instability may be obtained by considering the Helmholtz equation into which the difference equation for the oscillating flow over a flat plate may be transformed, namely,

$$X_{xx} + X_{yy} + \lambda_1^2 X = 0 \qquad (11)$$

It is well known that solutions to the Helmholtz equation may not be unique for given types of boundary conditions on a closed region since eigenfunctions corresponding to real eigenvalues can occur, i e, functions representing standing waves for which homogeneous boundary conditions occur on the boundary For the rectangular mesh area of width b and length a, the first eigenvalue associated with solutions of the Helmholtz equation with Dirichlet boundary conditions is the critical value of λ_1 just presented In terms of the relaxation procedure, it was shown in reference 5 that solutions of a relaxation problem of the form

$$[A]\{\phi\} = \{R\}$$

converge only when $[A]$ is positive definite and this holds for the unsteady problem when λ_1 is less than $\lambda_{1\,CRITICAL}$.

Integral equation solutions currently in use for the linearized subsonic unsteady solutions employ only the outgoing wave solution for the kernel function Similarly the outgoing wave solution is used to define Klunker-type (ref 11) boundary conditions on the outer boundary of the mesh region Since the boundary conditions are essentially Dirichlet-type, apparently the incoming wave solution is picked up during the numerical solution

In this section, we will discuss the effect of applying outgoing wave boundary conditions directly on the outer boundaries, the effect of using a coordinate transformation to move boundaries of the finite difference region to infinity, and the results of using an explicit solution rather than a sequential line relaxation solution

3 1 Variations in Outer Boundary Conditions

The Klunker-type boundary conditions define ϕ_1 on the upper and lower boundaries and set $\phi_{1_x} + i\omega\phi_1$ on the upstream and downstream boundaries of the finite difference region Since these boundary conditions apparently did not effectively sort out the incoming waves from the outgoing waves, alternative conditions were explored These included using an outgoing (radiation-type) condition on all four boundaries and also a porous wall boundary condition on the upper and lower boundaries The mathematical forms for these boundary conditions are summarized in table 1 The porous wall conditions could be varied to form either a "free jet" by making the parameter R (the porosity parameter) very large, or a "solid wall" condition by making the parameter R small In practice, the parameter is usually fixed by some empirical method for specific wind tunnel conditions, but for the current work the interest is on how the stability of the relaxation solution may be dependent on its value.

Table 1 –Equations for Boundary Conditions

BOUNDARY CONDITIONS	BOUNDARY	EQUATION
1. OUTGOING WAVE	UPSTREAM	$\phi_{1x} - i\omega\dfrac{M}{1-M}\phi_1 = 0$
	DOWNSTREAM	$\phi_{1x} + i\omega\dfrac{M}{1+M}\phi_1 = 0$
	UPPER	$\phi_{1y} + \dfrac{i\omega\sqrt{K}}{1-M^2}\phi_1 = 0$
	LOWER	$\phi_{1y} - \dfrac{i\omega\sqrt{K}}{1-M^2}\phi_1 = 0$
2. POROUS WALL	UPPER	$\phi_{1x} + i\omega\phi_1 + \dfrac{1}{R}\phi_{1y} = 0$
	LOWER	$\phi_{1x} + i\omega\phi_1 - \dfrac{1}{R}\phi_{1y} = 0$

The pilot program was modified so that all six combinations of outer boundary conditions shown in table 2 could be run, that is, either of the two conditions on the upstream and downstream boundaries could be run with any one of the three boundary conditions specified for the upper and lower boundaries The "free-jet" and "solid wall" boundary

Table 2 –Types of Boundary Conditions

UPSTREAM AND DOWNSTREAM BOUNDARIES	UPPER AND LOWER BOUNDARIES
1. KLUNKER	1. KLUNKER
2. OUTGOING WAVE	2. POROUS WALL FREE JET (LARGE R) INTERMEDIATE SOLID WALL (SMALL R)
	3. OUTGOING WAVE

conditions also were programmed explicitly and thus could be applied without the need for fixing a value for R The test example consisted of a two-dimensional airfoil of vanishing thickness oscillating in harmonic pitch at a Mach number of 0 9 For this case, and for the mesh dimensions that are used, the reduced frequency above which relaxation solutions are expected to be unstable according to Eq (10) is about 0 1 The examples were run for a very coarse mesh (17 x 10), and the overrelaxation factor (ORF) was varied to make sure the solution instabilities were not due to too large an ORF

The results of the calculations may be summarized as showing that the alternate boundary conditions used did not significantly improve the convergence of the solution In some cases, a slight increase in the value of reduced frequency was observed for which convergent solutions could be obtained No combination of boundary conditions would provide solution convergence above a reduced frequency of 0 18 Since the exact values of ω at which a relaxation solution stops converging and starts diverging cannot be exactly determined anyway, the results of this investigation were not considered promising

3 2 Coordinate Transformation

A second concept explored in hopes of removing the relaxation solution stability problem was a coordinate transformation that permits the boundary conditions at infinity to be used on the boundaries of the finite difference region, that is, the physical region to infinity is mapped into the limited area of the finite difference mesh in the calculation plane The particular form of transformation that was used is that suggested by Carlson (ref 12) which, as he points out, allows for a physically realistic behavior of the solution at infinity The physical plane is divided into three regions by perpendicular lines through the leading and trailing edges of the airfoil (See fig 1) The physical plane coordinates (x,y) are related to the calculation plane coordinates (ξ,η) by the following relations

in region I where $\xi \leqslant -1$

$$x = -1 + \tan\left[(\pi\ 2)(\xi + 1)\right] + \tan\left[(\pi\ 2)(\xi + 1)^3\right]$$

in region II, where $-1 < \xi < 1$

$$x \quad \xi\left\{\left[(6 - \pi)\ 4\right] + \left[(\pi - 2)\ 4\right]\xi^2\right\}$$

and in region III, where $1 \cdots \xi$

$$x \quad 1 + \tan\left[(\pi\ 2)(\xi - 1)\right] + \tan\left[(\pi\ 2)(\xi - 1)^3\right]$$

and

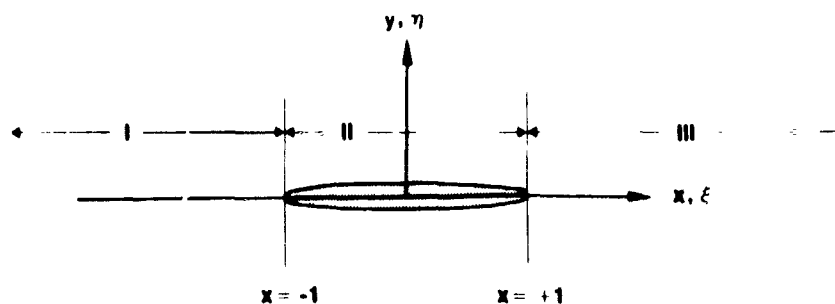$$y = \tan(\pi\ 2)\eta$$

Figure 1.-Subdivision of Flow Field for Coordinate Transformation

Two different boundary conditions were used   The first consisted simply of making $\phi_1 = 0$ on all four boundaries, the second of using the outgoing wave conditions discussed in the preceding section Here, the outgoing wave condition was applied at the midpoint between the boundary and the point adjacent to the boundary

These changes did not solve the relaxation solution stability problem For a given Mach number for example, relatively little (if any) change was noted in values of reduced frequency at which the solution became unstable

It is of interest to note that the combination of the coordinate transformation and the outgoing wave boundary condition provided results for the flat plate which very closely matched corresponding data from the NASA subsonic air force program (refs 13 and 14) A comparison of results from Klunker-type boundary conditions with results from outgoing wave conditions together with the coordinate transformation is shown in figure 2 It should be noted that the former results are for a 42 x 30 mesh while the latter results are for a significantly coarser 28 x 20 mesh

3 3 Complete Direct Solution

A 'semidirect" solution procedure was examined by the authors in reference 5 The form of the equation solved at that time was

$$\left[A(\lambda_1)\right]\left\{\phi_1^{(n)}\right\} = \left\{R(\phi_1^{(n-1)})\right\} \tag{12}$$

where $\{\phi_i^{(n)}\}$ contained an element for each interior mesh point In other words there was still an iteration required to update the vector $[R(\phi_i^{(n-1)})]$ on the right-hand side Although very efficient for the small meshes for which it was used (i e , permitted by the in-core solution capability), it was subject to the same type of solution instability as the relaxation solutions However, it is possible to rewrite the equation so that all unknowns are on the left hand side and the solution may be calculated without iteration This complete or full direct procedure should provide answers over the full range of values except for the specific values of λ_1 for which the matrix $[A(\lambda_1)]$ is singular

This procedure was first tested with a one-dimensional problem There was no problem in obtaining solutions near the singular points However, accuracy, as measured against the analytic answers, did present difficulties, which are discussed in detail in section 4
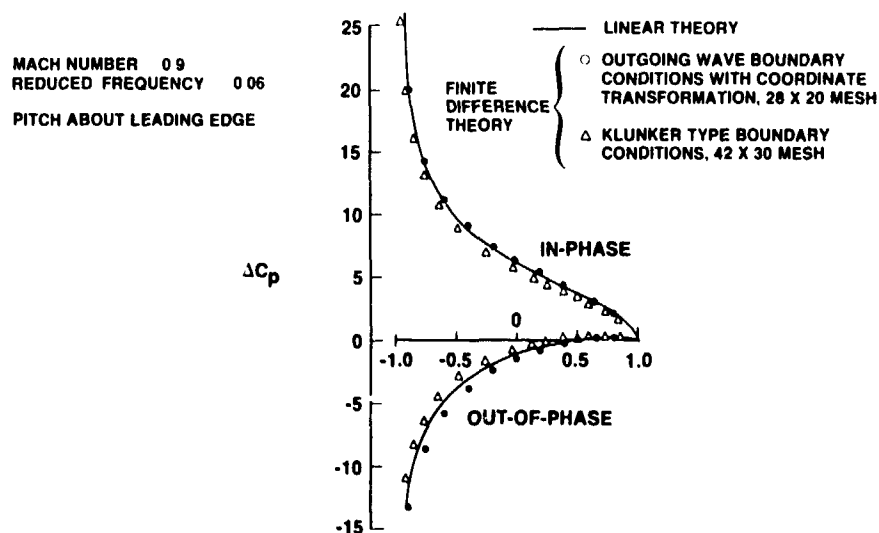

Figure 2 –Jump in Pressure Coefficient Across a Flat Plate Oscillating in Pitch

The full direct solution was also investigated for use with two-dimensional problems One formulation that was used included the coordinate transformation and the outgoing wave boundary conditions discussed above Use of the latter significantly reduced the bandwidth of the $[A]$ matrix over what it would have been had Klunker-type outer boundary conditions been used, thus increasing the number of mesh points that could be handled by the in-core solution routines

The resulting program was used on the sample problem of the airfoil of vanishing thickness oscillating in pitch As with the one-dimensional program, no trouble was encountered in obtaining solutions at frequencies well above values that had proved critical for the relaxation solution However, once the neighborhood of the critical value had been reached or exceeded, very poor correlation with corresponding solutions from the NASA subsonic unsteady flow program was obtained, that is, as the value λ_1 was increased from subcritical values to supercritical values, correlation with the NASA program went from very good to very poor The characteristics of this lack of correlation are discussed in detail in section 4

The original direct solution package did not contain a pivoting capability Since concern was expressed about numerical accuracy of the solution in the neighborhood of the matrix singularities a solution routine including partial pivoting with equilibration was inserted in the program Although it could be determined that pivoting was used during the solution, the results remained exactly the same to the number of significant digits retained

In summary the full direct solution provides solutions at values of λ_1 above the critical value The solutions do not correlate well with corresponding solutions from the NASA subsonic unsteady flow program and are thus not considered reliable Since these solutions have been obtained using routines that include partial pivoting, the lack of correlation does not appear to be due to numerical problems inverting the matrices The problem may be due to the restriction to a relatively small number of mesh points because of a limitation of the in-core solution routine and or due to the type of boundary conditions This seems to be borne out by the results from the study of the one-dimensional problem for which an error analysis is easy to obtain This is discussed in detail in section 4

4. NUMERICAL ACCURACY FOR LARGER VALUES OF λ_1

The accuracy of the finite difference procedure of this report may be discussed in several different contexts Previous reports (by the authors in refs 1 5, and 6 and Traci et al in refs 7 8, and 9) have included numerical examples the results of which are compared either with the experimental data of Tijdeman and Schippers (ref 10) or with other analytical data These analytical data may be for strictly subsonic flow (flow at high Mach number over a flat plate) or more detailed transonic calculations including full shock effects such as those by Magnus and Yoshihara (ref 15) The discussion here concentrates on the relationship between the critical value of λ_1 (critical in terms of relaxation solution stability) and the accuracy of the finite difference solutions relative to more exact linear solutions The examples to be discussed do not include shock effects

Section 4 1 discusses results from a one dimensional analog to the finite difference model Section 4 2 discusses some two-dimensional finite difference results compared with kernel function solutions

4 1 The One-Dimensional Problem

In order to gain insight into the unsteady transonic problem as formulated in this paper, a one-dimensional version of the flat plate problem was investigated The one-dimensional analog of the two-dimensional equation, Eq (6), for a flat plate may be obtained by dropping the ϕ_0 terms and the $\phi_{1_{yy}}$ term Dividing the resulting equation by K, we have

$$\phi_{1_{xx}} - 2i\lambda_1 M\phi_{1_x} + \lambda_1^2 (1 - M^2)\phi_1 = 0 \tag{13}$$

$$\lambda_1 = \frac{\omega M}{1 - M^2}$$

The exact general solution to Eq (13) is

$$\phi_1(x) = C_1 e^{i\lambda_1(1+M)x} + C_2 e^{-i\lambda_1(1-M)x} \tag{14}$$

where C_1 and C_2 may be determined once the boundary conditions (end conditions) are specified An approximate solution over an interval $[a,b]$ may also be found by transforming Eq (13) to a finite difference equation with the solution being obtained by either a full direct solution (similar to that discussed in sec 3 3) or by a point relaxation procedure

The interest here is in comparing answers obtained from the finite difference solution with corresponding answers from the exact solution For this, the maximum error quantity E for a given reduced frequency ω_K is defined as

$$E(\omega_K) = \max_{I = 1, IMAX} \left| \phi_{1_{1_{EXACT}}} - \phi_{1_{1_{FINITE\ DIFFERENCE}}} \right| \tag{15}$$

The investigation is aimed at determining the effect of the kind of boundary conditions used on $E(\omega_K)$ First, it is clear from the exact solution that the solution for a given reduced frequency, ω, or λ_1 is made up of components with two substantially different wavelengths For a given finite difference mesh (a given number of mesh points and specified mesh spacing), it would be expected that the short wavelength component would be less accurately represented than the long wavelength component, that is, a solution that is made up predominantly of the short wavelength component would be less accurately determined using a finite difference calculation than a solution made up predominantly of the long wavelength component This has indeed proved to be the case, as shown by examples presented in figure 3 Here two combinations of Dirichlet and Cauchy boundary conditions were used to obtain solutions, the first was set up so that the solution would consist solely of the short wavelength component and is denoted by the Δ-symbols in figure 3, and the second, so that the solution would consist solely of the long wavelength component and is denoted by the O-symbols The error level for the long wavelength component is significantly lower than that for the short wavelength component
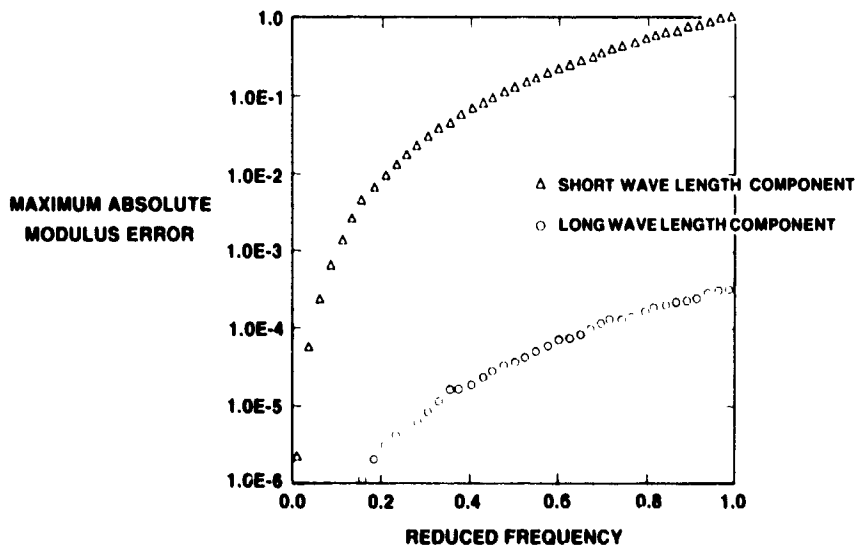

Figure 3 - Comparison of Error Curve for Long and Short Wavelength Solutions

Second, it is of interest to know how the error varies with frequency An analysis of a similar equation was made by Fischer and Usmani in reference 16 The equation studied was of the form

$$\psi_{xx} + \lambda_1^2\psi = 0 \tag{16}$$

and is simply related to our one-dimensional ϕ_1 equation by the transformation

$$\phi_1 = \psi e^{i\lambda_1 Mx} \tag{17}$$

with the analysis based on equally spaced mesh points Application of their analysis to the ψ equation, Eq 16, shows that for small values of $h\lambda_1$, where h is the distance between adjacent mesh points, and Dirichlet end conditions

$$E(\omega_K) \quad E_1 = \frac{Eh^2\lambda_1^3}{\sin[\lambda_1(b-a)]} \tag{18}$$

for some constant E which is independent of the reduced frequency and mesh spacing In view of the close relation between the ϕ_1 and ψ equations, we would expect the error behavior in the finite difference solution to be similar in both cases Eq. (18) displays several interesting characteristics For example, the predicted error is directly proportional to the square of the mesh point spacing h and the third power of λ_1 or, for fixed Mach number, the third power of the reduced frequency ω Also, the presence of the sin $[\lambda_1(b-a)]$ in the denominator of the equation introduces singularities in the error curve at values of ω (or λ_1) for which $\lambda_1(b-a) = n\pi$ These values of λ_1 correspond to eigenvalues of the analytical solution (Eq. 14) , i e , they are values of λ_1 for which there is no unique analytical solution In view of the close relation between ϕ_1 and ψ equations, it is expected that the error behavior would also be the same for ϕ_1

The presence of the singularities in the curve of maximum absolute modulus error versus reduced frequency is shown in figure 4 by the Δ-symbols It would appear that the eigenvalues for the analytic system do not coincide exactly with the eigenvalues for the finite difference system as noted by the distortions in the curves with which the points have been connected. The calculation was set up so that $E(\omega_k)$ would be evaluated at five points between each analytic eigenvalue The singular behavior is the result of the evaluation cf the C_1 and C_2 from a set of simultaneous equations that are a function of the applied boundary conditions This set of equations may be written in the form
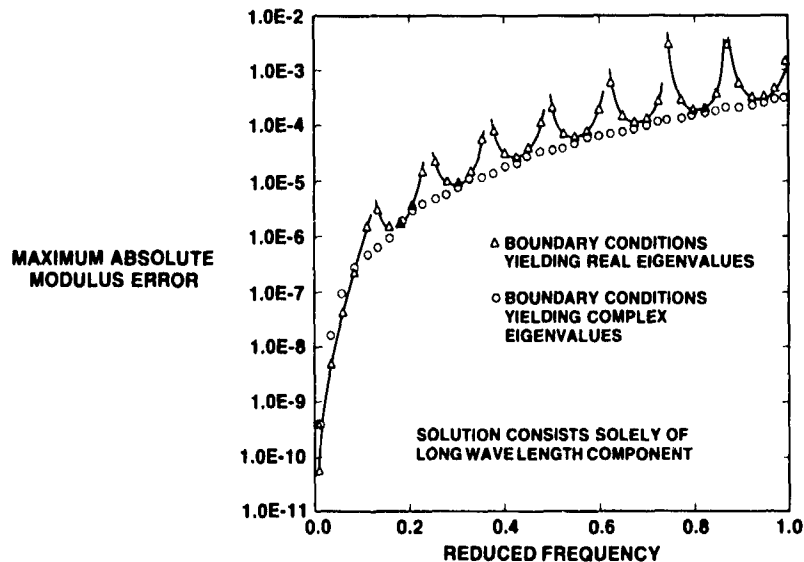
$$[\alpha(\lambda_1)]\{C\} = \{\gamma\}$$

Figure 4.–Comparison of Error Curves for Boundary Conditions Yielding All-Real and Complex Eigenvalues

where α is a 2 x 2 matrix which is a function of λ_1 (or ω), C is the two-element column matrix made up of C_1 and C_2 The forms of α and γ are a function of the nature of boundary (end) conditions, i e , whether they are Dirichlet, Neumann, or Cauchy Moreover, for certain values of λ_1, the determinant of α will be equal to zero These certain values are eigenvalues For values of λ_1 that correspond to eigenvalues, the solution for C_1 and C_2 is not unique, that is, for λ_1 equal to eigenvalues, there is no exact solution to Eq (13)

It is interesting to note that the values of λ_1, which are eigenvalues of α, may be either all-real or complex depending on the nature of the boundary conditions It is readily shown that Dirichlet conditions on both ends or Neumann conditions on both ends lead to all-real eigenvalues However, for certain combinations, such as mixed conditions (Dirichlet on one end and Cauchy on the other), the eigenvalues may be made complex Under these circumstances, we would not expect the violent peak and valley behavior of the error plots that result from the all-real eigenvalues This is indeed confirmed with the results shown in figure 4 when the boundary conditions are such as to yield complex eigenvalues

This problem was originally studied to see if it would shed light on the relaxation solution instability problem In particular it was of interest to see if relaxation solutions could be obtained for boundary (end) conditions for which the eigenvalues are complex However, tests with a relaxation solution of the one-dimensional system have not converged and thus having complex eigenvalues does not seem to materially affect the convergence

In addition, it was noted that Eq (18) implied that the error was proportional to λ_1^3 or ω^3 An example of this is shown in figure 5 where an error curve for an example in which the singularity behavior has been suppressed is compared with a curve proportional to ω^3 The correlation between the two is very good Also included is a curve, which is proportional to ω^4 as is predicted by a conventional truncation analysis of the finite difference equation

In summary analysis and experiment of the one-dimensional equation shows that the error from the finite difference solution is proportional to $h^2\lambda_1^3$ and thus the number of points has to be expanded (or more specifically the mesh spacing reduced) in proportion to the 3 2 power of the frequency in order to retain accuracy The level of the error is determined by the boundary conditions which in turn determine the relative contributions to the solution by the long and short wavelength components The relatively larger part the long wavelength component plays the smaller the level of error Superimposed on this general error curve can be a series of peaks and valleys with the peaks centered around the values of λ_1 (or ω) that correspond to the real eigenvalues of the system of finite difference equations and are dependent on the boundary conditions If the eigenvalues are complex the peak and valley behavior of the error curve is suppressed

These results would indicate that for certain choices of boundary conditions and sufficiently fine mesh spacing adequately accurate results may be obtained in the two-dimensional case using a full direct solution method
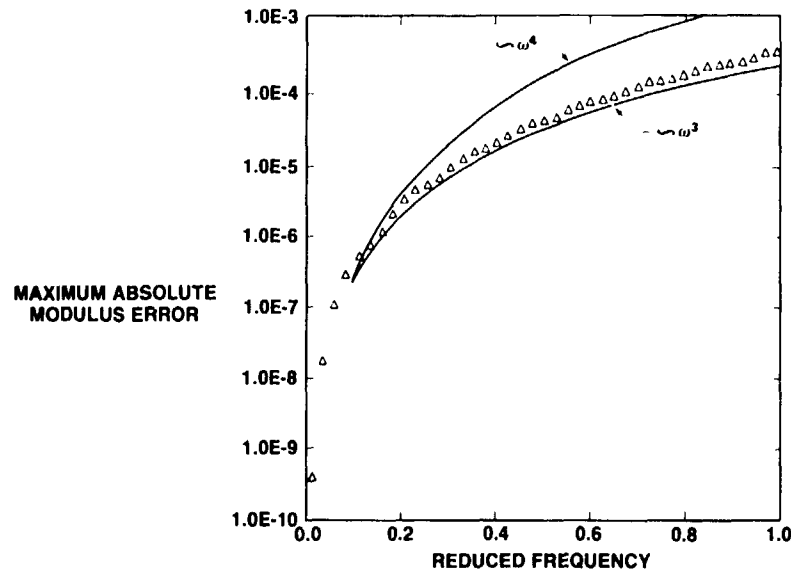
Figure 5 –Variation of Error Curve With Reduced Frequency

4 2 Two-Dimensional Examples

As noted in section 3, a complete direct solution using outgoing wave boundary conditions permits the obtaining of solutions at large values of reduced frequency, and solution stability no longer is a problem However, for the mesh sizes used, the correlation between the finite difference solutions and linear theory becomes very poor Results are presented here for a two-dimensional airfoil of vanishing thickness oscillating in pitch in a free stream of M = 0 9 Under these conditions, relaxation solutions would be expected to be unstable at reduced frequencies (based on the semichord) above 0 1 according to Eq (10) Results were obtained using both the linear theory program and the finite difference program Very good correlation between the two theories was obtained at ω = 0 06 (see fig 2) and very poor correlation at ω - 0 3 as shown in figure 6 The correlation is significantly degraded even at ω - 0 09 as shown in figure 7 To test whether this phenomenon was a function of λ_1 rather than ω, the same problem was rerun at a Mach number of 0 4 with reduced frequencies so that the values of λ_1 were the same Correlation between results from linear and finite difference calculations, as shown in figures 8 and 9, was good at ω - 0 6 (corresponding to ω = 0 06 at M = 0 9) and poor at ω = 0 9 (corresponding to ω = 0 09) The results at ω - 3, which are not shown, were very poor Thus, the results from the full two-dimensional transonic problem (although with nonmixed flow) appear to follow the same pattern as the results from the very simplified one-dimensional example Indeed, the poor results of M 0 9, ω 0 09 and at M 0 4 ω - 0 9 appear to be due to the same cause as the peaks in the error curve shown in figure 4

These results were checked using a direct solution routine incorporating partial pivoting with equilibration The results were not changed although it was possible to tell that the pivoting portion of the routine had been used Thus the errors encountered with the two-dimensional calculations do not seem to be due to numerical problems resulting from ill-conditioned matrices Increasing the number of mesh points in order to improve correlation was not feasible with available computer resources
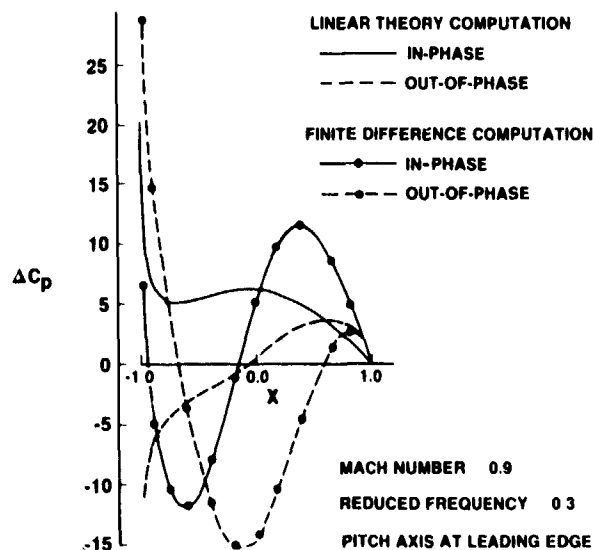

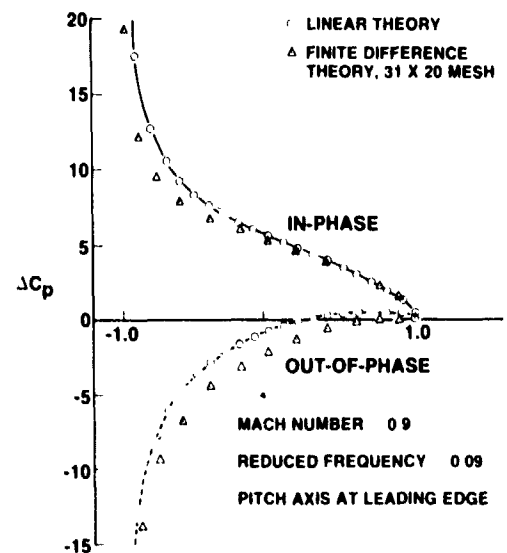Figure 6 –Jump in Pressure Coefficient Across
a Flat Plat Oscillating in Pitch

Figure 7 –Jump in Pressure Coefficient Across
a Flat Plate Oscillatin gin Pitch

Figure 8–Jump in Pressure Coefficient Across
a Flat Plate Oscillating in Pitch

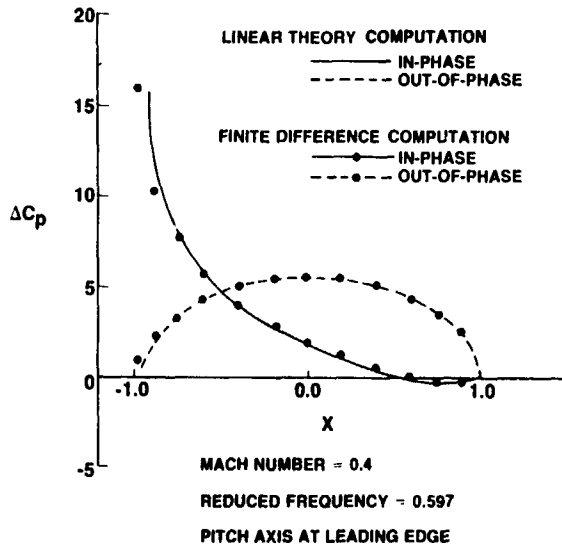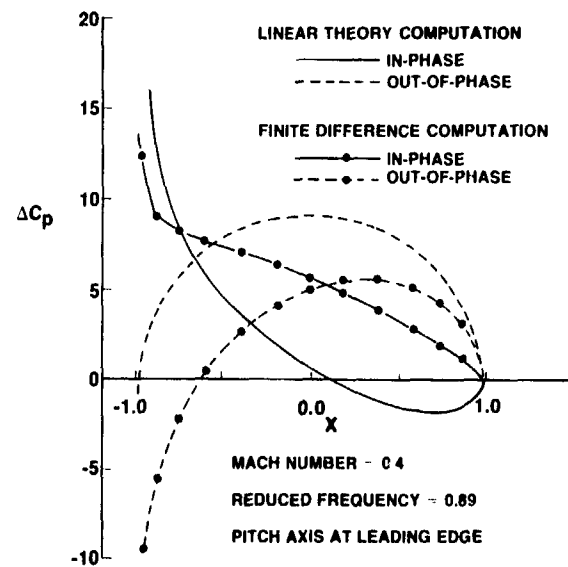Figure 9 –Jump in Pressure Coefficient Across
a Flat Plate Oscillating in Pitch

5. RESULTS FOR A RECTANGULAR WING

In a preceding report by the authors (ref 5), a pilot program for three-dimensional flow was described This program was used to calculate the pressure distributions over an aspect ratio 5 rectangular wing oscillating in harmonic pitch The calculations were performed for both a flat plate and a NACA 64A006 profile configuration, in a flow with a free-stream Mach number of 0 875 and with a reduced frequency based on the root semichord of 0 06 A mesh of 44 points in the flow direction, 32 points in the spanwise direction for the full span, and 26 points in the vertical direction was used The finite difference region extended about one chord length in front of the leading edge and behind the trailing edge, about seven chord lengths above and below the wing surface, and slightly more than a semispan beyond the wingtip

The computation time for the finite difference calculations was on the order of 7 to 8 CPU seconds for each iteration and 8 to 9 seconds for each far-field update This was for a CDC 6600 computer using the Kronos 2 1 operating system A significant saving over these costs could be achieved for symmetrical wings with a mean angle of attack of 0⁰ by taking advantage of the symmetry properties of the flow Under these limitations, the steady velocity potential is symmetric, the unsteady potential is antisymmetric with respect to the vertical coordinate, and the calculations need be carried out only over one-fourth of the total finite difference region

The analyses were made using column relaxation It was noted in reference 5 that, for the two-dimensional problem, row relaxation was much more efficient than column relaxation in terms of reaching a specified degree of convergence in a minimum number of iterations It was determined that in using row relaxation for mixed flow, additional terms must be included in the finite difference equation for hyperbolic points to avoid solution instabilities These additional terms have not proved enough to avoid instabilities in the three-dimensional row relaxation solution, and it is assumed that the two-dimensional analysis of reference 5 should be extended to the three-dimensional equations For the case to be shown, the converged solution (in this case the ERROR of Eq (9) was to be less than 10^{-4}) was of the order of 180 iterations with the initial unsteady velocity potential distribution set to zeros

The steady-state pressure distribution for a NACA 64A006 profile is shown in figure 10 It was obtained using a program developed by Ballhaus and Bailey (ref 17) The jump in pressure coefficient due to harmonic pitch about the
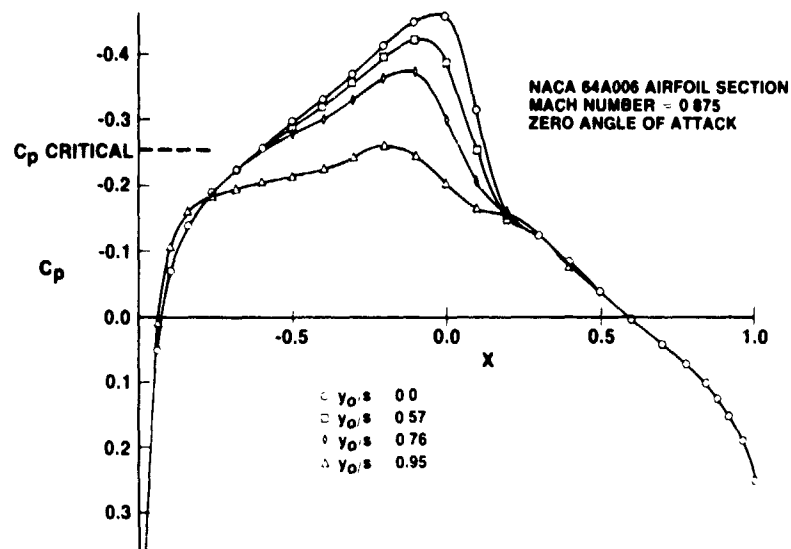

Figure 10 –Steady-State Pressure Coefficient Distributions for an Aspect Ratio 5 Rectangular Wing

planform leading edge is shown in figures 11 and 12 Three different results are presented The first results are from the
NASA subsonic unsteady three-dimensional airloads program using linear theory (refs 13 and 14) These should compare
directly with the second set of results calculated using the finite difference program and a flat plate airfoil section The
third data set is from using the finite difference program with the steady velocity potential distribution from the
nonlinear steady-state solution for the wing with a NACA 64A006 profile In addition a two-dimensional result from
finite difference theory for the same airfoil section is shown in the planform root plane

Generally, the linear results correlate very well with the corresponding finite difference results for a flat plate The
results including thickness display the pressure rise in the neighborhood of the shock that has been characteristic of
corresponding experimental measurements (see for example ref 10) The three-dimensional results show a significant
softening of the pressure rise in comparison with the two-dimensional results These results differ from those presented in
refs 5 and 6 because of a corrected scale factor on the steady-state velocity potential Of concern is the apparent
intensifying of the shock effect at the midpoint of the semispan of the wing The reason for this result, which is not
expected physically, is currently attributed to the way the finite difference operators are handled The program is written
to use central differencing for subsonic points (as determined from steady flow) and backward differencing for supersonic
points An abrupt change in the pattern of subsonic and supersonic points occurs on the chord adjacent to the one with the
sharpest shock effects It may be that use of the shock point operator would result in a more physically acceptable
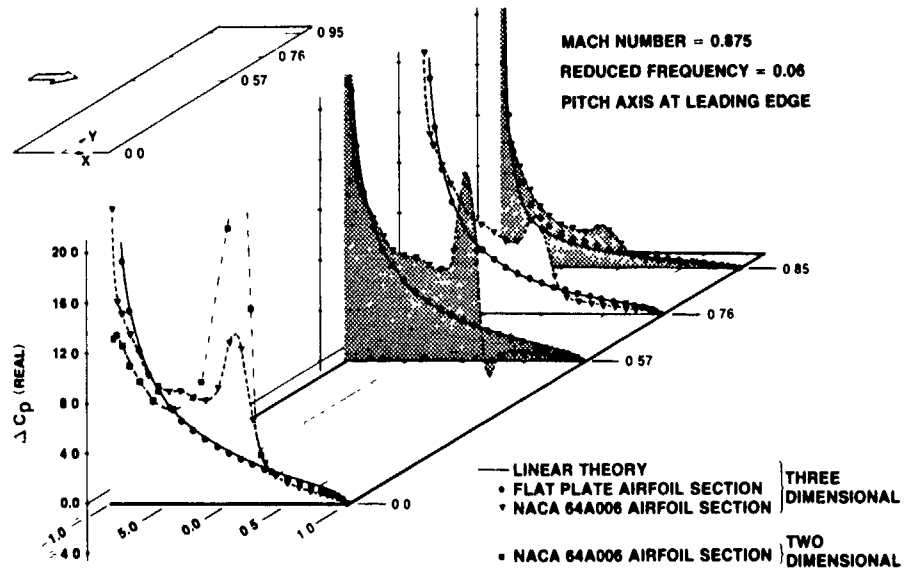pressure distribution There are no experimental data available at this time for comparison purposes

Figure 11 –Pressure Coefficient Distribution for an Aspect Ratio 5 Rectangular Wing
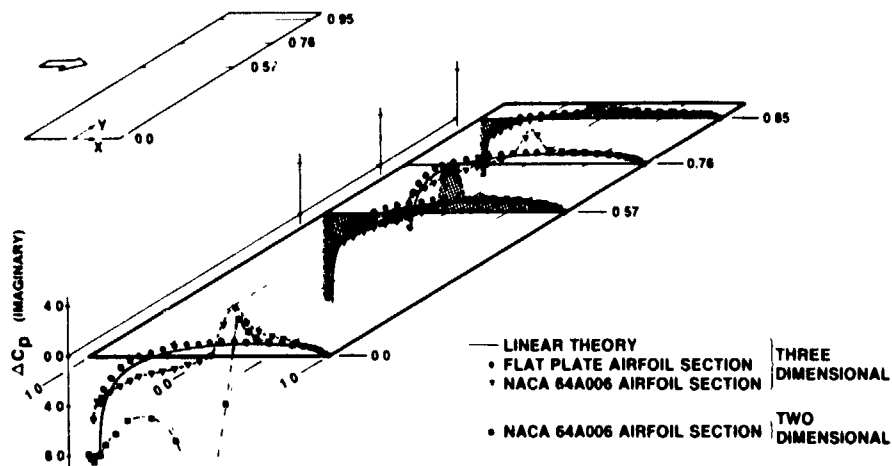Oscillating in Pitch, Real Component

Figure 12 –Pressure Coefficient Distribution for an Aspect Ratio 5 Rectangular Wing
Oscillating in Pitch, Imaginary Component

6. SUPERSONIC FREE STREAM

Of significant interest is the inclusion of transonic flow effects in the calculation of oscillating air forces where the free-stream flow is slightly supersonic. Of particular interest to the current work is whether or not the relaxation solutions become unstable in the same fashion when the free stream is supersonic as when it is subsonic.

The differential and finite difference equations are the same for both the subsonic and supersonic free-stream cases. The flow characteristics are sketched in figure 13, which shows the boundary conditions that were used in a pilot two-dimensional program. The unsteady velocity potential at the upstream boundary is set to zero. Since the flow is supersonic at the downstream boundary and backward differencing is used in the supersonic regions, boundary conditions need not be specified at the downstream boundary. Porous wall boundary conditions were convenient to use on the upper and lower boundaries. However, in practice, these boundaries should be set far enough out so that they do not affect the flow over the wing and thus the pressure is independent of the porosity factor.
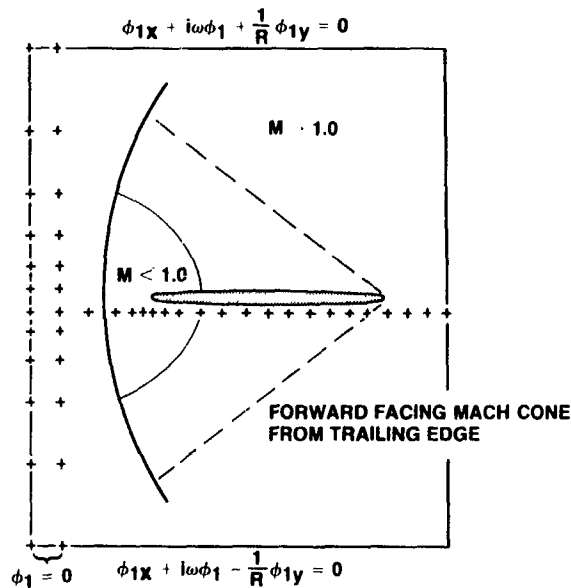
$$\phi_{1x} + i\omega\phi_1 + \frac{1}{R}\phi_{1y} = 0$$

$$\phi_1 = 0 \qquad \phi_{1x} + i\omega\phi_1 - \frac{1}{R}\phi_{1y} = 0$$

Figure 13 – Boundry Conditions for Problem With Supersonic Free Stream

As discussed by Traci et al (ref 9), the flat plate problem in which the steady-state velocity potential is constant may be solved by a single downstream pass with the relaxation procedure since nowhere in the flow is any point affected by points in the downstream columns. The problem of mixed flow with the pocket of subsonic flow buried within the supersonic flow is quite a different matter. Traci et al noted relaxation solution instabilities in the neighborhood of $M = 1.0$ and, for the supersonic case, obtained two-dimensional solutions at $M = 1.10$ but not at $M = 1.05$. A priori, one may suspect that the presence of the subsonic region will provide characteristics similar to those found for the subsonic free-stream case, which resulted in instabilities in the relaxation solutions for values of reduced frequency and Mach number, which makes λ_1 greater than that corresponding to the system eigenvalues.

In practice, numerical examples do not appear to admit such a simple explanation. A circular-arc airfoil was analyzed at two Mach numbers, $M = 1.05$ and 1.15. A simple pitching oscillation was studied. Our results have the characteristics of converging for a number of iterations and then diverging. Here the maximum difference between ϕ_1 for successive iterations was used as a measure of convergence. If the convergence criterion was met before the divergence started, one would assume that one had obtained a valid solution. Under these circumstances, the use of overrelaxation and underrelaxation factor (URF) increased the tendency for divergence. Hence, the calculations were run with ORF = URF = 1.0. The net result was that at $M = 1.15$, with a relatively small subsonic region, the convergence characteristics were improved by raising the reduced frequency. At $M = 1.05$ with the attendant large subsonic region about the airfoil leading edge, convergence improved by decreasing the reduced frequency. This latter behavior is what would be expected from experience with the subsonic free-stream problem.

There does appear to be stability problems with the relaxation process in the supersonic free-stream problem as well as with the subsonic problem. We suspect both have the same origins, that is, the eigen characteristics of the problem. However, numerical examples with the supersonic free-stream problem do not give consistent convergence divergence behavior at $M = 1.05$ and $M = 1.15$. It is assumed that a full direct solution as described above would provide solutions, but this has not been tried.

7. CONCLUSIONS

This paper has further explored a particular finite difference formulation for analyzing unsteady transonic flow over harmonically oscillating lifting surfaces. The results are not conclusive with respect to the eventual usefulness of the procedure in practical situations. A means for avoiding instabilities with relaxation procedures was not found. However, it is shown that a direct solution procedure may be used to obtain results at values of Mach number, reduced frequency and size of solution region above those critical for relaxation solutions. It is surmised that the direct solution could be used to solve convergence problems in the supersonic regime as well as in the subsonic regime. This procedure must be investigated with respect to large sets of finite difference points as well as alternate boundary conditions, to prove its practicality.

On the basis of a one-dimensional analysis, it was found that the accuracy of the finite difference procedure was proportional to $h^2 \lambda_1^3$, so that the finite difference spacing must be varied inversely to the 3 2 power of frequency if accuracy is to be retained For the larger values of reduced frequency at values of Mach number close to one, this will mean working with very large sets of finite difference points How the use of nonuniform mesh point spacing would affect this conclusion has not been examined In addition to the general error level, there are large positive excursions in error caused by the presence of real eigenvalues These excursions can be suppressed by proper selection of boundary conditions that result in the replacement of the real eigenvalues by complex eigenvalues

Finally, three-dimensional results have been presented for a moderate aspect ratio rectangular wing with a NACA 64A006 airfoil section

8. REFERENCES

1   F Edward Ehlers, *A Finite Difference Method for the Solution of the Transonic Flow Around Harmonically Oscillating Wings*, NASA CR-2257, January 1974

2   E M Murman and J D Cole, "Calculation of Plane Steady Transonic Flow," AIAA paper 70-188, January 1970

3   J A Krupp and E M Murman, "Computation of Transonic Flows Past Lifting Airfoils and Slender Bodies," *AIAA Journal* vol 10, July 1972, pp 880-887

4   J A Krupp, "The Numerical Calculation of Plane Steady Transonic Flows Past Thin Lifting Airfoils," Doctor of Philosophy Thesis, University of Washington, 1971, also Boeing Scientific Research Laboratories, document D180-12958-1, June 1971

5   W H Weatherill, F E Ehlers and J D Sebastian, *Computation of the Transonic Perturbation Flow Fields Around Two- and Three-Dimensional Oscillating Wings*, NASA CR-2599, December 1975

6   W H Weatherill, F E Ehlers, and J D Sebastian, "On the Computations of the Transonic Perturbation Flow Field Around Two- and Three-Dimensional Oscillating Wings," AIAA paper 76-99 January 1976

7   R M Traci, E D Albano, J L Farr, Jr and H K Cheng, *Small Disturbance Transonic Flows About Oscillating Airfoils*, TR-AFFDL-TR-74-37, June 1974

8   R M Traci, J L Farr, and E Albano, Perturbation Method for Transonic Flows About Oscillating Airfoils " AIAA paper 75-877, presented at the AIAA 8th Fluid and Plasma Dynamics Conference, Hartford, Connecticut, June 16-18, 1975

9   R M Traci, E D Albano, and J L Farr Jr , *Small Disturbance Transonic Flows About Oscillating Airfoils and Planar Wings*, AFFDL-TR-75-100, August 1975

10 H Tijdeman, and P Schippers, *Results of Pressure Measurements on an Airfoil With Oscillating Flap in Two-Dimensional High Subsonic and Transonic Flow (Zero Incidence and Zero Mean Flap Positions)*, NLR report TR 73078 U, August 1973

11 E B Klunker, *Contributions to Methods for Calculating the Flow About Thin Lifting Wings at Transonic Speeds*, NASA TN D-6530, November 1971

12 Leland A Carlson, *Transonic Airfoil Analysis Using Cartesian Coordinates*, NASA CR-2577, August 1975

13 W S Rowe, B A Winther, and M C Redman, *Prediction of Unsteady Aerodynamic Loadings Caused by Trailing Edge Control Surface Motions in Subsonic Compressible Flow-Analysis and Results*, NASA CR-2003, March 1972

14 M C Redman, W S Rowe, and B A Winther, *Prediction of Unsteady Aerodynamic Loadings Caused by Trailing Edge Control Surface Motions in Subsonic Compressible Flow-Computer Program Description*, NASA CR-112015, March 1972

15 R J Magnus and H Yoshihara, "Calculations of Transonic Flow Over an Oscillating Airfoil," AIAA paper 75-98, January 1975

16 C F Fischer and R A Usmani, "Properties of Some Tridiagonal Matrices and Their Application to Boundary Value Problems," *SIAM Journal on Numerical Analysis*, vol 6, No 1, March 1969

17 W F Ballhaus and F R Bailey, 'Numerical Calculation of Transonic Flow About Swept Wings " AIAA paper 72-677, presented at the AIAA 5th Fluid and Plasma Dynamics Conference, Boston, Massachusetts, June 26-28, 1972

Numerical Solution of the Unsteady
Transonic Small-Disturbance Equations*

M. M. Hafez, M. H. Rizk, and E. M. Murman
Flow Research Company, P. O. Box 5040, Kent, Washington 98031

This paper examines two problems that occur in the small unsteady harmonic perturbation approach (Weatherill, et al.[1] and Traci, et al.[2]) of calculating transonic flutter problems. The first problem involves a numerical instability that occurs in the relaxation procedure for solving the reduced potential equation. This instability results in a critical reduced frequency (for a given Mach number) beyond which relaxation solutions are divergent. A numerical treatment of Helmholtz's equation by iterative techniques is examined, and a one-dimensional model is computed to demonstrate a suggested solution. The second problem is to properly treat the movement of a shock wave caused by the harmonic perturbation of the body. This shock movement is described by a special equation, which is derived from a consistent perturbation expansion for the nonlinear differential equation and from shock-jump relations.

INTRODUCTION

For transonic aeroelastic and flutter calculations, Weatherill, et al.[1] and Traci, et al.[2] have reported a numerical method for computing small transonic unsteady harmonic perturbations to a steady flow. They express the potential function as a series of increasing powers of a small parameter, which measures the amplitude of an unsteady disturbance to the boundary (for example, a thin airfoil undergoing harmonic oscillation). This expression results in a sequence of boundary value problems for the perturbation potentials. The zeroth order is just the steady problem and is solved by a type-dependent finite-difference scheme with a line relaxation procedure. The first-order problem results in a linear equation of mixed type for the perturbation potential and is solved by the same procedure. This method, however, is successful only for small, reduced frequencies. Beyond a critical frequency (for a given Mach number), the relaxation solutions diverge.

Weatherill, et al.[1] analyzed the convergence of the relaxation procedure for the perturbation potential. The finite-difference approximation results in a matrix that is not always positive definite (depending on the reduced frequency). In this paper we suggest a remedy to this problem and compute a simple illustrative example. The main idea is to multiply the system of algebraic equations by the conjugate transpose of the system matrix. Hence, relaxation procedures are guaranteed to converge. This method is described in the first part of the paper.

In the second part, we investigate the problem of the shock movement caused by unsteady perturbations. In Weatherill's[1] and Traci's[2] work, the shock is not perturbed from the position calculated from the steady solution. For some problems, however, the shock motion is important and affects the whole flow field. To account for these effects, we derive, from a perturbation expansion for the shock-jump conditions, an equation representing the shock movement. The appropriate jumps at the unperturbed (steady) shock position are obtained by an analytical continuation of upstream and downstream conditions. To account for the shock movement, we impose the appropriate jumps on the perturbation potential with a shock-fitting procedure.

For steady perturbations calculated by an integral equation method, Nixon[3] has reported an alternative approach using the method of strained coordinates. In this paper we adopt the same approach for small harmonic perturbations computed by finite-difference methods. In this approach, the coordinates are strained in such a way that the shock is always fixed at its steady-state position. The perturbation of the jump conditions (in the strained coordinates) yields the same equations as the weak solution of the (linear) perturbed equation; hence, no shock fitting is necessary. The perturbed equation, however, is more complicated because it has nonhomogeneous terms accounting for the shock movement. Also, the boundary condition for the perturbed potential is altered (the airfoil is distorted so that the shock location is unchanged by the perturbation).

Finally, we show that the strained-coordinate method is equivalent to the direct method of transferring the jump conditions to the steady-state shock location. A numerical example for a one-dimensional model flow is discussed.

BASIC GOVERNING EQUATIONS

The unsteady transonic small-disturbance equation can be written in the form

$$(\beta \phi_t + \alpha \phi_x)_t = (K\phi_x - \frac{1}{2} \phi_x^2)_x + (\phi_y)_y \qquad (1)$$

where the $\beta\phi_{tt}$ term is neglected for low frequencies. The jump conditions, admitted by the weak solution of Eq. (1), are

$$\beta\left(\frac{\partial X^D}{\partial t}\right)^2 - \alpha\left(\frac{\partial X^D}{\partial t}\right) = <k - \phi_x> + \left(\frac{\partial X^D}{\partial y}\right)^2 , \tag{2a}$$

$$[\![\phi]\!] = 0 , \tag{2b}$$

where $<\phi>$ and $[\![\phi]\!]$ denote the average and the jump of ϕ across the shock $X = X^D(y;t)$. To complete the formulation of the problem, we must include the tangency boundary condition, a far-field behavior, and a Kutta condition for lifting airfoils.

For small harmonic perturbations, we let

$$\phi = \phi^0(x,y) + \varepsilon\mathrm{Re}\left[e^{i\omega t}\phi^1(x,y)\right] + \cdots , \tag{3}$$

where the oscillating airfoil has the following boundary condition:

$$\phi_y(x,0) = f_0'(x) + \varepsilon\mathrm{Re}\left[e^{i\omega t}f_1'(x)\right] . \tag{4}$$

The zeroth-order problem is given by

$$(K - \phi_x^0)\phi_{xx}^0 + \phi_{yy}^0 = 0 , \tag{5a}$$

$$\phi_y^0(x,0) = f_0'(x) , \tag{5b}$$

and the first-order problem (where the β term is neglected) is given by

$$(K - \phi_x^0)\phi_{xx}^1 + \phi_{yy}^1 - \phi_{xx}^0\phi_x^1 = \alpha i\omega\phi_x^1 \tag{6a}$$

$$\phi_y^1(x,0) = f_1'(x) . \tag{6b}$$

The boundary conditions (5b) and (6b) are applied in the airfoil mean surface. Note that Eq. (6.1) is linear with discontinuous coefficients. Its solution admits jumps only at that place where the steady shocks occur. We discuss this problem in part II.

In part I we discuss the convergence of the line-relaxation procedure applied to the algebraic system of equations that result from the finite-difference approximation of Eq. (6).

Part I: CONVERGENCE OF RELAXATION PROCEDURES USED FOR THE TRANSONIC SMALL HARMONIC PERTURBATION EQUATION

Convergence Analysis

Equation (6) gives the perturbation potential. Using type-dependent finite-difference schemes to solve Eq. (6), we obtain a system of algebraic equations in the following form:

$$A\phi = f , \tag{7}$$

where A is the system matrix, ϕ is a vector for the unknowns at the grid points, and f is a vector for the nonhomogeneous terms and the boundary conditions.

Equation (7) is solved by a line-relaxation procedure. Weatherill, et al.[1] observed the frequency-dependent limitation on the convergence of the relaxation method. In principle, relaxation procedures converge if and only if A is positive definite.* Since the eigenvalues of A are functions of ω, we must find a critical frequency, namely, the value of ω for which the smallest eigenvalue becomes zero. Above this value, relaxation procedures diverge. To solve Eq. (7) by a relaxation procedure that converges regardless of the value of ω, we must modify Eq. (7) so that the new system matrix is positive definite. Thus, we modify both sides of Eq. (7) by A^*, the conjugate transpose of A, to give

---

*For the case of interest here, A must have positive diagonal elements (submatrices).

$$A*A\phi = A*f$$

or
$$A_1\phi = f_1 \; , \qquad\qquad\qquad (8)$$

where
$$A_1 = A*A$$

$$f_1 = A*f \; .$$

A_1 is positive definite except when ω is the natural frequency, in which case A is singular. If $\underline{A \text{ is not singular}}$, Eqs. (7) and (8) are equivalent and have the same solution. Relaxation procedures will always converge for the new system, Eq. (8) (as long as the relaxation factor is positive and less than 2). The disadvantage of this remedy is that the bandwidth of $A*A$ is almost twice that of A, so the rate of convergence may be slow. In particular, if A is ill-conditioned, $A*A$ will be even more so. For high frequencies the grid size must be quite small, hence the number of equations is large, and the eigenvalues are close to each other. The smallest eigenvalue of $A*A$ will be very close to zero. In this case, shifting the eigenvalues from zero is useful. In the following, we compute a one-dimensional model of Eq. (6) by a relaxation procedure, as well as by direct inversion, for different values of ω.

Computational Example

The Helmholtz equation was suggested by Weatherill, et al.[1] for studying the divergence of relaxation solutions that he and his colleagues encountered when solving the unsteady transonic flow equation. The Helmholtz equation

$$\phi_{xx} + \phi_{yy} + \omega^2\phi = 0, \quad 0 < x < L_1$$

$$0 < y < L_2 \; ,$$

with ϕ given on the boundaries, is simpler than the original equation, but produces similar behavior when we attempt to solve it by relaxation. That is, for values of ω greater than a specific value ω_{cr}, line relaxation diverges. The one-dimensional analog to the Helmholtz equation produces the same behavior, yet it is easier to handle. We therefore consider the boundary value problem

$$\phi_{xx} + \omega^2\phi = 0, \qquad 0 < x < 1 \qquad\qquad (9a)$$

$$\phi(0) = \phi_L \; , \qquad\qquad\qquad (9b)$$

$$\phi(1) = \phi_R \; . \qquad\qquad\qquad (9c)$$

To solve the above problem numerically, we choose a set of J discrete points x_j with uniform spacing Δx in the interval of interest ($0 < x < 1$). We write the finite-difference approximation to equation (9a) at each of the points. Central-difference formulas are used to approximate the ϕ_{xx} term, and this approximation leads to the following system of algebraic equations, whose solutions approximate the solution of problem (9) at the set of discrete points x_j,

$$A\phi = f \; . \qquad\qquad\qquad (10)$$

Here, A is a tridiagonal matrix of order J,

$$A = \begin{bmatrix} 1 & -s & 1 \end{bmatrix} \; ,$$

$$S = 2 - \omega^2\Delta x^2 \; ,$$

$$f^T = \begin{bmatrix} -\phi_L & 0 & 0 \cdots 0 & -\phi_R \end{bmatrix} \; ,$$

where f^T denotes the transpose of f and where ϕ is the vector whose jth element ϕ_j approximates the solution of problem (9) at the point

$$x_j = j\Delta x \; .$$

The system of equations that result from multiplying Eq. (10) by $A*$ is

$$A\phi = A^2\phi = Af = f \; . \qquad\qquad\qquad (11)$$

When applying the Gauss-Seidel iterative method (point relaxation) to Eq. (11), we calculate the $n+1^{st}$ iteration with the relation

$$\phi_j^{n+1} = \phi_j^n + \Delta\phi_j^n , \qquad j = 1, 2, \cdots J ,$$

where

$$\Delta\phi_j^n = -\frac{\lambda}{a_j} (C_{j-2}\phi_{j-2}^{n+1} - 2SC_{j-1}\phi_{j-1}^{n+1} + a_j\phi_j^n$$

$$- 2SC_{j+1}\phi_{j+1}^n + C_{j+2}\phi_{j+2}^n - \hat{f}_j)$$

$$j = 1, 2, \cdots J .$$

Here, λ is the relaxation factor,

$$a_j = \begin{cases} S^2 + 2 , & 2 \le j \le J-1 \\ S^2 + 1 , & j = 1 , J \end{cases}$$

$$C_j = \begin{cases} 1 , & 1 \le j \le J \\ 0 , & j < 1 , j > J \end{cases}$$

$$\hat{f}^T = \begin{bmatrix} S\phi_L & -\phi_L & 0 & 0 & \cdots & 0 & -\phi_R & S\phi_R \end{bmatrix} .$$

By numerical examples we demonstrated that relaxation, when applied to Eq. (11), converges for those values of ω that cause it to fail when applied to Eq. (10). In each case we calculated the direct solution of Eqs. (10) and (11). As expected, they were identical. We also obtained the exact solution of Eqs. (9), and, by comparing it to the solution of Eqs. (10) or (11), we were able to determine the truncation error effect. We applied point relaxation with $\phi_L = \frac{1}{2}$, $\phi_R = 1$, and $J = 9$ to both systems (10) and (11). For a value of ω below π ($\omega = \pi/2$) , we found that both cases converge. For a value of ω greater than π ($\omega = 3\pi/2$) , we found that the iterative method converges when applied to system (11), but diverges when applied to system (10). Table I shows the results obtained for this case ($\omega = 3\pi/2$) . The first column of the table gives the value of x_j at which the solution is found. The second column shows the point relaxation (Gauss-Seidel) solution of Eq. (11) after a hundred iterations. The relaxation factor λ is equal to 1.65. The third column of table I gives the solution of both systems (10) and (11) obtained by Gauss elimination, and the last column gives the exact solution of the boundary-value problem (9). The difference between the values of the last two columns is attributable to the truncation error; i.e., it is attributable to approximating the differential equation by a set of algebraic equations. As the value of ω decreases, the truncation error decreases, and the rate of convergence increases. For $\omega = \pi/2$ and $J = 5$, the difference between the exact solution and the solution of the approximating matrix equation is less than 0.5%. Moreover, after 100 iterations, the error $\Delta\phi_j^n$ was 10^{-7} when equation (11) was solved by relaxation methods and was 10^{-15} when equation (10) was solved by relaxation methods.

		Table I	
x_j	Relaxation	ϕ_j Direct Inversion	Exact
0.0	0.5000	0.5000	0.5000
0.1	-0.0025	-0.0036	-0.0084
0.2	-0.5195	-0.5065	-0.5151
0.3	-0.9428	-0.8969	-0.9094
0.4	-1.1776	-1.0881	-1.1055
0.5	-1.1667	-1.0377	-1.0606
0.6	-0.9067	-0.7568	-0.7845
0.7	-0.4518	-0.3078	-0.3374
0.8	0.0980	0.2094	0.1832
0.9	0.6204	0.6802	0.6640
1.0	1.0000	1.0000	1.0000

Part II: SHOCK MOVEMENT CAUSED BY UNSTEADY PERTURBATION

Equation For Shock Movement

The problem can be examined in two different ways. First, we perturb the shock and

transfer the perturbed jump conditions to the old position (the steady state). These transferred conditions are imposed on the perturbation potential.

In the second approach, following Nixon,[3] the method of strained coordinates is used. The coordinates are strained so that the shock is always fixed at its steady-state location (in the strained coordinates). The differential equation governing the perturbation potential, in the strained coordinates, contains nonhomogeneous terms that account for the shock movement. Also, the boundary condition is distorted.

Following Cheng and Hafez*,[4] the shock is perturbed in the same way the flow field is perturbed; namely, let

$$X^D(y;t) = X^O(y) + \varepsilon \text{Re}\left[e^{i\omega t}X^1(y)\right] + \cdots .$$ (12)

The jump conditions (eqs. 2a and 2b) are given in terms of the averages and the jumps across the unknown perturbed shock $X^D(y;t)$. The appropriate jumps at the unperturbed shock $X^O(y)$ may be obtained by analytical continuation of upstream and downstream conditions. For example, consider the jump in a quantity u at X^D, namely $[\![u]\!]_{X^D}$. Up to first order, this jump can be expressed in terms of $[\![u]\!]_{X^O}$, $[\![u_x]\!]_{X^O}$ and X^1, as shown in figure 1.
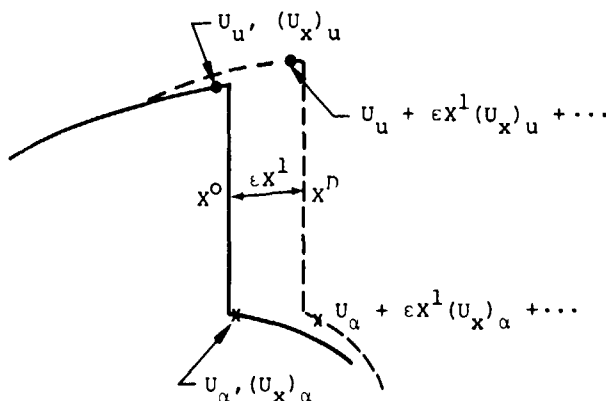
Figure 1   Perturbation of a Discontinuous Function

We can write

$$[\![u]\!]_{X^D} = U_\alpha + \varepsilon X^1(U_x)_\alpha + \cdots - \left[U_u + \varepsilon X^1(U_x)_u + \cdots\right]$$

$$= (U_\alpha - U_u) + \varepsilon X^1\left[(U_x)_\alpha - (U_x)_u\right] + \cdots$$

$$= [\![U]\!]_{X^O} + \varepsilon X^1 [\![U_x]\!]_{X^O} + \cdots ;$$

similarly

$$<u>_{X^D} = <u>_{X^O} + \varepsilon X^1 <U_x>_{X^O} + \cdots .$$

Now, consider condition (2a) expanded in terms of ε :

$$[\![\phi^O + \varepsilon\phi^1 + \cdots]\!]_{X^D} = [\![\phi^O + \varepsilon\phi^1 + \cdots]\!]_{X^O}$$

$$+ \varepsilon X^1[\![\phi_x^O + \varepsilon\phi_x^1 + \cdots]\!]_{X^O} + \cdots = 0 .$$ (13)

The zeroth and first-order relations are given by,

$$\text{for } \varepsilon^O, \quad [\![\phi^O]\!]_{X^O} = 0 ,$$ (14)

$$\text{for } \varepsilon^1, \quad [\![\phi^1]\!]_{X^O} = -X^1[\![\phi_x^O]\!]_{X^O} .$$ (15)

Similarly, condition (2a) gives,

$$\text{for } \epsilon^0, \quad \langle K - \phi_x^0 \rangle_{X^0} = -\left(\frac{\partial X^0}{\partial y}\right)^2 , \tag{16}$$

$$\text{for } \epsilon^1, \quad i\omega\alpha X^1 = \left\langle \phi_x^1 + X^1 \phi_{xx}^0 \right\rangle_{X^0} - 2\frac{\partial X^0}{\partial y}\frac{\partial X^1}{\partial y} . \tag{17}$$

Equation (17) is an ordinary differential equation in X^1 . Together with Eq. (15), it imposes the proper jump conditions on ϕ^1 . A shock-fitting procedure is necessary since the weak solution of the (linear) perturbed system (6) admits discontinuities other than the conditions that result from perturbing the jumps admitted by the fully nonlinear system (1).

Simplification For Normal Shock

For a locally normal shock, the term $\dfrac{dX^0}{dy}\dfrac{dX^1}{dy}$ in Eq. (17) is neglected; hence,

$$i\omega\alpha X^1 = \left\langle \phi_x^1 + X^1 \phi_{xx}^0 \right\rangle_{X^0} . \tag{18}$$

Eliminating X^1 between (15) and (18), we have

$$\left\langle \phi_x^1 \right\rangle_{X^0} [\![\phi_x^0]\!]_{X^0} + \left\langle i\omega\alpha - \phi_{xx}^0 \right\rangle_{X^0} [\![\phi^1]\!]_{X^0} = 0 . \tag{19}$$

Equation (19) is the jump condition to be imposed on ϕ^1 . After ϕ^1 is calculated, we can evaluate X^1 from Eq. (18) or (15).

A Shock-Fitting Procedure For the ϕ^1 Problem

First, we solve the steady problem ϕ^0 , using, for example, Murman's fully conservative schemes. From the ϕ^0 solution, we let $[\![\phi_x^0]\!]_{X^0} = a$ and $\langle i\omega\alpha - \phi_{xx}^0 \rangle_{X^0} = b$, where X^0 is considered part of the ϕ^0 solution. The first point downstream of the shock X^0 is identified by S.P., as shown in figure 2.
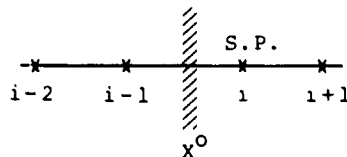

Figure 2   Shock Points and Shock Location

At this point, we replace the finite-difference equation for ϕ^1 by the following relation:

$$\frac{a}{2}\left(\frac{\phi_{i+1}^1 - \phi_i^1}{\Delta x} + \frac{\phi_{i-1}^1 - \phi_{i-2}^1}{\Delta x}\right) + b(\phi_i^1 - \phi_{i-1}^1) = 0 . \tag{20}$$

Eq. (20) is a first-order approximation of Eq. (19).

The shock is treated as an internal boundary with a boundary condition in the form of

$$a_1 \phi^+ + b_1 \phi_x^+ = c_1 ,$$

where a_1 , b_1 , and c_1 are constants, (+) denotes the conditions just downstream of the shock, and c_1 contains the conditions on the upstream side of the shock.

Computational Example

Considering the one-dimensional form of Eq. (1), neglecting the $\beta\phi_{tt}$ term, and setting $\alpha = 2$, we obtain the equation

$$2\phi_{xt} = (K - \phi_x)\phi_{xx} , \quad X_L < x < X_R . \tag{21a}$$

We are interested in solving the problem with the following boundary conditions:

$$\left. \begin{array}{l} \phi(X_L,t) = 0 \ , \ \phi_x(X_L,t) = 3 \\[2mm] \phi(X_R,t) = \epsilon \cos \omega t \end{array} \right\} \tag{21b}$$

We let

$$\phi = \phi^O + \epsilon \hat{\phi} = \phi^O + \epsilon \mathrm{Re} \left\{ e^{i\omega t} \phi^1 \right\} + \cdots \ ,$$

where Re denotes the real part of $e^{i\omega t}\phi^1$. The governing equation, boundary conditions, and shock-jump condition for ϕ^O are respectively given by

$$(K - \phi_x^O)\phi_{xx}^O = 0 \ , \quad X_L < x < X_R \tag{22a}$$

$$\left. \begin{array}{l} \phi^O(X_L) = \phi_L^O = 0 \ , \quad \phi_x^O(X_L) = \psi_L^O = 3 \\[3mm] \phi^O(X_R) = \phi_R^O = 0 \ , \end{array} \right\} \tag{22b}$$

$$\phi_x^{O-} + \phi_x^{O+} = 2K \ , \tag{22c}$$

where $(-)$ and $(+)$ denote conditions just upstream and downstream of the shock, respectively.

For the purpose of our example, we choose

$$K = 1$$

$$X_L = -\frac{1}{3} \ , \quad X_R = 1 \ .$$

Then, the solution for problem (22) is

$$\phi^O = \left\{ \begin{array}{ll} 3(x + \frac{1}{3}) \ , & -\frac{1}{3} < x < 0 \\[4mm] 1 - x \ , & 0 < x < 1 \end{array} \right.$$

The equation, boundary conditions, and shock-jump conditions governing ϕ^1 are given respectively by (noting that $\phi_{xx}^O = 0$ for the present problem)

$$(K - \phi_x^O)\phi_{xx}^1 - 2i\omega\phi_x^1 = 0 \ , \tag{23a}$$

$$\left. \begin{array}{l} \phi^1(X_L) \equiv \phi_L^1 = 0 \ , \ \phi_x^1(X_L) = \psi_L^1 = 0 \\[3mm] \phi^1(X_R) \equiv \phi_R^1 = 1 \end{array} \right\} \tag{23b}$$

$$\phi_x^{1+} - i\omega\phi^{1+} = -\phi_x^{1-} - i\omega\phi^{1-} \ . \tag{23c}$$

Eq. (23c) is the application of Eq. (18) to the present example.

We are interested in solving problem (23) numerically, in particular, by point relaxation. The shock whose steady-state position X^O has been determined from the solution of system (22) to be $X^O = 0$ divides our region of interest $(-1/3,1)$ into two intervals. To approximate problem (23) by a set of algebraic equations, we choose a set of J' discrete points with a uniform spacing $\Delta x'$ in the interval $-1/3 < x < 0$ and a similar set of J points with uniform spacing Δx in the interval $0 \leq x < 1$ such that, in the first interval,

$$x_j = -\frac{1}{3} + j\Delta x' \ , \quad j = 1,2,\cdots J' \ ,$$

and, in the second interval,

$$x_J = (J - 1)\Delta x , \quad J = 1, 2, \cdots J .$$

We write, for each point x_j in the supersonic region, the finite-difference approximation of Eq. (23a). In this case the derivatives are approximated by backward difference formulas so that

$$\phi_1^1 = \phi_L^1 + \Delta x' p' \psi_L' ,$$

$$\phi_2^1 = \frac{1}{p'^*}(-p' \phi_L^1 + 2\phi_1^1) ,$$

$$\phi_j^1 = \frac{1}{p'^*}(-p' \phi_{j-2}^1 + 2\phi_{j-1}^1) , \quad j = 3, 4, \cdots J' ,$$

where ϕ_j^1 is the solution approximating the value of $\phi(x_j)$,

$$p' = 1 + i \frac{\omega \Delta x'}{K - \phi_x^o} ,$$

and p'^* is the complex conjugate of p' . Since we are using backward difference formulas in the supersonic region, we obtain the solution by marching toward the right in one sweep, with no iteration required. After finding the solution in the supersonic region, which is zero in our particular example, we can consider the following boundary-value problem in the subsonic region:

$$(K - \phi_x^o)\phi_{xx}^1 - 2i\omega\phi_x^1 = 0 , \quad 0 < x < 1 , \tag{24a}$$

$$\left.\begin{array}{l} \phi_x^1(0) - i\omega\phi^1(0) = \gamma \\[2ex] \phi^1(1) = \phi_R^1 \end{array}\right\} , \tag{24b}$$

where the value of γ may be obtained from the solution of the supersonic region

$$\gamma = - \frac{\phi_{J'}^1 - \phi_{J'-1}^1}{\Delta x'} - i\omega\phi_{J'}^1 .$$

Now, using central difference formulas at each of the points x_j in the subsonic region approximating the differential equation (24a), we obtain the following set of algebraic equations:

$$B\phi = g , \tag{25}$$

where B is a tridiagonal matrix of order J ,

$$B = \begin{bmatrix} p & \alpha_j & p^* \end{bmatrix} ,$$

$$p = 1 + i \frac{\omega \Delta x}{K - \phi_x^o} ,$$

$$\alpha_j = \begin{cases} -2\beta \equiv -2(1 + ip\omega\Delta x) & j = 1 \\[1ex] -2 , & j \neq 1 \end{cases} ,$$

$$g^T = \begin{bmatrix} 2p\gamma\Delta x & 0 & 0\cdots & 0 & -p^*\phi_R^1 \end{bmatrix} ,$$

ϕ is the vector whose j^{th} element ϕ_j approximates the solution of problem (24) at the point $x_j = (j-1)\Delta x$. The system of equations that result from multiplying Eq. (25) by B^* is

$$\hat{B}\phi = B^*B\phi = B^*g \equiv \hat{g} . \tag{26}$$

When applying the Gauss-Seidel iterative method (point relaxation) to Eq. (26), we calculate the n+1st iteration with the relation

$$\phi_j^{n+1} = \phi_j^n + \Delta\phi_j^n , \qquad j = 1, 2, \cdots , J ,$$

where

$$\Delta\phi_j^n = - \frac{\lambda}{a_j} \left[p^2 d_{j-2}\phi_{j-2}^{n+1} + b_{j-1}\phi_{j-1}^{n+1} + a_j\phi_j^n \right.$$

$$\left. + c_{j+1}\phi_{j+1}^n + p*^2 d_{j+2}\phi_{j+2}^n - \hat{g}_j \right] , \quad j = 1, 2, \cdots , J$$

and where

$$a_j = \begin{cases} 4\beta\beta* + pp* , & j = 1 \\ 8 + pp* , & j = 2 \\ 2(2 + pp*) , & 3 \le j \le J-1 \\ 4 + pp* , & j = J \end{cases} ,$$

$$b_j = \begin{cases} 0 , & j = -1 \\ -2(2\beta+p) , & j = 1 \\ -4p , & j \ge 2 \end{cases} ,$$

$$c_j = \begin{cases} -2(2\beta* + p*) , & j = 2 \\ -4p* , & 3 \le j \le J , \\ 0 , & j = J+1 \end{cases}$$

$$d_j = \begin{cases} 1 , & 1 < j < J \\ 0 , & j < 1 , j > J \end{cases} ,$$

$$\hat{g}^T = \left[-4\beta*p\gamma\Delta x, \ 4p\gamma\Delta x, \ 0 , \ 0 , \ \cdots , \ 0 , \ -p*^2\phi_R^1 , \ 2p*\phi_R^1 \right] .$$

We tested the iterative solutions of Eqs. (25) and (26). For $\omega = \pi/2$ and $J = 4$, point relaxation converged when applied to either of the equations. The difference between the exact solution and the solution of the approximating matrix equation was less than 10%. After 100 iterations, the error $\Delta\phi_j^n$ was 10^{-14} when we used Eq. (25), and it was 10^{-6} when we used Eq. (26). For $\omega = 3\pi/2$ and $5\pi/2$, and $J = 10$, we found that the iterative process converges when applied to (26), but it diverges when applied to (25). Tables II and III respectively show the results obtained for $\omega = 3\pi/2$ and $\omega = 5\pi/2$. The first column in these tables is the value of x_j at which a solution is obtained. The second column includes the iterative solution of the real part of ϕ to Eq. (26) after 700 iterations, with a relaxation factor of 1.85 for table II and 1.8 for table III. The third column is the real part of the solution to equations (25) and (26), which is obtained by Gauss elimination. The fourth column is the real part of the exact solution to problem (24). The last three columns are the imaginary part of the iterative, direct, and exact solutions, respectively.

Using Eq. (15), we obtain the following expression for the shock displacement:

$$X^1 = \frac{1}{4} [\![\phi^1]\!]$$

for $\omega = 3\pi/2$, $X^D = -\epsilon \frac{1}{4} \sin \omega t$,

for $\omega = 5\pi/2$, $X^D = \epsilon \frac{1}{4} \sin \omega t$.

Table II

	Re(ϕ)			Im(ϕ)		
x_j	Iterative Solution	Direct Solution	Exact Solution	Iterative Solution	Direct Solution	Exact Solution
0.0	0.0392	-0.1282	0.0000	1.0703	0.9331	1.0000
0.1	-0.4684	-0.5537	-0.4539	0.9704	0.7691	0.8910
0.2	-0.8717	-0.8612	-0.8090	0.6568	0.4323	0.5877
0.3	-1.0855	-0.9860	-0.9876	0.1998	-0.0062	0.1564
0.4	-1.0661	-0.9019	-0.9510	-0.2992	-0.4544	-0.3090
0.5	-0.8203	-0.6265	-0.7071	-0.7300	-0.8179	-0.7071
0.6	-0.4045	-0.2178	-0.3090	-0.9979	-1.0202	-0.9510
0.7	0.0881	0.2381	0.1564	-1.0442	-1.0188	-0.9876
0.8	0.5487	0.6455	0.5877	-0.8592	-0.8139	-0.8070
0.9	0.8762	0.9186	0.8910	-0.4839	-0.4487	-0.4539
1.0	1.0000	1.0000	1.0000	0.0000	0.0000	0.0000

Table III

	Re(ϕ)			Im(ϕ)		
x_j	Iterative Solution	Direct Solution	Exact Solution	Iterative Solution	Direct Solution	Exact Solution
0.0	0.2525	0.2144	0.0000	-0.9485	-0.8768	-1.0000
0.1	0.9191	0.8369	0.7071	-0.4568	-0.4379	-0.7071
0.2	1.0723	0.9945	1.0000	0.3593	0.3072	0.0000
0.3	0.6293	0.6028	0.7071	1.0640	0.9605	0.7071
0.4	-0.1741	-0.1286	0.0000	1.2828	1.1727	1.0000
0.5	-0.9118	-0.8091	-0.7071	0.9021	0.8304	0.7071
0.6	-1.1956	-1.0747	-1.0000	0.1278	0.1166	0.0000
0.7	-0.8815	-0.7837	-0.7071	-0.6267	-0.5872	-0.7071
0.8	-0.1442	-0.0915	0.0000	-0.9623	-0.9050	-1.0000
0.9	0.6182	0.6319	0.7071	-0.7059	-0.6668	-0.7071
1.0	1.0000	1.0000	1.0000	0.0000	0.0000	0.0000

An Alternative Approach Using the Method of Strained Coordinates

Instead of Eq. (3), we use an exapansion of ϕ in strained coordinates (s,τ) as follows:

Let
$$\phi(x,y;\tau) = \phi_0(s,y) + \epsilon \text{Re}\left\{ e^{i\omega\tau}\phi_1(s,y)\right\} + \cdots , \tag{27}$$

$$x = s + \epsilon \text{Re}\left\{ e^{i\omega\tau}X_1(s)\right\} + \cdots , \tag{28}$$

$$t = \tau . \tag{29}$$

In particular, the shock location in the physical plane X^D is related to the shock location in the strained coordinates by the following relation:

$$X^D = S^D + \epsilon \text{Re}\left\{ e^{i\omega\tau}X_1(S^D)\right\} + \cdots . \tag{30}$$

That is, $X_1(S^D)$ is the shock movement.

The transformation derivatives are given by

$$\frac{\partial}{\partial x} = (1 - \epsilon e^{i\omega\tau}X_{1s} + \cdots)\frac{\partial}{\partial s} , \tag{31}$$

$$\frac{\partial}{\partial t} = \frac{\partial}{\partial \tau} - (\epsilon i \omega e^{i\omega\tau} X_1 + \cdots)\frac{\partial}{\partial s} . \tag{32}$$

Using (27) and (28) in Eq. (1) (with $K = 1$, $\alpha = 2$ and neglecting the β term) yields

$$(1 - \phi_{os})\phi_{oss} + \phi_{oyy} = 0 , \tag{33}$$

and

$$\phi_{1ss} + \phi_{1yy} = (\phi_{os}\phi_{1s})_s + 2i\omega(\phi_1 - X_1\phi_{os})_s$$

$$+ \left[X_{1s}(\phi_{os} - \phi_{os}^2)\right]_s + X_{1s}(\phi_{os}^2 - \tfrac{1}{2}\phi_{os}^2)_s , \tag{34}$$

while using (27) and (28) in Eqs. (2a) and (2b) yields

$$\langle\phi_{os}\rangle = 1 , \qquad [\![\phi_o]\!] = 0 , \tag{35}$$

and

$$\langle\phi_{1s}\rangle = X_{1s}(S^D) + 2i\omega X_1(S^D) , \qquad [\![\phi_1]\!] = 0 . \tag{36}$$

Note that Eqs. (35) and (36) are the jump conditions admitted by the weak solutions of Eqs. (33) and (34), respectively. The boundary conditions in the physical plane are transformed to

$$\phi_{oy}(s_1 o) = W_o(s) \quad \text{on the airfoil, and} \tag{37}$$

$$\phi_{1y}(s_1 o) = W_1(s) + X_1(s)W_{os}(s) \quad \text{on the airfoil} . \tag{38}$$

Equations (33), (35), and (37) determine the steady state, while Eqs. (34), (36), and (38) determine the perturbation potential in the strained coordinates.

Conservative Difference Equations For an Alternative Approach

For the steady-state problem, centered differences are used in the subsonic region, backward differences in the supersonic region, a parabolic-point operator at the sonic line (to exclude expansion shock), and a shock-point operator at the shock point to impose the right jump condition (conservation of mass).

For the perturbation potential, a parabolic-point operator and a shock-point operator are needed. Also, $X_1(S_o)$ is unknown.

We first consider the parabolic-point operator. In (x,y,t) coordinates, $\phi_x = 1$ at the sonic line. To guarantee finite acceleration ϕ_{xx} at the sonic line, Eq. (1) reduces to

$$\phi_{yy} = 2\phi_{xt} . \tag{39}$$

Parabolic-point operators in (s,y,τ) coordinates are given by

$$\phi_{oyy} = 0 , \tag{40}$$

$$\phi_{1yy} = 2i\omega(\phi_{1s} - X_{1s}\phi_{os}) . \tag{41}$$

In Eqs. (40) and (41) centered differences are used everywhere.

Equation (34) at $(\phi_{os} = 1)$ reads

$$(1 - \phi_{os})\phi_{1ss} = \phi_{oss}\left[\phi_{1s} - (X_{1s} - 2i\omega X_1)\right] . \tag{42}$$

To keep ϕ_{1ss} finite at the $(\phi_{os} = 1)$, we must satisfy the following condition:

$$\phi_{1s} = X_{1s} + 2i\omega X_1 , \quad \text{at } \phi_{os} = 1 . \tag{43}$$

Equation (43) is used to determine the shock movement Δ (assuming, for example,

$$X_1(s) = \Delta S(1 - S)/S^D(1 - S^D)$$

as in Nixon's[3] work). Note that Eq. (43) is consistent with Eq. (36) when the shock strength vanishes.

We next consider the shock-point operator. Equation (34) is written in a conservative form. A fully conservative scheme that admits the appropriate jumps (Eq. 36) is written as follows:

$$\text{(Shock-Point Operation)}_i = \text{(Elliptic Operator)}_i + \text{(Hyperbolic Operator)}_i . \qquad (44)$$

The y terms are central differenced.

After algebraic manipulation, Eq. (44) reduces to (neglecting y terms for a locally normal shock)

$$\frac{U^+ + U^-}{2} = X_{1s}(S^D) + 2i\omega X_1(S^D) , \qquad (45)$$

where

$$U^+ = \frac{\phi_{1,i+1} - \phi_{1,i}}{\Delta X} ,$$

$$U^- = \frac{\phi_{1,i-1} - \phi_{1,i-2}}{\Delta X} .$$

Equation (45) is a first-order approximation of jump condition (36).

EQUIVALENCE OF THE TWO METHODS

Finally, we want to show that these results are consistent with the previous approach and that the two approaches are equivalent. We substitute Eq. (28) into Eq. (3), together with a Taylor series expansion for ϕ^O around the point x,y, and collect terms of equal orders. The result is

$$\phi(x,y,t) = \phi^O(s,y) + \epsilon Re e^{i\omega t}\left[\phi^1(s,y) + X_1(s)\phi_s^O(s,y)\right] + \cdots . \qquad (46)$$

Comparing Eqs. (46) and (27), we find

$$\phi^O(s,y) = \phi_O(s,y) ,$$

$$\phi^1(s,y) + X_1(s)\phi_s^O(s,y) = \phi_1(s,y) . \qquad (47)$$

The equation for $\phi^1(s,y)$ reads

$$\phi_{ss}^1 + \phi_{yy}^1 = (\phi_s^O\phi_s^1)_s , \qquad (48)$$

with the boundary condition

$$\phi_y^1(s,0) = W_1(s) \qquad (49)$$

on the airfoil and the shock-jump conditions

$$[\![\phi^1]\!] = -X_1(S^D) [\![\phi_s^O]\!] , \qquad (50)$$

$$\langle\phi_s^1\rangle + X_1(S^D) \langle\phi_{ss}^O\rangle = 2i\omega X_1(S^D) . \qquad (51)$$

Equations (48), (49), (50), and (51) were used before with a shock-fitting procedure to determine ϕ^1. Hence, the two systems are equivalent.

CONCLUSIONS

We have considered two problems that are important in the calculation of unsteady transonic flow for flutter prediction. For the first problem, we have proposed an iterative method for solving the unsteady perturbation potential equation; this method converges for frequencies beyond a previously encountered critical frequency. We have tested this method on a one-dimensional problem and found that it worked. The rate of convergence, however, is quite slow.

For the second problem, we have derived an expression for the perturbed shock position for unsteady transonic calculations like those of Weatherill, et al.,[1] and Traci, et al.[2]. This result provides us with a consistent method for predicting the shock motion of small unsteady harmonic purturbations. A simple one-dimensional example has been calculated.

REFERENCES

1. Weatherill, W. H., Ehlers, F. E., and Sebastian, J. H. (1975) "Computation of the Transonic Perturbation Flow Fields Around Two- and Three-Dimensional Oscillating Wings," NASA CR-2599.

2. Traci, R. M., Abano, E. D., and Farr, J. L., Jr. (1975) "Perturbation Method For Transonic Flows About Oscillating Airfoils," AIAA Paper No. 75-877.

3. Nixon, D. (1977) "Perturbation of a Discontinuous Transonic Flow," AIAA Paper No. 77-206.

4. Cheng, H. K. and Hafez, M. M. (1973) "Equivalence Rule and Transonic Flows Involving Lift," AIAA Paper No. 73-88.

REPORT DOCUMENTATION PAGE

1. Recipient's Reference	2. Originator's Reference	3. Further Reference	4. Security Classification of Document
	AGARD-CP-226	ISBN 92-835-0197-7	UNCLASSIFIED

5. Originator	Advisory Group for Aerospace Research and Development North Atlantic Treaty Organization 7 rue Ancelle, 92200 Neuilly sur Seine, France

6. Title
UNSTEADY AIRLOADS IN SEPARATED AND TRANSONIC FLOW

7. Presented at	the 44th Meeting of the AGARD Structures and Materials Panel held in Lisbon, Portugal on 19–20 April 1977.

8. Author(s)	9. Date
Various	July 1977

10. Author's Address	11. Pages
Various	286

12. Distribution Statement	This document is distributed in accordance with AGARD policies and regulations, which are outlined on the Outside Back Covers of all AGARD publications.

13. Keywords/Descriptors		
Aerodynamic loads	Flight maneuvers	Military aircraft
Boundary layer separation	Aerodynamic stability	Predictions
Transonic flow	Unsteady flow	Loads (forces)

14. Abstract

The first session reviewed the prediction and description of the separated flow environment and the essential effects of airframe response on individual aircraft components. These effects may lead to failures of primary or secondary structures when exceeding design stress limits, or design fatigue loads. This is a special concern for military aircraft where flight operation at extreme manoeuvre conditions associated with flow separation frequently occurs. The scope of study included analytical approaches, windtunnel tests, as well as flight test techniques and data evaluation.

The second session dealt with flutter, aeroservoelastic instabilities involving coupling with active control systems, and other static and dynamic aeroelastic problems, which can be dangerous flight safety phenomena and which must therefore be predicted with accuracy and prevented. Margins of safety are least in the transonic speed range which is consequently the most critical speed regime. However, no dependable theoretical methods are yet available for predicting unsteady transonic airloads on lifting surfaces and control surfaces. Accurate prediction of the latter becomes more important for active control systems used in load alleviation. In addition to improving analytical confidence, a dependable approach could reduce the cost of aeroelastic model and flight flutter tests.

AGARD Conference Proceedings No. 226 Advisory Group for Aerospace Research and Development, NATO. UNSTEADY AIRLOADS IN SEPARATED AND TRANSONIC FLOW Published July 1977 286 pages The first session reviewed the prediction and description of the separated flow environment and the essential effects of airframe response on individual aircraft components. These effects may lead to failures of primary or secondary structures when exceeding design stress limits, or design fatigue loads. This is a special concern for military aircraft where flight operation at extreme manoeuvre conditions associated with flow P.T.O.	AGARD-CP-226 Aerodynamic loads Boundary layer separation Transonic flow Flight maneuvers Aerodynamic stability Unsteady flow Military aircraft Predictions Loads (forces)
AGARD Conference Proceedings No. 226 Advisory Group for Aerospace Research and Development, NATO. UNSTEADY AIRLOADS IN SEPARATED AND TRANSONIC FLOW Published July 1977 286 pages The first session reviewed the prediction and description of the separated flow environment and the essential effects of airframe response on individual aircraft components. These effects may lead to failures of primary or secondary structures when exceeding design stress limits, or design fatigue loads. This is a special concern for military aircraft where flight operation at extreme manoeuvre conditions associated with flow P.T.O.	AGARD-CP-226 Aerodynamic loads Boundary layer separation Transonic flow Flight maneuvers Aerodynamic stability Unsteady flow Military aircraft Predictions Loads (forces)
AGARD Conference Proceedings No. 226 Advisory Group for Aerospace Research and Development, NATO. UNSTEADY AIRLOADS IN SEPARATED AND TRANSONIC FLOW Published July 1977 286 pages The first session reviewed the prediction and description of the separated flow environment and the essential effects of airframe response on individual aircraft components. These effects may lead to failures of primary or secondary structures when exceeding design stress limits, or design fatigue loads. This is a special concern for military aircraft where flight operation at extreme manoeuvre conditions associated with flow P.T.O.	AGARD-CP-226 Aerodynamic loads Boundary layer separation Transonic flow Flight maneuvers Aerodynamic stability Unsteady flow Military aircraft Prediction Loads (forces)
AGARD Conference Proceedings No. 226 Advisory Group for Aerospace Research and Development, NATO. UNSTEADY AIRLOADS IN SEPARATED AND TRANSONIC FLOW Published July 1977 286 pages The first session reviewed the prediction and description of the separated flow environment and the essential effects of airframe response on individual aircraft components. These effects may lead to failures of primary or secondary structures when exceeding design stress limits, or design fatigue loads. This is a special concern for military aircraft where flight operation at extreme manoeuvre conditions associated with flow P.T.O	AGARD-CP-226 Aerodynamic loads Boundary layer separation Transonic flow Flight maneuvers Aerodynamic stability Unsteady flow Military aircraft Prediction Loads (forces)

separation frequently occurs. The scope of study included analytical approaches, windtunnel tests, as well as flight test techniques and data evaluation.

The second session dealt with flutter, aeroservoelastic instabilities involving coupling with active control systems, and other static and dynamic aeroelastic problems, which can be dangerous flight safety phenomena and which must therefore be predicted with accuracy and prevented. Margins of safety are least in the transonic speed range which is consequently the most critical speed regime. However, no dependable theoretical methods are yet available for predicting unsteady transonic airloads on lifting surfaces and control surfaces. Accurate prediction of the latter becomes more important for active control systems used in load alleviation. In addition to improving analytical confidence, a dependable approach could reduce the cost of aeroelastic model and flight flutter tests.

Papers presented at the 44th Meeting of the AGARD Structures and Materials Panel held in Lisbon, Portugal on 19–20 April 1977,

---